A detailed study of the inner disks of FU Ori objects and the star-disk boundary

Thesis by
Adolfo Sjoberg de Carvalho

In Partial Fulfillment of the Requirements for the
Degree of
Doctor of Philosophy in Astrophysics

CALIFORNIA INSTITUTE OF TECHNOLOGY
Pasadena, California

2026
Defended August 14, 2025

Adolfo Sjoberg de Carvalho
ORCID: [0000-0002-9540-853X]

To Maria Esther Sjoberg Ferreira de Carvalho, or as I knew her, Mãe.

ACKNOWLEDGEMENTS

I would like to begin by thanking my thesis advisor, Lynne Hillenbrand, for her wise and patient guidance these past 5 years. She was always available for long meetings discussing new ideas, the importance of revisiting old ideas, and admiring the richness of high resolution spectra. I leave every meeting excited about my work and encouraged. I thank her for always holding me to the highest standard and I look forward to many future years of collaboration.

I am eternally grateful for all the wonderful friends I have made here at Caltech. Thank you to Ivey, Sam, and Tony for your friendship from our very first classes together, when we organized evening study sessions over Zoom so I would not be alone in my room in Texas the entirety of first year. Thanks to Jean for many fun conversations and teaching me to surf and to Nik for great nights at the Opera and LA Phil. Thanks to Dee for all the fun times at random rock concerts and to Jakob for always being such a positive presence. Thank you Ed for the innumerable great pub nights, soccer (football) matches, and for introducing me to The Last Dinner Party.

Thanks to Jerry Xuan, for being a fantastic roommate and a better friend. I enjoyed our three years living together – the board game nights, cheese boards, movie nights, and dinners we cooked together. I will miss those times.

Thank you to Dr. Evan Nunez-Cravin and Rataéja Sholes-Cravin for the Jazz nights, Smash Bros gaming sessions and pizza parties, and for always reminding me of the importance of kindness and love for others in all we do. Thanks to recent graduates, Sarah Blunt, Ryan Rubenzahl, Mia de los Reyes, Nitika Yadlapalli Yurk, Devon Cody, and Max Goldberg for welcoming me into the department, guiding me in my first couple of years, and our continued fun times and enduring friendship.

Thank you to my committee, Dimitri Mawet, Geoff Blake, Konstantin Batygin, and Phil Hopkins, for the enlightening and educational conversations we have had. Thank you to Greg Doppmann for your mentorship during my time at Keck and since. I enjoyed sharing an office with you and I thank you for showing me the ropes on NIRSPEC my first times using it and for your help on the data reduction pipeline development. Finally, I thank you for your friendship then and now. My stay on the Big Island gave me some of the best times of my life.

To my partner, Jessie Miller, thank you for your companionship, love, and support.

Thank you, finally, to my family. Henrique, for always being an amazing brother and a constant supporter of everything I've done. Thank you, Dad, for everything you have done to prepare me for the challenges of graduate school and academia, and the immense sacrifices you have made for us. Thank you, Silvia, for joining our family and helping to raise Henrique and me.

Agradeço também à minha família no Brasil: especialmente minha tia Selma, minha prima Thais e meu tio Reynaldo. Obrigado pelo seu carinho e apoio. Amo vocês e sempre sinto sua falta.

ABSTRACT

FUOrs are young stellar objects (YSOs) whose disks undergo an instability that raises the disk-to-star accretion rate by a factor of 1,000 to 10,000, and sustain this elevated accretion rate for up to 100s of years. The outbursts may be a phase through which all young low-mass stars pass in the early stages of their formation and could have played a role in the thermal processing of material in the Solar System. In this thesis, I present a thorough and comprehensive study of the inner disks of FUOrs and the properties of the accreting stars themselves.

In Chapter I, I contextualize FUOr accretion disks in the timeline of pre-main sequence stellar evolution and discuss some of the major open questions in the study of FUOrs today. I address the mechanisms proposed to trigger FUOr outbursts and how the work in this thesis, as well as future observations, can constrain existing models for each trigger mechanism.

In Chapter II, I introduce the disk modeling infrastructure that I use to study FUOrs and to constrain physical parameters like their masses and mass accretion rates. I include a tutorial of how different parameters in the accretion disk model impact the spectral energy distributions (SEDs) and high resolution spectra. Finally, I give a recommendation for a consistent approach to estimating and interpreting the luminosities of FUOrs and enumerate some important caveats to consider when using the accretion disk model in this Thesis.

In Chapters III-VI, I rigorously test the accuracy of the accretion disk model with SEDs, and high and low resolution spectra, spanning visible to NIR wavelengths. The focus of Chapters III and IV is the photometric and spectroscopic evolution of V960 Mon following the first 3 years after the peak of its outburst. Disk model fitting indicates that the inner radius of the disk expanded as the post-peak accretion rate decreased. The rate of expansion of the inner radius is consistent with the magnetosphere re-establishing itself as the accretion flow weakens. Chapter V follows the evolution of HBC 722 in the first 10 years of its outburst. In this source, the size of the accretion-dominated inner disk grows over a 5 year period, indicating that the instability driving the outburst can ignite a larger region of the disk than where it began. In Chapter VI, I apply the disk model to V883 Ori, a FUOr with a rich molecular millimeter emission spectrum, to measure physical properties of its inner disk. I find that the visible light from the source is unexpectedly bright for its

NIR-derived extinction value, but that the discrepancy can be explained by material near the source scattering light toward the observer along a less-extincted line of sight.

In Chapter VII, I compute bolometric corrections for measuring the accretion luminosity of a FUOr from a single photometric observation. The bolometric corrections are tabulated for a broad range of accretion luminosities using the filters of 6 photometric surveys/observatories: ZTF, Gaia, LSST, 2MASS, Roman, and WISE. The work includes A_V to in-band extinction calibrations for each filter assuming the underlying SED of a FUOr. The bolometric corrections agree with more rigorously-derived accretion luminosities of 4 FUOrs. They are useful when estimating the peak accretion luminosity of a FUOr given a measured value from one epoch and a lightcurve for the source, and for converting lightcurves to accretion rate evolution of a disk during its outburst.

In Chapter VIII, I use cross-correlation functions (CCFs) of high resolution near-infrared spectra to compute the maximum rotational broadening in the disks of 20 FUOrs and to test a critical assumption of the accretion disk model. Measuring rotational broadening in FUOrs is challenging due to the differential rotation of the disk. I reveal a means of using CCFs of observed and modeled H band spectra to measure the maximum rotational broadening in the disk while accounting for differential rotation. I then apply the technique to Keck/NIRSPEC spectra of 20 FUOrs to measure $v_{\rm max}$ in the disks. I also compute the CCFs for Y, J, H, and K band spectra of FUOrs and find almost all show the expected differential rotation. I also compute the same CCFs for model spectra to show that the degree of observed differential rotation depends on the size of the active accretion region in the disk.

In Chapter IX, I use the infrastructure presented in the previous Chapters to measure the physical parameters of 4 well-known FUOrs. Two of them, V1057 Cyg and V1515 Cyg, are among the first known FUOrs and have been studied since the 1970s. The third is BBW 76, one of the oldest known FUOrs, and the fourth is Gaia 17bpi, which began its outburst in 2017 and appears to be returning to its pre-outburst state.

In Chapters X and XI, I present the first detection of the FUV continuum in FU Ori, as well as an NUV spectroscopic survey of 6 FUOrs. Using the FUV continuum flux of FU Ori and a newly-fit disk model, I demonstrated that the 40 year-old model for the star-disk interface at FU Ori cannot match the observed spectrum. I then applied the same technique to the bluest wavelengths of all 6 sources in the NUV

survey and found that they have UV emission in excess of the disk model spectrum, but inconsistent with the emission predicted by the classical boundary layer model proposed for FUOrs.

Chapters XII and XIII contain a high resolution spectral atlas of 15 – 20 FUOrs using Keck/HIRES and Keck/NIRSPEC. In total, the atlas covers 0.47 to 2.40 microns at spectral resolutions of 15,000 (NIRSPEC) to 35,000 (HIRES). In the two chapters, I briefly compare the spectra of FUOrs at high resolution. The data from the atlases appear throughout the other chapters in this Thesis.

I conclude the Thesis with Chapter XIV, in which I summarize several upcoming observational technologies that, when combined with the data and models presented in this thesis, will produce a complete picture of the FUOr variable class.

PUBLISHED CONTENT AND CONTRIBUTIONS

Carvalho, Adolfo S., Lynne A. Hillenbrand, Gregory J. Herczeg, and Kevin France (2025). "The Near-Ultraviolet Spectra of FU Orionis Accretion Disks." In: *ApJL, submitted*.
A.S.C aided in data acquisition, led the analysis and interpretation, and wrote the manuscript.

Carvalho, Adolfo S., Lynne A. Hillenbrand, and Á. Kóspál (2025). "The Hot Inner AU of V883 Ori." In: *ApJ, submitted*.
A.S.C aided in data acquisition, led the analysis and interpretation, and wrote the manuscript.

Carvalho, Adolfo S., Greg Doppmann, Kyle B. Westfall, Debora Pelliccia, J. Xavier Prochaska, Joseph Hennawi, Frederick B. Davies, Max Brodheim, Feige Wang, and Ryan Cooke (Oct. 2024). "Robust Support for Semi-automated Reductions of Keck/NIRSPEC Data Using PypeIt." In: *RNAAS* 8.10, 271.
A.S.C led the development of a new module to reduce spectroscopic data from NIRSPEC, as well as an independent code notebook to complete the necessary data reduction steps and analyze the data, and wrote the manuscript., p. 271. DOI: 10.3847/2515-5172/ad8bb5. arXiv: 2410.19991 [astro-ph.IM].

Carvalho, Adolfo S., Lynne Hillenbrand, Jerome Seebeck, and Kevin Covey (Aug. 2024). "An Expanding Accretion Disk and a Warm Disk Wind as Seen in the Spectral Evolution of HBC 722." In: *ApJ* 971.1, 44.
A.S.C led the modeling of the disk, aided in data acquisition and analysis, and wrote the manuscript., p. 44. DOI: 10.3847/1538-4357/ad5286. arXiv: 2405.20251 [astro-ph.SR].

Carvalho, Adolfo S. and Lynne A. Hillenbrand (Nov. 2024). "Bolometric Corrections for FU Ori Object Accretion Disk Luminosities." In: *ApJL* 976.1, L5.
A.S.C contructed the models, wrote software to compute the filter-convolved fluxes using published filter profiles, analyzed the resulting fluxes, fit the data to produce bolometric corrections, and wrote the manuscript., p. L5. DOI: 10.3847/2041-8213/ad8cdf. arXiv: 2410.22270 [astro-ph.SR].

Carvalho, Adolfo S., Lynne A. Hillenbrand, Kevin France, and Gregory J. Herczeg (Oct. 2024). "A Far-ultraviolet-detected Accretion Shock at the Star–Disk Boundary of FU Ori." In: *ApJL* 973.2, L40.
A.S.C led the analysis of the data and its interpretation, as well as writing the manuscript., p. L40. DOI: 10.3847/2041-8213/ad74eb. arXiv: 2408.11033 [astro-ph.SR].

Carvalho, Adolfo S., Lynne Hillenbrand, and Jerome Seebeck (Dec. 2023). "Disk Cooling and Wind Lines as Seen in the Spectral Line Evolution of V960 Mon." In: *ApJ* 958.2, 140.
A.S.C led the modeling of the disk combining several published datasets, analyzed

new data, and wrote the manuscript., p. 140. DOI: 10.3847/1538-4357/acff59. arXiv: 2310.02465 [astro-ph.SR].

Carvalho, Adolfo S., Lynne A. Hillenbrand, Franz-Josef Hambsch, Shawn Dvorak, Michael Sitko, Ray W. Russell, Victoria Hammond, Michael Connelley, Michael C. B. Ashley, and Matthew J. Hankins (Aug. 2023). "Modeling the Multiwavelength Evolution of the V960 Mon System." In: *ApJ* 953.1, 86.
A.S.C assembled publically available data and used this to compute the disk models that constrain the system parameters. A.S.C. then led the interpretation of the evolution of the system and wrote the manuscript., p. 86. DOI: 10.3847/1538-4357/ace2cb. arXiv: 2306.15107 [astro-ph.SR].

Carvalho, Adolfo S. and Christopher M. Johns-Krull (May 2023). "A Simple Code for Rotational Broadening of Broad Wavelength Range High-Dispersion Spectra." In: *RNAAS* 7.5, 91.
A.S.C assembled the data to compare the code with other techniques, formalized the code for publication and distribution, and wrote the manuscript.., p. 91. DOI: 10.3847/2515-5172/acd37e. arXiv: 2305.09693 [astro-ph.IM].

CONTENTS

Acknowledgements iv
Abstract vi
Published Content and Contributions ix
Contents x
List of Figures xv
List of Tables xliv
Chapter I: Introduction 1
1.1 An overview of the main stages of star formation 1
1.2 So what exactly are FUOrs? 3
1.3 The missing trigger of FU Ori outbursts 5
1.4 The aims of this Thesis 11
Chapter II: A New Framework for Fitting FUOr Disk Spectra 12
2.1 Computing the Spectrum of a Disk 13
2.2 Fitting Disk Models to Observed Spectra 16
2.3 The Importance of Incorporating High Resolution Spectra in SED Fitting 17
2.4 What Luminosity Should One Adopt for FUOrs? 20
2.5 Limitations of the disk model 28
Chapter III: Modeling the Multiwavelength Evolution of the V960 Mon System 33
3.1 Introduction 33
3.2 Data 35
3.3 Disk Model and Fitting 39
3.4 Photometric Evidence of Temperature Evolution in the Disk 47
3.5 The Passive Disk Contribution to L and M Band 54
3.6 Discussion 56
3.7 Summary and Conclusion 59
3.8 Acknowledgements 60
3.9 Appendix: Photometry used in Figure 1 61
Chapter IV: Disk Cooling and Wind Lines As Seen In the Spectral Line Evolution of V960 Mon 62
4.1 Introduction 62
4.2 Data 64
4.3 Modeling the High Dispersion Spectra 66
4.4 Evidence of Disk Cooling in the High-Dispersion Spectra 71
4.5 Lines with Excess Absorption Relative to the Disk Model 77
4.6 Forbidden Emission 88
4.7 Discussion 91
4.8 Conclusion 95
4.9 Acknowledgements 96

4.10 Appendix: Optical HWHD Measurements and the Keplerian Disk Model . . . 96
4.11 Appendix: Attempts to fit the TiO Bandheads . . . 96
4.12 Appendix: All Orders of the HIRES Spectra and Residuals . . . 98
Chapter V: An Expanding Accretion Disk and a Warm Disk Wind As Seen In the Spectral Evolution of HBC 722 . . . 99
5.1 Introduction . . . 99
5.2 Data . . . 101
5.3 SED Fits . . . 106
5.4 The Disk Model in High Resolution Spectra . . . 111
5.5 Lines with Excess Absorption or Emission Relative to the Disk Model 117
5.6 Interpretation . . . 131
5.7 Summary and Conclusions . . . 141
5.8 Acknowledgements . . . 142
5.9 Appendix: Progenitor Spectral Type . . . 142
5.10 Appendix: Line Profiles of O I Wind Lines . . . 144
5.11 Appendix: The Temperature Sensitivity and Time Evolution of the CO (3-0) Band . . . 145
Chapter VI: The Hot Inner AU of V883 Ori . . . 148
6.1 Introduction . . . 148
6.2 Data . . . 150
6.3 Disk Model Fits . . . 155
6.4 Discussion . . . 161
6.5 Conclusion . . . 166
6.6 Acknowledgements . . . 167
6.7 Appendix: Aperture Photometry on the Pan-STARRS Stacked Images 167
6.8 Appendix: 20 Years of Ground-based Photometry of V883 Ori . . . 168
6.9 Appendix: Posterior Distributions of the Disk + Scattered Light Model 169
Chapter VII: Bolometric Corrections for FU Ori Object Accretion Disk Luminosities . . . 172
7.1 Introduction . . . 173
7.2 Applying A Full-Spectrum Disk Model to Photometric Observations 174
7.3 Computing Accretion Luminosity . . . 176
7.4 Application to Two Well-Studied FU Ori Systems . . . 180
7.5 Conclusions . . . 183
7.6 Acknowledgements . . . 184
7.7 Appendix: New Constant-Temperature Bolometric Corrections . . . 185
Chapter VIII: Cross Correlation Analysis of the Keck/NIRSPEC High Resolution Spectroscopic Survey of FUOrs . . . 187
8.1 Using CCFs in H band to Measure $v_{\rm max}$ . . . 187
8.2 The Wavelength Dependence of Rotational Broadening in FUOrs Revealed by CCF Analysis . . . 191
Chapter IX: New Physical Parameters for Four Well-Known FUOrs . . . 213
9.1 V1057 Cyg . . . 214
9.2 V1515 Cyg . . . 216

9.3 BBW 76 . . . 219
9.4 Gaia 17bpi . . . 221
Chapter X: An FUV-detected Accretion Shock at the Star-Disk Boundary of FU Ori . . . 229
10.1 Introduction . . . 229
10.2 Data and Calibration . . . 231
10.3 The FUV Spectrum of FU Ori . . . 233
10.4 Fitting the FUV Excess Emission . . . 233
10.5 Discussion . . . 239
10.6 Conclusions . . . 245
10.7 Acknowledgements . . . 247
10.8 Appendix: Line Profiles of Common CTTS FUV Emission Features 247
10.9 Appendix: Previous Analysis of the FU Ori NUV Spectrum . . . 249
10.10Appendix: Revisiting the $\dot{M}$ and A_V of FU Ori . . . 251
10.11Appendix: Detecting the Continuum Blueward of 1200 Å . . . 252
Chapter XI: The Near-Ultraviolet Spectra of FU Orionis Accretion Disks . . . 255
11.1 Introduction . . . 255
11.2 Data . . . 257
11.3 Modeling the Spectra . . . 258
11.4 NUV Emission Lines . . . 263
11.5 Discussion . . . 267
11.6 Conclusions . . . 272
11.7 Appendix: STIS 2D Spectra and Detection Criteria For Fainter Sources 273
11.8 Appendix: Posterior Distributions for the UV Excess Blackbody Fits 273
11.9 Appendix: BP Tau as a Representative CTTS . . . 274
Chapter XII: A Keck/HIRES Spectral Atlas of FU Ori Objects . . . 280
12.1 Outflow-tracing features . . . 280
12.2 The HIRES Spectral Atlas . . . 283
Chapter XIII: A Keck/NIRSPEC Atlas of FUOrs . . . 322
13.1 Plots of the Keck/NIRSPEC Spectra . . . 322
13.2 Recommendations for Future Keck/NIRSPEC Observers . . . 323
Chapter XIV: Summary and Future Directions . . . 360
14.1 New Visible and NIR Surveying Capabilities . . . 360
14.2 Millimeter Observations of FUOrs Can Probe Disk Chemistry . . . 363
14.3 JWST as a Rapid Follow-Up Instrument of Newly Discovered Outbursts 365
14.4 Upgraded Interferometry for FUOr Multiplicity and Disk Inclinations 365
Bibliography . . . 368
Appendix A: Robust support for semi-automated reductions of Keck/NIRSPEC data using PypeIt . . . 403
A.1 Introduction . . . 403
A.2 Updates to PypeIt . . . 404
A.3 Telluric Contamination Correction . . . 405
Appendix B: A Simple Code for Rotational Broadening of Broad Wavelength Range High-Dispersion Spectra . . . 408
B.1 Introduction . . . 408

B.2 Broadening by Direct Integration 409
B.3 Conclusion 411

LIST OF FIGURES

Number *Page*

1.1 A schematic showing the inner region of a disk during the CTTS magnetospheric accretion stage (left) and during an FU Ori outburst (right). The physical parameters of the sample CTTS on the left are: $M_* = 0.6\ M_\odot$, $R_* = 2\ R_\odot$, and $R_T \sim 3\ R_*$. The location of the R_T and the dust sublimation region is informed by values from NIR interferometry (GRAVITY Collaboration et al., 2021). The FUOr schematic representative of the temperature structure of the inner disk of FU Ori itself (Zhu, Jiang, et al., 2020; Carvalho, Hillenbrand, France, et al., 2024). 4

2.1 A comparison of the disk models constructed using only blackbodies (blue) versus those constructed using synthetic stellar spectra (red). . 13

2.2 Sample SED fits to the photometry of V960 Mon (left) and the spectrophotometry of HBC 722 (right). Descriptions of the objects, fits, and data can be found in Chapters 3 and 5, respectively. This Figure is a reproduction of Figure 8 from Carvalho, Hillenbrand, Hambsch, et al. (2023) and Figure 4 from Carvalho, Hillenbrand, Seebeck, and Covey (2024). 16

2.3 Disk models showing how changing different parameters impacts the SED. In each panel, a single parameter is varied while keeping all others fixed. 18

2.4 A demonstration of the impact of $T_{\rm max}$ on template-based extinction measurements. All 3 model spectra used initially have $A_V = 0$ and are normalized to 1.0 at $\lambda = 2.15\ \mu$m. The A_V value reported in the caption is the "correction" necessary to match the template, which is negative of the spectum needs to be reddened. **Left:** A model spectrum with $T_{\rm max} = 7500$ K will appear bluer than the template ($T_{\rm max} = 6000$ K), causing the fit to underestimate the extinction. **Right:** A model spectrum with $T_{\rm max} = 4500$ K will appear redder than the template, causing the fit to overestimate the extinction. . . . 19

2.5 The effect of varying $R_{\rm outer}$ on the disk model spectrum and the estimated A_V when normalized at K band. **Left:** A reproduction of Figure 6 from (Carvalho, Hillenbrand, Hambsch, et al., 2023) showing how the chosen $R_{\rm outer}$ value in a disk model impacts the flux, especially for $\lambda > 2$ μm. **Right:** A model with $T_{\rm max} = 6000$ K and $R_{\rm outer} = 50$ $R_\odot$ computed with $A_V = 0$ (blue), then reddened by $A_V = 0.4$ mag to match the template, which has $T_{\rm max} = 6000$ K and $T_{\rm outer} = 150$ $R_\odot$. 20
2.6 The effect of varying $v_{\rm max}$ and $T_{\rm max}$ on absorption features in the high resolution disk models. 21
2.7 Same as Figure 2.6 but showcasing the spectra in the NIR. Notice that in contrast to the visible range, features are much more strongly affected by the rotational broadening than by changes in disk temperature. 22
2.8 A comparison of different luminosity measurements for FUOrs, showing also the importance of inclination. **Left:** The ratio of isotropic-emission-derived luminosity to true disk luminosity as a function of source inclination. **Right:** The $L_{\rm acc}$ values of FUOrs measured from their K band brightnesses via bolometric corrections compared with the $L_{\rm bol}$ values reported by Connelley and Reipurth (2018). The grey $y = x$ line is plotted for reference. 23
2.9 Deriving the luminosity of a FUOr from its lightcurve. **Left:** The multiband lightcurve of Gaia 17bpi, showing the pre-outburst state of the object, its rapid rise, and its slow fade in the past 8 years. **Right:** The $L_{\rm acc}$ curve for Gaia 17bpi, derived from bolometric corrections to the photometric points in the left panel. 26
2.10 CDFs of the $R_{\rm inner}$ values estimated for the FUOrs in Table 2.2 assuming 4 different temperatures. The grey and black lines show the R_* values for the 1 and 2 Myr PARSEC isochrones, respectively. . . 27
2.11 The region of the HIRES spectra containing the TiO 8860 Å band for 14 FUOrs and one EX Lup-type object. Important spectra features are marked with grey vertical lines. 30
2.12 The region of the disk model spectrum containing the TiO 8860 Å band for 3 potential $v_{\rm max}$ values. Notice that for increased rotational broadening, the TiO feature is difficult to distinguish from the Paschen absorption. 32

3.1 The multiband lightcurve of V960 Mon, showing photometry from many sources spanning U band to the W1 and W2 filters of WISE/NEOWISE. The outburst and rapid fade of the target is clear in all bands, with the amplitude tending to decrease toward the red. Photometry that is more sparsely sampled (WISE, Gaia) is shown connected by lines to highlight the trend in the outburst and exponential fade. The black and lime vertical dashes mark the dates on which the HIRES and SpeX spectra, respectively, were collected. 36
3.2 Orders of the HIRES spectrum taken closest to outburst that are used to compute the χ^2 surface described in Section 3.3. The fiducial model for the outburst spectrum is shown in red. Large mismatches between the data and model are seen in certain spectral lines; the extra depth (and blueshift in particular Fe II lines) in the data is due to wind absorption, which is not included in our disk model, but will be the subject of a future paper. 40
3.3 Same as Figure 3.2 for the next three orders used. 41
3.4 Same as Figure 3.2 for three reddest orders used. Here, in addition to wind absorption that is not included in the model, there is also uncorrected telluric absorption in the data that appears as narrow lines toward the right of the bottom panel (grey shaded region). . . . 42
3.5 The χ^2 surface for the outburst spectrum and high resolution models with varying M_* and $R_{\rm inner}$ values, $\log(\dot{M}) = -4.6\ M_\odot\ {\rm yr}^{-1}$ and $i = 15°$. The mininmum χ^2 value is found in the region that is intersected by the $v_{\rm max} \sin i = 60$ km s^{-1}. The width of the minimum allows for an uncertainty of 5 km s^{-1} on that value, which we use to constrain the SED fits. 45
3.6 The SED model compared with the photometry from the outburst epoch, with varying values of $R_{\rm outer}$. Notice that the longer wavelength data points favor increasingly larger values of $R_{\rm outer}$, an inconsistency that can be rectified by adding a passive disk component exterior to the adopted $R_{\rm outer}$ for the active accretion disk. 46
3.7 The posteriors from the full SED fit to the outburst SED. All of the parameters are well-constrained, with the exception of A_V. 48

3.8 The results of the MCMC fit restricted to 3 parameters, with $M_* = 0.59\ M_\odot$, $i = 15°$, and $R_{\rm inner} = 2.11\ R_\odot$ fixed to their best-fit values shown in Figure 3.7. **Left:** The posterior distributions shown as a `corner` plot. With the fixed system parameters, the $\dot{M}$ and A_V converge and are consistent with the best-fit values found from the full SED fit. **Right:** The resulting SED models, with the full fit shown in blue and the reduced parameter fit shown in red. The good agreement between the two indicates fixing the chosen parameters did not significantly affect the fit. The error bars on the photometry represent 0.01 mag precision. 49

3.9 V magnitude of V960 Mon versus color temperature of V960 Mon, computed using the Ballesteros (2012) conversion from $B-V$ to $T_{\rm eff}$. $B-V$ is adjusted assuming $E(B-V) = 0.53$ 50

3.10 The SpeX spectra compared with the best-fit outburst model and the model generated using the extrapolated system parameters described in Section 3.4. The flux uncertainty is shown with an error bar in the upper right. Overall, the models are in good agreement with the NIR disk emission. However, there are significant discrepancies in between the molecular features in the data and the models, and generally the pure accretion disk models produce poor fits to the L and M bands. The models consistently predict a much stronger H band peak than the data predict, especially at outburst. The discrepancies are further discussed in Section 3.5 and Paper II. 52

3.11 Temperature profiles adopted for the high resolution models of the HIRES epochs. 53

3.12 Color magnitude diagrams for V960 Mon using combined photometry from sources shown in Figure 3.1. Model curves are computed with $M_* = 0.6\ M_\odot$, $A_V = 1.6$ mag, and $d = 1120$ pc (Kuhn and Hillenbrand, 2019). The grey curves show lines of constant $\dot{M}$ and varying $R_{\rm inner}$. The colored curves show lines of $\dot{M}$ varying along with $R_{\rm inner}$ according to Equation 3.6 for different assumed values of B_*. **Top Two Plots:** V vs $B-V$ and I vs $V-I$ from AAVSO and other sources, along with our models. **Lower Left:** Gaia G vs $BP-RP$ photometry, converted to AB magnitudes, plotted alongside our models. The Gaia photometry is very well matched by the models. **Lower Right:** i vs $r-i$ using the ROBOTT (USB) photometry. The ROBOTT photometry spans only the initial steep fade in the lightcurve, prior to JD 2457400. 54

3.13 A model of the system for the 2015-01-15 SpeX epoch, incorporating both an active (red line) and a passive (blue dashed line) disk component. The active disk component is the same model as that shown in Figure 3.10 for the 2015-01-15 epoch, but computed with $R_{\rm outer} = 25\ R_\odot$. The passive disk component uses a flared disk model with a linearly increasing flare angle, described in Section 3.5. Notice that the addition of the passive disk allows the model to better match the H band molecular features, the K band continuum, and the L and M band excess. 56

4.1 The epochs of our HIRES spectra are shown (vertical solid lines) relative to the AAVSO B (black circles) and Gaia BP (grey connected points) lightcurves of V960 Mon. The lightcurve illustrates the rapid post-outburst fade and eventual plateauing in later epochs. The quiescent B magnitude reported in Kóspál, Ábrahám, Moór, et al. (2015) is shown as the black horizontal line for reference. The Dec 10 2014 HIRES epoch is marked with a dot-dashed line due to overlap with the Dec 9 2014 epoch. 64

4.2 The HIRES spectra shown in a time-series, with bluer to redder spectra indicating earlier to later epochs. The lower set of curves in each panel are the residuals after subtracting the disk model appropriate to each epoch. See Figures 2-4 of Paper I for the direct comparison between the outburst epoch spectrum (bluest line here) and the disk model. Strong excess absorption in certain lines (marked) is attributed to wind contributions in the spectra; see §4.5. Outside of these lines, the typical RMS value of the residuals is < 3 %. The remaining 28 orders are shown in Appendix 4.12. 66

4.3 The effect of varying $\dot{M}$ and $R_{\rm inner}$ on the width and depth of absorption lines with different EPs. **Left:** Models of the Ca I 6439 (upper panel) and Si II 6347 (lower panel) lines for different values of $\dot{M}$. Notice the Ca I 6439 line broadens as $\dot{M}$ decreases, whereas the Si II 6347 line only changes in depth. **Right:** Models of the same two lines for different values of $R_{\rm inner}$. Notice here that the $T_{\rm max}$ dependent broadening still dominates in the Ca I line as $R_{\rm inner}$ decreases, making the line counter-intuitively broader. However, in Si II, the broadening decreases with increasing $R_{\rm inner}$, as expected due to the decrease in the maximum Keperian velocity. 69

4.4 The Ca I 6439 (upper profiles) and Si II 6347 (lower profiles) absorption lines shown for the different epochs of the HIRES spectra. Notice the Si II line becomes narrower, in addition to weaker, consistent with an increase in $R_{\rm inner}$, while the broadening of the Ca I line remains relatively unchanged. 70

4.5 The HWHD measurements of several isolated absorption lines in the HIRES outburst (9 Dec 2014) spectrum (black) and the spectral model (red). Empty symbols show lines that are isolated and easily measured in the data but appear severely blended in the models. Although there are some line-by-line inconsistencies (largely due to imperfections in the PHOENIX models), neither set of measurements is significantly correlated with wavelength. The data and the disk model also have similar standard deviations and the scatter in the HWHD measurements does not vary with wavelength. The error bars shown reflect the uncertainty in the width parameter fit used to compute the HWHD measurements. 72

4.6 The equivalent width evolution (black squares) of two higher EP and two lower EP lines in the spectrum of V960 Mon. The AAVSO V band lightcurve is plotted (green points) for reference, showing the evolution of the continuum brightness over the spectral epochs. **Left Column:** The evolution of the 5316 Fe II line and 8862 Paschen line equivalent widths, which both closely follow the lightcurve of the target in their decreasing strength. The EW measurement for the 8862 Paschen line is blended with the Fe I 8866 line, but the Fe I line does not vary in time. **Right Column:** The evolution of the 5328 Fe I line and 6439 Ca I line, which both follow an inverse trend to the lightcurve in their growth, similarly strengthening as the target fades and plateauing at later times. 74

4.7 The 8750 Å and 8862 Å Paschen lines in the HIRES spectra (left column) and the residual spectrum (right column). Notice the lines have been removed to within a few % in every epoch, indicating the modeled $T_{\rm max}$ change reproduces the evolution of the Paschen series accurately. The 8750 Å line is blended with the 8751 Si I line and the 8862 Å line is blended with an Fe I line at 8866 but both are well-modeled, do not show any evolution, and do not appear in the residuals. The emission residual in the lower right panel at -200 km s^{-1} is due to TiO absorption in the model that is not present in the data. We discuss this discrepancy in Appendix 4.11. 75

4.8 Equivalent width ratios in the 6400 Åregion used to show temperature evolution. **Left:** The equivalent width ratios of the Ca I 6439 line and the Fe I 6456 line as a function of time in the HIRES spectra. **Right:** The equivalent width ratios of the same lines in the PHOENIX grid in the blue background and the ratios in the HIRES spectra shown in the red color map, with larger equivalent width ratio values as darker shades. 76

4.9 Equivalent width ratios in the 5300 Åregion used to show temperature evolution. **Left:** The equivalent width ratios of the Fe I 5328 line and the Fe II 5316 line as a function of time in the HIRES spectra. **Right:** The equivalent width ratios of the same lines in the PHOENIX grid in the blue background and the ratios in the HIRES spectra shown in the red color map, with larger equivalent width ratio values as darker shades. 77

4.10 The Hβ and Hα lines in each of the HIRES epochs as seen in the original data (left) and as residuals after removing the disk contribution (right). Both lines initially show a high velocity blue-shifted absorption component, that weakens rapidly over time and becomes an emission feature in Hα. The profiles also contain a slow component that moves redward. The emission components of the Hα profile are both peaked at $\pm$60 km s^{-1} and strengthen consistently relative to continuum. The absorption in the upper left panel at +185 km s^{-1} is the Cr II 4864 Å line. Notice it is well-removed by the model and is much weaker in the upper right residual panel. 80

4.11 The Na D 5889 line (top row) and Ca II IRT lines (lower three rows), shown in the data (left column) and residuals (right column). The Ca II IRT lines show a weakening fast blue-shifted component and a $\pm$60 km s^{-1} emission component similar to those seen in the H lines. Note that the +100 km s^{-1} absorption is due to Hydrogen Paschen line blending with the IRT. This is well-matched by our disk model and mostly removed in the residuals column. The Na D lines are saturated from -10 to 0 km s^{-1}, which matches the narrow absorption seen in the latest epoch, indicating there may be a constant slow wind covering almost the entire visible emission region of the disk. 81

4.12 High EP lines in the HIRES spectra of V960 Mon, smoothed with a $\sigma = 5$ pixel Gaussian for clarity. Epochs are shown in different colors, where redder indicates later epochs when the target is dimmer and, according to our disk model, cooler. The black vertical lines mark $\pm$60 km s^{-1}, the estimated $v_{\rm max}$ at outburst, as a reference for the line widths. The C I 9095 line is significantly contaminated by telluric absorption, but its similar evolution to the other lines is still apparent. 83

4.13 The EW ratio of the Si II 6347 line to the Fe I 6400 line for the HIRES spectra, showing that the ratio decreases in time and is consistent with a decreasing temperature. The color scheme in the left and right panel both show lighter red for larger EW ratios. **Left:** The timeseries of the EW ratios. **Right:** The EW ratios of the same lines as measured in the PHOENIX grid (blue contoured background) and in the HIRES spectra (red contours). 84

4.14 The EW ratio of the O I 8446 line to the Fe I 8688 line for the HIRES spectra, showing that the ratio decreases in time and is consistent with a decreasing temperature. The color scheme in the left and right panel both show lighter red for larger EW ratios. **Left:** The timeseries of the EW ratios. **Right:** The EW ratios of the same lines as measured in the PHOENIX grid (blue contoured background) and in the HIRES spectra (red contours). 84

4.15 Fe II lines in the HIRES spectra. Notice their behavior is similar to the high EP lines shown in Figure 4.12, rapidly shrinking over time. This effect is strongest in the lines with higher EP, indicating sensitivity to the hot wind component. The Fe II lines here seem to trace the disk behavior at lower EPs and bluer wavelengths, and trace the wind at higher EPs and redder wavelengths. 86

4.16 Lines in the HIRES spectra which show the central absorption feature shown as a time series progressing from blue to red color. Notice that across the range of lines and EPs, the narrow feature shows a consistent width ~ 20 km s^{-1} and is centered at 0 km s^{-1}. The feature grows as the target fades, absorbing against the disk continuum to additional depth that is almost equivalent to the depth of the disk contribution of many of the lines 87

4.17 Selected regions of the residuals of our fits to the HIRES spectra, compared with log $g = 1.5$, $T_{\rm eff} = 7000$ K (green) and $T_{\rm eff} = 9000$ (magenta) K PHOENIX models. Notice the residual features are consistent with the features seen in these hot model atmospheres, with a tendency for later epochs to more closely resemble the 7000 K atmosphere. This may indicate that the component of the system probed by the residuals is cooling as the disk cools. The HP lines in the lower right panel are strongly affected by Stark broadening in the PHOENIX atmospheres. That we do not see this in the disk model or the data indicates that the contribution from the narrower/weaker HP lines in cooler atmospheres is necessary to match the data. . . . 89

4.18 The [O I] 6300, [N II] 6583, [S II] 6731 emission lines in the HIRES spectra. All three features are blue-shifted, with emission components ranging from -60 km s^{-1} to -10 km s^{-1}. The emission in the [O I] λ6300 and [N II] λ6583 lines is mostly at higher velocities, whereas the [S II] λ6731 line shows both a -40 km s^{-1} component and a nearly 0 km s^{-1} component. 90

4.19 The Keplerian velocity at the luminosity weighted mean radius of each wavelength bin in the outburst spectrum model. Spectral absorption features appear as annuli with greater total flux at the slightly greater radii are needed to compensate for the absorption. 97

4.20 The TiO bandhead at 8860 in our models, the HIRES spectra, and the model residuals, shown for all of the HIRES epochs and for three different models. **Left:** Models computed assuming $R_{\rm outer}$ = 12 $R_\odot$. Notice the time (and therefore $\dot{M}$) dependence of the TiO bandhead is much stronger for this model. **Center:** Models using $R_{\rm outer}$ = 25 $R_\odot$. Already, there is little change in the TiO bandhead with time, and it clearly overpredicts the absorptions. **Right:** Models using $R_{\rm outer}$ = 45 $R_\odot$. The TiO bandhead is essentially insensitive to $\dot{M}$ in these models and continues to overestimate the absorption we see. 98

5.1 A simplified diagram of the HBC 722 system near the outburst peak. The color gradient represents the radial temperature profile in the disk atmosphere, which is assumed plane-parallel and peaks at $T_{\rm max}$ = 5700 K with $L_{\rm acc}$ = 71 $L_\odot$. The depicted height of the disk atmosphere above the midplane is representative of the τ = 1 surface in the Zhu, Jiang, et al. (2020) simulation of the FU Ori system. The midplane (in maroon) is marked for reference and given a height similar to the average scale height in the Zhu, Jiang, et al. (2020) simulation. The outer, passive disk represents that modeled in Section 5.3, which is reprocessing the bright inner disk emission. The fast outflow lines represent a magnetocentrifugal wind following the BP82 solutions, which appear consistent with what we observe in the the wind-sensitive lines of the spectrum **(Section 5.5)**. 101

5.2 The multiband lightcurve of HBC 722, illustrating the rapid rise during outburst, brief post-outburst fade (“dip") and subsequent rise and “plateau." Filters are as given in the legend; see text for details. Green and red triangles show ZTF photometry shifted by $g - 0.9$ and $r - 0.4$ to overlap with the V and R photometry. Square points in the 3.4 and 4.6 μm bands mark the Spitzer/IRAC photometry from Kóspál, Ábrahám, Acosta-Pulido, et al. (2016), distinguishing it from the WISE and NEOWISE measurements. Left-pointing arrows indicate the progenitor photometry taken prior to 2009 (Miller, Hillenbrand, et al., 2011). Epochs of our optical HIRES spectra are shown as vertical black dashed lines, while epochs of infrared SpeX and TripleSpec spectra are marked with short vertical magenta lines. 103

5.3 The `corner` plot for the MCMC fit of the outburst epoch SED showing the posterior distributions for the $\dot{M}$, $R_{\rm inner}$, i, and A_V model parameters. The median (mode) parameter values in the posterior distributions are marked by the red (blue) horizontal and vertical lines. 109

5.4 The 3 epochs of NIR spectra that trace the major parts of the lightcurve – the outburst peak (purple), the dip (blue), and the plateau (green). From outburst to the dip to the plateau, the evolution of the spectra is consistent with a general increase in $R_{\rm outer}$ and a decrease in the minimum $T_{\rm eff}$ of the model grid used to generate the disk model spectrum. Right panel includes extended wavelength coverage, and in order to match the photometry, a model for the passive disk in the outburst and dip epochs. For the plateau epoch, the active disk is large enough that a passive disk component is not necessary to model the spectrum in the $3 - 5$ μm range. 111

5.5 Selected orders from the HIRES spectra corresponding to the 3 SpeX epochs shown in Figure 5.4. Notice the strong agreement with the disk model spectrum that was derived to fit the lower resolution infrared spectrum, across a large range of visible wavelengths that include many atomic species. The most discrepant lines (e.g., Fe II 5018) trace wind absorption and are discussed in Section 5.5 while others (e.g., Li I 6707) exhibit a narrow blue-shifted absorption that grows over time and are discussed in Section 5.5 113

5.6 Selected orders from the NIRSPEC spectrum (in black), spanning 1.0-2.2 μm. Grey vertical lines mark locations of strong telluric absorption. The plateau epoch model is shown in green. The lines tracing the wind outflow, such as Paβ and Brγ, as well as several disk atmosphere lines including Ti I, Mg I, and Fe I, are marked with cyan vertical lines. 116

5.7 CCFs computed for 3 HIRES orders that are covered in 15/16 HIRES epochs, showing the evolution of the disk absorption over time. The purple profile indicates the 25 Sept 2010 outburst epoch, the blue profiles are those spanning the dip (Dec 2010 - Jan 2013) and the green profiles show the epochs in the plateau (2013-2022). The dotted grey lines show the approximate velocities of the peak absorption ($\pm$55 km s^{-1}), whereas the solid grey line marks the -10 km s^{-1} at which we see a narrow absorption feature growing over time (see Section 5.5). For most of the epochs and across the HIRES wavelength range, the line profiles are a consistent width, indicating an unchanging $v_{\rm max}$ over time. 117

5.8 Hβ (upper row) and Hα (lower row) lines in the HBC 722 HIRES spectra. The Hβ line is not covered in the outburst epoch, so only the dip (left panel) and plateau (right panel) epochs are shown. The outburst Hα profile is shown in the inset in the bottom left panel. The lines are highly variable as the target evolves but all consistently trace a massive outflow with $v = -10$ to -30 km s^{-1}. 119

5.9 The evolution Na I D 5889 line in the HIRES spectra shown for the 3 main stages of the lightcurve: the outburst (left), the dip (center), and the plateau (right). Notice the line profile during the outburst epoch looks very similar to the profiles during the plateau. However, during the dip, the profiles are dominated by wind absorption and show almost no disk broadening in the red wing. 119

5.10 The evolution Fe II 5018 (upper row) and Mg I 5183 (middle row) and K I 7699 (lower row) lines in the HIRES spectra shown for the 3 main stages of the lightcurve: the outburst (left), the dip (center), and the plateau (right). Notice the line profiles during the outburst epoch look very similar to the profiles during the plateau. However, during the dip, the profiles are dominated by wind absorption and show almost no disk broadening in the red wing. The narrow, blue-shifted absorption traced by several Ti I lines (see Section 5.5) can be seen growing stronger in the plateau epochs of the Fe II 5018 profiles and their rest-wavelengths are marked with grey vertical lines. The epochs of the Fe II 5018 line are the same as the Mg I 5183 line, so we only print them once. In the K I panels, the narrow absorption at −80, −130, −350, and −400 km s^{-1} is due to telluric features and should be disregarded. 122

5.11 Ca II lines in the HBC 722 HIRES spectra. The upper row shows the Ca II K line at 3933 Å for the spectra that cover it, including the outburst epoch (left), dip epoch (center), and the most recent plateau spectrum (right). The outburst epoch spectrum did not cover the Ca II IRT 8498 Å line so we only show the dip (left) and plateau epochs (right) that do cover it. Both sets of lines show similar profile behavior, particularly in the red-shifted emission. The wind absorption in the Ca II K line is much stronger than in the Ca II IRT. The blue-shifted absorption in the Ca II K profiles blends into two Fe I features at −450 km s^{-1} and −275 km s^{-1} (3927.919 Å and 3930.296 Å, respectively). 123

5.12 A selection of lines possessing the narrow absorption features in HBC 722. The features deepen toward later times, eventually almost dominating the absorption in some lines. The blue-shifted line center indicates it is tracing a low-velocity outflow. 126

5.13 A selection of NIR atomic lines in the NIRSPEC spectrum spanning the Y to J band that show the same narrow absorption features we see in the HIRES spectra. The feature is at the same blue-shift and has a similar width to its visible-range counterparts, indicating it traces the same material. 127

5.14 An examination of the likely temperature of the red-optical TiO absorption in HBC 722. **Left:** The 7070 Å - 7170 Å region of the HIRES spectra showing the emergent TiO absorption in the most 2021 epoch compared to previous epochs where it did not appear. Notice that the bandheads in the red spectrum are offset -10 km s^{-1} from their typical wavelengths, as highlighted by the grey vertical lines. The outburst (25 Sept 2010), penultimate (29 Nov 2019), and most recent (07 Aug 2021) spectra are shown in black, blue, and orange, respectively. A 3500 K, log$g$ = 1.5 PHOENIX model spectrum, rotationally broadened to 10 km s^{-1}, blue-shifted by 10 km s^{-1}, and scaled by 0.2, is shown in grey for reference. The scaled PHOENIX model has TiO absorption similar to that seen in the data. **Right:** CCFs computed with the TiO bandhead that appears in the 2021 HIRES spectrum (red in left panel). Notice that the strongest peak appears at 3500-3800 K and is blue-shifted by -10 km s^{-1}. . . . 128

5.15 A CCF analysis of the NIR CO absorption in HBC 722. **Left:** The CO (2-0) and (3-1) bands from the Keck/NIRSPEC 30 Oct 2023 spectrum (blue), the HJST/IGRINS 20 Nov 2014 spectrum (orange) and the high resolution disk model spectrum (black). As in the HIRES spectra, we see a narrow excess absorption feature that grown stronger from 2014 to 2023. **Right:** The CCFs of the CO (2-0) band computed with different $T_{\rm eff}$ PHOENIX model spectra. At cooler temperatures, the red-shifted disk emission becomes apparent, whereas the hotter temperature profiles are dominated by the blue-shifted wind absorption. 130

5.16 The progenitor data compared with models using the Fang, Hillenbrand, et al. (2020) reported best-fit parameters and our adopted parameters. **Left:** The 1998 Norris spectrum, binned to R = 1000, showing deep TiO absorption more consistent with the veiled late-type (M4-M5, green) model spectrum than the unveiled K7 model (blue). **Right:** The progenitor SED (black dots), using photometry from Miller, Hillenbrand, et al. (2011), compared with the different models for the progenitor spectrum (color lines). The model with our adopted $T_{\rm eff}$ = 3100 K, R_* = 2.8 $R_\odot$, r_{7465} = 0.7 and A_V = 2.5 mag, shown in green, is a good fit to both the SED and the Norris spectrum. 144

5.17 Line profiles of red/NIR O features known to trace winds, shown in the HIRES spectra for the outburst epoch (left column), dip epochs (middle column) and plateau epochs (right column). **Upper Row:** The line profiles of the O I 7773 Å triplet, which is typically only seen in higher temperature atmospheres. The absorption at +250 km s^{-1} is disk atmospheric absorption from the Fe I 7780 feature. **Lower Row:** The O I 8446 Å triplet, which appeared only in our dip and plateau epochs. The grey lines at −390 and −420 km s^{-1} mark the locations of the Ti I 8434.961 and 8435.653 Å lines, both of which have EP = 0.8 eV. The broader absorption marked at −310 km s^{-1} is mostly due to the Paschen line at 8837 Å. 145

5.18 Time evolution of the *H* band CO absorption in HBC 722. **Top Panel:** The CO (3-0) band from the Keck/NIRSPEC 30 Oct 2023 spectrum (blue), the HJST/IGRINS 20 Nov 2014 spectrum (orange) compared with the high resolution disk model spectrum (black). **Bottom Panels:** CCFs between the HBC 722 spectra and PHOENIX model atmospheres with different $T_{\rm eff}$. **Left:** The CCFs for the CO (3-0) band in the IGRINS spectrum. **Middle:** The CCFs for the CO (3-0) band in the NIRSPEC spectrum. **Right:** CCFs computed with (2-0) band for the IGRINS spectrum. Here, the disk absorption is seen at lower temperatures than in the NIRSPEC epoch, but at higher temperatures, the profile still shows strong narrow blue-shifted absorption at -15 km s^{-1}. 147

6.1 V883 Ori as seen in the Pan-STARRS $g - z$ color image. The green ellipse shows the projected shape of the disk on the sky (scaled ×12 for visibility), assuming an inclination of 38.3° and a position angle of 32.4° (Cieza, Ruíz-Rodríguez, et al., 2018). The green arrow shows the axis of rotation of the disk (Lee, Lee, et al., 2019). The position angle and inclination of the disk indicate it is the primary illumination source for the bright nebula that extends ∼ 70″ to the southeast. The nebula is known as IC 430. 151

6.2 The reddest several orders of the 2003 (orange) and 2011 (blue) Keck/HIRES spectra, where the signal-to-noise is suitable, plotted along with the disk model described in Section 6.3 (black). The model reproduces the weak absorption features well, but misses portions of several HI and CaII profiles that arise in winds. Strong telluric features are present at the reddest wavelengths shown and are marked by grey vertical lines. 153

6.3 Select orders from the 2023 Keck/NIRSPEC spectrum (magenta) compared with the disk model described in Section 6.3 (black). The model matches the majority of the absorption features accurately from 1.0 μ to 2.3 μm. Grey vertical bands mark regions of strong telluric absorption. 154

6.4 A diagram of the system showing the geometry of the scattering surfaces and obscuring screen relative to the disk and the observer. The illustrated disk (in orange) angle is set to the 38.3° disk inclination. The vertical black arrow marks the 400 au projected spatial width of the LRIS trace on-sky, while the size of the disk illustration is the 100 au dust disk radius. 156

6.5 The model V883 Ori spectra compared with visible and NIR spectra. **Upper panel:** The complete disk + scattering model (black) compared with the LRIS and SpeX spectra (magenta). The disk component is shown in red and the scattered light component shown in blue. Historical photometry of the source is shown as green symbols: triangles for PanSTARRS, squares for 2MASS, and circles for WISE. The WISE photometry includes significant thermal emission from the dust surrounding V883 Ori, while the SpeX LXD spectrum is dominated by emission from only the inner disk. **Lower panel:** The dereddened SpeX spectrum and accompanying dereddened best-fit models, to better highlight the NIR fit. The A_V used for dereddening the spectrum is 20.78 mag. As established from the joint model, this is much greater than A_V (scatt), causing the rapid upward slope toward the visible. 159

6.6 Posterior distributions for $L_{\rm acc}$ and $T_{\rm max}$ computed from the distributions of M_*, $\dot{M}$, and $R_{\rm inner}$. The posterior distribution for A_V for the disk component is shown for reference, as it is often covariant with $T_{\rm max}$. The lack of strong covariance our posteriors indicates we have successfully broken the degeneracy typically present in SED fitting of accretion disk models. 160

6.7 A lightcurve of V883 Ori, spanning the past 20 years of observations. The arrows to the left of the plot mark the brightness of the source at 0.8, 3.5, and 4.8 μm, taken in 1963, 1975, and 1975, respectively (Allen et al., 1975). The source has remained at essentially the same brightness for at least the past 60 years. The triangles mark points from Pan-STARRS, while $*$ symbols mark points from ZTF. The tan and grey squares mark NEOWISE $W1$ and $W2$ points, respectively. The symbols on the plot are larger than the photometric uncertainties for all points except NEOWISE. 164

6.8 The sources of heating in the V883 Ori disk. The heating from the central star is negligible since the disk dominates the luminosity of the system. The midplane viscous heating, while dominant in the inner 3 au of the disk, falls below the heating due to irradiation from the accretion luminosity of the disk. 166

6.9 The posterior distributions of all 8 parameters of the disk + scattering models. They are all well-constrained and show minimal covariance. 171

7.1 The normalized filter profiles for the LSST, Roman, and WISE filters (colored lines), plotted against our fiducial $\dot{M} = 10^{-4.5}\ M_\odot\ {\rm yr}^{-1}$ FU Ori object SED model (black). The filled boxes at the top show the approximate total wavelength coverage of each survey or mission. The optical ZTF and Gaia filters overlap the LSST bands, and the 2MASS filters overlap the Roman bands. 176

7.2 The bolometric corrections (filled circles) and our polynomial fits (solid lines). The visible range surveys in the top row are ZTF (left), Gaia (center), and LSST (right). The infrared surveys along the bottom are Roman (left), 2MASS (center), and WISE (right). 177

7.3 The M_{Ks} versus extinction-corrected $J - Ks$ color magnitude space, with the locations of V960 Mon (blue point) and HBC 722 (green "x") are marked. The grid of accretion disk model values is plotted in grey, with constant $R_{\rm outer}$ tracing approximately vertical lines and constant $L_{\rm acc}$ approximately horizontal. The values at the top of the grid mark $R_{\rm outer}$ in units of $R_\odot$ for each set of models and values along the lower boundary of the grid mark a few $L_{\rm acc}$ values in units of $L_\odot$ for reference. Models with $R_{\rm outer} > 200\ R_\odot$ converge in this color space. Notice that both V960 Mon and HBC 722 lie along tracks that agree with their measured $R_{\rm outer}$ values (blue and red text, respectively) in this space. 183

8.1 The results of the H band CCF best-fit used to measure the rotational broadening in V883 Ori. **Left:** The mean CCF from 8 H band orders of the NIRSPEC spectrum of V883 Ori (magenta) and the best-fitting mean CCF from the model grid, corresponding to a $v_{\rm max}$ = 135 km s^{-1}. The stronger blue-shifted absorption in V883 Ori is likely due to a rotating disk wind traced by molecular bands like CO (3-0), as has been reported in HBC 722 (Calvet, Hartmann, et al., 1993; Carvalho, Hillenbrand, Seebeck, and Covey, 2024). **Right:** The reduced χ^2 values for the grid of model CCFs and the V883 Ori CCF. The best-fit value is marked with a × symbol. 189

8.2 The measured $v_{\rm max}$ values for each object in our NIRSPEC sample. . 190

8.3 The CCFs and reduced χ^2 values for the two epochs of FU Ori NIRSPEC spectra. 190

8.4 Same as Figure 8.3 for V1515 Cyg. 192

8.5 Same as Figure 8.3 for HBC 722. 193

8.6 Same as Figure 8.3 for Parsamian 21. 194

8.7 Same as Figure 8.3 for V733 Cep. 194

8.8 Same as Figure 8.3 for V1735 Cyg. 194

8.9 Same as Figure 8.3 for Gaia 17bpi. 195

8.10 Same as Figure 8.3 for Gaia 18dvy. 195

8.11 Same as Figure 8.3 for PGIR 20dci. 196

8.12 Same as Figure 8.3 for RNO 1B. 196

8.13 Same as Figure 8.3 for RNO 1C. 197

8.14 Same as Figure 8.3 for RNO 54. 197

8.15 Same as Figure 8.3 for V900 Mon. 197

8.16 Same as Figure 8.3 for V960 Mon. 198
8.17 Same as Figure 8.3 for L1551 IRS 5. 198
8.18 Same as Figure 8.3 for PP 13S. 198
8.19 Same as Figure 8.3 for V2775 Ori. 199
8.20 Same as Figure 8.3 for BBW 76. 199
8.21 Same as Figure 8.3 for V883 Ori. 199
8.22 Same as Figure 8.3 for V582 Aur. 200
8.23 The CCFs produced from disk models with $R_{\rm outer}$ = 150 $R_\odot$ of the Y (blue), J (green), H (red), and K (brown) band NIRSPEC spectra. The brown dashed line shows the K band CCF produced from a disk model with $R_{\rm outer}$ = 25 $R_\odot$. Notice that the expected narrowing of line widths at longer wavelengths is stronger for larger $R_{\rm outer}$ and becomes negligible for small $R_{\rm outer}$ values. 202
8.24 The flux-weighted mean radius from which the continuum for each wavelength bin arises. As the $R_{\rm outer}$ value for the disk model increases, the more the annuli at larger radii dominate the continuum NIR emission. At outburst, the K band continuum arises mostly from the $R \sim 12\ R_\odot$ region of the disk, whereas in the plateau the K band continuum probes out to $R \sim 45\ R_\odot$. However, the radii probed by the visible range (0.3 - 0.8 μm) are relatively unchanged. 203
8.25 The CCFs of each band in the two NIRSPEC epochs for FU Ori. The blue line is Y band, green is J band, red is H band, and brown is K band. The profile shapes are relatively consistent between the epochs and show that in both cases, K band rotational broadening is less than at shorter wavelengths. 203
8.26 The same as Figure 8.25 but for HBC 722. 204
8.27 The same as Figure 8.25 but for Parsamian 21. Note that the spectra for Parsamian 21 were taken on 20220731 (J/H), 20220801 (K) and 20231101 (Y). 204
8.28 The same as Figure 8.25 but for V733 Cep. 205
8.29 The same as Figure 8.25 but for V1515 Cyg. 205
8.30 The same as Figure 8.25 but for V1735 Cyg. 206
8.31 The same as Figure 8.25 but for Gaia 18dvy. 206
8.32 The same as Figure 8.25 but for PGIR 20dci. 207
8.33 The same as Figure 8.25 but for RNO 1B. 207
8.34 The same as Figure 8.25 but for RNO 1C. 208

8.35 The same as Figure 8.25 but for RNO 54. 208
8.36 The same as Figure 8.25 but for V900 Mon. 209
8.37 The same as Figure 8.25 but for V960 Mon. 209
8.38 The same as Figure 8.25 but for L1551 IRS 5. 210
8.39 The same as Figure 8.25 but for PP 13S. 210
8.40 The same as Figure 8.25 but for V2775 Ori. 211
8.41 The same as Figure 8.25 but for V883 Ori. 211
8.42 The same as Figure 8.25 but for V582 Aur. 212
9.1 The posterior distribution for $\dot{M}$, M_*, $R_{\rm inner}$, $\cos i$, and A_V for the model fit to V1057 Cyg. The red lines mark the median values, blue lines mark modal values. 216
9.2 The posterior distribution for $T_{\rm max}$, $L_{\rm acc}$, and A_V of V1057 Cyg. . . . 217
9.3 The best-fit models V1057 Cyg model compared with the SpeX spectrum to which it was fit. Gaia photometry is included for approximate reference of the the visible range flux of the source near the epoch of the 2015 SpeX observation. 217
9.4 The posterior distribution for $\dot{M}_1$, $\dot{M}_2$, M_*, $R_{\rm inner}$, $\cos i$, and A_V for the model fit to V1515 Cyg. 219
9.5 The posterior distribution for $T_{\rm max}$, $L_{\rm acc}$, and A_V of V1515 Cyg. . . . 220
9.6 The best-fit models for each epoch of V1515 Cyg spectra, compared with the observed spectra. Gaia $G_{\rm BP}$, G, and $G_{\rm RP}$ data, taken in 2017 between the spectroscopic epochs, is plotted to show the photometric decline of the source. 220
9.7 Same as Figure 9.7 for BBW 76. 222
9.8 Same as Figure 9.8 for BBW 76. 223
9.9 The best-fit models for BBW 76 for the 2015 and 2023 observations. Gaia photometry from 2017 is included to mark the steady visible range decline in the source. 223
9.10 The NIR evolution of Gaia 17bpi, from 2018 to 2023. Despite the relatively large change in flux, there is little change in the slope, resulting in a surprisingly colorless evolution. This is not unprecedented – HBC 722 showed similarly little color evolution when it faded in 2012 (Carvalho, Hillenbrand, Seebeck, and Covey, 2024). . . 224
9.11 The posterior distributions for the 7 parameter 2 epoch SED fit for Gaia 17bpi. 226

9.12 The $L_{\rm acc}$, $T_{\rm max}$, and A_V distributions for each epoch in the Gaia 17bpi SED fit. 227
9.13 The two-epoch best-fit models for Gaia 17bpi. 228
10.1 The COS spectrum of FU Ori with the regions selected to represent continuum highlighted in light blue. Regions in black represent those masked out due to observed or potential line emission. The pink points with error bars mark the binned down continuum points we fit in Section 10.4. The vertical cyan lines mark locations of prominent H_2 features in typical CTTS spectra France, Arulanantham, et al. (2023), while identified bright or well-known (but marginally detected) atomic emission lines are marked and labeled in maroon. The vertical shaded regions denote masked geocoronal emission. 234
10.2 The FUV and NUV STIS spectra (dark blue) and the continuum points we derived from the COS spectrum (pink circles with error bars). Our combined disk + shock model fit is shown (light blue) along with the individual model components, with the disk model in green and the 16,275 K blackbody component in maroon. Notice the sharp transition from the disk-dominated spectrum to the excess emission dominated spectrum at the 2060 Å continuum break. The model components have all been reddened to our adopted A_V = 1.5 mag and using the Whittet et al. (2004) extinction curve, which has a weaker 2200 Å bump than the commonly used Cardelli et al. (1989) curve. The effect of the bump can be seen as an undulation from 2000 Å to 2800 Å in the otherwise featureless reddened excess component blackbody spectrum. 235
10.3 The `corner` plot for our MCMC fit for the FU Ori FUV excess. Our adopted best-fit values are marked by the navy vertical lines, showing the medians of the histograms. The modal values, marked by light blue dotted lines, are identical to the median values. The contours in the 2-d histogram mark the 0.5, 1.0, 1.5, and 2.0 σ levels, while the vertical dashed lines mark the 16th and 84th percentiles in the 1-d histograms. 237

10.4 The $L_{\rm FUV}$ (this work) and L_X (Kuhn and Hillenbrand, 2019) for FU Ori, compared with YSOs in Taurus (Yang et al., 2012). FU Ori has among the highest L_X and has the highest $L_{\rm FUV}$ of the sample. The range of $L_{\rm FUV}$ for FU Ori reflects the two values we calculate depending on the assumed geometry of the emission region. The sources that have $L_{\rm FUV} > 0.05\ L_\odot$ are T Tau, HD 143006, and RY Tau, which are much earlier spectral types than the FU Ori central object would be (K1, G3, and G0, respectively, Herczeg and Hillenbrand, 2014). . 246

10.5 Selected bright emission line doublets commonly studied in the FUV spectra of YSOs. The data are plotted in black and the uncertainty on each point is shown in light grey. The blue and red lines mark the blue and red components of the doublets. The vertical cyan dashed lines mark the rest-wavelengths of H_2 lines and the vertical magenta dotted lines mark the rest frequencies of known features that may be contaminating the doublet line profiles (Cl I 1351.657, Fe II 1352.487, and O IV] 1401.17). 249

10.6 Detected bright emission lines commonly seen in the FUV spectra of YSOs. The data are plotted in black and the uncertainty on each point is shown in red. The rest-frequency of each line marked by the vertical grey line. Notice that, if present, the C I 1656 feature is only marginally detected. 250

10.7 The `corner` plot for the fit with a variable $T_{\rm FUV}$, $R_{\rm eff}$, $\dot{M}$ and A_V. The dark blue vertical and horizontal solid lines mark the median values of the histograms, while the light blue dotted lines mark the modal values. The agreement between the two in all but the $T_{\rm FUV}$ parameter show that the posterior distributions are well-behaved. The contours in the 2-d histogram mark the 0.5, 1.0, 1.5, and 2.0 σ levels, while the vertical dashed lines mark the 16th and 84th percentiles in the 1-d histograms. 253

10.8 The net counts in the COS G130M spectra from 1150 Å to 1200 Å. The λ_{cen} = 1309 Å points are shown in maroon and the λ_{cen} = 1222 Å points are shown as dark blue squares. The counts have been resampled to a grid with 100-pixel-wide bins. Prior to binning, we masked the spectrum following the procedure described in Section 10.2. We assume the uncertainties on each bin are Poisson-distributed. Notice that there are several bins with $\sim$ 10 counts, indicating a $> 3\ \sigma$ continuum emission detection. 254

11.1 The G230L and G430L spectra for each of our objects (dark blue), along with the disk (green) and disk + UV excess (light blue) models for each of the FUOrs in the survey. The shaded regions show the range of the 16th and 84th percentile models from the MCMC samples. The UV excess in each panel (maroon) matches the flux level of the binned continuum points (salmon) blueward of 2300 Å. The flux upper limits for V1057 Cyg, HBC 722, and BBW 76 are shown as empty triangles. 259

11.2 The excess emission observed in the STIS spectra and its luminosity for each FUOr in the survey. **Upper Panel:** The ratio of the observed binned STIS spectra used to fit the blackbody excess model and the disk models binned to the same wavelength sampling. Notice that for all the FUOrs in the sample, the NUV flux is at least 2× as bright as the disk model predicts at 2200 Å and for many the flux ratio is > 10 (for HBC 722 and V1057 Cyg, this is true at 2400 Å, despite the lack of data at 2200 Å). **Lower Panel:** The L_{excess} measurements for each of the FUOrs compared with their disk-model-derived L_{acc}. The mean and standard deviation on the UV excess luminosities (excluding BBW 76) are marked by the purple line and shading, respectively. . . 262

11.3 The STIS G230L spectra of the 6 FUOrs and the CTTS BP Tau for reference. The spectra are sorted top-to-bottom in order of decreasing signal-to-noise. The grey vertical lines mark the locations of the emission features discussed in Section 11.4. 264

11.4 Comparisons of the line luminosities in the FUOr sample and a representative CTTS (BP Tau). **Top:** The C II] (black circles), Fe II] (red triangles), and Mg II (blue squares) line luminosities for the FUOr sample and the CTTS BP Tau. Error bars are drawn but are smaller than the symbols for most measurements. The empty circle (triangle) for HBC 722 (BP Tau) represents the 3σ upper limit on the C II] (Fe II]) luminosity. The FUOrs are sorted left-to-right in order of increasing $L_{\rm acc}$. **Middle:** The same line C II] and Fe II] luminosities divided by the Mg II luminosities. **Bottom:** The $L_{\rm CII]}$ measurements plotted against the $L_{\rm acc}$ for the FUOrs. The black line shows the best-fit relation described in Section 11.4. 276

11.5 The two-dimensional rectified `x2d` HST/STIS images for each of our sources. The white hashes mark the locations of the C II] 2326, Fe II] 2500, and Mg II 2800 features and the surface brightness units are 10^{-14} erg s^{-1} cm^{-2} Å^{-1} arcsec^{-2}. Notice that the traces of FU Ori, V1515 Cyg, and V960 Mon are all detected down to at 1800 Å. BBW 76 is only marginally detected at 2100 Å. V1057 Cyg is only detected redward of the C II feature, with barely any continuum until 2400 Å, and HBC 722 is only detected redward of 2450 Å. 277

11.6 Spectrally averaged spatial cuts in the 2d spectra of V1057 Cyg (left), HBC 722 (middle) and BBW 76 (right). The spectral averaging was over $\sim$ 75 Å and the legend shows the mean wavelength of each bin. 277

11.7 **The posterior distributions for the blackbody fit described in Section 11.3. The red vertical and horizontal lines mark the median values for histogram, while the blue lines mark the modal values. The magenta line marks the $R_{\rm BB} \propto T_{\rm BB}^{-2}$ relation, anchored at the median $L_{\rm excess}$ value for each source.** 278

11.8 The G230L spectrum of BP Tau (black) compared with the median (brown line) and range (brown filled region) of G230L spectra of 50 CTTSs in the ULLYSES sample. The grey lines mark the locations of the NUV emission lines discussed in Section 11.4. Notice that there is no sign of the Fe II] emission feature at 2505 in either BP Tau or the ULLYSES sample. 279

12.1 The Hα line profiles of FUOrs captured with Keck/HIRES. As can be seen in the spectra of V960 Mon and HBC 722, the profiles can be highly variable. The lines all show a wide range of absorption velocities, sometimes reaching -500 km s^{-1}. The vertical grey line indicates the rest velocity of each line. 281
12.2 The Hβ line profiles of FUOrs captured with Keck/HIRES. As can be seen in the spectra of V960 Mon and HBC 722, the profiles can be highly variable. The lines all show a wide range of absorption velocities, sometimes reaching -500 km s^{-1}. The vertical grey line indicates the rest velocity of each line. 284
12.3 Na I D line profiles of FUOrs captured with Keck/HIRES. As can be seen in the spectra of V960 Mon and HBC 722, the profiles can be highly variable. The lines all have several absorption components, indicating a multi-layered structure to the outflow. The vertical grey line indicates the rest velocity of each line. 285
12.4 The Ca II IRT line profiles for each component of the triplet. Each of the three components is impacted on the red-shifted side by increasingly severe HP absorption from the 8502 Å, 8545 Å, and 8665 Å lines. The blue-shifted absorption profiles vary between the components due to the relative line strengths of the three. The vertical grey line indicates the rest velocity of each line. 286
12.5 The line profiles for the Fe II 5018 Å and Li I 6707 Å features. In most FUOrs, the Fe II 5018 line shows both disk-broadened absorption in the wings and a blue-shifted core indicative of low-velocity wind absorption. The Li I 6707 line, despite expectations that it should trace the disk atmosphere closely, shows surprising diversity in its profiles. 287
12.6 The Keck/HIRES spectra of 15 FUOrs, continuum normalized and offset for ease of comparison. The colors of the spectra of HBC 722 and V960 Mon mark different epochs spanning the first few years after the peaks of each the outbursts in each object. The spectra of Gaia 17bpi, V900 Mon, V733 Cep, and RNO 1b are all low signal-to-noise and have been smoothed by a Gaussian kernel with $\sigma = 5$ pixels. The non-smoothed spectra for the sources are also shown in light green. 288
12.7 Figure 12.6 continued. 289

12.8 Figure 12.6 continued. 290
12.9 Figure 12.6 continued. 291
12.10 Figure 12.6 continued. 292
12.11 Figure 12.6 continued. 293
12.12 Figure 12.6 continued. 294
12.13 Figure 12.6 continued. 295
12.14 Figure 12.6 continued. 296
12.15 Figure 12.6 continued. 297
12.16 Figure 12.6 continued. 298
12.17 Figure 12.6 continued. 299
12.18 Figure 12.6 continued. 300
12.19 Figure 12.6 continued. 301
12.20 Figure 12.6 continued. 302
12.21 Figure 12.6 continued. 303
12.22 Figure 12.6 continued. 304
12.23 Figure 12.6 continued. 305
12.24 Figure 12.6 continued. 306
12.25 Figure 12.6 continued. 307
12.26 Figure 12.6 continued. 308
12.27 Figure 12.6 continued. 309
12.28 Figure 12.6 continued. 310
12.29 Figure 12.6 continued. 311
12.30 Figure 12.6 continued. 312
12.31 Figure 12.6 continued. 313
12.32 Figure 12.6 continued. 314
12.33 Figure 12.6 continued. 315
12.34 Figure 12.6 continued. 316
12.35 Figure 12.6 continued. 317
12.36 Figure 12.6 continued. 318
12.37 Figure 12.6 continued. 319
12.38 Figure 12.6 continued. 320
12.39 Figure 12.6 continued. 321

13.1 The line profiles of He I 10830 and Paβ in FUOrs. **Left:** The He I 10830 Å triplet for the FUOrs in our NIRSPEC survey. Notice the diversity of line profiles and maximum outflow absorption velocities. The vertical solid grey lines mark the components of the triplet, while the dashed line marks the nearby Si I 10827 Å line and the dotted line marks an Mg I 10811 Å line. **Right:** The Paβ line for the FUOrs in the survey. It is much weaker than the visible range Hα or Hβ (see Chapter 12), but does show variability between epochs. The spectra of FU Ori and V1057 Cyg show this most dramatically, but it can also be seen in HBC 722. 325
13.2 All of the FUOr spectra taken for the Keck/NIRSPEC survey with sufficient signal at 1 μm for high resolution spectroscopy. Shown here is Y Band order 76. 326
13.3 Same as Figure 13.2 for Y Band order 75. 327
13.4 Same as Figure 13.2 for Y Band order 74. 328
13.5 Same as Figure 13.2 for Y Band order 73. 329
13.6 Same as Figure 13.2 for Y Band order 72. 330
13.7 Same as Figure 13.2 for Y Band order 71. 331
13.8 Same as Figure 13.2 for Y Band order 70. 332
13.9 Same as Figure 13.2 for Y Band order 69. 333
13.10 All of the FUOr spectra taken for the Keck/NIRSPEC survey with sufficient signal at 1.2 μm for high resolution spectroscopy. Shown here is *J* Band order 66. 334
13.11 Same as Figure 13.10 for *J* Band order 65. 335
13.12 Same as Figure 13.10 for *J* Band order 64. 336
13.13 Same as Figure 13.10 for *J* Band order 63. 337
13.14 Same as Figure 13.10 for *J* Band order 62. 338
13.15 Same as Figure 13.10 for *J* Band order 61. 339
13.16 Same as Figure 13.10 for *J* Band order 60. 340
13.17 Same as Figure 13.10 for *J* Band order 59. 341
13.18 Same as Figure 13.10 for *J* Band order 58. 342
13.19 Same as Figure 13.10 for *J* Band order 57. 343
13.20 All of the FUOr spectra taken for the Keck/NIRSPEC survey with sufficient signal at 1.6 μm for high resolution spectroscopy. Shown here is *H* Band order 51. 344
13.21 Same as Figure 13.20 for *H* Band order 50. 345

13.22 Same as Figure 13.20 for *H* Band order 49. 346
13.23 Same as Figure 13.20 for *H* Band order 48. 347
13.24 Same as Figure 13.20 for *H* Band order 47. 348
13.25 Same as Figure 13.20 for *H* Band order 46. 349
13.26 Same as Figure 13.20 for *H* Band order 45. 350
13.27 Same as Figure 13.20 for *H* Band order 44. 351
13.28 All of the FUOr spectra taken for the Keck/NIRSPEC survey. Shown here is *K* Band order 36. 352
13.29 Same as Figure 13.28 for *K* Band order 35. 353
13.30 Same as Figure 13.28 for *K* Band order 34. 354
13.31 Same as Figure 13.28 for *K* Band order 33. 355
13.32 Same as Figure 13.28 for *K* Band order 32. 356
14.1 The distance horizon to FUOrs for LSST and SPHEREx, calculated from the bolometric corrections for a range of A_V to the source. The shaded regions represent a range of assumed FUOr luminosities from 10 $L_\odot$ to 300 $L_\odot$. The square marks the furthest known FUOr, L222_1 and the circle marks the most embedded known FUOr. The dashed line marks the horizon for VLT/GRAVITY to resolve the < 2 AU inner region FUOrs to measure the disk inclination. 362
A.1 An example of plots from PypeIt showing major steps in the data reduction process. **Upper Left:** A sample quality assurance plot from the wavelength calibration of Order 60 in the J band. **Upper Right:** Order 60 of the A0V telluric standard spectrum (black) and the PHOENIX model (red) used to remove the Paβ line to produce a telluric absorption spectrum. **Bottom Panel:** A plot of Order 65 of the science spectrum (black), the telluric spectrum (green) and the telluric-corrected spectrum (red). Notice that the fringing is also removed by the division by the telluric absorption spectrum. 407

B.1 Results from rotationally broadening spectra using the two methods, direct integration and convolution. **Left:** A 5500 K PHOENIX (Husser et al., 2013) atmosphere model, broadened to 30 km s^{-1} using the two methods and assuming a limb darkening coefficient of 0.6. We show a small piece of spectrum to better distinguish the individual line profiles. The wavelength ranges ($\Delta\lambda$) and mean wavelengths ($\bar{\lambda}$) of each spectrum are given in the legend. Notice the "fast" convolution matches the direct integration almost perfectly when the wavelength range is small and the region of interest is near the center of that range. In that case, the result is the same as using the "slow" method. However, for the larger wavelength range, where we are now far from the mean central wavelength, the broadening accuracy is much worse. The direct integration case is computed on the $\Delta\lambda = 2800$ Å case. **Right:** The times for the two broadening method as a function of the length of the array being broadened. Notice the rapid increase in time for the convolution method compared to integration. The spectra shown are sampled at $d\lambda \sim 0.01$, so $\Delta\lambda = 1000$ is a 10^5 element array. The grid used for the integration has $N_r = 10$ and $N_\theta = 100$, the default values for our function. 411

LIST OF TABLES

Number *Page*

2.1 Physical parameters for FUOrs derived using the disk model described in this Thesis. Note that parameters like $\dot{M}$, $R_{\rm inner}$ and the emergent $T_{\rm max}$ and $L_{\rm acc}$ all vary over the course of an outburst. The parameters reported in this Table reflect the state of each system at the time of observation. For V1057 Cyg, V1515 Cyg, and BBW 76, the epoch is 2014 – 2016. The distance references are as follows: FU Ori (Kounkel et al., 2018; Roychowdhury and Hillenbrand, 2024a); V1057 Cyg (Szabó, Kóspál, Ábrahám, Park, Siwak, Green, Moór, et al., 2021); V1515 Cyg (Szabó, Kóspál, Ábrahám, Park, Siwak, Green, Pál, et al., 2022a); V960 Mon (Kuhn and Hillenbrand, 2019); HBC 722 (Kuhn and Hillenbrand, 2019); BBW 76 (Gaia Collaboration, Vallenari, et al., 2023); RNO 54 (Hillenbrand, Carvalho, van Roestel, et al., 2023); V890 Aur (Hillenbrand, Carvalho, Stern, et al., 2025a); V883 Ori (Kounkel et al., 2018). Many of the distances in this table have been updated from those adopted by Connelley and Reipurth (2018) and used in Table 2.2. 14

2.2 $L_{\rm acc}$ values compared with the $L_{\rm bol}$ values in Connelley and Reipurth (2018), using the distances, K band measurements, and A_V therein. When available, inclinations were obtained from Kóspál, Cruz-Sáenz de Miera, et al. (2021), Pérez et al. (2020), Cieza, Ruíz-Rodríguez, et al. (2018), and Carvalho, Hillenbrand, Seebeck, and Covey (2024). All others, marked with brackets, are assumed to be 60°. 25

3.1 V960 Mon System parameters at each HIRES epoch. Parameters in the first epoch are all best-fit parameters from the procedure described in Section 3.3. For later epochs, $\dot{M}$ and $R_{\rm inner}$ are estimated using the color-temperature method in Section 3.4. The parameters shown in italics in later epochs are fixed. 53

3.2 Photometry from AAVSO, Gaia, Gattini, and WISE, shown in Figure 3.1. The full, machine-readable version of the table is available in the online journal 61

4.1 Spectroscopic Observations Log 65

5.1 Spectroscopic Observations Log 107

6.1 Best-fit values for the `dynesty` MCMC disk + scattering model. . . . 158

6.2 The V, R, I, $W1$, and $W2$ band photometry of V883 Ori show in Figure 6.7. The full table is available in the online journal. 170
7.1 Polynomial coefficients c_0, c_1, c_2 in front of absolute magnitudes (see Equation 7.2) for the bolometric corrections of FU Ori objects. Also provided are $A_{\lambda,\mathrm{disk}}/A_V$ values specifically computed for the viscous disk model. 178
7.2 Comparison between the measured accretion luminosities (L_{true}) for HBC 722 and V960 Mon, and those we estimate using our BCs ($L_{\mathrm{bol,disk}} = L_{\mathrm{acc}}$). 182
7.3 Polynomial coefficients c_0, c_1, c_2 in front of absolute magnitudes (see Equation 7.2) for the bolometric corrections of FU Ori objects using models of a constant $T_{\mathrm{max}} = 6,000$ K. Additional information for each filter can be found in Table 7.1. 186
8.1 The v_{max} measurements for FUOr with a Keck/NIRSPEC H band spectrum. While V1057 Cyg is included in this table for completeness, the CCFs are likely tracing the extreme wind absorption in this source, rather than disk broadening. 191
11.1 HST/STIS Observations Log 258
11.2 The adopted disk model parameters for each object in the sample. Note that parameters like $\dot{M}$, R_{inner} and the emergent T_{max} and L_{acc} all vary over the course of an outburst. The parameters reported in this Table reflect the state of each system at the time of observation. The distance references are as follows: FU Ori (Kounkel et al., 2018; Roychowdhury and Hillenbrand, 2024a); V1057 Cyg (Szabó, Kóspál, Ábrahám, Park, Siwak, Green, Moór, et al., 2021); V1515 Cyg (Szabó, Kóspál, Ábrahám, Park, Siwak, Green, Pál, et al., 2022a); V960 Mon (Kuhn and Hillenbrand, 2019); HBC 722 (Kuhn and Hillenbrand, 2019); BBW 76 (Gaia Collaboration, Vallenari, et al., 2023). 260
11.3 The best-fit blackbody component parameters and NUV emission line luminosities for each object in the sample. The best-fit blackbody component parameters for FU Ori are adopted from **Carvalho_FUVSpectrumFUOri_2024ApJ**, since that analysis includes FUV data that can better constrain T_{BB}. 275

13.1 The observing log for the Keck/NIRSPEC Survey we conducted from 2022-2023. The exposure times are the total on-source integration time and are reported in seconds. 357
13.2 Table 13.1 continued. 358
13.3 Table 13.1 continued. 359

Chapter 1

INTRODUCTION

The primary subject of this thesis is a class of outbursting accreting young stellar objects (YSOs), called FU Ori objects (FUOrs). These objects take on mass at a rate $10,000\times$ greater than their non-outbursting counterparts during episodes that can last up to 100s of years. It has been argued that all low mass ($M_* < 2\ M_\odot$) young stars undergo a stage during their formation during which they experience these episodic accretion outbursts. There is even some evidence that our own Solar System has undergone such an outburst.

There are many misconceptions about FUOrs and what is known about them to date. To better contextualize the place of these objects in the story of star and planet formation, I will begin with an overview of the main stages of star formation. I will then give a review of the history of FUOrs as a class of YSOs and how the structure of the inner disk changes during an FU Ori outburst. Following this, I will discuss the primary sets of theories for what triggers such extreme outbursts and how observations can constrain or rule out different theories. In the final sections of this chapter, I will broadly describe the questions this Thesis aims to answer.

1.1 An overview of the main stages of star formation

Star formation in a galaxy begins in giant molecular clouds, where gas densities can reach $10^3 - 10^6$ cm^{-3} (Draine, 2011). As gravity attracts the dense material to itself, density fluctuations in the cloud (pre-stellar cores) grow rapidly, until reaching a point (often called the Jeans density, Jeans, 1902), where the gravity overwhelms the gas (and magnetic field) pressure support. The material then collapses toward the center of mass until a sufficiently high temperature and density is achieved at the core of the cloud to halt the collapse. This, then, is a protostar.

The following steps for the stages of pre-main-sequence evolution were first clearly laid out in Adams et al. (1987). Following the collapse of the pre-stellar core, the protostar is still surrounded by a dense envelope of cloud and dust. The emission from the contracting protostar is powered by the heat of gravitational energy being converted to radiation. The remaining material from the collapse, in order to conserve the initial angular momentum of the cloud, settles into a disk around the

protostar. This is often referred to as the “protoplanetary disk".

Over the next few 100 kyr, the protostar will accrete material from and, via powerful outflows, clear away its envelope. Once the star is a few Myr in age, the majority of its initial disk mass has also dissipated via accretion onto the star and evaporative processes that drive disk material into the circumstellar medium. As the disk clears, all that will remain is the protostar, as well as any planets or planetesimals that may have formed around it in its protoplanetary disk. The protostar will continue to contract until its core reaches sufficient density to ignite hydrogen fusion, at which point it will join the stellar zero age main sequence.

These steps in pre-main sequence evolution can also be divided into stages empirically by the shapes of their spectral energy distributions (SEDs). Using mostly near-infrared (NIR) photometric observations of objects in Ophiuchus, Lada and Wilking (1984) found three classes of SEDs, which were explicitly delineated in Lada (1987) as: “protostars,” “T-Tauri star,” and “post T-Tauri stars.” These were assigned to SED Classes I, II, and III. The traditional definitions of these classes, based on the spectral slope of the SED in the IR ($\alpha = d \log \lambda F_\lambda / d \log \lambda$) are briefly enumerated below. The α boundaries provided are those defined in Greene et al. (1994).

1. Class I: the SED is entirely dominated by emission from the envelope. $\alpha > 0.3$.
2. Class II: the envelope has mostly dissipated and the SED is much more flat, with excess emission in the NIR/MIR mostly from the protoplanetary disk and envelope emission in the FIR. The SED contribution from the protostar can be clearly seen and the SED is much broader than a blackbody. $-1.6 < \alpha < -0.3$.
3. Once the disk has mostly dispersed, the emission is dominated by the star, with only a very small IR excess relative to the blackbody. $\alpha < -1.6$.

There are two additional stages that have been delineated since the original classification: Class 0 and Flat Spectrum. Class 0 sources (Barsony, 1994) emit almost all of their light in the FIR and millimeter wavelengths, and represent the earliest stages of the collapse of the pre-stellar core. Flat Spectrum sources (Greene et al., 1994) have SEDs with intermediate slopes between Class I and Class II: $-0.3 < \alpha < 0.3$.

The eruptive YSOs I will discuss in this thesis span the Class I to Class II stages in their SEDs. As will be discussed below, the Class II sources appear to be have

recently entered this evolutionary stage, as they have larger disk masses than most of the known Class II YSOs.

1.2 So what exactly are FUOrs?

The namesake of the class, FU Ori, was discovered when it began its outburst in 1937 (Wachmann, 1954). The source brightened by 5 magnitudes in the visible range and exhibited a spectrum unlike any other star observed at the time. After almost three decades of observations following its outburst, the first notion that FU Ori might be a YSO was raised by Herbig (1966). In this work, Herbig proposed that the eruption might be the first observation of a prestellar core collapsing to form a protostar.

Over the following 10 years, 2 more FUOrs were identified: V1057 Cyg and V1515 Cyg. Comparing the apparent frequency of the outbursts with the known YSO population led Herbig (1977) to presented a new theory for FUOrs: that they are merely T Tauri stars (TTSs) experiencing some transient, energetic event. Herbig (1977) also argued that these events should not be once-in-a-lifetime for young stars but may repeat over the first few Myr post-formation.

In the following decade, an answer to the mysterious outbursts was provided by the work of Hartmann and Kenyon (1985a), who hypothesized that they were caused by sudden increases in the disk-to-star accretion rate. They also demonstrated that the observed line profiles of FUOrs could be reproduced using a modified form of the thin, viscously heated accretion disk developed by Shakura and Sunyaev (1973). The radial temperature profile for FUOr accretion disks was presented in a more thorough paper (Kenyon, Hartmann, and Hewett, 1988), in which the model was shown to successfully match the spectra of three FUOrs. The temperature profile proposed for FUOr disks is nearly identical to the Shakura and Sunyaev (1973) profile,

$$T_{\rm eff}(r)^4 = \frac{3GM_*\dot{M}_{\rm acc}}{8\pi\sigma_{SB}r^3}\left[1-\sqrt{\frac{R_{\rm inner}}{r}}\right], \tag{1.1}$$

where M_* is the stellar mass, $\dot{M}_{\rm acc}$ is the disk-to-star accretion rate, $R_{\rm inner}$ is the innermost radius of the disk, σ_{SB} is the Stefan-Boltzmann constant, and G is the gravitational constant. An important modification is that for $r < \frac{49}{36}R_*$ (where the temperature profile attains its maximum), the disk is set to be isothermal. Thus $T_{\rm eff}\left(r < \frac{49}{36}R_*\right) = T_{\rm max} \equiv T_{\rm eff}\left(\frac{49}{36}R_*\right)$. The luminosity of the disk, $L_{\rm acc}$, is given by

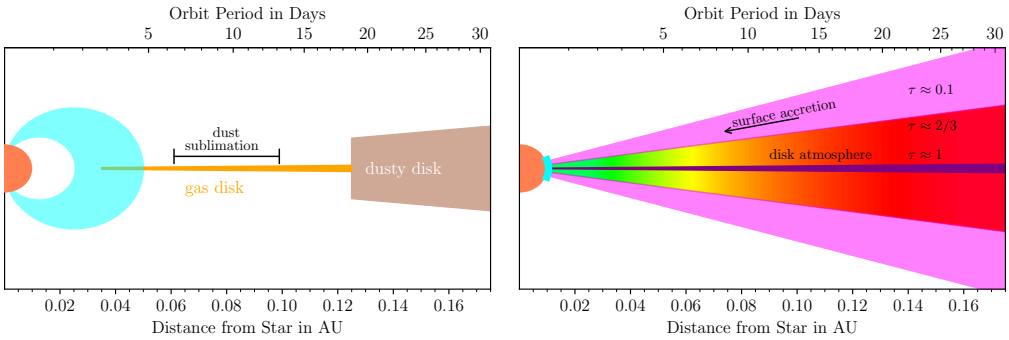

Figure 1.1: A schematic showing the inner region of a disk during the CTTS magnetospheric accretion stage (left) and during an FU Ori outburst (right). The physical parameters of the sample CTTS on the left are: $M_* = 0.6\ M_\odot$, $R_* = 2\ R_\odot$, and $R_T \sim 3\ R_*$. The location of the R_T and the dust sublimation region is informed by values from NIR interferometry (GRAVITY Collaboration et al., 2021). The FUOr schematic representative of the temperature structure of the inner disk of FU Ori itself (Zhu, Jiang, et al., 2020; Carvalho, Hillenbrand, France, et al., 2024).

the equation

$$L_{\rm acc} = \frac{1}{2}\frac{GM_*\dot{M}}{R_{\rm inner}}. \tag{1.2}$$

The gas near the star is assumed to be in Keplerian rotation, and therefore follows a Keplerian velocity profile. However, the observed orbit velocity, v_K, of a given annulus at r is projected on the sky according the the inclination, i, of the annulus with respect to the observer. Thus $v_{\rm obs}$ is given by

$$v_{\rm obs}(r) = v_K(r)\sin i = \sqrt{\frac{GM_*}{r}}\sin i. \tag{1.3}$$

At the stellar surface, the velocity reaches its maximum and we obtain another useful quantity, $v_{\rm max} = v_{\rm obs}(R_*)$. Since we always assume that the gas is in Keplerian orbit around the star, the choice of $v_{\rm max}$ prescribes the (viewer projected) velocity profile in units of R_* uniquely.

In the model that FU Ori outbursts are in fact disk accretion events in CTTSs, the accretion rate reaches values of $10^{-5} - 10^{-4}\ M_\odot\ {\rm yr}^{-1}$ (Hartmann and Kenyon, 1996). The resulting increase to the ram pressure of the accretion flow crushes the magnetosphere of the CTTS and the inner disk reaches the stellar surface. A schematic of this is shown in Figure 1.1. While the observations can be modeled with a vertically thin accretion disk, the disk has a distinct vertical structure. The viscous heating is able to rapidly raise the midplane temperature to the $\sim 2,500$

K necessary to ionize species like Ca, Mg, and Fe. The abundant freed electrons produce large amounts of H^-, which has a large continuous opacity at temperatures of $3,000-6,000$. The H^- can efficiently trap the viscous heat and raise the midplane temperature as high as $35,000$ K near the star (Zhu, Jiang, et al., 2020; Nayakshin and Elbakyan, 2024).

The hot midplane supports above it a plane-parallel atmosphere in hydrostatic equilibrium with the stellar gravity, not unlike a simplified model for a stellar photosphere. The atmosphere is shown in the schematic in Figure 1.1, with the color scale representing the radial temperature profile.

There are several lines of evidence that indicate the evolutionary state of FUOrs is likely Class I or early Class II. The first is that analysis of the SEDs of the majority of known FUOrs are consistent with Flat Spectrum or Class I sources (Gramajo et al., 2014). Those that have SEDs more consistent with Class II sources still seem to have large envelope masses, indicating that they have only recently entered the Class II stage and have not fully cleared out their envelopes. A second line of evidence is the large disk masses of FUOrs, as seen with ALMA. The majority of FUOr disks observed with ALMA have disk-to-star mass ratios greater than 0.1. Such large disk masses are typically associated with very young Class I source (Manara et al., 2023).

The final line of evidence I will mention is the fact that there is a visible range spectrum of the FUOr HBC 722 that is fully consistent with a typical accreting Class I/II YSO. The spectrum is presented in Chapter 5. It shows that, prior to its outburst, HBC 722 had an M4 spectral type and, based on its Hα luminosity, a mass accretion rate of $8 \times 10^{-8}\ M_\odot\ \mathrm{yr}^{-1}$. The accretion rate is high for Class II YSOs (Manara et al., 2023), but in the range seen for Class I sources (Fiorellino et al., 2023). This visible range spectrum of a pre-outburst FUOr provides the strongest constraints on the properties of the pre-outburst object, as well as conclusive evidence that the progenitors of FUOrs are indeed Class I/II YSOs undergoing magnetospheric accretion.

1.3 The missing trigger of FU Ori outbursts

A critical missing piece of the outburst puzzle remains the actual trigger of such a massive outburst. In the picture of magnetospheric accretion, there are small scale instabilities like local vortices or rapid changes to the magnetic field topology that can lead to low amplitude, $\Delta V \sim 2$ mag, accretion outbursts (Fischer et al.,

2023a). Even larger-amplitude, $\Delta V \sim 3-4$ mag, but shorter-lived accretion bursts like EX-Lup-type events, can happen spontaneously in a massive young disk with efficient inward radial transport of material (Cecil and Flock, 2024).

Despite the large amplitudes of EX Lup bursts, they only last a few months or up to 2 years (Fischer et al., 2023a). The fact that they are short-lived indicates that the amount of mass ($\dot{M} \times \Delta t = 2 - 4 \times 10^{-7}\ M_{\odot}$; Sicilia-Aguilar, Kóspál, et al., 2012; Sicilia-Aguilar, Fang, et al., 2015; Wang, Herczeg, et al., 2023) accreted per event is relatively low compared to FU Ori outbursts. FU Ori itself, assuming an accretion rate of at least $10^{-4.5}\ M_{\odot}\ \mathrm{yr}^{-1}$ (Carvalho, Hillenbrand, France, et al., 2024) over the past 87 years, has accreted almost 3 M_{Jup} of material.

If we assume a relatively flat surface density profile in the inner disk and a surface density of $\Sigma = 10^4\ \mathrm{g\ cm}^{-2}$, the total mass accreted by the star extends to 1 au. Given the likely lower surface density profile of the pre-outburst disk (e.g., Williams and McPartland, 2016), the outburst would have to have started at around 2-5 au to encompass enough material to power the burst we continue to observe today. However, at 2-3 au, the disk is highly inviscid due to the low ionization fraction and temperature (Gammie, 1996), so it is difficult to produce the high accretion rate seen in FU Ori outbursts.

This has led rise to the proposal of external triggers, which might disrupt the disk of a CTTS and lead to an FU Ori outburst. The four main classes of external triggers are: planet engulfment, binary or flyby encounters, and late-stage envelope infall.

Planet engulfment

Planet engulfment was proposed as one of the first theories to explain FU Ori outbursts (Herbig, 1977). Although the outburst itself has been found to result from an accretion event, recent work has revived a version of the hypothesis as a source of mass to feed the burst. Nayakshin, Owen, et al. (2023) show that if a Jupiter mass planet is in a tight orbit ($a_p < 0.1$ au) and the star undergoes an EX Lup type eruption, the high temperature reached in the disk midplane can unbind the atmosphere of the young planet. The unbound Jovian atmosphere can then provide a mass reservoir to extend the duration of the otherwise short-lived burst.

This model is compelling as an explanation for a few mysteries observed in FU Ori itself. The first is that the active accretion region is constrained (via NIR interferometry) to be ~ 0.3 au (Lykou, Ábrahám, Chen, et al., 2022). This is much smaller than the few au mentioned above as the necessary feeding zone size. Another

is that the disk of FU Ori has a mass of only $\sim 7-20\ M_{\rm Jup}$ (Pérez et al., 2020; Lykou, Ábrahám, Chen, et al., 2022), meaning the disk to star mass ratio is < 0.04 and the disk is therefore unlikely to be gravitationally unstable. This further complicates the ability to trigger an outburst in the disk at a few au. A Jovian planet serving as a mass reservoir near the star allows for a small active region and alleviates the need to trigger the outburst far out in the disk.

There are also, of course, challenges to the model. The most glaring of these is the need to efficiently form, and then rapidly migrate, such a massive planet to a close-in orbit. The first exoplanet discovered around a Sun-like star, 51 Pegasi b, is one such close-in giant planet (Mayor and Queloz, 1995), and since its discovery dozens of these hot Jupiters have been found[1]. The exact formation mechanism for hot Jupiters planets remains a mystery, with competing theories favoring in-situ formation, formation in the disk followed by disk-driven migration, or high eccentricity migration (see Dawson and Johnson, 2018, and references therein). Furthermore, observations of older planetary systems indicate that giant planets are much less common around lower mass stars. For the low mass FUOrs (e.g., RNO 54, V890 Aur, HBC 722, BBW 76: Hillenbrand, Carvalho, van Roestel, et al., 2023; Hillenbrand, Carvalho, Stern, et al., 2025b; Carvalho, Hillenbrand, Seebeck, and Covey, 2024, this thesis), the chance of rapidly forming a hot Jupiter becomes exceedingly small. This hypothesis may explain the outbursts in more massive systems like FU Ori and V883 Ori, but it is unlikely that the very low mass FUOrs are driven by the evaporation of hot Jupiters.

Binary or fly-by encounters

The idea that FU Ori outbursts could be triggered by the tidal interaction of the disk of the FUOr with a binary companion was first proposed by Bonnell and Bastien (1992). In this model, the outburst is triggered at the periastron passage of the binary system and should therefore be periodic. The binarity of FU Ori (Wang, Apai, et al., 2004; Reipurth and Aspin, 2004), as well as other famous FUOrs like Z CMa (Koresko et al., 1991), and V1057 Cyg (Green et al., 2016), appears to support this theory.

Another version of this theory is that the triggering encounter is not the periastron passage of a bound binary companion but rather a flyby of an unbound member of the star's birth cluster. Hydrodynamical simulations of such flyby encounters at a

[1] `https://exoplanetarchive.ipac.caltech.edu/`

range of impact parameters and orbit orientations (Cuello, Dipierro, et al., 2019; Cuello, Louvet, et al., 2020) are able to reproduce many of signatures observed in scattered light images of the circumstellar environments of eruptive YSOs (Zurlo et al., 2024a). Returning to the case of Z CMa, a large filamentary structure seen in scattered light can be reproduced in hydrodynamical simulations assuming the binary system experienced a flyby collision with a third object (Dong et al., 2022). A nearby infrared source at the end of the filament is suggested to be the interloper.

The flyby or binary interaction scenario is a compelling explanation for some FU Ori outbursts, but not all. While some have been found to be binaries, stellar mass companions to the objects V1515 Cyg and HBC 722 have been ruled out with high sensitivity, high spatial resolution NIR observations (Green et al., 2016). As for the known binary FUOrs, the two main challenges to the interaction-driven outbursts are the potential frequency (or paucity) of such interactions and the long orbit times of the systems compared with the recency of their outbursts.

In the case of FU Ori, the separation between the components of the binary is $\sim$ 200 au and the binary is known to be bound (ruling out a hyperbolic flyby, Pueyo et al., 2012). Assuming the system is at its periastron now, has a semimajor axis of $\sim$ 200 au, and that the masses of the components are 0.6 $M_\odot$ and 1.2 $M_\odot$ (Beck and Aspin, 2012), the period of the orbit is $\sim$ 2000 years. It is therefore unlikely that the periastron passage could have triggered the outburst.

Late-stage envelope infall

The discovery of a likely accretion streamer in FU Ori (Hales et al., 2024) and polarimetric imaging of outbursting YSOs showing large, filamentary structures surrounding many well-known sources (Zurlo et al., 2024a) has renewed interest in the envelope-infall-driven outburst theory. The idea originates from the notion that the transfer of mass from envelope to disk might be more rapid than the transfer of disk onto star (Bell and Lin, 1994). This would naturally cause mass to build up in the disk, rendering it potentially gravitationally unstable or, in the picture of Bell and Lin (1994), unstable to the classical thermal instability.

Envelope infall in the FUOr-like sources V346 Nor and L1551 IRS 5 have also been suggested potentially be connected to the outburst (Momose et al., 1998; Kóspál, Ábrahám, Csengeri, et al., 2017). In both of these sources, as well as FU Ori, the envelope infall rates are estimated to be $10^{-7} - 10^{-6}$ $M_\odot$ yr^{-1}, much lower than the disk-to-star accretion rates of $10^{-5} - 10^{-4}$ $M_\odot$ yr^{-1}, but higher than the expected

quiescent state mass accretion rates of $10^{-8} - 10^{-7}$ $M_{\odot}$ yr^{-1}. This supports the idea that the envelope loads mass onto the disk faster than the disk can be depleted, leading to an outburst during which the mass is impulsively removed from the disk.

An advantage of this scenario in explaining outbursts is that it enables large reservoirs of mass to accumulate at radii several AU away from the central star (Pavlyuchenkov et al., 2020). As mentioned above, the outburst trigger location is expected to be far out in the disk in order to provide the necessary mass to power the long-lived outburst. The pile-up of material is aided by the existence of the MRI dead zone in the disk at a few AU. The weak accretion/turbulence predicted in this region will naturally cause the excess material infalling from the envelope to pile up at its outer edge. Models where the material piles up at around 5 – 10 AU for high envelope infall rates most sucessfully reproduce FUOr-like outbursts (Maksimova et al., 2020).

The feasibility of the infall-driven outburst hypothesis relies in part on better understanding the ubiquity of accretion streamers or infalling envelopes around eruptive YSOs. Constraining this requires deep observations of each object, because bright molecular gas tracers like ^{12}CO and ^{13}CO are contaminated by emission from large scale outflows in the objects and can rapidly become optically thick. Detecting the streamers and accurately measuring the masses contained in them is best done with C^{18}O, which is much fainter and thus harder to detect than the brighter CO isotopologues. Another observational challenge is the large distances to much of the FUOr sample, which makes high angular resolution critical to finding true infalling streamers. Dedicated large programs with ALMA will likely be necessary to comprehensively survey the envelopes of FUOrs and other eruptive YSOs and constrain the frequency of streamers. Improved sensitivity of millimeter-wavelength facilities like ALMA (via the Wideband Sensitivity Upgrade) and JVLA (via the Next Generation VLA) will aid in these deeper searches for accretion streamers as well.

How can we identify the trigger?

Identifying the trigger mechanism for FU Ori outbursts is crucial to illuminating how frequently they occur during a disk's lifetime and whether they might affect all young stars or only a select few. If the outburst trigger relies on a rare event like a flyby interaction, a collision with ejected gas, or extreme evaporation of a young hot

Jupiter, it is extremely unlikely to repeat[2]. On the other hand, if the trigger relies on infall from the circumstellar envelope, delayed-onset accretion following binary periastron passage, or some mechanism intrinsic to young, massive disks, a system may experience several FU Ori outbursts during its first few Myr.

Similarly, if the trigger mechanism relies on the occurrence of rare events or specific orbit architectures it is unlikely (or impossible) that all young stars will undergo a "FUOr" stage during their formation. If, instead, the outburst is triggered by infall from the circumstellar envelope or a high disk to stellar mass ratio, the only restriction this likely places on the FUOr stage is that it must happen early after the formation of the disk. Any YSO may undergo a FUOr stage in these cases.

A necessary step to better understand the trigger and the ubiquity of FU Ori outbursts in the YSO population is knowing the properties of the central stars in these systems. For most FUOrs known today, the only way to do this is to indirectly infer the properties of the central star based on the dynamics of the disk surrounding it during the outburst. This leaves many basic properties of FUOrs, such as their mass distribution, radius distribution, and accretion rate distribution, still unknown. Is there a tendency for FUOrs to be very low mass stars? Or is their mass distribution representative of the Class I/II YSO population generally? Similarly, the canonical mass accretion rate usually cited for FUOrs is $10^{-5} - 10^{-4}$ $M_{\odot}$ yr^{-1} (e.g., Hartmann and Kenyon, 1996; Audard et al., 2014; Fischer et al., 2023a), but how are these values derived and what about the outbursts sets this range[3]? Another canonically adopted value is that the luminosity of a source in outburst will be 100 $L_{\odot}$, which is the typical value adopted for FU Ori. However, in the past 10 years, new FUOrs have been discovered with much lower luminosities, despite otherwise meeting the photometric and spectroscopic requirements to be classified as FUOrs (e.g., Gaia 17bpi and V890 Aur Hillenbrand, Peña, et al., 2018; Hillenbrand, Carvalho, Stern, et al., 2025a). Are the outbursts in these objects different from "typical" FU Ori outbursts?

[2]In the case of the young hot Jupiter, this is not strictly true. It is conceivable that the planet's atmosphere is not stripped away entirely during a single event and that enough material remains to feed future outbursts.

[3]A model of the triggering and evolution of the classical thermal instability in FUOrs has recently shown that objects with accretion rates in this range belong to the "hot branch" of the thermal instability, while eruptive objects that do not reach these accretion rates fail to trigger the instability (Nayakshin and Elbakyan, 2024).

1.4 The aims of this Thesis

The work in this thesis represents an attempt to build a clearer picture of these objects on both an individual and class-wide basis. The first step in this endeavor has been to test the limits of the disk model in its ability to reproduce the observed spectra of FUOrs.

To this end, I have built a new framework to fit the SEDs of FUOrs incorporating constraints from their high resolution spectra and established new means of constraining parameters such as $L_{\rm acc}$, $T_{\rm max}$, and $v_{\rm max}$ for each object. I have applied these developments to study the time evolution of two FUOrs in the first 5-10 years of their outbursts and produce new measurements of physical properties for long studied objects like V883 Ori, V1057 Cyg and V1515 Cyg. I have also identified a new and unexpected UV emission component, in excess of the emission from the viscous disk, that sheds new light on the physics of the star-disk boundary in FUOrs.

Chapter 2

A NEW FRAMEWORK FOR FITTING FUOR DISK SPECTRA

In principle, the implementation of the Kenyon, Hartmann, and Hewett (1988) disk model is relatively straightforward. One need only discretize the disk radially into several annuli, each representing a single $T_{\rm eff}$ value prescribed by Equation 1.1. A spectrum with the appropriate $T_{\rm eff}$ can be assigned to each annulus, and then summing the area-weighted fluxes from each annulus, we obtain a spectrum representing the disk. An important caveat in this model is that it represents only the inner ~ 0.5 au of the disk. Further out, the temperatures are cool enough that contribution of dust both in absorption and emission cannot be neglected and a more detailed treatment becomes necessary.

Historically, there have been two approaches to constructing a disk model spectrum. At high resolution, the model constitutes area-weighting spectra of standard stars with $T_{\rm eff} = 3,000-9,000$ (e.g., Kenyon, Hartmann, and Hewett, 1988; Welty, Strom, Edwards, et al., 1992; Herbig et al., 2003). To model the SEDs, the spectra are replaced with blackbody functions, due to the challenge of obtaining large libraries of standard star spectra with the necessary temperature sampling and wavelength coverage.

More recently, with the broad distribution of accurate synthetic stellar spectral libraries with dense sampling of both surface gravity $\log g$ and $T_{\rm eff}$, disk models have taken advantage of these for their annulus spectra (e.g., Rodriguez and Hillenbrand, 2022; Liu et al., 2022). This enables us to compute model SEDs spanning broad wavelength ranges while retaining crucial information about the atomic and molecular absorption features of the spectra. As shown in Figure 2.1, the blackbody-only SEDs are comparable to the stellar-spectrum-based SEDs in the wavelength range $0.4 - 5.0$ μm, and can thus be used to model SEDs constructed from multiband photometry reasonably well. For $\lambda < 0.4$ μm, the bound-free continuous opacity of metals like Mg, Al, and Si become non-negligible (Travis and Matsushima, 1968), as does the Balmer break for higher temperatures. In the NIR, the blackbody SEDs miss the strong molecular absorption, which can be important to constraining the outer radius of the active disk (Carvalho, Hillenbrand, Seebeck, and Covey, 2024).

The disk model I have worked with is based on that initially developed in Rodriguez

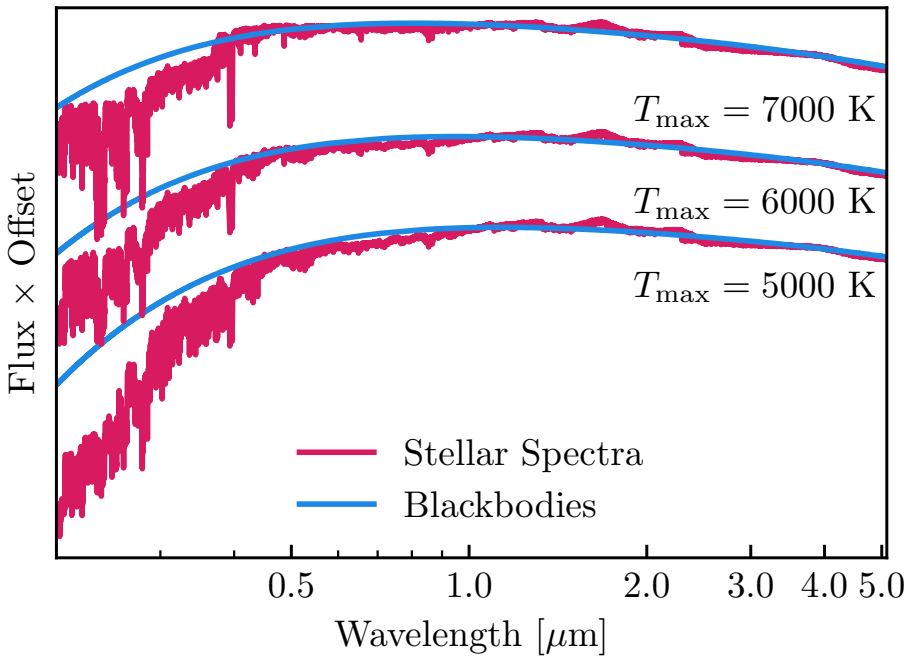

Figure 2.1: A comparison of the disk models constructed using only blackbodies (blue) versus those constructed using synthetic stellar spectra (red).

and Hillenbrand (2022). The SEDs shown in Figure 2.1 are from this model. In this Chapter, I detail the improvements made to the Rodriguez and Hillenbrand (2022) model to expand its flexibility and ability to rapidly produce high resolution spectral models spanning $0.1 - 5.0$ μm. I will then demonstrate the importance of modeling the high resolution spectra of FUOrs to better constrain the SED fits. I will also discuss limitations of the disk model and what can be learned from the spectral features it fails to reproduce.

2.1 Computing the Spectrum of a Disk

In the previous Chapter, I gave a general description of the Kenyon, Hartmann, and Hewett (1988) disk model for FU Ori objects, including the prescriptions for the temperature profile (Equation 1.1), accretion luminosity (Equation 1.2), and the Keplerian orbit velocity profile (Equation 1.3). While these equations together do describe the emergent spectrum of the disk atmosphere, they are insufficient to compare with observations. In order to do that, there are 4 additional parameters that must be accounted for: i, the inclination of the disk with respect to the observer, d, the distance to the disk, A_V, the extinction along the line of sight, and $R_{\rm outer}$, the outermost edge of the disk that can be described via this thin viscous accretion disk

model[1].

The implementation of the disk model that I will describe here is that which we demonstrated in Carvalho, Hillenbrand, Hambsch, et al. (2023) and Carvalho, Hillenbrand, Seebeck, and Covey (2024). The model has been successfully applied to fit the visible and NIR spectra of 9 FU Ori objects thus far. The best-fit parameters for these objects are presented in Table 2.1.

Table 2.1: Physical parameters for FUOrs derived using the disk model described in this Thesis. Note that parameters like $\dot{M}$, $R_{\rm inner}$ and the emergent $T_{\rm max}$ and $L_{\rm acc}$ all vary over the course of an outburst. The parameters reported in this Table reflect the state of each system at the time of observation. For V1057 Cyg, V1515 Cyg, and BBW 76, the epoch is 2014 – 2016. The distance references are as follows: FU Ori (Kounkel et al., 2018; Roychowdhury and Hillenbrand, 2024a); V1057 Cyg (Szabó, Kóspál, Ábrahám, Park, Siwak, Green, Moór, et al., 2021); V1515 Cyg (Szabó, Kóspál, Ábrahám, Park, Siwak, Green, Pál, et al., 2022a); V960 Mon (Kuhn and Hillenbrand, 2019); HBC 722 (Kuhn and Hillenbrand, 2019); BBW 76 (Gaia Collaboration, Vallenari, et al., 2023); RNO 54 (Hillenbrand, Carvalho, van Roestel, et al., 2023); V890 Aur (Hillenbrand, Carvalho, Stern, et al., 2025a); V883 Ori (Kounkel et al., 2018). Many of the distances in this table have been updated from those adopted by Connelley and Reipurth (2018) and used in Table 2.2.

Object	M ($M_\odot$)	$\log\dot{M}$ ($M_\odot$ yr^{-1})	$R_{\rm inner}$ ($R_\odot$)	inc (deg)	A_V (mag)	d (pc)	$T_{\rm max}$ (K)	$L_{\rm acc}$ ($L_\odot$)
FU Ori	0.60	−4.49	3.52	35	1.50	404	5970	86
V1057 Cyg	1.61	−5.17	2.67	8	2.72	795	6357	63
V1515 Cyg	0.69	−5.24	1.82	2	2.23	960	6585	34
V960 Mon	0.59	−4.96	2.69	15	1.60	1120	5550	38
HBC 722	0.20	−4.18	3.65	79	2.30	745	5840	85
BBW 76	0.2	−5.12	1.41	16	0.43	1040	6380	17
RNO 54	0.23	−3.45	4.5	50	3.9	1400	7000	265
V890 Aur	0.17	−5.48	1.04	6	1.8	1500	6218	8.4
V883 Ori	1.3	−3.9	5.9	38	20.8	388	7045	458

The most computationally expensive part of producing a high resolution disk model spectrum is computing the rotational broadening, which must be done for each annulus individually. An improvement we make to the Rodriguez and Hillenbrand (2022) model is that rather than applying a rotational broadening kernel to the spectrum in narrow wavelength ranges, we compute our rotational broadening for

[1]Note that this is **not** the outer edge of the entire circumstellar disk. Typical values for $R_{\rm outer}$ in our models range from 0.12 − 0.5 au, while the full disks of FUOrs have radii of 10s to 100s of au (e.g., Cieza, Ruíz-Rodríguez, et al., 2018; Pérez et al., 2020; Kóspál, Cruz-Sáenz de Miera, et al., 2021).

the entire spectrum at once by numerically integrating over the annulus

$$F_{\rm broad}(r, \lambda, T_{\rm eff}) = \frac{1}{2\pi} \int_0^{2\pi} F(r, \lambda(\theta), T_{\rm eff}) d\theta \tag{2.1}$$

where

$$\lambda(\theta) = \lambda \times \left(1 + \frac{v_{\rm kep}(r)}{c} \sin(\theta)\ \sin(i)\right), \tag{2.2}$$

and θ is the azimuthal angle in the disk. A discussion of the benefit of this approach versus kernel-based broadening is given in Appendix B.

The total disk model spectrum is then given by

$$F_{\rm disk}(\lambda) = 2\pi \left(\frac{\cos(i)}{2\pi d^2}\right) \left(e^{-0.4\ A_\lambda}\right) \int_{R_{\rm inner}}^{R_{\rm outer}} F_{\rm broad}(r, \lambda, T_{\rm eff})\ r\ dr, \tag{2.3}$$

where A_λ is the line of sight extinction at the observed wavelength, usually prescribed by an extinction law. In the $0.3 - 5.0$ μm wavelength range where we usually perform our fits, the popularly used Fitzpatrick (1999) galactic average extinction law, suffices. In the UV, we prefer to use the extinction law from Whittet et al. (2004), which has a higher total-to-selective reddening value of $R_V = 3.63$, compared with the $R_V = 3.1$ found for the galactic average. Extinction mapping of star forming regions in the Milky Way shows greater R_V values along sightlines with greater A_V (Zhang and Green, 2025). The Whittet et al. extinction law also assumes a smaller "UV bump" at 2175 Å, which we find fits the UV spectra of FU Ori objects well (Carvalho, Hillenbrand, France, et al., 2024).

An additional improvement to the Rodriguez and Hillenbrand (2022) disk model implementation that I explored was adding a radial log$g$ profile to the disk spectra. A version of the code with this implemented was used for the fits to V960 Mon, adopting $\log g(r_i) = GM_*/r_i^2$ for each annulus i with central radius r_i. This choice is justified in Chapter 3. However, when more closely comparing the high resolution model spectra with the observed HIRES spectra, we found that simply fixing log$g$ = 1.5 provided slightly better fits and thus did not use the log$g(r)$ profile when fitting spectra of other sources. This is consistent with the estimate that the red-optical and NIR arise mostly from $r \sim 3\ R_{\rm inner}$.

For the disk models implemented in Chapters 10 and 11, the log$g(r)$ was kept because models using only log$g$ = 1.5 underpredicted the flux in the blue-optical and UV. This is likely due to the fact that much of that emission comes from very close to the central star, and therefore is better represented by log$g$ = 3.

2.2 Fitting Disk Models to Observed Spectra

With the full disk SED model in hand, it is possible to fit the actual observed SEDs of FUOrs. The data we fit are typically either photometric points spanning the visible to NIR (usually $BVRI$ or $griz$ and JHK filters) or visible and NIR medium resolution flux-calibrated spectra ("spectrophotometry"). Particularly in the NIR, where the disk spectra show strong H_2O absorption between J and K band (Connelley and Reipurth, 2018), the spectrophotometry is more effective for constraining disk models than the JHK photometric points. Sample fits to the objects V960 Mon and HBC 722 are shown in Figure 2.2.

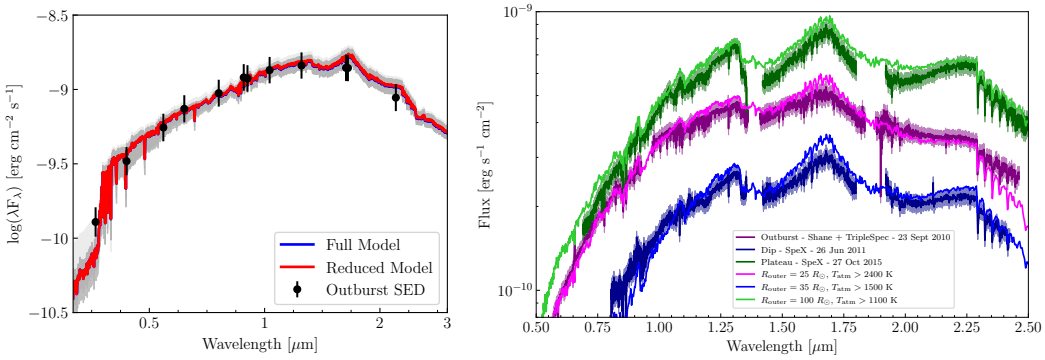

Figure 2.2: Sample SED fits to the photometry of V960 Mon (left) and the spectrophotometry of HBC 722 (right). Descriptions of the objects, fits, and data can be found in Chapters 3 and 5, respectively. This Figure is a reproduction of Figure 8 from Carvalho, Hillenbrand, Hambsch, et al. (2023) and Figure 4 from Carvalho, Hillenbrand, Seebeck, and Covey (2024).

The fitting itself is typically done via log-likelihood minimizing Markov Chain Monte Carlo (MCMC) sampling. The parameters we typically choose to fit are M_*, $\dot{M}$, $R_{\rm inner}$, i, and A_V. As in many SED fitting problems, it is necessary to adopt a value for d. While it is popular to simply adopt the parallax-based distance measurement from the Gaia mission (Gaia Collaboration, Prusti, et al., 2016) in such a situation, this is not appropriate for most FUOrs. FUOrs usually have significant nebulosity surrounding them, which interferes with the ability to compute a precise parallax for the source. An alternative way to estimate distances to FUOrs is to instead associate them with other neighboring YSOs which do have good Gaia parallax measurements and adopt the median value for the cluster (e.g., Kuhn and Hillenbrand, 2019).

As is demonstrated below, many of the parameters that I seek to fit are degenerate with one-another. Therefore, I seek to impose as many constraints on them as possi-

ble. When a full SED of the pre-outburst source is available, I leverage the expected pre-outburst $T_{\rm eff}$ to narrow the range of masses explored by the sampler. Some disks, like FU Ori and V883 Ori, have inclination measurements available from ALMA millimeter continuum imaging of their outer disks (Cieza, Ruíz-Rodríguez, et al., 2018; Pérez et al., 2020). It is not strictly the case that the inner and outer disks of FUOrs should be aligned, so I do not fix the i values but instead sample them from a Gaussian prior centered at the value found for the outer disk. In the case of V883 Ori and V960 Mon, I have retrieved best-fit i values in perfect agreement with the outer disk ALMA values (Carvalho et al.,2025a, submitted; Carvalho, Hillenbrand, Hambsch, et al., 2023).

The most important constraint we place on the SED fits, which also serves to constrain i somewhat, is on the allowed rotational broadening of spectral lines, $v_{\rm max}$, produced by the model. For each combination of M_*, $R_{\rm inner}$, and i explored by the samplers, we require that the resulting $v_{\rm max}$ value be drawn from a Gaussian distribution centered on the $v_{\rm max}$ estimated from a high resolution spectrum of the source. The technique usually relies on some form of varying $v_{\rm max}$ for a fiducial disk model, comparing with a high resolution spectrum, and and minimizing the χ^2 value between the two.

For visible range spectra, this can be somewhat sensitive to the adopted fiducial disk model parameters, due to the sensitivity of the absorption lines to the $T_{\rm max}$ value (see Section 2.3 and Chapter 4). In Chapter 8, I present a way to measure the $v_{\rm max}$ for a disk using high resolution NIR spectra, which are much less sensitive to the $T_{\rm max}$ of the disk.

2.3 The Importance of Incorporating High Resolution Spectra in SED Fitting

Even when using the stellar spectra to compute the disk model SED, however, it is not sufficient to fit only the SED to low resolution spectra. This is because when constructing a disk model and fitting it to observed data, the primary quantities the SED can constrain are $T_{\rm max}$ and $L_{\rm acc}$ for a disk. Consequently, there are several parameters that can be degenerate in an SED-only model. For example, in both the $T_{\rm max}$ and $L_{\rm acc}$ equations, the stellar mass and accretion rate appear as a product, $M_*\dot{M}$. The similar dependence on $R_{\rm inner}$ between the two quantities $\left(R_{\rm inner}^{-1}\right.$ versus $\left.R_{\rm inner}^{-3/4}\right)$ also introduces some degeneracy between that parameter and $M_*\dot{M}$. To complicate matters further, the overall luminosity of the disk is degenerate with the assumed i, due to projection of the flux along our line of sight, and the $T_{\rm max}$ is degenerate with

the assumed A_V.

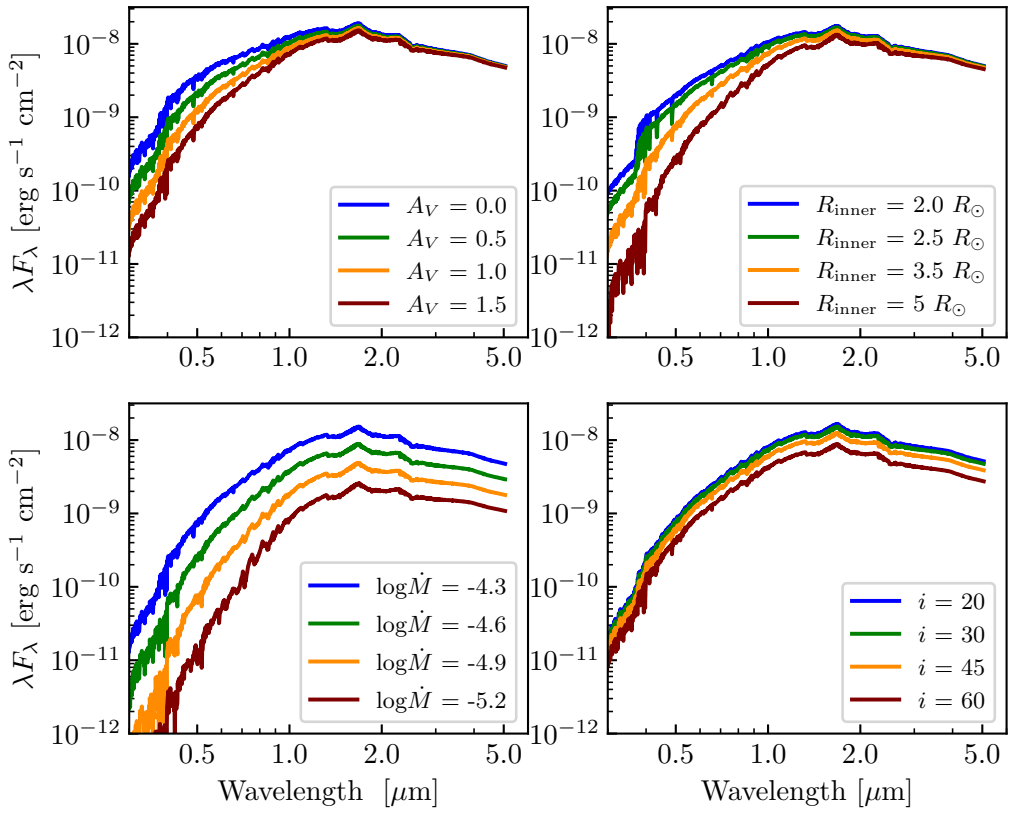

Figure 2.3: Disk models showing how changing different parameters impacts the SED. In each panel, a single parameter is varied while keeping all others fixed.

This degeneracy between different parameters in the SED models is illustrated in Figure 2.3. In each panel of the figure, the one of the model parameters is varied, while all others are kept constant. Notice that in the upper two panels, the change to A_V affects the bluer wavelengths of the SED in much the same way as the change to $R_{\rm inner}$, due to the strong sensitivity of $T_{\rm max}$ to $R_{\rm inner}$. In the lower two panels, the mild degeneracy between $\dot{M}$ (really $M_*\dot{M}$) and i is shown.

The degeneracy between $T_{\rm max}$ and A_V can severely impact template-matching as a means of estimate the extinction to a FUOr. This is the method adopted by Connelley and Reipurth (2018) in their NIR spectroscopic survey of FUOrs. However, the range of $T_{\rm max}$ values for the objects spans almost 3000 K (see, e.g., Chapters 3 and 9). However, for low A_V values, the $T_{\rm max}$ of the FUOr cannot be neglected when dereddening to a template.

All illustration of this problem is shown in Figure 2.4. In the Figure, all 3 models

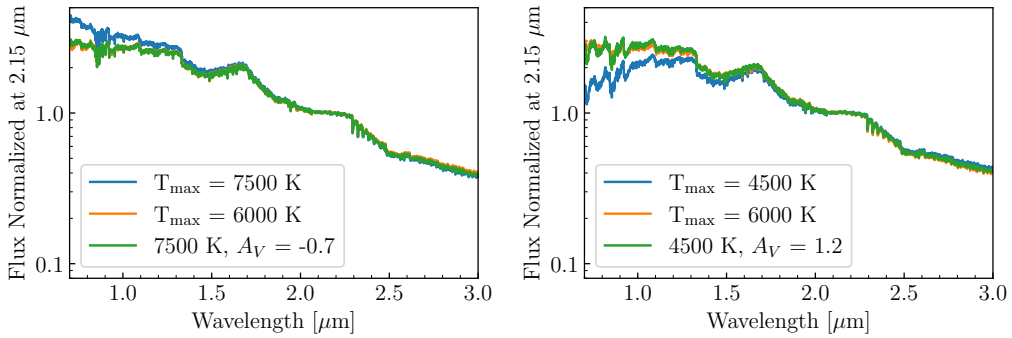

Figure 2.4: A demonstration of the impact of $T_{\rm max}$ on template-based extinction measurements. All 3 model spectra used initially have $A_V = 0$ and are normalized to 1.0 at $\lambda = 2.15$ μm. The A_V value reported in the caption is the "correction" necessary to match the template, which is negative of the spectum needs to be reddened. **Left:** A model spectrum with $T_{\rm max} = 7500$ K will appear bluer than the template ($T_{\rm max} = 6000$ K), causing the fit to underestimate the extinction. **Right:** A model spectrum with $T_{\rm max} = 4500$ K will appear redder than the template, causing the fit to overestimate the extinction.

used are computed with $A_V = 0$. The template spectrum is a model with $T_{\rm max} = 6000$ K, close to the $T_{\rm max}$ of FU Ori. If the $T_{\rm max}$ of the observed object is greater than that of the template, then the measured A_V may be underestimated. For $\Delta T_{\rm max} = 1500$ K, the underestimate is $\Delta A_V = -0.7$ mag. If the $T_{\rm max}$ of the object is less than that of the template, then A_V can be overestimated. For $\Delta T_{\rm max} = -1500$ K, the overestimate is $\Delta A_V = 1.2$ mag.

Another less significant effect, but one which can still be bothersome for low ($A_V < 5$ mag) values is the impact of the $R_{\rm outer}$ parameter on the K band flux of a model. This is demonstrated in Figure 2.5. If the observed target has $T_{\rm max} = 6000$ K and $R_{\rm outer} = 50$ $R_\odot$, then when normalized to 1 at $\lambda = 2.15$ μm, the source will appear bluer than a template that has the same $T_{\rm max}$ and $R_{\rm outer} = 150$ $R_\odot$. This is because the source with a smaller $R_{\rm outer}$ has less flux at K band relative to those with larger $R_{\rm outer}$ values. Normalizing instead to a continuum region of H or J band can mitigate this problem, since they show relatively little variation over a broad range of $R_{\rm outer}$ values (see Figure 2.5, left panel).

Breaking the degeneracy in the SED models requires incorporating information from high resolution spectra. The benefit of modeling high resolution spectra along with the lower resolution SEDs is that the absorption lines of the spectra are sensitive to the rotational broadening in the disk, $v_{\rm max}$, and the maximum disk temperature, $T_{\rm max}$, but are not impacted by A_V or d. The impact of $T_{\rm max}$ and $v_{\rm max}$ values on disk

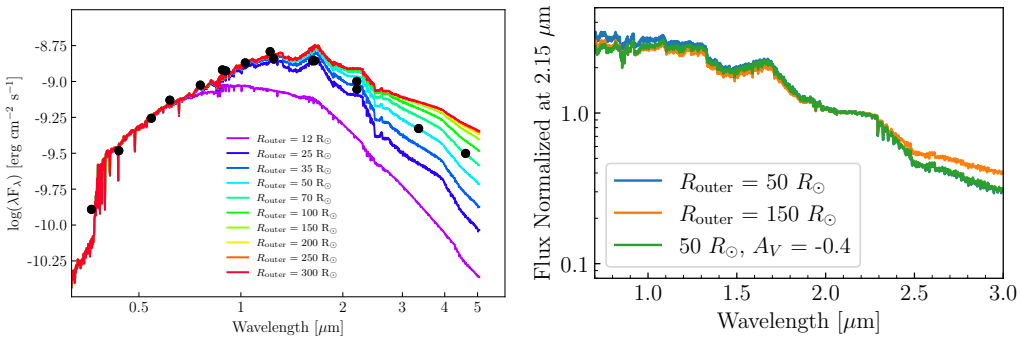

Figure 2.5: The effect of varying $R_{\rm outer}$ on the disk model spectrum and the estimated A_V when normalized at K band. **Left:** A reproduction of Figure 6 from (Carvalho, Hillenbrand, Hambsch, et al., 2023) showing how the chosen $R_{\rm outer}$ value in a disk model impacts the flux, especially for $\lambda > 2$ μm. **Right:** A model with $T_{\rm max}$ = 6000 K and $R_{\rm outer}$ = 50 $R_\odot$ computed with A_V = 0 (blue), then reddened by A_V = 0.4 mag to match the template, which has $T_{\rm max}$ = 6000 K and $T_{\rm outer}$ = 150 $R_\odot$.

model spectra is demonstrated in Figure 2.6.

The sensitivity of features like the Fe I 5328 line and the H Paschen lines at 8400 Å to 9000 Å to $T_{\rm max}$ can be used to approximate $T_{\rm max}$ for the disk directly. In Chapter 4, I investigate this in detail, showing several features that trace the a decreasing $T_{\rm max}$ in the disk of V960 Mon as the source faded following the peak of its outburst. We also used the relative strengths of temperature sensitive features in the spectrum of RNO 54 to constrain its $T_{\rm max}$ value (Hillenbrand, Carvalho, van Roestel, et al., 2023).

In Figure 2.6, the impact of increased disk broadening on the absorption lines can be clearly seen. At higher $v_{\rm max}$ values, the profiles of the strongest absorption features become very box-like, while weaker features are no longer seen. At lower $v_{\rm max}$ values, the instrumental broadening becomes non-negligible, and the lines no longer show the expected double-peak. This is apparent in the spectra of face-on FUOrs like V960 Mon, V1515 Cyg, V890 Aur, and V2775 Ori (see the spectra in Chapters 12 and 13).

2.4 What Luminosity Should One Adopt for FUOrs?

The luminosity of the disk of a FUOr during outburst (particularly the peak luminosity value) is an important quantity to consider when studying the impact of the outburst on the disk and its environment. Different means of measuring the luminosity of a FUOr, however, persist in the literature (e.g., Audard et al., 2014;

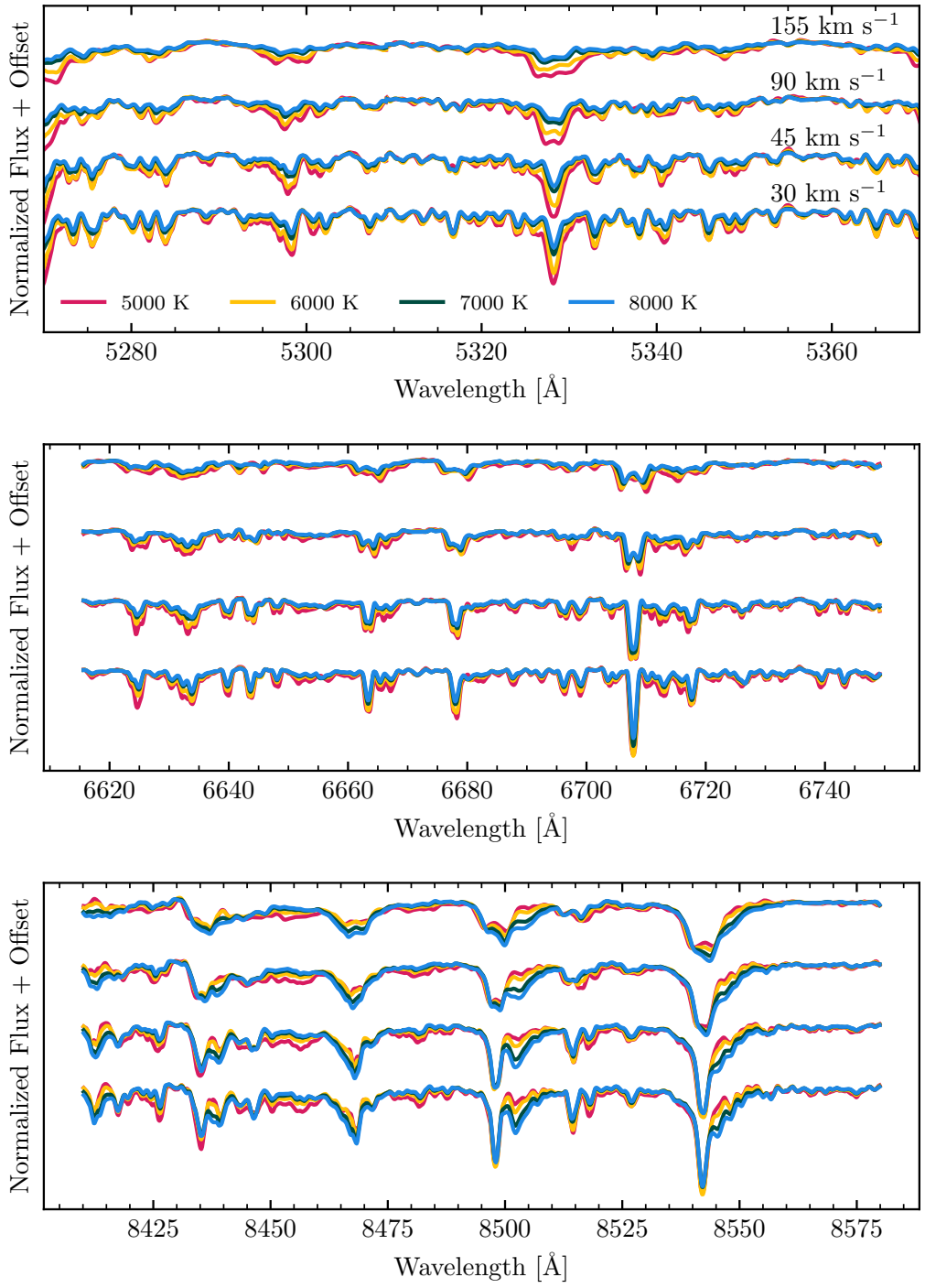

Figure 2.6: The effect of varying $v_{\max}$ and $T_{\max}$ on absorption features in the high resolution disk models.

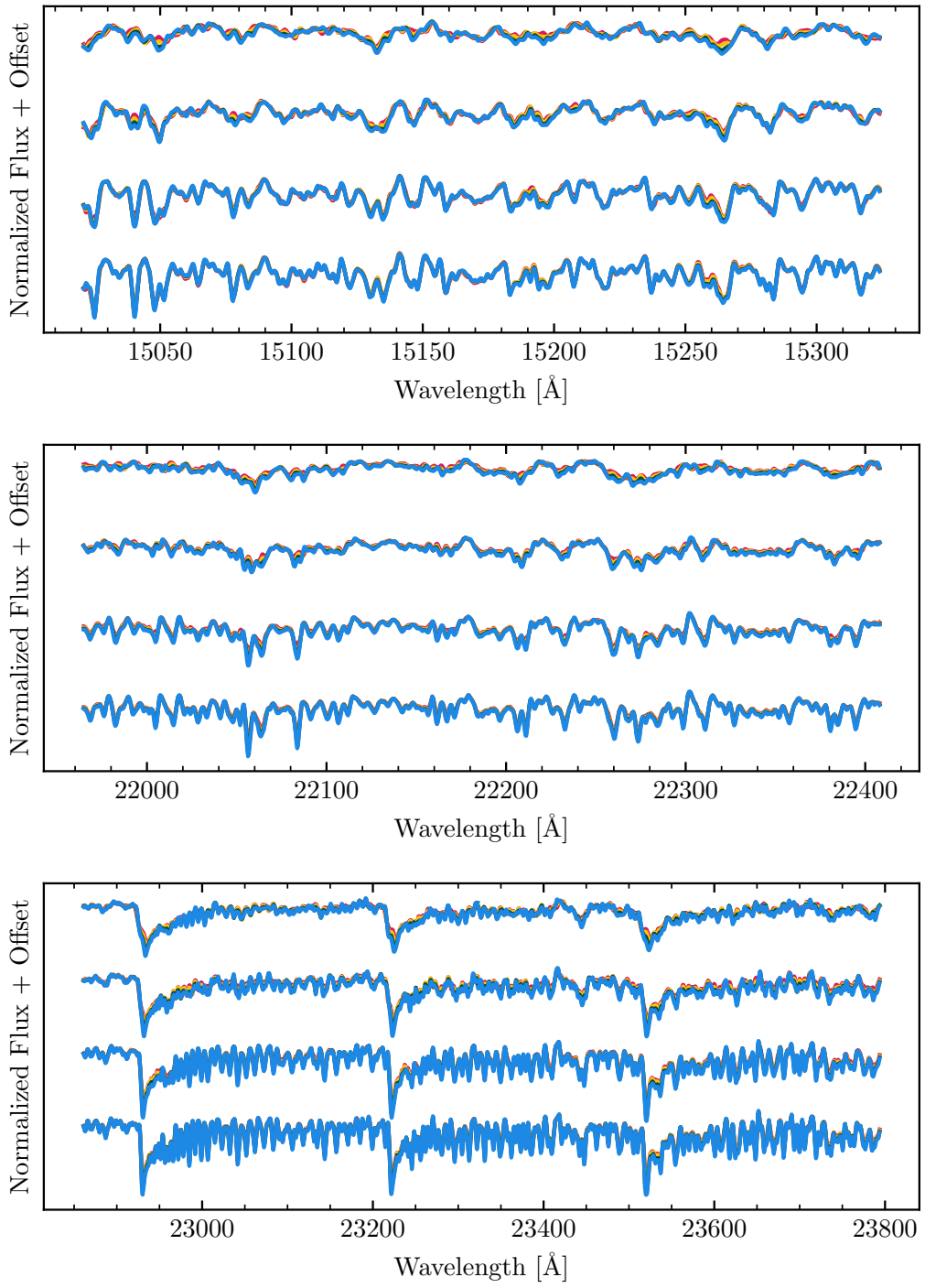

Figure 2.7: Same as Figure 2.6 but showcasing the spectra in the NIR. Notice that in contrast to the visible range, features are much more strongly affected by the rotational broadening than by changes in disk temperature.

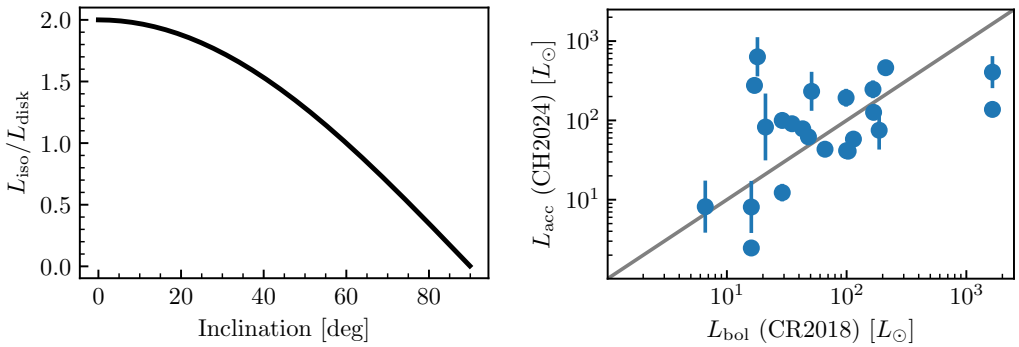

Figure 2.8: A comparison of different luminosity measurements for FUOrs, showing also the importance of inclination. **Left:** The ratio of isotropic-emission-derived luminosity to true disk luminosity as a function of source inclination. **Right:** The $L_{\rm acc}$ values of FUOrs measured from their K band brightnesses via bolometric corrections compared with the $L_{\rm bol}$ values reported by Connelley and Reipurth (2018). The grey $y = x$ line is plotted for reference.

Connelley and Reipurth, 2018). One of the most common measurements to use, largely due to the significant line-of-sight extinction to FUOrs and by analogy to Class 0/I protostars, is the bolometric luminosity of the source, $L_{\rm bol}$.

In principle, $L_{\rm bol}$ captures the emission from the inner disk that has been reprocessed by the circumstellar material and is emitted at mostly IR wavelengths. This emission is less susceptible to the effects of extinction and should therefore be an accurate measurement of the luminosity of the source. While this is the case for the mostly-isotropic and quiescent emission of Class 0/I protostars, the same does not hold for FUOrs. The first challenge is with the projection effect of the disk inclination. Since the disk dominates the emission, and disk emission is non-isotropic, its inclination must be considered when computing luminosity.

For a given flux density, F_λ, the corresponding luminosity from a FUOr is $L_\lambda = 2\pi d^2 F_\lambda / \cos(i)$, rather than the typical $L_\lambda = 4\pi d^2 F_\lambda$. Ignoring the effect of disk inclination impacts the estimated luminosity in a stochastic, rather than systematic, way. The over- or underestimation of $L_{\rm disk}$ using the isotropic emission assumption to compute luminosity, $L_{\rm iso}$, is shown in Figure 2.8.

For FUOrs, even computing a reliable $L_{\rm bol}$ in the traditional sense is non-trivial due to the historically sparse time sampling of NIR-FIR spectroscopic surveys. Since many of the known FUOrs have been detected in the past 15 years (Contreras Pena et al., 2025), they will not have 2MASS/WISE/Akari/Herschel photometry from their

in-outburst states. And, since many of the objects can evolve dramatically on 5-10 year timescales (e.g., Audard et al., 2014; Szabó, Kóspál, Ábrahám, Park, Siwak, Green, Moór, et al., 2021), the time between these surveys can also inhibit accurate calculation of $L_{\rm bol}$ for objects in outburst prior to 2015. Binary FUOrs are also not resolved in many of the previous MIR/FIR surveys, meaning the $L_{\rm bol}$ for objects like Z CMa and RNO 1b/c is not representative of the actual outburst luminosity.

In order to remedy this, I propose that $L_{\rm acc}$ be used instead of $L_{\rm bol}$ when discussing luminosities of FUOrs. The $L_{\rm acc}$ of a FUOr can be estimated from a single-band observation using the bolometric corrections provided in Chapter 7. These bolometric corrections have been computed for a broad range of possible source $L_{\rm acc}$ values using the accretion disk model described in this Chapter. The bolometric corrections are produced for several visible and NIR filters for current and upcoming surveys, enabling measurements of $L_{\rm acc}$ for historical lightcurves of currently outbursting FUOrs and those of newly discovered ones.

An example of using bolometric corrections to compute $L_{\rm acc}$ for FUOrs is shown in the right panel of Figure 2.8. The $L_{\rm acc}$ values are computed using the K band photometry of FUOrs published in Connelley and Reipurth (2018). I adopted the same distances and A_V values reported in Connelley and Reipurth (2018) for each source in order to compare $L_{\rm acc}$ with their reported $L_{\rm bol}$. I omit Z CMa from the comparison because at K band, the companion to the FUOr dominates the emission from the system (Hinkley et al., 2013). For sources which do not have literature i measurements, I assumed $i = 60°$. The inclinations adopted from Kóspál, Cruz-Sáenz de Miera, et al. (2021) are based on their radiative-transfer model best-fit values. The resulting $L_{\rm acc}$ values are also given in Table 2.2, along with the values used to derive them. The uncertainties on $L_{\rm acc}$ are the result of propagating the A_V uncertainties reported in Connelley and Reipurth (2018).The median $L_{\rm acc}$ in Table 2.2 is 86 $L_\odot$.

Note that the $L_{\rm acc}$ values reported here refer to the state of each system at the epoch of the K band photometry, most of which was taken between 2014 and 2016 (Connelley and Reipurth, 2018). While these provide a more true representation of the state of the accretion disk at the time of observation, directly comparing the objects in the class requires considering the evolution of their outbursts. V1057 Cyg, for instance, had faded by more than 3 magnitudes since its peak, while HBC 722 and V960 Mon were both near the peaks of their outbursts when this survey was conducted.

An advantage of using the bolometric corrections is the ability to estimate the peak

Table 2.2: $L_{\rm acc}$ values compared with the $L_{\rm bol}$ values in Connelley and Reipurth (2018), using the distances, K band measurements, and A_V therein. When available, inclinations were obtained from Kóspál, Cruz-Sáenz de Miera, et al. (2021), Pérez et al. (2020), Cieza, Ruíz-Rodríguez, et al. (2018), and Carvalho, Hillenbrand, Seebeck, and Covey (2024). All others, marked with brackets, are assumed to be 60°.

Object	K (mag)	Distance (pc)	A_V (mag)	i (deg)	$L_{\rm bol}$ $L_\odot$	$L_{\rm acc}$ $L_\odot$
RNO 1b	8.34	930	14.5 ± 1.0	[60]	1652	138^{+15}_{-13}
RNO 1c	7.73	930	19.5 ± 4.0	[60]	1652	406^{+207}_{-137}
PP 13S	10.82	450	56.5 ± 5.0	[60]	51	233^{+156}_{-93}
L1551 IRS5	9.21	147	25.5 ± 2.0	79	29	12^{+3}_{-2}
V582 Aur	8.18	1300	5.6 ± 1.2	[60]	168	126^{+16}_{-15}
Haro 5a/6a	9.85	388	57.5 ± 5.0	68	18	634^{+429}_{-255}
V883 Ori	5.53	388	22.5 ± 1.0	38	212	462^{+50}_{-45}
V2775 Ori	8.43	428	27.5 ± 1.0	[60]	29	100^{+11}_{-10}
FU Ori	5.79	400	1.5 ± 0.2	35	66	43^{+1}_{-1}
IRAS 05450+0019	8.76	388	31.5 ± 1.0	[60]	35	91^{+10}_{-9}
V900 Mon	7.51	1100	13.5 ± 2.0	14	99	193^{+44}_{-36}
V960 Mon	7.42	1100	1.5 ± 0.4	15	48	62^{+3}_{-2}
BBW 76	8.60	1800	1.6 ± 0.2	20	114	58^{+1}_{-1}
Parsamian 21	9.55	500	2.5 ± 0.5	37	16	2^{+0}_{-0}
V1515 Cyg	7.95	1050	3.5 ± 0.4	0	103	41^{+2}_{-2}
HBC 722	6.31	550	3.7 ± 0.5	79	17	276^{+15}_{-14}
V2494 Cyg	8.37	600	17.5 ± 5.0	[60]	187	75^{+50}_{-30}
V1057 Cyg	6.59	550	3.9 ± 1.6	10	100	42^{+7}_{-6}
V2495 Cyg	11.79	600	49.5 ± 9.0	[60]	21	82^{+124}_{-49}
CB 230	10.27	300	26.5 ± 7.0	[60]	7	8^{+8}_{-4}
V1735 Cyg	7.54	950	12.5 ± 2.0	[60]	166	247^{+56}_{-46}
HH 354 IRS	10.83	300	31.5 ± 7.0	[60]	16	8^{+8}_{-4}
V733 Cep	8.29	800	11.5 ± 1.0	[60]	43	78^{+8}_{-8}

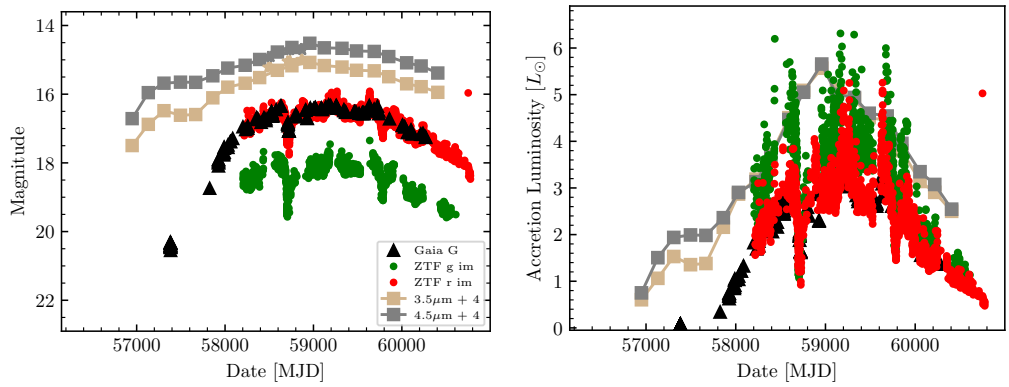

Figure 2.9: Deriving the luminosity of a FUOr from its lightcurve. **Left:** The multiband lightcurve of Gaia 17bpi, showing the pre-outburst state of the object, its rapid rise, and its slow fade in the past 8 years. **Right:** The $L_{\rm acc}$ curve for Gaia 17bpi, derived from bolometric corrections to the photometric points in the left panel.

$L_{\rm acc}$ value of a FUOr directly from its lightcurve. This will enable converting the single-epoch measurements presented in Table 2.2 to the true distribution of peak $L_{\rm acc}$ values for FUOrs. With a complete visible/NIR spectrum of each source to constrain M_* and $R_{\rm inner}$ for a source one can then also estimate the $\dot{M}$ evolution over the course of an outburst as well as the distribution of peak $\dot{M}$ values for FUOrs.

An example of applying the bolometric corrections to compute $L_{\rm acc}$ during an outburst is provided in Figure 2.9. In the Figure, the $L_{\rm acc}$ is computed for the source Gaia 17bpi, a low luminosity FUOr that began its outburst in 2017 (Hillenbrand, Peña, et al., 2018). The bolometric corrections used here are from the constant temperature $T_{\rm max} = 6,000$ K grid, which is computed specifically to optimize the correction for low-luminosity FUOrs. The data shown in the lightcurve are from the NEOWISE survey (Mainzer et al., 2011), ZTF (Bellm et al., 2019), and the Gaia Photometric Alerts Service (Hodgkin et al., 2021). The bolometric corrections applied to all of the lightcurves, spanning 0.5μm to 4.5μm, provide $L_{\rm acc}$ estimates that are consistent within 50%, which is similar to the accuracy of this technique as discussed in 7. The assumed distance to the source is $d = 1250$ pc (Kuhn and Hillenbrand, 2019), the inclination is chosen to be $i = 75°$, which gives an upper bound on the source distance, and $A_V = 2$ mag is estimated from a comparison between the source NIR spectrum and that of FU Ori.

With the ability to estimate $L_{\rm acc}$ for several FUOrs with one single photometric measurement, it becomes possible to test broader assumptions about the underlying

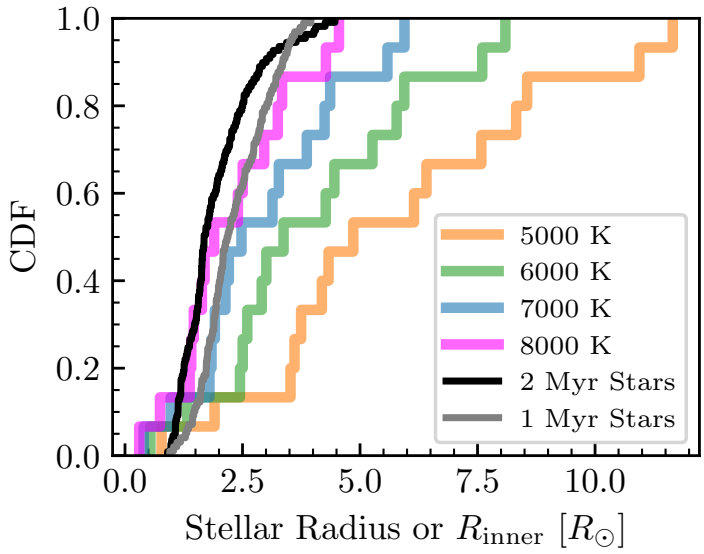

Figure 2.10: CDFs of the $R_{\rm inner}$ values estimated for the FUOrs in Table 2.2 assuming 4 different temperatures. The grey and black lines show the R_* values for the 1 and 2 Myr PARSEC isochrones, respectively.

sources. One application of this is to constrain $R_{\rm inner}$ of the population of FUOrs at a given time, by assuming a range of $T_{\rm max}$ values for the sample and computing $R_{\rm inner} = \sqrt{\frac{3}{4\pi\sigma}\left(\frac{6^6}{7^7}\right)\frac{L_{\rm acc}}{T_{\rm max}}}$. The resulting $R_{\rm inner}$ values derived from the $L_{\rm acc}$ in Table 2.2, are summarized as cumulative distribution functions (CDFs) and shown in Figure 2.10. Compared with 1 Myr and 2 Myr PARSEC Nguyen et al. (2022) isochrones, the FUOrs have generally larger $R_{\rm inner}$. If the standard $R_{\rm inner} = R_*$ assumption is applied, this suggests that FUOrs are indeed generally inflated relative to their non-outbursting peers, potentially the result of their intense accretion.

The challenge of estimating the inclination to FUOrs remains, but significant progress is being made on this front using ALMA and optical interferometric instruments like VLT/MATISSE, VLT/GRAVITY, VLT/PIONEER, and CHARA/MIRCX (e.g., Cieza, Casassus, et al., 2016; Pérez et al., 2020; Kóspál, Cruz-Sáenz de Miera, et al., 2021; Labdon et al., 2021; Lykou, Ábrahám, Chen, et al., 2022; Lykou, Ábrahám, Cruz-Sáenz de Miera, et al., 2024). While more recently detected outbursts tend to be further away and thus difficult to spatially resolve, spectroscopic modeling and careful consideration of the properties of the pre-outburst source can help constrain inclination as well.

As is always the problem when estimating a luminosity, the A_V and distance to

FUOrs is important. For A_V, an estimate can be obtained by comparing the NIR spectrum of a source with that of FU Ori (e.g., Connelley and Reipurth, 2018, caveat the challenges discussed in Section 2.3). Thanks to the Gaia mission (Gaia Collaboration, Prusti, et al., 2016), distance estimates to FUOrs are becoming more reliable. Note that due to the frequent presence of nebular emission around these sources, in addition to their optical variability, it is not sufficient to simply adopt the reported Gaia parallax to the source. Instead, it is preferable to identify their kinematic association with other nearby YSOs, which enables a reasonably precise ($< 10\%$ uncertain) distance estimate (e.g., Kuhn and Hillenbrand, 2019; Kuhn and Hillenbrand, 2020; Roychowdhury and Hillenbrand, 2024b).

2.5 Limitations of the disk model

In the following Chapters, I will further demonstrate the efficacy of the relatively simple model I have presented so far. However, it is important to also bear in mind the limitations of the model. Several assumptions are made in the construction of these disk spectra and questioning each is both worthwhile and necessary. Some of the shortcomings on the disk model in matching observations have been highlighted in the past by the work of Herbig et al. (2003). I will address these and others in this section.

The thin disk assumption

The most immediate assumption that can be questioned in this model is that the disk is geometrically thin, but optically thick. As has been shown in simulations, the inner disk of FUOrs is not geometrically thin, but can extend vertically as high as $z = R_*$ due to the extremely high temperatures produced by viscous heating (Popham, Narayan, et al., 1993; Popham, Kenyon, et al., 1996; Zhu, Jiang, et al., 2020). However, empirically, we still see that the disk model matches the line profiles of disk absorption features at high resolution (see Chapters 3 and 5), though for temperatures much lower than the midplane temperatures seen in simulations.

This can be understood by considering that the emergent spectrum is not probing the midplane but rather the material above the midplane where the continuous opacity reaches an optical depth of $\tau = 1$. In fact, Zhu, Jiang, et al. (2020) demonstrate in their simulation that the radial temperature profile at $\tau = 1$ is almost exactly that of the thin, viscous accretion disk, despite tracing large vertical heights in the disk ($z \sim r$). When fitting the thin, viscous disk model to FUOrs, the derived temperature

profile can be treated as a minimum temperature at each radius, while the midplane may be $2 - 10\times$ hotter.

The accuracy limits of synthetic stellar spectra

The disk model I use relies entirely on pre-computed synthetic stellar spectra. This means that there is no real radiative transfer done when computing the disk spectrum. Such a heavy reliance on synthetic spectra makes the model susceptible to the same inaccuracies that plague attempts to model single-temperature stellar atmospheres. While the spectra are excellent matches to low- and medium-resolution data, at high resolution the mismatches become clear.

The 8860 Å TiO feature

A persistent problem in the modeling of FUOr accretion disks has been the over-prediction of the strength of the 8860 Å TiO feature relative to observations. This was raised as a critique of the disk model by (Herbig et al., 2003) and remains a challenge even in the synthetic spectral models constructed today.

Figure 2.11 shows the TiO feature in the Keck/HIRES spectra of 14 FUOrs. Although the strength of the absorption varies between objects, the feature can be seen in almost all of the FUOrs (the exceptions being V960 Mon and V1057 Cyg). The presence of the feature is especially clear in the narrow-line spectra of V1515 Cyg and V890 Aur.

In Figure 2.12, I show the same region in three disk model spectra. The model spectra were computed for an FU Ori-like disk, with $M_* = 0.6\ M_\odot$, $R_{\rm inner} = 3.52\ R_\odot$, and $\dot{M} = 10^{-4.5}\ M_\odot\ {\rm yr}^{-1}$. The $v_{\rm max}$ is set to 180, 100, and < 5 km s^{-1} by changing the disk inclination to the values 89°, 35°, and 1°. For larger values of rotational broadening, the absorption by the TiO bandhead is severely blended into the wing H Paschen line. This may, in part, explain the apparent absence of the feature in the spectra of objects that have $v_{\rm max} > 80$ km s^{-1} (see Chapter 8.1 for the measured values of $v_{\rm max}$ for each object).

It may also be that the temperature structure of the disk at the radii where the molecular absorption is strongest is not as simple as it is very close in to the star. While $T_{\rm eff} \propto r^{-0.75}$ reproduces the SED and (most) atomic absorption features well, the molecular absorption bands, including VO, TiO, and CO, are much less well-matched. It is possible also that the vertical thermal structure of the disk at the wind

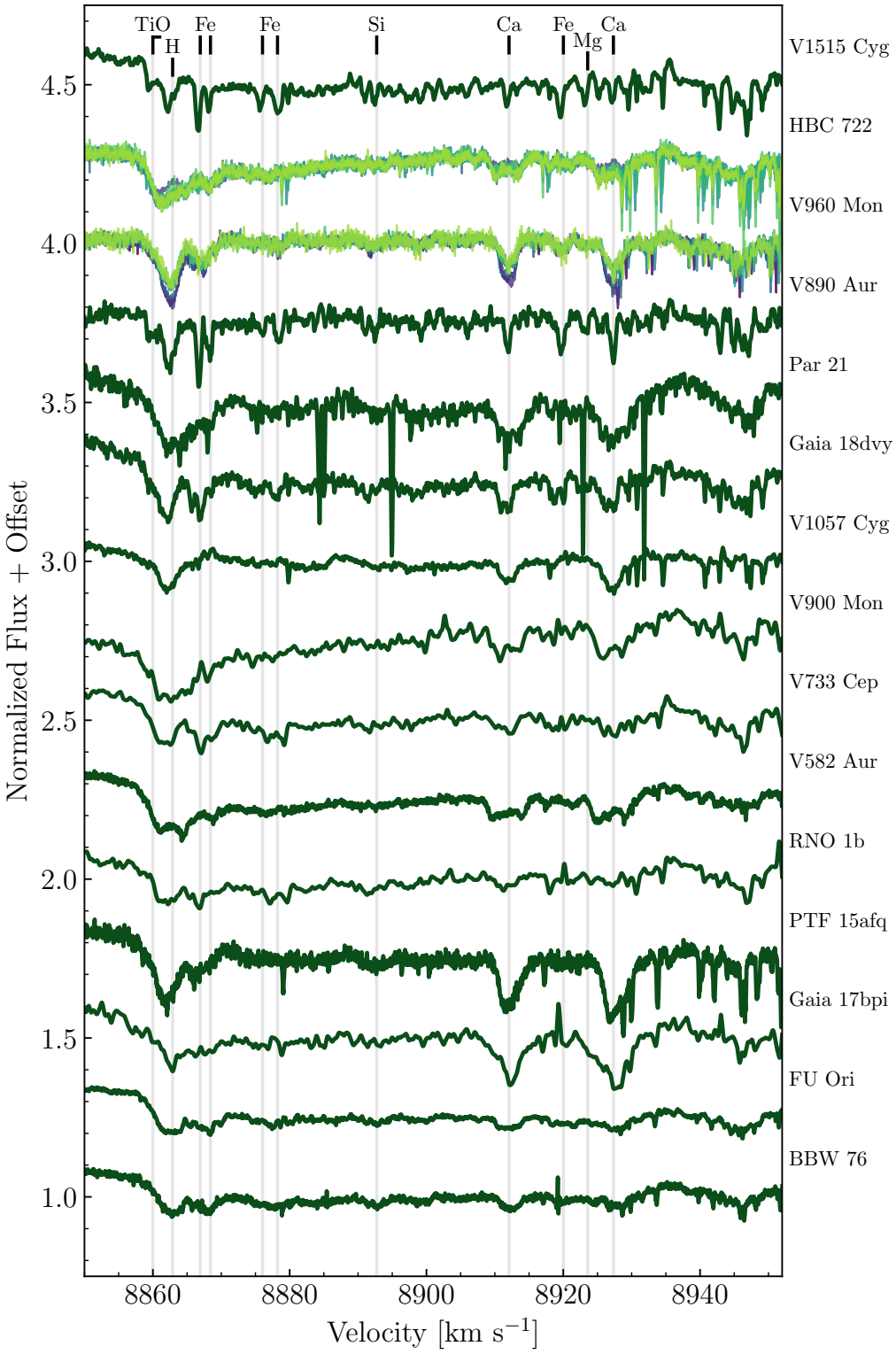

Figure 2.11: The region of the HIRES spectra containing the TiO 8860 Å band for 14 FUOrs and one EX Lup-type object. Important spectra features are marked with grey vertical lines.

launch point of the disk is more complex than the plane-parallel atmospheres we are using. As is discussed in Chapter 5, there is evidence that the visible range TiO features and the NIR 2.0 μm CO $\Delta\nu = 2$ bands show absorption from the outflow in HBC 722. Thus, the annuli bearing molecular absorption may be much closer-in to the star than the thin disk model predicts, and would be rotating at greater speeds. This would preferentially broaden molecular features and lower their absorption depth relative to nearby atomic features.

It should be noted also that the disk model spectra underpredict the strength of the Ca II doublet at 8912/8927 Å in most objects. This doublet has an excitation potential of ~ 7 eV (Moore and Merrill, 1968) and thus presumably traces hotter material in the disk. However, in disk models, the absorption strength of the doublet is almost unaffected by changes to $T_{\rm max}$, despite the its strong temperature dependence in the $T_{\rm eff} = 4,000 - 6,000$ K atmospheres. Furthermore, the strength of the doublet and its line profiles vary widely in the spectra of FUOrs. In objects like V582 Aur and HBC 722, the profiles are very flat-bottomed and box-like, clearly tracing the Keplerian rotation in the disk. In sources like Gia 17bpi and Par 21, however, the profiles have very broad wings reminiscent of the profiles of the Paschen lines.

It is likely that the Ca II doublet traces material near the boundary layer at the surface of the star or in the launch points of the outflow. In V960 Mon, the decreasing strength of the doublet as the disk cooled in the 3 years following the peak of its outburst indicates that the doublet may still be sensitive to $T_{\rm max}$ in the disk, despite model predictions. The potential temperature sensitivity of doublet, along with other features like the Si II 6341/6371 Å doublet, are discussed in more detail in Chapter 4.

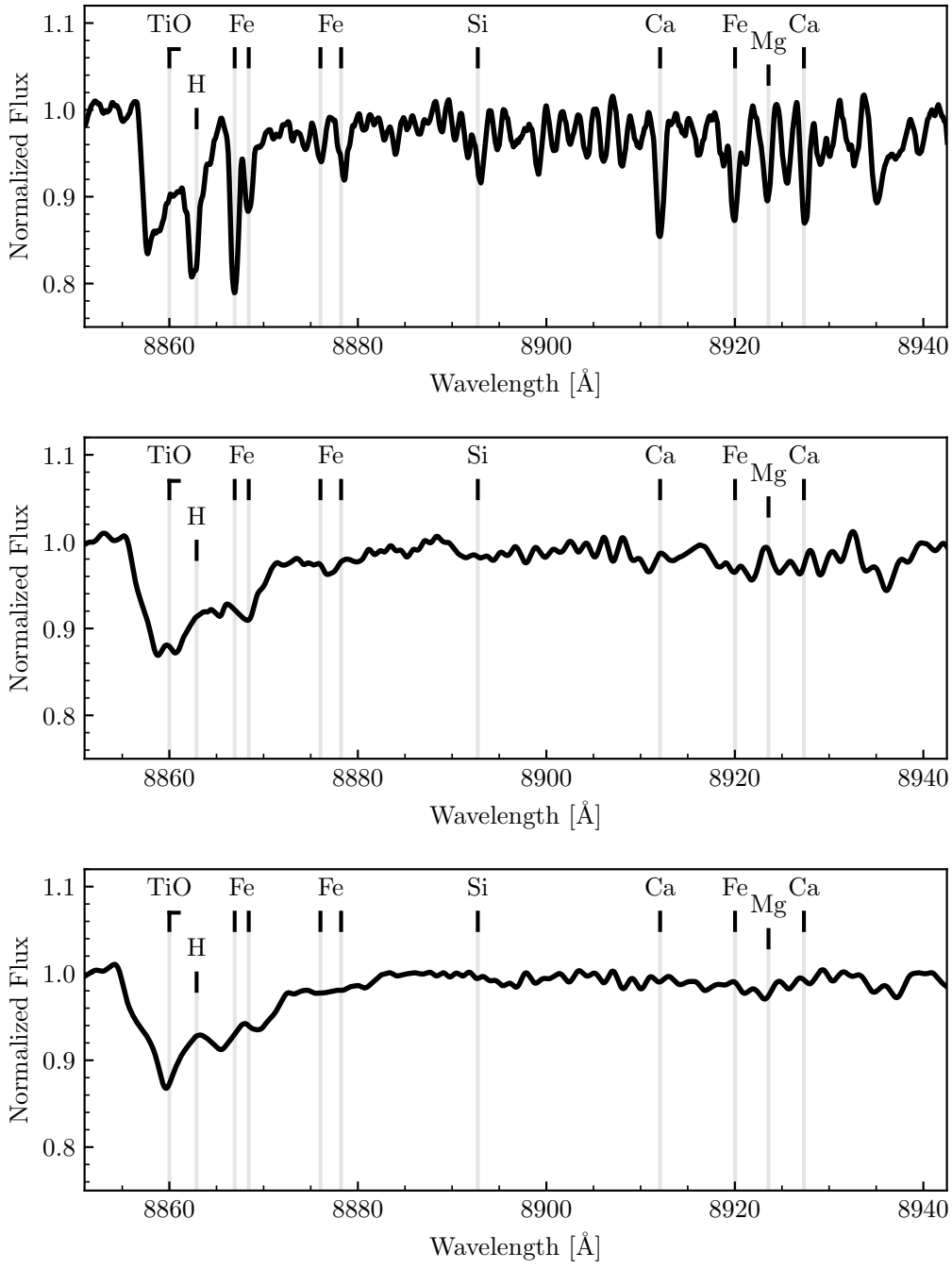

Figure 2.12: The region of the disk model spectrum containing the TiO 8860 Å band for 3 potential $v_{\max}$ values. Notice that for increased rotational broadening, the TiO feature is difficult to distinguish from the Paschen absorption.

Chapter 3

MODELING THE MULTIWAVELENGTH EVOLUTION OF THE V960 MON SYSTEM

Carvalho, Adolfo S., Lynne A. Hillenbrand, Franz-Josef Hambsch, Shawn Dvorak, Michael Sitko, Ray W. Russell, Victoria Hammond, Michael Connelley, Michael C. B. Ashley, and Matthew J. Hankins (Aug. 2023). "Modeling the Multiwavelength Evolution of the V960 Mon System." In: *ApJ* 953.1, 86, p. 86. DOI: 10.3847/1538-4357/ace2cb. arXiv: 2306.15107 [astro-ph.SR].

Abstract: We study the evolution of the FU Ori object V960 Mon since its outburst, using available multi-wavelength photometric time series over 8 years, complemented by several epochs of moderate-dispersion spectrophotometry. We find that the source fading can be well-described by a decrease in the temperature of the inner disk, which results from a combination of decreasing accretion rate and increasing inner disk radius. We model the system with a disk atmosphere model that produces the observed variations in multi-band photometry (this paper) and high resolution spectral lines (a companion paper).

3.1 Introduction

FU Ori objects are a class of stellar variable consisting of disk-bearing young stellar objects (YSOs) that have undergone eruptive outbursts. The outbursts reach optical amplitudes of $\Delta V \sim 4 - 6$ mag (Herbig, 1977) and are attributed to a significant increase in the accretion rate of the disk onto the central star (Hartmann and Kenyon, 1996). The relatively small sample of FU Ori objects seen to outburst show a variety of rise times and post-outburst fade timescales (Clarke et al., 2005).

Studying the evolution of the spectral energy distribution (SED) of such objects during the development of the outburst and also after its peak is critical to understanding the physics driving the outburst. High resolution spectra are also necessary to constrain system parameters independently of the broadband SED via the temperature and rotational broadening indicated by absorption lines.

V960 Mon is one of the most well-studied objects to have undergone an FU Ori outburst. The outburst was reported in late 2014 (Maehara et al., 2014; Hillenbrand, 2014; Reipurth and Connelley, 2015; Hackstein, Chini, et al., 2014) and the object

was followed in its post-outburst state by many photometric campaigns in the optical and near-infrared. The post-outburst fade of the object is remarkably short (as presented below in Figure 3.1) relative to other objects like V1057 Cyg (Szabó, Kóspál, Ábrahám, Park, Siwak, Green, Moór, et al., 2021).

Kóspál, Ábrahám, Moór, et al. (2015) gathered historical photometry of the target and found the progenitor SED is consistent with a 4000 K T-Tauri-like object. However, this assumed a distance to the target of 450 pc, whereas recent work has found a distance of 1120 pc (Kuhn and Hillenbrand, 2019). With the updated distance to the target, a single 4000 K young star is not luminous enough to account for the progenitor SED.

A possible remedy to this is that the system may be at least a binary, or a triple. One faint companion at 0.2 arcsec separation and a candidate companion at 0.1 arcsec separation have been detected using adaptive optics imaging of the system (Caratti o Garatti et al., 2015). In addition, Hackstein, Haas, et al. (2015) propose there is a close-in binary causing variation in the lightcurve at a 17 day period. However, this is inconsistent with the observed separations of either of the Caratti o Garatti et al. (2015) companions.

Spectroscopic evolution of V960 Mon was discussed in Park, Lee, et al. (2020) who presented high dispersion optical data from the Bohyunsan Optical Echelle Spectrograph (BOES) and near infrared data from Immersion Grating Infrared Spectrograph (IGRINS).

Here, we consider the photometric evolution of V960 Mon, complemented by several epochs of newly presented near-infrared moderate resolution spectra from IRTF/SpeX. The post-outburst fade was also sampled by us spectroscopically with high-resolution optical spectra from Keck/HIRES and Lick/APF, which we present in a companion paper (Carvalho et al. 2023b, in preparation), hereafter Paper II. That study will focus on the evolution of the high dispersion optical spectra and specifically the details of the line profile changes as the source has faded. In Paper II we also interrogate the evolving disk model presented below with respect to the spectroscopic evolution.

In this paper, we interpret the body of available photometric time series data in the context of an accretion disk model. In Section 3.2, we discuss the photometric and spectroscopic data we use in our analysis. Section 3.3 presents our improvements to the pure accretion disk model described in Rodriguez and Hillenbrand (2022) and

our modeling strategy for the V960 Mon system. In Section 3.4 we give evidence that disk cooling is driving the post-outburst fade, and provide evidence for the physical drivers of the cooling being a combination of decrease in accretion rate and increase in disk inner radius. We address the possible presence of a passive disk component in Section 3.5. We then discuss our results in the context of recent literature, and provide further interpretation of our analysis in Section 3.6. Our conclusions are briefly summarized in Section 3.7.

3.2 Data

Photometry

We use numerous archival sources and lightcurves assembled in previous literature of the target to study its post-outburst evolution across multiple bands spanning U in the near-ultraviolet to WISE/W2 in the mid-infrared.

Visible Range

The first 6 months post-outburst is well-sampled by the photometry assembled by and reported in Hackstein, Haas, et al. (2015). We use their data from Universitätssternwarte Bochum (USB) and The Remote Observatory Atacama Desert (ROAD). The data from USB were taken with RoBoTT (U, B, V, r, i, z) are labelled as ROBOTT in our plots.

We additionally use B, V, R, and I band lightcurves accessible in the American Association of Variable Star Observers (AAVSO) archive. The tight sampling of the data made it possible to follow the evolution of the closely during the early stages of the fade. To mitigate some of scatter in the photometry and enable better interpolation to observation dates of the spectroscopic data, we bin the AAVSO photometry in 10 day increments.

We also include photometry from the Gaia mission, which we accessed via the Gaia ESA Archive (Gaia Collaboration, Brown, et al., 2021; Riello et al., 2021). The Gaia BP, RP, and G band photometry show the outburst peak itself, in the MJD 56954 epoch. The Gaia photometry constrains the date and amplitude of the outburst peak and informs our interpretation of our other data on the system. It is especially important in our analysis below to confirm that the earliest epoch in the high dispersion spectra is representative of the outburst peak of the system.

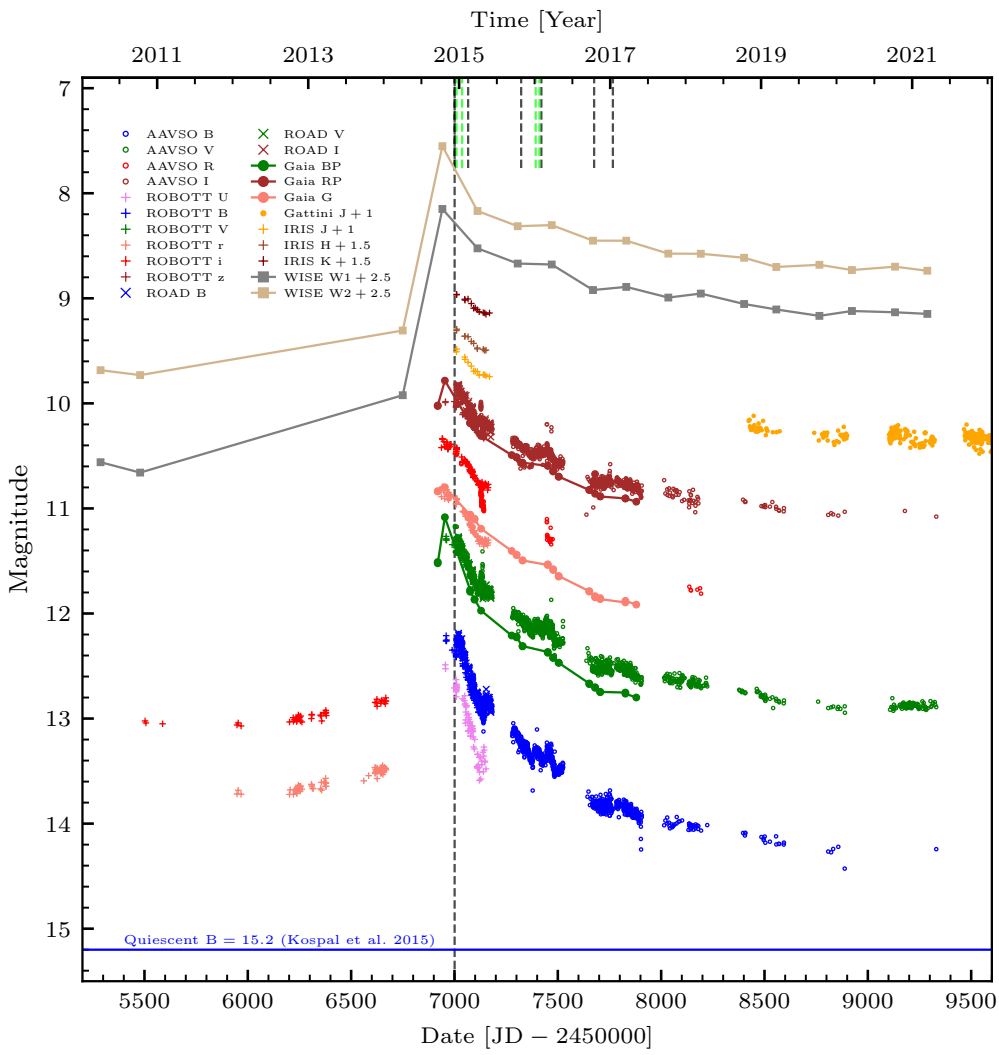

Figure 3.1: The multiband lightcurve of V960 Mon, showing photometry from many sources spanning U band to the W1 and W2 filters of WISE/NEOWISE. The outburst and rapid fade of the target is clear in all bands, with the amplitude tending to decrease toward the red. Photometry that is more sparsely sampled (WISE, Gaia) is shown connected by lines to highlight the trend in the outburst and exponential fade. The black and lime vertical dashes mark the dates on which the HIRES and SpeX spectra, respectively, were collected.

Infrared

We assemble the infrared lightcurves from several sources. Monitoring of the target in J, H, K bands was also done by Hackstein, Haas, et al. (2015) using the 0.8 m Infrared Imaging System (IRIS, Hodapp et al., 2010).

The Gattini infrared survey (Moore, Kasliwal, et al., 2016) provides J-band pho-

tometry of V960 Mon starting in September 2018, sampling the brightness of the target late along its plateau.

The object was also observed pre-outburst by the Wide-field Infrared Suvey Explorer (WISE) survey and post-outburst by the reactivation of the WISE mission as NEOWISE (Mainzer et al., 2011) which observes any given position approximately every six months. We use the $W1$ and $W2$ photometry, binning the point spread function fitting photometry from each visit to one point at the median epoch, median flux, and with error equivalent to the dispersion in the individual measurements. We perform the saturation correction provided in Cutri, Mainzer, et al. (2015) for the saturated observations following outburst.

There is a nearby source ($\sim 5''$ to the North), but the FU Ori object is well-resolved from it in all photometry included in this work. The full lightcurve, including all data described above, is shown in Figure 3.1. We include the pre-outburst B magnitude of the target reported by Kóspál, Ábrahám, Moór, et al. (2015) from 1953 and 1983 Palomar plates as a reference.

The photometry corresponding to the epoch of our high-dispersion spectrum shortly following the outburst (marked in Figure 3.1) is used to produce an SED of the target. The SED is used to fit our disk model (see Section 3.3 for the SED and the disk model-fitting procedure).

Multi-Wavelength Lightcurve and Photometric Evolution

Figure 3.1 shows the multi-band time-series photometry (lightcurve) of the target. Although V960 Mon has faded considerably from its peak brightness, the lightcurve shows a plateau from MJD 58500 to the present that is well above quiescence, indicating that the object is still accreting at a significant rate and has not yet fully returned to its pre-outburst low-state accretion rate.

The initial outburst spanned multiple magnitudes in every band shown in Figure 3.1. Using the quiescent state estimated by Kóspál, Ábrahám, Moór, et al. (2015), the ΔB of the outburst was approximately 3 magnitudes[1]. The ROBOTT r and i photometry shows outburst amplitudes of 2.8 and 2.6 magnitudes, respectively. Near-infrared J band photometry from the 2-micron All Sky Survey (2MASS, Cutri, Mainzer, et al., 2015) compared with IRIS J band photometry shows the object jumped by

[1]See also the historic lightcurve from Jurdana-Šepić and Munari (2016), constructed using Harvard photograpic plates, showing no previous evidence of eruptions from 1899 to 1989.

$\Delta J \sim 2.5$ mag. Even in the mid-infrared, the outburst amplitudes reach 2.5 and 2.2 for W1 and W2, respectively. The post-outburst fade measured by AAVSO B-band photometry shows that V960 Mon is still $\sim$ 1 magnitude brighter than at quiescence, while at J-band the Gattini photometry indicate the object is 1.6 mag brighter than at quiescence, and similarly in NEOWISE photometry the plateau is about 1.5 mag brighter than the faint-state WISE measurement.

Spectroscopy

Our disk models described in Section 3.3 are constrained by the photometry described above and by high and medium dispersion spectra.

Optical

We use a high dispersion visible range spectrum taken at the time of the object's outburst at the Keck Observatory using the HIgh Resolution Echelle Spectrograph (HIRES; Vogt et al., 1994). The spectrum covers 4780-9220 Å at a signal-to-noise of 170 at 7100 Å and was processed with the 2008 version of the MAKEE pipeline reduction package written by Tom Barlow[2].

The orders used in our accretion disk model fits are shown in Figures 3.2, 3.3, and 3.4. This spectrum is a part of a dedicated monitoring campaign which samples the post-outburst fade over several epochs, as indicated in Figure 3.1 and given in Table 3.1. The spectra from this campaign are discussed in detail in Paper II.

In the outburst spectrum, we compute the half-width-half-depth (HWHD) of several absorption lines across the optical range, and find that there is no correlation between wavelength of the line and HWHD. The measurements are discussed and shown in detail in Paper II. The mean and standard deviation of the measurements are 44 ± 5 km s^{-1}, consistent with the line-width measurements reported by Park, Lee, et al. (2020). As described below, this linewidth provides important constraints in the disk model that we explore for matching the lightcurve evolution.

We also measure a heliocentric system velocity of -43 km s^{-1}. This was determined by comparison of the spectrum with our high dispersion disk model, using it as a radial velocity reference. Our RV value is consistent with the system velocity of -42.6 km s^{-1} found for CO by Cruz-Sáenz de Miera et al. (2023, submitted), which is the RV value we adopt.

[2] `https://sites.astro.caltech.edu/~tb/makee/`

Infrared

Our analysis also makes use of data from the NASA InfraRed Telescope Facility (IRTF) SpeX spectrograph (Rayner, Toomey, et al., 2003). We include the outburst epoch SpeX spectrum of V960 Mon obtained on 19 Dec 2014 and published by Connelley and Reipurth (2018) who provide a detailed description of the data reduction. We also make use of SpeX data taken at several other epochs: 15 Jan 2015, 6 Jan 2016, and 24 Jan 2016, all of which are previously unpublished.

The SpeX observations were obtained using the cross-dispersed echelle gratings between 0.8 and 5.4 μm, using two spectrograph slit widths: 0.8″ (15 Jan 2015 and 24 Jan 2016) and 0.5″ (19 Dec 2014 and 6 Jan 2016). Spectral extraction, wavelength calibration, telluric correction, and flux calibration were done using the Spextool reduction package (Vacca et al., 2003; Cushing et al., 2004) running under IDL. K band photometry was also obtained on each night using the SpeX guide camera, and extracted using aperture photometry. Due to the use of a slit with variations in throughput from seeing and tracking changes, all SpeX spectra were normalized to the K band photometry.

The spectrophotometry from SpeX is an important supplement to the photometry when evaluating the success of our cooling accretion disk model.

3.3 Disk Model and Fitting

To constrain the physical parameters of the evolving V960 Mon system, we model the disk photosphere using a modified version of the model described in Rodriguez and Hillenbrand (2022). Our modifications to this model are described below. The model is based on the Shakura and Sunyaev (1973) viscous accretion disk radial temperature profile,

$$T_{\rm eff}^4(r) = \frac{3GM_*\dot{M}}{8\pi\sigma r^3}\left(1-\sqrt{\frac{R_{\rm inner}}{r}}\right), \tag{3.1}$$

where $R_{\rm inner}$ is the inner radius of the accretion disk, M_* is the mass of the central star, $\dot{M}$ is the stellar accretion rate, G is the gravitational constant, and σ is the Stefan-Boltzmann constant.

In this profile, a maximum temperature ($T_{\rm max}$) is reached at $r = 1.361\ R_{\rm inner}$. Interior to this radius, the temperature falls rapidly to 0. This is not physical for this system, where we assume $R_{\rm inner} \sim R_*$ (see, e.g., Hartmann and Kenyon, 1996). We therefore follow the example of Kenyon, Hartmann, and Hewett (1988) and set

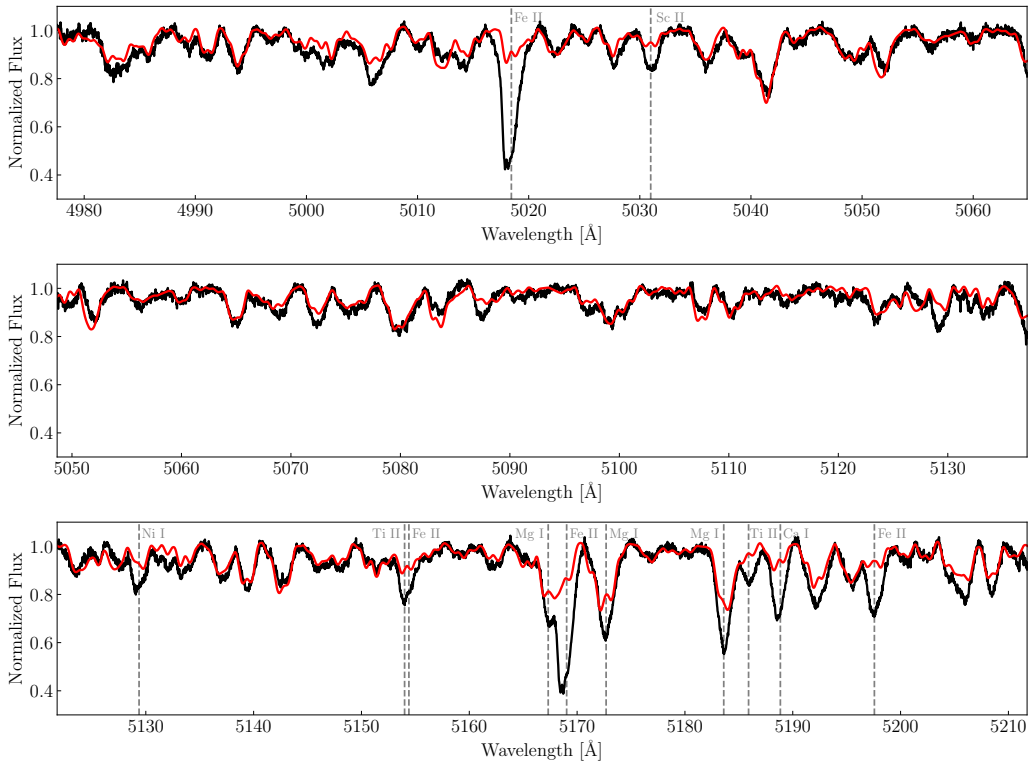

Figure 3.2: Orders of the HIRES spectrum taken closest to outburst that are used to compute the χ^2 surface described in Section 3.3. The fiducial model for the outburst spectrum is shown in red. Large mismatches between the data and model are seen in certain spectral lines; the extra depth (and blueshift in particular Fe II lines) in the data is due to wind absorption, which is not included in our disk model, but will be the subject of a future paper.

$T_{\rm eff}(r < 1.361\ R_{\rm inner}) = T_{\rm max}$. The annuli at each r value are then constructed from the appropriate PHOENIX (Husser et al., 2013) model using the calculated $T_{\rm eff}(r)$.

We fit the outburst SED of the target and the outburst HIRES spectrum using the modified model. We then use the photometry of the target to guide our modeling of the time-evolution of the system, which includes the evolution. The outburst epoch fitting procedure is described below, and the construction of models for later epochs is described in Section 3.4.

Improvements to the Rodriguez et al. 2022 Model

We have implemented several improvements to increase the accuracy of the model and its ability to rapidly compute high dispersion spectra. One important improvement is to the rotational broadening calculation. Rodriguez and Hillenbrand (2022) use the popular method of rotationally broadening spectra by convolution with the

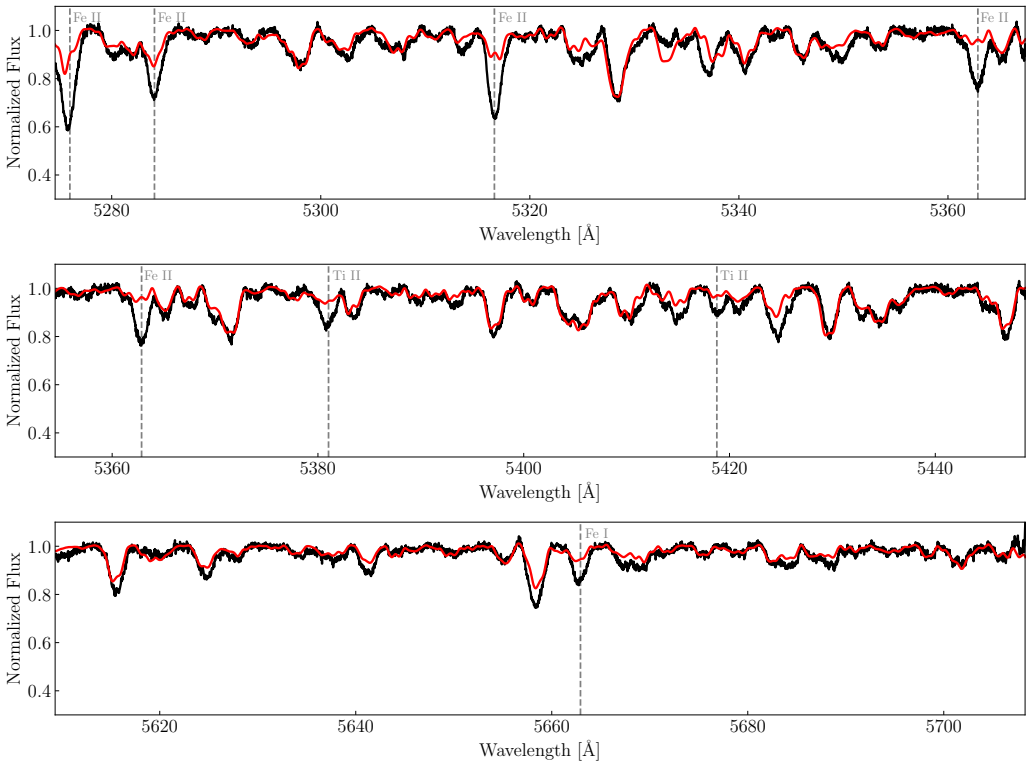

Figure 3.3: Same as Figure 3.2 for the next three orders used.

kernel

$$\phi(\lambda) = \left[1 - \left(\frac{\lambda - \lambda_0}{\lambda_{\max}(r)}\right)^2\right]^{-\frac{1}{2}}, \tag{3.2}$$

where $\lambda_{\max}(r) = \lambda_0 \frac{v_{\rm kep}(r)}{c} \sin i$, $v_{\rm kep}(r)$ is the Keplerian velocity of the annulus centered at r, i is the disk inclination, and c is the speed of light in a vacuum. This method is only valid in small wavelength ranges ($\sim$ 100 Å). Rotationally broadening a broadband high dispersion spectrum with this method requires convolving dozens of 100 Å segments at a time. This is extremely slow, and a different approach is needed to compute high dispersion models for the HIRES wavelength range of 4500 Å to 9000 Å quickly enough to reasonably use them for fitting.

We compute our rotational broadening by numerically integrating the disk

$$F_{\rm broad}(r, \lambda) = \int_0^{2\pi} F(r, \lambda(\theta)) d\theta \tag{3.3}$$

where

$$\lambda(\theta) = \lambda \times \left(1 + \frac{v_{\rm kep}(r)}{c} \sin(\theta)\, \sin(i)\right), \tag{3.4}$$

and θ is the azimuthal angle in the disk.

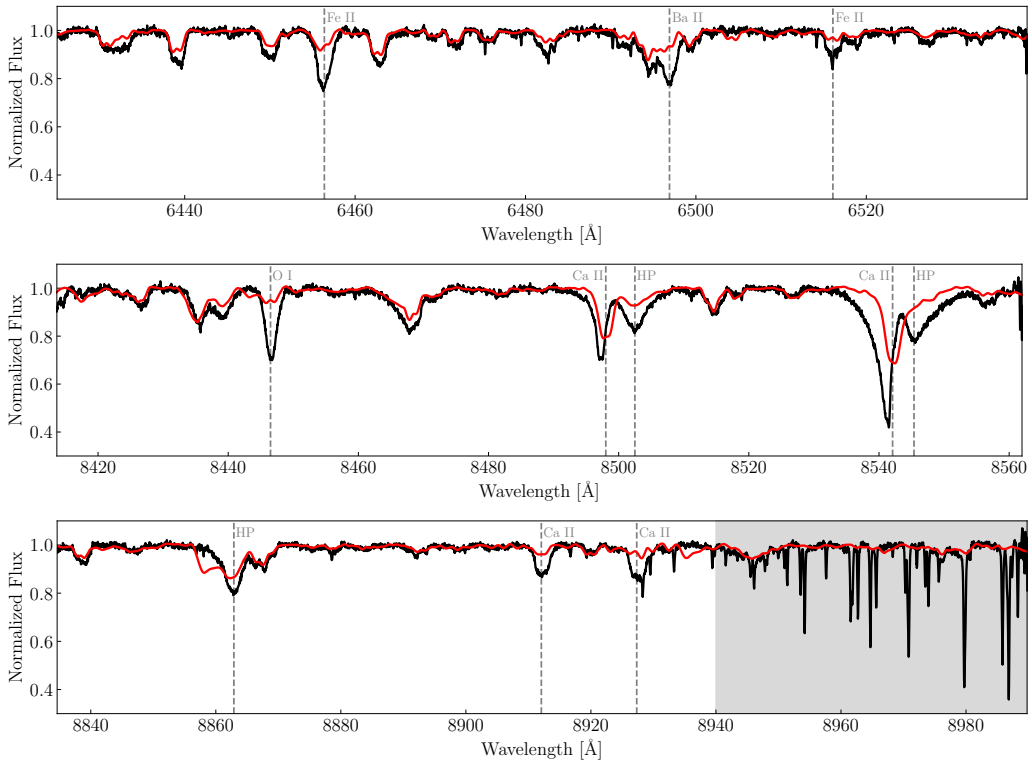

Figure 3.4: Same as Figure 3.2 for three reddest orders used. Here, in addition to wind absorption that is not included in the model, there is also uncorrected telluric absorption in the data that appears as narrow lines toward the right of the bottom panel (grey shaded region).

This greatly accelerates the model calculation because we can integrate the spectrum in one operation, rather than folding it into 100 Å chunks. (see Carvalho and Johns-Krull, 2023a for further detail). The accelerated method enables us to rapidly produce high resolution model spectra, limited only by the large amount of memory required for the atmosphere model grid.

Another significant improvement to the model is the calculation of log g at each annulus in the disk. For this calculation, we assume the gravity is dominated by the central star and neglect self-gravity from the disk, so that the acceleration g at an annulus with average radius r is given by

$$g(r) = \frac{G\ M_*}{r^2} \tag{3.5}$$

where G is the gravitational constant and M_* is the mass of the central star.

The prescription for the disk gravity given in Chiang and Goldreich (1997) is $g \sim \Omega^2 z$, where Ω is the Keplerian angular velocity and z is the height of the disk

atmosphere above the plane. Using $\Omega(r) = \sqrt{GM_*/r^3}$, we get $g \sim \frac{GM_*}{r^3}z$. If we assume that the disk flaring is constant and write $\alpha = \frac{z}{r}$, then $g \sim \alpha\frac{GM_*}{r^2}$, or $g \sim \alpha g_*$, where g_* is the gravitational acceleration due only to the star. For thin disks, our approximation greatly overestimates the gravity. However, as flaring increases, our approximation becomes more accurate. The inner disk model presented in Zhu, Jiang, et al. (2020) shows the flaring in the inner disk during an outburst may be as high as $z/r \sim 0.5 - 1$.

Modeling Strategy and Results

Our modeling strategy requires a broadband SED of the FU Ori object and a contemporaneous high resolution spectrum. In the case of V960 Mon, we construct the SED from the photometry shown in Figure 3.1 near the peak, and use the outburst HIRES spectrum from the 2014 December 9 epoch.

Using the two sets of data, we can constrain the mass of the central object, M_*, the innermost radius of the accretion disk, $R_{\rm inner}$, the inclination of the target, i, the accretion rate, $\dot{M}$, and the extinction to the target, A_V.

Directly fitting the high dispersion spectrum alone proved challenging for a variety of reasons. One in particular is that there are broad combinations of the model parameters which produce fits with similar errors. The error surface then has many deep, steep-walled local minima that are difficult for optimization algorithms to escape from to find the global minimum.

Fitting the SED alone is not as significant a challenge, but the SED is quite limited in its ability to constrain many physical parameters simultaneously. The inclination of the system is degenerate with the overall luminosity, and the extinction to the system, A_V, is degenerate with the maximum temperature in the disk. These degeneracies result in broad posteriors in our SED fits when using uniform priors on the physical parameters.

Combining the data to fit both the SED and high dispersion spectrum simultaneously is also challenging because the data volumes and ranges are vastly different. Defining properly scaled error terms in the combined space is unclear and requires further study.

We therefore adopt a hybrid approach: using a course sampling of the χ^2 surface of the high dispersion data to inform priors on the parameters of the SED fit. This way, we impose both physically motivated and data-driven constraints on the most

difficult-to-disentagle parameters such as M_* and $\dot{M}$, which are highly covariant in the SED.

Fitting the High Dispersion Spectrum

Before fitting the high dispersion spectrum, we compute several high dispersion models, spanning a broad range of i, M_*, $\dot{M}$, and $R_{\rm inner}$ parameter space. The widths of the absorption lines (see the empirical HWHD measurement above, and the $v \sin i \sim 60$ km s^{-1} inference discussed in Paper II) are much smaller than the Keplerian velocities expected near the surface of young stars (150 – 300 km s^{-1}, assuming M_*, R_* values from 0.5 Myr PARSEC isochrones, Nguyen et al., 2022). This immediately implies that the system is relatively face-on, with $i < 30°$.

Varying $T_{\rm max}$, by choosing different values of $M_*\dot{M}$ and $R_{\rm inner}$, and comparing with the observed outburst spectrum allows us to estimate a reasonable $T_{\rm max}$ range of 6500 K $< T_{\rm max} <$ 8000 K. Assuming then reasonable $R_{\rm inner}$ values based on the R_* values in the 0.5 Myr PARSEC isochrones (Nguyen et al., 2022) for 0.1 $M_\odot < M_* <$ 2 $M_\odot$, gives a range of 1.5 $R_\odot < R_{\rm inner} <$ 5 $R_\odot$.

We fix the system inclination to 15°, the best-fit value from the radiative transfer modeling in Kóspál, Cruz-Sáenz de Miera, et al. (2021). This choice of inclination agrees well with our expectation that the system is relatively face-on, despite the broad error bars reported in Kóspál, Cruz-Sáenz de Miera, et al. (2021). We continuum-normalize the models following the same normalization procedure applied to the HIRES spectra (see Paper II), eliminating A_V as a parameter for the χ^2 analysis.

Having established a reasonable range of M_*, $\dot{M}$, and $R_{\rm inner}$ values to explore, and fixing the other model parameters, we compute a grid of high dispersion models. We explore a range of 0.3 $M_\odot < M_* <$ 1.4 $M_\odot$, 1.5 $R_\odot < R_{\rm inner} <$ 2.9 $R_\odot$, and $-5 < \log \frac{\dot{M}}{M_\odot \text{ yr}^{-1}} < -4$ in steps of 0.1 $M_\odot$, 0.1 $R_\odot$, and 0.1 dex, respectively. For each of the high-dispersion models, we compute the χ^2 value.

We inspect the slices of the χ^2 cube along the $\dot{M}$ dimension and find the $\dot{M} = 10^{-4.6}$ $M_\odot$ yr^{-1} contains a minimum with physically reasonable values of M_* and $R_{\rm inner}$ that are also consistent with the estimated $v_{\rm max} \sin i \sim 60$ km s^{-1}. The slice is shown in Figure 3.5. For reference, we draw lines of constant $v_{\rm max} \sin i = v_{\rm kep}(R_{\rm inner}) \sin i$.

Notice the valley of minimum χ^2 values approximately intersects the 60 km s^{-1} line at $M_* = 0.6$ $M_\odot$ and $R_{\rm inner} = 2.2$ R$_\odot$. We adopt these as our best-fit parameters from

the χ^2 fit and will use them to construct the priors for the MCMC fits to the SED (Section 3.3).

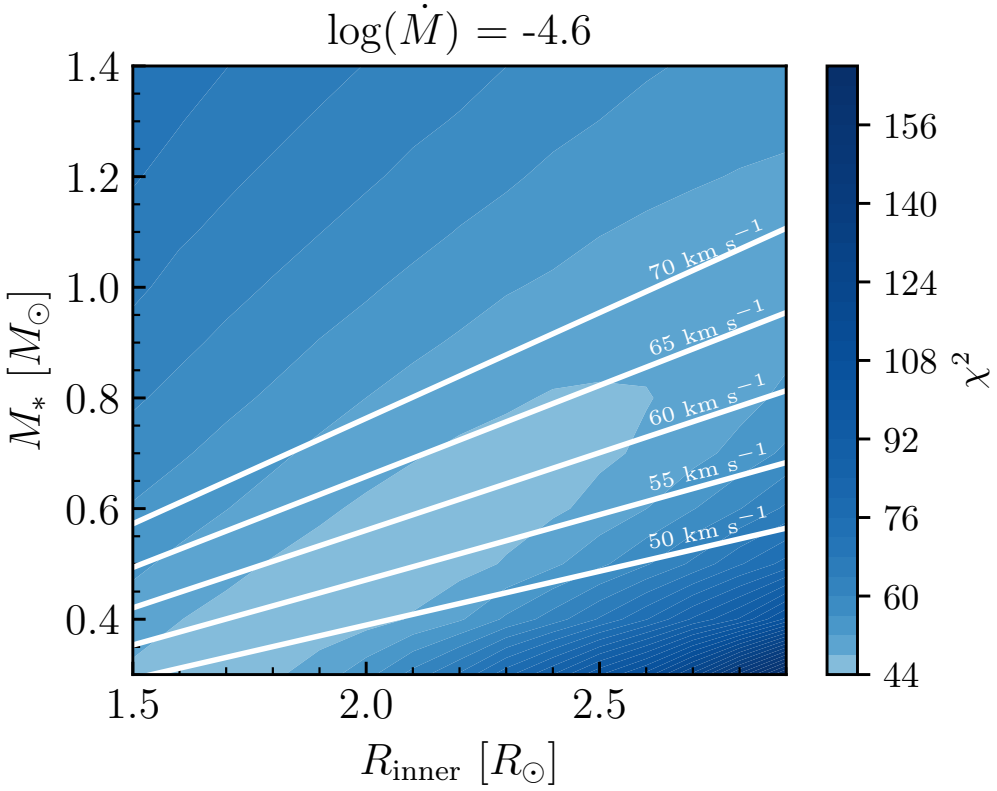

Figure 3.5: The χ^2 surface for the outburst spectrum and high resolution models with varying M_* and $R_{\rm inner}$ values, $\log(\dot{M}) = -4.6$ $M_\odot$ yr^{-1} and $i = 15°$. The mininmum χ^2 value is found in the region that is intersected by the $v_{\rm max} \sin i = 60$ km s^{-1}. The width of the minimum allows for an uncertainty of 5 km s^{-1} on that value, which we use to constrain the SED fits.

Fitting the SED

The first prior we impose on the SED fits is that the M_* should be drawn from the Kroupa (2001) Initial Mass Function (IMF), to properly reflect the lower probability that M_* would be large.

We then use the estimated $v_{\rm max} \sin i \sim 60$ km s^{-1} from the high dispersion data to construct a joint prior on M_* and $R_{\rm inner}$. At each iterative step, we compute $v_{\rm max} \sin i = \sqrt{GM_*/R_{\rm inner}} \sin i$. We then impose that the resulting value be drawn from a Normal distribution, with a mean of $\bar{v} = 60$ km s^{-1} and standard deviation

of σ_v = 5 km s^{-1}. The σ_v value is chosen from the approximate width of the valley in the χ^2 plane, and thus represents the uncertainty on the best-fit parameters.

To account for the uncertainty in the i reported in Kóspál, Cruz-Sáenz de Miera, et al. (2021), we construct a skew-normal prior distribution for i. The parameters of the distribution are chosen such that the bounds of the 95 % confidence interval match the Kóspál, Cruz-Sáenz de Miera, et al. (2021) likely range. Finally, we fix $R_{\rm outer}$ to be 45 R$_\odot$, which is approximately where the model reaches the dust sublimation temperature. We find that when varying $R_{\rm outer}$, values around 45 R$_\odot$ are marginally preferred. We demonstrate the effect of varying $R_{\rm outer}$ on the SED in Figure 3.6.

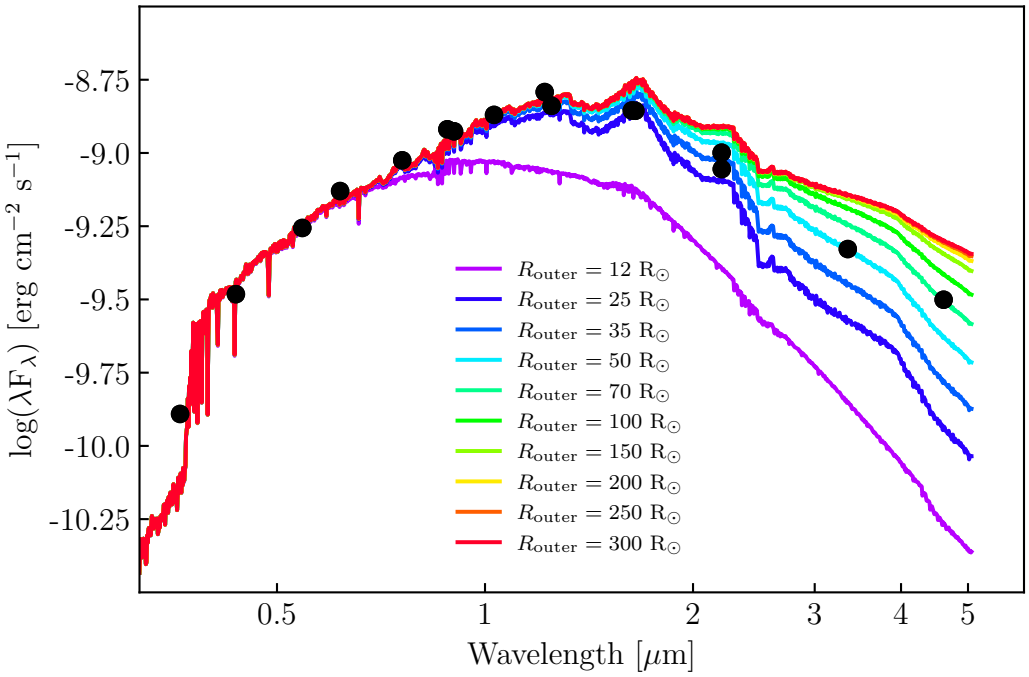

Figure 3.6: The SED model compared with the photometry from the outburst epoch, with varying values of $R_{\rm outer}$. Notice that the longer wavelength data points favor increasingly larger values of $R_{\rm outer}$, an inconsistency that can be rectified by adding a passive disk component exterior to the adopted $R_{\rm outer}$ for the active accretion disk.

We fit the SED in two major steps via MCMC using the `emcee` package (Foreman-Mackey et al., 2013). In the first step, we allow M_*, $\dot{M}$, $R_{\rm inner}$, i, and A_V to vary , imposing the priors described above. The `corner` (Foreman-Mackey, 2016) plot showing the posterior histograms for this fit is shown in Figure 3.7.

The parameters are generally all well-constrained, with the exception of A_V. They

are also consistent with the estimates from the high dispersion model fits. We therefore fix $M_* = 0.59\ M_\odot$, $R_{\rm inner} = 2.11\ {\rm R}_\odot$, and $i = 14.76°$ and in the second step fit only the $\dot{M}$ and A_V. The posteriors for this second fit are shown in Figure 3.8, along with the SED models from the full and reduced-parameter fit. This second SED model is almost indistinguishable from that produced in the first step of the SED fit and the $\dot{M}$ and A_V best-fit values are consistent with the posteriors in the first step.

We therefore adopt as the best-fit parameters for the system: $M_* = 0.59\ M_\odot$, $R_{\rm inner} = 2.11\ {\rm R}_\odot$, $\dot{M} = 10^{-4.59}\ M_\odot\ {\rm yr}^{-1}$, $i = 15°$, and $A_V = 1.61$. This best-fit model is the one shown in Figures 3.2, 3.3, and 3.4, in comparison to the observed high dispersion spectrum over the orders that were used to compute the initial χ^2 cube.

Our best-fit system parameters for the disk yield an $L_{\rm acc} \sim 100\ L_\odot$ at outburst. For a 0.6 $M_\odot$, 1 Myr star, the PARSEC isochrones predict that the stellar luminosity should be $L_* = 0.85\ L_\odot$. Thus, the central star contributes less than 1 % of the total luminosity of the FU Ori object, and thus can be ignored in our modelling procedure.

We take the values of M_*, i, and A_V as fixed and unchanging, with the justification for adopting a constant A_V provided in 3.4. However, we consider the derived $R_{\rm inner}$ and $\dot{M}$ parameters as references for the outburst epoch of the system only. In Section 3.4 we discuss the temperature evolution of the system, and the effect of varying these two parameters. We assume that during the photometric fade, these are the only two system parameters which change and argue that this is sufficient to explain the variation in both the photometry and spectrophotometry (discussed below) and the high dispersion spectra (Paper II).

3.4 Photometric Evidence of Temperature Evolution in the Disk

The post-outburst fade of V960 Mon can be explained by a decrease in $T_{\rm max}$ in the disk, driven by a decrease in $\dot{M}$ and an increase in $R_{\rm inner}$. We ignore any stellar contribution to the system, as justified above based on the luminosity arguments.

The early fade of the system is well-sampled by several photometric surveys, enabling us to study the fade in color-magnitude space for several bands. We primarily make use of the AAVSO, ROAD, and ROBOTT photometry for our analysis. We use the photometry to study the color-temperature of the system, estimate the variation in accretion rate during the post-outburst fade, and demonstrate that $R_{\rm inner}$ is changing along with the $\dot{M}$ over time.

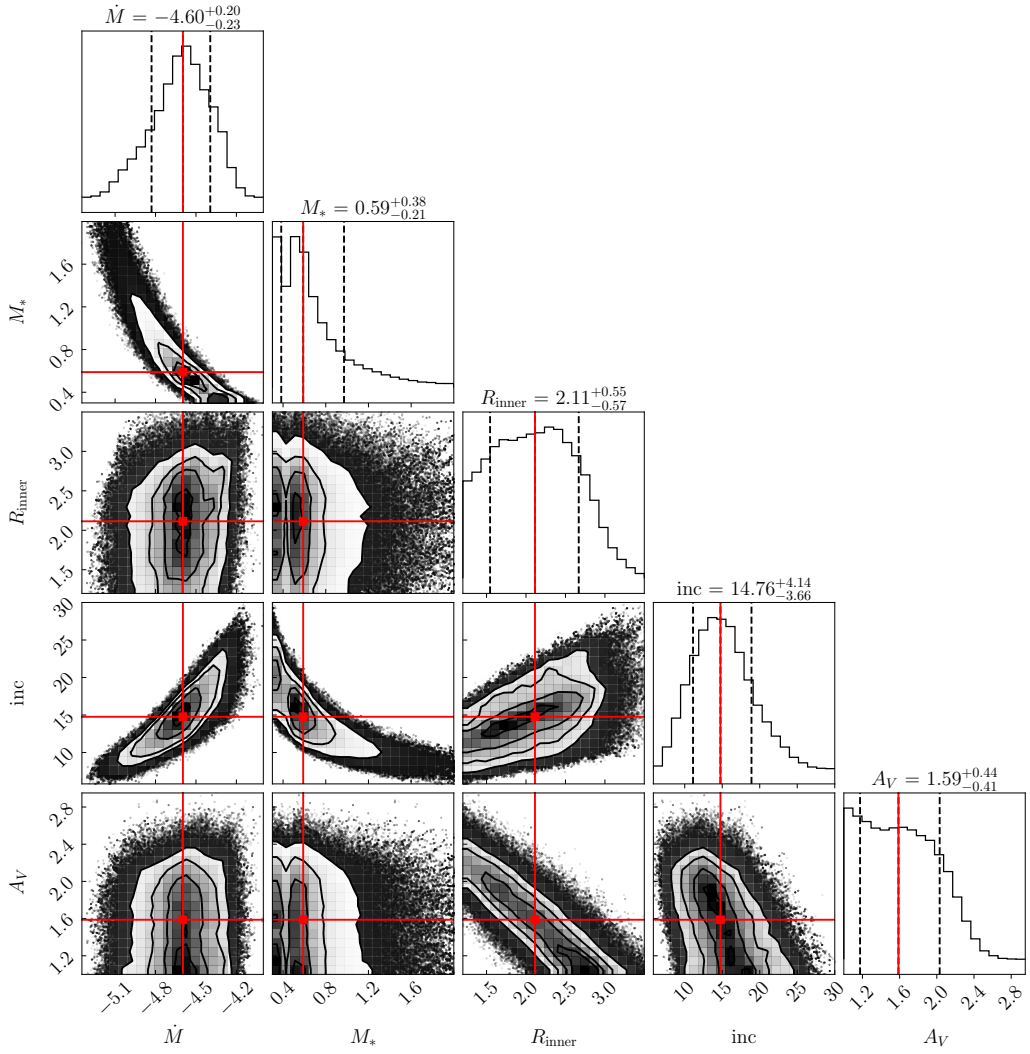

Figure 3.7: The posteriors from the full SED fit to the outburst SED. All of the parameters are well-constrained, with the exception of A_V.

The color temperature of the system

We first compute the color-temperature variation in the system, using the AAVSO B and V photometry. We adjust the V magnitudes using the best-fit $A_V = 1.61$ and use $(B-V) - E(B-V)$, assuming the typical interstellar value $R_V = 3.1$ (Cardelli et al., 1989). We then use the Ballesteros (2012) calibration to convert the $(B-V) - E(B-V)$ values to temperatures. The color-magnitude diagram with the color temperature conversion is shown in Figure 3.9.

The color temperature of the disk at outburst is approximately 6500 K, and cools to 5000 K before reaching the plateau after MJD = 58500. In order to estimate the appropriate disk parameters at later epochs, we explore use of the estimated color

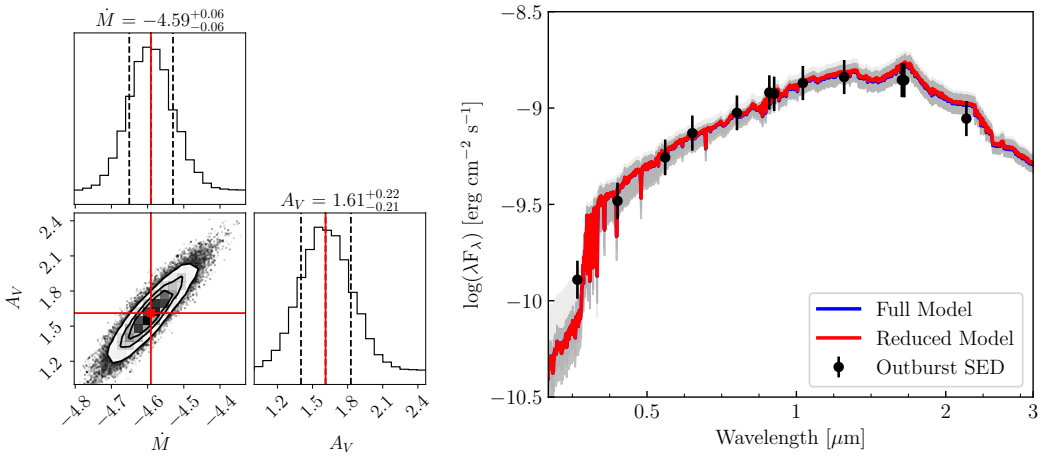

Figure 3.8: The results of the MCMC fit restricted to 3 parameters, with $M_* = 0.59\ M_\odot$, $i = 15°$, and $R_{\rm inner} = 2.11\ R_\odot$ fixed to their best-fit values shown in Figure 3.7. **Left:** The posterior distributions shown as a `corner` plot. With the fixed system parameters, the $\dot{M}$ and A_V converge and are consistent with the best-fit values found from the full SED fit. **Right:** The resulting SED models, with the full fit shown in blue and the reduced parameter fit shown in red. The good agreement between the two indicates fixing the chosen parameters did not significantly affect the fit. The error bars on the photometry represent 0.01 mag precision.

temperature evolution and the best-fit system parameters at outburst as a starting point. We can then scale the system parameters (particularly $\dot{M}$ and $R_{\rm inner}$) to model the post-outburst disk in a physically motivated and consistent way.

In T Tauri systems, the innermost accretion boundary is typically estimated to be set by the pressure balance between the magnetic field energy density $P_B = \frac{B^2}{8\pi}$ and the accretion ram pressure $P_{\rm ram} = \frac{1}{2}\rho v^2$. One thus derives the classic equation

$$R_{\rm inner} = \left[\frac{B_*^4 R_*^{12}}{2GM_*\dot{M}^2}\right]^{\frac{1}{7}}, \tag{3.6}$$

where R_* is the stellar radius and B_* is the stellar surface field strength (Hartmann, Herczeg, et al., 2016).

This shows immediately that $R_{\rm inner} \propto \dot{M}^{-2/7}$. Recall then that plugging $r = 1.361\ R_{\rm inner}$ into Equation 3.1 gives

$$T_{\rm max}^4 = \frac{3GM_*\dot{M}}{56\pi\sigma R_{\rm inner}^3}, \tag{3.7}$$

from which we see $T_{\rm max} \propto \dot{M}^{\frac{1}{4}} R_{\rm inner}^{-\frac{3}{4}}$. Using now the fact that $R_{\rm inner} \propto \dot{M}^{-\frac{2}{7}}$, we can write $T_{\rm max} \propto \dot{M}^{\frac{13}{28}}$.

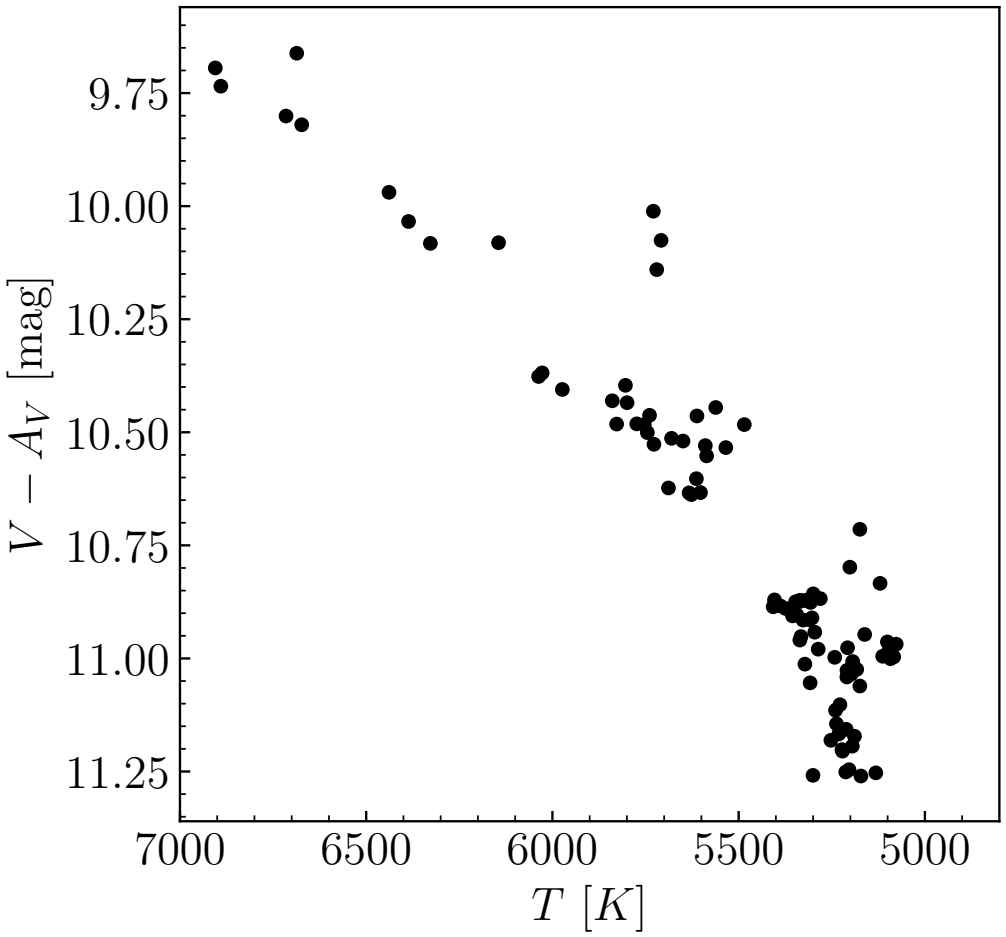

Figure 3.9: V magnitude of V960 Mon versus color temperature of V960 Mon, computed using the Ballesteros (2012) conversion from $B - V$ to $T_{\rm eff}$. $B - V$ is adjusted assuming $E(B - V) = 0.53$

This gives us a way to scale the estimated mass accretion rate at outburst, to that at later epochs by using the relative color temperatures between epochs, while accounting for expected increase in $R_{\rm inner}$. We demonstrate good agreement between this model, with an increasing $R_{\rm inner}$, and the photometric evolution in Section 3.4.

Using $T_{\rm max} \propto \dot{M}^{\frac{13}{28}}$ at a given time and the temperature difference between the outburst epoch and each HIRES epoch, we can estimate the $\Delta\dot{M}$ over time as

$$\frac{T_{\rm epoch}}{T_{\rm outburst}} = \left(\frac{\dot{M}_{\rm epoch}}{\dot{M}_{\rm outburst}}\right)^{\frac{13}{28}} \tag{3.8}$$

The accretion rates we calculate with Equation 3.8 (and resulting $R_{\rm inner}$ values) at each HIRES epoch are reported in Table 3.1. The temperature profiles for these

system parameters are shown in Figure 3.11.

We confirm the efficacy of this means of estimating the $\dot{M}$ and $R_{\rm inner}$ of the disk for a given epoch by comparing our models with the SpeX spectrophotometry, shown in Figure 3.10. The SpeX epoch closest to outburst (19 Dec 2014, cyan spectrum) is consistent with our model using the best-fit outburst parameters derived above. We then scale the $\dot{M}$ and $R_{\rm inner}$ to the later epochs and those models are consistent as well. The 24 Jan 2016 epoch (red spectrum) is well-matched by the model that uses $\log\dot{M} = -4.75$ and $R_{\rm inner} = 2.37\ R_{\odot}$.

We also compare the integrated luminosities of the SEDs and the models in the 0.7-2.5 μm range and find them to be in good agreement. The earlier two SpeX epochs, have integrated luminosities of 46 (cyan curve) and 49 (blue curve) $L_{\odot}$ and the two models have luminosities of 49 and 48 $L_{\odot}$, with discrepancies of $\sim 2\%$. The later epochs have luminosities of 31 (orange curve) and 36 (red curve) $L_{\odot}$ and the model has a luminosity of 35 $L_{\odot}$, in better agreement with the red curve but still within 15 % of the orange curve.

We address the mismatches between the model and the data in the deep molecular bands of the H and K bands in detail in Paper II. In Section 3.5 we address the long-wavelength mismatches, in L and M bands of the SpeX spectra, which we find can be accounted for by including a passive disk component that reproduces the observed excess above the pure-accretion disk model.

Considering the overall evolution of the system, the change in accretion rate is relatively small, with $\dot{M}_{2017} = 0.6\ \dot{M}_{\rm outburst}$. If we assumed only that

$$\frac{\Delta\dot{M}}{\dot{M}_{\rm outburst}} \propto \frac{\Delta L_{\rm bol}}{L_{\rm bol,\ outburst}} \propto 10^{-0.4\ \Delta V}, \tag{3.9}$$

and used the $\Delta V \sim 1.5$ since outburst, we would find $\dot{M}_{2017} \sim 0.25\ \dot{M}_{\rm outburst}$.

Color-Magnitude Evolution during the Post-Outburst Fade

In Hackstein, Haas, et al. (2015), the authors point out that the evolution of V960 Mon post-outburst in color-magnitude space does not convincingly follow the A_V vector across all color spaces. In fact, while the initial fade (MJD < 7300) is well-matched by an A_V of 0.5 magnitudes, that amount of extinction significantly overpredicts the amount of fading and reddening in redder color spaces.

In Figure 3.12, we show the photometry in four color-magnitude diagrams (CMDs): $(B-V,\ V)$, $(V-I,\ I)$, $(BP-RP,\ G)$, $(r-i,\ i)$. In these four spaces, the necessary

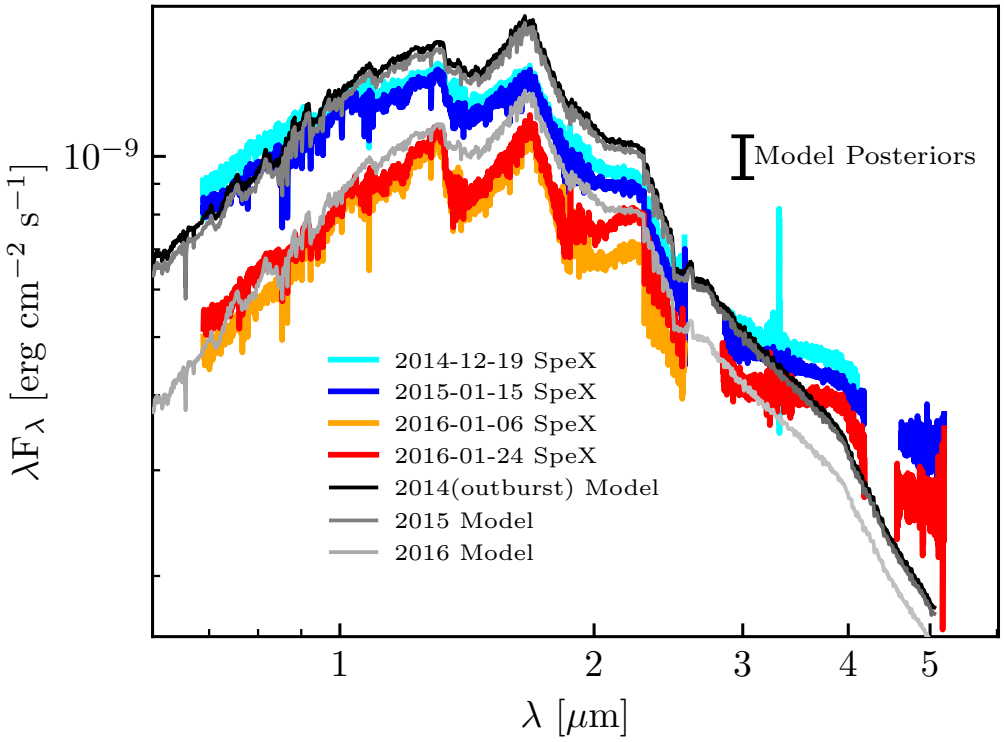

Figure 3.10: The SpeX spectra compared with the best-fit outburst model and the model generated using the extrapolated system parameters described in Section 3.4. The flux uncertainty is shown with an error bar in the upper right. Overall, the models are in good agreement with the NIR disk emission. However, there are significant discrepancies in between the molecular features in the data and the models, and generally the pure accretion disk models produce poor fits to the L and M bands. The models consistently predict a much stronger H band peak than the data predict, especially at outburst. The discrepancies are further discussed in Section 3.5 and Paper II.

amount of extinction to match the evolution of the target differs significantly, as described in Hackstein, Haas, et al. (2015). In fact, not only does the magnitude of extinction fail to match across the four CMDs, the corresponding reddening fails to match the reddening in the photometry. This is especially egregious in the $(V-I,\ I)$ diagram, where the slope of the photometry is much steeper than the slope of the A_V vector.

We thus conclude that the A_V variation is negligible and we propose that the evolution of the target can be better explained by a change in $T_{\rm max}$ that is driven by a simultaneous decrease in $\dot{M}$ and an accompanying increase in $R_{\rm inner}$. We model several SEDs with different $\dot{M}$ and $R_{\rm inner}$ values and compute the magnitudes in several

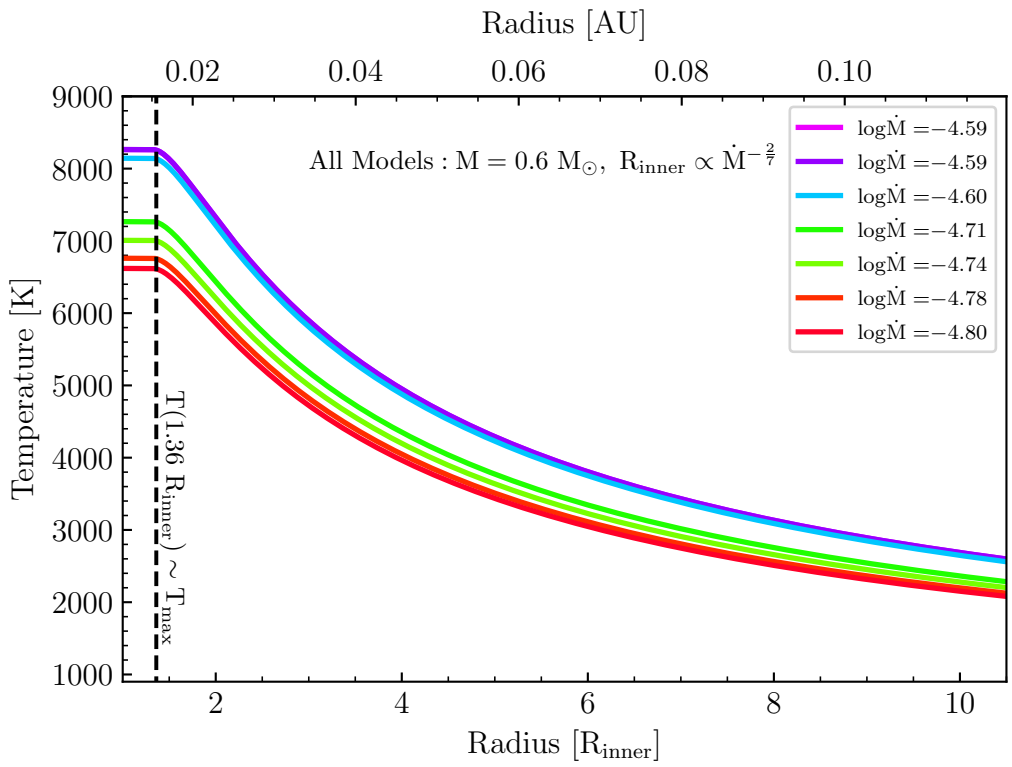

Figure 3.11: Temperature profiles adopted for the high resolution models of the HIRES epochs.

Epoch	log$\dot{M}$ ($M_\odot$ yr^{-1})	$R_{\rm inner}$ ($R_\odot$)	M_* ($M_\odot$)	A_V (mag)	i (°)
2014-12-09	-4.59	2.11	0.59	1.61	15
2014-12-10	-4.59	2.11	*0.59*	*1.61*	*15*
2015-02-09	-4.60	2.13	*0.59*	*1.61*	*15*
2015-10-27	-4.72	2.29	*0.59*	*1.61*	*15*
2016-02-02	-4.75	2.35	*0.59*	*1.61*	*15*
2016-10-14	-4.78	2.40	*0.59*	*1.61*	*15*
2017-01-13	-4.81	2.44	*0.59*	*1.61*	*15*

Table 3.1: V960 Mon System parameters at each HIRES epoch. Parameters in the first epoch are all best-fit parameters from the procedure described in Section 3.3. For later epochs, $\dot{M}$ and $R_{\rm inner}$ are estimated using the color-temperature method in Section 3.4. The parameters shown in italics in later epochs are fixed.

bands using the filter profile package `speclite`. We use the `get_ab_magnitude` function along with the filter response profiles. We convert AB magnitudes to Vega magnitudes as appropriate. The modeled CMDs are also plotted in Figure 3.12. The increasing $R_{\rm inner}$ reddens the target more rapidly than just the decreasing $\dot{M}$, which

is consistent with the photometric evolution in several color spaces.

The maximum recession rate of $R_{\rm inner}$ implied by these models can be estimated by focusing on the rapid fade from MJD 56935 to MJD 57163. The photometry corresponding to this period shows a $\Delta V \sim 0.3$ magnitudes and is well-sampled by both AAVSO and ROAD. The $\dot{M}$ for that epoch would be $10^{-4.75}$ $M_\odot$ yr^{-1}, corresponding to $R_{\rm inner} \sim 2.4$ $R_\odot$. This is a recession of 0.25 R$_\odot$ in 228 days. The implied recession rate, then, is ~ 8.8 m s^{-1} or 1870 AU Myr^{-1}, This recession rate gives a viscous timescale $\sim$ 100 times greater than those typically associated with T Tauri accretion disks (Armitage et al., 2003).

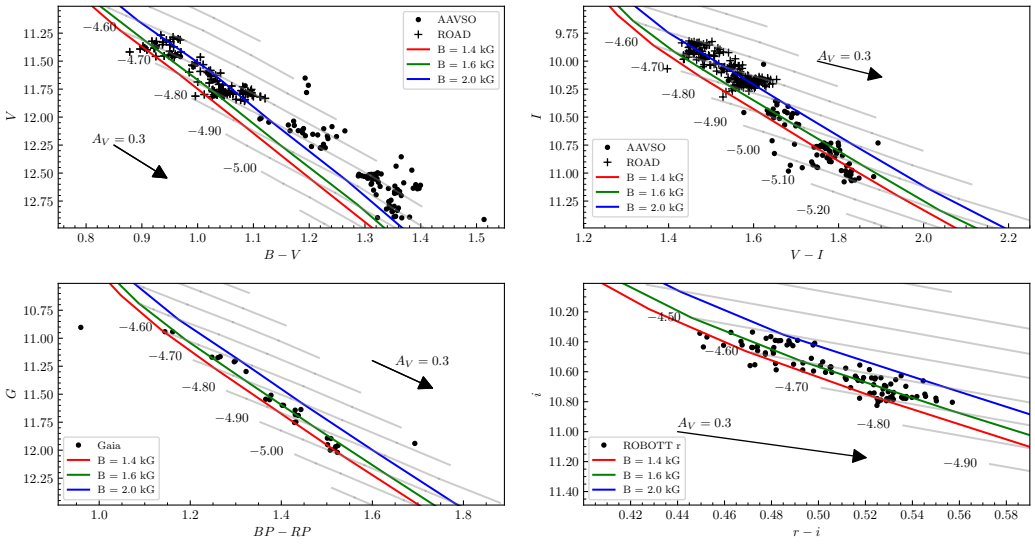

Figure 3.12: Color magnitude diagrams for V960 Mon using combined photometry from sources shown in Figure 3.1. Model curves are computed with $M_* = 0.6$ $M_\odot$, $A_V = 1.6$ mag, and $d = 1120$ pc (Kuhn and Hillenbrand, 2019). The grey curves show lines of constant $\dot{M}$ and varying $R_{\rm inner}$. The colored curves show lines of $\dot{M}$ varying along with $R_{\rm inner}$ according to Equation 3.6 for different assumed values of B_*. **Top Two Plots:** V vs $B - V$ and I vs $V - I$ from AAVSO and other sources, along with our models. **Lower Left:** Gaia G vs $BP - RP$ photometry, converted to AB magnitudes, plotted alongside our models. The Gaia photometry is very well matched by the models. **Lower Right:** i vs $r - i$ using the ROBOTT (USB) photometry. The ROBOTT photometry spans only the initial steep fade in the lightcurve, prior to JD 2457400.

3.5 The Passive Disk Contribution to L and M Band

As can be seen in Figure 3.10, the SpeX spectra (and the W1 and W2 photometry) show a clear L and M band excess that we do not model with our active accretion

disk model. Increasing the $R_{\rm outer}$ parameter in our model does not account for the excess, and, as discussed in Section 3.3, overestimates the flux in K band.

We find that adding a passive disk component to the system accounts for the majority of this excess, though matching the SpeX L and M bands precisely is challenging. To compute the contribution of the passive disk, we modify the passive disk prescription given in Chiang and Goldreich (1997). We assume a slightly flared disk, with linearly increasing flare angle, such at that a given radius r, the height of the disk surface, h, is set by $\frac{h}{a} = \eta \left(\frac{a}{a_i}\right)^{\beta}$.

We estimate the effective temperature, $T_{\rm eff}$, of the passive disk reprocessing the disk accretion flux to be given by a version of Chiang and Goldreich (1997) Equation 1. We generalize the expression to allow for contributions to $T_{\rm eff}$ from multiple sources. The modified version is shown below:

$$T_{\rm eff}(a) \approx \left(\frac{\alpha}{2}\right)^{1/4} \left(\sum_{\rm i}^{\rm N\ sources} \frac{r_i^2}{a^2}\, T_i^4 \right)^{1/4} . \tag{3.10}$$

This allows us to incorporate different annuli of the active disk centered at radii of r_i and effective temperatures T_i. α gives the grazing angle at which the incoming radiation strikes the disk. We only model the emission from the two innermost active disk annuli, and since $a >> r_i$, α will not change significantly between the two.

We compute α assuming the dominant flux is coming from a given annulus of the inner disk, rather than a central star. This new geometry would result in a α given approximately by

$$\alpha \approx \arctan\left(\frac{h}{a - a_i}\right) - \arctan\left(\frac{h}{a - r_i}\right). \tag{3.11}$$

We then use Planck functions $B_\nu(T_{\rm eff})$ to model the reprocessed emission from the annuli of the passive disk and integrate the flux.

We fix the a_i value to be equal to $R_{\rm outer}$ of the active component. To best match the K band continuum, we must decrease $R_{\rm outer}$ of the active disk from 35 $R_\odot$ to 25 $R_\odot$. Otherwise, the passive disk contribution causes the total model to overestimate the K band flux. We vary the η and β flaring parameters and find that the flaring law that best matches the decrease in K band, the sudden rise at L band, and the flat M band, is given by $\frac{h}{a} = 0.08 \left(\frac{a}{a_i}\right)^{1.0}$. This is in good agreement with the flaring law found for FU Ori by Lykou, Ábrahám, Chen, et al. (2022), though they find a shallower power law index of 0.13. The final model is shown in Figure 3.13.

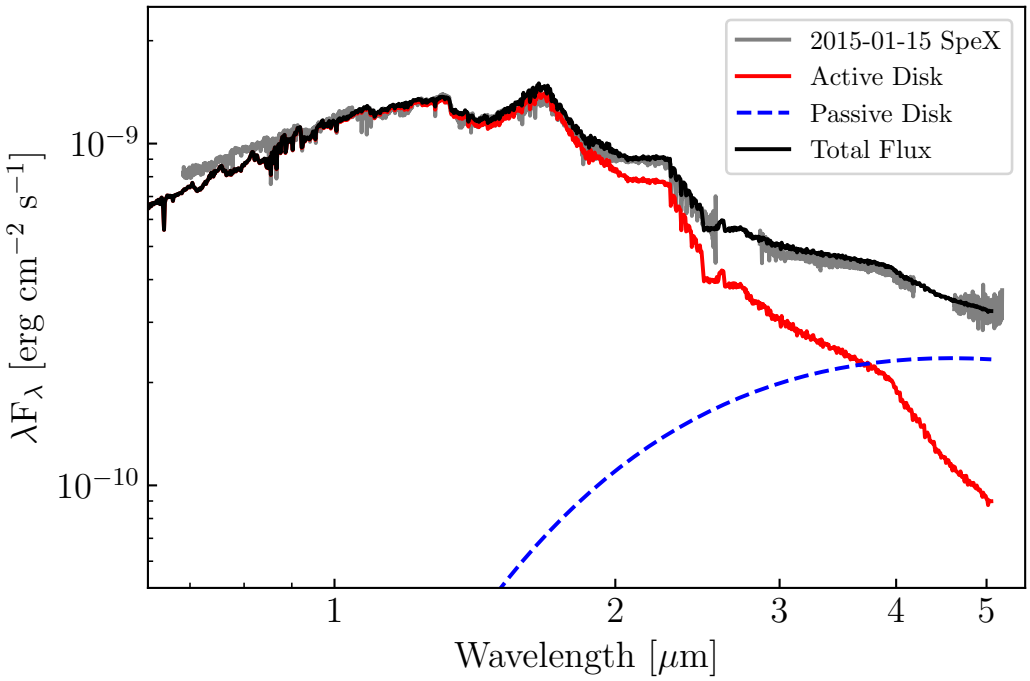

Figure 3.13: A model of the system for the 2015-01-15 SpeX epoch, incorporating both an active (red line) and a passive (blue dashed line) disk component. The active disk component is the same model as that shown in Figure 3.10 for the 2015-01-15 epoch, but computed with $R_{\rm outer} = 25\ R_\odot$. The passive disk component uses a flared disk model with a linearly increasing flare angle, described in Section 3.5. Notice that the addition of the passive disk allows the model to better match the H band molecular features, the K band continuum, and the L and M band excess.

3.6 Discussion

Our accretion disk model consistently reproduces the evolution of V960 Mon during its post-outburst fade from 2015-2017 in multiple color-magnitude spaces, as well as in the high dispersion spectra that are discussed in Paper II.

Combining constraints from the outburst SED and HIRES spectrum, we are able to constrain the system parameters to: $\dot{M} = 10^{-4.59}\ M_\odot\ {\rm yr}^{-1}$, $A_V = 1.61$ mag, $M_* = 0.59\ M_\odot$, $R_{\rm inner} = 2.11\ {\rm R}_\odot$, and $i = 15°$.

Using the outburst SED we have compiled, the 1120 pc distance to the target, and the best-fit $A_V = 1.61$ mag, we compute an $L_{\rm bol} = 107\ L_\odot$. If we compute the $L_{\rm acc}$ expected from the system parameters at outburst, we get $L_{\rm acc} = 113\ L_\odot$. This indicates we may be missing some flux, perhaps in the NUV. Integrating our model SED gives $L_{\rm bol,model} = 90\ L_\odot$. However, as shown in Figure 3.13, a model of just the active disk misses a significant amount of flux in the NIR. Our inclusion of a

passive disk component to the model (see Section 3.5) accounts for this missing flux by reproducing the L and M band excesses.

Comparison with previous results

Our derived parameters are generally consistent with those found in other literature on the target. Though we use the inclination posteriors reported in Kóspál, Cruz-Sáenz de Miera, et al. (2021) as a prior in our fits, the SED fit finds a best-fit inclination consistent with theirs. Our best-fit $R_{\rm inner}$ value is a bit larger than their reported $R_* = 1.69\ R_\odot$, but they have a broad 68 % credible region, extending to $R_* = 6.45\ R_\odot$ on the larger side.

The best-fit A_V value is in good agreement with the 1.5 mag measured by Connelley and Reipurth (2018), and is somewhat smaller than the 2.4 mag estimated by Carvalho and Hillenbrand (2022). This may indicate that the DIB method overestimates A_V values for $E(B-V) > 0.5$.

Our mass is slightly smaller than that estimated for the progenitor object in Kóspál, Ábrahám, Moór, et al. (2015). However, using a distance estimate of 1120 pc, it is difficult to reconcile the SED of a 0.6 $M_\odot$ or 0.75 $M_\odot$ object with the progenitor SED compiled by Kóspál, Ábrahám, Moór, et al. (2015).

Though the color temperatures we computed from the Ballesteros (2012) calibration do not match the $T_{\rm max}$ values for the temperature profiles, they do match the temperatures at $r \sim 3\ R_*$. This is consistent with the result of radiative transfer modeling of FU Ori by Calvet, Hartmann, et al. (1993), who find that that the optical continuum arises predominantly from the $r \sim 3\ R_*$ annulus. Since the color temperatures are derived from $B-V$ colors, we expect the estimated temperature to be that of the $r \sim 3\ R_*$ region of the disk.

The outburst amplitudes across the photometric bands are somewhat consistent with the outbursts modeled in Hillenbrand and Rodriguez (2022) and Liu et al. (2022). The outburst is slightly greater amplitude at shorter wavelengths ($\Delta B \sim 3$ mag) and smaller in the NIR ($\Delta W2 \sim 2.2$ mag). However, this is not as drastic a difference as that predicted in Hillenbrand and Rodriguez (2022). This can be explained by two effects not modeled by Hillenbrand and Rodriguez: the pre-outburst accretion shock and the post-outburst variable passive disk. A significant contribution from the magnetospheric accretion shock in the bluer bands (especially U) would increase expected pre-outburst U and B magnitude and decrease the outburst amplitude in those bands.

For the NIR outburst amplitude, we expect the passive disk should be more luminous after outburst, as the incident radiation has both a greater $T_{\rm eff}$ and overall luminosity. This will increase the post-outburst passive disk contribution to the SED, increasing the outburst amplitude in the reddest bands, especially W1 and W2. Therefore, it is not entirely surprising that the outburst would have an approximately similar amplitude across all optical/NIR photometric bands.

The case for a cooling inner disk

We find that the exponential post-outburst fade of V960 Mon is well-explained by the inner disk cooling over time. The cooling is primarily driven by a decrease in the disk accretion rate, which in turn causes the $R_{\rm inner}$ to increase.

Our investigation of the evolution of the system in four CMDs shows that a model wherein the disk cools is a better fit to the data than one wherein the extinction increases. A single extinction vector cannot reproduce the slope and magnitude of the color variation of the system in the 4 CMDs consistently. In fact, assuming the $\Delta J \sim 0.9$ mag fade is due to extinction, and using $A_J/A_V = 3.55$ (Mathis, 1990), we obtain a corresponding A_V increase of 3.2 mag, which is much greater than the ΔV observed.

A cooling inner disk (though accompanied by an increase in A_V) is also proposed to explain the long-term fading of V1057 Cyg (Szabó, Kóspál, Ábrahám, Park, Siwak, Green, Moór, et al., 2021). In their model, Szabó, Kóspál, Ábrahám, Park, Siwak, Green, Moór, et al. (2021) vary the product $M_*\dot{M}$ and A_V over time, finding that an exponential decrease in $\dot{M}$ and a factor 2 increase in A_V is consistent with the SED evolution of the target over 50 years. It is possible that the increase in A_V might be substituted for an increase in $R_{\rm inner}$ in this system to better fit the data. The slopes of the CMDs shown in their Figure 7 are inconsistent with either $\dot{M}$ or A_V vectors. However, comparing their $\mathrm{d}V/\mathrm{d}(V-I)$, the overall fading and reddening in the CMD is approximately consistent with the $\mathrm{d}V/\mathrm{d}(V-I)$ we obtain from our model. Rather than varying A_V, varying $R_{\rm inner}$ over time could better explain the slope seen in the CMDs.

Ultimately, a cooling inner disk is more consistent with the photometric evolution of systems like V960 Mon and V1057 Cyg than only increasing A_V. We discuss the issue of varying $R_{\rm inner}$ in Section 3.6, supported by evidence presented in Section 3.4.

The case for an increasing $R_{\rm inner}$

Using the time-evolution of the object in color-magnitude space and the fixed $\dot{M}_{\rm outburst} = 10^{-4.59}\ M_\odot\ {\rm yr}^{-1}$, we have estimated the $\dot{M}$ as a function of time for the system. Assuming only $\dot{M}$ varies over time, we find $\dot{M} = 10^{-5.05}\ M_\odot\ {\rm yr}^{-1}$ for the 2017 HIRES epoch. This represents a maximum decrease of a factor of 2.9 in the accretion rate since outburst.

For the February 2016 epoch, we find that $R_{\rm inner} = 2.4\ R_\odot$ and $\dot{M} = 10^{-4.75}\ M_\odot\ {\rm yr}^{-1}$ fits the SpeX spectrum well (See Section 3.4). For this same epoch, varying only $\dot{M}$ gives an estimate of $10^{-4.89}\ M_\odot\ {\rm yr}^{-1}$, which is a poor fit to the SpeX spectrum. This difference indicates that varying only $\dot{M}$ causes us to underestimate it at later times.

The question that arises then is whether our use of Equation 3.6 is physically reasonable in this system. For a 0.6 $M_\odot$, 2.1 $R_\odot$ star (corresponding to a $\sim$ 0.7 Myr central star; Baraffe et al., 2015), we can solve for the necessary B_* such that $R_{\rm inner} = R_*$. Doing this gives a value of $\sim$ 1.4 kG, well within the range of, and in fact at bit smaller than, typical T Tauri star surface field strengths (Johns-Krull, 2007).

Though this B_* value is slightly smaller than that of the track along which the photometry evolves in Figure 3.9, there are factors of order unity, such as the partition of pressure support between gas pressure and magnetic field pressure, which might contribute to this difference. Another possible contribution to the pressure support in the system is that of the magnetic field of the disk, which may be comparable to the B_* value we estimate here (Donati et al., 2005; Zhu, Jiang, et al., 2020).

We find that this relation between $\dot{M}$ and $R_{\rm inner}$ is consistent with what we observe in the high dispersion spectra, as presented in Paper II. Of note is the fact that there are many subtleties in the spectral data, with line strength and line broadening that is sometimes nonintuitive in terms of behavior with excitation potential or wavelength, but in fact can be well-explained by the disk model.

3.7 Summary and Conclusion

We have demonstrated that a single accretion disk model can be used to fit the SED and high dispersion spectrum of V960 Mon at outburst. The model can then be modified by varying $\dot{M}$ and $R_{\rm inner}$ in physically consistent ways to reproduce the photometric evolution of the system during its post-outburst fade.

In summary:

1. We have modified the accretion disk model described in Rodriguez and Hillenbrand (2022) to more accurately and rapidly produce both SEDs and high dispersion model spectra.

2. We introduced a hybrid technique for using high dispersion spectra of FU Ori objects to inform priors on contemporaneous SED fits of the targets. The technique produces best-fit system parameters near the lightcurve peak of $\dot{M} = 10^{-4.59}\ M_\odot\ \mathrm{yr}^{-1}$, $A_V = 1.61$ mag, $M_* = 0.59\ M_\odot$, $R_{\mathrm{inner}} = 2.11\ \mathrm{R}_\odot$, and $i = 15°$. We find $R_{\mathrm{outer}} = 45\ R_\odot$ produces models most consistent with the K band photometry. The L_{acc} computed from these parameters is 113 $L_\odot$, in good agreement with the $L_{\mathrm{bol}} = 107\ L_\odot$ computed by integrating the outburst epoch SED.

3. We used the color-temperature evolution of the system, along with the derived relation $T_{\mathrm{eff}} \propto \dot{M}^{-13/28}$, to trace the photometric evolution of the system. To better match the evolution as seen in the CMDs, we allowed R_{inner} to vary, assuming a justified $R_{\mathrm{inner}} \propto \dot{M}^{-2/7}$. We assume all other system parameters are fixed during this time.

4. We investigated the contribution of a passive disk to emission at L and M band in the NIR, finding a simple blackbody representation produces a consistent model, even improving the agreement with the H and K band. The K, L, and M band are well-matched by reducing the R_{outer} of the active component to 25 $R_\odot$ and introducing a passive component with a flaring law of $\frac{h}{a} = 0.08\left(\frac{a}{a_i}\right)$.

We study the evolution of the system at high dispersion in Paper II. In future work, we will expand this technique to other well-known FU Ori objects. For other objects that show an exponential fade, a cooling inner disk driven by a decrease in $\dot{M}$ and increase in R_{inner} may be the best explanation for the systems' fading.

3.8 Acknowledgements

We thank Antonio Rodriguez for insightful conversations and comments.

We thank the American Association of Variable Star Observers for their dedicated sampling of the post-outburst lightcurve of this target in multiple bands.

We thank the referee for a careful review of our work.

3.9 Appendix: Photometry used in Figure 1

A significant fraction of the photometry used in Figure 3.1 can be found on a variety of public databases and in Hackstein, Haas, et al. (2015). We present in Table 3.2 the photometry used in Figure 3.1, and throughout this work, that is not already published. All of the photometry from RoBoTT, ROAD, and IRIS can be found in the CDS table associated with Hackstein, Haas, et al. (2015).

Epoch (JD - 2450000.5)	Flux (mag)	Flux Uncertainty (mag)	Source/Facility	Band
7010.51	12.25	0.01	AAVSO	B
7010.51	12.25	0.01	AAVSO	B
7012.10	12.27	0.01	AAVSO	B
7012.11	12.28	0.01	AAVSO	B
7013.10	12.27	0.01	AAVSO	B
7013.10	12.29	0.01	AAVSO	B
7014.10	12.28	0.01	AAVSO	B
7014.10	12.27	0.01	AAVSO	B
7015.10	12.24	0.01	AAVSO	B
7015.10	12.27	0.01	AAVSO	B
7016.09	12.28	0.01	AAVSO	B
7016.09	12.27	0.01	AAVSO	B
...	...	...	...	...

Table 3.2: Photometry from AAVSO, Gaia, Gattini, and WISE, shown in Figure 3.1. The full, machine-readable version of the table is available in the online journal

Chapter 4

DISK COOLING AND WIND LINES AS SEEN IN THE SPECTRAL LINE EVOLUTION OF V960 MON

Carvalho, Adolfo S., Lynne Hillenbrand, and Jerome Seebeck (Dec. 2023). "Disk Cooling and Wind Lines as Seen in the Spectral Line Evolution of V960 Mon." In: *ApJ* 958.2, 140, p. 140. DOI: 10.3847/1538-4357/acff59. arXiv: 2310.02465 [astro-ph.SR].

Abstract: We follow up our photometric study of the post-outburst evolution of the FU Ori object V960 Mon with a complementary spectroscopic study at high dispersion that uses time series spectra from Keck/HIRES. Consistent with the photometric results reported in Carvalho et al. 2023, we find that the spectral evolution of V960 Mon corresponds to a decrease in the temperature of the inner disk, driven by a combination of decreasing accretion rate and increasing inner disk radius. We also find that although the majority of the absorption lines are well-matched by our accretion disk model spectrum, there are several strong absorption line families and a few emission lines that are not captured by the model. By subtracting the accretion disk model from the data at each epoch, we isolate the wind/outflow components of the system. The residuals show both broad and highly blueshifted profiles, as well as narrow and only slightly blueshifted profiles, with some lines displaying both types of features.

4.1 Introduction

FU Ori outbursts produce photometric brightenings that reach optical amplitudes of $\Delta V \sim 4 - 6$ mag, and that are associated with episodes of significantly enhanced accretion (Hartmann and Kenyon, 1996) in young stellar objects (YSOs). The accretion rates during these outbursts may increase by factors 10^2 to 10^4, leading to proposals that YSOs may accrete a significant fraction of their mass during the events (see Fischer et al., 2023b, for a review).

In December 2014, the relatively unknown young stellar object V960 Mon underwent a large outburst, which was initially reported as a suspected FU Ori object by Maehara et al. (2014). V960 Mon has several other YSOs nearby, is surrounded by diffuse dust emission, and its status as an FU Ori object was quickly confirmed

by followup observations (Hillenbrand, 2014; Reipurth and Connelley, 2015; Hackstein, Chini, et al., 2014). The outburst peaked at $V \sim 11.2$ magnitudes and had a relatively flat outburst amplitude across the spectrum, with $\Delta B \sim 3$ reported by Kóspál, Ábrahám, Moór, et al. (2015) and a ΔW2 ~ 2.2 from the Widefield Infrared Survey Explorer (WISE, Mainzer et al., 2011). Carvalho, Hillenbrand, Hambsch, et al. (2023, hereafter Paper I) Figure 1 provides the full multiband lightcurve to date.

In the months and years following the outburst, the target faded approximately exponentially, eventually reaching a plateau of $B \sim 14$ ($V \sim 13$) after 2018, as can be seen in Figure 4.1. Though the target faded rapidly post-outburst, since reaching the plateau in 2018 its brightness has remained essentially unchanged and is still 1.2 mag brighter in the B band than pre-outburst.

In Paper I, we presented a disk model that successfully reproduces the color-magnitude evolution of the target during its exponential fade. We used photometry gathered near the outburst epoch and a single high dispersion spectrum from the same time to determine the best-fit system parameters in the pure-accretion scenario. The stellar and disk parameters that best explain the outburst peak are: $M_* = 0.59\ M_\odot$, $R_{\rm inner} = 2.11\ R_\odot$, and $\dot{M} = 10^{-4.59}\ M_\odot\ {\rm yr}^{-1}$, corresponding to $T_{\rm max} = 8240$ K, $L_{\rm acc} = 113\ L_\odot$, and $v_{\rm max} = 60$ km s^{-1}. Our analysis in Paper I assumed a distance to the target of 1120 pc (Kuhn and Hillenbrand, 2019).

The model described in detail in Paper I is used here to study the spectral evolution of the V960 Mon system at high dispersion. We followed the exponential decline over several years, from the initial outburst to the beginning of the plateau, as indicated in Figure 4.1. In this paper, we present the spectra, gathered with Keck/HIRES, and demonstrate that our accretion disk model is able to accurately reproduce the spectral evolution over a broad range of optical wavelengths during the fade.

We then isolate the excess absorption and emission in the spectrum by subtracting our high resolution model from the data. In this way, we are able to analyze a spectrum of the non-disk components in the system.

We begin by discussing our reduction and continuum normalization of the HIRES spectra in Section 4.2. We then give a brief summary of our disk model from Paper I, followed by a discussion of the spectral line evolution in the system in Section 4.3. We show evidence for a cooling inner disk and how that is traced by the absorption lines in the HIRES spectra (and reproduced by our model) in

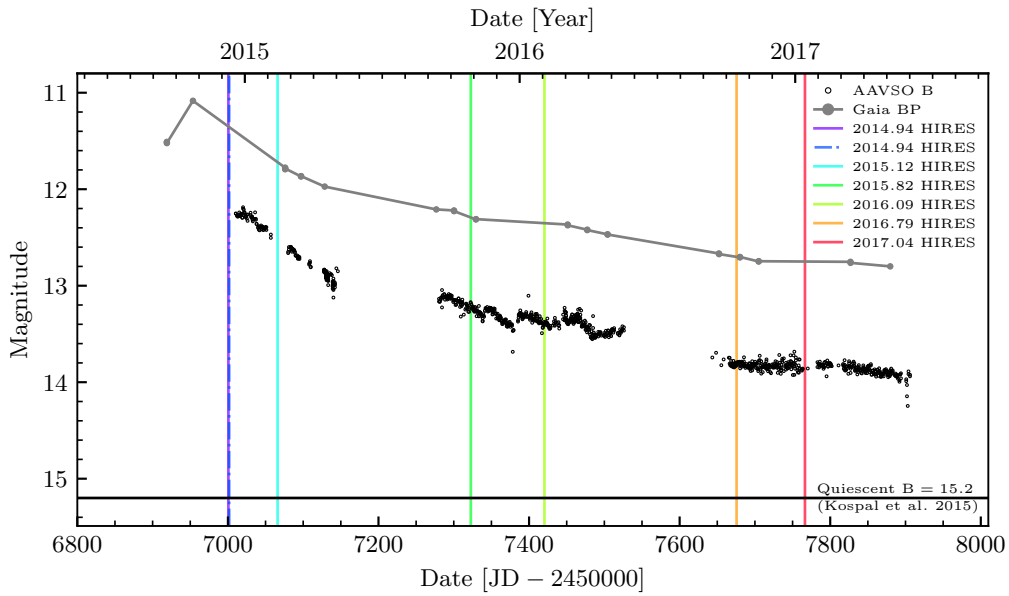

Figure 4.1: The epochs of our HIRES spectra are shown (vertical solid lines) relative to the AAVSO B (black circles) and Gaia BP (grey connected points) lightcurves of V960 Mon. The lightcurve illustrates the rapid post-outburst fade and eventual plateauing in later epochs. The quiescent B magnitude reported in Kóspál, Ábrahám, Moór, et al. (2015) is shown as the black horizontal line for reference. The Dec 10 2014 HIRES epoch is marked with a dot-dashed line due to overlap with the Dec 9 2014 epoch.

Section 4.4. Once we have subtracted the model spectra from the data, we analyze the excess absorption/emission spectrum, which is presented in Section 4.5. We identify several forbidden emission lines in the spectrum, which grow as the target fades, and we show those in Section 4.6. We discuss our results in the context of existing FU Ori object and other young star literature in Section 4.7 and summarize our conclusions in Section 4.8.

4.2 Data

We obtained visible range high-dispersion spectra from the Keck Observatory's HIgh Resolution Echelle Spectrograph (HIRES; Vogt et al., 1994), covering 4780-9220 Å. Table 4.1 gives the epochs, instruments, and S/N for the spectra. The spectra were processed with the 2008 version of the MAKEE pipeline reduction package written by Tom Barlow[1].

We normalize the spectra by fitting the continuum using a regularized Asymmetric

[1] `https://sites.astro.caltech.edu/~tb/makee/`

Table 4.1: Spectroscopic Observations Log

Date	Instrument	S/N at 7100 Å	Exposure Time (s)
2014-12-09	HIRES	170	600
2014-12-10	HIRES	117	315
2015-02-09	HIRES	98	245
2015-10-27	HIRES	97	300
2016-02-02	HIRES	147	600
2016-10-14	HIRES	80	180
2017-01-13	HIRES	52	180

Least-Squares technique (Eilers and Boelens, 2005). The regularization parameter allows for more or less flexible continuum fits and the technique is more robust to the edges of the spectrum than polynomial fitting. Orders with emission lines (e.g., Hα, weak forbidden emission lines, and the Ca II Infrared Triplet) need special treatment. We mask emission lines in the spectrum and use the linear interpolation from the redward continuum point to the blueward continuum point on either side of the lines as the continuum under those lines. Several orders from the continuum-normalized HIRES outburst epoch spectrum are illustrated in Figure 4.2.

As is mentioned in Paper I, we compute the half-width-half-depth (HWHD) of several absorption lines in the outburst spectrum (taken 9 December, 2014) across the optical range, and find no correlation between wavelength of the line and HWHD. The measurements are discussed and shown in Section 4.3. The mean and standard deviation of the measurements are 44 ± 5 km s^{-1}, consistent with the line-width measurements reported by Park, Lee, et al. (2020).

We compute the equivalent widths (EWs) of select lines via direct integration, taking the continuum to be 1.0 following our normalization described above. The procedure for the equivalent width measurement and uncertainty estimation is described in detail in Carvalho and Hillenbrand (2022) and our results for V960 Mon are presented in Section 4.4.

We measure a heliocentric system velocity of +43.0 km s^{-1}, which is roughly consistent with the $v_{\rm LSR} = 23.81$ km s^{-1} ($v_{\rm helio} \sim 40$ km s^{-1}) measured by Cruz-Sáenz de Miera et al. (2023).

The 7 epochs of HIRES data, along with the residuals from the high dispersion disk model described below, are shown in Figure 4.2.

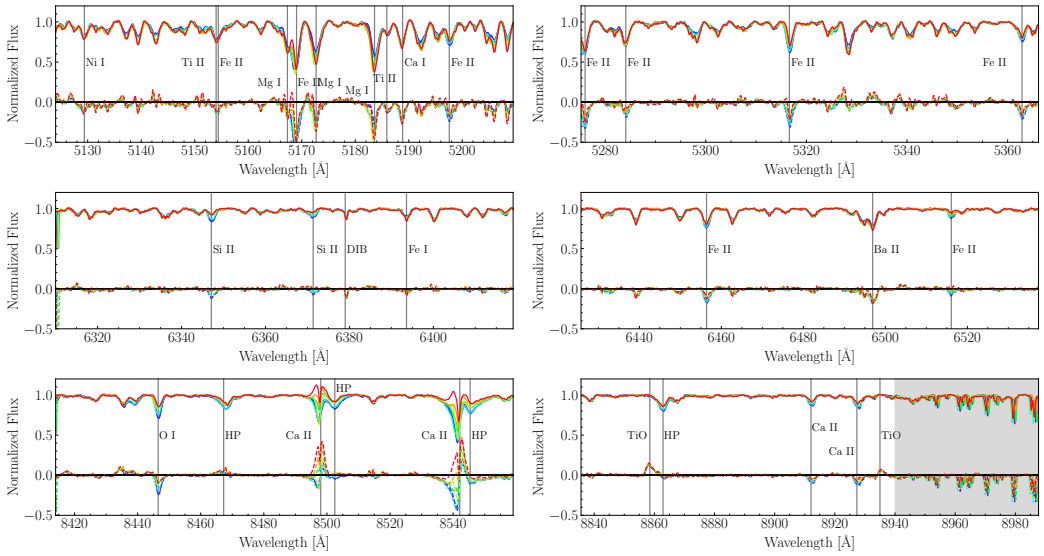

Figure 4.2: The HIRES spectra shown in a time-series, with bluer to redder spectra indicating earlier to later epochs. The lower set of curves in each panel are the residuals after subtracting the disk model appropriate to each epoch. See Figures 2-4 of Paper I for the direct comparison between the outburst epoch spectrum (bluest line here) and the disk model. Strong excess absorption in certain lines (marked) is attributed to wind contributions in the spectra; see §4.5. Outside of these lines, the typical RMS value of the residuals is < 3 %. The remaining 28 orders are shown in Appendix 4.12.

4.3 Modeling the High Dispersion Spectra

We use the disk model described in Paper I to model the high dispersion data. We briefly summarize the model below, as well as the technique we adopt to model the evolution of the system from outburst to later epochs. We describe how temperature-sensitive lines behave in the model in terms of their presence and broadening We also discuss the effect of varying the accretion rate and innermost radius on the high dispersion models and the strong agreement with what we observe in the HIRES spectra.

A Recap of the Disk Model

We assume that the system can be well-approximated by a thin accretion disk, following the Shakura and Sunyaev (1973) model, with the change that for radii interior to that of the maximum temperature, $T_{\rm max}$, we impose a flat profile, following Kenyon, Hartmann, and Hewett (1988). Therefore, the radial temperature profile in

the model is given by:

$$T_{\rm eff}^4(r) = \frac{3GM_*\dot{M}}{8\pi\sigma r^3}\left(1-\sqrt{\frac{R_{\rm inner}}{r}}\right), \tag{4.1}$$

for $r \geq \frac{49}{36}\,R_{\rm inner}$ and $T_{\rm eff}^4(r) = T_{\rm max}$ for $r < \frac{49}{36}\,R_{\rm inner}$. Here, M_* is the mass of the central star, $\dot{M}$ is the accretion rate, $R_{\rm inner}$ is the innermost radius of the accretion disk, while σ is the Stefan-Boltzmann and G the gravitational constant, respectively.

We use PHOENIX (Husser et al., 2013) model atmosphere spectra[2] corresponding to the $T_{\rm eff}$ of each annulus of the disk, following the temperature profile in Equation 4.1. We find that using only the $\log g = 1.5$ atmospheres gives a better match to the high dispersion spectra than the $g(r)$ model implemented in Paper I. The change does not affect the SED fits from Paper I.

To account for turbulence in the disk like that seen in simulation of FU Ori presented by Zhu, Jiang, et al. (2020), we apply 20 km s^{-1} of spherical broadening to the atmospheres using the direct integration method in Carvalho and Johns-Krull (2023a). The broadening is similar to stellar rotational broadening, but without limb darkening. This initial broadening step helps to better match the individual line profiles, which do not show the narrow double-peaks typical of Keplerian rotation in a thin disk, but instead have a flat-bottomed, box-like profile. We then apply the disk Keplerian broadening as described in Paper I.

In Paper I, we found that as the target fades, the color-magnitude evolution is well-matched by varying both $\dot{M}$ and $R_{\rm inner}$. The exact scaling between the two quantities is that given by the canonical truncation radius equation (Equation 6 of Paper I), which yields $R_{\rm inner} \propto \dot{M}^{-2/7}$. We use the color-temperature calculated in Paper I at each HIRES epoch from the AAVSO photometry to estimate the appropriate $\dot{M}$, assuming the scaling $T \propto \dot{M}^{13/28}$. We compute a $T_{\rm max}$ at each epoch ranging from 8300 K to 6600 K. See Figure 11 of Paper I for the resulting temperature profiles.

The high dispersion disk models computed from the lightcurve evolution are generally very good fits to the HIRES spectra. The models reproduce the absorption lines across the entire spectral range well, with the exception of certain features we believe trace non-disk absorption and emission components (including "wind" lines like Hα, Ca II and high excitation potential (EP) lines like Si II and C I, see Section 4.5). The typical RMS of the residuals, excluding these and other key excess features that are not accounted for in the disk model, is < 3 %.

[2]Downloadable at: `http://svo2.cab.inta-csic.es/theory/newov2/index.php`

Temperature-Sensitive Lines: Differential Broadening

In the canonical FU Ori disk model (Kenyon, Hartmann, and Hewett, 1988; Calvet, Hartmann, et al., 1993), the spectral line broadening is given by the Keplerian rotation of the gas disk. Therefore, for a given spectral line, the broadening should be proportional to $\sqrt{GM_*/r_{\rm line}}$, where $r_{\rm line}$ is the radius in the disk where the line is expected to form. For lines with higher EP, one might expect $r_{\rm line} \sim R_{\rm inner}$, whereas lower EP lines are expected to form further out in the disk, on average. While this may be the case, we also find that the $\dot{M}$ in the model plays a role in determining the final observed line broadening.

We find that for lower EP lines belonging to neutral species such as Fe I and Ca I, lower values of $\dot{M}$ produce broader line profiles and higher $\dot{M}$ values produce narrower line profiles. In fact, the effect is so strong in these lines that it overwhelms the effect of varying $R_{\rm inner}$, as shown in Figure 4.3.

This is because for higher values of $\dot{M}$, the $T_{\rm eff}$ in the fastest-moving annuli is high enough that low EP lines from Ca I (e.g., Ca I 6439) and Fe I (e.g. Fe I 6393) are extremely weak or totally absent. The effect is especially pronounced in the $T_{\rm eff} > 7000$ K annuli. In this case, the low EP lines will not be broadened as significantly as lines that still appear in those hottest annuli, such as Si II 6347 and 6371.

As $\dot{M}$ decreases, we see in Figure 4.3 that the Ca I 6439 line grows broader because the fastest-moving, closest-in annuli are cool enough to show lower EP lines in absorption. The higher EP lines like Si II 6347 remain the same width throughout, because the innermost annuli do not get hot enough for the lines to disappear. Decreasing $\dot{M}$ only decreases the depth of the lines. This is clear in the lower left panel of Figure 4.3.

We see then, that this dependence on $\dot{M}$ in the line broadening is in fact a dependence on $T_{\rm max}$. This implies that changes to $R_{\rm inner}$ should elicit the same effect. Varying $T_{\rm max}$ via $R_{\rm inner}$, as we propose in Paper I, however, is expected to directly affect the rotational broadening of all lines by changing the maximum Keplerian velocity in the disk. The question becomes: are changes in the rotational broadening of lines due to the changes in the maximum Keplerian velocity distinguishable from those due to changes in $T_{\rm max}$?

The two panels in the right column of Figure 4.3 show our investigation of this in the Ca I 6439 and the Si II 6347 lines. In the Ca I line, the $T_{\rm max}$ effect dominates,

working to broaden the line as $R_{\rm inner}$ increases due to the overall decrease in $T_{\rm max}$. In the Si II line, the decreasing maximum Keplerian velocity dominates and we see the line narrows as we increase $R_{\rm inner}$.

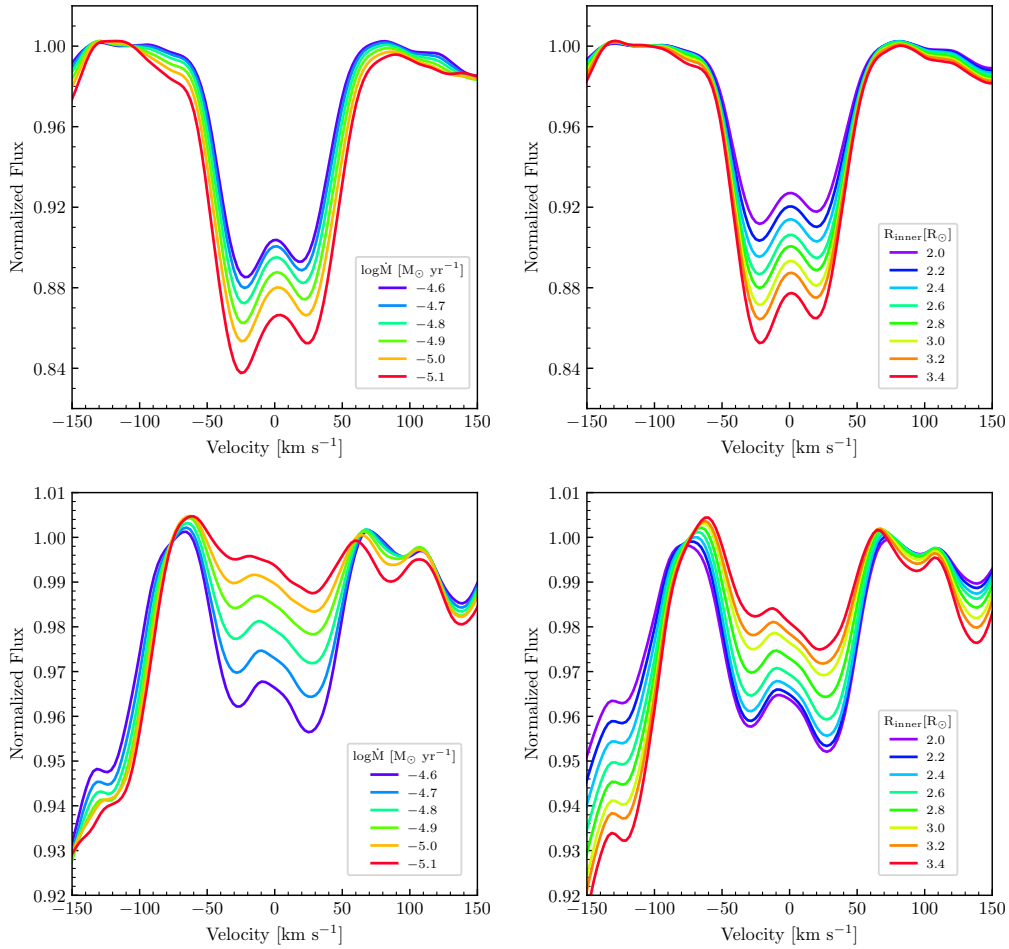

Figure 4.3: The effect of varying $\dot{M}$ and $R_{\rm inner}$ on the width and depth of absorption lines with different EPs. **Left:** Models of the Ca I 6439 (upper panel) and Si II 6347 (lower panel) lines for different values of $\dot{M}$. Notice the Ca I 6439 line broadens as $\dot{M}$ decreases, whereas the Si II 6347 line only changes in depth. **Right:** Models of the same two lines for different values of $R_{\rm inner}$. Notice here that the $T_{\rm max}$ dependent broadening still dominates in the Ca I line as $R_{\rm inner}$ decreases, making the line counter-intuitively broader. However, in Si II, the broadening decreases with increasing $R_{\rm inner}$, as expected due to the decrease in the maximum Keperian velocity.

We find this is consistent with the broadening we see in the high dispersion spectra. Figure 4.4 shows the Si II and Ca I lines over time as observed in the HIRES spectra at different epochs. The Ca I line remains at a relatively constant width, tending

toward slightly broader at later epochs. This is what we expect from a decreasing $\dot{M}$ and increasing $R_{\rm inner}$, as seen in Figure 4.3. The Si II line narrows rapidly toward later epochs, as we might expect from the discussion above and as is shown in Figure 4.3. As we discuss in Section 4.5, the Si II line does not arise entirely from the disk, so its rapid narrowing is not only due to the increase in $R_{\rm inner}$.

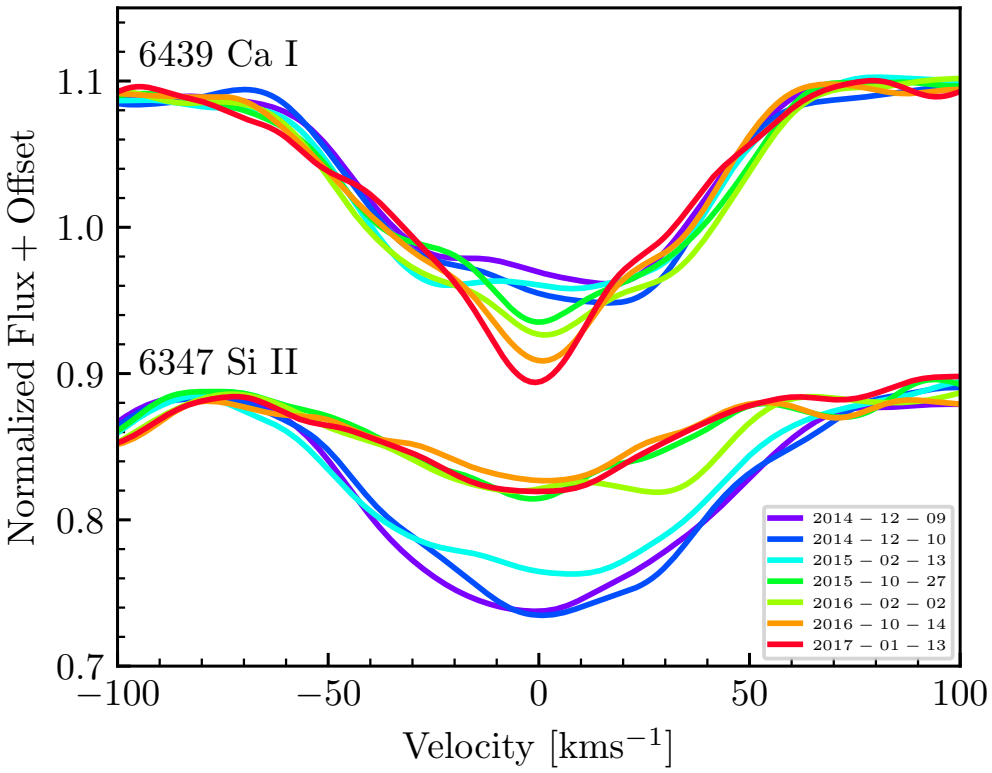

Figure 4.4: The Ca I 6439 (upper profiles) and Si II 6347 (lower profiles) absorption lines shown for the different epochs of the HIRES spectra. Notice the Si II line becomes narrower, in addition to weaker, consistent with an increase in $R_{\rm inner}$, while the broadening of the Ca I line remains relatively unchanged.

Line Broadening as a Function of Wavelength

Half-width half-depth measurements have been used by many authors to argue for the presence (Welty, Strom, Strom, et al., 1990; Park, Lee, et al., 2020) or absence (Herbig et al., 2003) of disk broadened spectral lines in FU Ori stars. However, due to the differential broadening of different spectral lines based on their location of formation in the disk, as just discussed (Section 4.3), it is not straightforward to connect a HWHD vs wavelength (or even EP) relation to the physics of the disk.

We measured the HWHD values for several lines in the observed outburst spectrum

and in outburst epoch model spectrum of V960 Mon (shown in Figure 4.5. To estimate the uncertainty of the HWHD measurements, we fit disk profiles to the lines and multiplied the fractional 1σ uncertainty in the width parameter of the fit by our HWHD value. While there is a generally decreasing (though not statistically significant) trend in HWHD vs wavelength over broad regions of the spectrum, there is significant scatter in the measurements of even neighboring lines. This is in agreement with the results presented in Zhu, Espaillat, et al. (2009a), which also shows that for FU Ori, the disk model predicts almost no wavelength dependence in HWHD measurements made in the optical.

Both the slightly decreasing trend with wavelength and the large scatter are consistent with the high resolution disk model, as shown in Figure 4.5. The HWHD measurements from our high resolution model have a slightly lower median than those in the HIRES data. However, attempting a model with slightly greater median broadening gives a worse fit to the data, with greater chi-squared values. For more direct comparison between the two datasets, we scale the model HWHD values to have the same median as the HIRES values.

Linear fits to the two HWHD vs wavelength relations give slopes of -3.8 $\times 10^{-4}$ km s^{-1} Å^{-1} and -9.3 $\times 10^{-4}$ km s^{-1} Å^{-1} with low significance Pearson test p values of 0.33 and 0.40 for the data and model respectively. The scatter of 2.1 km s^{-1} in the HIRES HWHD measurements is greater than any wavelength-dependent change in width predicted by the disk model over the 5000-9000 Å wavelength range.

4.4 Evidence of Disk Cooling in the High-Dispersion Spectra

We look to the behavior of temperature sensitive absorption lines in the high dispersion spectra to confirm the temperature evolution of the disk that is seen in the photometric models presented in Paper I. We will focus on two sets of lines: those with very high EP values ($>$ 7 eV) and those with relatively lower EP values ($<$ 3 eV). In general, we find that the high EP lines weaken rapidly as the target fades, while the low EP lines become deeper over the same time. This is expected for a target that is cooling, as the higher energy levels depopulate and fill the lower energy levels.

One challenge to interpreting the behavior of the highest EP lines in the HIRES spectra is that some lines are significantly stronger than the models predict them to be. We believe this is evidence that the highest EP lines, such as Si II 6347 and 6371, O I 8446, Ca II 8912/8927 and C I 9111 trace a non-disk (potentially outflowing)

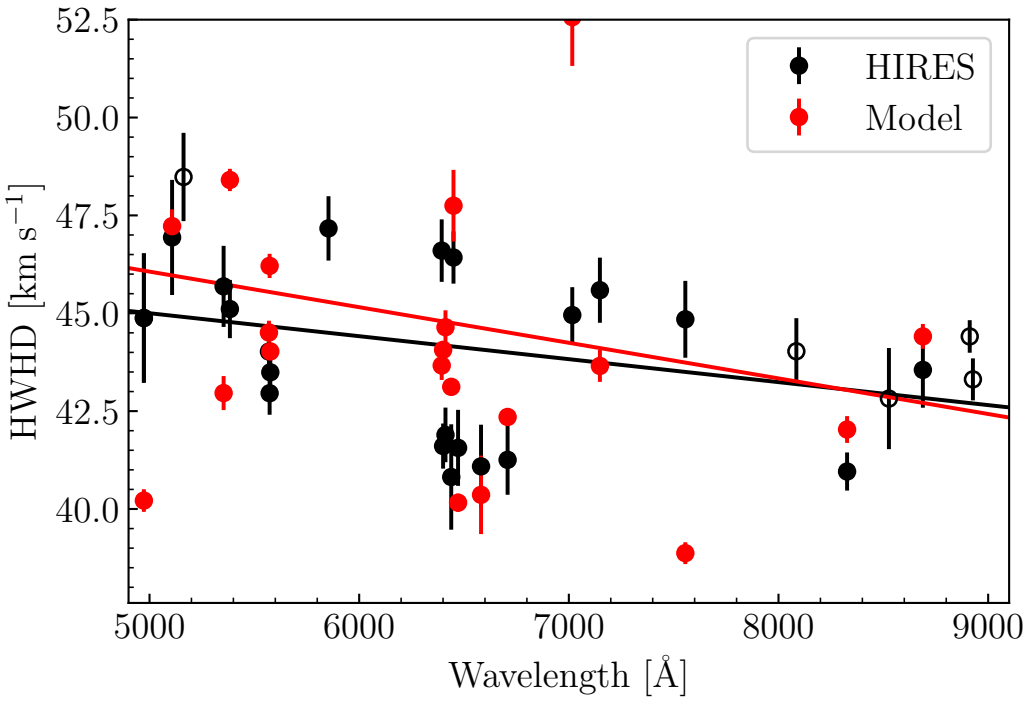

Figure 4.5: The HWHD measurements of several isolated absorption lines in the HIRES outburst (9 Dec 2014) spectrum (black) and the spectral model (red). Empty symbols show lines that are isolated and easily measured in the data but appear severely blended in the models. Although there are some line-by-line inconsistencies (largely due to imperfections in the PHOENIX models), neither set of measurements is significantly correlated with wavelength. The data and the disk model also have similar standard deviations and the scatter in the HWHD measurements does not vary with wavelength. The error bars shown reflect the uncertainty in the width parameter fit used to compute the HWHD measurements.

component in the system. We will discuss these lines in detail in Section 4.5. The high EP lines we will focus on in this section are those that do not appear to be influenced by wind.

To illustrate the general time evolution of the lines in our HIRES spectra of V960 Mon, we have chosen four lines to highlight: two high-EP and two low-EP. The high EP regime is represented by the Paschen series lines of H I (hereafter HP), with the HP 8862 Å line serving as a specific example, and the Fe II 5316 line. These are both isolated features that show dramatic decreases in line strength as the target fades. The low EP lines are represented by the Fe I 5328 line and the Ca I 6439 line. The Fe I 5328 feature (which is in reality a blend of low EP Fe I lines) is especially temperature sensitive, increasing in strength dramatically as the target

fades (see Figure 4.2). The Ca I 6439 line has the advantage of being isolated, so it clearly shows the flat-bottomed line profile characteristic of FU Ori objects (though the profile develops a rest-velocity excess absorption feature over time, as discussed in Section 4.5. It also grows significantly in time, as seen in the profiles shown in Figure 4.4.

We quantify the weakening or strengthening of lines we will discuss in this section by computing their EWs at each HIRES epoch. The measurements are shown in Figure 4.6 with the V band lightcurve from Paper I plotted alongside the measurements as a reference for the brightness evolution of the target. In the Figure, we see that the shape of the EW curves qualitatively either follows or mirrors that of the V band lightcurve, depending on the line. The high EP Paschen line and the Fe II 5316 line both show decreasing EW measurements over time. The Paschen line closely follows the lightcurve, with a greater slope matching the initial rapid fade of the target, then plateauing at later epochs. The lower EP lines, Fe I 5328 and Ca I 6439, both mirror the lightcurve, growing rapidly during the early epochs and plateauing at larger values later.

The time evolution of the H I Paschen Series

As can be seen in Figure 4.7, our disk model is a good match to the line strength of the HP 8862 line at outburst and its subsequent time evolution. We interpret this to mean three things: the HP lines are good tracers of disk temperature; our outburst model $T_{\rm max} \sim 8300$ K is sufficiently high to describe the initial HP depth; and the line evolution supports our proposed temperature evolution of the disk. We note that the HP lines blueward of 8350 Å are not detected, which is consistent with our model predictions, due to blending with other features and minimal time evolution. Of the lines blueward of 8350 Å, only the 8345.5 Å line varies by more the $\sim 1\%$.

The exponential decrease of the HP 8862 line is a strong indication that the line is closely tracing the decrease of $T_{\rm max}$, which is driving the brightness decrease in V960 Mon. We note that this differs somewhat from the behavior of the Fe II 5316 line, which also decreases in strength, but shows a more linear decline in time. The difference in evolution can be explained by the relative temperature sensitivities of the two lines. The HP lines are strongest in very hot atmospheres and will weaken quickly as the hottest components of the disk cool. This makes the HP lines very sensitive to the $T_{\rm max}$ in the disk. The Fe II lines span a broader range of temperatures and are relatively temperature insensitive in our disk models. Therefore, as the disk

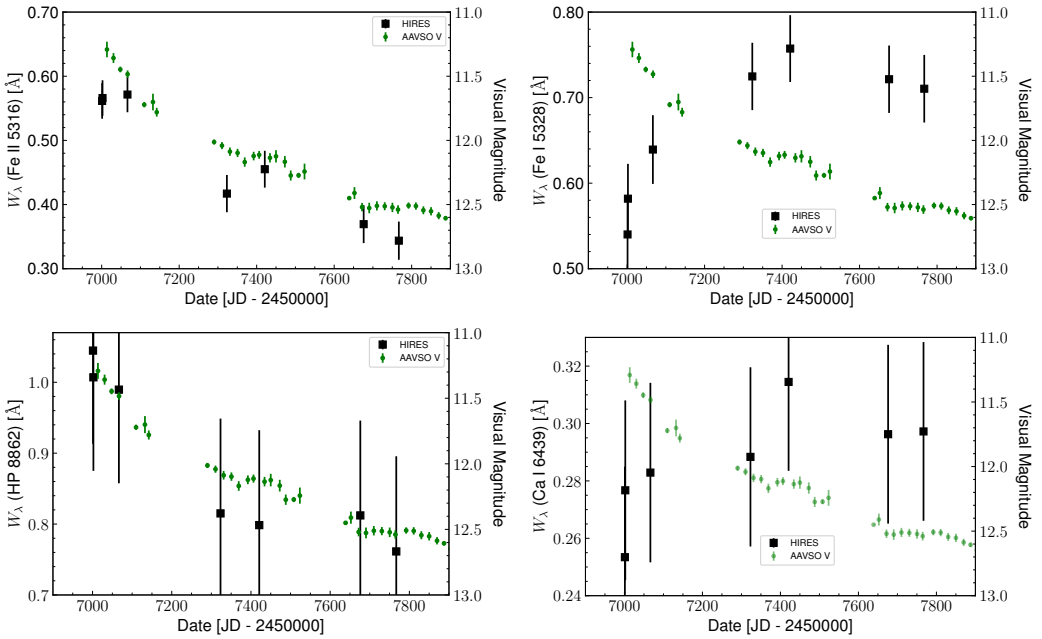

Figure 4.6: The equivalent width evolution (black squares) of two higher EP and two lower EP lines in the spectrum of V960 Mon. The AAVSO V band lightcurve is plotted (green points) for reference, showing the evolution of the continuum brightness over the spectral epochs. **Left Column:** The evolution of the 5316 Fe II line and 8862 Paschen line equivalent widths, which both closely follow the lightcurve of the target in their decreasing strength. The EW measurement for the 8862 Paschen line is blended with the Fe I 8866 line, but the Fe I line does not vary in time. **Right Column:** The evolution of the 5328 Fe I line and 6439 Ca I line, which both follow an inverse trend to the lightcurve in their growth, similarly strengthening as the target fades and plateauing at later times.

cools, the EW of the Fe II lines may decrease but the annuli in which the line largely forms will simply shift radially inward, slowing the weakening of the line.

The time evolution of the low EP metal lines

We also see evidence of disk cooling in the behavior of temperature-sensitive low EP lines, such as Fe I 5328 and Ca I 6439. The region of the disk from which the optical continuum arises is at 5000-7000 K, which is hot enough that the majority of the Ca and Fe is ionized. This makes the Ca I and Fe I lines particularly sensitive temperature tracers (Gray, 2008).

One supporting argument for the cooling disk was presented in Section 4.3, we attribute the slight broadening of the Ca I 6439 line in time to the cooling of the innermost annuli. Another argument is that the Fe I and Ca I lines increase in

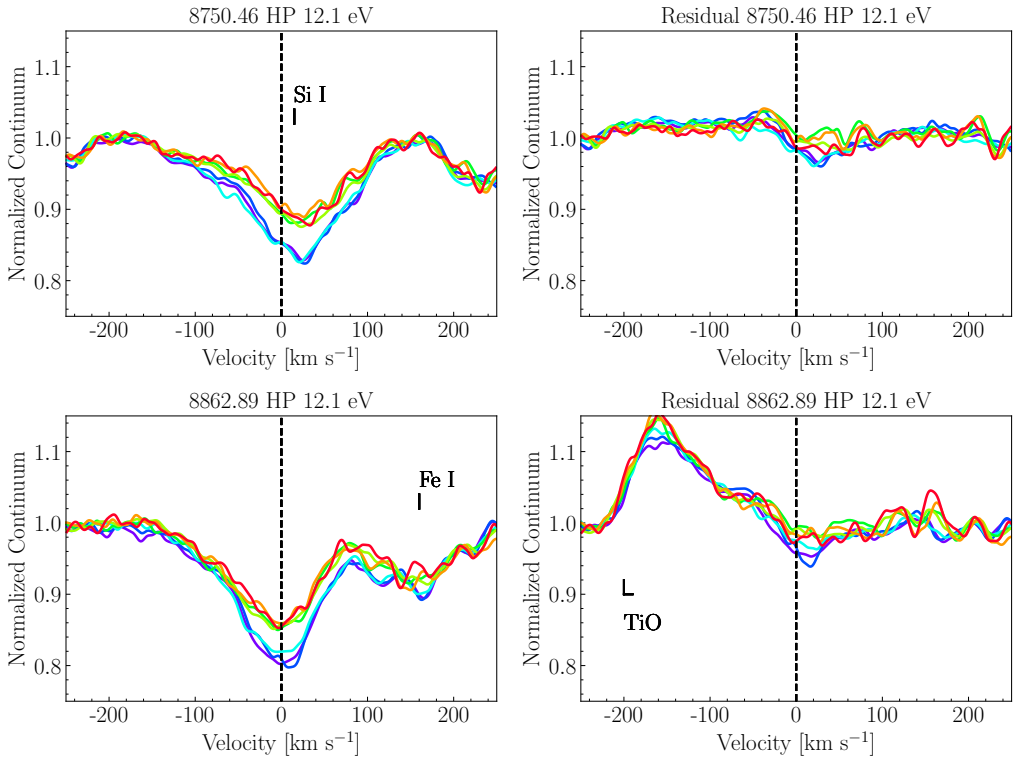

Figure 4.7: The 8750 Å and 8862 Å Paschen lines in the HIRES spectra (left column) and the residual spectrum (right column). Notice the lines have been removed to within a few % in every epoch, indicating the modeled $T_{\rm max}$ change reproduces the evolution of the Paschen series accurately. The 8750 Å line is blended with the 8751 Si I line and the 8862 Å line is blended with an Fe I line at 8866 but both are well-modeled, do not show any evolution, and do not appear in the residuals. The emission residual in the lower right panel at -200 km s^{-1} is due to TiO absorption in the model that is not present in the data. We discuss this discrepancy in Appendix 4.11.

strength significantly as the target fades. The line strength increase is seen clearly in the EW measurments of the Fe I 5328 and Ca I 6439 lines in Figure 4.6.

In order to more directly constrain disk properties from the equivalent width measurements of the low EP lines, we compute the equivalent width ratios of these lines to neighboring lines. Using equivalent width ratios allows us to investigate the local gravity and temperature from the regions where the lines were emitted without worrying about contributions from continuum opacity.

We focus our analysis on two line ratios in particular: the 6439/6456 ratio, between the Ca I 6439 line and the Fe II 6456 line, and the 5328/5316 ratio, between the Fe I 5328 line and the Fe II 5316 line. The denominators of the line ratios are chosen for

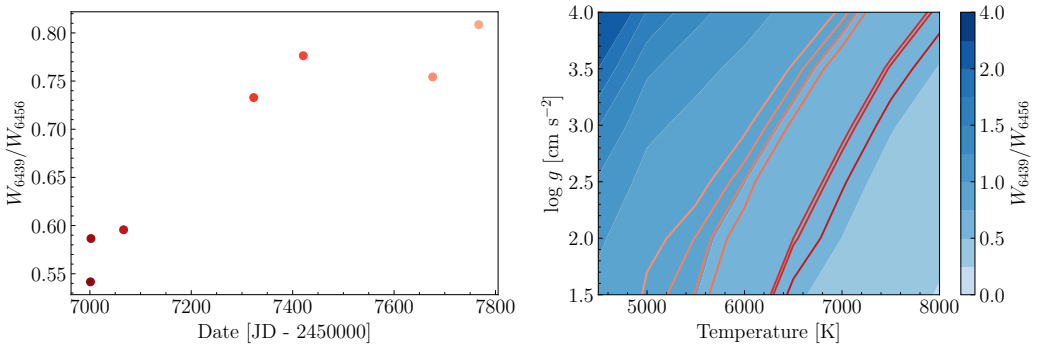

Figure 4.8: Equivalent width ratios in the 6400 Åregion used to show temperature evolution. **Left:** The equivalent width ratios of the Ca I 6439 line and the Fe I 6456 line as a function of time in the HIRES spectra. **Right:** The equivalent width ratios of the same lines in the PHOENIX grid in the blue background and the ratios in the HIRES spectra shown in the red color map, with larger equivalent width ratio values as darker shades.

two reasons: in the case of Fe II 6456, the line remains unchanged in the spectra, allowing a good comparison with the evolution of the Ca I 6439 line, whereas for Fe II 5316, its evolution is opposite that of Fe I 5328, potentially making the ratio more temperature sensitive.

We study these two line ratios by comparing to computed expected line ratios in the PHOENIX grid, for a range of temperatures (5000 K - 9000 K) and range of gravities (log g = 1.5 - log g = 4.0). This gives us an equivalent width ratio surface, on which we can plot the equivalent width ratios we compute in the HIRES spectra. Placing the equivalent width measurements on their appropriate contours shows the corresponding temperature and gravity for that ratio in the PHOENIX grid.

The resulting contour plots are shown in Figure 4.8 and 4.9, along with the timeseries of the ratios for reference. As predicted from our model, both sets of ratios are initially consistent relatively high temperatures and evolve toward cooler ones. In fact the 5328/5316 ratio is a good match to the predicted $T_{\rm max}$ evolution of the system.

Ultimately, both the high EP HP lines and the low EP neutral atomic lines show good agreement with our model of a cooling disk. Both sets of lines also support our $T_{\rm max}$ estimate for the outburst epoch, particularly in the fact that the HP line depths are well-matched for that epoch and those that follow.

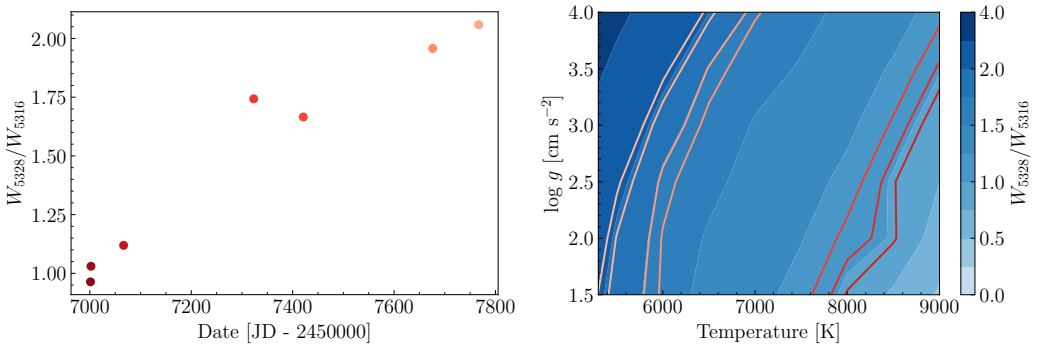

Figure 4.9: Equivalent width ratios in the 5300 Åregion used to show temperature evolution. **Left:** The equivalent width ratios of the Fe I 5328 line and the Fe II 5316 line as a function of time in the HIRES spectra. **Right:** The equivalent width ratios of the same lines in the PHOENIX grid in the blue background and the ratios in the HIRES spectra shown in the red color map, with larger equivalent width ratio values as darker shades.

4.5 Lines with Excess Absorption Relative to the Disk Model

In the high dispersion spectra, there are three distinct families of features which are not well-matched by our pure-accretion disk models. This section highlights lines showing high-velocity, blue-shifted excess absorption; then lines showing broad, rest-velocity absorption that shrinks over time; and lines showing a narrow, rest-velocity absorption that grows over time.

The high-velocity blue-shifted features include lines which typically trace winds in young stars and show absorption velocities as high as -200 km s^{-1}. These may probe the wind/outflow acceleration region in the disk. We find that the broad, rest-velocity absorption in high EP lines may trace a hot wind, with $T \sim 8000 - 9000$ K. The narrow, rest-velocity absorption in lower EP lines may in turn trace the outflow as it cools. We describe the line families individually below and discuss possible physical mechanisms from which they may arise.

Blue Excess Absorption

There is evidence of a fast moving and evolving outflow in the traditional wind-tracing lines in the V960 Mon spectra. We identify several morphological features in the Hα, Hβ, Na I D, and Ca II Infrared Triplet (IRT) lines, shown in Figures 4.10 and 4.11. The lines trace different velocity components in the flow and the variations in those components over time.

In the outburst epoch and the two epochs shortly after outburst ($\sim$ 1 month after) we

see a strong, blue-shifted absorption component in Hα and Hβ extending to -200 km s^{-1}. The component is strongest in Hα and disappears sometime between February 2015 and October 2015, over which time the source faded by 0.8 mag in the B band. There is a distinct component seen in Hβ with an absorption peak at -110 km s^{-1} that disappears between October 2015 and February 2016, but then reappears during the October 2016 epoch. The feature again disappears by the January 2017 epoch and is not apparent in later spectra shown in Park, Lee, et al. (2020).

There is also a slower absorption component in the H lines, which shows an absorption peak around -30 km s^{-1} in both Hα and Hβ at the outburst epoch, but moves to slower velocities at later times. In the January 2017 epoch, the component has slowed to -10 km s^{-1}.

The Hβ line has a red-shifted absorption wing that is similar in slope to the disk-tracing atomic features. That the absorption likely arises in the disk is confirmed by the fact it is almost fully removed in by our disk-model subtraction, as seen in the right column of Figure 4.10. The blue-shifted absorption features discussed above persist in the residuals, indicating they are indeed tracing outflow components.

The especially fast absorption in the H lines is absent in the other wind tracers. The slower component, however, is visible in both H lines and the Ca II IRT. At the outburst epoch, there is a distinct absorption minimum at -30 km s^{-1}, which slows over time to -10 km s^{-1}. The change in velocity of this absorption is most noticeable in the Ca II IRT profiles. We note also that the Ca II IRT profiles appear quite different from one another in the HIRES spectra, despite being a triplet (Figure 4.11, left column). We find that this is due to the differing levels of HP blending each line experiences, and when the disk (and therefore HP) contribution is subtracted, the lines show similar profiles, as expected (Figure 4.11, right column).

The Na D lines are remarkably featureless compared with the other wind lines. They are saturated from -10 to 0 km s^{-1}, indicating the presence of a slow wind that covers the entire optical continuum emission region. The blue wings of the lines extend to -100 km s^{-1}, tracing a much slower component than the Hα and Hβ lines. There is also a component at -60 km s^{-1} that is slightly deeper at earlier epochs, but the change is relatively small compared to that in the other wind lines.

Hα shows consistent red-shifted and blue-shifted emission components at velocities of ± 60 km s^{-1}. The blue-shifted emission appears in the earliest epochs despite the significant wind absorption, and toward later epochs rises to equal the strength of

the red-shifted component (see also the 2019 epochs of Park, Lee, et al., 2020). The red- and blue-shifted emission features are also apparent in the profiles of the Ca II IRT lines in later epochs. On closer inspection, the feature may be discernable as an inflection point in the profiles of the Ca II IRT lines in early epochs, as well as the Hβ line profiles. Strangely, the peaks of the emission in the Ca II IRT lines are consistent with the locations of the peaks in Hα in the data, but after removing the disk contribution, the peaks shift to lower velocities ($\pm$ 40 km s^{-1}).

The locations of the peaks of these emission components is approximately consistent with the Keplerian velocity at the innermost radii of the accretion disk. We interpret that the emission arises from a hot boundary layer, which may be shocking against the stellar photosphere.

The deep, narrow, low velocity absorption component may trace an outflow with a wide opening angle, as has been observed in T Tauri systems (e.g. Whelan et al., 2021). These low velocity absorption features are typically attributed to disk winds in T Tauri systems, which may indicate we are also seeing a slower disk wind.

In summary, we have demonstrated in this sub-section that several of the strong lines traditionally used to diagnose inflowing and outflowing gas in young stellar objects can have contributions from disk absorption in FU Ori type systems. Subtraction of the disk component reveals both inflowing possible boundary layer material, and outflowing slow and fast winds.

Broad Central Absorption

The evolution of the especially high EP lines mentioned briefly in Section 4.4 (due to Si II, Si I, O I, Ca II, and C I) is shown in Figure 4.12. The lines follow a similar evolution to that of the HP lines, indicating the lines all trace a rapidly cooling hot component of the system. However, unlike the HP lines, these lines are significantly stronger in our spectra than in the disk model (especially in the earliest epochs) and can be clearly seen in the residuals in Figure 4.2. The profile shapes are also very similar in the residuals after we subtract the disk model. The significant difference in depths and profile shapes for these lines from the predictions in our disk model indicate the majority of the absorption traced by them is not accounted for in our model. We note that the residual depths are much smaller in the later epochs, indicating the absorption excess relative to the disk model has almost full disappeared by the 2017 epoch.

The component traced by the high EP lines appears to be somewhat dynamically

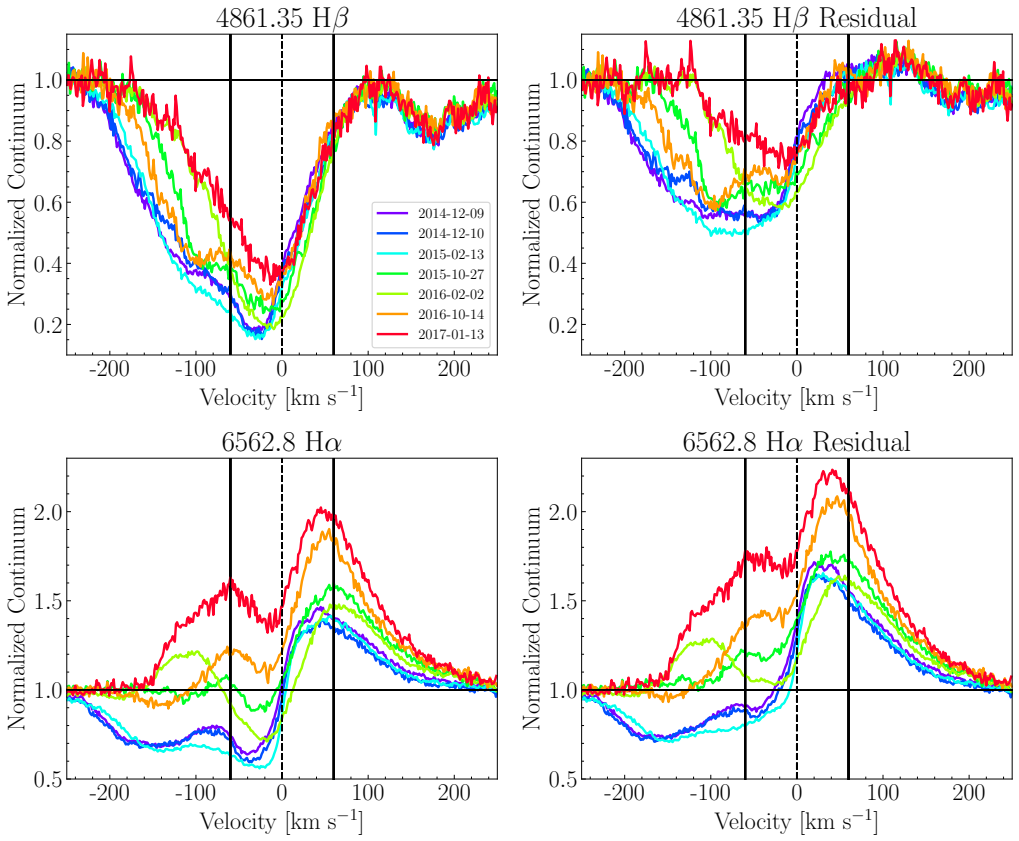

Figure 4.10: The Hβ and Hα lines in each of the HIRES epochs as seen in the original data (left) and as residuals after removing the disk contribution (right). Both lines initially show a high velocity blue-shifted absorption component, that weakens rapidly over time and becomes an emission feature in Hα. The profiles also contain a slow component that moves redward. The emission components of the Hα profile are both peaked at $\pm$60 km s^{-1} and strengthen consistently relative to continuum. The absorption in the upper left panel at +185 km s^{-1} is the Cr II 4864 Å line. Notice it is well-removed by the model and is much weaker in the upper right residual panel.

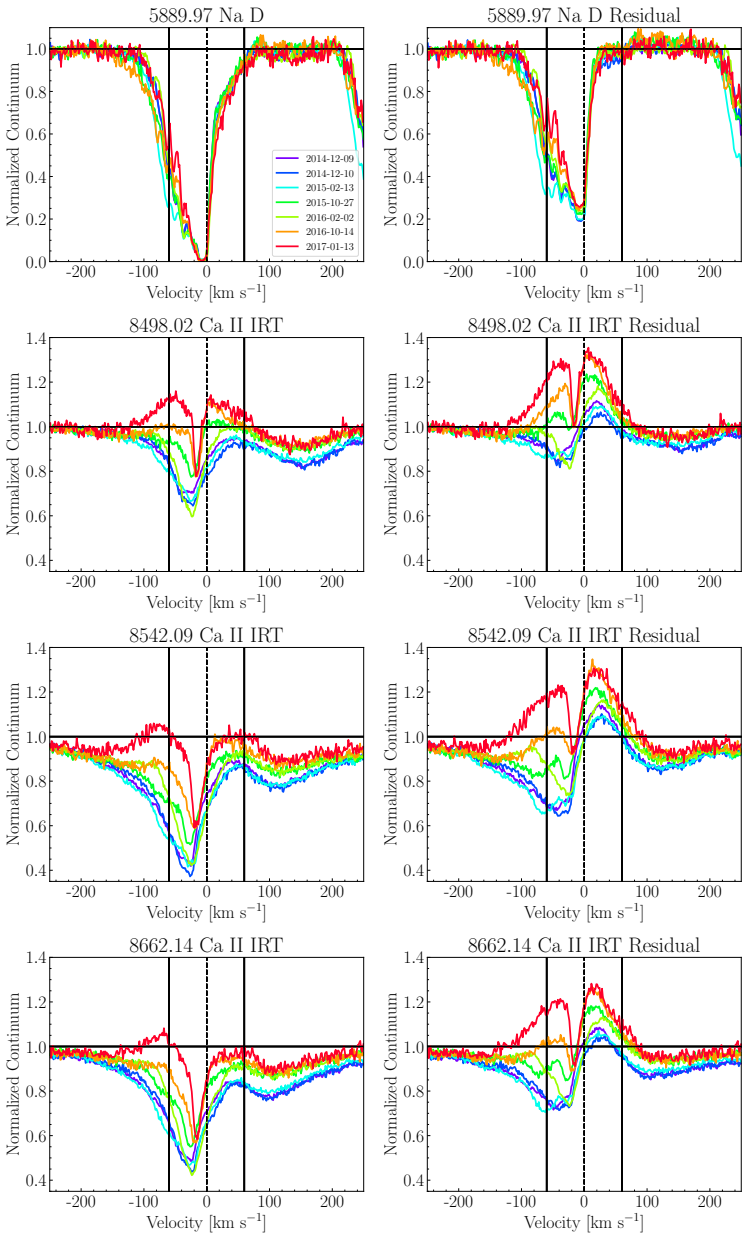

Figure 4.11: The Na D 5889 line (top row) and Ca II IRT lines (lower three rows), shown in the data (left column) and residuals (right column). The Ca II IRT lines show a weakening fast blue-shifted component and a ±60 km s^{-1} emission component similar to those seen in the H lines. Note that the +100 km s^{-1} absorption is due to Hydrogen Paschen line blending with the IRT. This is well-matched by our disk model and mostly removed in the residuals column. The Na D lines are saturated from −10 to 0 km s^{-1}, which matches the narrow absorption seen in the latest epoch, indicating there may be a constant slow wind covering almost the entire visible emission region of the disk.

different from the disk. The lines show a largely round-bottomed profile, almost consistent with profiles of high v sin i stellar features. The wings of the lines show relatively consistent 60 km s^{-1} broadening, which may be attributed to the disk broadening as is seen in other features. However, the line core shows an initial $40 - 50$ km s^{-1} broadening which decreases as the line weakens, narrowing to only $20 - 30$ km s^{-1}. The lines appear centered at the system rest velocity, implying they are tracing a particularly slow, albeit hot, outflow.

To better quantify the evolution of these high EP lines and to try to understand the implications for the temperature conditions in this additional component, we again use equivalent width ratios like those described in Section 4.4. For our investigation, we choose two lines: Si II 6347 and O I 8446. These lines are high EP (8.1 eV and 9.5 eV, respectively), show a dramatic decrease in strength over time, and are well-isolated from other photospheric lines and telluric lines. For the denominators in the line ratios, we choose the Fe I 6400 and 8688 lines, both of which show almost no time variability.

The time-series of the 6347/6400 and 8446/8688 ratios are shown in Figures 4.13 and 4.14. Both sets of ratios show an initial rapid fade, similar to that of the HP lines, followed by a plateau, closely following the structure of the V band lightcurve. The $T_{\rm eff}$ vs log g contour plot for the 6347/6400 ratio shows that the line ratio is initially consistent with a ~7000 K temperature atmosphere and as the target fades the ratio is more consistent with that seen in ~5800 K atmospheres.

The contour plot for the 8446/8688 ratios also shows a similar evolution, where the ratio is initially consistent with $\sim$ 5700 K atmospheres and evolves to be more consistent with $\sim$ 5200 – 5300 K atmospheres. Both sets of ratios indicate then that this excess component is cooling as the target fades. They also show, however, that different wavelengths are indeed tracing regions with different temperatures. This is consistent with the expected $T_{\rm eff}(\lambda)$ relation expected for accretion disks and indicates that the continuum at 6400 Å arises from a warmer region of the disk than that at 8400 Å. We can use the temperatures described above and the wavelengths of the line ratios to find that at outburst, $dT/d\lambda \sim 0.65$ K/Å whereas at the 2017 epoch, $dT/d\lambda \sim 0.45$ K/Å.

Taking the temperature from the 6347/6400 ratio at outburst to be $\sim$ 7000 K and the temperature from the 8446/8688 ratio to be $\sim$ 5700, we can also estimate that the lines arise from the $r \sim 2\ R_*$ and $r \sim 3\ R_*$ annuli respectively. That would in turn mean an average $\frac{dT}{d\lambda} \sim 0.62$ K Å^{-1} across the red range of the optical spectrum.

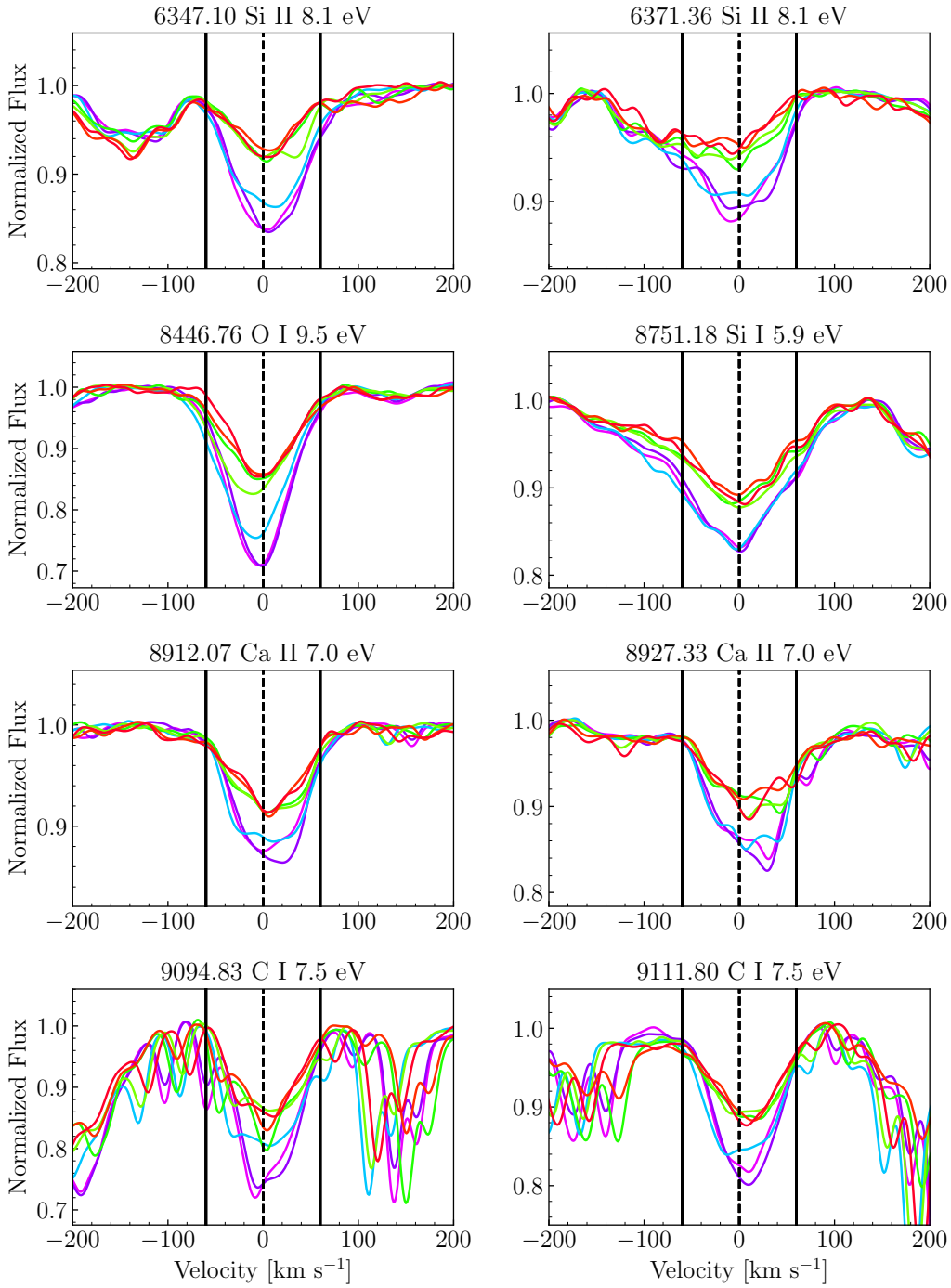

Figure 4.12: High EP lines in the HIRES spectra of V960 Mon, smoothed with a $\sigma = 5$ pixel Gaussian for clarity. Epochs are shown in different colors, where redder indicates later epochs when the target is dimmer and, according to our disk model, cooler. The black vertical lines mark ±60 km s^{-1}, the estimated $v_{\rm max}$ at outburst, as a reference for the line widths. The C I 9095 line is significantly contaminated by telluric absorption, but its similar evolution to the other lines is still apparent.

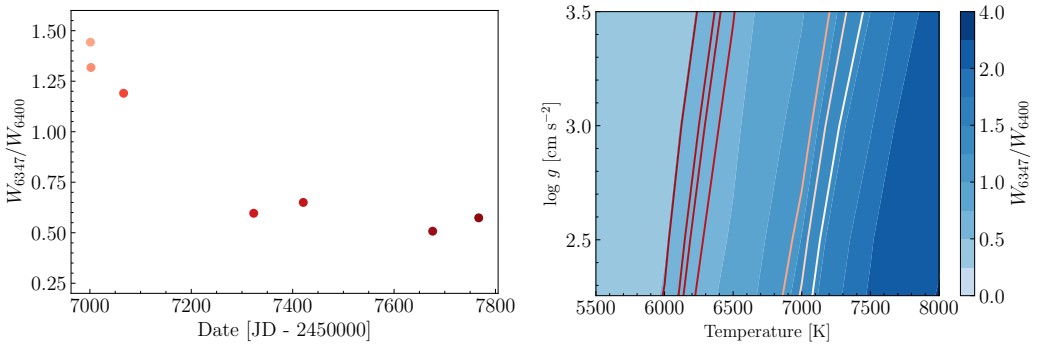

Figure 4.13: The EW ratio of the Si II 6347 line to the Fe I 6400 line for the HIRES spectra, showing that the ratio decreases in time and is consistent with a decreasing temperature. The color scheme in the left and right panel both show lighter red for larger EW ratios. **Left:** The timeseries of the EW ratios. **Right:** The EW ratios of the same lines as measured in the PHOENIX grid (blue contoured background) and in the HIRES spectra (red contours).

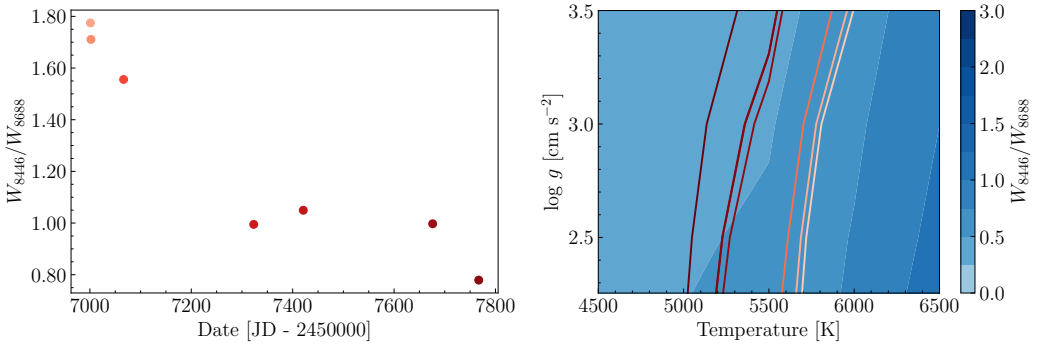

Figure 4.14: The EW ratio of the O I 8446 line to the Fe I 8688 line for the HIRES spectra, showing that the ratio decreases in time and is consistent with a decreasing temperature. The color scheme in the left and right panel both show lighter red for larger EW ratios. **Left:** The timeseries of the EW ratios. **Right:** The EW ratios of the same lines as measured in the PHOENIX grid (blue contoured background) and in the HIRES spectra (red contours).

We now turn our attention to some cooler lines, namely moderate EP lines of Fe II that also show broad excess absorption relative to the disk model. Similarly to the high EP lines, the Fe II lines (shown in Figure 4.15) also decrease in strength significantly as V960 Mon fades. The effect is not as dramatic as that seen in the high EP lines such as Si II 6347, but it is notable. The Fe II lines are also much stronger than predicted in the disk models, as can be seen for the Fe II 5316 and 5362 lines in Figure 4.2. These two facts imply the Fe II lines may trace the same excess component as the high EP lines.

However, there are also Fe II lines, especially those blueward of 5200 Å, that show almost no time evolution. The FeII lines which most closely follow the evolution of the high EP lines in Figure 4.12 are those between 5200-7000 Å having EPs between 3.0-4 eV. We note that these FeII lines are also typically gravity sensitive in single-atmosphere models, but when varying the log g of our disk model, we do not see significant gravity sensitivity.

In summary, in this sub-section we have demonstrated that there is a family of lines with deep broad profiles in V960 Mon that have distinctly deeper depths, and very different broadening shapes relative to the disk model. These lines come exclusively from high and intermediate excitation potential species. We speculate that they originate in the hot components of the wind, near its point of origin in the disk.

Narrow Central Absorption

Several lines in the spectra at later epochs show an excess narrow absorption feature centered at the system velocity. The feature deepens over time, but does not broaden, maintaining a relatively consistent $\sim$ 20 km s^{-1} half-width measured from the intersection of the narrow component with the disk component. The lines exhibiting this feature most prominently are shown in Figure 4.16.

Narrow central absorption lines span most of the optical range covered by the HIRES spectra but seem especially prominent between 4900 Å $< \lambda <$ 8400 Å. The lines with excess narrow absorption components predominantly occupy a narrow range of somewhat high EPs: 2.5 – 3.5 eV, such as Ca I (shown in detail in Figure 4.4) and Fe I though there are a few at lower EPs, including the Ba II and Li I features (all shown in Figure 4.16). A comparison with the PHOENIX model spectra shows the depths of many of these features are consistent with $T_{\rm eff} \sim 5000 - 7000$ K atmospheres. The lines are also generally temperature-sensitive and grow deeper in the PHOENIX

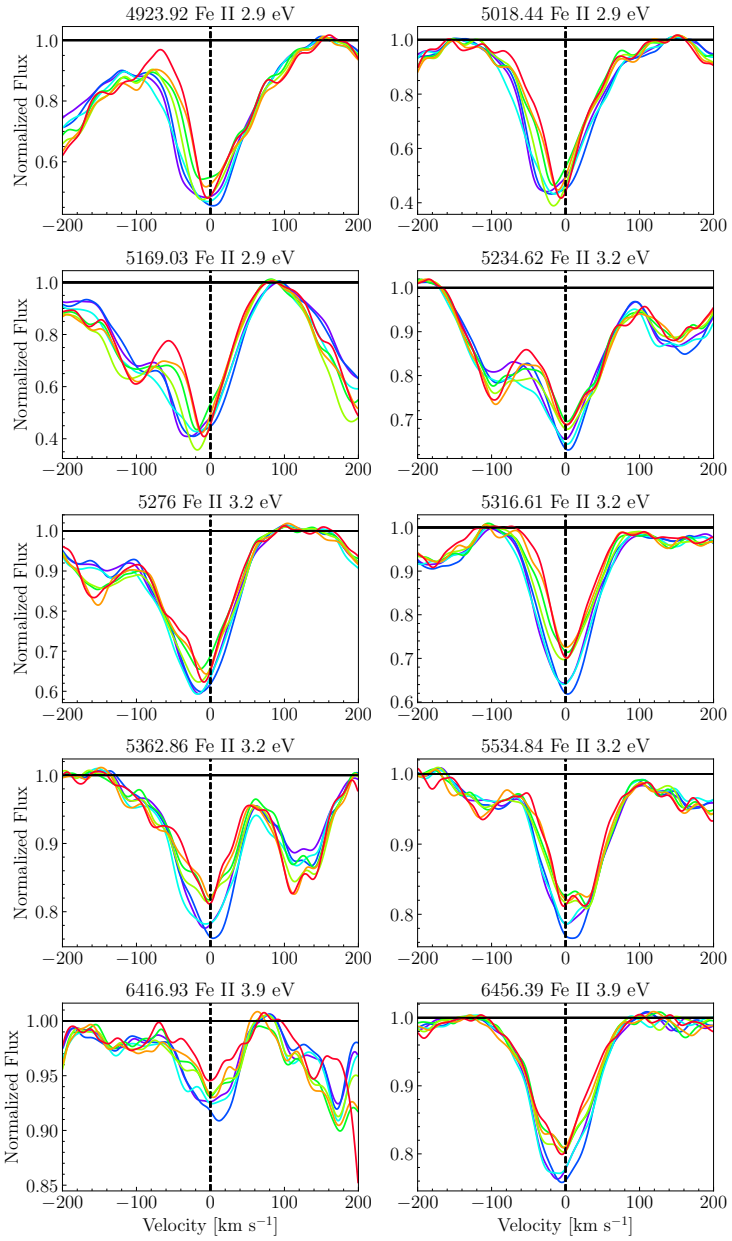

Figure 4.15: Fe II lines in the HIRES spectra. Notice their behavior is similar to the high EP lines shown in Figure 4.12, rapidly shrinking over time. This effect is strongest in the lines with higher EP, indicating sensitivity to the hot wind component. The Fe II lines here seem to trace the disk behavior at lower EPs and bluer wavelengths, and trace the wind at higher EPs and redder wavelengths.

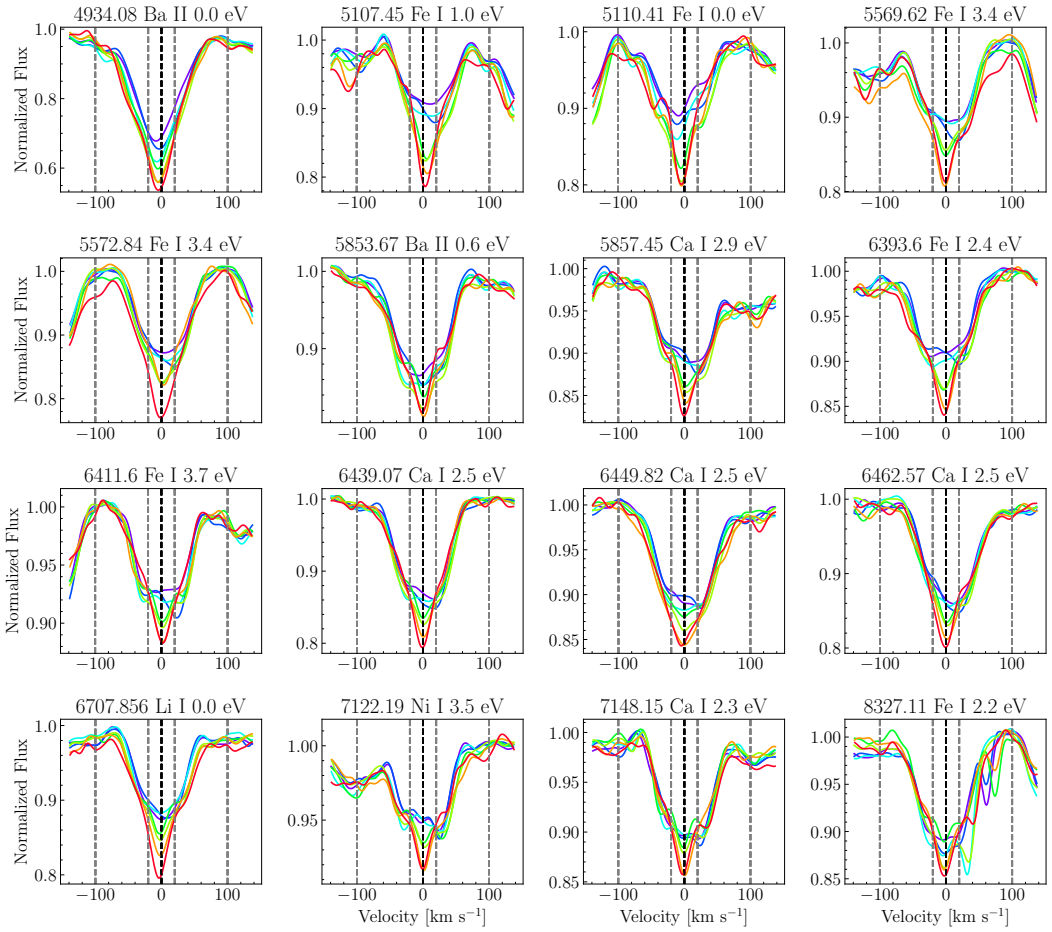

Figure 4.16: Lines in the HIRES spectra which show the central absorption feature shown as a time series progressing from blue to red color. Notice that across the range of lines and EPs, the narrow feature shows a consistent width $\sim$ 20 km s^{-1} and is centered at 0 km s^{-1}. The feature grows as the target fades, absorbing against the disk continuum to additional depth that is almost equivalent to the depth of the disk contribution of many of the lines

atmosphere models as $T_{\rm eff}$ is lowered from 7000 K to 5000 K.

The somewhat high temperatures at which we expect these features, the fact that they appear at the system velocity, and their growth as the high EP lines discussed in Section 4.5 shrink, implies a connection between the two families of lines. As mentioned in Section 4.5, the high EP lines shown in Figure 4.12 are all initially much deeper than predicted by our disk model, but over time their strength decreases to be more consistent with the models at later epochs. We have also shown that the evolution of the lines is consistent with this hot excess component cooling over time.

The low velocity of the absorption may be consistent with absorption by a slow

outflow at a distance of $r \sim 4 - 5\ R_{\rm inner}$. This region would be consistent with broadening < 35 km s^{-1} as we see in this excess. If the outflow cools as the disk cools, the highest EP levels may depopulate and fill the 2.5-3.5 EP levels, contributing to increased absorption in those species.

When we isolate the high and low EP excess absorption by subtracting the disk model from the data, we can get a spectrum of this non-disk component. Parts of the residual spectrum are shown in Figure 4.2, but we reproduce it in better detail in Figure 4.17. In Figure 4.17, the residual spectrum is shown compared to two log g = 1.5 PHOENIX atmospheres, one with $T_{\rm eff}$ = 9000 K and another with $T_{\rm eff}$ = 7000 K. For better comparison with the line widths we see in the residuals, we broadened both models to $v \sin i$ = 30 km s^{-1}.

The outburst epoch residual spectrum possesses features that are quite similar to those seen in the 9000 K spectrum (e.g., Si II 6347 and 6371, Fe II 6456, and O I 8446). As the target fades, features that are similar to those in the 7000 K spectrum (e.g. Ca I 6439, 6449, and 6463) grow stronger. The upper left panel of Figure 4.17 shows this well, where there are several lines in the 4750-4850 Å range that are not in the 9000 K atmosphere but can be seen in the residual spectrum. The lower left panel of Figure 4.17 shows the same fact in another wavelength range. In this panel, the Fe II 6456 line appears in both the 9000 K and 7000 K atmospheres, where the Ca I 6439 and 6449 lines are not expected in the hotter atmosphere. They are indeed generally weaker initially. However, as the target fades, the Ca I features in the residual spectrum deepen until they are consistent in depth with those seen in the 7000 K spectrum. The inverse case is shown in the upper right panel of the Figure, where the Si II features weaken over time, which is again what we may expect from a residual component cooling.

In summary, in this sub-section we have demonstrated that there is a family of narrow absorption lines in V960 Mon that grows in strength over time against the “continuum" of the disk photosphere, which produces disk-broadened profiles in many of the same lines. We speculate that the lines may trace a slow-moving, cooler component of the wind that was initially traced by the excess high EP absorption discussed in Section 4.5.

4.6 Forbidden Emission

The [S II] 6731 emission feature was reported in the spectrum of V960 Mon by Park, Lee, et al. (2020), and they discuss the growth of the feature at later epochs.

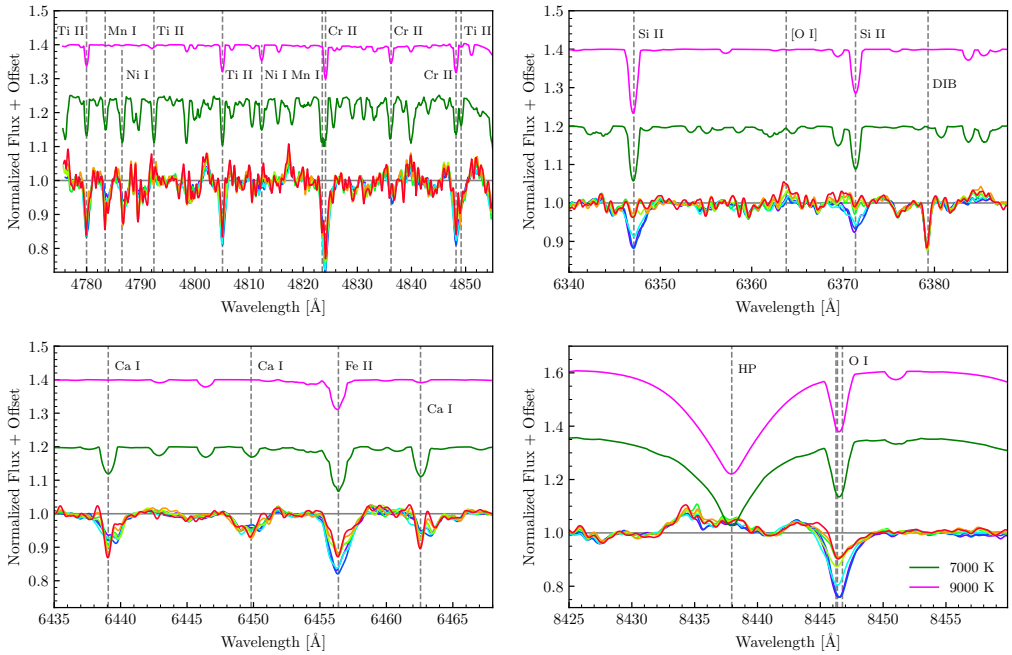

Figure 4.17: Selected regions of the residuals of our fits to the HIRES spectra, compared with log g = 1.5, $T_{\rm eff}$ = 7000 K (green) and $T_{\rm eff}$ = 9000 (magenta) K PHOENIX models. Notice the residual features are consistent with the features seen in these hot model atmospheres, with a tendency for later epochs to more closely resemble the 7000 K atmosphere. This may indicate that the component of the system probed by the residuals is cooling as the disk cools. The HP lines in the lower right panel are strongly affected by Stark broadening in the PHOENIX atmospheres. That we do not see this in the disk model or the data indicates that the contribution from the narrower/weaker HP lines in cooler atmospheres is necessary to match the data.

We recover this feature and its growth in our HIRES spectra. We also find the [O I] 6300 and [N II] 6583 emission features. The maximum normalized flux of the [O I] 6300 line is a bit greater than that of the [S II] 6731 line. The [O I] and [N II] fluxes also increase relative to the continuum at later epochs. The features as seen in the HIRES spectra are shown in Figure 4.18.

The weaker components of these two doublets, the [S II] line at 6716 Å and [OI] line at 6363 Å, are tentatively identifiable in the latest epoch but are barely 1 % above continuum. The doublet of the [N II] line falls in between orders in the HIRES spectra. Detecting the 6716 Å and 6363 Å emission in the data is complicated by line blending with nearby photospheric lines, namely the Fe I 6715 and 6362 absorption lines, which are sufficiently broadened to blend with the neighboring forbidden emission features. Fortunately, the Fe I lines can be removed using our

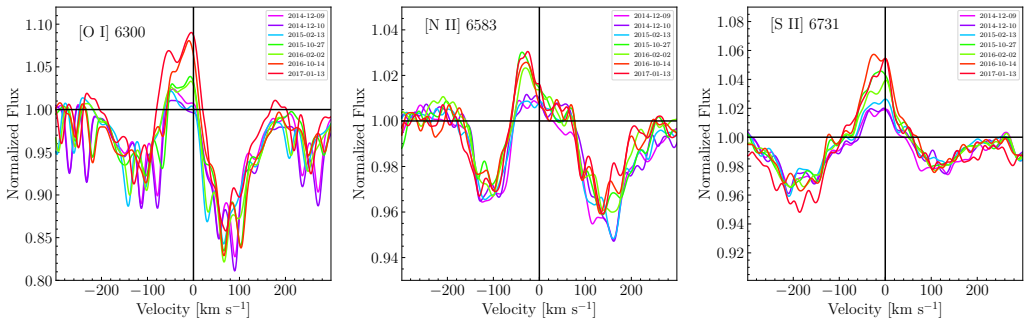

Figure 4.18: The [O I] 6300, [N II] 6583, [S II] 6731 emission lines in the HIRES spectra. All three features are blue-shifted, with emission components ranging from -60 km s^{-1} to -10 km s^{-1}. The emission in the [O I] λ6300 and [N II] λ6583 lines is mostly at higher velocities, whereas the [S II] λ6731 line shows both a -40 km s^{-1} component and a nearly 0 km s^{-1} component.

high dispersion models of the HIRES spectra. Looking at the residuals, the features appear clearly and show similar structure to the 6731 Å and 6363 Å features. The stronger 6731 Å and 6300 Å are also clearly seen in the residuals and retain the amplitude we see in the data.

The line profiles show a velocity structure different from that we see in the absorption features. The emission is predominantly blue-shifted in all three main lines, indicating they are tracing outflows from the FU Ori object. They also show multiple velocity components, the velocities of which differ slightly from line to line. To measure the widths and central velocities of the components, we use the `optimize` toolkit in `scipy` to do least-squares fitting of a sum of two Gaussian functions to the line profiles. The fits are quite noisy because the detections of the lines are weak and not all epochs are well-described by a sum of two Gaussians. However, the best-fit parameters provide a general picture of the composition of the forbidden emission.

The [S II] 6731 line has two distinct peaks, one at essentially system rest velocity and one at -30 km s^{-1}. Both peaks have a HWHM of $\sim$ 15 km s^{-1}. The [O I] line also has a peak at system rest velocity but its blue-shifted component is closer to -50 km s^{-1}. Its components are also both broader, with HWHM values of $\sim$ 20 km s^{-1}. The [N II] line seems dominated by a single component at -30 km s^{-1}, which has a HWHM of $\sim$ 25 km s^{-1}, though there may also be a weak rest-velocity component.

The $v \sin i = -30\,\mathrm{km\,s^{-1}}$ peak is consistent with the velocity of the narrow absorption component in the wind lines described in Section 4.5.

4.7 Discussion

The accretion disk model presented in Paper I successfully reproduces most of the variability seen in the spectra, as can be seen in the residuals presented in Figure 4.2. There are also many features in the residuals that are not captured by the disk model, either because they are classic wind tracers, such as Hα, the CaII triplet and the Na D lines, or because they trace some other, unmodeled component of the system (see Section 4.5).

Disk absorption and the gravity and temperature dependencies

The observed high-dispersion spectra are reasonably well-reproduced by models of an accretion disk photosphere. However, great care is needed in understanding and disentangling the effects of temperature and surface gravity in the disk, from the wind components.

The lines that are typically used as gravity indicators cannot be used to determine the gravity of FU Ori objects because they are often sensitive to outflows and are therefore dominated by outflow absorption. This is the case for the Na D lines and many other highly gravity-sensitive features (see Section 4.5 for a discussion of these and other wind lines). We therefore must rely on other gravity indicators in the spectrum of V960 Mon, in the weaker optical atomic lines that are known to trace the disk.

To explore the gravity sensitivity of the absorption lines in the spectrum, we computed a grid of high dispersion models using the outburst epoch best-fit parameters and in each we fixed the log $g(r)$ to be one of 0.5, 1.0, 1.5, 2.0, 2.5, 3.0, or 3.5. We then compared the change in the spectra due to the variation of log g with the time-evolution of the HIRES spectra.

Although we do see some evolution in the high EP lines discussed in Section 4.5, they remain at least a factor of 2 deeper in the data than in the models, indicating once again that they are likely tracing excess absorption not accounted for in our disk model. The Fe II lines are also much deeper in the data than in any of the models, similarly indicating that they may also in part trace this hot excess absorption component. Hartmann and Calvet (1995a) show that the Fe II lines in other FU Ori objects, such as FU Ori itself or V1515 Cyg, are consistent with wind absorption models. We do not see blue shifted absorption in these profiles, but they may trace a slower outflowing component.

For the other gravity sensitive lines, such as Ti I 8435, explaining the line evolution

seen in the HIRES spectra with only a change in the disk gravity would require a very large log g increase (at least $\sim$ 2 dex). In general, we find that the overall spectrum is more consistent with the lower gravity models (log $g \sim 1.5$) than models that use a $g(r)$ profile. However, this should also be tested with the gravity sensitive features in the near-infrared, such as the CO (2-0) and (3-1) bandheads.

Ultimately, we find that it is critical to look at the disk-integrated model spectrum to study gravity sensitivity of different features, rather than looking at them atmosphere-by-atmosphere. The gravity sensitivity of a given feature is a function of the effective temperature of the atmosphere and may not extend across broad temperature ranges. Therefore, the temperature blending in the full integrated disk spectrum may counteract or weaken the gravity sensitivity of lines like Ti I 8435.

The evolution of the Fe I and Ca I lines, on the other hand, is insensitive to log g but consistent with a $\sim 1000 - 2000$ K decrease in $T_{\rm eff}$. The lower EP Fe I lines are especially temperature sensitive and grow rapidly as the target fades. The higher EP Fe I lines do not vary as significantly initially, but consistently show the growing narrow central absorption feature at later times. We also see a similar pattern in the Ca I features. The Ca I 6439 and 6462 features show little evolution except the growth of the narrow central absorption.

The relative lack of gravity sensitivity and significant temperature sensitivity of these two species in the temperature ranges we expect (5000 - 7000 K) are indicative that the narrow central absorption is not tracing a higher gravity component of the system but rather one that is cooling.

Wind features

The wind lines shown in Section 4.5 show evidence of a multicomponent outflow that evolves over the course of the post-outburst fade. The primary components we identify are: a fast-moving (-200 km s^{-1}) component traced by the Hα and Hβ lines, a slower component (-50 to -30 km s^{-1}) traced initially by Hα, Hβ, and the Ca II IRT, and a very slow component (-10 to 0 km s^{-1}), traced by all lines (the Na I D doublet in all epochs and the other lines at later epochs). The velocities probed by the emission components in the [O I], [N II], and [S II] forbidden emission lines discussed in Section 4.6 are also consistent with some of the slower components seen in the wind lines.

The fastest component of the wind that is visible in the -200 km s^{-1} absorption of the Hα and Hβ lines is similar in shape to that seen in the Na I D and Hβ lines of

other FU Ori objects like V1057 Cyg or FU Ori (Hartmann and Calvet, 1995a). This absorption is consistent with a high mass-outflow rate, $\dot{M}_{\rm out}$, during the outburst, as demonstrated in models of disk winds during FU Ori outbursts (Calvet, Hartmann, et al., 1993; Milliner et al., 2019a).

As the target fades, however, we see this high velocity component disappears, indicating the $\dot{M}_{\rm out}$ is much lower. Following estimated $\dot{M}_{\rm out} \sim 0.1\dot{M}_{\rm acc}$ described in Calvet, Hartmann, et al. (1993), we would expect that the high velocity component would remain relatively deep, because we only predict a 40% decrease in $\dot{M}_{\rm acc}$. To preserve the $L_w/L_{\rm acc}$ they describe (which is also supported by Zhu, Jiang, et al., 2020), we would require a much more massive wind corresponding to the apparent velocity decrease, which would likely make it optically thick.

The slow component of the outflow, visible in Hα, Hβ, the Na D lines and the Ca II IRT, ranges from -10 km s^{-1} to -30 km s^{-1}. In the Na I D lines in particular, this component is saturated, indicating it may be a very massive outflow and absorbs against a large area of the disk from which the visible continuum arises. In the other lines, the component is initially more blue-shifted (up to -50 km s^{-1}) but slows to -10 km s^{-1} over time. The persistence of the component in Na I, and its appearance in the Hα, Hβ, and Ca II IRT lines at later epochs suggests the outflow is present during the course of the initial outburst, throughout the fade and into the plateau. It may be that the faster outflow traced by the other lines obscures the slower component we see in Na I.

This absorption is also consistent in velocity with the -30 km s^{-1} component we see in the [S II], [O I], and [N II] forbidden emission (Section 4.6). This may be evidence of the a disk wind similar to that seen in T Tauri stars (Whelan et al., 2021), though it may be much more massive.

The forbidden emission lines shown in Section 4.6 may allow us to differentiate between different outflow components. The [O I] 6300 emission line has the highest critical density of the three emission features ($n_c \sim 2 \times 10^6$ cm^{-3}) and also shows the highest velocity emission feature (-50 km s^{-1}). This may be emission from a region closer to $R_{\rm inner}$, where the wind density and escape velocity may be higher. The [S II] emission, which has the lowest critical density ($n_c \sim 2 \times 10^4$ cm^{-3}, may in turn probe a region further from $R_{\rm inner}$, and therefore is lower velocity.

Both the [S II] and [O I] features also have $v \sim 0$ km s^{-1} emission features at similar strengths to their blue-shifted emission. This very low velocity emission is

consistent with the low velocity components of the forbidden emission observed in T Tauri disks, which are believed to be trace slow-moving disk winds (as opposed to the “high velocity components" that are usually attributed to jets; see Pascucci et al., 2023, for a review). It is possible that due to the increase in $T_{\rm eff}$ and $L_{\rm bol}$ of the source irradiating the outer disk, the wind that is launched may be more massive than that in T Tauri systems. This would be consistent with the finding by Cruz-Sáenz de Miera et al. (2023) that FU Ori outflows observed in cooler molecular emission are indeed be more massive than those of T Tauri systems.

Using the de-reddened fluxes of our SED models at each HIRES epoch, we are able to estimate the total flux in the emission lines. Though the target fades significantly over time, we find that the fluxes of the [O I] 6300 and [S II] 6731 lines are relatively constant, perhaps increasing slightly over time. The measured median fluxes for the lines are $\log \lambda F_\lambda(6300) = -14.2 \pm 0.34$ and $\log \lambda F_\lambda(6731) = -13.9 \pm 0.11$ erg s^{-1} cm^{-2}. Using the distance to the target of 1120 pc, we estimate line luminosities of $\log(L_{6300}/L_\odot) = -3.66 \pm 0.34$ and $\log(L_{6731}/L_\odot) = -3.36 \pm 0.11$. For the [O I] 6300 line, these values are almost 1.5 dex greater than the $\log(L_{6300}/L_\odot) \sim -5$ reported for several Classical T Tauri Stars by Fang, Pascucci, et al. (2018).

The Hα and Ca II IRT lines show a strong red-shifted emission component, centered at +60 km s^{-1}, which grows stronger over time. Toward later epochs, the strong absorption features in Hα and Ca II IRT also become dominated by blue-shifted emission at -60 km s^{-1}. The Hα profiles shown in Park, Lee, et al. (2020) for their 2018 epochs continue to show the double-peaked Hα emission, and the peaks remain at $v \sim \pm 60$ km s^{-1}. The velocities of the emission peaks are consistent with the $v_{\rm kep} \sin i$ of $R_{\rm inner}$. This may be evidence of emission from the innermost radius of the disk, tracing the accretion boundary with the star.

For the broad/shrinking and narrow/growing low-velocity absorption excess components, we believe these can be attributed to some sort of excess, outflowing material above the disk atmosphere. The rest-velocity absorption profile is consistent with observations of disk winds through [O I] emission profiles in face-on circumstellar disks (Fang, Wang, et al., 2023). The notion of a hot excess component cooling and a cooler component appearing is also consistent with the behavior in the coronal X-Ray emission of the system (Kuhn and Hillenbrand, 2019).

4.8 Conclusion

In Paper I, we presented a means of modeling the SED of the V960 Mon system at outburst using information from our HIRES spectrum at outburst to constrain the SED fit and break some existing degeneracies between physical parameters in the model. We also presented a means of estimating the $\dot{M}$ and $R_{\rm inner}$ of the system for subsequent epochs as the system faded post-outburst.

In this work, we used the disk parameters in Paper I to construct high spectral resolution models at each observational epoch in our high spectral resolution time series data set, in order to better understand the evolution of both disk and non-disk components of the V960 Mon system. We have shown:

1. Our high resolution model disk spectrum accurately reproduces the evolution of disk absorption features across the 4000-9000 Å range of the HIRES spectra during the post-outburst fade of the V960 Mon system.

2. The HIRES spectra show evidence of temperature evolution that is consistent with our predicted SED evolution of the system.

3. We are able to isolate absorption and emission from non-disk components of the V960 Mon system, including a strong multicomponent outflow, by subtracting our model disk spectrum from the HIRES spectra.

    a) We detect [O I], [N II], and [S II] emission that is consistent with the multicomponent forbidden emission from CTTS disk systems, though these likely trace much more massive outflows because they tend to be as bright shock emission from jets.

    b) At outburst, the spectra show a very massive, high-velocity outflowing wind that weakens and largely disappears as the target fades.

    c) Several high EP lines in the spectra show strong and broad rest-velocity excess absorption, which weakens as the target fades. Correspondingly, lower EP lines show a narrow rest-velocity excess that strengthens as the target fades. We interpret this as evidence of a slow-moving, cooling outflow in the system.

Further high-resolution follow-up of the system will be crucial to understanding how it compares at later epochs to the older, more mature FU Ori outbursts that have been well-studied.

4.9 Acknowledgements

We thank the Association of Amateur Variable Star Observers for their dedicated high-cadence sampling of the post-outburst lightcurve of this target, which we have reproduced in Figure 1, and discussed for multiple bands in Paper I.

We thank the anonymous referee for their detailed comments which helped improve the manuscript.

4.10 Appendix: Optical HWHD Measurements and the Keplerian Disk Model

In past studies of FU Ori objects, the HWHD or FWHD measurements of spectral lines have been used to estimate the location in the disk from which spectral lines arise (Herbig et al., 2003; Park, Lee, et al., 2020). However, repeated investigations of line width in FU Ori objects have found little variation in the line widths as a function of wavelength, particularly in the optical.

Historically, this observation has been raised as evidence against the canonical $T \propto R^{-3/4}$ and $v \sim v_K$ models used. This is because the line width measurements are assumed to follow a velocity profile similar to that shown in Figure 4.19. The velocity profile is derived by taking the $v_{\rm kep}$ at the luminosity weighted mean radius of each wavelength bin in our outburst SED model.

Contrary to these expectations, however, we find that measurements of the HWHD in our Keplerian, thin disk, $T \propto R^{-3/4}$ disk model are relatively consistent with those we measure in the HIRES spectra (see Section 4.3). Though there is some slope in the measurements, tending toward narrower lines at redder wavelengths, the correlation is not significant. Furthermore, the widths of individual spectral lines is not sufficient to estimate the radial locations of the annuli from which the lines arise due to the differential broadening effect described in Section 4.3. The limited utility of HWHD measurements of spectral lines in the visible range is also pointed out in Zhu, Espaillat, et al. (2009a), where the authors argue that much broader wavelength ranges must be used. Zhu, Espaillat, et al. (2009a) find that lines around 5 μm do indeed have significantly narrower profiles than those in the visible.

4.11 Appendix: Attempts to fit the TiO Bandheads

We generally find some inconsistency between the predictions of the disk model in the NIR and the data, particularly in its ability to match molecular features. In Paper I, we show that our model is capable of reproducing the spectrophotometry of V960 Mon in the NIR near the outburst peak. However, the model fails at later

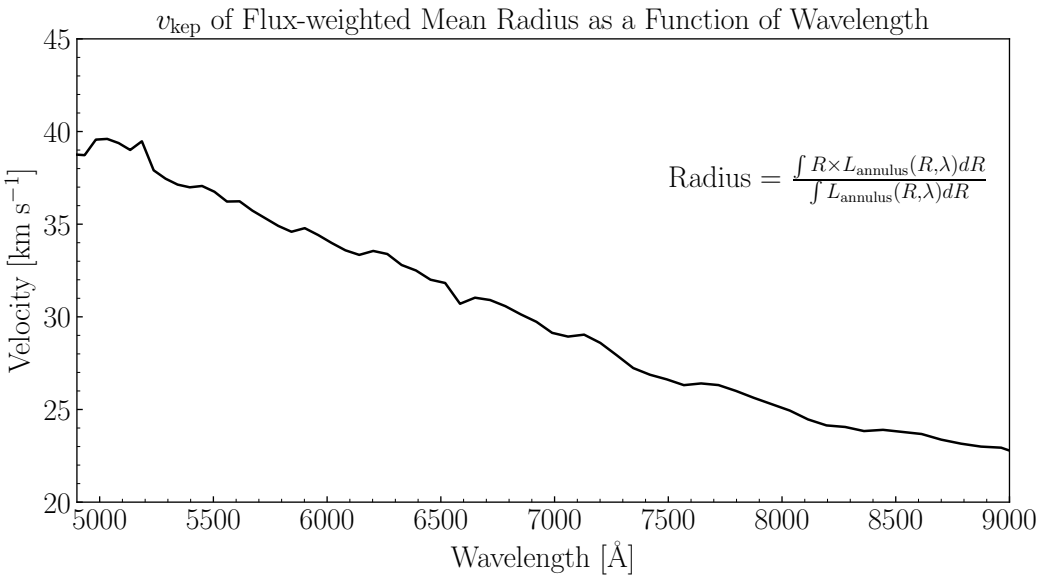

Figure 4.19: The Keplerian velocity at the luminosity weighted mean radius of each wavelength bin in the outburst spectrum model. Spectral absorption features appear as annuli with greater total flux at the slightly greater radii are needed to compensate for the absorption.

epochs when the H_2O H band features are significantly deeper. The difficulty in matching molecular absorption consistently across our disk model begins near the 8600 Å region, where the model predicts multiple strong TiO bands should be visible between I and Y band, but they do not appear in the data.

The problem with the red/NIR TiO bandheads in FU Ori objects is also mentioned by Herbig et al. (2003) in their attempts to use a disk model to model the spectra of FU Ori and V1057 Cyg. Their model uses only three stellar templates, chosen to represent three different temperatures in the disk, but they find the same problem, indicating that the issue does not arise from our choice of spectral model grid. Herbig et al. (2003) find that in both objects, the model predicts a very strong TiO 8860 bandhead, though in FU Ori and V1057 Cyg (as in V960 Mon), only the Paschen line at 8860 appears in the object spectra.

In our attempts to fit the TiO Bandhead at 8860 Å we find that the bandhead is best-replicated by having a disk that truncates at $R_{\rm outer}$ = 12 $R_\odot$, which is very compact, extending only to 6 $R_{\rm inner}$. A comparison between the bandhead in the data and the models with varying $R_{\rm outer}$ values is shown in Figure 4.20. An active disk component like that is too small because if it were truncated at such short radii, would have an outermost temperature of 4500 K. With this as the outermost

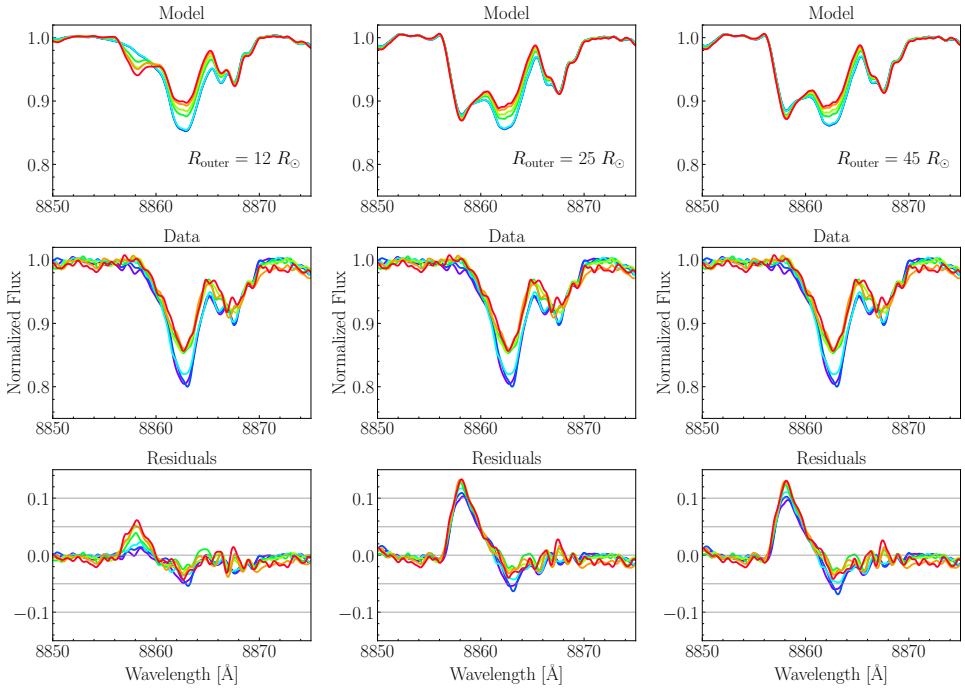

Figure 4.20: The TiO bandhead at 8860 in our models, the HIRES spectra, and the model residuals, shown for all of the HIRES epochs and for three different models. **Left:** Models computed assuming $R_{\rm outer} = 12\,{\rm R}_\odot$. Notice the time (and therefore $\dot{M}$) dependence of the TiO bandhead is much stronger for this model. **Center:** Models using $R_{\rm outer} = 25\,{\rm R}_\odot$. Already, there is little change in the TiO bandhead with time, and it clearly overpredicts the absorptions. **Right:** Models using $R_{\rm outer} = 45\,{\rm R}_\odot$. The TiO bandhead is essentially insensitive to $\dot{M}$ in these models and continues to overestimate the absorption we see.

(minimum) temperature of the active disk, no region of the active component would be cool enough to produce any of the NIR molecular features.

4.12 Appendix: All Orders of the HIRES Spectra and Residuals

All of the HIRES spectral orders from our 7 observations, including those shown in Figure 4.2.

Chapter 5

AN EXPANDING ACCRETION DISK AND A WARM DISK WIND AS SEEN IN THE SPECTRAL EVOLUTION OF HBC 722

Carvalho, Adolfo S., Lynne Hillenbrand, Jerome Seebeck, and Kevin Covey (Aug. 2024). "An Expanding Accretion Disk and a Warm Disk Wind as Seen in the Spectral Evolution of HBC 722." In: *ApJ* 971.1, 44, p. 44. DOI: 10.3847/1538-4357/ad5286. arXiv: 2405.20251 [astro-ph.SR].

We present a comprehensive analysis of the post-outburst evolution of the FU Ori object HBC 722 in optical/near-infrared (NIR) photometry and spectroscopy. Using a modified viscous accretion disk model, we fit the outburst epoch SED to determine the physical parameters of the disk, including $\dot{M}_{\rm acc} = 10^{-4.0}\ M_\odot\ {\rm yr}^{-1}$, $R_{\rm inner} = 3.65\ R_\odot$, $i = 79°$, and a maximum disk temperature of $T_{\rm max} = 5700$ K. We then use a decade of optical/NIR spectra to demonstrate a changing accretion rate drives the visible-range photometric variation, while the NIR shows the outer radius of the active accretion disk expands outward as the outburst progresses. We also identify the major components of the disk system: a plane-parallel disk atmosphere in Keplerian rotation and a 2-part warm disk wind that is collimated near the star and wide-angle at larger radii. The wind is traced by classic wind lines, and appears as a narrow, low-velocity, deep absorption component in several atomic lines spanning the visible spectrum and in the CO 2.29μm band. We compare the wind lines to those computed from wind models for other FU Ori systems and rapidly accreting young stellar disks and find a 4000-6000 K wind can explain the observed line profiles. Fitting the progenitor spectrum, we find $M_* = 0.2\ M_\odot$ and $\dot{M}_{\rm progenitor} = 7.8 \times 10^{-8}\ M_\odot\ {\rm yr}^{-1}$. Finally, we discuss HBC 722 relative to V960 Mon, another FU Ori object we have previously studied in detail.

5.1 Introduction

FU Ori-type sources are a class of Young Stellar Object (YSO) that have undergone extreme ($\Delta V \sim 4 - 6$ mag) outbursts attributed to rapid increases in their circumstellar-to-star disk accretion rates. While ~ 30 of these objects have been identified since the eruption of FU Ori itself in 1936 (Herbig, 1966), the mechanisms triggering and driving the outbursts remain elusive.

The recent outbursts of the FU Ori objects HBC 722 (Semkov and Peneva, 2010) and V960 Mon (Maehara et al., 2014) have provided unique opportunities to study outbursts as they evolve, in unprecedented detail. These outbursts happened well into the era of deep all-sky surveys, enabling multi-wavelength characterization that was not possible for the “classic" FU Ori objects like FU Ori itself, V1057 Cyg, and V1515 Cyg. Both outbursts were both promptly followed-up, with the outburst peaks captured by several observatories with high precision photometry, intermediate resolution spectrophotometry, and high-resolution spectroscopy (Miller, Hillenbrand, et al., 2011; Hillenbrand, Reipurth, et al., 2015).

In the years following these two outbursts, the targets were revisited by many of these same facilities, enabling detailed study of the spectral evolution of the objects (e.g. Lee, Park, et al., 2015; Park, Lee, et al., 2020; Carvalho, Hillenbrand, Hambsch, et al., 2023; Carvalho, Hillenbrand, and Seebeck, 2023). Continued observations of these targets by the American Association of Variable Star Observers (AAVSO) and the ease of access to their publicly available data has also provided crucial multi-band photometry to contextualize the spectroscopic observations.

Following a similar approach to the work in Carvalho, Hillenbrand, Hambsch, et al. (2023) and Carvalho, Hillenbrand, and Seebeck (2023) for V960 Mon, here we use several Keck/HIRES, IRTF/SpeX, and Palomar/TripleSpec spectra to supplement the existing photometry of HBC 722 and better understand the many components in the accretion/outflow system.

Our picture of the system near the outburst peak is shown in Figure 5.1, illustrating the various absorption and emission components that we detect in the spectra of the object. Our interpretation of the structure of the inner disk region is consistent with past studies of FU Ori objects (Calvet, Hartmann, et al., 1993; Hartmann and Kenyon, 1996; Zhu, Jiang, et al., 2020). The presence of each component is identified empirically and is agnostic to the potential outburst trigger or active instability in this system. In our data, we are able to clearly identify absorption from a rotating, plane-parallel disk atmosphere, a high-velocity collimated disk wind, a low-velocity disk wind with a wide opening angle, and emission from the winds. The disk atmosphere is generally consistent with a modified viscously-heated accretion disk (Shakura and Sunyaev, 1973; Kenyon, Hartmann, and Hewett, 1988; Rodriguez and Hillenbrand, 2022), while the disk winds are similar to the Blandford and Payne (1982, hereafter BP82) magnetocentrifugal wind model.

Over the course of this article, we will present our evidence for the existence of each

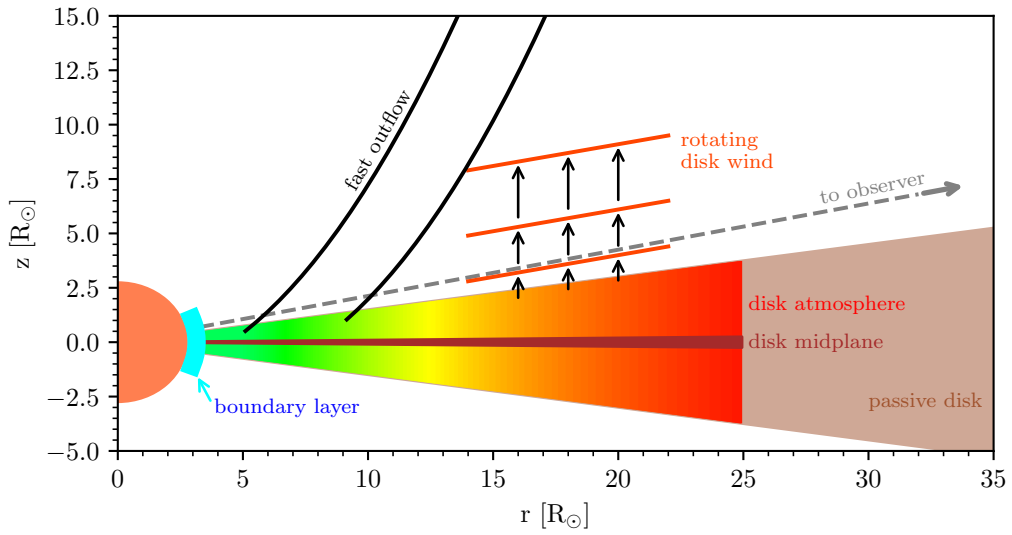

Figure 5.1: A simplified diagram of the HBC 722 system near the outburst peak. The color gradient represents the radial temperature profile in the disk atmosphere, which is assumed plane-parallel and peaks at $T_{\rm max}$ = 5700 K with $L_{\rm acc}$ = 71 $L_\odot$. The depicted height of the disk atmosphere above the midplane is representative of the τ = 1 surface in the Zhu, Jiang, et al. (2020) simulation of the FU Ori system. The midplane (in maroon) is marked for reference and given a height similar to the average scale height in the Zhu, Jiang, et al. (2020) simulation. The outer, passive disk represents that modeled in Section 5.3, which is reprocessing the bright inner disk emission. The fast outflow lines represent a magnetocentrifugal wind following the BP82 solutions, which appear consistent with what we observe in the the wind-sensitive lines of the spectrum **(Section 5.5)**.

of these components and how they varied as HBC 722 evolved through the 3 main stages of its post-outburst lightcurve.

In Section 5.2, we describe the different datasets we used and the data reduction steps for the spectra. We then explain, in Section 5.3, the SED fits with which we predict the time-evolution of the outer boundary of the active region of the disk and its atmosphere. In Section 5.4 we present our high resolution models of the system. In Section 5.5 the wind components of the system are identified in the high resolution spectra. We then provide an interpretation and summary of our analysis in Section 5.6.

5.2 Data

To understand the parameters of the HBC 722 system both at outburst and as they evolve in time, we combine several years of photometry, flux-calibrated medium-

resolution spectra, and high resolution spectra. We mostly rely on previously unpublished data, though we include some published data in our analysis. The spectra sample the lightcurve well, especially in the 3 main epochs: the outburst peak, the subsequent fade (which we refer to as the “dip"), and the second outburst into the plateau phase. An observing log for the spectra is given in Table 5.1.

Photometry

We use photometry from Miller, Hillenbrand, et al. (2011), Semkov, Peneva, et al. (2013), and Semkov, Ibryamov, et al. (2021), as shown in Figure 5.2.

To briefly summarize the photometric evolution of the system: HBC 722 began a slow rise in 2009 ($\Delta V/\Delta t \sim -1$ mag yr^{-1}), which culminated in a strong ($\Delta V \sim -4$ mag) outburst in late 2010. The outburst maximum brightness lasted only a few days before the object began to fade. In the following months, the object faded at a rate of $\Delta V/\Delta t \sim 2$ mag yr^{-1}, reaching a post-outburst minimum brightness in May 2011 before steadily brightening again at a rate of $\Delta V/\Delta t \sim -0.75$ mag yr^{-1} until late 2013. Since 2014, the system brightness has remained relatively constant, with occasional $|\Delta V| \sim 0.1$ mag variations over several months.

Medium Resolution Spectrophotometry

We make use of several medium resolution flux-calibrated spectra to study the photometric evolution of the spectrum simultaneously with the changing molecular absorption.

Near the outburst epoch, the visible range medium resolution spectrum we use to constrain the model is from September 16, 2010, taken using the Kast spectrograph (Miller and Stone, 1993) on the Lick observatory 3 m Shane Telescope. The near-infrared (NIR) medium resolution spectrum was taken on September 25, 2010, with the TripleSpec spectrograph (Herter et al., 2008) on the Palomar 5 m Hale telescope. Details of the data reduction for both spectra can be found in Miller, Hillenbrand, et al. (2011). We use these spectra without further manipulation or reduction beyond that described in Miller, Hillenbrand, et al. (2011).

For the “dip" and “plateau" epochs, NIR medium resolution spectra were taken with the SpeX spectrograph (Rayner, Toomey, et al., 2003) on the 3 m NASA Infrared Telescope Facility (IRTF) on June 26, 2011, and October 27, 2015. The spectrum from 2015 has been previously published as part of the Connelley and Reipurth (2018) survey of FU Ori objects and the data reduction is described there.

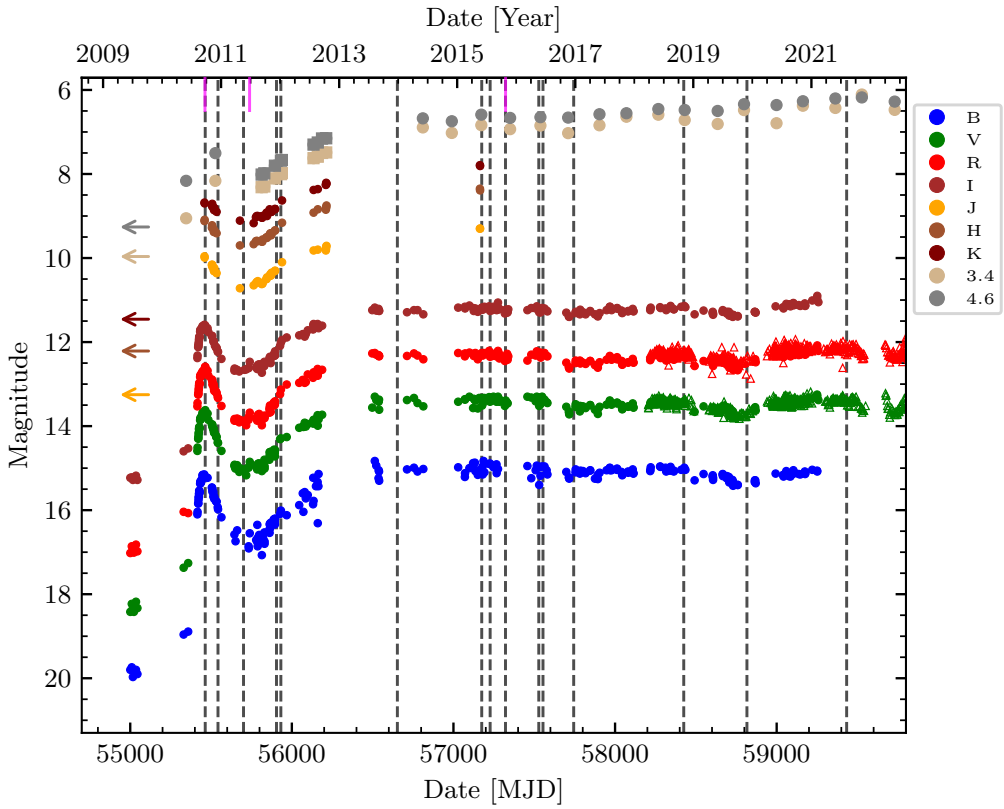

Figure 5.2: The multiband lightcurve of HBC 722, illustrating the rapid rise during outburst, brief post-outburst fade (“dip") and subsequent rise and “plateau." Filters are as given in the legend; see text for details. Green and red triangles show ZTF photometry shifted by $g - 0.9$ and $r - 0.4$ to overlap with the V and R photometry. Square points in the 3.4 and 4.6 μm bands mark the Spitzer/IRAC photometry from Kóspál, Ábrahám, Acosta-Pulido, et al. (2016), distinguishing it from the WISE and NEOWISE measurements. Left-pointing arrows indicate the progenitor photometry taken prior to 2009 (Miller, Hillenbrand, et al., 2011). Epochs of our optical HIRES spectra are shown as vertical black dashed lines, while epochs of infrared SpeX and TripleSpec spectra are marked with short vertical magenta lines.

The previously unpublished (2011) SpeX observations were obtained using the cross-dispersed echelle gratings between 0.8 and 2.45 μm, using the 0.5″ wide slit. Seeing was 0.5-0.7″, with light to heavy cirrus. Spectral extraction, wavelength calibration, telluric correction, and flux calibration were done using the Spextool reduction package (Vacca et al., 2003; Cushing et al., 2004). Observations of the A0V standard HD 205314 obtained immediately prior and at similar airmass were used for telluric correction and spectral slope calibration. Contemporaneous K band photometry was used to correct for slit losses by fixing the flux level of the spectrum at 2.2 μm.

High Resolution spectra

Keck/HIRES

We obtained visible range high-dispersion spectra from the Keck Observatory's HIgh Resolution Echelle Spectrograph (HIRES; Vogt et al., 1994). The spectra were taken in slightly different spectrograph settings over time, but broadly overlap in their wavelength coverage. Table 5.1 gives the epochs, coverage, and resolution for the spectra.

The spectra with 3600-7500 Å coverage were obtained upon request by the California Planet Search collaboration and processed using their standard reduction scripts (Howard et al., 2010); the first such spectrum was published previously by us in Miller, Hillenbrand, et al., 2011. The spectrum for 14 November 2010 was obtained from the Keck Observatory Archive (PI: G. Herbig) and was processed by their automated pipeline, which uses the MAKEE pipeline reduction package written by Tom Barlow[1]. All other spectra were processed with the 2008 version of MAKEE.

We normalize the spectra by fitting the continuum using a regularized Asymmetric Least-Squares-based algorithm (Eilers and Boelens, 2005). The technique relies on non-parameteric least-squares fitting with a regularization term to smoothly reproduce major features in the data. The error function the algorithm aims to minimize is $S = \Sigma_i d_i^2 + \lambda \Sigma_i (\Delta^2 z_i)^2$, where d_i is the residual between y_i, the input, and z_i, the model. The $\Delta^2 z_i$ term is the second derivative of the model and ensures the smoothness of the fit. The regularization parameter, λ, enables us to tune the smoothness of the continuum fits to avoid removing broad molecular absorption features or blended atomic features (see Oller-Moreno et al., 2014, Section III.A for a clear description of the algorithm).

[1] `https://sites.astro.caltech.edu/~tb/makee/`

The technique is also more robust to the edges of the spectrum than polynomial fitting. Orders with emission lines (e.g., Hα, weak forbidden emission lines, and the Ca II Infrared Triplet) need special treatment. We mask emission lines in the spectrum and use the linear interpolation from the redward continuum point to the blueward continuum point on either side of the lines as the continuum under those lines. The normalized spectra are shown in Section 5.4.

We measure a heliocentric system velocity of -10.0 km s^{-1} for the system by centering the disk profiles of isolated disk lines (e.g., Ca I 6439, Ca I 6449, and Li I 6707).

Keck/NIRSPEC

We obtained a NIR spectrum spanning 1.0-2.5 μm on 30 October 2023 using the Keck Observatory Near InfraRed SPECtrograph (NIRSPEC, McLean et al., 1998; Martin et al., 2018; López et al., 2020). The spectrum was taken in good weather and seeing, yielding a signal-to-noise ratio of $\sim$ 300. Four sets of spectrograph settings were required to cover the wavelength range, one for each of Y, J, H and K bands (the coverage and resolution are given in Table 5.1). We acquired the spectra in ABBA nod pairs to facilitate efficient background subtraction, nodding the telescope $\sim 6''$ along the slit between integrations. The exposure times differed in each band due to the target SED and the different filter throughput values. The exposure numbers and times for each band were as follows: 8×30 s (Y), 8×30 s (J), 4×60 s (H), 8×10 s (K).

We reduced the spectrum using the newly developed NIRSPEC pipeline (Carvalho, Doppmann, et al., 2024) in the `PypeIt` package (Prochaska et al., 2020). The pipeline uses the lamp flats to identify the edges of the orders of the spectra, which it then traces to construct slit masks. The slits are then extracted and rectified. We use Ar, Xe, Kr, Ne arc lamp spectra to wavelength-calibrate the spectra. `PypeIt` fits the emission lines with Gaussian profiles to identify their centroids in pixel space. We then manually identify the emission lines using the references produced by Greg Doppmann and published on the NIRSPEC instrumentation webpage[2]. The A/B nod pairs are then subtracted from one another and the target traces extracted using an optical extraction algorithm. The A0V telluric standards and the lamp flats are then used to estimate the sensitivity and blaze functions prior to coadding the individual spectra.

[2] `https://www2.keck.hawaii.edu/inst/nirspec/cals.html`

We telluric corrected the spectra by first continuum normalizing the telluric standard spectrum and fitting an A0V PHOENIX (Husser et al., 2013) stellar model spectrum to it. We then continuum normalize the target spectrum and divide it by the telluric spectrum. The continuum normalization was done using the same procedure we used for the HIRES spectra.

Gemini/IGRINS

We also use a spectrum from the Immersion GRating INfrared Spectrograph (IGRINS, Park, Jaffe, et al., 2014) to study the observed NIR variability at high resolution. The spectrum was taken on November 20, 2014 when IGRINS was installed on the Harlan J. Smith Telescope at the McDonald Observatory and was previously published by Lee, Park, et al. (2015). The spectrum was reduced using the IGRINS Pipeline Package (Lee, Gullikson, et al., 2017) and is available on the Raw and Reduced IGRINS Spectral Archive[3]. We continuum normalize the IGRINS spectrum using the same procedure as we used for the HIRES and NIRSPEC spectra.

5.3 SED Fits

We adopt a viscous accretion disk model that follows the Shakura and Sunyaev (1973) temperature profile,

$$T_{\rm eff}(r)^4 = \frac{3GM_*\dot{M}_{\rm acc}}{8\pi\sigma_{SB}r^3}\left[1-\sqrt{\frac{R_{\rm inner}}{r}}\right], \tag{5.1}$$

where $R_{\rm inner}$ is the innermost radius of the disk, M_* is the stellar mass, $\dot{M}_{\rm acc}$ is the mass accretion rate (hereafter we will simply use $\dot{M}$ for the disk-to-star accretion rate during the FU Ori outburst), σ_{SB} is the Stefan-Boltzmann constant, and G is the gravitational constant. Following Kenyon, Hartmann, and Hewett (1988), we set $T_{\rm eff}(r < \frac{49}{36}R_{\rm inner}) = T_{\rm eff}(\frac{49}{36}R_{\rm inner}) = T_{\rm max}$. Kinematically, the gas is assumed to be in Keplerian orbit around the star and thus follows the velocity profile: $v_{\rm Kep}(r) = \sqrt{GM_*/r}$. Our model is described in detail in Carvalho, Hillenbrand, Hambsch, et al. (2023).

We fit the model to our spectrophotometry of HBC 722 to constrain the physical parameters of the disk and how they evolve post-outburst. We first fit the outburst epoch, allowing several system parameters to vary. We then fix most of the parameters to their outburst epoch best-fit values and demonstrate that the post-outburst

[3] `https://igrinscontact.github.io`

Table 5.1: Spectroscopic Observations Log

Date	Instrument	Band (μm)	$\lambda/\Delta\lambda$
2010-09-25	Keck/HIRES	0.36 – 0.79	30,000
2010-11-14	”	0.43 – 0.86	”
2010-12-13	”	0.43 – 0.86	”
2011-05-20	”	0.36 – 0.79	”
2011-12-10	”	0.47 – 0.92	”
2012-01-06	”	0.44 – 0.86	”
2013-12-27	”	0.47 – 0.92	”
2015-06-02	”	0.47 – 0.92	”
2015-07-24	”	0.47 – 0.92	”
2015-10-27	”	0.47 – 0.92	”
2016-05-20	”	0.47 – 0.92	”
2016-06-15	”	0.47 – 0.92	”
2016-12-22	”	0.47 – 0.92	”
2018-11-03	”	0.47 – 0.92	”
2019-11-29	”	0.47 – 0.92	”
2021-08-07	”	0.36 – 0.79	”
2010-09-16	Lick/Kast	0.35 – 1.00	6000
2010-09-23	Palomar/TripleSpec	0.90 – 2.50	2700
2011-06-26	IRTF/SpeX	0.80 – 2.50	2000
2015-10-27	”	0.70 – 5.00	”
2014-11-20	Gemini/IGRINS	1.40 – 2.50	45,000
2023-10-30	Keck/NIRSPEC	1.00 – 2.50	15,000

evolution can be modeled by changing just $\dot{M}$ and $R_{\rm outer}$. We detail these two main modeling stages below.

Fitting the Outburst Epoch SED

We constrain the HBC 722 system outburst epoch parameters by fitting an SED constructed from 2 medium-resolution spectra taken at the peak of the outburst and spanning 0.4-2.5 μm: the 16 September 2010 Lick/Kast spectrum and the 23 September 2010 Palomar/TripleSpec spectrum (Miller, Hillenbrand, et al., 2011). Since our focus in the SED fit is to match the continuum and broad molecular emission in the target, we resample the spectra to a grid with $\lambda/\Delta\lambda = 100$. This also accelerates the model construction (and therefore fitting) significantly.

Our SED fitting technique follows a similar procedure to that outlined in Carvalho, Hillenbrand, Hambsch, et al. (2023), combining information from existing literature and the high resolution spectra to constrain an MCMC (`emcee`, Foreman-Mackey et al., 2013) fit. The parameters we will need to compute our models are: M_*,

$\dot{M}$, $R_{\rm inner}$, A_V, $R_{\rm outer}$, d (the distance to the target), and i (the disk inclination). We will also demonstrate in Section 5.3 that we will need to also vary $T_{\rm min}$, the coolest temperature atmosphere model used in the accretion disk model, where for $T(r) < T_{\rm min}$, $F_\lambda(r) = B_\lambda(T(r))$. For the fits described below, we fix $T_{\rm min} = 2400$ K.

The existence of pre-outburst observations of the target (Fang, Hillenbrand, et al., 2020; Miller, Hillenbrand, et al., 2011) enables us to use the progenitor M_* and R_* to guide our modeling of the post-outburst state. The pre-outburst visible range spectrum indicates the progenitor had a $T_{\rm eff} = 3100$ K, while the pre-outburst SED (Miller, Hillenbrand, et al., 2011) indicates an $R_* = 2.8\ R_\odot$, corresponding to $M_* = 0.2\ M_\odot$ in the 10^5 yr PARSEC (Nguyen et al., 2022) isochrone (see Appendix 5.9 and Fang, Hillenbrand, et al., 2020). We therefore fix $M_* = 0.2\ M_\odot$ for our disk model. We can then restrict the $R_{\rm inner} \geq R_* = 2.8\ R_\odot$. We also adopt the Gaia-derived 745 pc as the distance to the target (Kuhn and Hillenbrand, 2020).

The 25 Sept 2010 HIRES spectrum shows clear disk-like absorption line profiles that are consistent with a maximum disk velocity, $v_{\rm max} \sim 90$ km s^{-1} (see samples from the spectra in Section 5.4 and Section 5.4). The line profiles are distinctly non-Gaussian and are characterized by having flat “cores" and are well-matched by Keplerian rotation profiles. We use this to impose a prior on the $R_{\rm inner}$ and inclination (i) in the MCMC fit by requiring that $v_{\rm max}$ should be drawn from a Gaussian distrubution centered at 90 km s^{-1} with an uncertainty of 10 km s^{-1}.

Since we have $d = 745$ pc and $M_* = 0.2\ M_\odot$, we only need to fit $\dot{M}$, $R_{\rm inner}$, i, and A_V. The very weak K band emission in this epoch implies an "active" region much smaller than the $R_{\rm outer} \sim 100\ R_\odot$ typically assumed for FU Ori objects (e.g., Rodriguez and Hillenbrand, 2022). For this epoch we fix $R_{\rm outer} = 25\ R_\odot$, which matches the data well (and larger values overestimate the K band continuum flux). We discuss the $R_{\rm outer}$ value for this and other epochs of HBC 722 spectra in Section 5.3.

The `corner` (Foreman-Mackey, 2016) plot with the results of the fit is shown in Figure 5.3. The posterior distributions are well-behaved, with good agreement between the modal and median values for each of the 4 parameters, so we take as our best-fit model parameters: $\dot{M} = 10^{-4.0}\ M_\odot$ yr^{-1}, $R_{\rm inner} = 3.65\ R_\odot$, $i = 79°$, and $A_V = 2.3$ mag. The best-fit $A_V = 2.3$ mag is slightly smaller than our estimated $A_V = 2.5$ mag to the progenitor, but is still formally consistent with the value. The best-fit model is shown in Figure 5.4 as the outburst epoch model. The $R_{\rm inner}$ and i values are reflected in Figure 5.1, while the $\dot{M}$ sets the maximum temperature

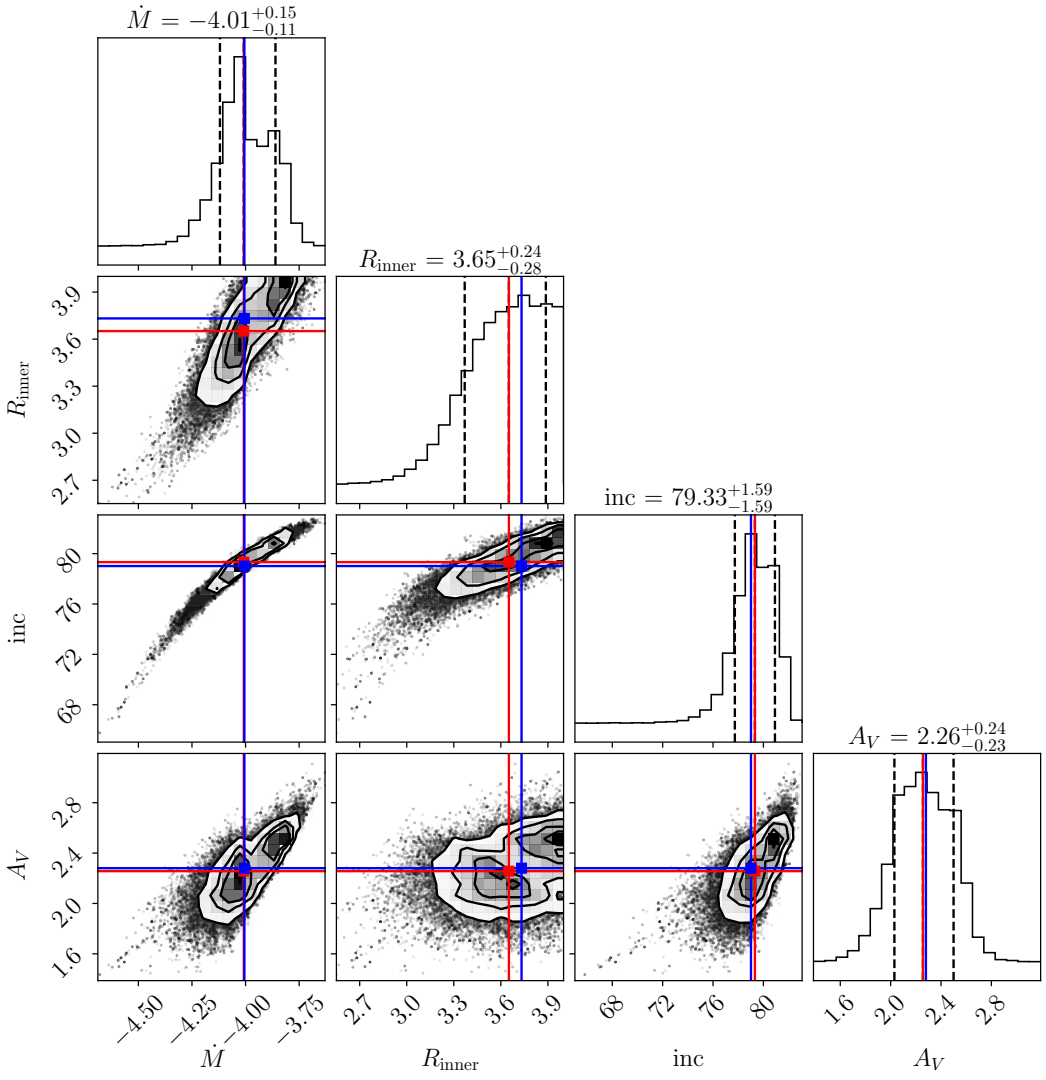

Figure 5.3: The `corner` plot for the MCMC fit of the outburst epoch SED showing the posterior distributions for the $\dot{M}$, $R_{\rm inner}$, i, and A_V model parameters. The median (mode) parameter values in the posterior distributions are marked by the red (blue) horizontal and vertical lines.

represented by the rainbow colorscale in the Figure.

Determining the Evolution of Disk Parameters

Following the procedure described in Section 5.3, we are able to successfully fit the outburst epoch Lick/Shane + Palomar/TripleSpec spectrophotometry well. We then sought to fit the other two NIR (IRTF/SpeX) spectra to better understand the system evolution in the dip (26 Jun 2011) and the plateau (27 Oct 2015).

We find that the color-magnitude evolution of the target as it faded into the dip

and brightened into the plateau is inconsistent with the model for the post-outburst fade of V960 Mon presented in Carvalho, Hillenbrand, Hambsch, et al. (2023), in which $R_{\rm inner} \propto \dot{M}^{-2/7}$ and $T_{\rm max} \propto \dot{M}^{13/28}$. Therefore, we do not assume the same behavior for this system and instead choose to fix $R_{\rm inner}$ in our models. The relatively constant-color evolution favors a fixed A_V mag over time, so we also fix that parameter. For these two fixed parameters, we adopt the best-fit values from Section 5.3: $R_{\rm inner} = 3.65\ R_\odot$ and $A_V = 2.3$ mag. Of the parameters that we varied in the MCMC fit described in Section 5.3, we only varied $\dot{M}$ to match the other two NIR spectrophotometric epochs. For the outburst epoch, we use the best-fit parameters described above, including $\dot{M} = 10^{-4.0}\ M_\odot\ {\rm yr}^{-1}$. For the dip, we find that $\dot{M} = 10^{-4.4}\ M_\odot\ {\rm yr}^{-1}$ best-matches the spectrum, whereas in the plateau we find a value of $\dot{M} = 10^{-3.9}\ M_\odot\ {\rm yr}^{-1}$.

Since the NIR data show a rapid increase in the strength of the H_2O absorption features between 1.3-1.4 μm and 1.8-1.9 μm, we found it necessary to also increase $R_{\rm outer}$ and decrease $T_{\rm min}$ for the 2011 (dip) and 2015 (plateau) epochs. This is further corroborated by the steady brightening of the 3-5 μm continuum flux (see Figure 5.2), especially after HBC 722 recovered from the dip. The brightening 3-5 μm continuum indicates that an increasing area of the disk is hotter than predicted by the passive disk model and is better matched by the viscously heated disk component.

The $T_{\rm min}$ for the outburst epoch is 2400 K, whereas matching the dip epoch requires a minimum of 1500 K and matching the plateau spectrum requires a minimum of 1100 K. We also find that between the outburst and the dip the $R_{\rm outer} = 25\ R_\odot$ grows to $R_{\rm outer} = 35\ R_\odot$, but then must increase by another 65 $R_\odot$ to match the plateau epoch spectrum. The implied outward motion of the outer boundary of the active region of the disk is 65 $R_\odot$ over the course of 1950 days. This translates to an outward velocity of 0.27 km s^{-1}.

The models are shown in Figure 5.4. The $\dot{M}$ progression described above enables us to match the overall flux level and I to J band slope well, while the $R_{\rm outer}$ and $T_{\rm min}$ progression produce an excellent match to the molecular absorption in J and H band and a good fit to the K band continuum. The larger $R_{\rm outer}$ values in the 2011 and 2015 epochs are critical to producing the appropriate continuum shape in H and K bands.

We also model the contribution of a passive disk for the 2010 (peak) and 2011 (dip) epochs to better match the WISE and Spitzer photometry at $3 - 5$ μm. The model we adopt is that of a passive disk irradiated by the inner actively accreting region

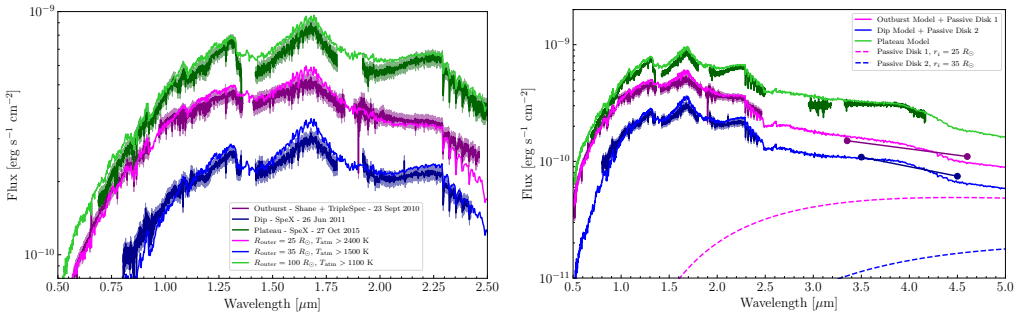

Figure 5.4: The 3 epochs of NIR spectra that trace the major parts of the lightcurve – the outburst peak (purple), the dip (blue), and the plateau (green). From outburst to the dip to the plateau, the evolution of the spectra is consistent with a general increase in $R_{\rm outer}$ and a decrease in the minimum $T_{\rm eff}$ of the model grid used to generate the disk model spectrum. Right panel includes extended wavelength coverage, and in order to match the photometry, a model for the passive disk in the outburst and dip epochs. For the plateau epoch, the active disk is large enough that a passive disk component is not necessary to model the spectrum in the $3-5$ μm range.

of the disk, as described in Carvalho, Hillenbrand, Hambsch, et al. (2023). We use three $T_{\rm eff}$ components in the model for the incident radiation, based on $T_{\rm max}$, $T(1.5\ R_{\rm inner})$ and $T(2.0\ R_{\rm inner})$ of the disk in each epoch. We assume a mildly flaring disk, with $\frac{h}{r} = 0.2\left(\frac{r}{r_i}\right)^{1.0}$, where h is the height of the disk atmosphere, r is the radial coordinate, and r_i is the inner radius of the passive disk. The flaring index of 1.0 is similar to that found for the outer disk of the other outbursting YSOs (Cieza, Ruíz-Rodríguez, et al., 2018). For both epochs, we set $r_i = R_{\rm outer}$, so that the passive disk begins where the active disk ends (see Figure 5.1 for an illustration of this in the outburst epoch).

For the 2015 (plateau) epoch, the $3-5$ μm spectrum is well-fit by the active disk model alone, indicating that the active region of the disk dominates the flux at those bands, and that the passive component may be detected only in longer wavelength observations. The models including the passive disk components are shown in the right panel of Figure 5.4.

5.4 The Disk Model in High Resolution Spectra

The HIRES and NIRSPEC spectra enable us to test the simple thin-disk viscous accretion disk model across a broad range of spectrum, with nearly continuous coverage from 0.4-2.5 μm. The broad wavelength range allows us to probe emission presumed to arise from a large fraction of the active region of the disk, from $r \sim R_{\rm inner}$ to $r \sim 10\ R_{\rm inner} = 36\ R_\odot$ (see Figure 8.24). In this section, we demonstrate the

strong agreement between our disk model and the data for the HIRES and NIRSPEC spectra, which we interpret as evidence of the presence of the disk atmosphere depicted in Figure 5.1.

The Accurately-predicted Visible Range Spectra

Using the system parameters derived from the SED fits, we predict high resolution spectra corresponding to the three epochs for which we modeled the medium-resolution spectrophotometry. We compare these predicted models to the three HIRES spectra that were taken nearly coincident with the medium-resolution spectra. The HIRES epochs we select are: 25 Sept 2010 (outburst), 20 May 2011 (dip), and 27 Oct 2015 (plateau). The high resolution spectra show significant evolution between the outburst, dip, and plateau stages. While we find that our models of the outburst epoch and the plateau epoch match the HIRES spectra well, the dip epoch is not very well-fit by the disk model, with the observations showing additional structure distinct from the line profiles predicted by the pure-disk model. The disk models and several of the HIRES spectral orders for the three epochs are shown in Figure 5.5.

The outburst epoch HIRES spectrum agrees with the $T_{\rm max}$ = 5700 K best-fit model for the outburst SED, especially toward the redder orders. The bluer orders, especially blueward of 4500 Å, are dominated by wind absorption that is not included in our model so the fits are worse there than in the red.

During the dip, the HIRES spectrum no longer looks like a disk spectrum. This seems surprising given the similarity between the dip epoch model and the 26 Jun 2011 SpeX spectrum. The inconsistency between the optical and near-infrared spectra may indicate that although the temperature profile still follows $T(r) \propto r^{-3/4}$, the disk atmosphere may no longer be rotating as a Keplerian disk would be. We discuss this possibility further in Section 5.6.

The plateau HIRES spectrum is also well-matched by the $T_{\rm max}$ = 6000 K plateau SED model. The absorption lines in the spectrum have also recovered their disk profiles, indicating the disk atmosphere has recovered its Keplerian velocity profile.

As was observed in the Carvalho, Hillenbrand, and Seebeck (2023) models of V960 Mon, the TiO bandhead at 8860 Å is predicted to be quite strong in all of our models but is totally absent in the data. This mismatch between the modeled and observed spectra of FU Ori objects was noted in Herbig et al. (2003) and Petrov and Herbig (2008) as a flaw with accretion disk models of these objects. Zhu,

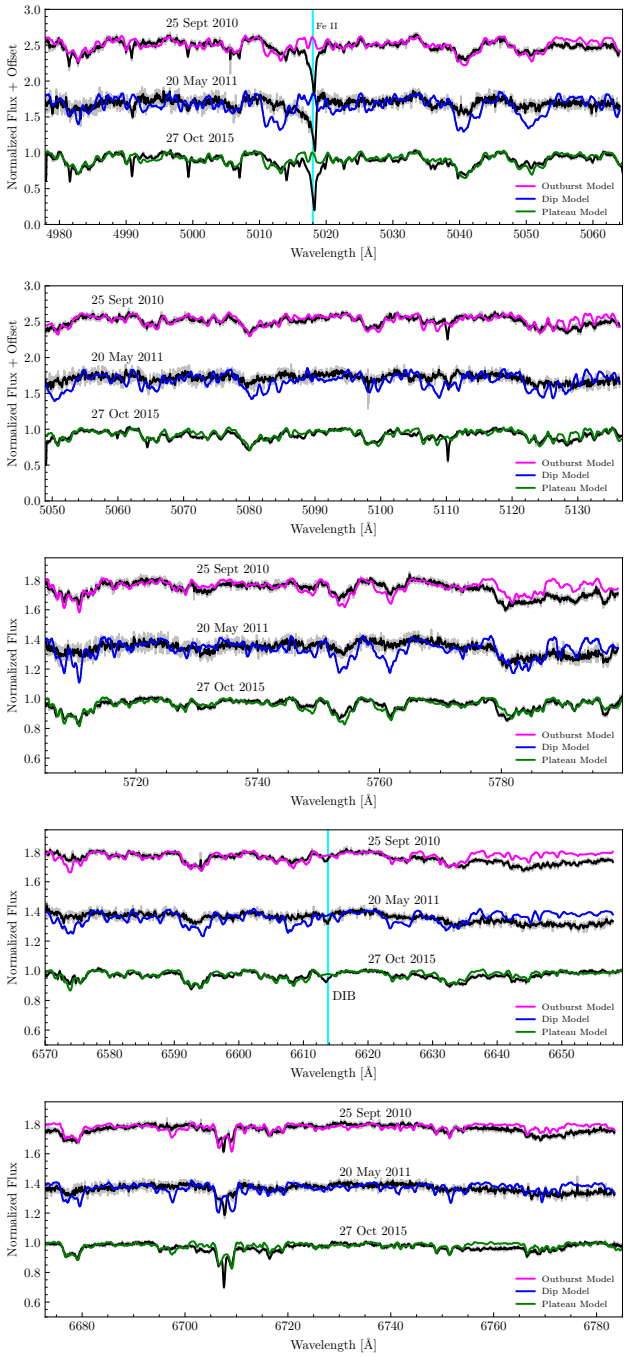

Figure 5.5: Selected orders from the HIRES spectra corresponding to the 3 SpeX epochs shown in Figure 5.4. Notice the strong agreement with the disk model spectrum that was derived to fit the lower resolution infrared spectrum, across a large range of visible wavelengths that include many atomic species. The most discrepant lines (e.g., Fe II 5018) trace wind absorption and are discussed in Section 5.5 while others (e.g., Li I 6707) exhibit a narrow blue-shifted absorption that grows over time and are discussed in Section 5.5

Espaillat, et al. (2009b) demonstrated that the excessively deep TiO absorption can be revolved by lowering the assumed $T_{\rm max}$ in the model so that the flatter part of the temperature distribution constributes relatively more in the visible range. The excess TiO absorption in our model of HBC 722 is surprising because the target is much cooler than V960 Mon, and, following the logic of Zhu, Espaillat, et al. (2009b), would not have such strong predicted TiO. This consistent TiO overprediction highlights a need to better understand the location in the disk where these features are formed to explain how the conditions differ from those assumed in our model.

The Accurately-predicted NIR Spectra

The disk model also predicts the line profiles in the 30 Oct 2023 NIRSPEC spectrum, which spans 1.0-2.5 μm. Though the spectrum was taken later than the plateau HIRES and SpeX epochs, the line profiles in the 1.0-2.5 μm wavelength range are relatively insensitive to the small difference in accretion rate between the two epochs.

Representative orders of the NIRSPEC spectrum are shown in Figure 5.6. For most of the atomic and molecular features across the entire NIRSPEC range, the disk model matches the data very closely. Major exceptions to this are wind-sensitive features (e.g. He I 10830 and the H absorption lines, Dupree et al., 2005). or low excitation potential (EP) lines tracing a disk wind (e.g., Ti I 10396 Å and Fe I 11879 Å, see Section 5.5). The excess absorption in Sr II 10326 relative to the disk model is an indicator of the very low gravity in the disk (Rayner, Cushing, et al., 2009) and a result of the strong departure in the line from the local thermodynamic equilibrium (LTE) assumptions in the model spectra (Korotin et al., 2020).

The lines that trace the disk absorption in the NIR tend to have higher EP than the disk tracing lines in the visible range (typically > 2 eV). It is notable that across the entire NIR range shown in Figure 5.6, the line profiles are matched in both depth and width by our disk model. This, combined with the good model-data agreement in HIRES, indicates that the plane-parallel disk atmosphere with Keplerian rotation is present in the system for the entire region of the disk that is probed by the 0.4-2.5 μm continuum.

The wind features in the NIR do not show the same dramatic high-velocity absorption we see in the HIRES spectra (discussed in Section 5.5). The absorption in both Paβ and Brγ are similar to the most recent plateau HIRES spectra, as might be expected. Both lines show blue-shifted absorption out to -200 km s^{-1}, consistent with the

absorption velocities seen in the later Hβ profiles, which indicates they are tracing the same massive wind (see Sections 5.6 and 5.6). The He I 10830 Å line shows a symmetric disk profile, indicating the line is tracing mostly the disk atmosphere and potentially the launching point of the rotating wind.

The CO absorption in the NIR spectra is particularly illuminating. Although the modeled CO (Δv = 3) bands are consistent with those observed in the NIRSPEC spectrum (see the analysis in Section 5.5), there is a significant discrepancy between the modeled CO (Δv = 2) bands and the data, where the observed CO (Δv = 2) bands show deep, narrow, blue-shifted absorption that is not predicted by the model. We attribute this absorption to a low-velocity disk wind, that is increasing in density over time. We show the CO (2-0) and (3-1) bands and contrast them to the disk model in Section 5.5 and we discuss their connection to the disk wind in Section 5.6.

Cross Correlation Analysis of the HIRES Spectra

To highlight the profile evolution of atomic lines in the HIRES spectra, we computed the cross-correlation function (CCF) between different spectral orders and a $T_{\rm eff}$ = 4500 K, log$g$ = 1.5 PHOENIX model stellar spectrum[4]. We chose 3 orders that appear in almost all HIRES epochs and represent a large fraction of the HIRES wavelength coverage: 5040-5130 Å, 6666-6783 Å, and 7060-7170 Å. The CCFs, shown in Figure 5.7, have clear disk line profiles in the outburst and plateau epochs. During the dip, as mentioned above, the profiles differ from disk absorption profiles and take on a more centrally absorbed structure.

As has been observed for many of the classical FU Ori objects (Herbig et al., 2003), there is little wavelength-dependence in the width of the line profiles across the visible range. This may in part be due to the phenomenon described in Carvalho, Hillenbrand, and Seebeck (2023, see also Figure 8.24) whereby atomic lines that probe different temperature components do not simply follow the expected continuum wavelength dependence. There are several lines in the redder visible orders (e.g., Ca II 8927 Å) that probe hotter regions of the disk than some of the lines in the bluer orders (e.g., Fe I 5328 Å).

Our detailed disk modeling, in addition to previous work (Welty, Strom, Edwards, et al., 1992; Zhu, Espaillat, et al., 2009b), has shown that the rotational broadening of

[4] $T_{\rm eff}$ = 4500 K is representative of the expected region in the disk from which the 5000-8000 Å continuum arises (see Figure 8.24). The log$g$ = 1.5 is similarly a typical expected gravity in this region.

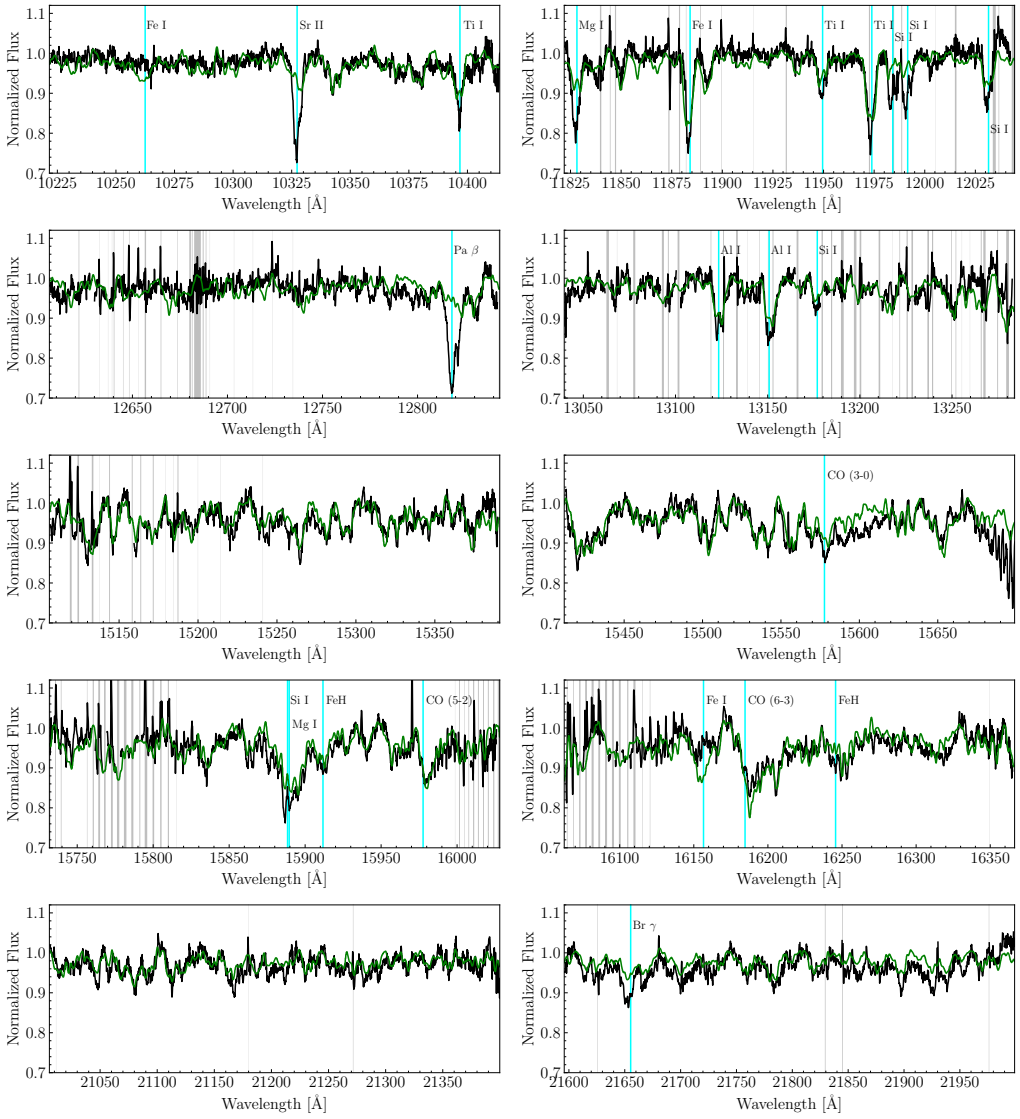

Figure 5.6: Selected orders from the NIRSPEC spectrum (in black), spanning 1.0-2.2 μm. Grey vertical lines mark locations of strong telluric absorption. The plateau epoch model is shown in green. The lines tracing the wind outflow, such as Paβ and Brγ, as well as several disk atmosphere lines including Ti I, Mg I, and Fe I, are marked with cyan vertical lines.

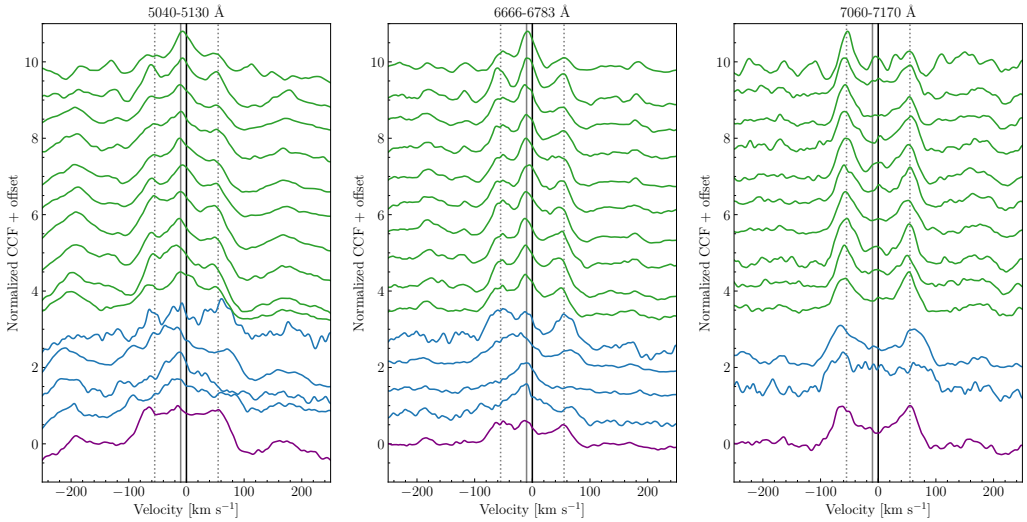

Figure 5.7: CCFs computed for 3 HIRES orders that are covered in 15/16 HIRES epochs, showing the evolution of the disk absorption over time. The purple profile indicates the 25 Sept 2010 outburst epoch, the blue profiles are those spanning the dip (Dec 2010 - Jan 2013) and the green profiles show the epochs in the plateau (2013-2022). The dotted grey lines show the approximate velocities of the peak absorption (± 55 km s^{-1}), whereas the solid grey line marks the -10 km s^{-1} at which we see a narrow absorption feature growing over time (see Section 5.5). For most of the epochs and across the HIRES wavelength range, the line profiles are a consistent width, indicating an unchanging $v_{\rm max}$ over time.

atomic lines in the optical wavelength range has a very weak wavelength dependence and that NIR observations are necessary to observe the phenomenon.

In the outburst and plateau epochs, the line profiles remain strongly disk-like and have peaks at ± 55 km s^{-1}. At later times in the plateau, we begin see a strong, narrow, blue-shifted absorption component that grows in strength against the disk absorption, which we discuss in Section 5.5. The centrally absorbed lines seen in the 13 Dec 2010 and 20 May 2011 CCFs are indicative of a departure from Keplerian rotation in these epochs and potentially increased turbulence in the disk atmosphere (see Section 5.6).

5.5 Lines with Excess Absorption or Emission Relative to the Disk Model

As in V960 Mon, the high resolution spectra of HBC 722 contain several lines that show absorption in excess of that predicted by the disk model. In this section we highlight several of these lines and describe their time-evolution.

We divide the lines into 2 main groups: the wind-tracing lines, many of which show

P-Cygni-like profiles and show both high- and low-velocity blue-shifted excess absorption, in addition to some emission, and a series of atomic lines with low-velocity and narrow blue-shifted absorption. We then also identify the molecular absorption that appears suddenly in the 2021 HIRES spectrum and the similar narrow CO absorption in the NIR spectra.

The Variable Profiles of Wind-tracing Lines

The lines typically known to trace outflows, Hβ, Hα, Fe II 5018 Å, Mg I 5183 Å, the Na I D doublet, and the Ca II H & K and Infrared Triplet (IRT) all show significant post-outburst evolution. Although in other YSO disk systems these features are also known to trace accretion, in FU Ori objects they are only known to trace outflows (Lima et al., 2010). We consider the line profiles of HBC 722 within the three main stages of post-outburst evolution discussed above: outburst (the 25 Sept 2010 epoch), dip (13 Dec 2010 - 06 Jan 2012), and plateau (27 Dec 2013 - 07 Aug 2021).

The outburst line profiles are generally similar to the plateau profiles, so we will discuss them together, though there remain some subtle differences between them that we will address. The spectrum of HBC 722 during the dip differs strongly from the outburst and plateau epochs, so we will address the line profile behavior during the dip separately. We will also then highlight the persistant low-velocity absorption present in all of the wind-tracing lines and the emission component of the Hα and Ca II IRT lines.

Regarding the Ca II lines, there are two important notes. First, in FU Ori objects, the strong blue-shifted wind absorption in the Hϵ line at 3970 Å blends into the red side of the Ca II H line profile. For our discussion we will focus on the Ca II K line since it is isolated. Second, of the lines in the Ca II IRT, we will focus on 8498 Å, because it is the only one covered in almost all of the HIRES spectra.

The Outburst and Plateau Profiles

As mentioned above, all of the wind line profiles look remarkably similar between the outburst epoch the plateau epochs. The lines all have multi-component blue-shifted absorption profiles and, in general, the red-shifted absorption is contained within the velocity range of the disk profile (see the absorption in the Hα line in Figure 5.8 compared with the disk profile CCFs in Figure 5.7), indicating the absorbing material is moving slower than the $v_{\rm max}$ of the disk model. We detail below the components of each of the wind lines and how they evolve during the

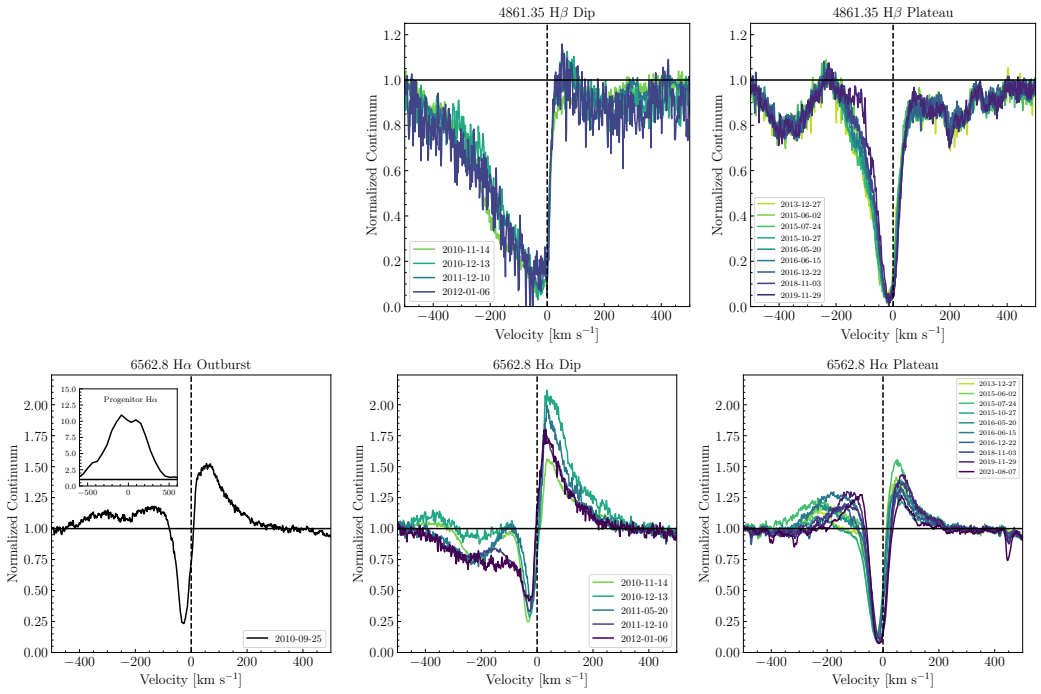

Figure 5.8: Hβ (upper row) and Hα (lower row) lines in the HBC 722 HIRES spectra. The Hβ line is not covered in the outburst epoch, so only the dip (left panel) and plateau (right panel) epochs are shown. The outburst Hα profile is shown in the inset in the bottom left panel. The lines are highly variable as the target evolves but all consistently trace a massive outflow with $v = -10$ to -30 km s^{-1}.

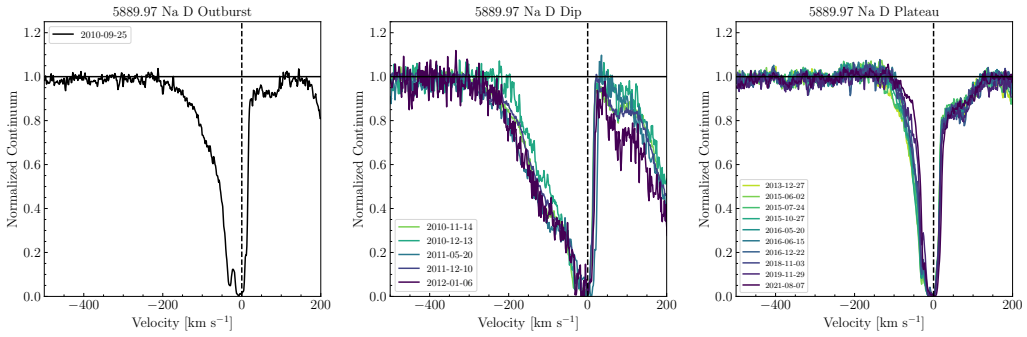

Figure 5.9: The evolution Na I D 5889 line in the HIRES spectra shown for the 3 main stages of the lightcurve: the outburst (left), the dip (center), and the plateau (right). Notice the line profile during the outburst epoch looks very similar to the profiles during the plateau. However, during the dip, the profiles are dominated by wind absorption and show almost no disk broadening in the red wing.

outburst and plateau epochs. The evolution of the profiles during the dip epochs is discussed in Section 5.5.

The Hα profiles are the most variable and complex of the wind lines, as can be seen in Figure 5.8. The blue-shifted Hα absorption has two primary components in the outburst epoch: one at high velocity, absorbing from -150 km s^{-1} to -300 km s^{-1} and one at lower velocity, absorbing from 0 km s^{-1} to -100 km s^{-1}. The high velocity component is not apparent in the plateau profiles, though in the profiles prior to 2016 there is a weak intermediate velocity absorption component ranging from -100 km s^{-1} to -250 km s^{-1}, which disappears after 2016. The low-velocity component persists almost unchanged and is especially deep, with a maximum absorption depth of 0.75 at -30 km s^{-1} that deepens during the plateau to almost 0.9 and slows to -15 km s^{-1}.

The spectrograph settings in the outburst epoch did not cover Hβ; during the plateau, however, the line profiles show only the slow wind component at -15 km s^{-1} that is persistent in Hα. With an absorption depth of 0.95, the slow component in Hβ is even deeper than in Hα.

The Na I D lines (shown in Figure 5.9) also primarily trace this deep, slow absorption, and are almost totally absorbed from 0 km s^{-1} out to -30 km s^{-1}. At outburst, the Na I D lines have a higher velocity component from -100 km s^{-1} to -200 km s^{-1}. In the plateau spectra, the faster component has disappeared and only the slow component remains. On the red side of the line, both outburst and plateau spectra show a disk-like absorption profile, though the absorption is around 2$\times$ deeper in the plateau than at outburst.

The Fe II 5018, Mg I 5183, and K I 7899 (Figure 5.10) lines evolve similarly in our spectra. All three lines have a relatively unchanging -15 km s^{-1} absorption component with an absorption depth of 0.8. The Fe II and K I lines lack the $v < -100$ km s^{-1} absorption present in the Mg II line at outburst (though it is also not in the Mg II plateau profiles). The red wing of the lines has a disk-like profile in both epochs, though its "boxiness" is more pronounced in the outburst epoch. The most dramatic change in both line profiles is the emergence of the narrow Ti I and Fe I absorption, which appears only after the dip and grows dramatically over time in the plateau stage. This absorption is discussed in more detail in Section 5.5.

The Ca II K line absorption (shown in Figure 5.11) is totally saturated in the outburst and plateau epochs. The profile is absorbed to ~ 0 from 0 to -60 km s^{-1} at outburst

and from 0 to -40 km s^{-1} in the plateau. It is difficult to determine whether the line has any high velocity absorption at outburst due to blending with several lines to the blue of Ca II K. The Ca II IRT (also in Figure 5.11) does not appear in the outburst spectrum, but we can discuss the line profiles in the plateau epochs. The lines show relatively little evolution during the plateau and their low-velocity, deep absorption is similar to that of the Fe II 5018 and Mg I 5183 lines. The blue-shifted absorption reaches a maximum depth of 0.8. The core of the absorption is at -15 km s^{-1} and the blue wing of the low-velocity component ends at -80 km s^{-1}. There is some hint of a higher velocity component from -80 km s^{-1} to -150 km s^{-1} in some epochs but not all.

The Dip Profiles

The wind absorption profiles during the dip show several features that do not appear in the outburst or plateau wind line profiles. The first notable difference is that all of the wind lines show a strong high-velocity absorption component with maximum velocities of -200 km s^{-1} (in Hβ, Fe II 5018, Na I D, Mg I 5183 and the Ca II IRT) up to -400 km s^{-1} (in Hα). The second is that the red-shifted disk absorption only appears in Mg I 5183.

Beginning again with the Hα line profiles, we see the high velocity blue-shifted absorption extending out to -400 km s^{-1}. The wind is absorbing against the blue wing of the Hα emission, which can be seen centered at -80 km s^{-1}. Taking into consideration the blue emission wing of the line, it becomes clear that the high velocity wind component blends into the low-velocity component. The low velocity component has weakened to a depth of 0.7 and slowed to a velocity of -20 km s^{-1}.

The high velocity absorption in the Hβ line appears to extend to similarly high velocities but there is a Fe I feature at 4854 Å that may be responsible for the absorption blueward of -300 km s^{-1}. However, there is certainly absorption from -200 km s^{-1} to -300 km s^{-1} that is not present in the plateau epochs. As in the outburst and plateau spectra, the Hβ absorption during the dip is deeper than the Hα absorption.

The distinction between the high velocity component and low velocity component is more clear in the Na I D lines, which show a clear “kink" at -80 km s^{-1}. The Na I D high velocity component only extends to -200 km s^{-1}. The low velocity component is consistent with that seen in the other wind lines and remains as strong as in the outburst and plateau epochs.

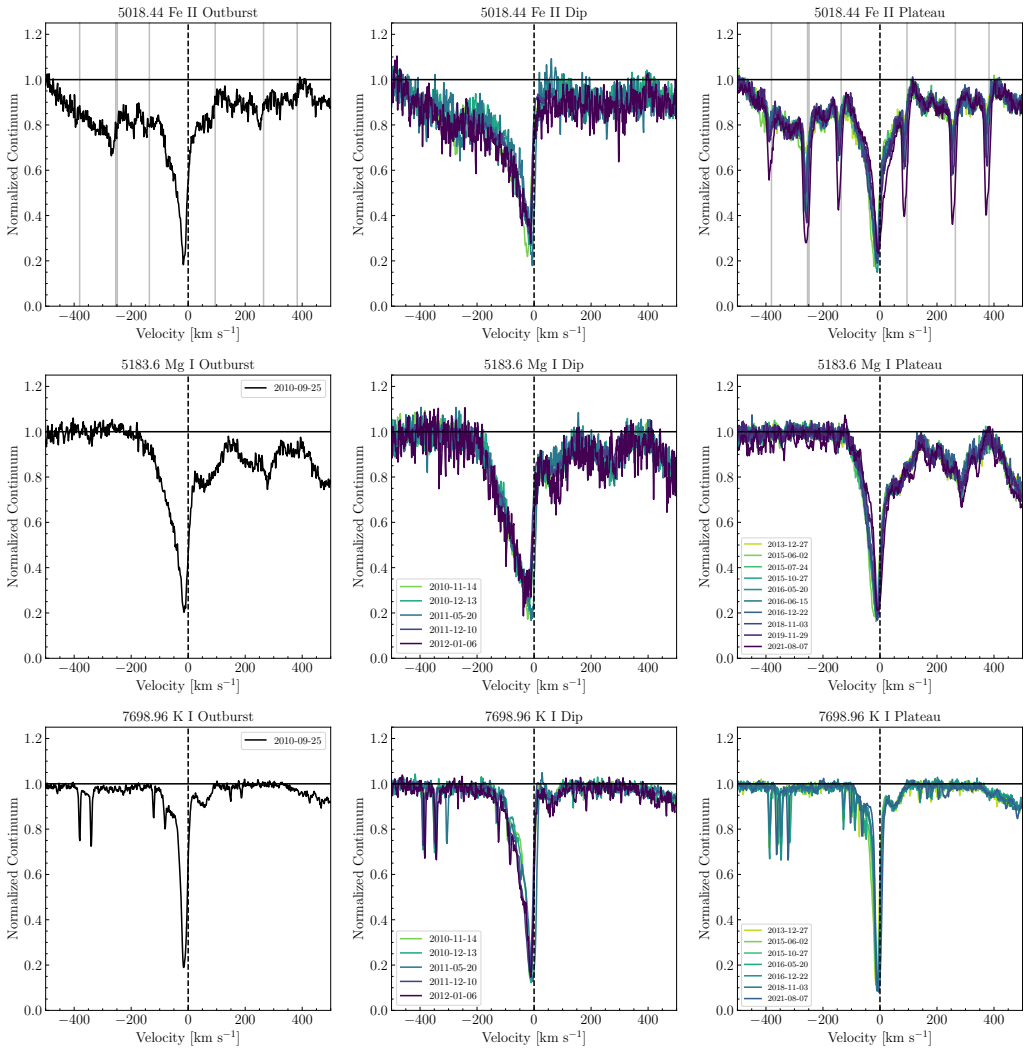

Figure 5.10: The evolution Fe II 5018 (upper row) and Mg I 5183 (middle row) and K I 7699 (lower row) lines in the HIRES spectra shown for the 3 main stages of the lightcurve: the outburst (left), the dip (center), and the plateau (right). Notice the line profiles during the outburst epoch look very similar to the profiles during the plateau. However, during the dip, the profiles are dominated by wind absorption and show almost no disk broadening in the red wing. The narrow, blue-shifted absorption traced by several Ti I lines (see Section 5.5) can be seen growing stronger in the plateau epochs of the Fe II 5018 profiles and their rest-wavelengths are marked with grey vertical lines. The epochs of the Fe II 5018 line are the same as the Mg I 5183 line, so we only print them once. In the K I panels, the narrow absorption at −80, −130, −350, and −400 km s^{-1} is due to telluric features and should be disregarded.

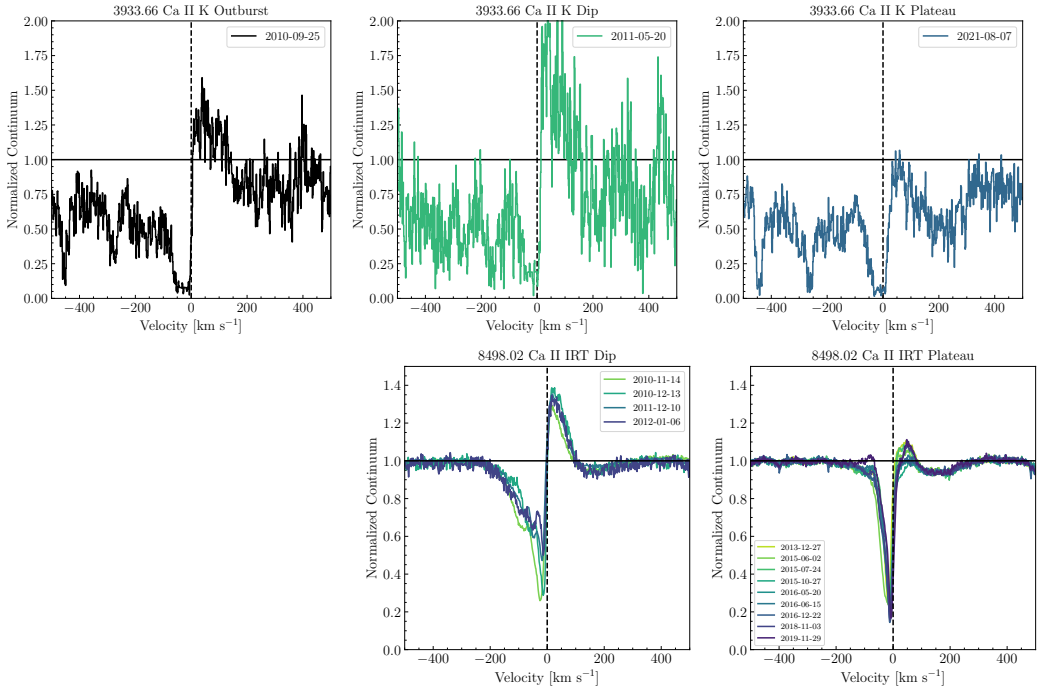

Figure 5.11: Ca II lines in the HBC 722 HIRES spectra. The upper row shows the Ca II K line at 3933 Å for the spectra that cover it, including the outburst epoch (left), dip epoch (center), and the most recent plateau spectrum (right). The outburst epoch spectrum did not cover the Ca II IRT 8498 Å line so we only show the dip (left) and plateau epochs (right) that do cover it. Both sets of lines show similar profile behavior, particularly in the red-shifted emission. The wind absorption in the Ca II K line is much stronger than in the Ca II IRT. The blue-shifted absorption in the Ca II K profiles blends into two Fe I features at -450 km s^{-1} and -275 km s^{-1} (3927.919 Å and 3930.296 Å, respectively).

In the Fe II 5018 and Mg I 5183 lines, the high velocity component also extends to -200 km s^{-1} and blends into the low velocity component, though the Fe II 5018 line has a slight kink at -80 km s^{-1} like that in the Na I D profiles. The K I line continues to only trace the lower velocity absorption, although it is deeper at -100 km s^{-1} than in the outburst or plateau epochs. A similarity between all of the profiles features highlighted in this section is that during the dip, their profiles are all distinctly wedge-shaped, with a nearly vertical slope near 0 km s^{-1} and almost no red shifted absorption.

The Ca II K line absorption remains relatively unchanged during the dip. Despite the apparently weaker blue-shifted absorption, the line minimum may still be consistent with zero due to the low signal-to-noise in the region. The Ca II IRT has a clear 2-component blue-shifted absorption profile, with absorption minima at -10 km

s^{-1}, -90 km s^{-1}, which later (by 2012) becomes a 3-component profile with a third minimum at -50 km s^{-1}. Though the slowest of the three can be attributed to the same absorbing material that has contributed to the low-velocity absorption in the other lines, the -50 km s^{-1} component is more difficult to explain. It may not be a distinct absorption component but rather an artifact of stronger blue-shifted emission that splits the broader absorption by filling in a narrow range of velocities during this epoch, as is the case in Hα.

The Persistent Slow Absorption Component

Despite the variability in the high-velocity absorption components of the wind lines, the low-velocity component remains relatively constant throughout the outburst, dip, and plateau epochs. In the Fe II 5018, Na I D, and Ca II IRT lines, this component is centered at around -10 km s^{-1} and has a half width at half depth (HWHD) of approximately $20 - 25$ km s^{-1}. In the Na I D lines the core is saturated, but ranges from 0 km s^{-1} to -20 km s^{-1}.

In the Balmer lines, the low-velocity component is more dynamic. The Hβ profile in the dip epochs appears to contain a low-velocity component that is centered at -40 or -50 km s^{-1}, though it is blended with the higher velocity component. In the plateau epochs, the component slows to -10 km s^{-1} with a HWHD of ~ 30 km s^{-1}. The line is nearly saturated at low velocities in both sets of spectra.

The Hα line at outburst shows a relatively faster low-velocity component, centered around -50 km s^{-1} with a HWHD of ~ 20 km s^{-1}. In the dip, the low-velocity component is initially similar to that at outburst but, in the 10 Dec 2011 and 06 Jan 2012 epochs, the component becomes a bit shallower and broader, with a HWHD of ~ 30 km s^{-1}. In the plateau spectra, The low-velocity component tends to slow from -30 km s^{-1} to -20 km s^{-1}. The HWHD remains ~ 25 km s^{-1}.

Emission in the Hα and Ca II Lines

In all (or most) of the HIRES epochs, the Hα and Ca II (K and IRT) profiles show both red- and blue-shifted emission components. The emission components are consistent with the emission expected for a hot, collimated disk wind, as we will discuss in Section 5.6. Here, we describe the characteristics of the emission in the two sets of lines and how it evolves post-outburst.

In the pre-outburst, progenitor spectrum, the Hα line shown in Figure 5.8 (left panel

inset) is purely in emission and extremely bright, with a peak-to-continuum flux ratio of 11.0. Accounting for the $R \sim 2000$ of the spectrograph used to obtain the spectrum (Fang, Hillenbrand, et al., 2020)[5], the width of the progenitor emission is ~ 250 km s^{-1}. In the post-outburst spectra, the red-shifted emission extends from 0 km s^{-1} to 200 km s^{-1}, though the emission peak is strongly absorbed blue-ward of 50 km s^{-1}. The blue-shifted emission extends to greater velocities than the red-shift emission, reaching -400 km s^{-1} in the outburst epoch and the 2013-2014 epochs of the plateau, potentially indicating forward-scattering of emission line by the outflow. The blue-shifted emission between 0 and -100 km s^{-1} may explain why the Hα absorption is shallower than the Hβ absorption, as is seen in V960 Mon (Carvalho, Hillenbrand, and Seebeck, 2023) and V1331 Cyg (Petrov, Kurosawa, et al., 2014).

Like Hα, the Ca II K line and the IRT also show some blue- and red-shifted emission, though during the plateau it is much weaker. The red side of the Ca II H line is heavily absorbed by the blue wing of the Hϵ line, so we cannot see any potential red-shifted emission in the feature. We will also focus on the 8498 Å component of the Ca II IRT, since it is the one most consistently covered by the HIRES spectra. However, the 2012-01-06 spectrum all three Ca II IRT components are visible and at their greatest peak-to-continuum ratios, enabling us to better compare the emission from all three. The ratios of the emission peaks of the three are 1:1:0.7 in increasing wavelength order. If the emission were optically thin, the expected peak flux ratios would be those of the $\log g_f$ values between the lines, or 1:9:5 (Ryabchikova et al., 2015), which indicates the source of the Ca II IRT optically thick, as is seen most T Tauri stars and Herbig Ae/Be stars (Hamann and Persson, 1992a; Hamann and Persson, 1992b).

The Ca II K and 8498 Å emission components are brightest during the dip, with peak-to-continuum ratios of 2.0 and 1.35, respectively. The emission of the Ca II K line extends to almost 150 km s^{-1}, almost as high velocity as the Hα emission. The maximum velocity of the Ca II IRT red-shifted emission peak is only 100 km s^{-1}, much slower than the Hα emission. The difference may be due to significant Paschen absorption to the red side of every IRT component, (e.g., line at 8502.49 Å may absorb the highest velocity emission from the wing of the Ca II 8498 Å line).

[5]To account for this, we measure the FWHM of the line, then divide by $2\sqrt{2}\ln 2$ to compute the appropriate measured Gaussian width σ_m. Assuming the instrument broadening is approximately Gaussian with a width σ_R, we can estimate the underlying line width by calculating $\sigma_{H\alpha} = \sqrt{\sigma_m^2 - \sigma_R^2}$.

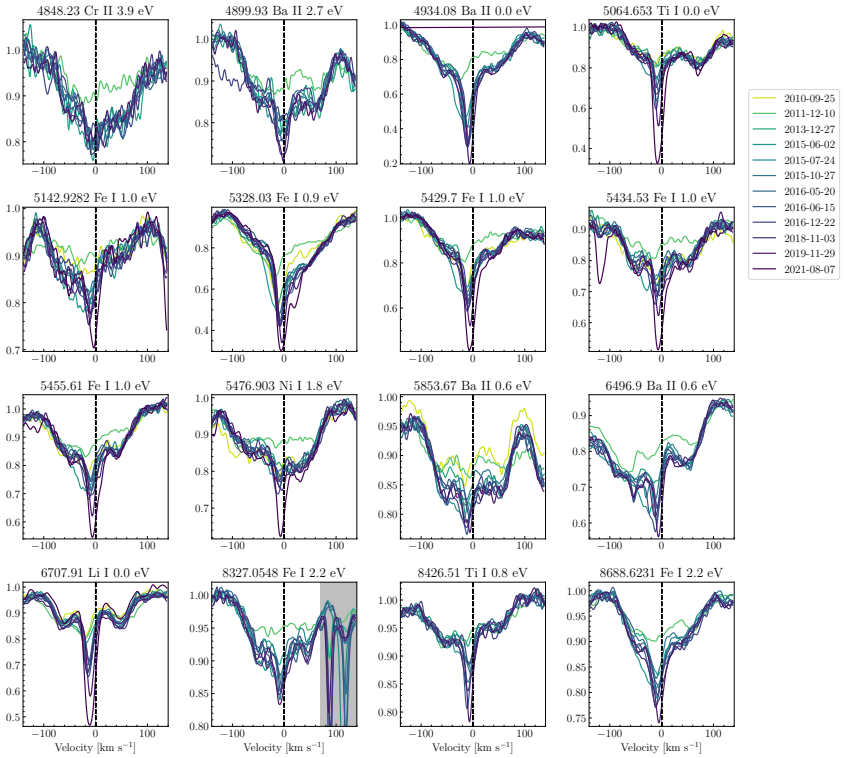

Figure 5.12: A selection of lines possessing the narrow absorption features in HBC 722. The features deepen toward later times, eventually almost dominating the absorption in some lines. The blue-shifted line center indicates it is tracing a low-velocity outflow.

For Hα and both sets of Ca II lines, the emission peak-to-continuum ratios are significantly anti-correlated with the brightness of the *R* band continuum, such that in the deepest part of the dip (the 13 Dec 2010 and 20 May 2011 spectra) the blue and red emission components are strongest.

A Forest of Narrow Blue-shifted Absorption

Above, we discussed the high-velocity blue-shifted absorption visible in the wind-sensitive lines. We also identified a low-velocity component in these lines. There is another, distinct, family of lines that show a similar narrow, low-velocity blue-shifted absorption component in the HBC 722 spectra, a subset of which we show in Figure 5.12. These lines are typically neutral species like Fe I and Ti I and almost all have low (< 1.5 eV) excitation potentials (EPs). We find 130 of these features in the HIRES spectra between 4800-8700 Å, the vast majority of which are Ti I lines with EP < 1.0.

The narrow, blue-shifted absorption can be seen weakly in the outburst spectrum

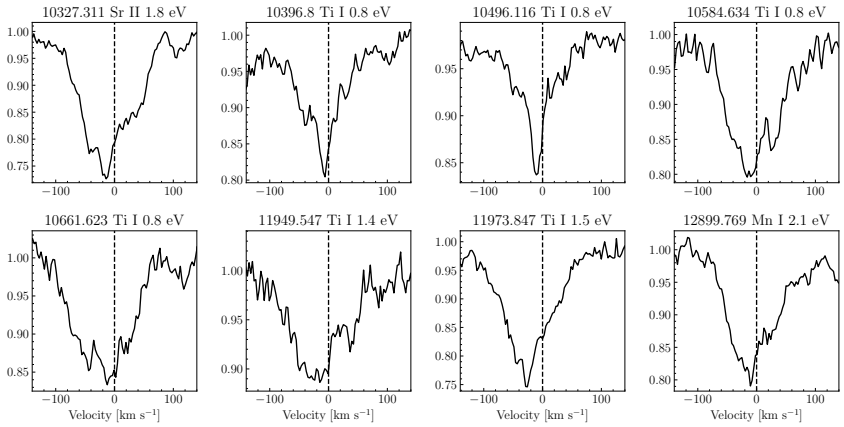

Figure 5.13: A selection of NIR atomic lines in the NIRSPEC spectrum spanning the Y to J band that show the same narrow absorption features we see in the HIRES spectra. The feature is at the same blue-shift and has a similar width to its visible-range counterparts, indicating it traces the same material.

but not in the dip spectra, though it reappears as soon as the target emerges from the dip. As can be seen in Figure 5.12, the feature appears consistently at -10 km s^{-1} and is very narrow, with a HWHD $\sim$ 10 km s^{-1}. We see it across the entire HIRES spectral range and, in the Aug 7 2021 spectrum it dominates over the disk absorption in several lines. Weak absorption lines tracing this feature are so ubiquitous, they appear 6 and 13 times over $\sim$ 800 km s^{-1} in the plateau line profile snippets in Figure 5.10 of the Fe II 5018 (upper right panel) Mg I 5183 (lower right panel) lines, respectively.

The strong absorption in the region surrounding the Fe II 5018 line is especially notable. There are 6 weak Ti I lines within $\pm$400 km s^{-1} of the Fe II 5018 line that reappear during the plateau phase and grow to be very strong during the plateau. The features have rest wavelengths (marked in Figure 5.10) of 5012.0676, 5014.187, 5014.276, 5016.1608, 5020.0263, 5022.868 and 5024.844 Å, though they are all blue-shifted by 10 km s^{-1}, and they all have 0.8 eV $<$ EP $<$ 0.9 eV (except 5014.187 Å, which has EP = 0 eV). During the plateau, they reappear and grow consistently in strength, some reaching depths of 70 % (e.g. Ba II 4934). The absorption is strongest and the growth more rapid in the lower EP features.

We also observe similarly narrow features in certain atomic lines in the Y and J bands of the NIRSPEC spectrum, shown in Figure 5.13. Unfortunately, many of the features suffer from severe blending with other atomic absorption lines, so the line profiles are not as clear as those in the HIRES spectra. However, both the Ti I

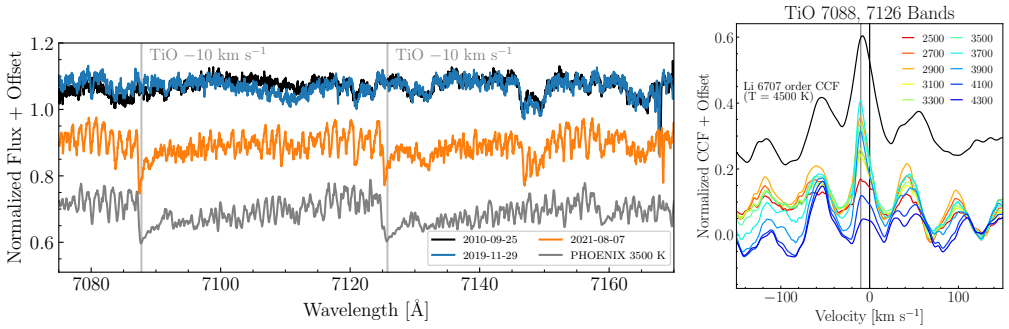

Figure 5.14: An examination of the likely temperature of the red-optical TiO absorption in HBC 722. **Left:** The 7070 Å - 7170 Å region of the HIRES spectra showing the emergent TiO absorption in the most 2021 epoch compared to previous epochs where it did not appear. Notice that the bandheads in the red spectrum are offset -10 km s^{-1} from their typical wavelengths, as highlighted by the grey vertical lines. The outburst (25 Sept 2010), penultimate (29 Nov 2019), and most recent (07 Aug 2021) spectra are shown in black, blue, and orange, respectively. A 3500 K, log$g$ = 1.5 PHOENIX model spectrum, rotationally broadened to 10 km s^{-1}, blue-shifted by 10 km s^{-1}, and scaled by 0.2, is shown in grey for reference. The scaled PHOENIX model has TiO absorption similar to that seen in the data. **Right:** CCFs computed with the TiO bandhead that appears in the 2021 HIRES spectrum (red in left panel). Notice that the strongest peak appears at 3500-3800 K and is blue-shifted by -10 km s^{-1}.

10396 Å and Ti I 10496 Å lines have profiles that are similar to the Ti I lines seen in the 2021 epoch of the HIRES spectra. Overall, in the NIR, the lines tend to be of slightly higher EP values than those in the visible, though they are still almost all < 1.5 eV.

In both the HIRES and NIRSPEC spectra, the deepest narrow absorption features appear in lines showing strong disk broadening already. We note that in the HIRES spectra the absorption depth of these narrow features grows rapidly, while the disk component of the profiles remains constant in both depth and width. This contrast demonstrates that the material carrying these lines must be absorbing against the underlying disk atmosphere. We interpret the behavior of these lines to be evidence of a low-velocity, wide angle disk wind, which we discuss in detail in Section 5.6.

TiO Absorption

In addition to the sudden increase in strength in the narrow low-EP absorption feature in the 7 Aug 2021 HIRES spectrum we also see strong TiO absorption bands at 7088 and 7126 that did not appear in any previous epochs. The spectral range

containing both bandheads is shown in Figure 5.14, compared with the previous HIRES epoch (29 Nov 2019) and the outburst epoch. Notice that in the 9 years between the 2010 outburst spectrum and the 2019 spectrum, there is almost no evolution in this wavelength range.

The bands are blue-shifted by $\sim$ 10 km s^{-1} and have widths of $\sim$ 10 km s^{-1}, consistent with the narrow blue-shifted absorption features described above. They are also relatively shallow, with bandhead absorption depths of 0.2, but they are similar in structure to those in a 3500 K, log$g$ = 1.5 atmosphere. A 3500 K, log$g$ = 1.5 PHOENIX model that has been rotationally broadened by 10 km s^{-1} is shown in Figure 5.14 for reference.

To better understand the line structure of the TiO absorption and where in the system it may originate, we performed a CCF analysis similar to that described in Section 5.4. Here, we computed the CCFs between the 2021 HIRES spectrum and several different $T_{\rm eff}$ PHOENIX models in the wavelength range of 7060 Å to 7170 Å. The temperature range we explored spanned 2500 K to 4300 K, though we found the strongest CCF power to be between 3000 K and 4000 K. The CCFs are plotted in the right panel of Figure 5.14. We also computed the CCF between the HIRES order containing the 6707 Li I feature and a $T_{\rm eff}$ = 4500 K PHOENIX model, to serve as a reference for the profiles of the atomic absorption features.

The line profiles of the TiO bands are similar to the line profiles of the atomic absorption in the rest of the HIRES spectrum. The lines show the double-peak of the disk absorption profile at ±60 km s^{-1} and the strong, narrow, blue-shifted absorption component that is dominant in the 2021 spectrum. The CCF peaks tracing this narrow component are also similar in width to the Li I order CCF. We therefore conclude that the TiO absorption traces the same component of the HBC 722 system as the narrow blue-shifted absorption in the low-EP atomic lines.

The CCF analysis shows that the preferred temperature for the TiO absorption feature is 3500-3700 K, though the 2900 K CCF peak is also quite strong. We discuss the implications of the TiO absorption in relation to the narrow blue-shifted atomic absorption and its preferred temperature range in Section 5.6.

CO Absorption

So far in this Section, we have discussed the typical visible and NIR wind features which we expect to probe a component not included in the disk model, as well as a new narrow absorption component not previously seen. Another notable

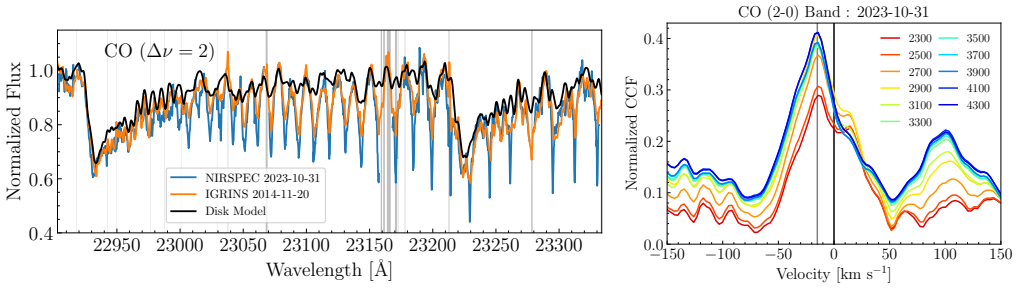

Figure 5.15: A CCF analysis of the NIR CO absorption in HBC 722. **Left:** The CO (2-0) and (3-1) bands from the Keck/NIRSPEC 30 Oct 2023 spectrum (blue), the HJST/IGRINS 20 Nov 2014 spectrum (orange) and the high resolution disk model spectrum (black). As in the HIRES spectra, we see a narrow excess absorption feature that grown stronger from 2014 to 2023. **Right:** The CCFs of the CO (2-0) band computed with different $T_{\rm eff}$ PHOENIX model spectra. At cooler temperatures, the red-shifted disk emission becomes apparent, whereas the hotter temperature profiles are dominated by the blue-shifted wind absorption.

discrepancy between the model and data appears in the CO (2-0) band at 2.29μm.

The CO (2-0) band is expected to originate in the disk and has been shown to match a disk profile well in other FU Ori objects (e.g., V960 Mon, Park, Lee, et al., 2020). However, the CO (2-0) band is dominated by narrow absorption lines much deeper than those predicted by the disk model, as can be seen in Figure 5.15, where we show the (2-0) bands in the IGRINS and NIRSPEC spectra compared with our disk model prediction.

Relative to the disk model spectrum, the (2-0) band shows a deep excess absorption component in both epochs. We note that the near-continuum wings of the lines in the (2-0) band are similar in width to the model lines, indicating that the absorption is growing *against* the underlying disk spectrum. The absorption is reminiscent of that seen growing in the HIRES spectra and which appears in some atomic features in the Y and J bands of the NIRSPEC spectrum.

We again turn to CCF analysis to study the temperature sensitivity of the line profiles of the CO (2-0). For consistency with our analysis of the visible range TiO absorption, we use the same log$g$ = 1.5 models, and explore 2300 K < $T_{\rm eff}$ < 4300 K. The wavelength ranges over which we computed the CCFs was 22920 – 23205 Å and the CCFs are shown in Figure 5.15. We will focus on the NIRSPEC spectrum here, but we discuss the CO (2-0) band in the IGRINS spectrum and the time evolution of the narrow CO absorption in Appendix 5.11.

In general, the higher $T_{\rm eff}$ CCFs are dominated by the blue-shifted wind absorption feature and only for $T_{\rm eff}$ < 3000 K do we see the red-shifted disk atmospheric absorption appear. Still, even the cooler model CCFs show strong wind absorption and a very weak red-shifted disk absorption profile. These facts indicate that the wind traced by CO (2-0) has a temperature range of 3000 K < $T_{\rm eff}$ < 4300 K, whereas the region of the disk from which the CO (2-0) atmospheric absorption arises has a temperature range of 2300 K < $T_{\rm eff}$ < 3000 K. The wind temperature range is consistent with the temperature range found for the TiO wind absorption discussed in Section 5.5. The disk temperatures are only slightly cooler than those predicted by our plateau epoch model (see Figure 8.24).

5.6 Interpretation

The fact that HBC 722 had dedicated follow-up following its 2010 outburst to collect spectra that sample the entire post-outburst lightcurve to date, enables us to construct a detailed picture of the system. We find that a multi-component accretion disk system, with high and low velocity warm disk wind components and an evolving disk, are all necessary to explain the observed data. In this Section, we describe our interpretation of the spectroscopic and photometric evolution of the HBC 722 system in light of the picture presented in Figure 5.1.

The α Disk

The primary component we observe is the accretion disk atmosphere, which at outburst has an $L_{\rm acc}$ = 71 $L_{\odot}$, dominating the emission from the system. The relatively simple disk model with $T_{\rm max}$ = 5700 K, M_{*} = 0.2 $M_{\odot}$, $\dot{M}_{\rm outburst}$ = $10^{-4.0}$ $M_{\odot}$ yr^{-1}, $R_{\rm inner}$ = 3.65 $R_{\odot}$, A_V = 2.3 mag, i = 79° and $R_{\rm outer}$ = 25 $R_{\odot}$ reproduces the data excellently. The model matches the spectrophotometry of HBC 722 (Figure 5.4) and is able to accurately predict the line profiles of the spectrum at high resolution spanning 0.4-2.5 μm (Figures 5.5 and 5.6).

Varying only 3 parameters in the model is also able to reproduce the evolution of the system post-outburst. The 0.3-1.3 μm spectrum at outburst, in the dip, and during the plateau can be reproduced by simply varying the $\dot{M}$ of the system from $\dot{M}_{\rm outburst}$ = $10^{-4.0}$ $M_{\odot}$ yr^{-1} to $\dot{M}_{\rm dip}$ = $10^{-4.4}$ $M_{\odot}$ yr^{-1} to $\dot{M}_{\rm plateau}$ = $10^{-3.9}$ $M_{\odot}$ yr^{-1}. The accretion luminosities and temperatures are correspondingly $L_{\rm acc}$ = 71 $L_{\odot}$ → 28 $L_{\odot}$ → 90 $L_{\odot}$ and $T_{\rm max}$ = 5700 K → 4500 K → 6000 K. The H_2O absorption at 1.35 μm and 1.8-2.0 μm, along with the 2.2 μm continuum, help to constrain the values of $R_{\rm outer}$ and $T_{\rm min}$ in each of the three stages.

In Section 5.3, we demonstrated that the spectophotometric evolution indicates an increasing $R_{\rm outer}$ value, from 25 $R_\odot$ at outburst to 35 $R_\odot$ in the dip and 100 $R_\odot$ in the plateau. During the earlier two epochs, a passive disk component starting at r_i = 25 $R_\odot$ and r_i = 35 $R_\odot$, respectively, is necessary to match the flux level of the $3-5$ μm photometry, whereas the 2015 spectrum is well-fitted with only a passive disk component. This is consistent with a model wherein the viscous accretion region of the disk propagates outward and "activates" the passive disk.

Accompanying the increase in $R_{\rm outer}$, we also found that the $T_{\rm min}$ value of the active disk evolved from 2400 K to 1500 K to 1100 K. The decreasing $T_{\rm min}$ is consistent with the outer boundary of the high-viscosity, high accretion rate region of the object propagating outward. The decreasing $T_{\rm min}$ may also indicate cooler annuli are establishing plane-parallel disk atmospheres with significant molecular absorption, rather than simply emitting as blackbodies. The outward propagation rate of 0.27 km s^{-1} is well below the expected sound speed of the disk midplane Zhu, Jiang, et al. (2020). Future simulations are necessary to test the ability of different instabilities to propagate outward in the disk as we observe in this system.

Notably, we showed in Section 5.4 that the HIRES (outburst and plateau epochs) and NIRSPEC spectra are closely-matched by the high resolution spectra predicted by our disk model. That spectra of FU Ori objects are consistent with disk model spectra has been shown for some of the classic objects like FU Ori and V1057 Cyg (Kenyon, Hartmann, and Hewett, 1988; Welty, Strom, Edwards, et al., 1992; Zhu, Espaillat, et al., 2009b) but many of these studies rely on relatively isolated regions of the spectrum, usually in visible wavelengths (e.g., 6100-6200 Å). Here, we demonstrate agreement between model and data to within $\sim$ 5 % for the entire 0.4-2.5 μm spectrum, excepting only lines known to trace massive disk winds, as discussed in Section 5.5. This bolsters the veracity of a high viscosity, relatively thin ($h_p/r < 0.02$, where h_p is the disk pressure scale height, Zhu, Jiang, et al., 2020) accretion disk as a model for the innermost regions of FU Ori accretion disks.

Although the α disk model successfully reproduces the intermediate resolution spectra in all epochs and the HIRES and NIRSPEC spectra during the outburst and plateau, the model is a poor fit to the HIRES spectra during the dip. This is not a difficiency in the disk model but rather illustrates that during the dip the spectra show a distinct and different average line profile. In the dip spectra, the atomic line profiles generally do not show the tidy Keplerian disk profiles seen before and after (see Section 5.4). Rather, the CCFs show that the atomic lines are dominated by the

low-velocity narrow absorption component, and have relatively triangular profiles. Interestingly, the CCFs of the reddest order do show much more disk-like profiles than are seen in the bluer orders.

Altogether, this may be an indication that as the accretion rate decreased during the dip and the innermost annuli cooled, the region nearest the star became dominated by turbulence rather. The triangular line profiles can be reproduced by convolving a Keplerian disk kernel ($v_{\rm kep} \sim 90$ km s^{-1}) with a spherically rotationally broadened line ($v_{\rm rot} \sim 30 - 40$ km s^{-1}). This is similar to the ~ 20 km s^{-1} turbulence observed in the V960 Mon system Carvalho, Hillenbrand, and Seebeck (2023) and in the Zhu, Jiang, et al. (2020) simulation of FU Ori, though it is at a higher velocity and is only seen during the dip. Such high turbulence would imply that the Shakura and Sunyaev (1973) viscosity parameter $\alpha \sim 1 - 5$ in the innermost region of the disk during the dip. However, the turbulent motion we observe may not necessary translate to an elevated viscosity in the α disk model but may instead by due to the disruption of the inner disk by the decrease in accretion rate.

The High Velocity Collimated Outflow

In the outburst spectrum, during the dip, and early into the plateau, a very high velocity $v \sim 100 - 400$ km s^{-1} wind can be seen as blue-shifted absorption in the Hα line profiles. Lower velocity regions of this outflow can also be observed in some of the other wind lines discussed in Section 5.5: Hβ (dip, 100 – 300 km s^{-1}), Na I D (outburst and dip, 100 – 250 km s^{-1}), Fe II 5018 and Mg I 5183 (dip, 100 – 200 km s^{-1}), Ca II IRT (dip, 100 – 250 km s^{-1}).

The highest velocity wind absorption is seen especially in the dip in the Hα line. During the dip, the absorption reaches a depth of ~ 0.3 at -200 km s^{-1} to -300 km s^{-1}. The absorption then weakens at higher velocities but is still ~ 0.1 at -400 km s^{-1}.

The line profiles of the Na I D, Fe II 5018, and Mg I 5183 lines are consistent with those created with the BP82 magnetocentrifugally driven disk wind model. The solid curves in our Figure 5.1 are generated using the BP82 prescription for the streamlines of the outflow. The pure-absorption case for Model MHD1i of Milliner et al. (2019b) illustrates the BP82 model with the best-match to the profiles in HBC 722 being the 55° inclination case shown in their Figure 14.

The BP82 solutions predict winds that accelerate and decrease in density as they rise. This may be observable in the different maximum velocities seen in different

wind lines. When the wind is denser and nearer the disk, it is traced by all of the wind lines, so we see the -100 km s^{-1} to -200 km s^{-1} component in the Ca II IRT, Na I D, Fe II 5018, and Mg I 5183 lines. During the dip, we also see this component in the Hβ line. However, as the wind accelerates, the only line strong enough to trace the more diffuse material is Hα. Therefore, we see the -200 km s^{-1} to -400 km s^{-1} absorption in Hα.

The Hα line profiles of HBC 722 shown in Lee, Park, et al. (2015) have 10 more epochs sampling the dip, which help to clarify the evolution of the profiles immediately post-outburst and as the target recovers from the dip more clearly. As can be seen in our Figure 5.8 and Figure 1 of Lee, Park, et al. (2015), the high velocity component in Hα is strongest as the target is fading and when it reaches its minimum brightness in the dip. As the target brightens, starting in August 2012, the Hα line dramatically changes over just 28 days from one showing absorption to -400 km s^{-1} to showing only low velocity wind absorption. The rapid disappearance of the high velocity component must be due to a change in the wind structure, where either the wind no longer reaches such high velocities or the absorbing material is too diffuse to be detected.

The Zhu, Jiang, et al. (2020) magneto-hydrodynamical (MHD) simulation of the FU Ori outburst provides some potential context for interpreting our observations. They find a wind that accelerates a relatively short distance above the disk atmosphere, where the estimated optical depth is $\tau \sim 0.01$. The wind quickly reaches velocities along the rotation axis of $v_z > 50$ km s^{-1}, velocities along the disk radial axis of $v_r > 100$ km s^{-1}, and rotational velocities of $v_\phi > 100$ km s^{-1}. The high inclination of HBC 722 implies the projected velocities from the outflow in our direction will be dominated by v_r and v_ϕ. Given the rapid wind acceleration in the r direction, the v_r component may be more responsible for the high-velocity blue-shifted wind absorption than the v_z. The absorption would be present only in the strongest wind lines due to the lower optical depth in the region where the wind reaches the velocities we observe.

The Low Velocity Disk Wind

The low-velocity absorption seen consistently in the wind-tracing lines (Section 5.5) can be attributed to a wide opening-angle, rotating disk wind, like that modeled in Calvet, Hartmann, et al. (1993). The massive wind modeled by Calvet, Hartmann, et al. (1993) was demonstrated to match the line behavior of FU Ori, particularly

for deeper absorption lines like Fe II 5018, in Hartmann and Calvet (1995b). As we show in Section 5.5, the cores of the line profiles are typically centered at −10 to −30 km s^{-1}, while the blue wing of the profiles terminate near the blue-shifted wing of the disk model line profiles (e.g., the Hα line in Figure 5.5). This is mainly the behavior that was successfully modeled for deep atomic absorption (Calvet, Hartmann, et al., 1993; Hartmann and Calvet, 1995b) and the Na I D doublet (Milliner et al., 2019b) in FU Ori.

This low-velocity disk wind may also be traced by other absorption lines, as discussed in Section 5.5 and shown in the CCFs in Figure 5.7. The low EP, neutral atomic lines in both the HIRES and NIRSPEC *Y* and *J* band spectra all show a growing absorption component that is blue-shifted between −5 km s^{-1} and −15 km s^{-1}, consistent with the lower range of velocities probed by the wind lines. Although this feature has not been seen in other FU Ori objects (except perhaps V960 Mon), it appears in lines that have been previously identified as wind-tracing lines at high mass outflow rates in FU Ori, V1057 Cyg, and Z CMa (Welty, Strom, Edwards, et al., 1992).

The structure of the absorption is also reminiscent of that identified in the bluer low EP neutral species lines in the spectrum of V1057 Cyg, dubbed the "shell features" by Herbig et al. (2003). The features are attributed to condensations in the wind absorbing against the host star. They are not consistently seen in other FU Ori objects, implying V1057 Cyg may be a special case. Potentially, as the HBC 722 system ages it will reveal more narrow absorption features as the wind evolves.

The growth of the disk wind absorption in HBC 722 is also seen in the CO (2-0) band. Between the 2014 IGRINS spectrum and the 2023 NIRSPEC spectrum, the feature doubled in depth, ultimately dominating the absorption profiles of the band. Generally, the wind seems to be traced by the higher-temperature features of the CO (2-0) band, similar to the temperatures traced by the HIRES TiO 7088/7126 Å absorption (see Section 5.5).

Altogether, the slow disk wind absorption component seen in the wind lines is consistently also seen absorbing against the disk spectrum across the entire visible/NIR. The growing absorption may be due to an increasing mass reservoir accumulating in the disk wind. As the outburst progresses and propagates outward and more material is lifted into the wind, the wind can be seen in increasingly weak absorption lines, like the many very weak Ti I lines that appear in the 2021 HIRES epoch.

In the Zhu, Jiang, et al. (2020) MHD simulation, lower portion of the wind acceleration region, where the highest layers of the disk atmosphere begin to show vertical motion, the density is still comparable to lower in the disk atmosphere, with an optical depth around $\tau = 0.1$. The model predicts that in this region the material will still rotate at roughly the local $v_{\rm Kep}$, though the v_r is predicted to be around $10 - 20$ km s^{-1} and $v_z \sim 50$ km s^{-1}.

Considering the high inclination of HBC 722, the observed absorption line velocities would be around -10 km s^{-1} to -20 km s^{-1}, depending on the strength of the line. This is exactly what we see for the low-velocity absorption in the wind lines, the narrow, growing atomic and visible range TiO absorption features, and the deep CO ($\delta v = 2$) bands. Zhu, Jiang, et al. (2020) find that for the FU Ori system, the wind has an $\dot{M}_{\rm out} \sim 0.1\ \dot{M}_{\rm acc}$, which would mean a $\dot{M}_{\rm out} \sim 10^{-6}$ to $10^{-5}\ M_\odot$ yr^{-1} for HBC 722.

Emission from the Warm Disk Wind

There are only 5 lines that show emission in any of the epochs of HIRES spectra: the Ca II K line, Hα line and the Ca II IRT. Both Hα and the Ca II lines are heavily wind absorbed blueward of 0 km s^{-1}, as discussed above, but both blue- and red-shifted emission components can be seen in almost all epochs. In both sets of lines, the line peak-to-continuum ratio is inversely correlated with the R band continuum flux level, indicating the disk continuum may be out-shining most of the emission.

The Hα emission is strongest during the first two epochs in the dip, reaching a peak-to-continuum ratio of 2.0, whereas during the plateau, due to the increased continuum brightness, the ratio is only 1.25. The blue side shows a clear emission component similar to that seen in the red side, though it is weaker in the outburst and dip epochs due to wind absorption. The blue emission strengthens to equal the red emission peak as the wind absorption weakens (as in the V960 Mon system, Park, Lee, et al., 2020; Carvalho, Hillenbrand, and Seebeck, 2023).

Similarly, the Ca II IRT reaches a maximum peak-to-continuum ratio of 1.35 during the dip which decreases to 1.1 during the plateau. As discussed in Section 5.5, the ratios of the individual emission line peaks of the Ca II IRT show that the emission source is optically thick.

Many of these points are consistent with the observations of the wind line profiles in the V960 Mon spectra (Carvalho, Hillenbrand, and Seebeck, 2023), as well as those of FU Ori (though FU Ori does not show Ca II emission). We therefore propose that

the emission in these systems is due to a warm wind, similar to those seen in high accretion rate Classical T Tauri Star (CTTS) systems (e.g. the strong accreter RW Aur, Alencar et al., 2005). The emission seen in lines like Hα in these systems has been demonstrated to arise not only from the magnetospheric accretion but also in large part from hot disk and stellar winds (Kurosawa et al., 2011; Petrov, Kurosawa, et al., 2014).

A warm, line-emitting wind has been modeled in the past for FU Ori objects (Croswell et al., 1987), using a spherically symmetric geometry and a plane-parallel geometry. Their Hα line profile models for a wind with $\dot{M}_w = 10^{-6} - 10^{-5}\ M_\odot\ \mathrm{yr}^{-1}$ are a good match to the Hα lines we observe in HBC 722 and V960 Mon. However, their predicted Na I D line profiles have emission components, whereas we do not see emission in our data. Their plane-parallel geometry $\dot{M}_w = 10^{-6}\ M_\odot\ \mathrm{yr}^{-1}$ model line profiles, on the other hand, somewhat under-predict the Hα emission but are more similar to the Na I D line.

To better understand the impact of different wind geometries and temperature profiles, we also compare our results models of CTTS disk winds. One example is the strong difference between the profiles generated by more collimated winds, potentially originating from the star or the innermost region of the disk, and those with wider opening angles being launched from the disk surface. In the model line profiles presented by Kurosawa et al. (2011), the more collimated wind models are consistent with the Hα profiles observed in HBC 722 and V960 Mon shortly after their outburst peaks, though wider opening angle models better match the profiles of these systems at later times. We also see a similar progression in the Hα lines of V1057 Cyg over time (Szabó, Kóspál, Ábrahám, Park, Siwak, Green, Moór, et al., 2021). Though the wind mass loss rates modeled by Kurosawa et al. (2011) are much lower than those we expect in FU Ori systems, the comparison may indicate an initially more collimated wind that becomes dominated by a slower, wider opening-angle component over time.

Another instructive set of CTTS wind models comes from Lima et al. (2010). They compute several Hα profiles for a Blandford and Payne (1982) hot disk wind under different model conditions, include the wind mass outflow rate, $\dot{M}_w$, and the maximum temperature attained in the wind $T_{\mathrm{MAX,w}}$. Several of their profiles are consistent with those we see in the later epochs of the HBC 722 and V960 Mon spectra, especially the emission on the red side of the profile. One of their findings is that strong blue-shifted absorption appears at particular combinations of $\dot{M}_w$ and

$T_{\rm MAX,w}$ (10^{-9} $M_\odot$ yr^{-1} and 9000 K, for example) and that the required $T_{\rm MAX,w}$ to see absorption decreases with $\dot{M}_w$. They state that for systems with very high mass loss rates ($> 10^{-8}$ $M_\odot$ yr^{-1}), the critical $T_{\rm MAX,w}$ could be as low as 6000 K. In FU Ori systems, where mass loss rates may be as high as $> 10^{-7}$ to 10^{-6} $M_\odot$ yr^{-1}, this may allow wind temperatures to be even cooler and still show the blue-shifted absorption.

An important detail about the Lima et al. (2010) disk wind models is that their winds are slower (by a factor of 10-100), denser (by ∼1.5 dex) and cooler (by ∼2000 K) near the wind launching points on the disk surface. This would allow the deep, fast, blue-shifted Hα absorption to appear in a relatively warmer part of the wind, perhaps around 5000-6000 K, while the denser, cooler region of the wind, nearer the launching point, would be traced by the low-velocity atomic and molecular absorption we highlighted in Sections 5.5, 5.5, and 5.5. In this way, the model may also be consistent with the predictions made by the cold wind models in Calvet, Hartmann, et al. (1993) and Milliner et al. (2019b).

Therefore, we propose that, as is the case in V960 Mon (Carvalho, Hillenbrand, and Seebeck, 2023), the emission components of Hα and the Ca II IRT originate in a boundary layer between the accretion disk and the central star. The variability in the emission is then caused by the boundary layer being absorbed by the disk atmosphere and wind. When the accretion rate is lower, the disk atmosphere is dimmer and the boundary layer appears brighter by contrast.

Comparison with V960 Mon

In contrast to the V960 Mon system we studied in Carvalho, Hillenbrand, Hambsch, et al. (2023), we find here that the $R_{\rm inner}$ of HBC 722 is constant in time. The relatively colorless evolution of the system does not match the predictions made by the $R_{\rm inner} \propto \dot{M}^{-2/7}$ model found to match the exponential fade of V960 Mon. The constant $R_{\rm inner}$ may place an upper limit on the magnetic field of the HBC 722 central star or at least its ability to provide pressure support against the ram pressure of the accretion flow. For the system parameters during the low accretion rate state in the dip, using the magnetospheric truncation radius equation (Hartmann, Herczeg, et al., 2016), we estimate an upper bound for the stellar magnetic field of $B_* < 1.3(1/\xi)^{1/4}$ kG, where ξ is an order unity correction factor.

Another possibility is that the high inclination of the system prevents us from directly observing the variation in the innermost annulus of the disk. If the disk atmosphere

is sufficiently flared, it may absorb the emission from $r < 3.65\ R_\odot$. The HIRES spectra with coverage blueward of 4000 Å are not as well-matched by the disk model and have many absorption lines that show wind excess relative to the model line profiles. This may indicate that the emission from the $r < 3.65\ R_\odot$ annuli of the disk is obscured by self-absorption from the disk and wind absorption from the collimated, high-velocity outflow.

The second strong contrast between the V960 Mon disk and the HBC 722 disk is the expansion of $R_{\rm outer}$ in HBC 722, which was not found for V960 Mon. In V960 Mon, the 3-5 μm emission is matched by an active disk component with $R_{\rm outer} \sim 25\ R_\odot$ and a passive disk beyond that in both the 2015 and 2016 epochs. The HBC 722 outburst and dip spectra also require a 2-component active + passive disk model, though with different $R_{\rm outer}$ values between the epochs. The plateau spectrum, however, requires only an active disk with the large $R_{\rm outer} = 100\ R_\odot$. The difference in the $R_{\rm outer}$ evolution in the two systems hints at potentially distinct outburst mechanisms in the two systems.

The evolution of the V960 Mon system post-outburst hints at an outside-in instability, originating further out in the disk then propagating inward. This would be consistent with something like gravitational instability in the disk, which has been observed at large scales in millimeter and NIR imaging (Weber, Pérez, Zurlo, et al., 2023a). The outward propagation of the instability in HBC 722 indicates the trigger is likelier to have originated closer to the central star. This would be more consistent with a thermal-instability-driven outburst, though how the instability can extend to larger $R_{\rm outer}$ is not clearly understood (Nayakshin, Cruz Sáenz de Miera, et al., 2024).

Despite the differences in the evolution and geometry of the two systems, there are several elements in common between them. An especially important one is the emergence of the narrow absorption component that strengthens over time, which in HBC 722 we can attribute to a low velocity disk wind. In V960 Mon, the essentially 0 km s^{-1} central velocity of the component makes this scenario less clear, but not impossible. The fact that the absorption grows as HBC 722 brightens/remains bright, whereas in V960 Mon it grows as the target fades may be evidence of a difference between the sources of the absorption. Detailed wind models of these systems are necessary to test the low-velocity high-line-opacity disk wind picture.

The two systems also show very similar wind line evolution, where they initially show higher velocity blue-shifted absorption that over time weakens and becomes dominated by always-present low velocity absorption component and red-shifted

emission (in the case of the Hα and Ca II lines). As discussed in Section 5.6, this is also seen in V1057 Cyg and may be due to evolution in the velocity structure of the wind over years and decades following the outburst that may be in common between the three systems.

Comparison with Previous Literature

Our best-fit models tend to produce lower $T_{\rm max}$ and higher $\dot{M}$ than the previously published $T_{\rm max} > 7000$ K and $\dot{M} \sim 10^{-5}\ M_\odot\ {\rm yr}^{-1}$ (Kóspál, Ábrahám, Acosta-Pulido, et al., 2016; Rodriguez and Hillenbrand, 2022; Liu et al., 2022). This is due to two main differences in our approach to the model fitting: we assume a much smaller mass for the central object (0.2 $M_\odot$, compared with the previously typical 0.6 $M_\odot$) and we use the line broadening from the high resolution spectra to directly constrain $R_{\rm inner}$ and i parameters in the SED fit.

The smaller mass, which we demonstrated to be more consistent with the progenitor spectrum than the previously assumed $M_* = 0.6\ M_\odot$ (Miller, Hillenbrand, et al., 2011; Kóspál, Ábrahám, Acosta-Pulido, et al., 2016) implies a central star radius of $R_* = 2.8\ R_\odot$ (see Appendix 5.9); much greater than the $R_* = 1.51\ R_\odot$ derived from matching isochrones. While our best-fit $i = 79^{+2}_{-2}$ deg agrees with the 73^{+6}_{-15} deg reported by Kóspál, Ábrahám, Acosta-Pulido, et al. (2016), our constraint on $v_{\rm max} \sin\ i$ also required a large $R_{\rm inner} = 3.65^{+0.2}_{-0.3}\ R_\odot$ for the system, which is expected from the large progenitor radius though greater than the previous to 2.0 $R_\odot$ (Rodriguez and Hillenbrand, 2022; Liu et al., 2022) values derived from SED fitting alone. The inclusion of the rotational broadening from the high resolution spectra as a constraint on the radius is critical to breaking the degeneracy in SED fitting between $M_*\dot{M}$ and $R_{\rm inner}$ and helps to provide a more reliable estimate of $R_{\rm inner}$.

Despite the differences in our derived physical parameters of the disk, our best-fit $A_V = 2.3$ mag (0.7-1.0 mag smaller than previous results) and adopted distance to the source ($\sim$ 200 pc farther away, Connelley and Reipurth, 2018) counteract one another to give a similar $L_{\rm acc}$ estimate. The effect of our smaller M_*, edge-on disk orientation, and similar $L_{\rm bol}$ conspire to require a much larger $\dot{M}$ than before. The large $R_{\rm inner}$ for the system drives the $T_{\rm max}$ to be much lower, since $T_{\rm max} \propto L_{\rm acc}/R^2_{\rm inner}$. We find our $T_{\rm max} \sim 5700 - 6000$ K is a better match to high resolution spectra at outburst and in the plateau than higher $T_{\rm max}$ models.

The increasing $R_{\rm outer}$ over time that we discuss in Section 5.6 was also identified by Kóspál, Ábrahám, Acosta-Pulido, et al. (2016). Using $3 - 5\ \mu$m photometry from

WISE and Spitzer in their SED fits, they report an initial $R_{\rm outer} \sim 19\ R_\odot$ that expands to 60 $R_\odot$ between JD 2455500 to JD 2456300, which are similar to the values we report and imply an expansion rate only 1.5× faster than the one we find.

5.7 Summary and Conclusions

We have used several years of photometry and spectroscopy of the HBC 722 system to constrain the behavior of the components in the system. This has also enabled us to better understand the nature of each of the components in this complex accretion disk .

The HBC 722 system is composed of 3 identifiable components: a viscous, active accretion disk, a low-velocity disk wind, and a high velocity collimated outflow. From our SED + spectroscopic fitting we are able to constrain the disk parameters at outburst and find that the disk begins with an $R_{\rm outer} = 25\ R_\odot$. Varying the $\dot{M}$, $R_{\rm outer}$ and $T_{\rm min}$ in the model to match the other epochs, we see that over time the active region expands from $R_{\rm outer} = 25\ R_\odot$ in 2010 to $R_{\rm outer} = 35\ R_\odot$ in 2011 to $R_{\rm outer} = 100\ R_\odot$ in 2015, and that $T_{\rm min}$ of the disk decreased over that same time.

We also see strong variability in the two outflow components. The high velocity outflow is much stronger during the dip than during the outburst or plateau, contrary to the expectation that the outflow velocity should correlate with the accretion rate. This may indicate a change in the geometry of the flow, such that during the dip the outflow is less collimated and the higher velocity material points more in the direction of the observer.

The low-velocity wind does not show much kinematic change but grows significantly in absorption strength over time. The absorption from this component even appears stronger than the disk absorption in some lines (e.g., Li I 6707) during the most recent HIRES epoch.

The high and low velocity wind components may also be the source of the emission in Hα and the Ca II lines if they are warm winds, with temperatures around 3000-5000 K. The line profiles are generally consistent with the profiles of hot wind models for CTTS systems. The exact wind temperature may not need to be as hot as that expected for CTTS winds, however, but could cool enough to be consistent with the atomic and molecular wind absorption we observe (Lima et al., 2010).

Our spectroscopic analysis of the progenitor of the system reveals it to be a low-mass but highly inflated CTTS, with $M_* = 0.2\ M_\odot$, $R_* = 2.8\ R_\odot$, and $\dot{M} = 7.8 \times 10^{-8}\ M_\odot$

yr $^{-1}$. The accretion rate is typical of Class I YSOs and among the highest for Class II YSOs in this mass range.

Comparisons between the spectral evolution of HBC 722 and V960 Mon hint at potentially different outburst mechanisms operating in the two systems. It may be that the different mechanisms can be classified according to their post-outburst photometric evolution. In that case, the outburst of HBC 722 is most similar to those of V1515 Cyg and FU Ori, whereas the V960 Mon outburst is more similar to that of V1057 Cyg, though with different fading timescales.

We strongly encourage more high and intermediate resolution follow-up of other FU Ori systems, especially in the short time following their outbursts. Sampling the post-outburst evolution (and ideally pre-outburst when possible) is critical to constraining the physics of the outburst mechanism.

5.8 Acknowledgements

The authors thank Mike Connelley for access to the 2015 SpeX SXD and LXD spectra published in Connelley and Reipurth, 2018. We also acknowledge Luke Bouma for the program add-on to obtain the 2021 Keck/HIRES spectrum. We thank the anonymous referee for their detailed comments and suggestions that improved the final manuscript.

This work has made use of the VALD database, operated at Uppsala University, the Institute of Astronomy RAS in Moscow, and the University of Vienna.

5.9 Appendix: Progenitor Spectral Type

To better constrain the physical parameters of our disk model, in particular M_*, we made use of the pre-outburst spectrum of the HBC 722 progenitor published in Fang, Hillenbrand, et al. (2020). The spectrum, spanning 5100-7800 Å, was obtained in 1998 with the Norris multi-object spectrograph on the Palomar 5-m Hale telescope at an estimated resolution $R \sim 2000$. Fang, Hillenbrand, et al. (2020) fit both empirical and model template spectra to the Norris spectrum to determine the spectral type, veiling, and A_V. In their first spectral type calculation, they report a spectral type of M4.4 ($T_{\rm eff} \sim 3000$ K) for the progenitor. However, the second step of their analysis included a post-outburst spectrum and their final spectral type of K6.6 adopted for the source, as reported in their Table 4, is not consistent with the pre-outburst Norris spectrum (see Figure 5.16). As a result, their final adopted L_* and A_V for the system are unreliable because they may have been derived by fitting the outburst spectrum,

rather than the progenitor spectrum.

To establish reliable $T_{\rm eff}$, R_*, A_V, and veiling values for the HBC 722 progenitor, we reanalyze the Norris spectrum and the pre-outburst SED (using the photometry from Miller, Hillenbrand, et al., 2011). We first use a $T_{\rm eff}$ = 3100 K BT-Settl model spectrum simultaneously produce models of both the SED and medium-resolution spectrum. This consistent with an M4.3 spectral type according to Fang, Hillenbrand, et al. (2020) (and close to their reported M4.4 from their initial spectral type fit), which we do find to be a good match for deep TiO absorption in the progenitor spectrum.

We then vary the angular size of the progenitor to match the H band flux and find R_* = 2.8 $R_\odot$, assuming our adopted distance of 745 pc, indicating the star was highly inflated relative to typical CTTSs (Baraffe et al., 2015; Nguyen et al., 2022). The final step is to vary the veiling, r_{7465}, and the A_V, until both the SED and Norris spectra are well-matched. Our best-fit values for the progenitor are then $T_{\rm eff}$ = 3100 K, a veiling of r_{7465} = 0.7 , A_V = 2.5 mag, and a R_* = 2.8 $R_\odot$. The $T_{\rm eff}$ and R_* correspond to M_* ∼ 0.2 $M_\odot$ in the 100 kyr PARSEC isochrone (Nguyen et al., 2022). The best-fit models (with and without veiling) are shown in Figure 5.16 alongside a model that adopts the Fang, Hillenbrand, et al. (2020) parameters for the system.

We can also follow the procedure in Herczeg and Hillenbrand (2008) to estimate the mass accretion rate of the progenitor based on the Hα line luminosity, $L_{\rm H\alpha}$. We first use the A_V-corrected continuum flux from the best-fit SED model, F_c = 2.388×10^{-15} erg s^{-1} cm^{-2} Å^{-1}, to estimate the flux of the Hα line. We then integrate the line from 6545 Å to 6580 Å to get $F_{\rm H\alpha} = 2.43 \times 10^{-13}$ erg s^{-1} cm^{-2} or , $L_{\rm H\alpha} = 4.19 \times 10^{-3}$ $L_\odot$, using the distance to the target, 745 pc. We convert this to an accretion luminosity using the prescription adopted in Herczeg and Hillenbrand (2008), $\log L_{\rm acc} = 1.2 \log H_\alpha + 2$, yielding $L_{\rm acc}$ = 0.14 $L_\odot$ and $L_{\rm acc}/L_{\rm bol}$ = 0.22. Using Equation 1 from Herczeg and Hillenbrand (2008), $\dot{M} \sim 1.25\, L_{\rm acc} R_* / (G M_*)$, we estimate $\dot{M} = 7.8 \times 10^{-8}$ $M_\odot$ yr^{-1}. This would make the HBC 722 progenitor one of the most rapidly accreting stars with M_* ∼ 0.2 $M_\odot$ (Manara et al., 2023), although it is consistent with measured accretion rates of Class I protostars (Fiorellino et al., 2023).

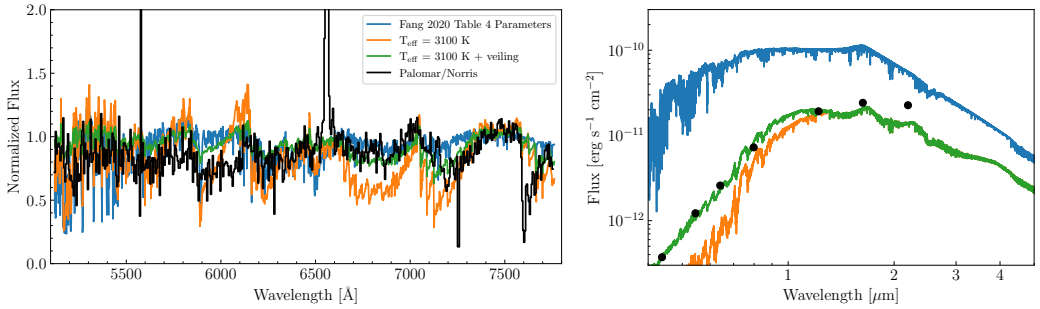

Figure 5.16: The progenitor data compared with models using the Fang, Hillenbrand, et al. (2020) reported best-fit parameters and our adopted parameters. **Left:** The 1998 Norris spectrum, binned to $R = 1000$, showing deep TiO absorption more consistent with the veiled late-type (M4-M5, green) model spectrum than the unveiled K7 model (blue). **Right:** The progenitor SED (black dots), using photometry from Miller, Hillenbrand, et al. (2011), compared with the different models for the progenitor spectrum (color lines). The model with our adopted $T_{\rm eff} = 3100$ K, $R_* = 2.8\ R_\odot$, $r_{7465} = 0.7$ and $A_V = 2.5$ mag, shown in green, is a good fit to both the SED and the Norris spectrum.

5.10 Appendix: Line Profiles of O I Wind Lines

In Section 5.5, we identify the main absorption components of several lines typically understood to trace outflows in young stars. Here, we include 2 lines that were omitted from that discussion: the O I 7773 Å triplet (at 7771, 7774, and 7775 Å) and the O I 8446 triplet (at 8446.25, 8446.36, and 8446.76 Å), both shown in Figure 5.17. We omit the O I triplets because the three components blended together make it difficult to identify the distinct velocity components we see in the other wind lines.

The O I 7773 triplet, which has an EP= 9.1 eV, is typically only present in higher temperature atmospheres or high $T_{\rm max}$ FU Ori objects (Hillenbrand, Carvalho, van Roestel, et al., 2023). Here, it appears almost entirely in excess of the disk model, which predicts a maximum depth of $\sim 5\%$ for the line. This indicates the triplet must arise entirely from some hotter region in the disk, potentially near the launch point of the collimated wind (i.e., near $R_{\rm inner}$). This may be corroborated by the blue-shifted absorption that can be seen at -30 km s^{-1} relative to the 8774 line. The triplet absorption is also shallower in the dip than in the outburst or plateau, which is the opposite of what we see in the other wind lines. If the triplet is sensitive here to the hottest region in the disk, the weaker absorption can be considered further evidence that the disk cools during the dip.

The behavior of the O I 8446 triplet, which also has an EP= 9.1 eV, differs from the

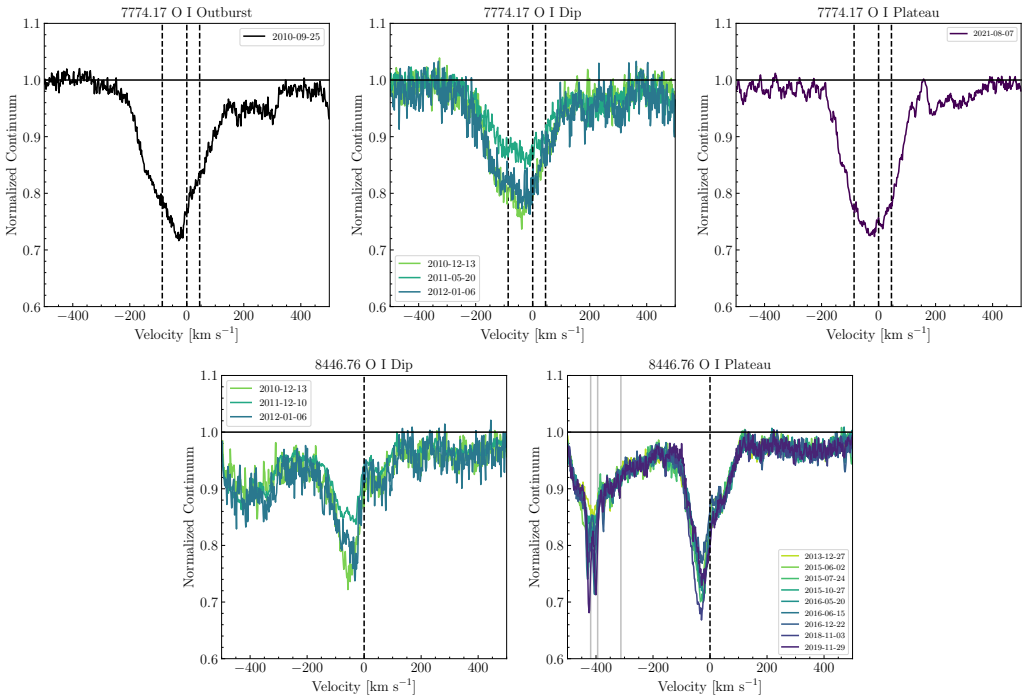

Figure 5.17: Line profiles of red/NIR O features known to trace winds, shown in the HIRES spectra for the outburst epoch (left column), dip epochs (middle column) and plateau epochs (right column). **Upper Row:** The line profiles of the O I 7773 Å triplet, which is typically only seen in higher temperature atmospheres. The absorption at +250 km s^{-1} is disk atmospheric absorption from the Fe I 7780 feature. **Lower Row:** The O I 8446 Å triplet, which appeared only in our dip and plateau epochs. The grey lines at −390 and −420 km s^{-1} mark the locations of the Ti I 8434.961 and 8435.653 Å lines, both of which have EP = 0.8 eV. The broader absorption marked at −310 km s^{-1} is mostly due to the Paschen line at 8837 Å.

O I 7773 lines. This triplet clearly shows blue-shifted wind absorption that extends to −100 km s^{-1} and red-shifted disk profile absorption, like we see in the Fe II 5018 line profiles. The lower velocity component of O I 8446 is at −50 km s^{-1}, faster than we see for the other wind features, and like O I 7773, it is shallower in the dip than in the plateau. Again this may indicate that these high EP O I triplets trace the hottest absorbing material in the system, close to the central star.

5.11 Appendix: The Temperature Sensitivity and Time Evolution of the CO (3-0) Band

In this appendix we explore the potential temperature ranges for the disk and wind absorption components of the CO bands in the NIRSPEC and IGRINS spectra. We expand the CCF analysis used in Section 5.5 for the CO (2-0) band in the NIRSPEC

spectrum to the CO (2-0) band in the IGRINS spectrum and the CO (3-0) bands of both spectra. For the CO (3-0) and (3-1) bands, the wavelength ranges over which we compute the CCFs are 15540 – 15640 and 23205 – 23305 Å. We also investigate the relative sensitivity of the CO (3-0), (3-1), and (2-0) bands to the low-velocity wind absorption.

Considering first the CO (3-0) bands (top panel of Figure 5.18) we see that there is little evolution between the IGRINS and NIRSPEC epochs and that the disk model generally matches the data closely. Accordingly, CO (3-0) band CCFs (middle row, Figure 5.18) show very clear disk profiles in both the NIRSPEC and IGRINS spectra. This remains the case almost regardless of the $T_{\rm eff}$ of the model used to compute the CCF.

One trend that appears is that higher $T_{\rm eff}$ models produce CCFs with slightly broader disk profiles, whereas the lower $T_{\rm eff}$ models show narrower profiles. This demonstrates two important properties of the accretion disk model: that a large region of the disk representing several $T_{\rm eff}$ values can contribute to any particular spectral feature and that the Keplerian broadening of the hotter (closer in) regions is greater than that of the cooler (further out) regions. The only significant difference between the two epochs in this band is that the cooler temperature CCFs in the NIRSPEC spectrum are narrower than those of the IGRINS spectrum. This may trace the coolest, slowest-moving material at large radii away from the star and may be evidence of $R_{\rm outer}$ continuing to expand between 2014 and 2023.

The CCFs computed for the CO (2-0) band in the IGRINS spectrum (bottom right panel, Figure 5.18) highlight the difference between the band in the two spectral epochs, as discussed in Section 5.5. In the IGRINS spectrum, the disk profiles seen at lower temperatures are much more clear than in the NIRSPEC spectrum. Although we also see the wind absorption component growing in prominence from the cooler model CCFs to the hotter ones, the feature does not dominate the profiles like we see in the NIRSPEC spectrum.

The IGRINS CO (2-0) band notably shows similar behavior to the CO (3-0) band: the CCFs computed with hotter models have broader disk profiles than those computed with the cooler models. The CO (2-0) disk profiles are also generally narrower than the CO (3-0) profiles, which was also identified by Lee, Park, et al. (2015). We generally see the trend in the NIRSPEC spectra for the cooler temperature CCFs. This is consistent with the idea that the K band continuum is dominated by emission from greater (and therefore slower-orbiting) radii than H band as predicted by the

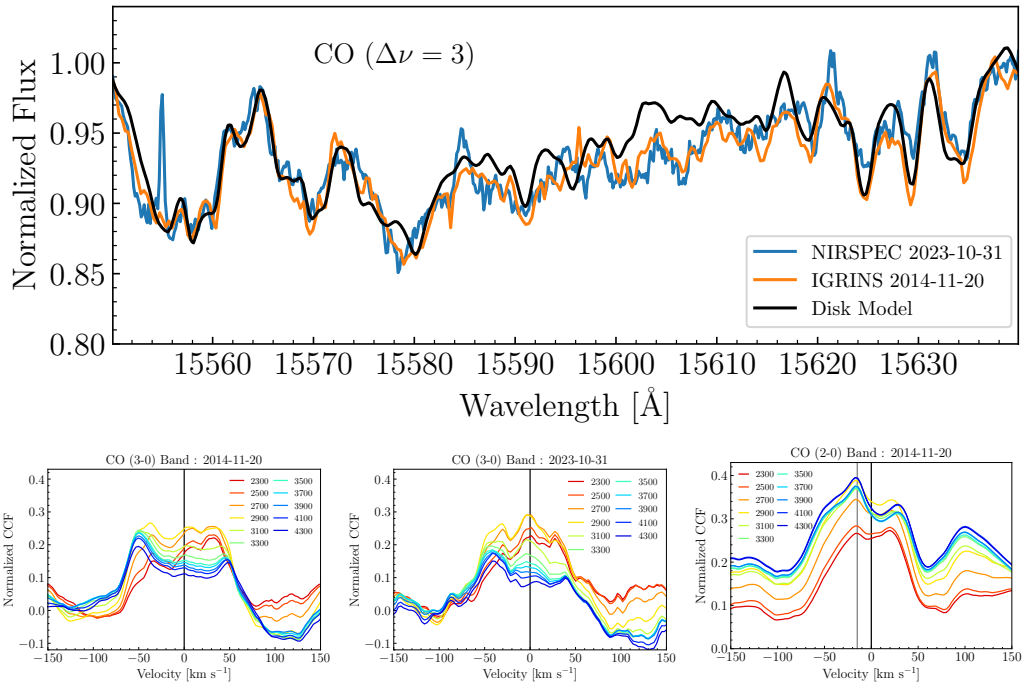

Figure 5.18: Time evolution of the *H* band CO absorption in HBC 722. **Top Panel:** The CO (3-0) band from the Keck/NIRSPEC 30 Oct 2023 spectrum (blue), the HJST/IGRINS 20 Nov 2014 spectrum (orange) compared with the high resolution disk model spectrum (black). **Bottom Panels:** CCFs between the HBC 722 spectra and PHOENIX model atmospheres with different $T_{\rm eff}$. **Left:** The CCFs for the CO (3-0) band in the IGRINS spectrum. **Middle:** The CCFs for the CO (3-0) band in the NIRSPEC spectrum. **Right:** CCFs computed with (2-0) band for the IGRINS spectrum. Here, the disk absorption is seen at lower temperatures than in the NIRSPEC epoch, but at higher temperatures, the profile still shows strong narrow blue-shifted absorption at -15 km s^{-1}.

expected $T(r)$ and $v(r)$ profiles of viscous accretion disks in Keplerian rotation (demonstrated in Figure 8.24).

Chapter 6

THE HOT INNER AU OF V883 ORI

Abstract: The V883 Ori system is a rapidly accreting young stellar object that has been used as a laboratory for studying the molecular inventory of young circumstellar disks with high luminosity. We simultaneously fit high resolution spectroscopy and medium resolution spectrophotometry of the system to constrain the physical conditions in the inner au. Using our thin viscous accretion disk model, we find $\dot{M} = 10^{-3.9\pm0.2}\ M_\odot\ \mathrm{yr}^{-1}$, $R_{\mathrm{inner}} = 5.86 \pm 1\ R_\odot$, $i = 38.2 \pm 3$ degrees and $A_V = 20.8 \pm 0.7$ mag, resulting in an accretion luminosity of 458 $L_\odot$ and maximum disk temperature of 7045 K. The optical portion of the SED greatly exceeds the flux level expected for a highly extincted accretion disk. We propose that the excess emission arises from a contribution due to scattering of the accretion disk spectrum off nearby envelope material that is viewed along a less-extincted line of sight. Additionally, we use photometric observations spanning 137 years to demonstrate that the source has accreted at least 18 M_{Jup} of disk material to date. Finally, we discuss the importance of considering both the viscous heating from the midplane and the consequent irradiation effects on the outer disk when modeling the temperature structure to reproduce millimeter-wavelength observations.

6.1 Introduction

There is a population of accreting young stellar objects (YSOs) known to undergo extreme photometric outbursts, during which the mass accretion rate onto the star increases by up to 10,000, causing the system to brighten by a factor of 100. The class prototype was defined when FU Ori itself rapidly brightened in 1937 by 6 magnitudes (in B band, Wachmann, 1954) and then remained at its elevated brightness for several decades (Herbig, 1977). By the 1990s, around 10 FU Ori-like objects (FUOrs) had been discovered and their spectra were shown to be consistent with those of thin, viscously-heated accretion disks (Kenyon, Hartmann, and Hewett, 1988; Hartmann and Kenyon, 1996).

Among these first half dozen or so discovered FUOrs was the V883 Ori system. Although it was only identified in 1993 as a FUOr in outburst, it is one of the brightest and longest-lived accretion outbursts, having potentially peaked in brightness sometime before 1888 (Pickering, 1890; Strom and Strom, 1993).

V883 Ori has been the target of several millimeter and submillimeter observations aimed at studying the molecular inventory of the disk. Due to the intense heat of the outburst, complex molecules that are typically trapped in ices in the midplane of the disk are released when the ices sublimate. The liberated molecules, now in gas phase, emit brightly at millimeter/submillimeter wavelengths. Although the details of this sublimation, like the new location of the H_2O snow line (Schoonenberg et al., 2017), are not well known, the rich millimeter emission line spectrum of V883 Ori is well documented (Cieza, Casassus, et al., 2016; van 't Hoff et al., 2018; Lee, Lee, et al., 2019; Tobin et al., 2023).

Modeling the emission from these molecules to interpret the millimeter spectra requires a detailed understanding of the radiation field in the disk. In non-outbursting YSOs, the majority of the relevant radiation is from the central star (in the visible/near-infrared) and the accretion columns shocking on the stellar surface (in the X-ray/ultraviolet, Öberg et al., 2023). In FUOrs, however, the star itself contributes minimally to the overall spectrum, while the magnetospheric accretion columns are expected to have been overwhelmed by the disk and thus also do not contribute much (Hartmann and Kenyon, 1996; Liu et al., 2022).

Instead, the near-ultraviolet (NUV), visible, and near-infrared (NIR) spectrum is dominated by emission from the viscously heated accretion disk itself. The far-UV (Carvalho, Hillenbrand, France, et al., 2024) and X-ray (Kuhn and Hillenbrand, 2019) are likely dominated by emission near the star-disk interface, either from enhanced magnetic activity during the outburst or a shock from the accretion flow along the surface of the disk. In V883 Ori, most of the NUV/visible flux is faint due to the high line-of-sight extinction to the central source. This has limited the ability to constrain the properties of the inner disk like the disk mass accretion rate, accretion luminosity, and maximum temperature.

The V883 Ori system was first identified as a potential YSO by Haro (1953), who observed the morphological similarity of the bright nebula that extends 67″ to the southeast of the point source (see Figure 6.1) to Herbig-Haro objects. The point source, which is V883 Ori, was then classified as a B-type star under 20 mag of extinction by Allen et al. (1975). Eventually, Strom and Strom (1993) highlighted the spectroscopic similarities between V883 Ori and FU Ori in low resolution optical spectra, identifying it as a FUOr. The FUOr classification of the source has since been re-affirmed by Connelley and Reipurth (2018).

Millimeter continuum observations of V883 Ori have revealed a large outer disk,

extending to 100 au, with an inclination of 38.3° and a position angle on the sky of 32.4° (Cieza, Casassus, et al., 2016). The orientation of the disk relative to the bright nebula is shown in Figure 6.1.

In this article, we present new measurements of the inner disk temperature, luminosity, and truncation radius, enabled by deep spectroscopic observations of the source from $0.4 - 4.2$ μm. We demonstrate that the visible range emission from V883 Ori, while faint, is much brighter than expected for a highly extincted FUOr and likely due to scattering in the surrounding nebula. We then discuss our model of the system and its implications for interpretation of the emission at longer wavelengths.

6.2 Data

To fully characterize the inner disk of V883 Ori, we combine several public and newly collected datasets spanning the 0.4 to 5 μm and wavelength range, including both and high and low resolution spectra. The data are described below.

High Resolution Spectroscopy

Visible (Keck/HIRES)

Two high dispersion red-optical spectra of V883 Ori were obtained on 5 October 2003 and 10 December 2011 using the HIgh RESolution spectrograph (HIRES, Vogt et al., 1994) on the W.M. Keck Observatory's Keck I telescope. The 2003 spectrum was obtained from the Keck Observatory Archive (PI: R. White) and was processed by their automated pipeline, which uses the MAKEE pipeline reduction package written by Tom Barlow[1]. The 2011 spectrum was also obtained from the Keck Observatory Archive (PI: L. Hillenbrand), but was extracted and reduced using the HIRES data reduction pipeline in PypeIt (Prochaska et al., 2020).

Both spectra were continuum normalized using the asymmetric least-squares detrending code described in Carvalho, Hillenbrand, and Seebeck (2023). The spectra both have a resolution of $R \equiv \lambda/\Delta\lambda = 37,000$ and have reasonable signal-to-noise from 6400 Å to 9000 Å. V883 Ori is very faint in the visible ($V \sim 20$ mag, see Section 6.4), requiring prohibitively long exposure times for greater sensitivity at shorter wavelengths. The position angle (PA) of the slit in the 2003 (2011) spectrum was to 72° (50°), so the nebula shown in Figure 6.1 is mostly excluded from the slit. Visual inspection of the 2D images confirm that there no extended nebular emission captured during the observations.

[1] `https://sites.astro.caltech.edu/~tb/makee/`

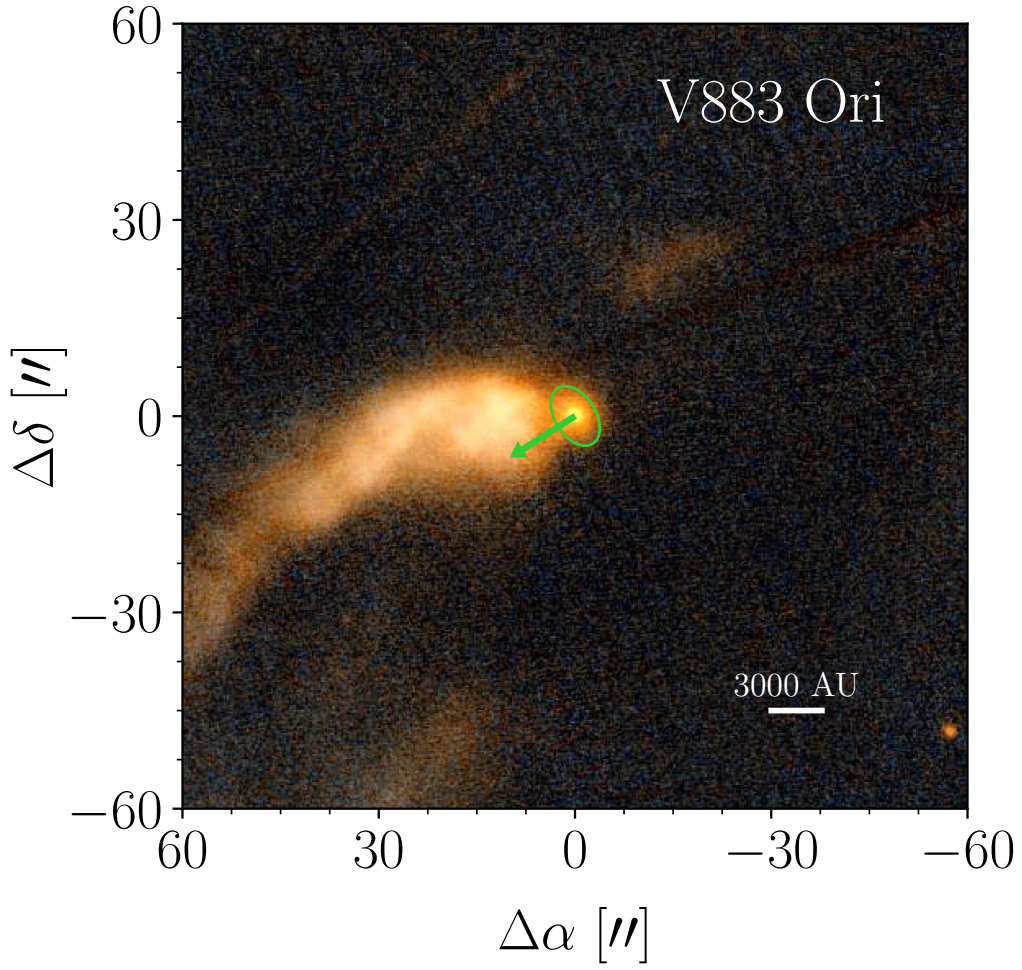

Figure 6.1: V883 Ori as seen in the Pan-STARRS $g-z$ color image. The green ellipse shows the projected shape of the disk on the sky (scaled ×12 for visibility), assuming an inclination of 38.3° and a position angle of 32.4° (Cieza, Ruíz-Rodríguez, et al., 2018). The green arrow shows the axis of rotation of the disk (Lee, Lee, et al., 2019). The position angle and inclination of the disk indicate it is the primary illumination source for the bright nebula that extends ∼ 70″ to the southeast. The nebula is known as IC 430.

Selected orders from the spectra are shown in Figure 6.2. Absorption features that trace the disk and those which trace the outflow in V883 Ori are marked in black and blue, respectively. The CaII IRT and OI have blue-shifted absorption that is variable between 2003 and 2011, indicating they are outflow features tracing a wind in the inner disk (Calvet, Hartmann, et al., 1993).

NIR (Keck/NIRSPEC)

We obtained a high resolution NIR spectrum of V883 Ori from $1 - 2.5$ μm on 31 Oct 2023 using the Keck Observatory's Near InfraRed SPECtrograph (NIRSPEC, McLean et al., 1998; Martin et al., 2018) using the NIRSPEC-1, NIRSPEC-3, NIRSPEC-5, and Kband-new filters to span the entire wavelength range. The exposure times for each band were 1200s, 480s, 360s, and 40s, respectively, to achieve a minimal signal-to-noise ratio (SNR) per pixel of 50 in each band. The slit PA was set to 0° to avoid the large nebula to the southeast.

The spectra were extracted and reduced using the NIRSPEC pipeline (Carvalho, Doppmann, et al., 2024) in the data reduction software package PypeIt (Prochaska et al., 2020). The telluric correction was performed using a high SNR spectrum of the A0V standard star HIP 102074, by first fitting an A0V template spectrum to remove the stellar hydrogen absorption, then continuum normalizing the remaining telluric spectrum to 1.0 (again using the asymmetric least-squares detrending code). We then divide the observed V883 Ori spectra by the normalized telluric spectrum. A description of the general procedure is given in Carvalho, Doppmann, et al. (2024). Select orders from the spectrum are shown in Figure 6.3

Spectrophotometry

NUV/Visible (Keck/LRIS)

We obtained a visible range flux-calibrated spectrum of V883 Ori on 3 February 2025 with the Low Resolution Imaging Spectrometer (LRIS, Oke et al., 1995; McCarthy et al., 1998; Rockosi et al., 2010). The spectrum spans 0.4 μm to 1.0 μm at $R = 400$ and has SNR increasing with wavelength from 20 in the blue to 200 in the red. The PA of the slit was set to $-45°$ to avoid the optical nebula to the southeast. The spectrum was extracted and flux-calibrated using the LRIS pipeline in `PypeIt` (Prochaska et al., 2020).

We scale the final spectrum by a factor of 4.0 to match the flux level of the IRTF/SpeX spectrum at 1.0 μm.

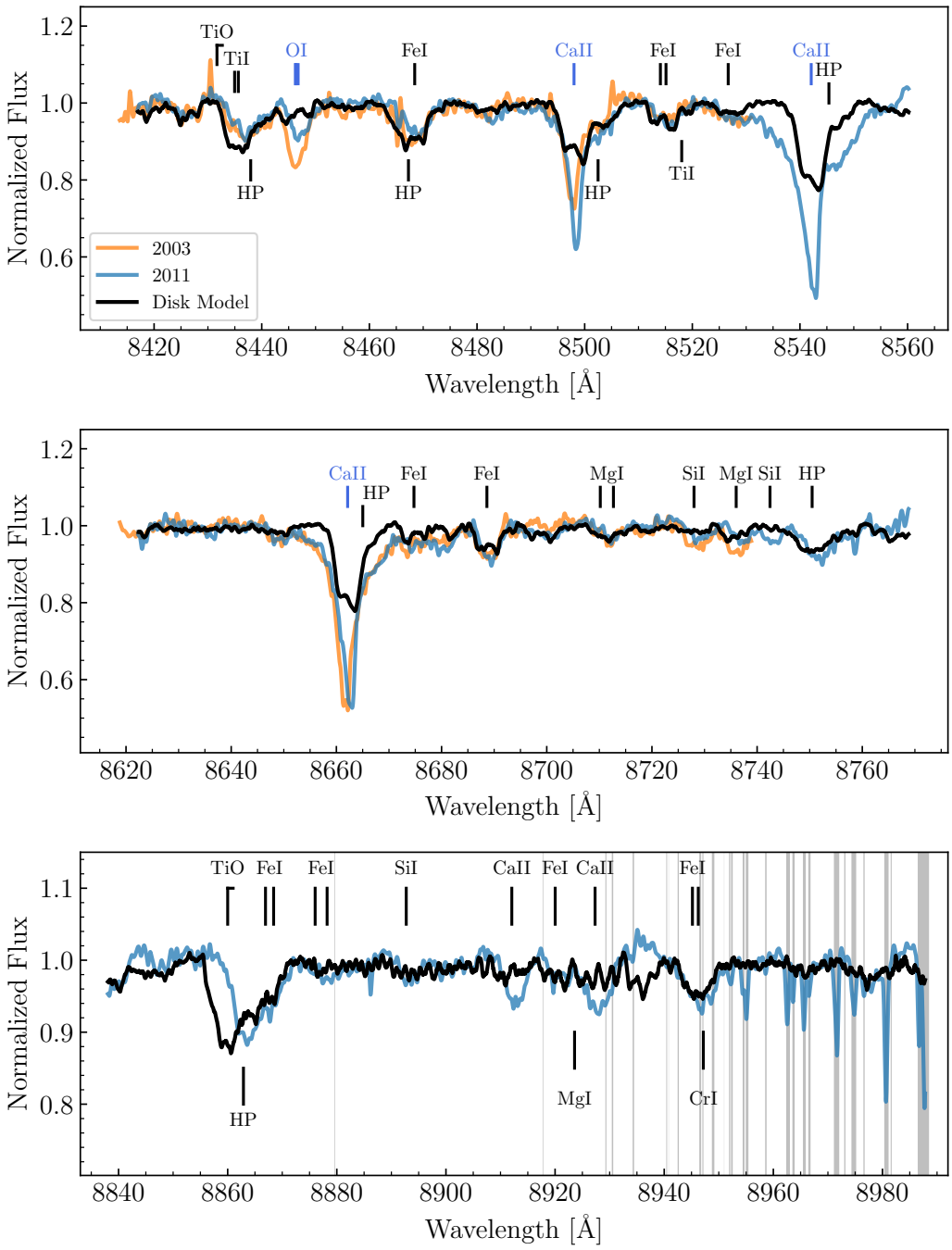

Figure 6.2: The reddest several orders of the 2003 (orange) and 2011 (blue) Keck/HIRES spectra, where the signal-to-noise is suitable, plotted along with the disk model described in Section 6.3 (black). The model reproduces the weak absorption features well, but misses portions of several HI and CaII profiles that arise in winds. Strong telluric features are present at the reddest wavelengths shown and are marked by grey vertical lines.

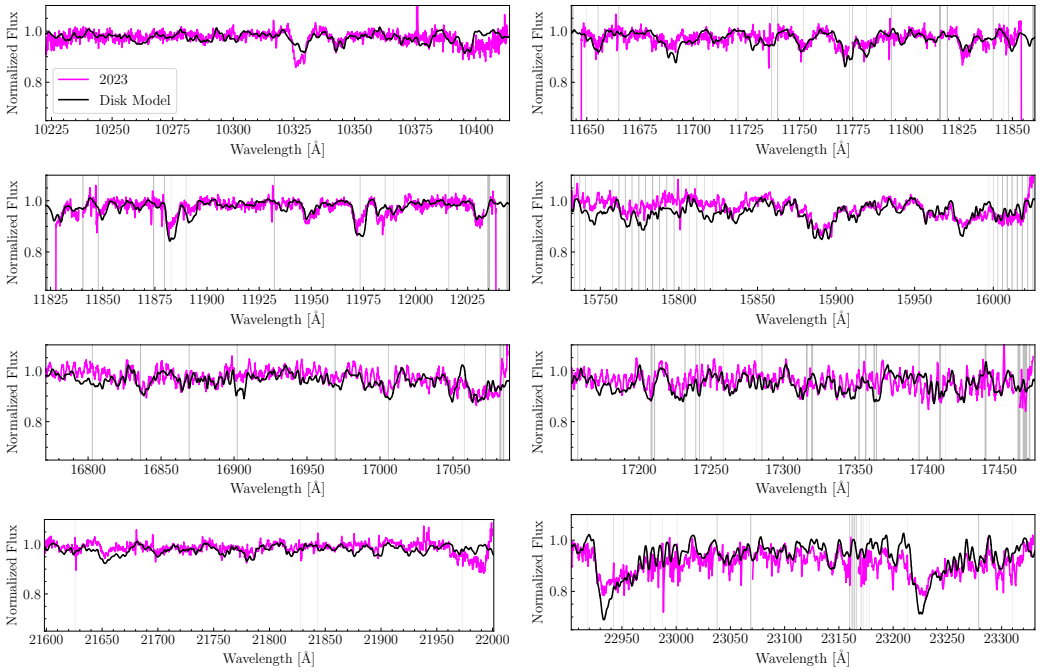

Figure 6.3: Select orders from the 2023 Keck/NIRSPEC spectrum (magenta) compared with the disk model described in Section 6.3 (black). The model matches the majority of the absorption features accurately from 1.0 μ to 2.3 μm. Grey vertical bands mark regions of strong telluric absorption.

NIR (Palomar/TripleSpec and IRTF/SpeX)

We use the 30 October 2015 NASA Infrared Telescope Facility (IRTF) SpeX SXD/LXD spectrum published in Connelley and Reipurth (2018). The spectrum spans 0.7 – 4.2 μm at high signal-to-noise and is shown in Figure 6.5.

Photometry

We obtained multiband photometry of V883 Ori from several archival datasets. The target appears reliably in the Two-Micron All Sky Survey (2MASS, Cutri, Skrutskie, et al., 2003), Wide-field Infrared Survey Explorer (WISE/NEOWISE, Wright et al., 2010; Mainzer et al., 2011; Cutri, Mainzer, et al., 2015), and Zwicky Transient Facility (ZTF, Bellm et al., 2019) point source catalogs. We also perform new aperture photometry on the source using the Pan-STARRS *grizy* stacked images (Chambers et al., 2019; Magnier et al., 2020; Waters et al., 2020; Flewelling et al., 2020) to obtain consistent and reliable measurements of the optical flux for comparison with our Keck/LRIS spectrum. The aperture photometry procedure is described in Appendix 6.7.

To contextualize the duration of the outburst and the current state of V883 Ori relative to past observations, we also assemble 20 years of ground-based photometry in V, R, and I bands. The data reduction and aperture photometry procedure for these are described in Appendix 6.8 and the lightcurve we produce is discussed in Section 6.4. While the source flux is reported in the ZTF stacked image catalog, the individual detections are unreliable, so we preform aperture photometry on individual ZTF image frames to include in our lightcurve. The ZTF photometry is also described in Appendix 6.8.

The NEOWISE data are binned by visit and each point in the lightcurve is the 3 sigma-clipped median flux for the observations in the visit, with the uncertainty given by the 3 sigma-clipped standard deviation of the measurements. The source is extremely bright in the $W1$ and $W2$ bands, so we apply the necessary saturation corrections[2].

6.3 Disk Model Fits

The visible/NIR spectrum of V883 Ori is shown in Figure 6.5. In this section, we describe an accretion disk model fit and demonstrate that a standard FU Ori disk model cannot fit the spectrum blueward of 1 μm. The emission in the NUV/visible is consistent with a less extincted disk, indicating it is dominated by scattered light with less line-of-sight extinction, while the NIR likely probes a line of sight directly to the inner disk. A cartoon illustrating the scenario is shown in Figure 6.4.

We fit the entire $0.4 - 2.5$ μm spectrum simultaneously with a thin, viscously heated accretion disk and a physically motivated scattering law. We describe the models we adopt and fitting procedure in detail below.

The Viscous Disk

The disk model we fit is a thin, viscously heated accretion disk following the formulation of Shakura and Sunyaev (1973) modified to be isothermal interior to $r = \frac{49}{36} R_{\rm inner}$ (Kenyon, Hartmann, and Hewett, 1988). The details of the model are given in Carvalho, Hillenbrand, and Seebeck (2023) and Carvalho, Hillenbrand, Seebeck, and Covey (2024).

For the distance to the source, we assume V883 Ori is a member of the Orion Nebula Cluster (ONC, Roychowdhury and Hillenbrand, 2024b) and adopt the Gaia-derived distance to the ONC of 388 pc (Kounkel et al., 2018). The parameters we vary in this

[2] `https://wise2.ipac.caltech.edu/docs/release/neowise/expsup/sec2_1civa.html`

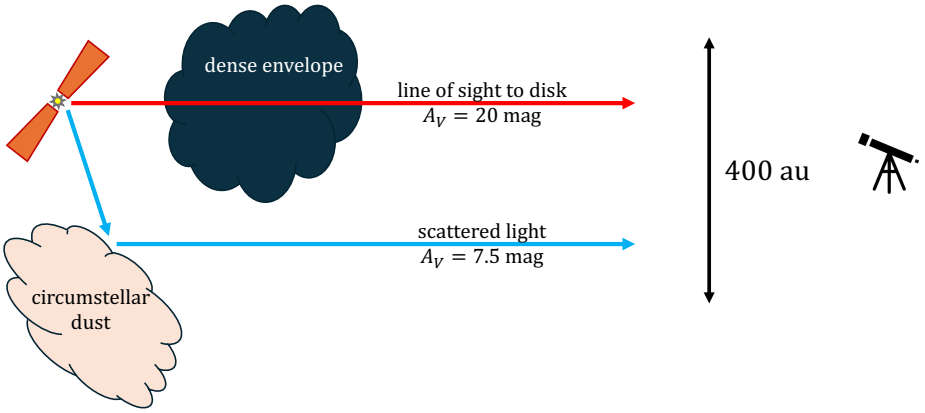

Figure 6.4: A diagram of the system showing the geometry of the scattering surfaces and obscuring screen relative to the disk and the observer. The illustrated disk (in orange) angle is set to the 38.3° disk inclination. The vertical black arrow marks the 400 au projected spatial width of the LRIS trace on-sky, while the size of the disk illustration is the 100 au dust disk radius.

part of the model are $\dot{M}$, M_*, $R_{\rm inner}$, the inclination (i), and the line of site extinction (A_V, using Fitzpatrick, 1999). V883 Ori has an extinction-corrected $J - K = 1.25$ magnitudes, so following the guidance of (Carvalho and Hillenbrand, 2024) we adopt $R_{\rm outer} = 300\ R_\odot$. Above this value, the $R_{\rm outer}$ parameter does not affect the NIR continuum in the model (see Figure 6 in Carvalho, Hillenbrand, Hambsch, et al., 2023). The choice of $R_{\rm outer}$ is also justified by the good match to the $3 - 4.2\ \mu$m region of the SpeX LXD spectrum (see Figure 6.5).

Attempting to fit an accretion-disk-only model to the entire SED is impossible due to the drastically different slopes of the visible and NIR. As can be seen in the bottom panel of Figure 6.5 and in Figure 3 of Connelley and Reipurth (2018), de-reddening the spectrum to the best-fit extinction value based on the NIR ($\sim$ 20 mag) results in an extremely steep de-reddened visible range spectrum that is 10^6 times brighter at 0.4μm than at 1 μm and gives a nonphysical $L = 8 \times 10^7\ L_\odot$. Fitting an accretion disk model to only the $1.0 - 2.5\ \mu$m region of the spectrum is possible and yields best-fit parameters that are consistent with those we report for our fiducial model but are not as well-constrained.

Scattered Light Model

For a source with the right inclination relative to the observer or surrounding envelope material and significant line-of-sight extinction to the inner disk, the scattered light from the disk becomes non-negligible. In the case of the large $A_V \sim 20$ mag estimated from NIR observations of V883 Ori (Strom and Strom, 1993; Connelley and Reipurth, 2018), the direct line-of-sight visible range flux is suppressed and must be dominated by scattering. Modeling the scattering is necessary to match the observed SED, which cannot be fit by a disk model alone (see Figure 6.5).

We use a simple 2 component scattered light model, assuming that the two physical phenomena dominating the scattering at these wavelengths is Rayleigh scattering and Mie scattering. We model the scattering of emission from the inner disk, $F_{\rm disk}(\lambda)$ into our line of sight as a sum of the two scattering laws,

$$F_{\rm scatt}(\lambda) = F_{\rm disk}(\lambda) \times \left[f_{\rm R} \left(\frac{9000}{\lambda} \right)^4 + f_{\rm Mie} \right]. \tag{6.1}$$

The fraction of Rayleigh scattering is given by f_R, while the fraction of light subject to Mie scattering is given by $f_{\rm Mie}$. The normalization of the Rayleigh component at 9000 Å is chosen as the wavelength where the scattering component begins to dominate, but is formally degenerate with the value of f_R. The two factors f_R and $f_{\rm Mie}$ treat only the total emergent scattered light flux along the line of sight of the observer. The model does not consider the effect of scattering phase function, since the scattered light is unresolved in our observations. For the sub-micron sized grains dominating the scattering, the Mie scattering opacity between $\lambda = 0.3\mu$m and $\lambda = 1.0\mu$m of most dust compositions is approximately constant (Ysard et al., 2018). After computing the scattered light spectrum, we redden it to A_V(scatt), which is distinct from the A_V to the viscous accretion disk.

Fitting Process and Results

The fit was performed using a log-likelihood minimizing Markov-Chain Monte Carlo (MCMC) technique with the nested sampling code `dynesty` (Speagle, 2020). We adopt uniform priors for 6 of the 8 total model parameters. The two priors we impose on the disk model MCMC fits are that we require that i be drawn from a normal distribution with mean $\mu = 38.3°$ and standard deviation $\sigma = 3°$ and that the maximum Keplerian broadening in the disk, $v_{\rm max} = \sqrt{GM_*/R_{\rm inner}} \sin i$ be drawn from a normal distribution with $\mu = 130$ km s^{-1} and $\sigma = 5$ km s^{-1}. The prior on i comes from the inclination of the outer disk, measured from exquisite millimeter

Table 6.1: Best-fit values for the `dynesty` MCMC disk + scattering model.

Parameter	Symbol	Value	Units
Disk Model			
Accretion Rate	$\log(\dot{M})$	$-3.89^{+0.22}_{-0.14}$	dex $M_\odot$ yr^{-1}
Stellar Mass	M_*	$1.34^{+0.37}_{-0.46}$	$M_\odot$
Truncation Radius	$R_{\rm inner}$	$5.86^{+0.94}_{-1.83}$	$R_\odot$
Inclination	i	$38.15^{+3.02}_{-2.93}$	deg
Extinction	A_V	$20.78^{+0.77}_{-0.67}$	mag
Scattered Light Model			
Rayleigh Factor	$\log f_R$	$-3.32^{+0.44}_{-0.45}$	...
Mie Factor	$\log f_{\rm Mie}$	$-2.31^{+0.07}_{-0.20}$	...
Extinction	A_V(scatt)	$7.84^{+0.96}_{-0.57}$	mag
Inner Disk Properties			
Accretion Luminosity	$L_{\rm acc}$	458^{+141}_{-80}	$L_\odot$
Max Disk Temperature	$T_{\rm max}$	7046^{+1405}_{-744}	K

imaging of the source (Cieza, Casassus, et al., 2016). The $v_{\rm max}$ constraint is based on our measurements of $v_{\rm max}$ in the disk using the NIRSPEC spectrum and we describe the procedure in more detail in Carvalho (2025, in prep).

Despite the large number of parameters, they are all extremely well-constrained and the fit to the 0.4 – 2.5 μm spectrum is excellent, as can be seen in Figure 6.5. The best-fit parameters of the model are summarized in Table 6.1. The posterior distribution for each parameter is shown in a `corner` plot in Appendix 6.9. Our best-fit parameters for the inner disk are $\dot{M} = 10^{-3.89}$ $M_\odot$ yr^{-1}, $M_* = 1.34$ $M_\odot$, $R_{\rm inner} = 5.86$ $R_\odot$, which produce $L_{\rm acc} = 458$ $L_\odot$ and $T_{\rm max} = 7046$ $L_\odot$. The best-fit inclination is $i = 38.15°$ and the disk is seen through $A_V = 20.78$ mag. The large extinction to the inner disk is confirmed by the strong 3 μm ice absorption (Connelley and Reipurth, 2018), which can be seen in Figure 6.5. The scattered light component is seen through $A_V = 7.84$ mag, indicating it follows a less extincted line-of-sight than the inner disk.

We also used the the posterior distributions of the disk model parameters to construct the distributions of $L_{\rm acc}$ and $T_{\rm max}$ values of the system. The distributions are shown in Figure 6.6. The median values of $L_{\rm acc} = 458$ $L_\odot$ and $T_{\rm max} = 7045$ K are reported in Table 6.1 along with the upper and lower uncertainties.

Using Keck/LRIS and IRTF/SpeX, we are able to observe the inner disk of V883 Ori and constrain its accretion luminosity and maximum disk temperature, along with the physical parameters of the system. The non-negligible contribution from

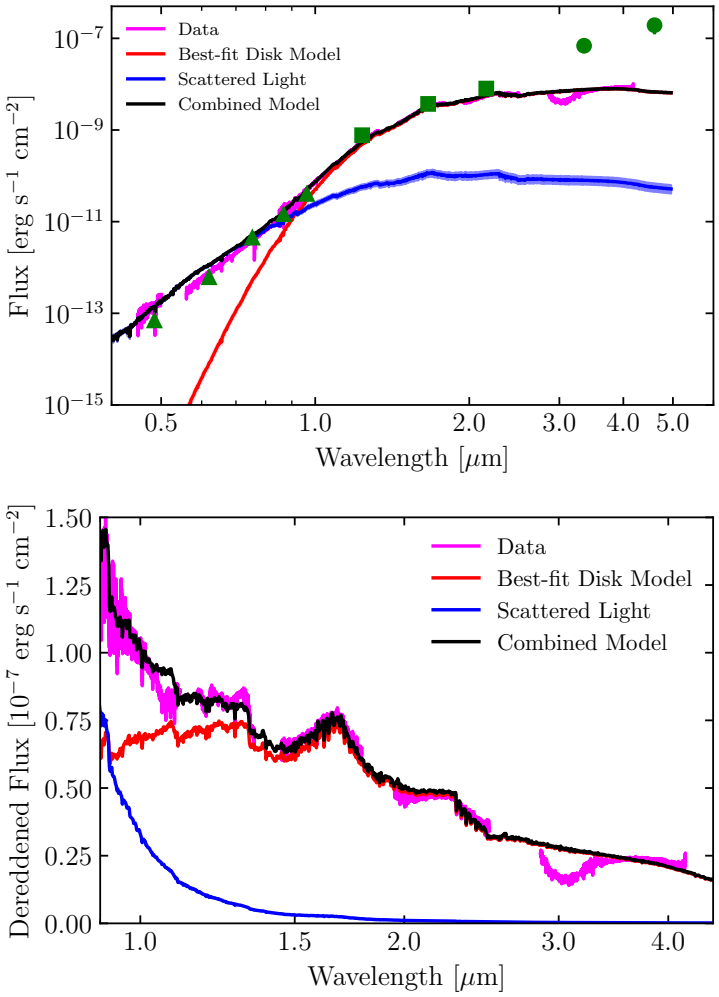

Figure 6.5: The model V883 Ori spectra compared with visible and NIR spectra. **Upper panel:** The complete disk + scattering model (black) compared with the LRIS and SpeX spectra (magenta). The disk component is shown in red and the scattered light component shown in blue. Historical photometry of the source is shown as green symbols: triangles for PanSTARRS, squares for 2MASS, and circles for WISE. The WISE photometry includes significant thermal emission from the dust surrounding V883 Ori, while the SpeX LXD spectrum is dominated by emission from only the inner disk. **Lower panel:** The dereddened SpeX spectrum and accompanying dereddened best-fit models, to better highlight the NIR fit. The A_V used for dereddening the spectrum is 20.78 mag. As established from the joint model, this is much greater than A_V (scatt), causing the rapid upward slope toward the visible.

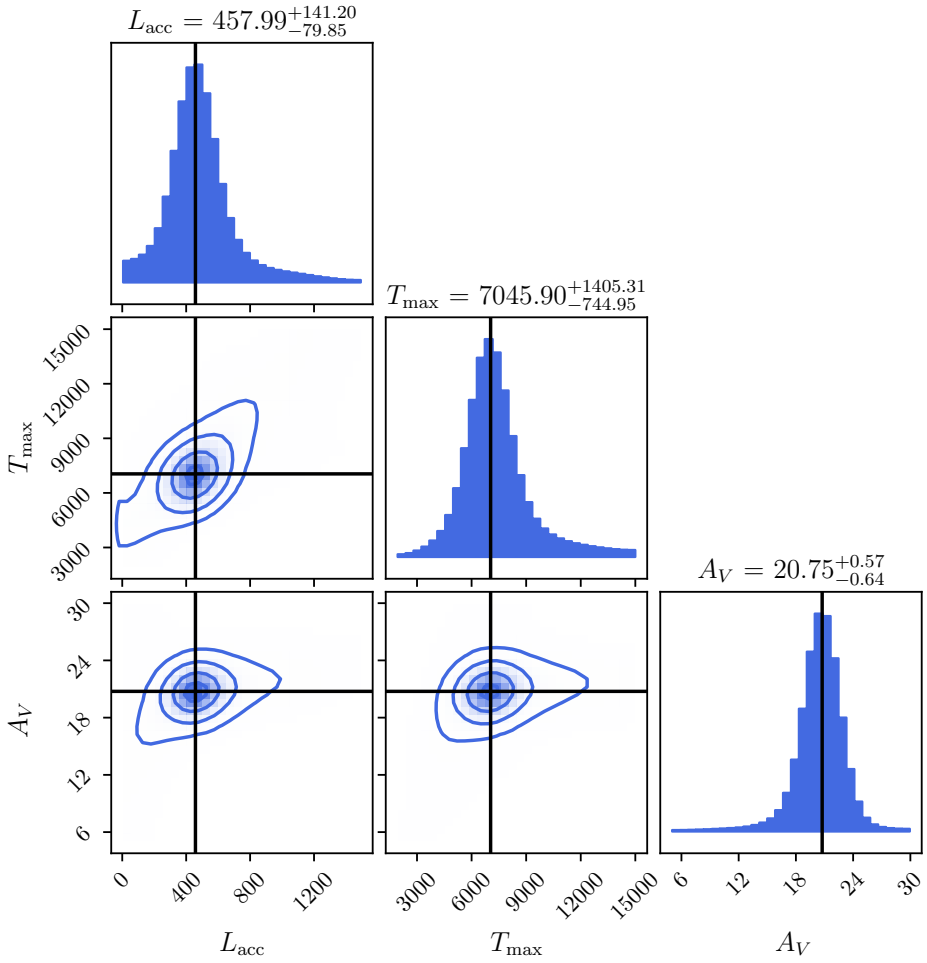

Figure 6.6: Posterior distributions for $L_{\rm acc}$ and $T_{\rm max}$ computed from the distributions of M_*, $\dot{M}$, and $R_{\rm inner}$. The posterior distribution for A_V for the disk component is shown for reference, as it is often covariant with $T_{\rm max}$. The lack of strong covariance our posteriors indicates we have successfully broken the degeneracy typically present in SED fitting of accretion disk models.

scattering in the visible range required modeling both the inner disk and the scattered light from the inner disk simultaneously. The combined model described in Table 6.1 is an excellent match to the spectrum of the system from $0.4 - 4.2$ μm.

The best fit stellar mass and disk inclination are both in good agreement with the $M_* = 1.3$ $M_\odot$ and $i = 38.3°$ derived from millimeter range observations of the system (Cieza, Casassus, et al., 2016). The $R_{\rm inner} = 5.86$ $R_\odot$ for the system is much larger than the $2.7 - 3.5$ $R_\odot$ radii expected for a 0.5-1 Myr old system (Baraffe et al., 2015), but FUOrs are likely to have inflated radii due to their rapid mass accretion (Hartmann and Kenyon, 1996). The ability of rapid mass accretion to inflate the radius of a star is seen in models of main sequence accretors in symbiotic binary systems (Lau et al., 2024).

6.4 Discussion

Using Keck/LRIS and IRTF/SpeX, we are able to observe the inner disk of V883 Ori and constrain its accretion luminosity and maximum disk temperature, along with the physical parameters of the system. The non-negligible contribution from scattering in the visible range required modeling both the inner disk and the scattered light from the inner disk simultaneously. The combined model described in Table 6.1 is an excellent match to the spectrum of the system from $0.4 - 4.2$ μm.

The best fit stellar mass and disk inclination are both in good agreement with the $M_* = 1.3$ $M_\odot$ and $i = 38.3°$ derived from millimeter range observations of the system (Cieza, Casassus, et al., 2016). The $R_{\rm inner} = 5.86$ $R_\odot$ for the system is much larger than the $2.7 - 3.5$ $R_\odot$ radii expected for a 0.5-1 Myr old system (Baraffe et al., 2015), but FUOrs are likely to have inflated radii due to their rapid mass accretion (Hartmann and Kenyon, 1996). The ability of rapid mass accretion to inflate the radius of a star is seen in models of main sequence accretors in symbiotic binary systems (Lau et al., 2024).

The Scattered Light Component

The visible range spectroscopy and spectrophotometry of V883 Ori are both many orders of magnitude brighter than is expected for a FUOr inner disk observed through $A_V = 20$ mag. The disk model shown in Figure 6.5 indicates that the source should barely be detectable blueward of 0.6 μm. Nevertheless, we see faint emission from V883 Ori across the whole visible range in the Pan-STARRS photometry and the Keck/LRIS spectrum, indicating a different emission component in the system must be dominating the visible spectrum.

The optical spectrum is also consistent with that of a FUOr, as was first reported in Allen et al. (1975). We affirm this with our LRIS spectrum. It is therefore more likely that the blue excess is due to the dust surrounding V883 Ori scattering the optical spectrum of the inner disk into our line of sight. This requires scattering only 0.5% of the radiation, which is typical of the fraction of starlight scattered by typical circumstellar disks (e.g., Wolff et al., 2017).

The source has been observed at high (~ 10 μJy) sensitivity with ALMA at angular resolutions spanning $0.04'' - 1.0''$ and fields of view from $0.3' - 1.0'$, covering both the point source and the extended nebula (Cieza, Ruíz-Rodríguez, et al., 2018; Lee, Lee, et al., 2019; Tobin et al., 2023). Matching the visible range excess emission with a stellar companion would require a luminosity of $L > 2.25$ $L_\odot$ assuming $A_V \sim 7.8$ and a temperature of $\sim 10,000$ K. This would imply a radius of 0.5 $R_\odot$, which is unphysically small for such a hot star. Furthermore, such a companion would be expected to disrupt the V883 Ori outer disk, which would be detectable in the millimeter dust emission and no such disruption to the disk has been reported.

Typically, in cases where the central source is highly extincted such that the visible/NIR are largely seen as scattered light, the extinction is due to the flared disk itself. These systems are edge-on, such that the disk obscures a direct line of sight to the star and the light from the star is mostly seen scattered off the side of the disk opposite the observer (e.g., HH 30 and IRAS04302+2247, Burrows et al., 1996; Padgett et al., 1999). The outer disk inclination of V883 Ori is too face-on for this scenario.

We propose instead that the visible light is scattered off the outer disk and nearby circumstellar material. The direct line of the sight to the inner disk is obscured by a cloud of dense envelope material, which produces the 20 magnitudes of optical extinction to the inner disk spectrum. The less extincted visible light is scattered off material near the disk but not obscured by this cloud, so we see it through a much lower A_V, as shown in Figure 6.4.

The full-width at half maximum (FWHM) of the optical extraction window used to extract the LRIS spectrum is $1.0''$, which translates to a physical size of 388 au at the source location. The dust continuum emission in the disk only extends to $0.25''$ or a radius of 100 au (Cieza, Casassus, et al., 2016). Large dust structures surrounding face-on FUOrs beyond their disks are seen in scattered light at flux ratios of $\sim 1\%$ of the inner disk luminosity (e.g., V960 Mon and FU Ori, Weber, Pérez, Zurlo, et al., 2023b; Zurlo et al., 2024a). In FU Ori, the light-scattering circumstellar

envelope extends more than 200 au from the source, despite the extremely compact disk radius of $\sim$ 11 au (Pérez et al., 2020).

The ^{12}CO and ^{13}CO millimeter emission from V883 Ori reveals a biconical outflow extending 5″ from the disk (Ruíz-Rodríguez et al., 2017). The same observations also show that within 0.5″ of the disk, the ^{12}CO emission suffers significant absorption. The absorption is attributed to a large dust column along the line of sight to the inner disk, which would be consistent with the visible/NIR observations presented here. It is possible that the large outflow in the system traces a nebula near the disk that is contributing to the scattered light component, as is seen in FU Ori (Hales et al., 2024).

The Enormous Mass Consumed by V883 Ori

The luminosity of V883 Ori has remained essentially constant for at least the past 60 years of observation, and plausibly longer, implied by Figure 6.7. This indicates that the mass accretion rate has remained at an extremely high $10^{-3.9}$ $M_\odot$ yr^{-1} that entire time. Over 60 years, the source has accreted a minimum of 8 $M_{\rm Jup}$ ($\dot{M} \times \Delta t$). In their simulation of an FU Ori outburst, Zhu, Jiang, et al. (2020) found that the mechanical energy removal by winds during the burst can be highly efficient, resulting in a 30% lower $L_{\rm acc}$ than the thin disk model predicts. Thus, for a given $L_{\rm acc}$, the actual $\dot{M}$ in the disk can be 3× greater. If this is the case in V883 Ori, the total accreted mass in 60 years could be as much as 24 $M_{\rm Jup}$.

The origin of the outburst is estimated to be around 1888, when the nebula was first reported by (Pickering, 1890). Strom and Strom (1993) argue that given the faint $B \sim 24$ mag arcsec^{-2} surface brightness of the nebula in 1975 and the fact that plates in 1888 were preferentially sensitive to blue light and much less sensitive generally, the nebula must have been much brighter. If the star is illuminating the nebula sufficiently that the nebula would be brightened by the outburst, then its accretion rate would have been even greater in the 1880's. If we conservatively assume that the accretion rate was at least the same at outburst as it is today, then the star has accreted at least 18 $M_{\rm Jup}$ (0.017 $M_\odot$). This is comparable to lower estimates for the total current disk mass (e.g., 0.02 $M_\odot$, Sheehan et al., 2022), although the disk mass has also been estimated to be as high as 0.54 $M_\odot$ (in radiative transfer modeling of dust continuum emission and adopting a dust-to-gas ratio of 0.01, Cieza, Ruíz-Rodríguez, et al., 2018).

Even if the disk mass is underestimated, the total mass accreted by V883 Ori during

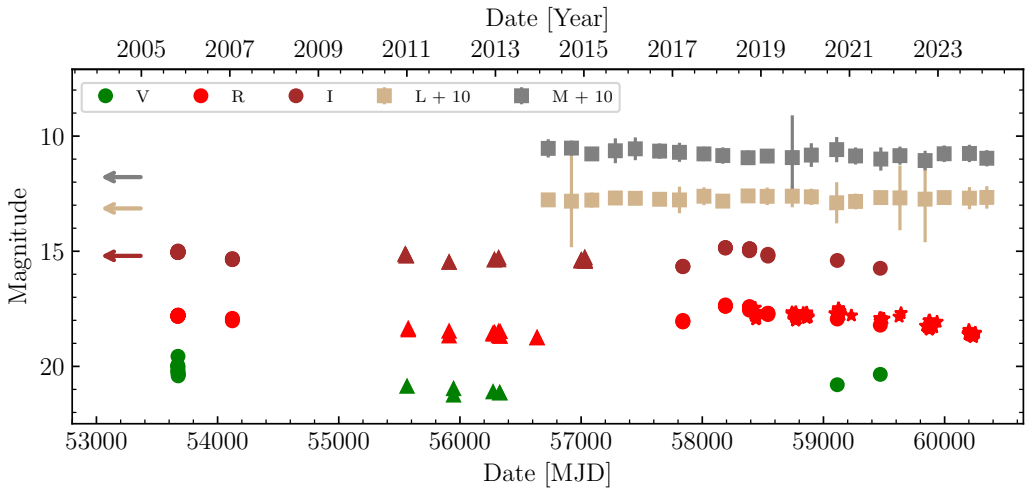

Figure 6.7: A lightcurve of V883 Ori, spanning the past 20 years of observations. The arrows to the left of the plot mark the brightness of the source at 0.8, 3.5, and 4.8 μm, taken in 1963, 1975, and 1975, respectively (Allen et al., 1975). The source has remained at essentially the same brightness for at least the past 60 years. The triangles mark points from Pan-STARRS, while $*$ symbols mark points from ZTF. The tan and grey squares mark NEOWISE $W1$ and $W2$ points, respectively. The symbols on the plot are larger than the photometric uncertainties for all points except NEOWISE.

this outburst may be a large fraction of the mass in the disk. FU Ori is a similar case. The system has been in outburst since 1937 (Wachmann, 1954) and has only faded by $\sim$ 1 mag since the burst. Today, the accretion rate is reported to be $10^{-4.49}$ $M\odot$ yr^{-1} (Carvalho, Hillenbrand, France, et al., 2024). Assuming that the accretion rate has been constant in the interesting of obtaining a conservative estimate of mass accreted, the total is 0.003 $M_{\odot}$, of almost half of the total current $M_{\rm disk} = 0.007 M_{\odot}$ (using the dust disk mass from Pérez et al., 2020, and assuming a dust-to-gas ratio of 0.01).

Irradiation Heating of the Outer Disk

As one of the closest FUOrs to the Sun, V883 Ori has been the target of several millimeter-range observations to study the molecular emission from the spatially-resolved outer disk. Interpreting the observed spectra, however, is challenging because it requires careful accounting for all potential heating sources in the disk and the disk environment.

One critical heating source in FUOr disks is the irradiation from the self-luminous inner disk. The extremely high accretion luminosity in the inner disk dominates the

UV to NIR flux. As we demonstrate below, this accretion luminosity also dominates the irradiation of the outer disk, whereas the central star's luminosity is irrelevant, and its irradiative effects inconsequential in the outer disk.

To investigate the impact of omitting inner disk irradiation from a heating budget of the outer disk, we construct an analytic heating model based on that of Fukue (2013). This model is distinct from that which we used to fit the visible/NIR SED of the source in Section 6.3 and is meant to illustrate the different contributions of accretion and irradiation to regions of the disk probed by millimeter-range observations. We compute the irradiation heating from both the star and inner disk as

$$Q_{\rm irr,*} = (1 - A)\left[\frac{R_* L_*}{3\pi^2 r^3} + \frac{L_*}{4\pi^2 r^2}\left(\frac{dH}{dr} - \frac{H}{r}\right)\right], \tag{6.2}$$

and

$$Q_{\rm irr,disk} = (1 - A)\left[\frac{L_{\rm acc}}{4\pi^2 r^2}\left(\frac{dH}{dr} - \frac{H}{r}\right)\right]. \tag{6.3}$$

In Equation 6.2, the first term $\frac{R_* L_*}{3\pi^2 r^3}$ accounts for the physical extent of the star, which slightly impacts the heating at $r < 10$ au. At larger radii, the star can be treated like a point source and the radiation angle of incidence on the disk, accounted for by the second term $\frac{L_*}{4\pi^2 r^2}\left(\frac{dH}{dr} - \frac{H}{r}\right)$, dominates. For the irradiation from the inner disk in Equation 6.3, we drop the first term since the disk is flat and the angle of incidence to small radii becomes extremely small. We assume that the albedo of the outer disk, A, is 0 for simplicity[3]. We adopt a stellar radius of $R_* = 2.7\ R_\odot$ and $L_* = 2.95\ L_\odot$, which correspond to a $M_* = 1.3\ M_\odot$ star at an age of 1 Myr (Baraffe et al., 2015). We assume that the disk scale height, $H(r) = H_0\,(r/r_0)^\gamma$, where $H_0 = 0.05$ au at $r_0 = 1$ au and the flare index $\gamma = 1.1$. For the disk $L_{\rm acc}$ we use our best-fit value of 458 $L_\odot$.

We also compare this to the viscous heating due to the high accretion rate in the system, which we model following the Shakura and Sunyaev (1973) model,

$$Q_{\rm visc} = \frac{3GM_*\dot{M}}{8\pi r^3}. \tag{6.4}$$

The three heating models are shown in Figure 6.8. While the viscous heating is dominant in the inner 2 au of the disk, by $r = 4$ au the irradiation from the inner disk is greater and by $r = 25$ au, $Q_{\rm irr,disk} = 10\ Q_{\rm visc}$.

[3]Our scattering model indicates it is not 0, but given the very small scattering factors, it is close enough to not meaningfully affect the calculation here.

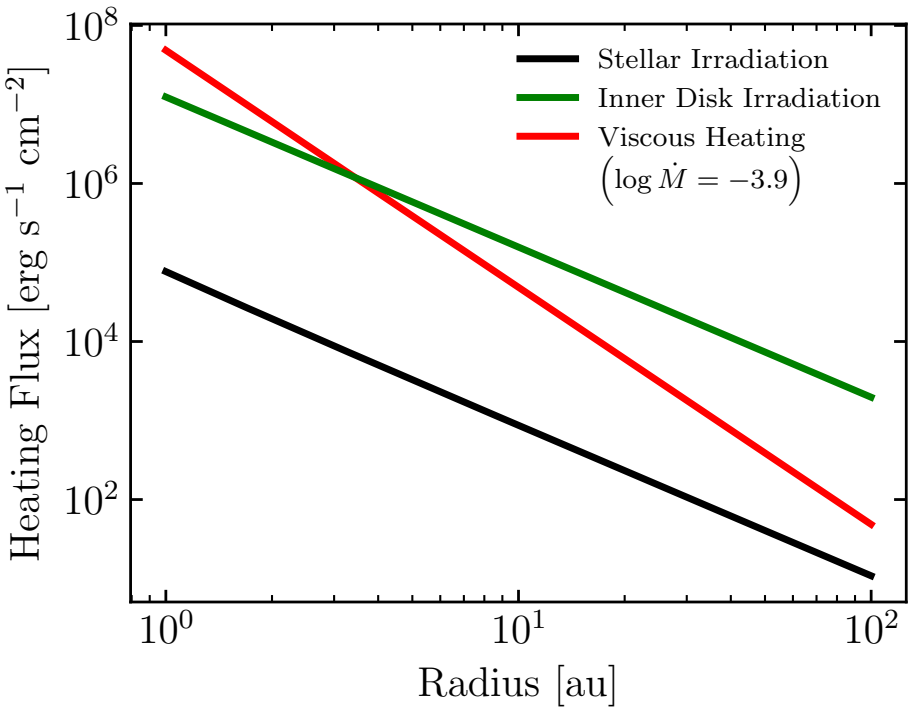

Figure 6.8: The sources of heating in the V883 Ori disk. The heating from the central star is negligible since the disk dominates the luminosity of the system. The midplane viscous heating, while dominant in the inner 3 au of the disk, falls below the heating due to irradiation from the accretion luminosity of the disk.

We note that the calculations above treat the inner disk as a luminous point source. A more detailed analysis that incorporates the radially extended nature of the inner disk and the true angle of incidence of the accretion flux on the flared outer disk is necessary to account for the correct outer disk dust temperature.

6.5 Conclusion

We use optical + NIR high and low resolution spectra to constrain a viscous accretion disk model for one of the brightest and longest-lived FU Ori outbursts, V883 Ori. We successfully model the spectrum from $0.4 - 4.2$ μm by assuming that the shorter wavelength component is due to scattered light from the inner disk observed at a lower line-of-sight extinction, A_V(scatt) = 7.84 mag, relative to the A_V = 20.78 mag along direct line-of-sight to the inner disk. The best-fit physical parameters of the disk model are $M_* = 1.34$ $M_\odot$, $\dot{M} = 10^{-3.89}$ $M_\odot$ yr^{-1}, $R_{\rm inner} = 5.86$ $R_\odot$, and $i = 38.15°$. The maximum temperature of the inner disk, given these parameters, is 7045 K and the accretion luminosity is 458 $L_\odot$.

We also provide a decades-long light curve of the source, demonstrating its consistent brightness in both the visible and NIR over the past 62 years of observations. The flat lightcurve indicates a relatively constant accretion rate, which can be integrated to show that the source has accreted at least 8 $M_{\rm Jup}$ since 1963 and has likely ejected ~ 1 $M_{\rm Jup}$ of material as outflows.

The inner disk maximum temperature and luminosity of the source should be considered when modeling both dust continuum emission and molecular emission. The tight constraints we provide for both will enable accurate modeling of the dust and gas temperature, and therefore more reliable estimates of the disk mass of V883 Ori. Given the large mass already accreted by the source, and competing theories for trigger mechanisms of FU Ori outbursts, an accurate measurement of the disk mass is critical to understanding the past and predicting the future evolution of this object.

6.6 Acknowledgements

The operation of the RC80 and Schmidt telescopes at Konkoly Observatory has been supported by the GINOP 2.3.2-15-2016-00033 and GINOP-2.3.2-15-2016-00003 grants of the National Research, Development and Innovation Office (NKFIH) funded by the European Union.

This work was also supported by the NKFIH NKKP grant ADVANCED 149943. Project no.149943 has been implemented with the support provided by the Ministry of Culture and Innovation of Hungary from the National Research, Development and Innovation Fund, financed under the NKKP ADVANCED funding scheme.

6.7 Appendix: Aperture Photometry on the Pan-STARRS Stacked Images

Due to the nebulosity in the vicinity of V883 Ori, the PSF photometry of the source in the Pan-STARRS point source catalog is unreliable for bands izy. In order to complete the photometric visible/NIR SED of V883 Ori, we downloaded $grizy$ $2' \times 2'$ cutouts from the image cutout service [4]. We then used the `photutils` package (Bradley et al., 2024) to extract the flux from the location of V883 Ori using a circular aperture with a $3''$ diameter. We estimate the background as the median pixel value in the image and subtract the total background counts within the aperture. We convert the total data number (DN) in our aperture to a magnitude using the formula in the Pan-STARRS stack images documentation[5]: $m_\lambda = -2.5 \log_{10}(DN) +$

[4] `https://ps1images.stsci.edu/cgi-bin/ps1cutouts`

[5] `https://outerspace.stsci.edu/display/PANSTARRS/PS1+Stack+images`

$25 + 2.5 \log_{10}(t_{\rm exp})$. The new photometry we find for V883 Ori (in AB magnitudes) is: $m_g = 21.27$, $m_r = 18.64$, $m_i = 16.27$, $m_z = 14.84$, $m_y = 13.62$. The conversions to Vega magnitudes, computed from the ratio of Vega zeropoints to AB zeropoints, are −0.095, 0.146, 0.37, 0.51, and 0.55, respectively.

6.8 Appendix: 20 Years of Ground-based Photometry of V883 Ori

The visible/NIR flux level (and therefore mass accretion rate) of V883 Ori has been remarkably constant over the past 60 years. In order to constrain the photometric evolution of the source in the last 20 years, we assembled V, R, and I band measurements from several ground-based facilities. The calibration, aperture extraction, and filter normalization of each data set is described in this Appendix. The aperture extraction generally follows a similar procedure as that described for the Pan-STARRS data, though our flux calibration step differs by observatory.

ZTF

The ZTF r band individual frames were obtained from the IPAC/IRSA ZTF Image Access tool[6]. We selected a 3 pixel aperture radius, which requires the smallest correction between aperture and PSF fitting photometry, according to the ZTF Explanatory Supplement. We again estimate the background as the median flux level in the image. We then extract the flux at the location of V883 Ori, apply the magnitude zero point of the image specified by the `MAGZP` header key, and add the aperture to PSF correction specified by the `APCOR3` header key.

To ensure the robustness of the extracted flux to aperture size choice, we also tested 4 and 5 pixel radii and found that the extracted fluxes are consistent with the 3 pixel values.

Konkoly Observatory, Instituto de Astrofisica de Canarias (IAC), and La Silla Observatory

Optical observations of V883 Ori were obtained at five different telescopes in Hungary, Spain, and Chile. Three telescopes were at Konkoly Observatory (Hungary): the 1 m RCC telescope equipped with a Princeton Instruments VersArray:1300b camera, pixel scale: 0″.31/pixel, field of view: 6.9′×6.4′ (V, R_C, I_C filters, data from 2005), the 90/60 cm Schmidt telescope equipped with an Apogee Alta U16 camera, pixel scale: 1″.03/pixel, field of view: 70′×70′ (R_C, I_C filters, data from 2017–2019), and the Astrosysteme ASA800 80 cm RC telescope equipped with an

[6] `https://irsa.ipac.caltech.edu/Missions/ztf.html`

FLI Microline camera, pixel scale: 0″55/pixel, field of view: 18′4×18′7 (V, r', i' filters, data from 2020–2022). The telescope we used at Teide Observatory (Canary Islands, Spain) was the Instituto de Astrofísica de Canarias 82 cm IAC80 telescope equipped with the CAMELOT E2V back illuminated chip, pixel scale: 0″304pixel, field of view: 10′4×10′4 (R, I filters, data from 2007). In Chile, we used the 60 cm Rapid Eye Mount (REM) telescope located at La Silla Observatory, equipped with the ROS2 multi-channel imaging camera, 0″58/pixel, field of view: 9′9×9′9 (g', r', i', z' filters, data from 2014–2015). At each observing night, 3-4 images were taken with each filter, with exposure times between 20–1080 s. The data was reduced following the usual steps for bias, dark, and flatfield correction.

For each image, we use an aperture with a 6 pixel radius, corresponding to an angular radius of 6″ on PSCH and $1-1.5''$ on RCC, RC80, and IAC80. The aperture size is chosen to minimize the chance of including emission from the nearby nebula while maximizing robustness to the highly variable seeing. We extract the flux at the location of V883 Ori and all Pan-STARRS catalog sources within 30' of V883 Ori. For PSCH, this accounts for half of the sources in the field of view, while for RCC, RC80, and IAC80, we use every Pan-STARRS source in the field. We take the background to the median flux level in the image.

We computed the magnitude of V883 Ori in each image relative to the Pan-STARRS catalogue objects in the field, using the g band values as reference for V band, r band as reference for r', R, and R_C, and i band as reference for i', I, and I_C. We took the 5-sigma-clipped median and standard deviations as our magnitude measurements and uncertainties on the measurements, respectively. The typical uncertainty on a measurement is $0.05-0.1$ mag. Many of the REM g' and r' images are not deep enough to detect V883 Ori, so they are omitted from the lightcurve.

To convert to a uniform set of V, R, and I band measurements in the Johnson filter system, we used the relative zero points between each filter and the Pan-STARRS filters, and then between the AB and Vega systems for each filter. The zero points were all obtained from the Spanish Virtual Observatory website[7].

6.9 Appendix: Posterior Distributions of the Disk + Scattered Light Model

Our MCMC `dynesty` models ran for 22,306 iterations. It reached a $d\log z$ of 0.01 and then stopping criterion of 1.0. The posterior distributions of each parameter are shown as a `corner` (Foreman-Mackey, 2016) plot in Figure 6.9.

[7] `https://svo2.cab.inta-csic.es/svo/theory/fps3/`

Table 6.2: The V, R, I, $W1$, and $W2$ band photometry of V883 Ori show in Figure 6.7. The full table is available in the online journal.

MJD	V	R	I	z	W1	W2	Facility
53671.0419	19.966	···	···	···	···	···	RCC
53671.0456	···	17.826	···	···	···	···	RCC
53671.0492	···	···	15.055	···	···	···	RCC
54121.9191	···	···	15.354	···	···	···	IAC80
54121.9330	···	···	15.364	···	···	···	IAC80
57839.7761	···	18.066	···	···	···	···	PSCH
57839.7784	···	···	15.651	···	···	···	PSCH
58429.3919	···	17.770	···	···	···	···	ZTF
58432.3703	···	17.823	···	···	···	···	ZTF
59114.1002	20.797	···	···	···	···	···	RC80
59114.1037	···	17.943	···	···	···	···	RC80
59114.1072	···	···	15.400	···	···	···	RC80
59265.0747	···	···	···	···	2.838	0.862	WISE
59473.4018	···	···	···	···	2.669	0.996	WISE

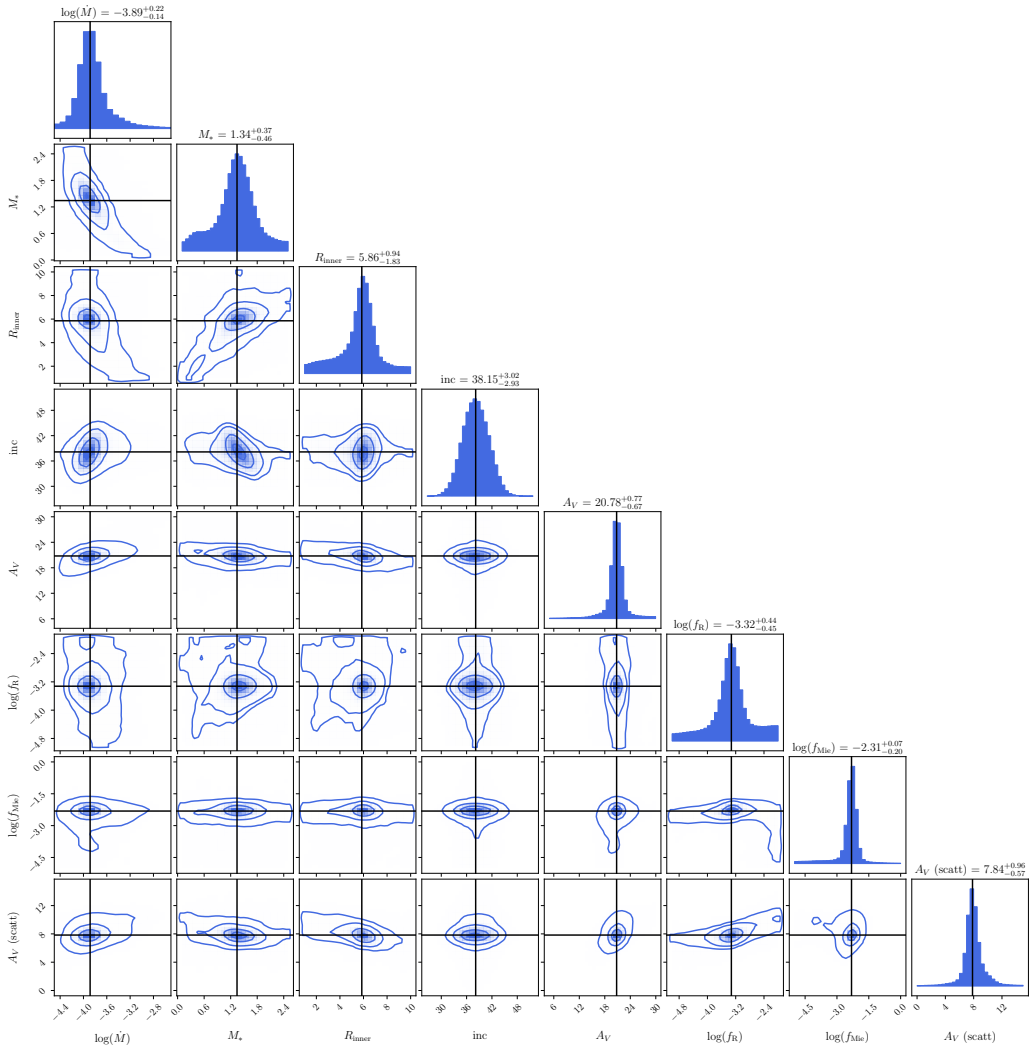

Figure 6.9: The posterior distributions of all 8 parameters of the disk + scattering models. They are all well-constrained and show minimal covariance.

Chapter 7

BOLOMETRIC CORRECTIONS FOR FU ORI OBJECT ACCRETION DISK LUMINOSITIES

Carvalho, Adolfo S. and Lynne A. Hillenbrand (Nov. 2024). "Bolometric Corrections for FU Ori Object Accretion Disk Luminosities." In: *ApJL* 976.1, L5, p. L5. DOI: 10.3847/2041-8213/ad8cdf. arXiv: 2410.22270 [astro-ph.SR].

Abstract: The accretion luminosity of an FU Ori disk is a fundamental system parameter, but a challenging one to estimate for all but the most well-studied systems. FU Ori objects are dynamically evolving accretion disks, especially close in time to the outburst epoch. They have a complex multi-temperature disk structure that results in distinctly shaped, broad SEDs. Detailed spectroscopic analysis is required for simultaneous constraint on relevant physical parameters such as the central stellar mass, inner disk radius, disk inclination, and disk accretion rate. However, outbursting systems that are deeply embedded and/or distant may be limited to only photometric measurement, and over only a narrow range of wavelengths. The bolometric corrections necessary to estimate accretion luminosities are not straightforward, and in particular can not be adopted from existing literature on isotropically radiating stars. We present bolometric corrections specific to astrophysical accretion disks for a variety of filters in ongoing and upcoming all-sky surveys.

Author Note: The bolometric corrections that were published as a part of this work are produced following a fixed $R_{\rm inner}$ value for the disk (as is discussed below) and therefore the $T_{\rm max}$ value varies as the $L_{\rm acc}$ value varies. However, the spectroscopic similarity of FUOrs in the visible range (see Chapter 12) indicates they have $T_{\rm max}$ values in the range of 5000 – 8000 K. For the lowest and highest luminosity FUOrs, the temperature difference between the models used to derive the bolometric corrections below and their $T_{\rm max}$ is large and can skew the bolometric correction. To account for this, I have computed a set of bolometric corrections for fixed $T_{\rm max}$, by forcing $R_{\rm inner}$ follows $\dot{M}^{-1/3}$. These perform better especially for low-luminosity FUOrs and give good agreement across visible and NIR wavelengths (see the lightcurve of Gaia 17bpi in Chapter 2). The new Table is given in this Chapter in the Appendix and will be publicly available on `github` at `https://github.com/Adolfo1519/FUOrBolCorr`.

7.1 Introduction

FU Ori outbursts occur when the accretion disks around young stellar objects (YSOs) undergo instabilities that increase their accretion rates by factors of 10^2 – 10^4 (Hartmann and Kenyon, 1996). The outbursts have been observed to last for decades and some objects, like V883 Ori, are estimated to have been in outburst for over 100 years (Strom and Strom, 1993). When YSOs are in this luminous, long-lived, outbursting state they are labeled as FU Ori objects.

Extreme accretion outbursts like those of FU Ori objects are proposed as a solution to the “luminosity problem", a timescale problem in stellar mass assembly (Kenyon, Hartmann, Strom, et al., 1990; Kenyon and Hartmann, 1995; Myers, 2010; Fischer et al., 2023a). The problem arises from the observation that measured mass accretion rates of quiescent Class 0 to Class II YSOs are much too low for the forming stars to acquire their eventual main sequence mass in the estimated lifetimes of the envelope (0.5 Myr) and disk (<5-10 Myr); Evans, 2011.

One of the greatest limitations to better understanding the FU Ori phenomenon is the small sample size, as fewer than 45 outbursts have been observed (Connelley and Reipurth, 2018; Guo et al., 2024). Fortunately, the number of FU Ori objects discovered each year has increased exponentially as more all sky surveys have turned on at different wavelengths (Hillenbrand 2025, in prep). While many of the early FU Ori outbursts (FU Ori, V1057 Cyg, V1515 Cyg) were discovered by astute professional astronomers, a large number of them in the 1980s-2000’s were found by dedicated citizen scientists. Most recently, the PTF/ZTF (Law et al., 2009; Bellm et al., 2019), Gaia (Gaia Collaboration, Prusti, et al., 2016), Gattini (Moore, Kasliwal, et al., 2016; De et al., 2020), VVV/VVVX (Minniti et al., 2010; Saito et al., 2024), and NEOWISE (Mainzer et al., 2011) time series photometry surveys have resulted in the detection of tens of FU Ori outbursts over the past 15 years, more than doubling the sample of observed outbursts.

In the coming years, two major all sky surveys will begin: the Rubin Observatory Legacy Survey of Space and Time (LSST), in the visible, and the Roman Observatory High Latitude Wide Area Survey and Galactic Microlensing Survey, in the infrared. The increased depth of these surveys relative to existing ones is expected to enable the observation of new FU Ori eruptions.

However, many of these objects will be distant, and likely at least partially embedded. They will be thus difficult to characterize in detail. In particular, it may be impossible with current capabilities to assemble comprehensive SEDs or obtain

even limited wavelength multi-epoch spectroscopy. For many, perhaps most, of the photometrically detected outbursts, only distinguishing lightcurves will be available.

Here, we provide a series of bolometric corrections for FU Ori objects in common photometric filters. We include those from both existing (ZTF, Gaia, 2MASS, NEOWISE) and upcoming (LSST, Roman) all sky time domain surveys. With the proper corrections for accretion disks from observed to bolometric magnitudes, and with further correction for distance and extinction to absolute bolometric magnitudes, the accretion luminosities (and thence accretion rates) of FU Ori objects can be constrained .

7.2 Applying A Full-Spectrum Disk Model to Photometric Observations

SED for a typical FU Ori object

We construct a model SED of an FU Ori object assuming that in the visible/near-infrared the emission is dominated by a viscously heated accretion disk. Our model follows the method put forth by Kenyon, Hartmann, and Hewett (1988) but includes additional elements, as described in detail in Carvalho, Hillenbrand, Hambsch, et al. (2023). We summarize the model here.

First, we assume the accretion disk is thin and viscously heated. We then adopt a modified version of the Shakura and Sunyaev (1973) α-disk temperature profile,

$$T_{\rm eff}^4(r) = \frac{3GM_*\dot{M}}{8\pi\sigma r^3}\left(1-\sqrt{\frac{R_{\rm inner}}{r}}\right), \tag{7.1}$$

where $R_{\rm inner}$ is the inner radius of the accretion disk, M_* is the mass of the central star, $\dot{M}$ is the stellar accretion rate, G is the gravitational constant, and σ is the Stefan-Boltzmann constant. We assume that $T_{\rm eff}(r < \frac{49}{36}R_{\rm inner}) = T_{\rm eff}(\frac{49}{36}R_{\rm inner}) = T_{\rm max}$ (Kenyon, Hartmann, and Hewett, 1988). We then populate the annuli of the disk with PHOENIX model spectra (Husser et al., 2013) with $\log g = 1.5$ and the appropriate $T_{\rm eff}(r)$.

For the physical parameters of the star and disk, we adopt those of FU Ori (Zhu, Jiang, et al., 2020): $M_* = 0.6\ M_\odot$, $R_{\rm inner} = 3.52\ R_\odot$, $R_{\rm outer} = 0.7$ AU. Since we will be computing bolometric corrections for various system luminosities, we vary $\dot{M}$ in the range $10^{-5.5} - 10^{-3.5}\ M_\odot\ {\rm yr}^{-1}$ to cover $8\ L_\odot < L_{\rm acc} < 845\ L_\odot$ and $3,300\ {\rm K} < T_{\rm max} < 10,500$ K. The grid of luminosities and effective temperatures slightly exceeds the range of values found in detailed modelling of FU Ori objects (Nayakshin and Elbakyan, 2024).

The model grid is computed for systems at distance d = 10 pc, with extinction A_V = 0 mag. We also assume the disk is face on (inclination $i = 0°$). Below, when applying the model grid to observations, the latter are corrected to these parameter values.

The filter profiles

We obtained filter profiles and photometric zero points from the Spanish Virtual Observatory (SVO) Filter Profile Service[1]. We selected several major large-area time domain surveys to represent: the on-going ZTF and Gaia, and the upcoming LSST optical surveys, the upcoming Roman near-infrared survey, and the recently completed NEOWISE mid-infrared survey that probes the most embedded YSOs. We additionally include the 2MASS J, H, and Ks bands due to the broad use of 2MASS as a calibration for other J, H, and K filter systems in various time domain surveys (e.g., Gattini-IR and WINTER: Moore, Kasliwal, et al., 2016; Lourie et al., 2020).

The filter profiles for LSST, Roman, and WISE are shown in Figure 7.1 for reference. Notice that the bolometric corrections will be largest for the u, g, $W1$, and $W2$ filters, while the SED of a typical FU Ori disk is relatively flat for $0.4 < \lambda < 1.3$ μm.

Bolometric Corrections

For each of the filters, we compute the observed photometric magnitude in our model, which is by construction the absolute magnitude. We then compute the bolometric correction, $BC_{\lambda,\mathrm{disk}} \equiv M_{\mathrm{bol,disk}} - M_{\lambda,\mathrm{disk}}$ between the absolute magnitude in the observed band and the bolometric magnitude, assuming a solar bolometric magnitude of $M_{\mathrm{bol},\odot} = 4.74$ (Willmer, 2018). The bolometric corrections are shown as a function of absolute magnitude, $M_{\lambda,\mathrm{disk}}$, in Figure 7.2.

We can fit the $BC_{\lambda,\mathrm{disk}}$ versus $M_{\lambda,disk}$ relation with a 2nd order polynomial:

$$BC_{\lambda,\mathrm{disk}} = c_0 + c_1 M_{\lambda,\mathrm{disk}} + c_2 M^2_{\lambda,\mathrm{disk}}, \tag{7.2}$$

where $BC_{\lambda,\mathrm{disk}}$ is the bolometric correction for a given filter, λ, and c_0, c_1, c_2 are the fit coefficients. The best-fit polynomials are also plotted in Figure 7.2. We report the coefficients and the reference wavelength of each filter in Table 7.1.

[1] `http://svo2.cab.inta-csic.es/svo/theory/fps3/index.php?mode=browse`

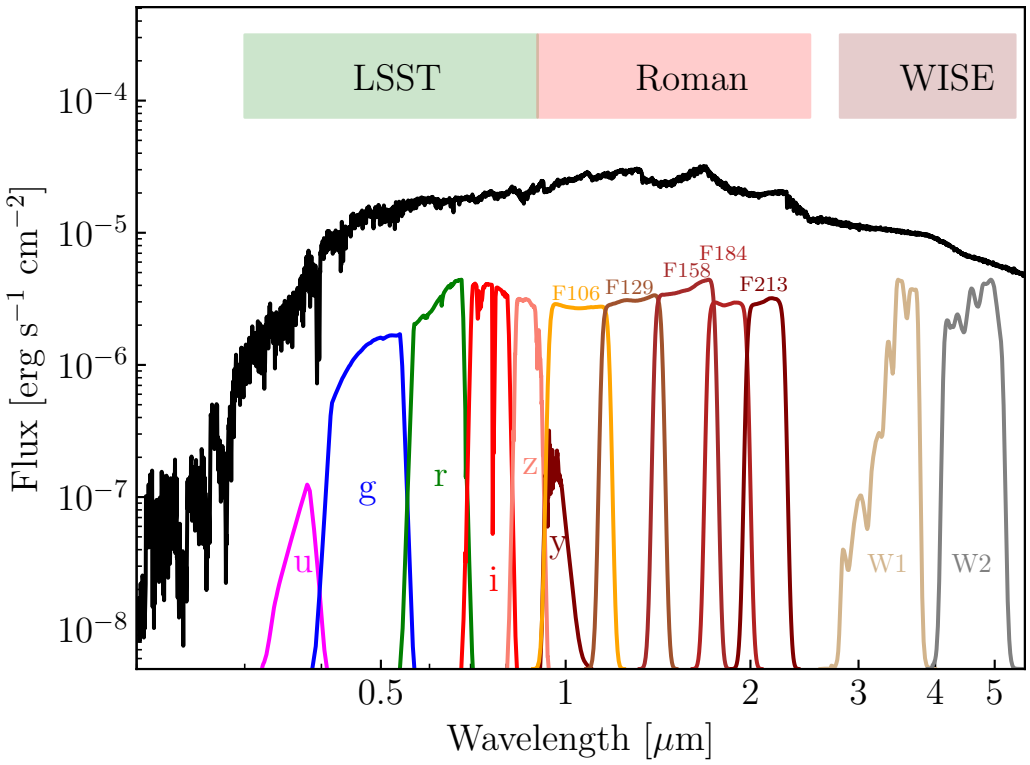

Figure 7.1: The normalized filter profiles for the LSST, Roman, and WISE filters (colored lines), plotted against our fiducial $\dot{M} = 10^{-4.5}\ M_\odot\ \mathrm{yr}^{-1}$ FU Ori object SED model (black). The filled boxes at the top show the approximate total wavelength coverage of each survey or mission. The optical ZTF and Gaia filters overlap the LSST bands, and the 2MASS filters overlap the Roman bands.

7.3 Computing Accretion Luminosity

Arriving at a luminosity estimate (in our case the L_{acc}) from photometric data requires two major corrections prior to applying the bolometric corrections presented in Section 7.2. The first is to determine the extinction to the source in the filters being used. The second is to correct for distance to the source by computing the distance modulus.

The unique SED and anisotropic emission from a viscous accretion disk requires that these corrections be treated differently from their analogs in standard stellar literature. We present the appropriate extinction corrections and distance modulus for FU Ori objects in the following section. We then describe how to apply the bolometric corrections to estimate L_{acc}.

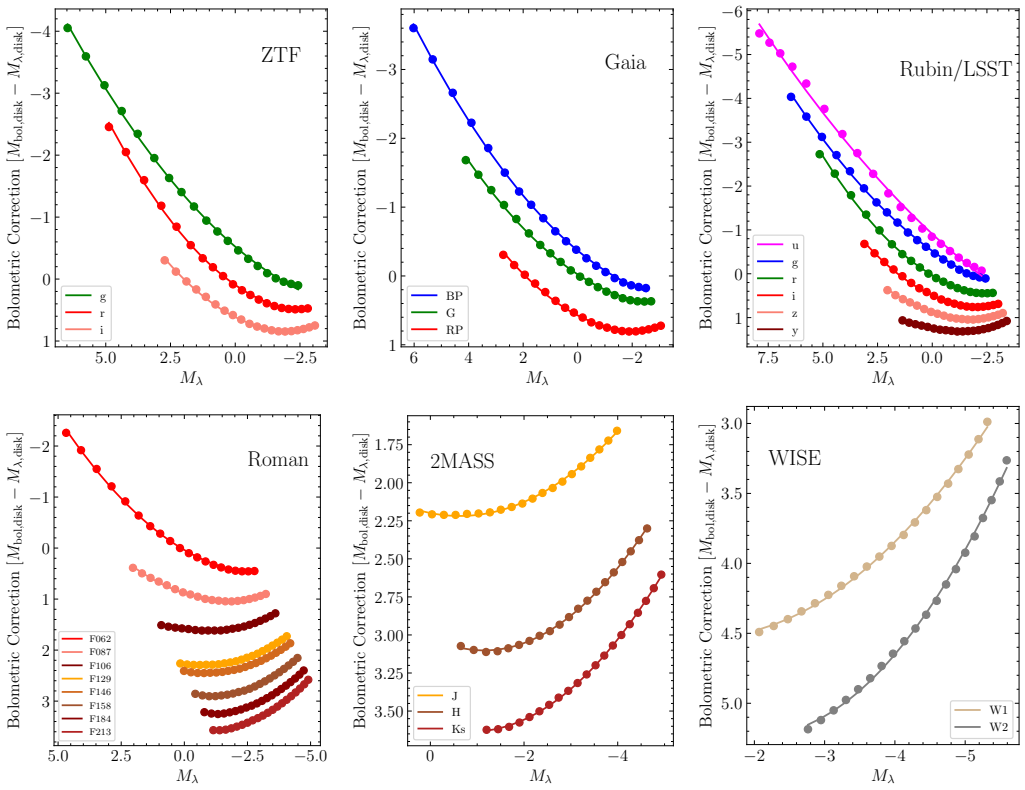

Figure 7.2: The bolometric corrections (filled circles) and our polynomial fits (solid lines). The visible range surveys in the top row are ZTF (left), Gaia (center), and LSST (right). The infrared surveys along the bottom are Roman (left), 2MASS (center), and WISE (right).

A_λ versus A_V for an accretion disk SED

An important step in the process of computing bolometric magnitudes – before applying the bolometric corrections – is the extinction correction to observed magnitudes, m_λ. When a broadband spectrum of an outbursting FU Ori system of obtainable, the A_V is often estimated by scaling the spectrum to match that of another modestly reddened, well-known FU Ori object (Connelley and Reipurth, 2018). Another technique is to use interstellar absorption of Diffuse Interstellar Bands (DIBs), which are not otherwise present in the spectra of FU Ori objects (Carvalho and Hillenbrand, 2022).

Whatever the means of estimating A_V, applying the extinction correction to photometry in other bands requires knowing how the extincted flux in that band relates to the extincted flux in the V band. For broadband filters like those in Gaia, the assumed SED of the source can affect the conversion between A_V and the extinction in the desired filter, $A_{\lambda,\rm disk}$ (as is known to be the case for stars, e.g., Zhang and

Table 7.1: Polynomial coefficients c_0, c_1, c_2 in front of absolute magnitudes (see Equation 7.2) for the bolometric corrections of FU Ori objects. Also provided are $A_{\lambda,\mathrm{disk}}/A_V$ values specifically computed for the viscous disk model.

Filter	λ_{ref} [Å]	c_0	c_1	c_2	$A_{\lambda,disk}/A_V$
Gaia BP	5041.61	-0.368	-0.326	-0.036	0.84
Gaia G	5850.88	-0.022	-0.260	-0.038	0.50
Gaia RP	7690.74	0.574	-0.205	-0.048	0.46
ZTF g	4746.48	-0.522	-0.357	-0.030	1.07
ZTF r	6366.38	0.097	-0.289	-0.051	0.72
ZTF i	7829.03	0.615	-0.208	-0.051	0.54
LSST u	3751.20	-0.907	-0.464	-0.018	1.47
LSST g	4740.66	-0.520	-0.358	-0.030	1.05
LSST r	6172.34	0.036	-0.295	-0.050	0.77
LSST i	7500.97	0.492	-0.229	-0.051	0.58
LSST z	8678.90	0.888	-0.164	-0.048	0.47
LSST y	9711.82	1.254	-0.098	-0.042	0.39
Roman F062	6141.54	0.038	-0.289	-0.046	0.68
Roman F087	8650.97	0.887	-0.162	-0.047	0.44
Roman F106	10465.04	1.594	-0.073	-0.043	0.32
Roman F129	12759.99	2.267	-0.081	-0.052	0.24
Roman F146	13049.63	2.409	-0.094	-0.053	0.18
Roman F158	15577.83	2.816	-0.146	-0.066	0.17
Roman F184	18290.96	3.156	-0.151	-0.066	0.14
Roman F213	21116.87	3.525	-0.118	-0.063	0.11
2MASS J	12350.00	2.200	-0.062	-0.049	0.26
2MASS H	16620.00	3.015	-0.153	-0.067	0.16
2MASS Ks	21590.00	3.589	-0.108	-0.062	0.11
WISE W1	33526.00	4.377	-0.237	-0.092	0.06
WISE W2	46028.00	4.586	-0.627	-0.153	0.04

Yuan, 2023).

To account for extinction effects, we thus also compute a suite of models with fixed $\dot{M} = 10^{-4.5}\ M_\odot\ \mathrm{yr}^{-1}$ and apply a range of A_V values from 0 mag to 20 mag using the Cardelli et al. (1989) curve, to determine the conversion between A_V and $A_{\lambda,\mathrm{disk}}$ for each filter. We then fit $A_{\lambda,\mathrm{disk}}$ versus A_V with a linear model, which is applicable for $0.5 < A_V < 20$ in the bluest bands and $0.1 < A_V < 20$ for $\lambda > 1.0\ \mu$m. The vertical offset in the linear fits is almost exactly 0 mag for all bands, so we simply give the slope, or $A_{\lambda,\mathrm{disk}}/A_V$ in Table 7.1. For targets with $A_V > 15$, the bolometric corrections in the bluer bands may not be reliable due to the radically steepened SED.

Distance Modulus for an Accretion Disk

Once the extinction to an FU Ori object is known, the distance to the target should be accounted for using the distance modulus. One important detail is that the emission is not isotropic but rather from a disk. Consequently, distance modulus should be modified to account for the projected area of the inclined disk. Whereas for a given flux F, the luminosity of an isotropically emitting target at a distance d is calculated by $L = 4\pi d^2 F$, for a disk with inclination i the expression becomes $L = 2\pi d^2 F/\cos i$.

To compare observed disks to our model, the distance modulus, is given by

$$m_\lambda - M_{\lambda,disk} = 5\log_{10}(d) - 5 + A_{\lambda,\mathrm{disk}} + C_i, \tag{7.3}$$

where $A_{\lambda,\mathrm{disk}}$ is the extinction in the observed band, $C_i = -2.5\log_{10}(\cos i)$, and i is the inclination of the observed disk. For a face-on system, $C_i = 0$, while for $i = 80°$, $C_i = 1.901$. Assuming an isotropic distribution of inclinations, a typical value for $\cos i = 1/2$. Thus, in the absence of information about the inclination of an object, a reasonable estimate is $C_i = 0.75$.

Disk Accretion luminosity

With an observed brightness in a given band, m_λ, and the proper distance modulus, the absolute magnitude of the disk $M_{\lambda,\mathrm{disk}}$ is computed by subtracting the distance modulus from m_λ, as in Equation 7.3. Then, using the coefficients in Table 7.1 and Equation 7.2, the bolometric correction $BC_{\lambda,\mathrm{disk}}$ can be computed. Next, the accretion brightness in absolute magnitudes is simply given by $M_{\mathrm{bol,disk}} = BC_{\lambda,\mathrm{disk}} + M_{\lambda,\mathrm{disk}}$.

Finally, converting this accretion brightness into the accretion luminosity $L_{\mathrm{acc}} = L_{\mathrm{bol,disk}}$ in $L_\odot$, can be done in the usual way:

$$L_{\mathrm{acc}} = 10^{-0.4(M_{\mathrm{bol,disk}} - M_{\mathrm{bol},\odot})} L_\odot, \tag{7.4}$$

where as before, $M_{\mathrm{bol},\odot} = 4.74$. If the stellar parameters are known or can be estimated, then the accretion rate can be subsequently inferred from $L_{\mathrm{acc}} = \frac{1}{2}\frac{GM_*\dot{M}}{R_{\mathrm{inner}}}$.

As noted above, the bolometric corrections for FU Ori disks are largest for the bluest (u, g) and the reddest (W1, W2) filters that are discussed here, and smaller at intermediate wavelengths. For any given outburst, the source may be detected from quiescence to the outburst state in one or more of these bands. So which bands are “best" for determining an accurate accretion luminosity? In addition to the issue

of the size of the bolometric correction with wavelength, there is also the issue of the size of the extinction correction with wavelength. A final consideration is the sensitivity of different wavelength ranges to physical parameters of the accretion disk, specifically the outer radius of the actively accreting disk, as discussed on the next section.

On balance, it appears as though red optical through short near-infrared bands (r,i,z,Y,J) optimally measure the accretion luminosity of the outburst. While they are less sensitive to the $\dot{M}$ of the system than bluer bands, they are not as significantly affected by the A_V. This makes them more robust to uncertainties in the adopted A_V value. The reddest NIR bands are least impacted by A_V but are contaminated by emission from the passive disk in the system, which decreases their capacity to directly trace the $L_{\rm acc}$. The rationale for these conclusions is provided below.

7.4 Application to Two Well-Studied FU Ori Systems

In this section, we consider several practical aspects of determining FU Ori accretion disk luminosities using bolometric corrections to photometric observations.

Comparison with previous results on L_{acc}

The reliability of the approach outlined above for estimating the accretion luminosity of FU Ori objects can be demonstrated by comparing results from this procedure with our previous detailed disk modeling for two objects: HBC 722 and V960 Mon.

Both systems have existing Gaia and WISE lightcurves. The accretion luminosity values we adopt as the “true" values for the systems are $L_{\rm true}$ = 100 $L_\odot$ for V960 Mon and $L_{\rm true}$ = 90 $L_\odot$ for HBC 722 (Carvalho, Hillenbrand, Hambsch, et al., 2023; Carvalho, Hillenbrand, Seebeck, and Covey, 2024). For V960 Mon, this is the luminosity measured at the peak of its outburst, whereas for HBC 722 we use the luminosity measured after 2015, when the source reached its bright plateau phase following a short-lived dip immediately after the temporary peak in early 2011.

The comparison between the $L_{\rm true}$ values derived from detailed multi-wavelength modelling and $L_{\rm acc}$ estimated here by applying BCs to single-band photometry, is given in Table 7.4. In most of the bands, the estimated luminosity is within 20% of the measured luminosity with the notable exception of the WISE bands. This can be interpreted as the approximate systematic uncertainty in the method, which dominates over the typically $< 1\%$ photometric uncertainty for data used to compute $L_{\rm acc}$. The BCs are calculated for and applicable to a broad range of source

luminosities, from 8 $L_\odot$ to 700 $L_\odot$. So long as the target, regardless of luminosity, has an FU Ori-like accretion disk, this method is applicable.

Cautions regarding WISE photometry use to compute L_{bol}

For FU Ori systems, photometry redward of K band has been demonstrated to increasingly (with wavelength) trace the passive disk component of the system (Liu et al., 2022; Carvalho, Hillenbrand, Hambsch, et al., 2023). It can also be sensitive to the outer boundary of the viscously heated region of the disk (Kóspál, Ábrahám, Acosta-Pulido, et al., 2016; Carvalho, Hillenbrand, Seebeck, and Covey, 2024). As a result, the WISE $W1$ and $W2$ photometry may overestimate the L_{acc} in some systems. This can be seen in the relatively large values of L_{acc} derived from $W1$ and $W2$ compared to those at other wavelengths.

For V960 Mon, Table 7.4 shows that $L_{acc}(W1) \sim 2L_{true}$ and $L_{acc}(W2) \sim 3L_{true}$. Consistent with these bolometric luminosity results, in the SED of V960 Mon, the viscous-disk-only model of Carvalho, Hillenbrand, Hambsch, et al. (2023) underestimates the $W1$ and $W2$ fluxes by factors of $\sim$ 2 and $\sim$ 3, respectively. The excess flux is accounted for in Carvalho, Hillenbrand, Hambsch, et al. (2023) by including a dust disk component in the system, beyond the active disk region, that is reprocessing the accretion luminosity.

We find that for reasonable assumptions of R_{outer} in the viscous disk model (e.g., $R_{outer} > 25\ R_\odot$), the case of V960 Mon represents an extreme instance of overestimating L_{acc} from $W1$ or $W2$. For targets where the viscous disk extends farther than $R_{outer} \sim 100\ R_\odot$, the passive disk contribution at $3.5 - 5\ \mu$m is negligible. This is exemplified in HBC 722, where the L_{acc} using the $W2$ photometry is relatively consistent with both L_{true} and the near-infrared estimates, though larger than the visible range estimates.

Estimating disk R_{outer} from infrared colors

In Section 7.4, we discussed how estimates of L_{acc} are susceptible to contamination in the $W1$ and $W2$ photometry from the non-active region of the disk. Moving to shorter wavelength photometry, such as JHK, we identify another consideration in estimating accurate L_{acc} values.

Carvalho, Hillenbrand, and Seebeck (2023) demonstrated that the 1.5 to 2.2 μm region of an FU Ori object SED is sensitive to the R_{outer} value of the active disk region. This is especially the case for $25 < R_{outer}/R_\odot < 100$, with larger values of

Table 7.2: Comparison between the measured accretion luminosities ($L_{\rm true}$) for HBC 722 and V960 Mon, and those we estimate using our BCs ($L_{\rm bol,disk} = L_{\rm acc}$).

	$L_{\rm acc}/L_\odot$	
Filter	V960 Mon	HBC 722
	$L_{\rm true} = 100 \pm 10$	$L_{\rm true} = 90 \pm 9$
Gaia BP	123	77
Gaia G	101	73
Gaia RP	105	87
ZTF g	···	85
ZTF r	···	84
2MASS J[a]	88	113
2MASS H[a]	67	106
2MASS Ks[a]	56	116
WISE W1[b]	240	157
WISE W2[b]	295	111

[a] The flux in J, H, and Ks is sensitive to the $R_{\rm outer}$ value in the model and for $R_{\rm outer} < 100\ R_\odot$, H and Ks underestimate the $L_{\rm acc}$.

[b] The flux from both WISE bands includes significant contribution from the passive disk and may overestimate $L_{\rm acc}$.

$R_{\rm outer}$ best discriminated in the 3 to 5 μm range of the SED (Carvalho, Hillenbrand, Seebeck, and Covey, 2024). This sensitivity to $R_{\rm outer}$ may present a challenge for interpreting $L_{\rm acc}$ from K or Ks band photometry.

In Table 7.4, although the J-band-inferred $L_{\rm est}$ is nearly $L_{\rm meas}$, the $L_{\rm est}$ values for V960 Mon steadily decrease toward the redder 2MASS bands. This is consistent with the small $R_{\rm outer} = 25 - 35\ R_\odot$ reported for the system. On the other hand, the $L_{\rm est}$ values for HBC 722 do not show this steady decrease with increasing wavelength and are in better agreement with the $L_{\rm est}$ from the visible (if slightly over-estimated). We expect this for HBC 722 because for the epoch we show here, $R_{\rm outer} > 100\ R_\odot$ (Carvalho, Hillenbrand, Seebeck, and Covey, 2024).

Assuming that the J band is a reasonable estimate of $L_{\rm acc}$ for $R_{\rm outer} > 25\ R_\odot$, we can use the $M_J - M_{Ks}$ color of the system to estimate $R_{\rm outer}$. We demonstrate this in Figure 7.3. Although the $M_{W1} - M_{W2}$ space would in principle be more sensitive to the $R_{\rm outer}$ in a system, the potentially significant contribution of the passive disk can

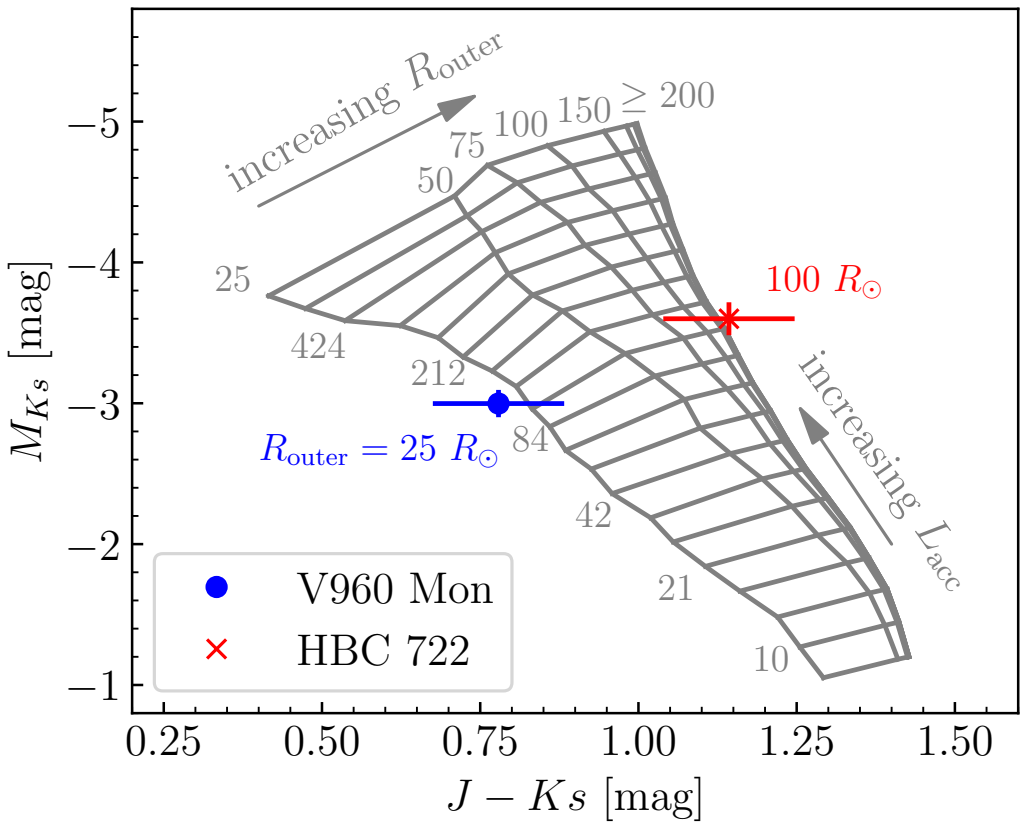

Figure 7.3: The M_{Ks} versus extinction-corrected $J-Ks$ color magnitude space, with the locations of V960 Mon (blue point) and HBC 722 (green "x") are marked. The grid of accretion disk model values is plotted in grey, with constant $R_{\rm outer}$ tracing approximately vertical lines and constant $L_{\rm acc}$ approximately horizontal. The values at the top of the grid mark $R_{\rm outer}$ in units of $R_\odot$ for each set of models and values along the lower boundary of the grid mark a few $L_{\rm acc}$ values in units of $L_\odot$ for reference. Models with $R_{\rm outer} > 200\ R_\odot$ converge in this color space. Notice that both V960 Mon and HBC 722 lie along tracks that agree with their measured $R_{\rm outer}$ values (blue and red text, respectively) in this space.

confound the diagnostic. In the M_{Ks} versus $M_J - M_{Ks}$ color magnitude space, the models computed for different $R_{\rm outer}$ are well-separated while remaining minimally affected by passive disk emission.

7.5 Conclusions

Using our semi-empirical viscous disk model, we have computed bolometric corrections between observed and absolute magnitudes for YSOs that are dominated by luminosity generated in accretion disks. We have also provided a guide for the full set of considerations needed in order to convert a brightness measurement m_λ

for an FU Ori accretion disk into an $L_{\rm acc}$ estimate, using bolometric corrections.

Our procedure accounts for the ways in which computing $L_{\rm acc}$ for a disk differs from the canonical methods developed to compute $L_{\rm bol}$ for stars, particularly due to the unique shape of the disk SED and the projection of flux in inclined disks. The shape of the SED impacts both the bolometric correction and the conversion from A_V to $A_{\lambda,\rm disk}$ because the flux is distributed across a much broader wavelength range than in stellar SEDs. Larger disk inclinations lead to a smaller fraction of $L_{\rm acc}$ reaching an observer, which can lead to systematic underestimation of $L_{\rm acc}$ if the emission is assumed to be isotropic. We also add a correction term to the traditional distance modulus calculation to incorporate the inclination of the disk when computing the absolute magnitude of accretion disks.

When applying the bolometric corrections we calculated to a typical FU Ori disk, the bands that will give bolometric-correction-derived luminosities most consistent with the true $L_{\rm acc}$ are those between the red-optical and J (or H) band. This wavelength range is where the SED is flattest and least affected by the assumed A_V or the presence of hot dust emission in the system.

Estimating $L_{\rm acc}$ with the bolometric corrections presented here will enable a self-consistent means of comparing accretion luminosities of FU Ori objects for several ongoing and upcoming all-sky-surveys. This will facilitate building a sample of objects that can be studied uniformly as more outbursts are detected, leading to statistical robustness for population studies.

Although we have computed the quantities and relations in the paper with FU Ori accretion disks in mind, there are elements of the work that can be applied to other disk systems. One that is universal is the need to correct for flux projection when estimating a disk luminosity from photometric data. The modified distance modulus we present in Equation 7.3 is applicable to calculating the absolute magnitude of emission from any astrophysical disk. The bolometric corrections are generally applicable for viscous accretion disks with maximum temperatures ranging from 3,300 K to 10,500 K. However, due to the modification to the Shakura and Sunyaev (1973) temperature profile, the results will be most reliable for redder bands, as bluer bands are more sensitive to the details of $T_{\rm eff}(r < \frac{49}{36}R_{\rm inner})$.

7.6 Acknowledgements

The authors thank Antonio Rodriguez for insightful conversations and suggestions.

7.7 Appendix: New Constant-Temperature Bolometric Corrections

The bolometric corrections provided in the text above allow the $T_{\rm max}$ of the disk to vary in the range of $3,500 - 10,000$ K in order to cover the large luminosity range. However, recent discoveries of low-luminosity FUOrs still showing spectra consistent with $T_{\rm max} \sim 5000 - 7000$ K (e.g., Hillenbrand, Peña, et al., 2018; Hillenbrand, Carvalho, Stern, et al., 2025a) indicate that the temperature range of the models used to compute the bolometric corrections is too broad. While this is acceptable for FUOrs with luminosities near the middle of the range $50 < L_{\rm acc}/L_{\odot} < 400$, those near the ends of the range will have less accurate luminosity estimates. In the case of sources with $L_{\rm acc} < 10$, the bolometric corrections will be based on models that are too red and thus over-estimate the correction. Table 7.3 contains bolometric corrections for models computed with a fixed $T_{\rm max} = 6,000$ K by adopting $M_{*} = 0.6\ M_{\odot}$ and $R_{\rm inner} = 3.52 \left(\frac{\dot{M}}{10^{-4.5}\ M_{\odot}\ {\rm yr}^{-1}} \right)^{-1/3}\ R_{\odot}$. The parameter $\dot{M}$ is then varied from $10^{-7}\ M_{\odot}\ {\rm yr}^{-1}$ to $10^{-3.5}\ M_{\odot}\ {\rm yr}^{-1}$.

Table 7.3: Polynomial coefficients c_0, c_1, c_2 in front of absolute magnitudes (see Equation 7.2) for the bolometric corrections of FU Ori objects using models of a constant $T_{\rm max} = 6,000$ K. Additional information for each filter can be found in Table 7.1.

Filter	c_0	c_1	c_2
Gaia BP	-0.513	0.014	-0.000
Gaia G	0.012	0.019	-0.000
Gaia RP	0.741	0.026	-0.000
ZTF g	-0.783	0.015	-0.001
ZTF r	0.185	0.014	0.001
ZTF i	0.794	0.029	-0.000
LSST u	-1.592	0.047	-0.006
LSST g	-0.781	0.015	-0.001
LSST r	0.102	0.012	0.001
LSST i	0.663	0.026	0.000
LSST z	1.056	0.031	-0.001
LSST y	1.351	0.027	-0.001
Roman F062	0.104	0.015	0.000
Roman F087	1.054	0.030	-0.001
Roman F106	1.624	0.017	-0.000
Roman F129	2.190	0.004	-0.000
Roman F146	2.335	0.002	-0.001
Roman F158	2.694	-0.010	-0.002
Roman F184	2.966	-0.014	-0.002
Roman F213	3.200	-0.011	-0.001
2MASS J	2.104	0.004	0.000
2MASS H	2.845	-0.015	-0.002
2MASS Ks	3.227	-0.011	-0.001
WISE W1	3.871	-0.003	-0.001
WISE W2	4.373	-0.002	-0.001

Chapter 8

CROSS CORRELATION ANALYSIS OF THE KECK/NIRSPEC HIGH RESOLUTION SPECTROSCOPIC SURVEY OF FUORS

Cross-correlation functions (CCFs) provide an efficient means of determining the average line profile among several in a spectrum. The CCF greatly improves the signal-to-noise ratio of the line profile relative to isolating individual lines. In regions of the spectrum with mixed or blended molecular and atomic absorption features, it can sometimes be the only way to analyze the structure of the line profiles.

The Keck/NIRSPEC survey of FUOrs that we conducted from 2022 to 2023 was designed to capture the most complete high resolution NIR spectra of FUOrs known at the time, spanning $1.0 - 2.4$ μm. In Chapters 5 and 6, I show how the spectra of HBC 722 and V883 Ori are very effectively reproduced by the disk model. In this chapter, I use this fact to compute the $v_{\rm max}$ in FUOrs based on their rotational broadening at H band, and to compare the observed line broadening from bluer to redder wavelengths with that predicted from the disk model. The spectra used in both analysis are shown in Chapter 13.

8.1 Using CCFs in H band to Measure $v_{\rm max}$

As discussed in Chapter 2, an effective means of using the high resolution spectrum of a FUOr to constrain SED fits has been to measure the Keplerian rotational broadening in the spectrum. Recall that if the material is in a Keplerian orbit around the central star, then its velocity at a given radius is $v_{\rm Kep}(r) = \sqrt{GM_*/r}$. The velocity we observe is projected along our line of sight according to the inclination, i, of the disk, so we observe $v_{\rm Kep}(r)\sin i$. The maximum velocity we observe is at $r = R_{\rm inner}$, and is given by $v_{\rm max} = \sqrt{GM_*/R_{\rm inner}}\sin i$.

The fact that $v_{\rm max}$ contains M_*, $R_{\rm inner}$ and i in its expression gives it the power to constrain these parameters in the SED model. Notice also that it isolates M_* from the $M_*\dot{M}$ product that appears in the expressions of $T_{\rm max}$ and $L_{\rm acc}$.

Measuring $v_{\rm max}$ directly from the rotational broadening of spectra lines is challenging because the formation radius of a given feature is a complex function of its excitation potential, the line oscillator strength, and the local disk properties (Carvalho, Hillenbrand, and Seebeck, 2023). It is generally true that the contin-

uum redder wavelengths probe cooler regions of the disk at larger r (see Figure D1 in Carvalho, Hillenbrand, Seebeck, and Covey, 2024), so one might imagine that measuring the $v \sin i$ of lines in the blue-optical or NUV would give the best estimate of $v_{\rm max}$. However, blueward of $\sim$ 5000 Å, the spectrum of FUOrs suffers heavy contamination from the strong outflows of the object and the NUV/FUV spectrum is dominated by outflow emission (Kravtsova, Lamzin, et al., 2007; Carvalho, Hillenbrand, France, et al., 2024).

In order to obtain estimates of $v_{\rm max}$ that are minimally impacted by absorption/emission from outflows and to account for the Keplerian velocity profile in the disk, we propose a new, cross-correlation-based technique using high resolution H band spectra. The H band is ideal due to its mix of atomic and molecular spectral features with a wide range of excitation potentials and in turn a wide range of formation radii in the disk. The line absorption in the region is also relatively insensitive to the maximum temperature in the disk, so the line widths are primarily set by the Keplerian rotational broadening.

To begin, we compute an accretion disk model based on the FU Ori system, using the system parameters from our model in (Carvalho, Hillenbrand, France, et al., 2024): $M_* = 0.6\ M_\odot$, $R_{\rm inner} = 3.52\ R_\odot$, $\dot{M} = 10^{-4.49}\ M_\odot\ {\rm yr}^{-1}$. Since we are continuum-normalizing the spectra, A_V and distance are irrelevant here. In order to vary the rotational broadening of the model absorption lines, we compute a grid of models with $i = 1^\circ - 89^\circ$. The resulting velocity range is $v_{\rm max} = 1 - 175$ km s^{-1}. We also compute a model with no rotational broadening.

To produce the reference grid of cross-correlation functions (CCFs), we first downsample the models to the wavelength sampling and resolution of the NIRSPEC spectrum in each of the ten H band orders. We then compute the CCF between the non-broadened model and each of the broadened models and the NIRSPEC H band spectrum.

We combine the CCFs of each order to produce a mean CCF following the guidance in Zucker (2003):

$$CCF_{\rm mean} = \sqrt{1 - \left(\prod_{1}^{10} CCF_i^2 \right)^{1/10}}, \tag{8.1}$$

where CCF_i is the CCF for a given H band spectral order. The resulting $CCF_{\rm mean}$ is a maximum-likelihood based combination of all 10 orders, minimizing the effects of artifacts near the wings of the CCF. The $CCF_{\rm mean}$ for the V883 Ori spectrum is

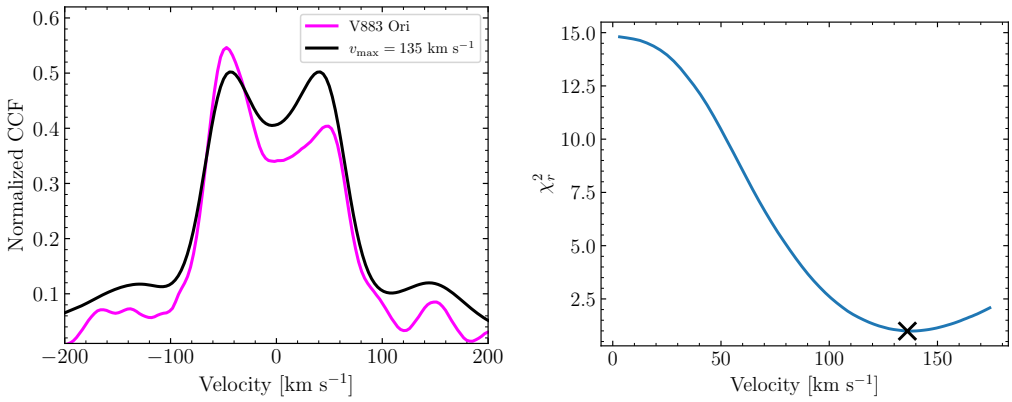

Figure 8.1: The results of the *H* band CCF best-fit used to measure the rotational broadening in V883 Ori. **Left:** The mean CCF from 8 H band orders of the NIRSPEC spectrum of V883 Ori (magenta) and the best-fitting mean CCF from the model grid, corresponding to a $v_{\rm max}$ = 135 km s^{-1}. The stronger blue-shifted absorption in V883 Ori is likely due to a rotating disk wind traced by molecular bands like CO (3-0), as has been reported in HBC 722 (Calvet, Hartmann, et al., 1993; Carvalho, Hillenbrand, Seebeck, and Covey, 2024). **Right:** The reduced χ^2 values for the grid of model CCFs and the V883 Ori CCF. The best-fit value is marked with a × symbol.

shown in Figure 8.1. We compute the reduced χ^2 between each of our model CCFs and the V883 Ori CCF to identify the correct best-fitting $v_{\rm max}$ value for the system. As shown in Figure 8.1, the best-fit value of $v_{\rm max}$ = 135 km s^{-1}.

Using this technique, we are able to measure the $v_{\rm max}$ values for all of the objects in our Keck/NIRSPEC survey for which we were able to obtain *H* band spectra. The $v_{\rm max}$ measurements are shown in Table 8.1 and and summarized in Figure 8.2. The plots of the CCFs and χ^2 values as a function of $v_{\rm max}$ are presented below. Note that the resolution of the NIRSPEC spectra is $\sim 15,000$, so the instrumental line broadening is 20 km s^{-1}. This places an upper bound on the rotational broadening in objects like V1515 Cyg, V2775 Ori, and PP 13S.

I have omitted the measurements for V1057 Cyg from Table 8.1 because they do not appear to reflect the actual rotational broadening in the disk. Despite the spectroscopic similarity of V1057 Cyg to FUOrs at medium/low resolution, the high resolution NIR spectrum, like the visible range spectrum, is dominated by wind absorption and emission features (see Chapter 13), even in *H* band. Thus, the spectral line profiles trace the kinematics of the outflow in the source, rather than the disk itself.

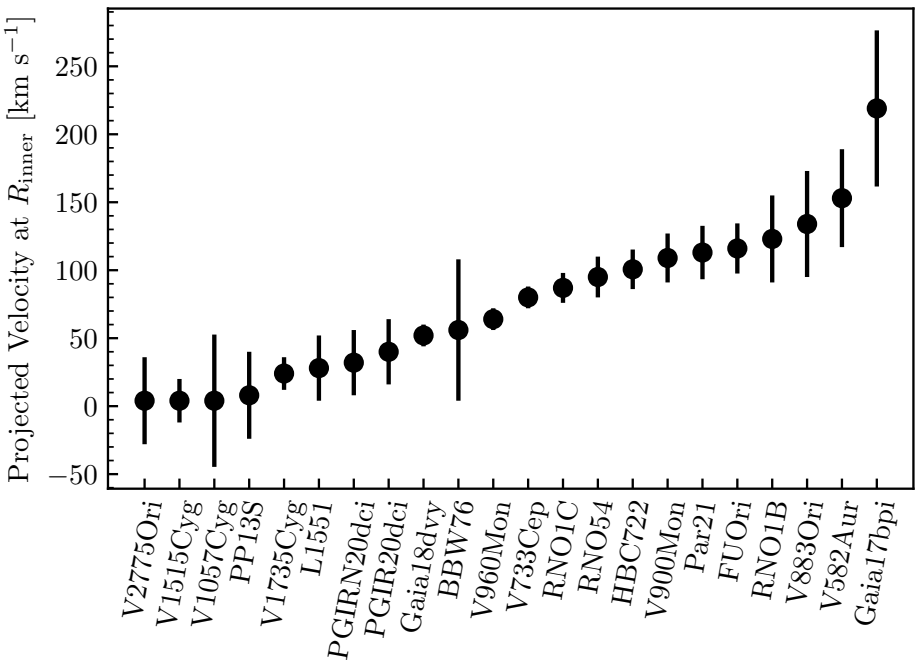

Figure 8.2: The measured $v_{\rm max}$ values for each object in our NIRSPEC sample.

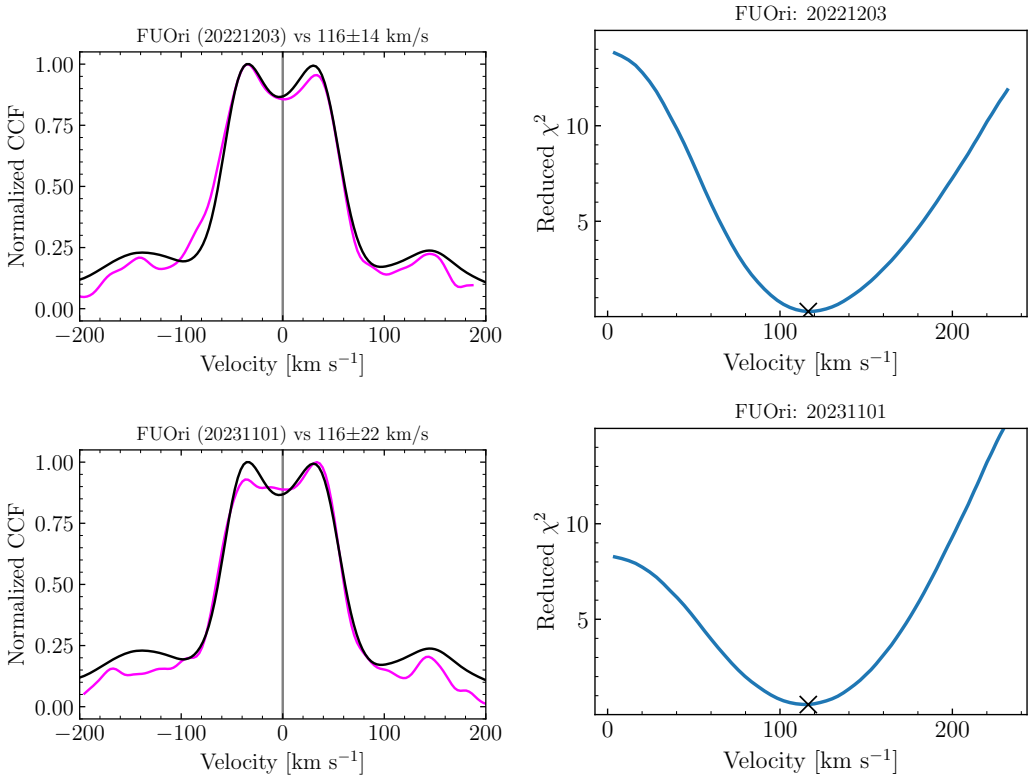

Figure 8.3: The CCFs and reduced χ^2 values for the two epochs of FU Ori NIRSPEC spectra.

Table 8.1: The $v_{\rm max}$ measurements for FUOr with a Keck/NIRSPEC H band spectrum. While V1057 Cyg is included in this table for completeness, the CCFs are likely tracing the extreme wind absorption in this source, rather than disk broadening.

Object	Date	$v_{\rm max}$ (km s^{-1})	σ_v (km s^{-1})
Gaia17bpi	2022-07-31	206	60
	2023-10-31	232	54
HBC 722	2022-07-31	102	7
	2022-12-03	102	15
	2023-10-30	98	19
Parsamian 21	2022-07-31	113	14
	2023-11-01	113	24
V733 Cep	2022-07-31	80	8
V1057 Cyg	2022-07-31	4	40
	2022-12-03	4	56
V1515 Cyg	2022-07-31	4	16
V1735 Cyg	2022-07-31	24	12
Gaia18dvy	2022-08-01	52	8
PGIR20dci	2022-08-01	32	24
	2023-10-30	40	24
FU Ori	2022-12-03	116	14
	2023-11-01	116	22
RNO 1B	2022-12-03	123	32
RNO 1C	2022-12-03	87	11
RNO 54	2022-12-03	95	15
V900 Mon	2022-12-04	109	18
V960 Mon	2022-12-04	64	8
L1551 IRS 5	2023-10-30	28	24
PP13S	2023-10-30	8	32
V2775 Ori	2023-10-30	4	32
BBW 76	2023-10-31	56	52
V883 Ori	2023-10-31	134	39
V582 Aur	2023-11-01	153	36

8.2 The Wavelength Dependence of Rotational Broadening in FUOrs Revealed by CCF Analysis

The idea that FUOrs have a thin, viscous accretion disk in approximately Keplerian rotation around the central star naturally implies that further away from the star, material will be orbiting more slowly. The temperature profile for the disk, $T \propto r^{-3/4}$, also shows that this slower rotating material should be cooler and therefore radiate at

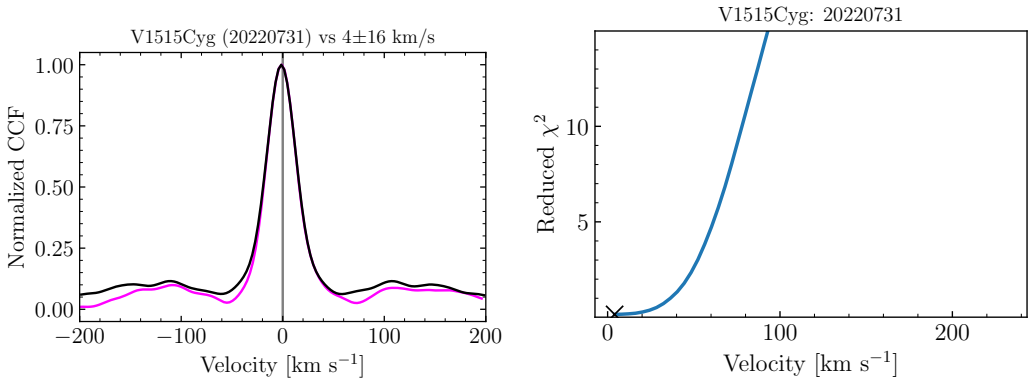

Figure 8.4: Same as Figure 8.3 for V1515 Cyg.

redder wavelengths. Therefore, when looking at high resolution spectra of FUOrs, absorption lines at redder wavelengths should have narrower profiles than absorption lines at bluer wavelengths. The effect should also be seen in the excitation potential of the lines: features with greater excitation potential should probe hotter material and have broader absorption lines than features with lower excitation potentials.

When modeling the high resolution visible range spectra of V1057 Cyg (pre-1994 fade event), Z CMa, and FU Ori, (Welty, Strom, Edwards, et al., 1992) found the absorption lines in both observations and the disk models did not follow this trend. Their models successfully reproduced a lack of correlation in rotational broadening with both wavelength and excitation potential. In this case, the model does, in fact, match the observed lack of correlation, despite the counter-intuitive nature of the result.

The lack of correlation between observed line broadening and wavelength or excitation potential is raised by Herbig et al. (2003) and Petrov and Herbig (2008) as arguments against the disk model. In their disk model spectra, the predicted correlations between observed line width and wavelength are strong, while remaining absent in their observed spectra of FU Ori and V1057 Cyg. Zhu, Espaillat, et al. (2009a) rebut these criticisms of the disk model by demonstrating that high resolution spectrum of FU Ori at 5 μm has much narrower absorption lines than the visible range spectrum, as expected. They also explain that the visible range spectra probe a region of the disk that is relatively radially isothermal, and that the temperature gradient is insufficient to produce the rotational broadening effects.

In Chapter 4, I applied these rotational broadening tests to V960 Mon and found, similarly to the above works, that the widths of lines in visible range spectra do

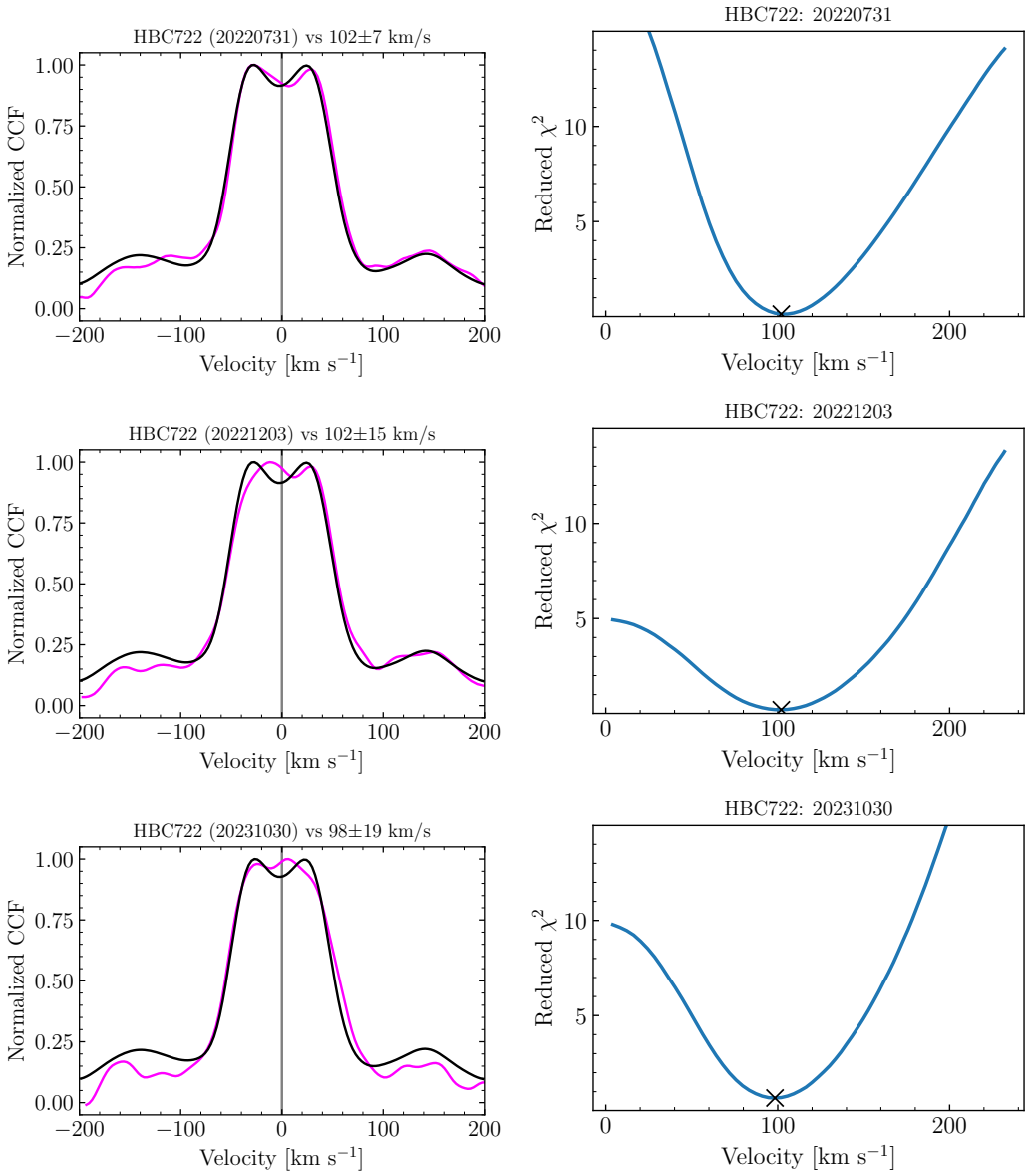

Figure 8.5: Same as Figure 8.3 for HBC 722.

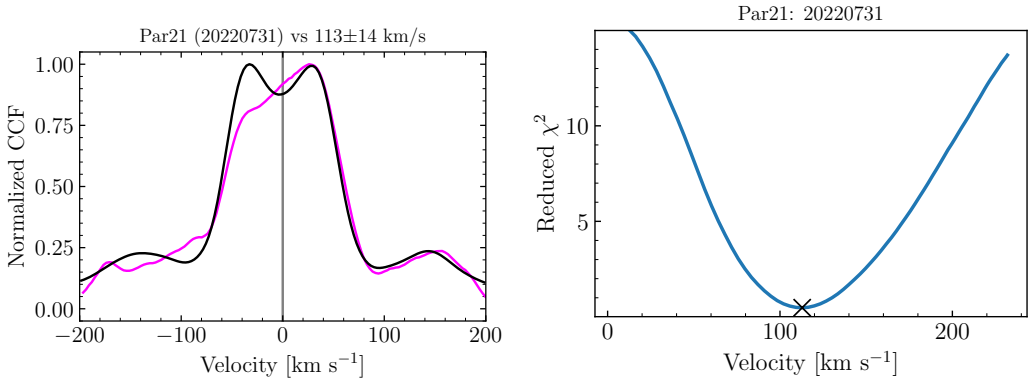

Figure 8.6: Same as Figure 8.3 for Parsamian 21.

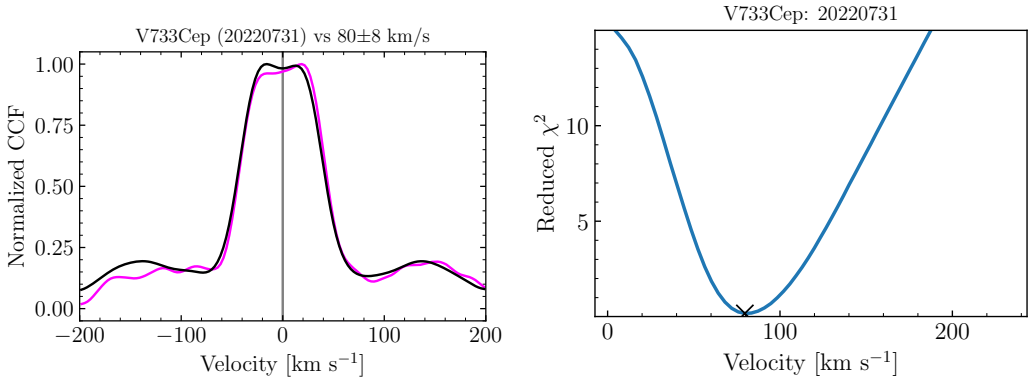

Figure 8.7: Same as Figure 8.3 for V733 Cep.

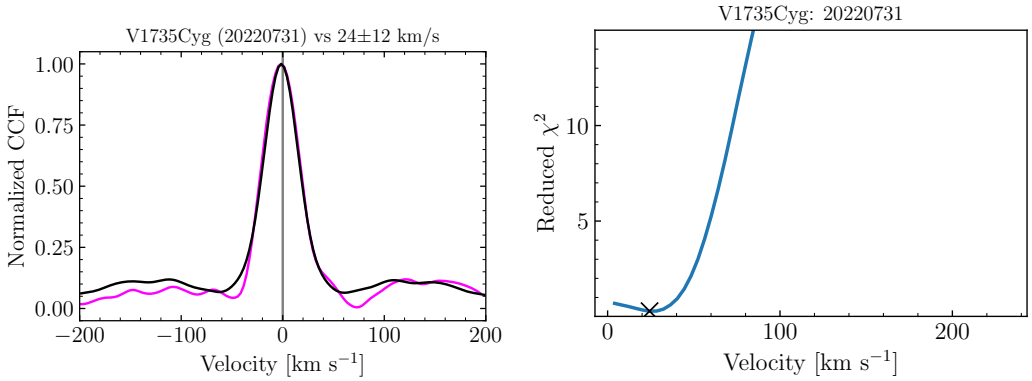

Figure 8.8: Same as Figure 8.3 for V1735 Cyg.

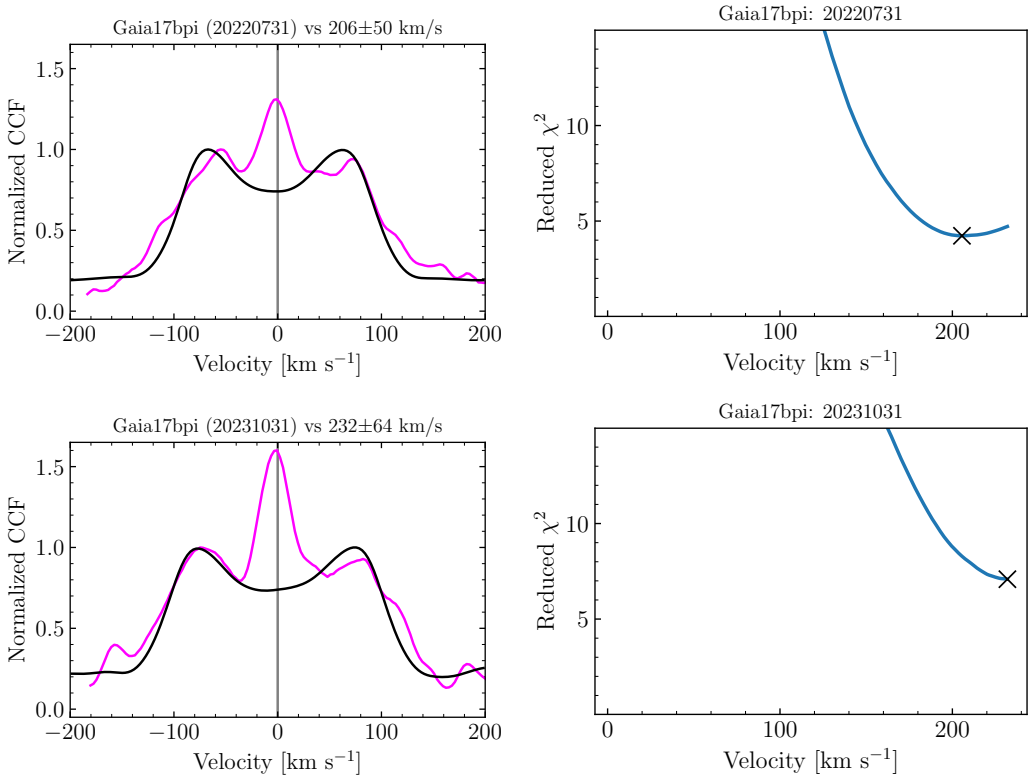

Figure 8.9: Same as Figure 8.3 for Gaia 17bpi.

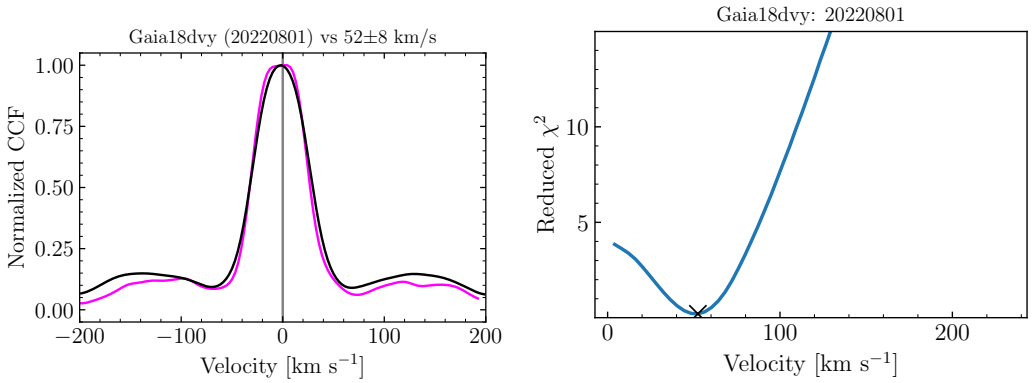

Figure 8.10: Same as Figure 8.3 for Gaia 18dvy.

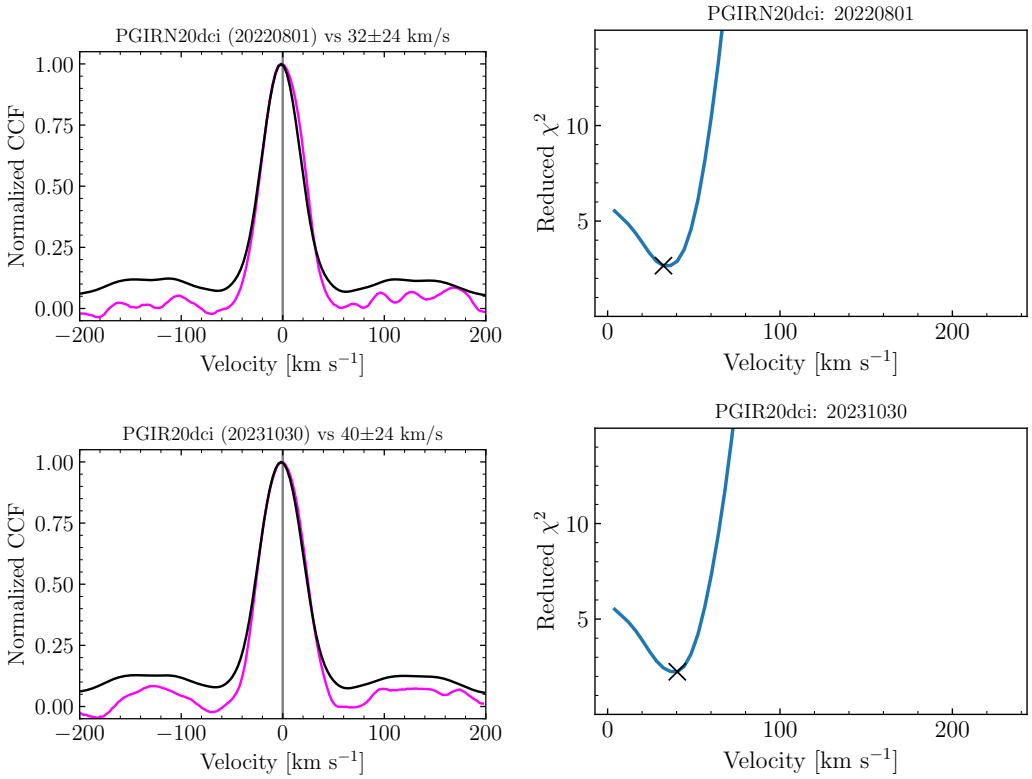

Figure 8.11: Same as Figure 8.3 for PGIR 20dci.

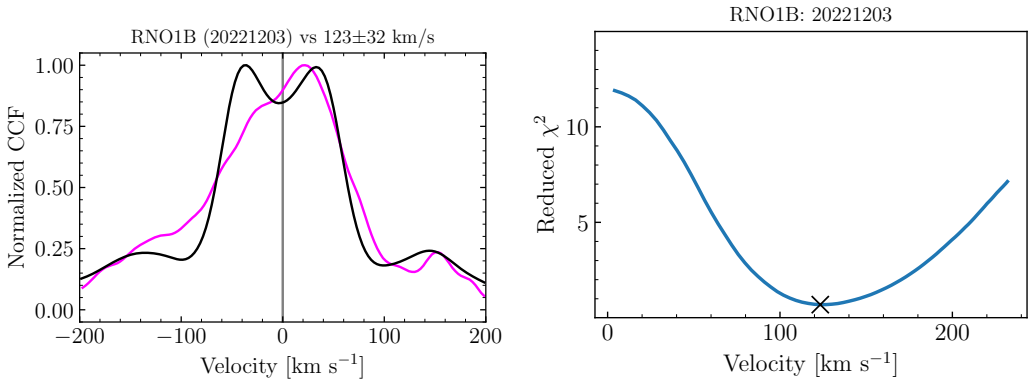

Figure 8.12: Same as Figure 8.3 for RNO 1B.

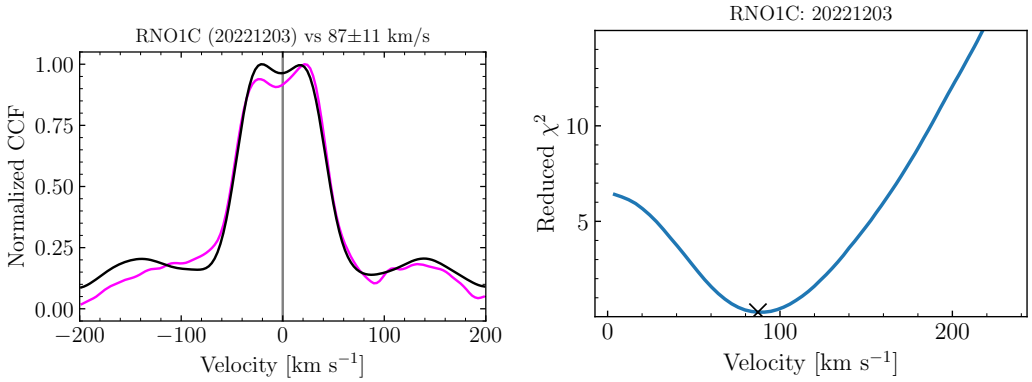

Figure 8.13: Same as Figure 8.3 for RNO 1C.

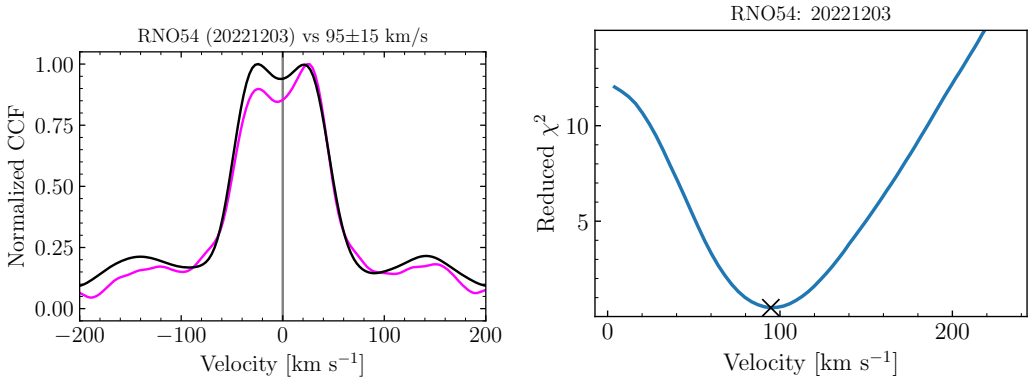

Figure 8.14: Same as Figure 8.3 for RNO 54.

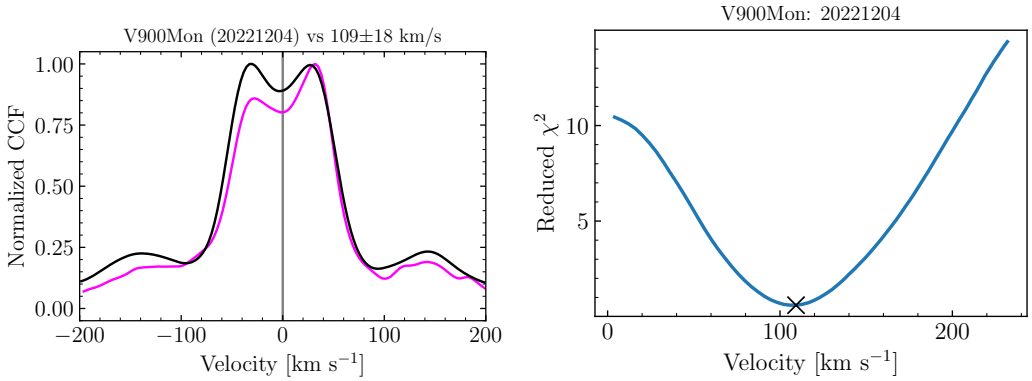

Figure 8.15: Same as Figure 8.3 for V900 Mon.

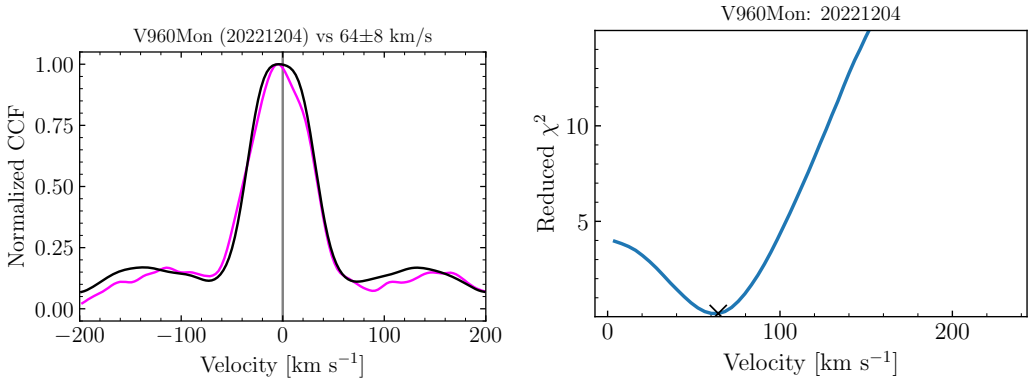

Figure 8.16: Same as Figure 8.3 for V960 Mon.

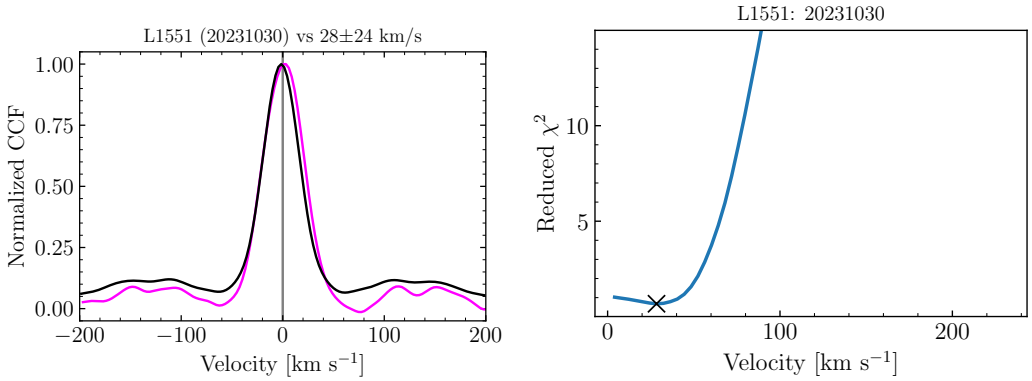

Figure 8.17: Same as Figure 8.3 for L1551 IRS 5.

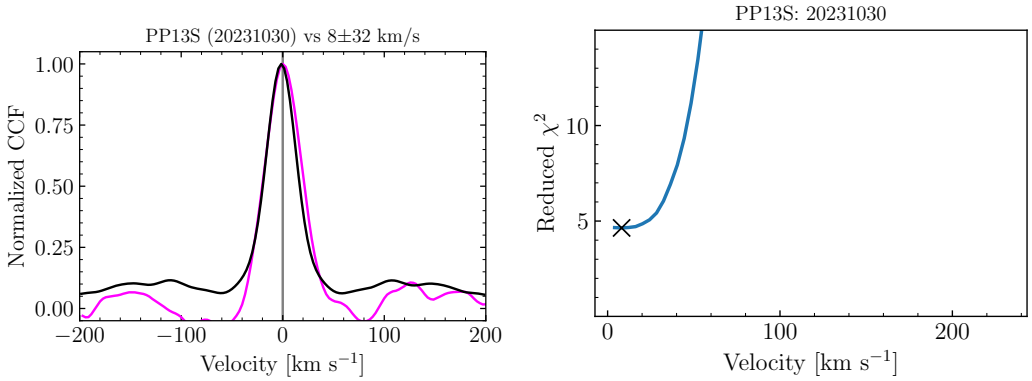

Figure 8.18: Same as Figure 8.3 for PP 13S.

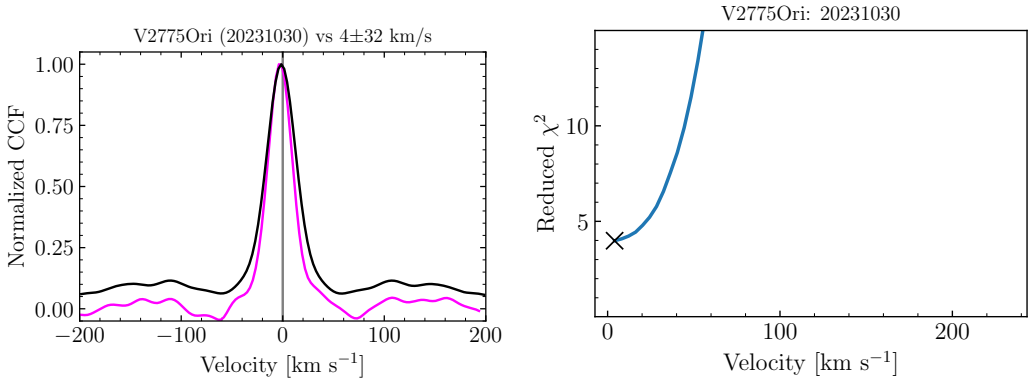

Figure 8.19: Same as Figure 8.3 for V2775 Ori.

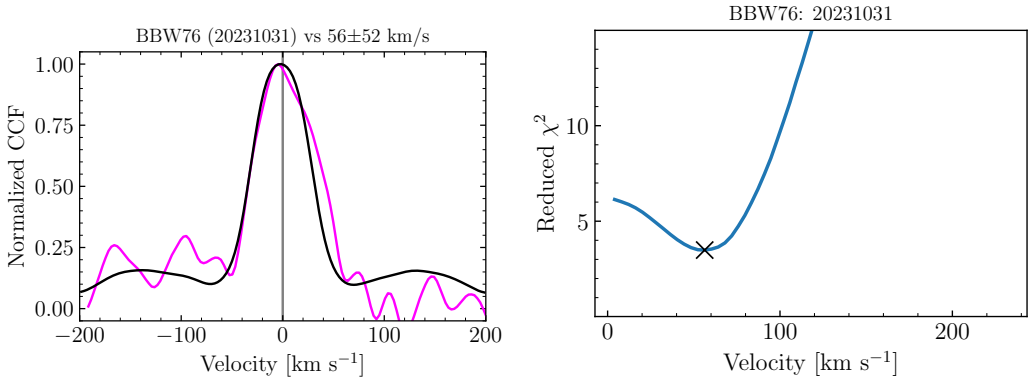

Figure 8.20: Same as Figure 8.3 for BBW 76.

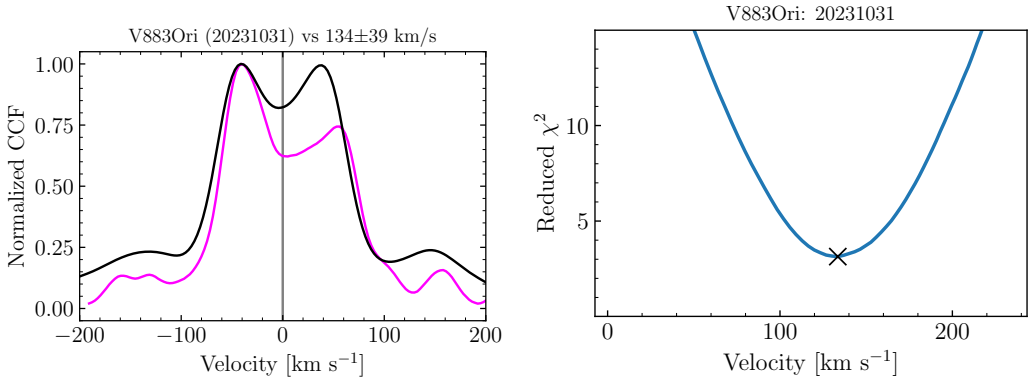

Figure 8.21: Same as Figure 8.3 for V883 Ori.

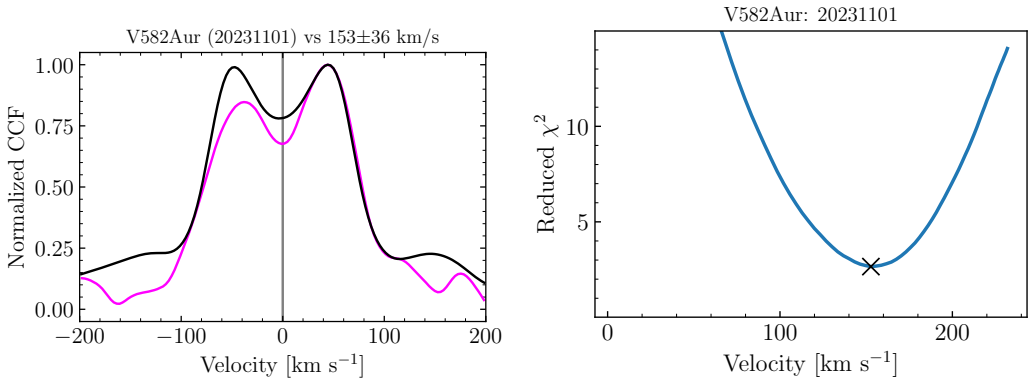

Figure 8.22: Same as Figure 8.3 for V582 Aur.

not correlate strongly with wavelength or excitation potential. I demonstrated then that, as described in Zhu, Espaillat, et al. (2009a) for FU Ori, the $T_{\rm max}$ of the disk model impacts the dependence of visible range rotational broadening on the observed line width. Higher $T_{\rm max}$ values in the disk will cause the region from which the visible range spectrum emerges to have a greater radial $T_{\rm eff}$ gradient. Thus, as Zhu, Espaillat, et al. (2009a) conclude, searching for the predicted differential disk rotation in visible range spectra will yield inconclusive results.

To rigorously test this effect in the large sample of FUOrs now known, we conducted CCF analysis of the Y, J, H, and K band spectra shown in Chapter 13. In each band, we compute a mean CCF following the technique described in Section 8.1. We then compare the CCFs from each band, as shown in Figures 8.25 through 8.42.

In the majority of FUOrs, the K band CCFs are clearly narrower than the Y or J band CCFs. There are some objects, however, wherein the expected narrowing of the CCF at longer wavelengths is not seen. In Figure 8.23, I show three sets of model CCFs (from the grid computed in Section 8.1) for different $v_{\rm max}$ values and the four bands. In all three model sets, for the fiducial $R_{\rm outer}$ = 150 $R_\odot$, the K band CCFs are indeed predicted to be narrower. In the models with $R_{\rm outer}$ = 25 $R_\odot$, the narrowing is not seen.

This can be explained by considering the flux-weighted mean radii probed by different spectral regions of the disk model as a function of $R_{\rm outer}$. A schematic of this for the different models of HBC 722 (see Chapter 5), is shown in Figure 8.24. A detailed discussion of the figure in the context of HBC 722 is given in Carvalho, Hillenbrand, Seebeck, and Covey (2024). In the Figure, the model labeled “Outburst" has $R_{\rm outer}$ = 25 $R_\odot$, “Dip" has $R_{\rm outer}$ = 35 $R_\odot$, and “Plateau" has $R_{\rm outer}$ = 100 $R_\odot$.

For models with larger $R_{\rm outer}$, the typical radius probed by the 2 μm region of the spectrum is much further out in the disk than for smaller $R_{\rm outer}$. Therefore, the differential rotation between 1 μm and 2 μm is much more extreme. The $v_{\rm Kep} \sin i$ values as a function of radius are shown in the right axis of the upper panel in Figure 8.24, for reference. The difference in $v_{\rm Kep} \sin i$ between $1 - 2$ μm for the Outburst and Dip models are negligible compared to that in the Plateau model. As I have demonstrated in Chapters 3, 5, and 6, the $R_{\rm outer}$ can vary from object to object, and even a lack of differential rotation from $1 - 2$ microns is predicted by the disk model for potentially many FUOrs.

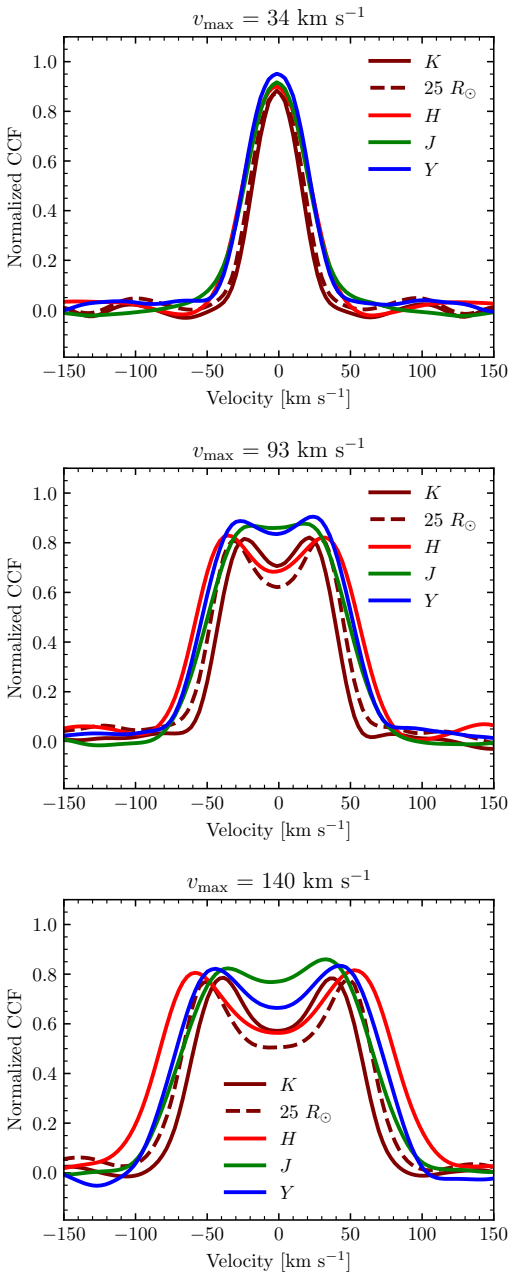

Figure 8.23: The CCFs produced from disk models with $R_{\rm outer}$ = 150 $R_\odot$ of the Y (blue), J (green), H (red), and K (brown) band NIRSPEC spectra. The brown dashed line shows the K band CCF produced from a disk model with $R_{\rm outer}$ = 25 $R_\odot$. Notice that the expected narrowing of line widths at longer wavelengths is stronger for larger $R_{\rm outer}$ and becomes negligible for small $R_{\rm outer}$ values.

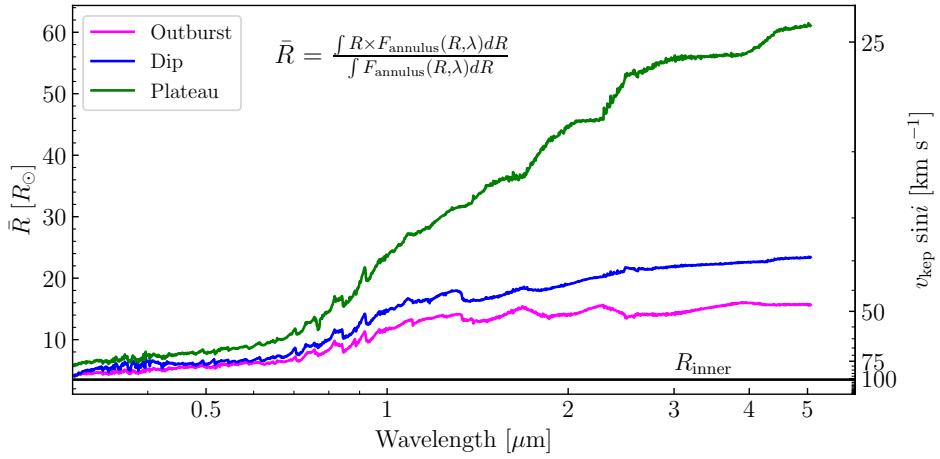

Figure 8.24: The flux-weighted mean radius from which the continuum for each wavelength bin arises. As the $R_{\rm outer}$ value for the disk model increases, the more the annuli at larger radii dominate the continuum NIR emission. At outburst, the K band continuum arises mostly from the $R \sim 12\ R_\odot$ region of the disk, whereas in the plateau the K band continuum probes out to $R \sim 45\ R_\odot$. However, the radii probed by the visible range (0.3 - 0.8 μm) are relatively unchanged.

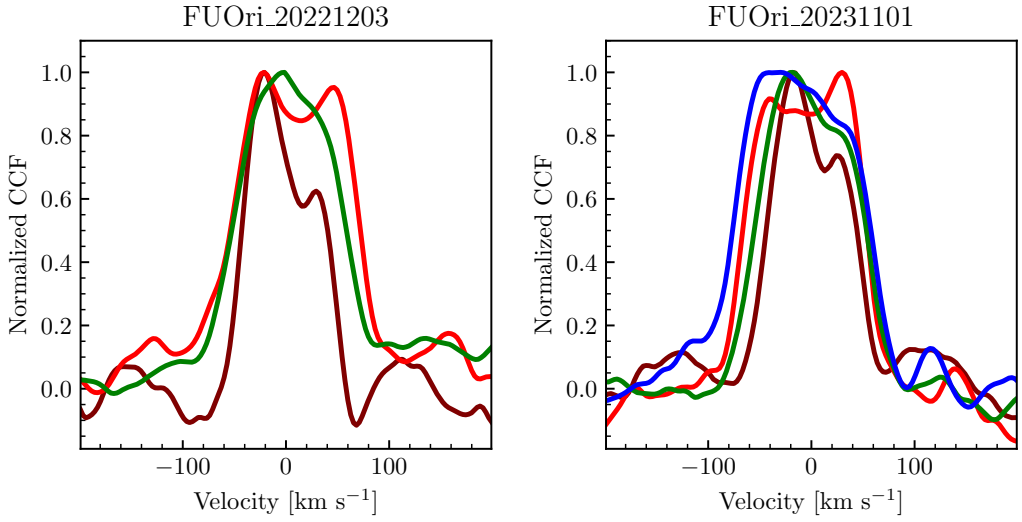

Figure 8.25: The CCFs of each band in the two NIRSPEC epochs for FU Ori. The blue line is Y band, green is J band, red is H band, and brown is K band. The profile shapes are relatively consistent between the epochs and show that in both cases, K band rotational broadening is less than at shorter wavelengths.

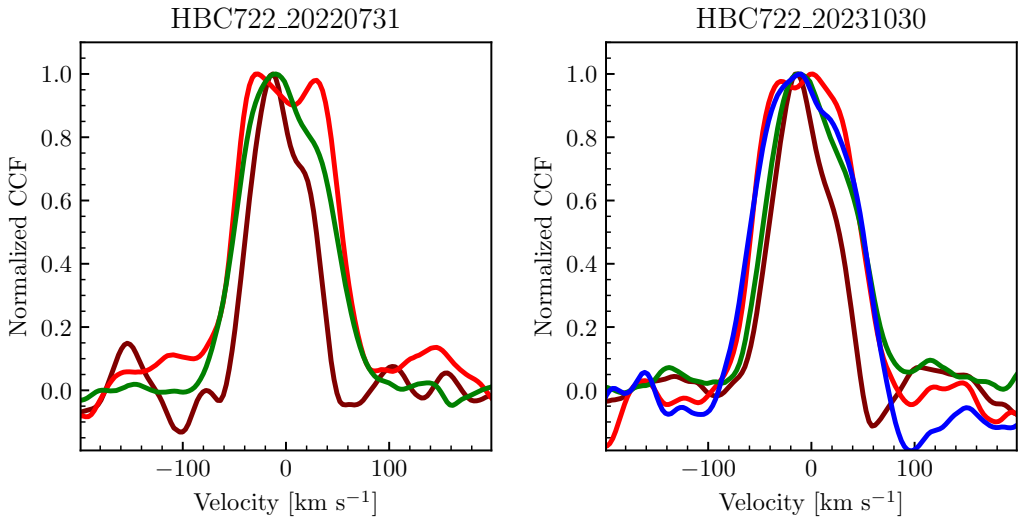

Figure 8.26: The same as Figure 8.25 but for HBC 722.

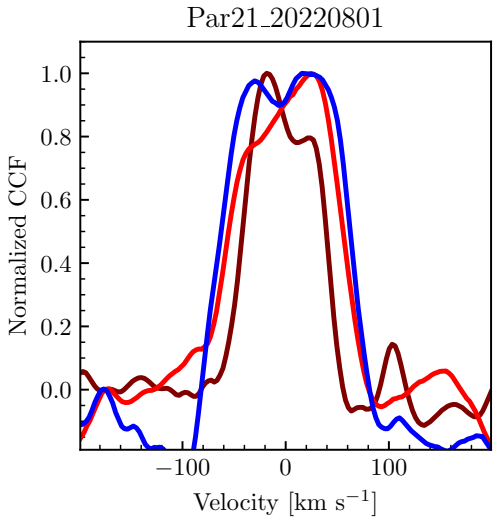

Figure 8.27: The same as Figure 8.25 but for Parsamian 21. Note that the spectra for Parsamian 21 were taken on 20220731 (J/H), 20220801 (K) and 20231101 (Y).

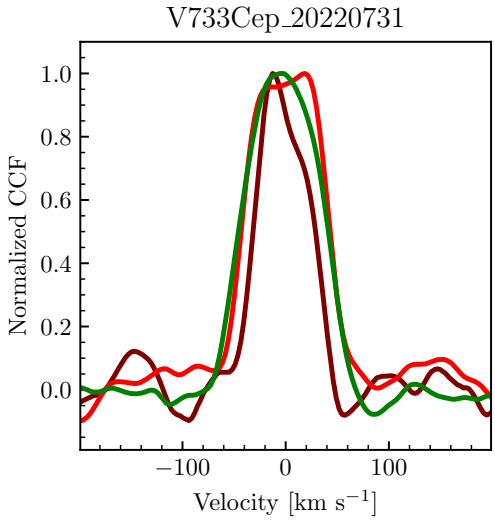

Figure 8.28: The same as Figure 8.25 but for V733 Cep.

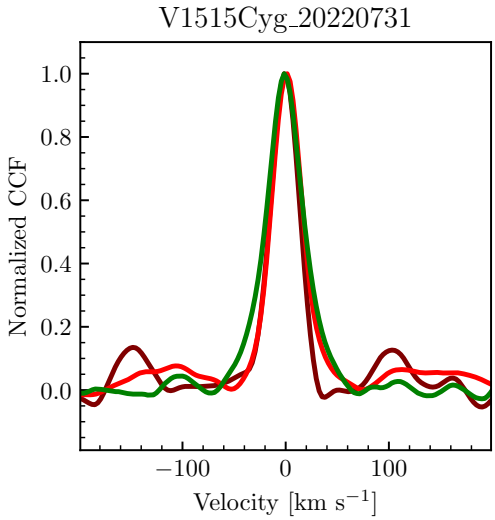

Figure 8.29: The same as Figure 8.25 but for V1515 Cyg.

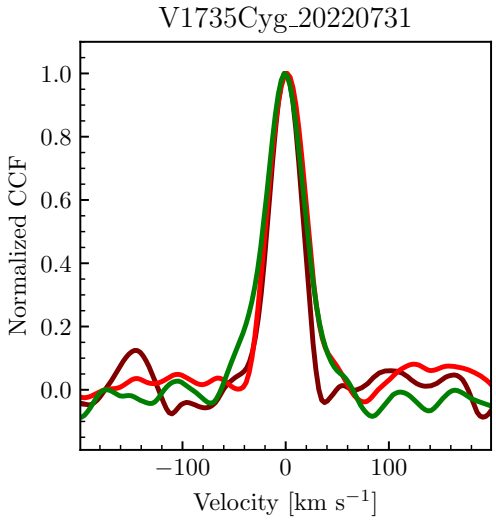

Figure 8.30: The same as Figure 8.25 but for V1735 Cyg.

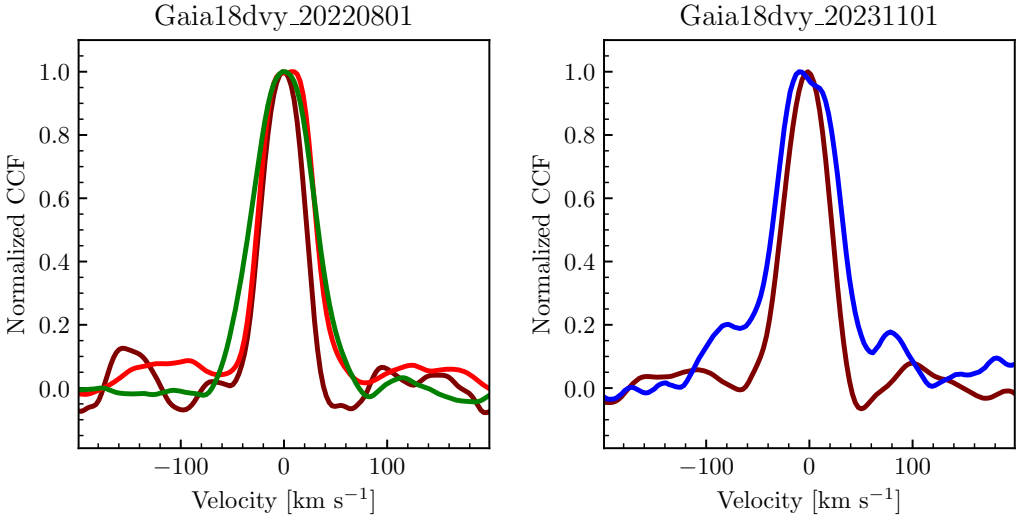

Figure 8.31: The same as Figure 8.25 but for Gaia 18dvy.

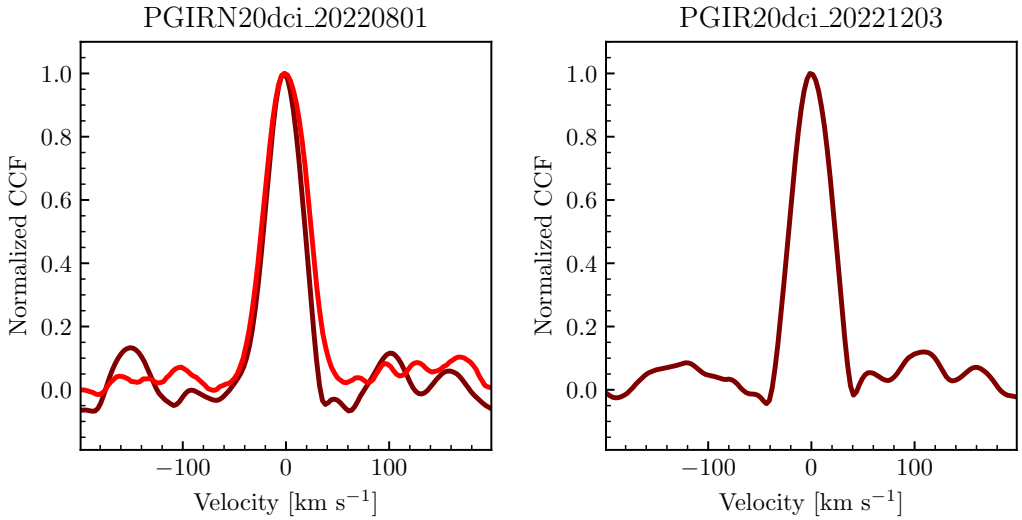

Figure 8.32: The same as Figure 8.25 but for PGIR 20dci.

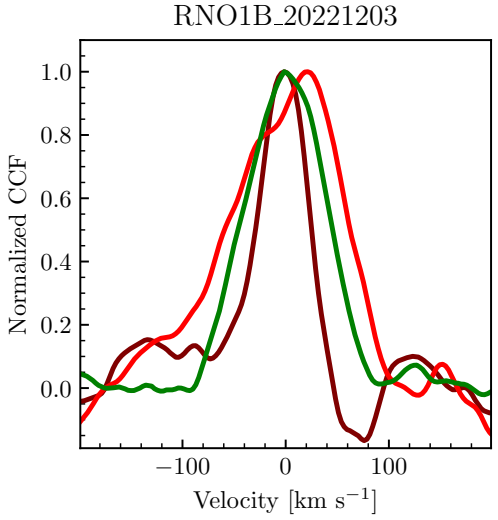

Figure 8.33: The same as Figure 8.25 but for RNO 1B.

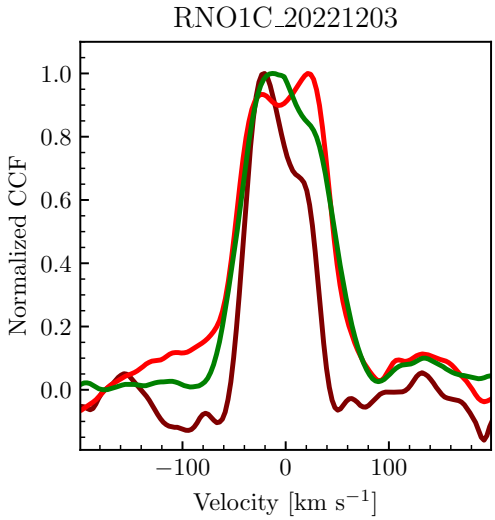

Figure 8.34: The same as Figure 8.25 but for RNO 1C.

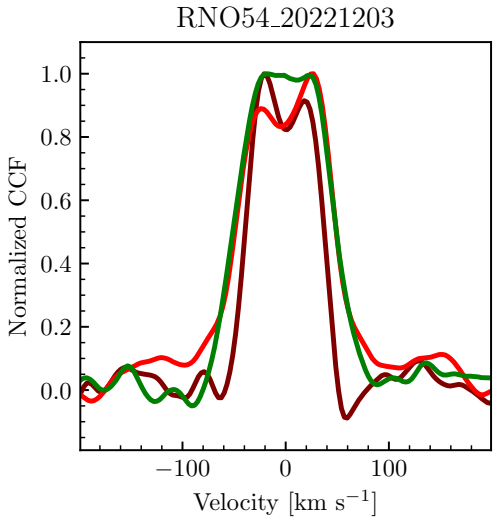

Figure 8.35: The same as Figure 8.25 but for RNO 54.

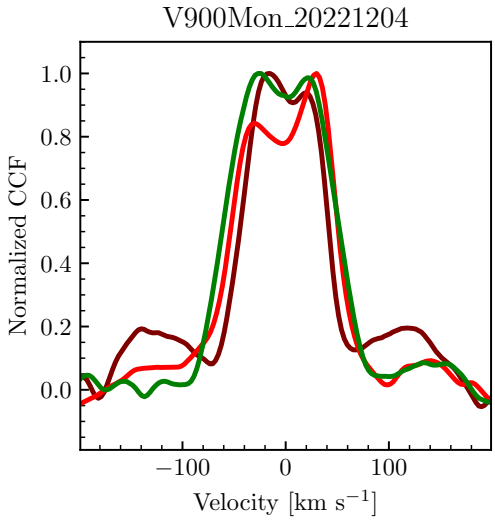

Figure 8.36: The same as Figure 8.25 but for V900 Mon.

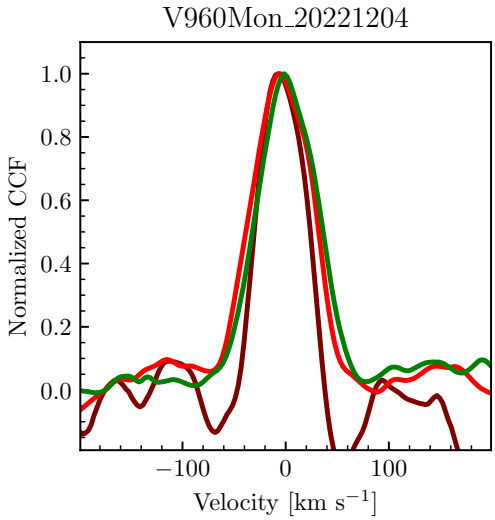

Figure 8.37: The same as Figure 8.25 but for V960 Mon.

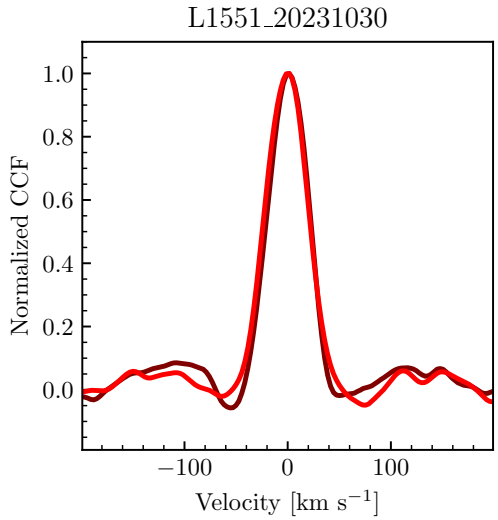

Figure 8.38: The same as Figure 8.25 but for L1551 IRS 5.

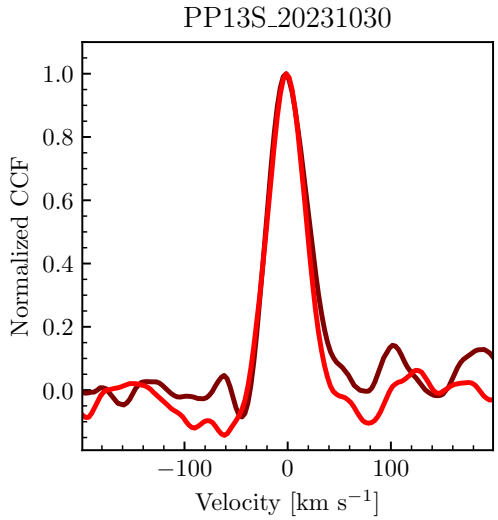

Figure 8.39: The same as Figure 8.25 but for PP 13S.

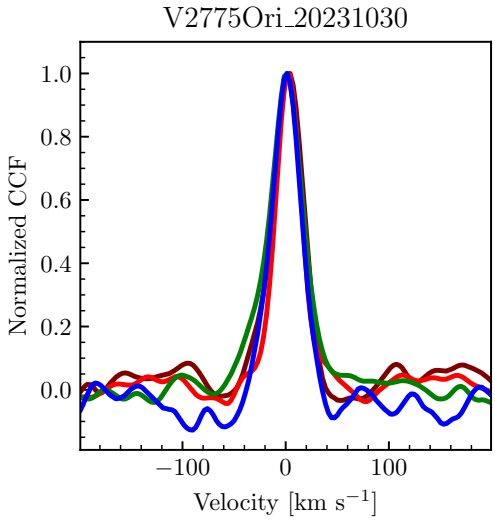

Figure 8.40: The same as Figure 8.25 but for V2775 Ori.

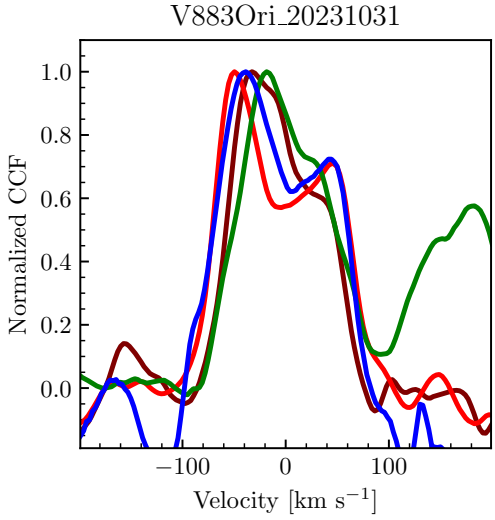

Figure 8.41: The same as Figure 8.25 but for V883 Ori.

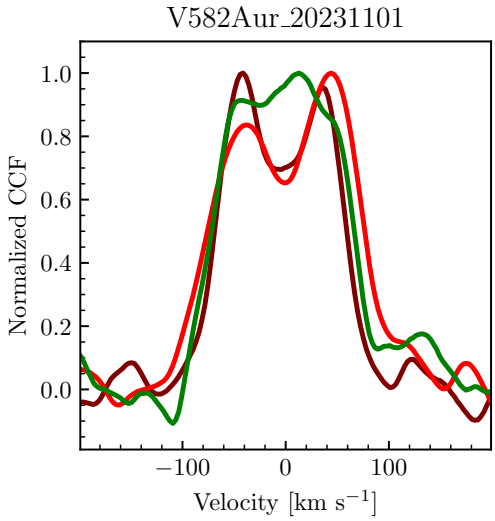

Figure 8.42: The same as Figure 8.25 but for V582 Aur.

Chapter 9

NEW PHYSICAL PARAMETERS FOR FOUR WELL-KNOWN FUORS

There are three well-known FUOrs that lack published physical parameters: BBW 76, V1057 Cyg, and V1515 Cyg. These objects are difficult to model for a variety of reasons. However, modeling them accurately became necessary to constrain the UV excess in the sources. Furthermore, these famous objects are accessible to several observatories, like ALMA and JWST, that enable investigation of the chemistry in the disk. Interpreting these observations requires detailed models for the radiation from the inner disk. It is also generally important to know as much as we can about each member of this relatively small class.

All three objects have faded over the past two decades. V1057 Cyg is much fainter than it was at the peak of its burst, while V1515 Cyg began a rapid decline in 2006 that has made it 1.5 mag fainter in 19 years. BBW 76 has been steadily fading in the past 30 years and the NIR has recently evolved dramatically from the typical NIR spectrum of a FUOr.

Modeling each of the objects required special consideration of evolution of the SED between observations. For all three objects, I combined the 2015 IRTF/SpeX spectrum from Connelley and Reipurth (2018) with the blue/visible HST/STIS spectrum taken in 2023/2024. The fading of all three objects can be attributed to their accretion rates decreasing, as photometric studies of all three have shown that the color evolution of the sources over this time period is inconsistent with increasing extinction (Siwak, Ogłoza, et al., 2020; Szabó, Kóspál, Ábrahám, Park, Siwak, Green, Moór, et al., 2021; Szabó, Kóspál, Ábrahám, Park, Siwak, Green, Pál, et al., 2022b). Thus, combining the 2015 NIR data with the 2023/2024 visible range data requires careful consideration of the color evolution of each object.

The fourth object I will disccuss in this Chapter is Gaia 17bpi. The outburst of the source is relatively unique for a FUOr, as it is low-luminosity and appears to potentially be short-lived, given the source has already faded by 2 mag since it attained its peak brightness in 2019/2020. The lightcurve of the source shows a pre-outburst NIR brightening (Hillenbrand, Peña, et al., 2018), which has been suggested to be evidence that the outburst began further out in the disk and moved

inward, a sign that it could have been triggered by gravitational instability (Cleaver et al., 2023).

In the following sections, I will detail the disk modeling for each object and the final determination of best-fit parameters. The general modeling procedure I follow has been described in detail in previous chapters, particularly Chapters 2, 3, and 5, so I will not repeat the description in this Chapter. Instead, I will focus on the results of the modeling. The distances I adopt for each source are reported in Table 2.1.

9.1 V1057 Cyg

The high resolution spectrum of V1057 Cyg was clearly that of a FUOr prior to 1996 (e.g., Welty, Strom, Edwards, et al., 1992). Since the fading event in 1994-1996, the spectrum has become wind-dominated and variable. Strong Fe I and Fe II lines show P Cygni profiles and, at times, even become purely emission features. The spectrum also shows variable [O I] 6363 Å, [S II] 6730 Å, and [Fe II] 7155 Å emission that is blue-shifted by $100 - 150$ km s^{-1}. There are almost no absorption features in the spectra of V1057 Cyg taken in the past 28 years that resemble their counterparts in other FUOrs. Nevertheless, the low resolution spectra of the source continue to resemble those of FUOrs (Connelley and Reipurth, 2018; Szabó, Kóspál, Ábrahám, Park, Siwak, Green, Moór, et al., 2021).

Given the inability to use NIR or visible range spectra taken since 1996 to constrain the $v_{\rm max}$ in V1057 Cyg, I adopted $v_{\rm max} = 40 \pm 10$ km s^{-1}. This is 10 km s^{-1} smaller than the value derived from high resolution disk model fitting by Welty, Strom, Edwards, et al. (1992). Given the significant photometric and spectroscopic evolution of V1057 Cyg in the 30 years since this measurement, it is likely that $v_{\rm max}$ of the source has decreased slightly in that time. Consider that the only parameter that could have changed in 30 years enough to impact $v_{\rm max}$ is $R_{\rm inner}$. Since $v_{\rm max} \propto R_{\rm inner}^{-1/2}$, a 10% change[1] in $v_{\rm max}$ would require a 20% increase in $R_{\rm inner}$. The resulting 20% decrease in $L_{\rm acc}$ and 15% decrease in $T_{\rm eff}$ is potentially consistent with the fading event in 1994-1996, and is similar to the estimated increase in $R_{\rm inner}$ estimated for V960 Mon in the years following the peak of its outburst (see Chapter 3).

I further constrain the fits by requiring that the models considered by the sampler have $4,500 < T_{\rm max}/{\rm K} < 6,500$. The lower temperature bound is set by the predicted very strong molecular absorption for cooler models, which is clearly not seen in the

[1] This is the typical uncertainty of the $v_{\rm max}$ measurements in Chapter 8.1.

SpeX spectrum. The upper temperature bound is set by the lack of a Balmer break in the HST/STIS spectrum. As can be seen in Figures 3.6 and 3.8, the models for V960 Mon near its outburst peak, when it had $T_{\rm max} \sim 8,000$ K, predict a strong Balmer break. Models with $T_{\rm max} > 6,500$ all show Balmer breaks much stronger than that seen in the NUV spectrum of V1057 Cyg (see Chapter 11 for that spectrum).

The posterior distributions of the physical parameters varied in the models, $\dot{M}$, M_*, $R_{\rm inner}$, $\cos i$, and A_V, are shown in Figure 9.1. As I did in Chapter 6, I also compute the posterior distributions for $T_{\rm max}$ and $L_{\rm acc}$ from the values of the physical parameters at each sample. The best-fit model, alongside the SpeX spectrum, is shown in Figure 9.3. The best-constrained parameters are $\log \dot{M} = -5.17^{0.15}_{-0.19}$ dex $M_\odot$ yr^{-1}, $R_{\rm inner} = 2.67^{+0.56}_{-0.07}$ $R_\odot$, and $A_V = 2.72^{+0.13}_{-0.46}$ mag. This A_V is smaller than the $A_V = 3.9 \pm 1.6$ mag reported by Connelley and Reipurth (2018), but agrees with their measurement within uncertainties.

The $\cos i$ posterior distribution generally favors very face-on inclination values, which yields a large uncertainty in the true $v_{\rm Kep}(R_{\rm inner})$ of the source and therefore a large uncertainty in M_*. A face-on inclination is consistent with the challenges Eisner and Hillenbrand (2011) found when trying to measure i from NIR interferometry. The best-fit median mass in the posterior distribution is $M_* = 1.61^{+0.77}_{-0.43}$ $M_\odot$, and $M_* > 2$ $M_\odot$ is clearly disfavored by the fits.

The pre-outburst photometry of V1057 Cyg suggests that M_* is unlikely to be < 1 $M_\odot$. According to Szabó, Kóspál, Ábrahám, Park, Siwak, Green, Moór, et al. (2021), the pre-outburst V band magnitude of V1057 Cyg was 14.5 ± 0.5. Assuming a source distance of 795 pc (Szabó, Kóspál, Ábrahám, Park, Siwak, Green, Moór, et al., 2021), the pre-outburst absolute V band magnitude was $M_V = 5 \pm 0.5$. According to a PARSEC 2 Myr isochrone (Nguyen et al., 2022), and assuming conservatively that the source pre-outburst had $A_V = 0$ (which is unlikely), $M_V = 5$ mag corresponds to $M_* = 1.5$ $M_\odot$. If $A_V = 1$ mag (2 mag), then $M_* \sim 2.0$ $M_\odot$ ($2.5 M_\odot$). For $M_* < 1$ $M_\odot$, $M_V > 6.2$, which means that the pre-outburst accretion luminosity would have to account for $\Delta V = 1.2$ of the source flux. This would require that $L_{\rm acc,preoutburst} = 3$ L_*, which is only attained assuming $\dot{M} > 10^{-6}$ $M_\odot$ yr $^{-12}$. Thus, the pre-outburst object would have to already be in an extreme accretion state.

[2]This is computed assuming that $L_{\rm acc} = (1 - R_*/R_{\rm inner}) G M_* \dot{M} / R_*$ and that $R_{\rm inner} \sim 2$ R_*, as reported in Pittman, Espaillat, Robinson, Thanathibodee, Lopez, et al. (2025).

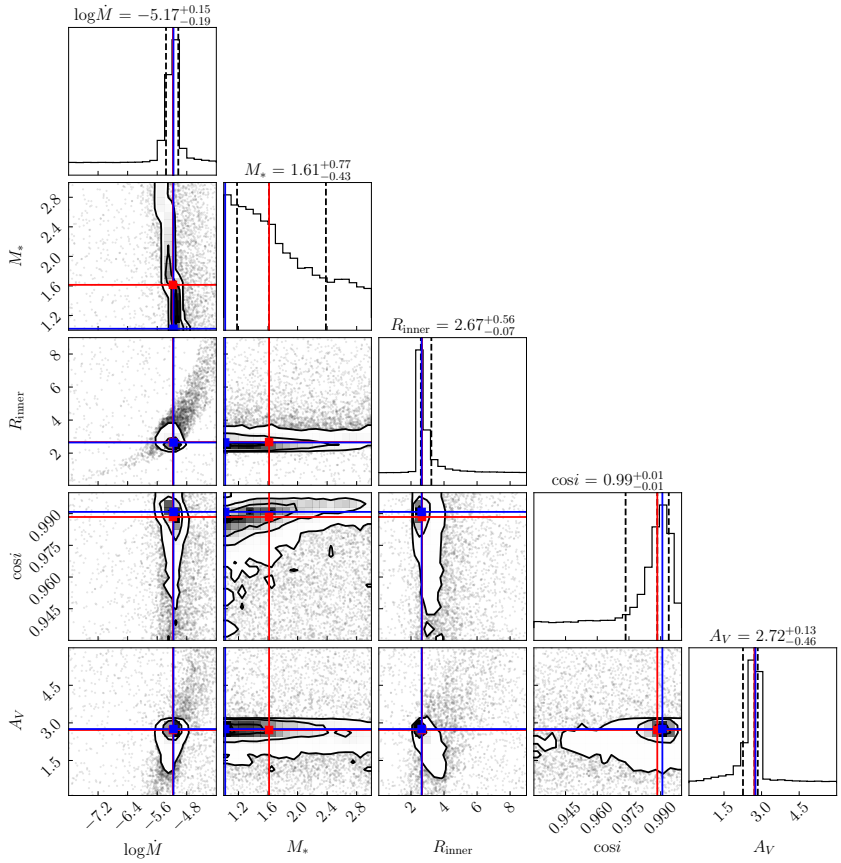

Figure 9.1: The posterior distribution for $\dot{M}$, M_*, $R_{\rm inner}$, $\cos i$, and A_V for the model fit to V1057 Cyg. The red lines mark the median values, blue lines mark modal values.

9.2 V1515 Cyg

I fit the SED of V1515 Cyg following a similar procedure as that described above for V1057 Cyg. For V1515 Cyg, the two spectroscopic epochs are 2015 (IRTF/SpeX from Connelley and Reipurth, 2018) and 2024 (HST/STIS from Carvalho et al., 2025b, submitted). For this source, the $v_{\rm max}$ value is more difficult to constrain, since it is consistently below the typical spectral resolution of observations. Nevertheless, it is clear that the object is extremely face-on, which produces the narrow absorption lines. This is also suggested by the difficulty in fitting an inclination to the interferometric data of the source (Eisner and Hillenbrand, 2011).

The face-on inclination makes constraining the mass of the object with any $v_{\rm max}$ value nearly impossible. Without an extremely precise inclination measurement of V1515 Cyg, small decreases in i yield large possible increases in the M_* parameter. The difference between 1° and 2° inclination in this context is equivalent to a factor

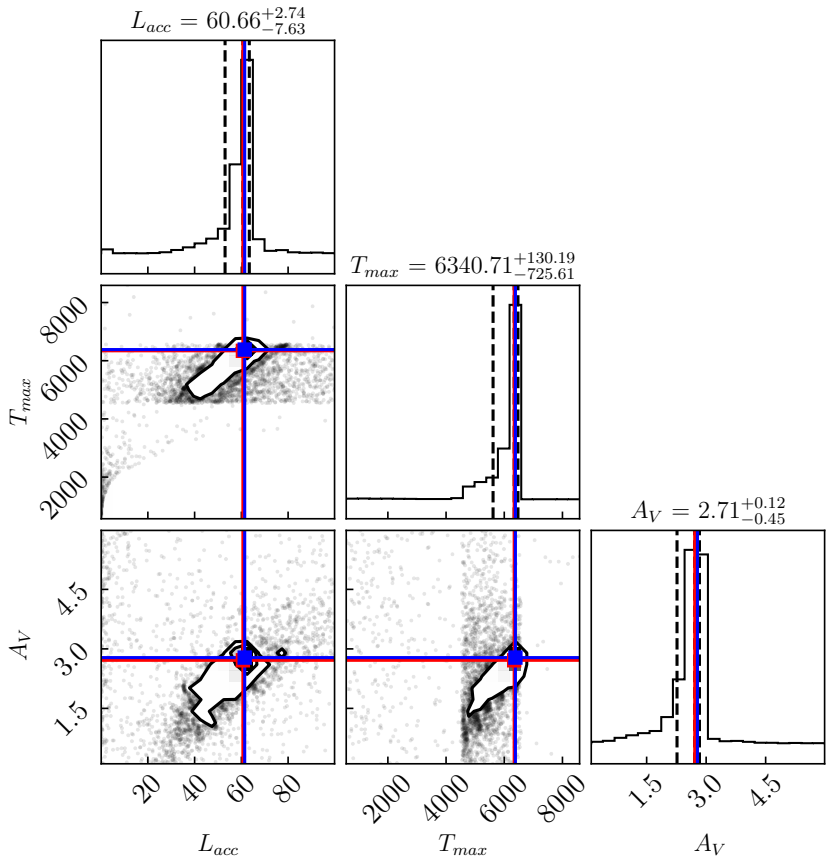

Figure 9.2: The posterior distribution for $T_{\rm max}$, $L_{\rm acc}$, and A_V of V1057 Cyg.

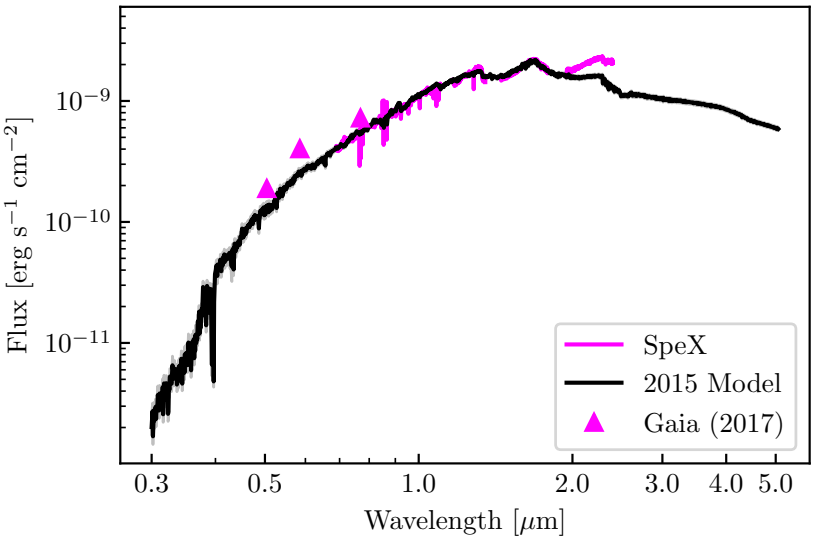

Figure 9.3: The best-fit models V1057 Cyg model compared with the SpeX spectrum to which it was fit. Gaia photometry is included for approximate reference of the the visible range flux of the source near the epoch of the 2015 SpeX observation.

of 2 increase in $(v_{\rm max}/\sin(i))^2 \propto M_*/R_{\rm inner}$.

To fit the two epochs jointly, I allowed the model to vary two values of $\dot{M}$, while requiring that the chosen M_*, $R_{\rm inner}$, i, and A_V be used to model both datasets at each sampler step. This, of course, assumes that a decreasing $\dot{M}$ is driving all of the visible range variation. As demonstrated in Chapter 3 for V960 Mon, this is not strictly always the case and other parameters like $R_{\rm inner}$ may evolve during the outburst as well. It is also possible that A_V might have increased during this time. Nevertheless, both data epochs are well-fit by varying only $\dot{M}$, so I adopted this simpler model. Following the same reasoning as in V1057 Cyg, I restricted the allowed temperature range for both epochs to be $4,500 < T_{\rm max}/{\rm K} < 6,500$.

The posterior distributions from the nested sampling are shown in Figure 9.4. The most tightly constrained parameters in the fit are $R_{\rm inner} = 1.82^{+0.21}_{-0.03}\ R_\odot$ and $A_V = 2.23^{+0.09}_{-0.17}$ mag. While both $\dot{M}$ and M_* have bimodial posterior distributions, the parameter $\dot{M}M_*$ is well-constrained on both cases. In 2015, the best-fit $\dot{M}_1 M_* = 10^{-5.44\pm0.03}\ M_\odot^2\ {\rm yr}^{-1}$ and $\dot{M}_2 M_* = 10^{-5.62\pm0.05}\ M_\odot^2\ {\rm yr}^{-1}$.

Although M_* is not very well-constrained in this source, the posterior distribution still shows that it is likely in the range $0.2 - 1.1\ M_\odot$. The distribution favors two potential solutions in that range: $M_* = 0.3 \pm 0.1\ M_\odot$ and $M_* = 1.0 \pm 0.1\ M_\odot$. Following a similar exercise as above, it is possible to consider the pre-outburst $B = 17.5 \pm 0.2$ mag (Szabó, Kóspál, Ábrahám, Park, Siwak, Green, Pál, et al., 2022a), which is $M_B = 7.6$. if $A_V = 0$ mag, the PARSEC 2 Myr isochrone again indicates that $M_* > 0.9\ M_\odot$. While accounting accretion excess, which is greater at B band than at V band, allows for smaller M_* values, the A_V is unlikely to be 0, requiring a brighter M_B. Thus, the greater mass, $M_* = 1.0\ M_\odot$ is favored.

The decreased accretion rate between 2015 and 2024 matches the steady fading of the source that began in 2005 (Szabó, Kóspál, Ábrahám, Park, Siwak, Green, Pál, et al., 2022a). The best fit luminosities and temperatures for each epoch were: $L_{\rm acc,1} = 31.5^{+1}_{-2}\ L_\odot$, $T_{\rm max,1} = 6526^{+28}_{-450}$ K, $L_{\rm acc,2} = 21.6^{+2}_{-2}\ L_\odot$, and $T_{\rm max,2} = 5862^{+50}_{-280}$ K. The posterior distributions for these, constructed from the values of the physical parameters in the samples are shown in Figure 9.5.

Applying the K band bolometric correction to the peak $K \sim 7$ mag brightness of V1515 Cyg, which it reached in 1974 (Szabó, Kóspál, Ábrahám, Park, Siwak, Green, Pál, et al., 2022a), and $A_V = 2.23$ mag, shows the source had a peak $L_{\rm acc} = 70\ L_\odot$. Assuming the luminosity change is entirely driven by $\dot{M}$, the peak

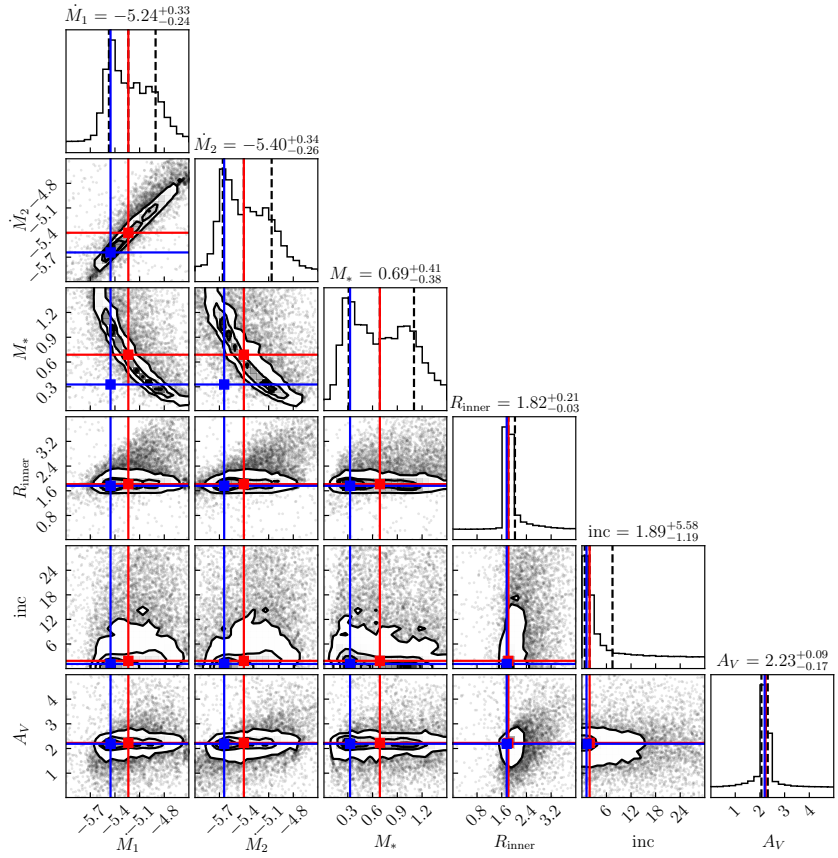

Figure 9.4: The posterior distribution for $\dot{M}_1$, $\dot{M}_2$, M_*, $R_{\rm inner}$, $\cos i$, and A_V for the model fit to V1515 Cyg.

$\dot{M}M_*$ of V1515 Cyg was $10^{-5.06}$ $M_\odot^2$ yr^{-1}. For $M_* = 0.3$ $M_\odot$, this corresponds to $\dot{M} = 10^{-4.54}$ $M_\odot$ yr^{-1}.

The best-fit models for the two spectroscopic epochs are shown in Figure 9.6. The models follow the spectroscopic evolution of the source well, despite the lack of visible range data to constrain the 2015 model.

9.3 BBW 76

As with V1515 Cyg, the two spectral epochs used to fit BBW 76 were the 2015 SpeX spectrum from (Connelley and Reipurth, 2018) and the 2023 HST/STIS spectrum from Carvalho et al. (2025b, submitted). I imposed the same temperature constraints on the models as for the two sources above, and followed the two-epoch fitting procedure described for V1515 Cyg. The posterior distributions of the fit are shown in Figure 9.7. The $L_{\rm acc}$ and $T_{\rm max}$ distributions for each epoch are given in Figure 9.8. The best-fit models, along with the two spectra used in the fits, are

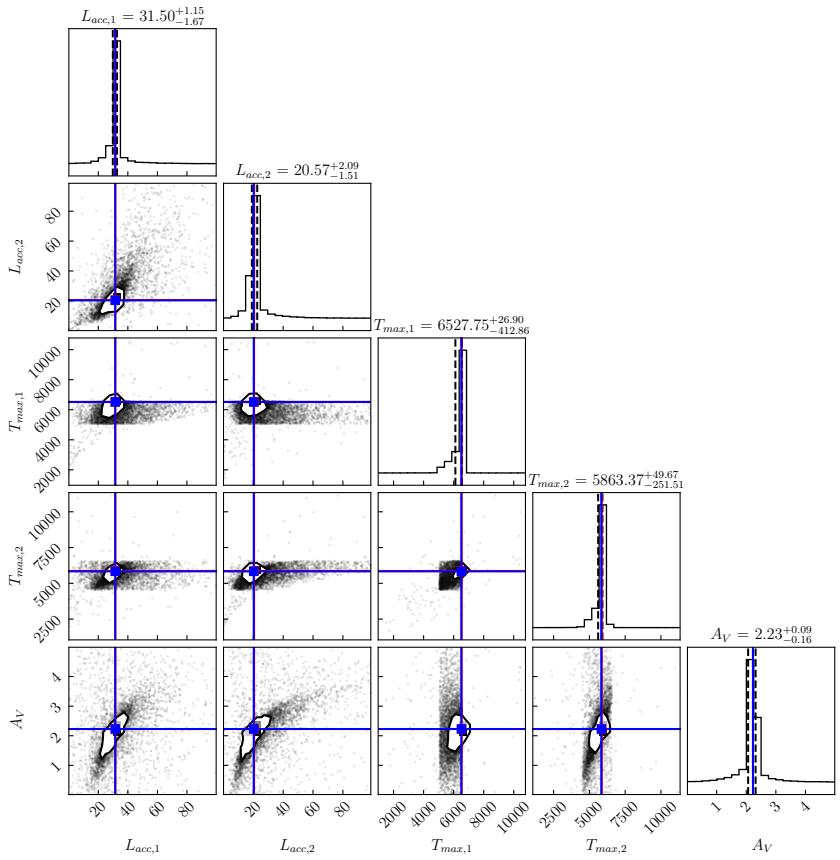

Figure 9.5: The posterior distribution for $T_{\rm max}$, $L_{\rm acc}$, and A_V of V1515 Cyg.

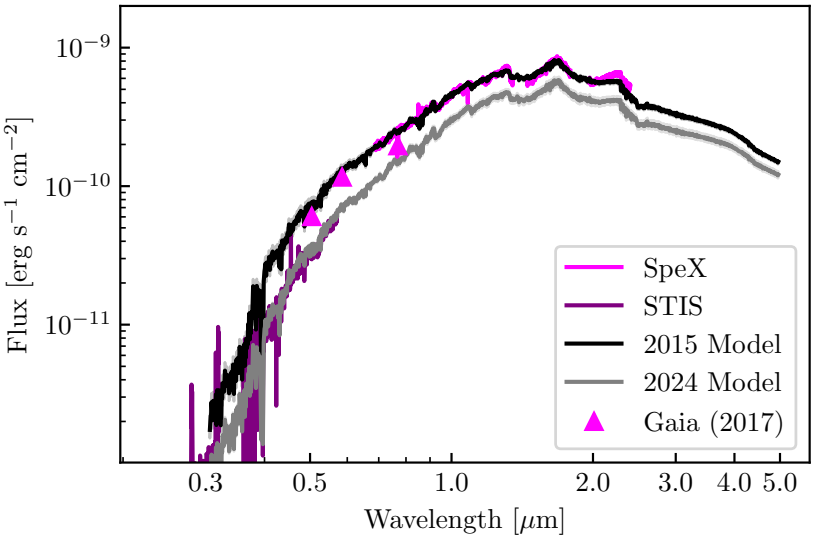

Figure 9.6: The best-fit models for each epoch of V1515 Cyg spectra, compared with the observed spectra. Gaia $G_{\rm BP}$, G, and $G_{\rm RP}$ data, taken in 2017 between the spectroscopic epochs, is plotted to show the photometric decline of the source.

presented in Figure 9.9.

For BBW 76, the source inclination is well-constrained to $i = 15^{+15}_{-5}$ degrees, which agrees well with the $i = 20^{+48}_{-3}$ degrees found for the outer disk using ALMA (Kóspál, Cruz-Sáenz de Miera, et al., 2021). The $A_V = 0.43^{+0.35}_{-0.14}$ mag is in mild disagreement with the $A_V = 1.6 \pm 0.2$ mag reported by (Connelley and Reipurth, 2018), but this may be due to some of the uncertainty in the method adopted by those authors when measuring small A_V, as discussed in Chapter 2.

The constraint on M_* is not particularly tight, but the fit clearly prefers solutions with $M_* < 0.5\ M_\odot$, with modal value of $M_* = 0.2\ M_\odot$ for the posterior distribution. The best-fit $R_{\rm inner} = 1.41^{+0.57}_{-0.05}\ R_\odot$ is reasonable for the low mass of the source. As is the case for V1515 Cyg, the $\dot{M}M_*$ values for both epochs are well-constrained, with $\dot{M}_1 M_* = 10^{-5.81\pm0.05}\ M_\odot^2\ {\rm yr}^{-1}$ and $\dot{M}_2 M_* = 10^{-6.0\pm0.1}\ M_\odot^2\ {\rm yr}^{-1}$. Adopting $M_* = 0.2\ M_\odot$, the values become $\dot{M}_1 = 10^{-5.12\pm0.05}\ M_\odot\ {\rm yr}^{-1}$ and $\dot{M}_2 = 10^{-5.3\pm0.1}\ M_\odot\ {\rm yr}^{-1}$.

The NEOWISE photometry of BBW 76 shows that it has been steadily fading over the last 15 years. The decreasing $L_{\rm acc}$ we find between 2015 and 2024 agree with this, as the source $L_{\rm acc}$ is now 6 $L_\odot$ fainter than in 2015. The constant-temperature bolometric corrections in Chapter 7 can be used to compute the luminosity of the source in 1983 using the $K = 7.4$ mag reported in Reipurth, Hartmann, et al. (2002). Assuming the source distance of 1040 pc and $A_V = 0.42$ mag, the $L_{\rm acc} = 50\ L_\odot$ in 1983. Reipurth, Hartmann, et al. (2002) argue that the source has been in outburst since before 1900, and that it must have had approximately its same brightness (i.e., $V \sim 11 - 12$). Thus, it is likely that the peak luminosity of BBW 76 was $L_{\rm acc,peak} < 100\ L_\odot$ and probably $L_{\rm acc} \sim 50\ L_\odot$.

9.4 Gaia 17bpi

When Gaia 17bpi was first detected and reported as a FUOr, it was the lowest-luminosity FUOr in the literature (Hillenbrand, Peña, et al., 2018). Attempts to fit its SED by Rodriguez and Hillenbrand (2022) and Cleaver et al. (2023) have in the past found a $M_* \sim 0.6\ M_\odot$ and a $R_{\rm inner} = 0.65\ R_\odot$ were necessary to match the SED. This mass radius combination, however, requires a much denser star than is expected for pre-main sequence protostars. For a system with an age of 2 Myr, which is typical for regions mostly populated by Class I/II YSOs (Manara et al., 2023), the stellar radius for $M_* = 0.6\ M_\odot$ is $R_* \sim 1.5\ R_\odot$ (Baraffe et al., 2015).

As shown in Chapter 2, the $L_{\rm acc}$ derived from bolometric corrections is $\sim 3 - 7\ L_\odot$, consistent with notion that it is one of the lowest luminosity FUOrs known. The

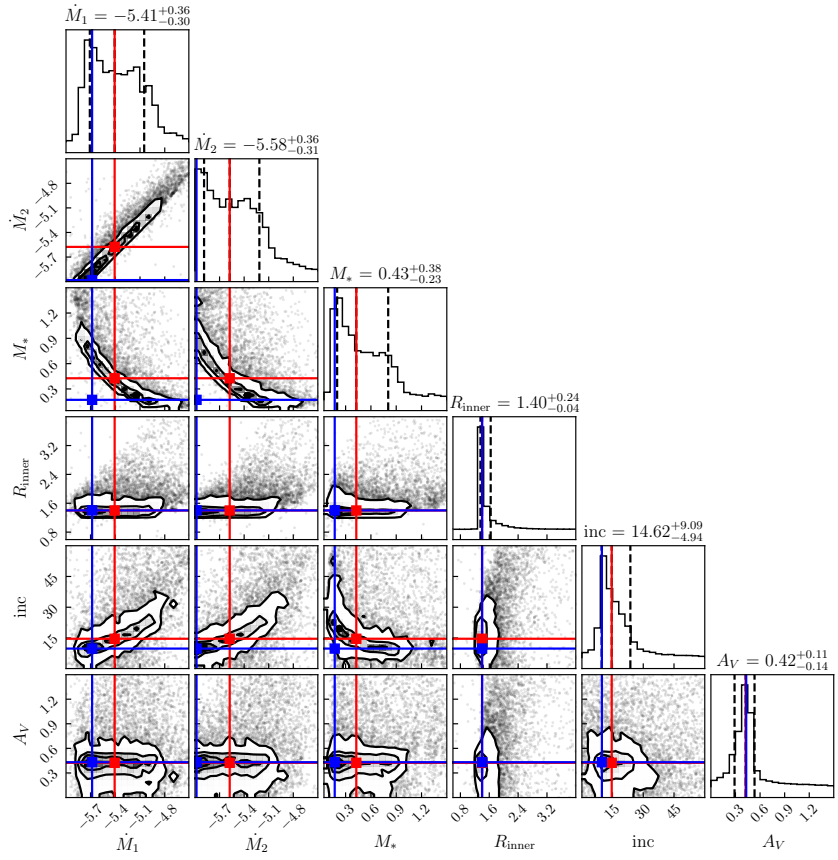

Figure 9.7: Same as Figure 9.7 for BBW 76.

medium resolution spectrum of the source lacks particularly deep molecular features like TiO or VO that might be expected for a very low $T_{\rm max}$, suggesting $T_{\rm max} > 5,500$ K. Considering the relations dictating $T_{\rm max}$ and $L_{\rm acc}$ (Equations 1.1 and 1.2), it is possible to relate $T_{\rm max}$ to $L_{\rm acc}$ via $R_{\rm inner}$,

$$T_{\rm max}^4 = \frac{3}{4\pi\sigma_{SB}} \left(\frac{6^6}{7^7}\right) \frac{L_{\rm acc}}{R_{\rm inner}^2}. \tag{9.1}$$

Thus, for the maximum $L_{\rm acc} = 7\ L_\odot$ estimated for Gaia 17bpi and assuming the coolest likely $T_{\rm max}$, the maximum $R_{\rm inner} = 1.2\ R_\odot$. The question remains then if, then, Gaia 17bpi might not simply be a low mass FUOr, like HBC 722, RNO 54, or V890 Aur. Turning again to the 2 Myr Baraffe et al. (2015) isochrone, a star with $R_* = 1.2\ M_\odot$ should have $M_* \sim 0.3\ M_\odot$. To observe the mean $v_{\rm max} = 215 \pm 30$ km s^{-1} measured in Chapter 8 for Gaia 17bpi is possible for $i > 80°$.

Constructing a single-epoch spectrum of Gaia 17bpi is challenging because of the rapid photometric evolution of the source. The particular challenge is in matching

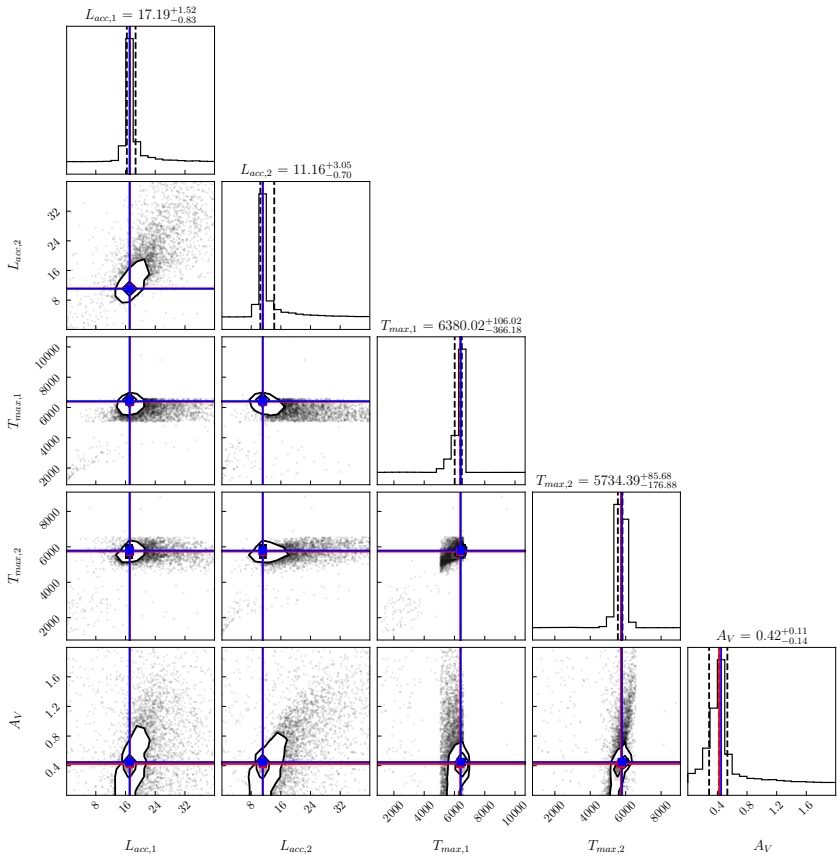

Figure 9.8: Same as Figure 9.8 for BBW 76.

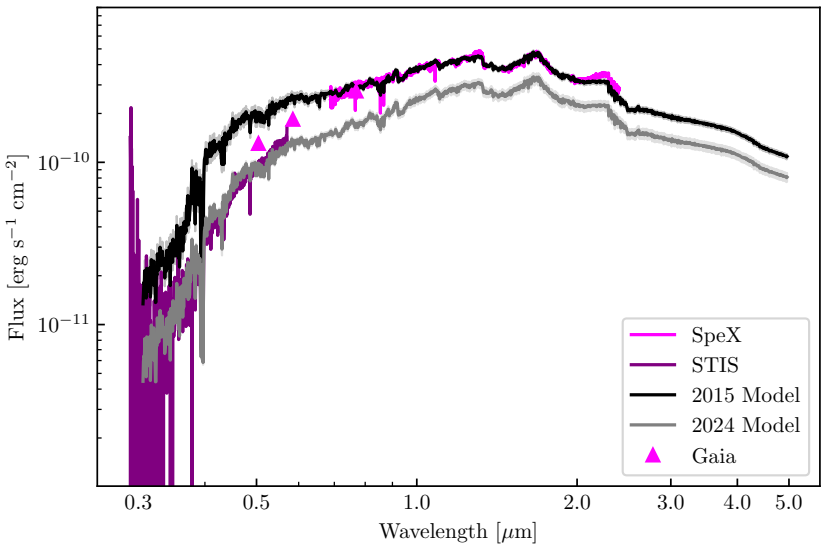

Figure 9.9: The best-fit models for BBW 76 for the 2015 and 2023 observations. Gaia photometry from 2017 is included to mark the steady visible range decline in the source.

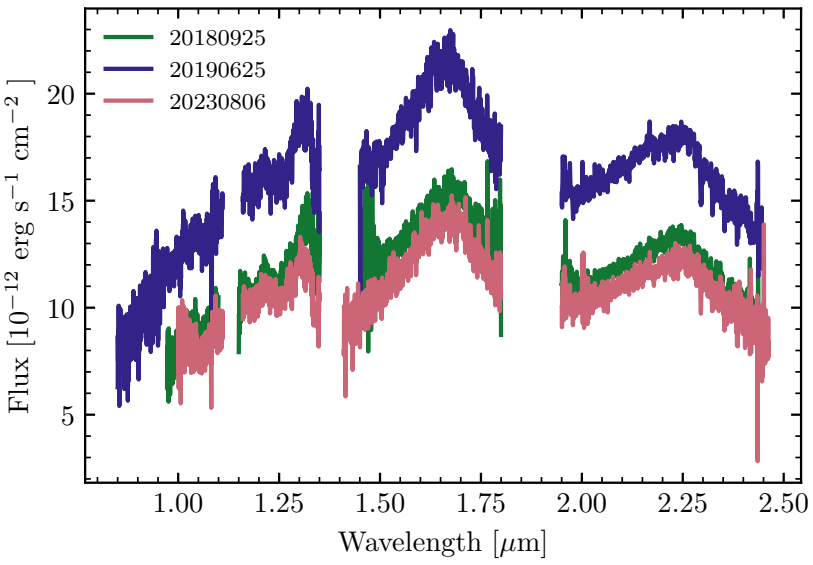

Figure 9.10: The NIR evolution of Gaia 17bpi, from 2018 to 2023. Despite the relatively large change in flux, there is little change in the slope, resulting in a surprisingly colorless evolution. This is not unprecedented – HBC 722 showed similarly little color evolution when it faded in 2012 (Carvalho, Hillenbrand, Seebeck, and Covey, 2024).

a flux-calibrated visible range spectrum to an available NIR spectrum of the source. The Palomar/TSPEC (NIR) and Palomar DBSP (visible) spectra published in Rodriguez and Hillenbrand (2022) were taken in June and July, 2019, respectively. In that month, specifically, Gaia 17bpi underwent a rapid and deep photometric decline (see Figure 2.9 in Chapter 2). Therefore, it is necessary to color-correct the DBSP spectrum to match the flux level and spectral slope it would have had during the TSPEC epoch. While Rodriguez and Hillenbrand (2022) apply a flat grey-body correction to the flux, I apply a power-law correction to match the contemporaneous ZTF photometry of the source.

To mitigate the potential bias that this necessary correction might impose on a single-epoch fit to Gaia 17bpi, I include the TSPEC spectrum published in Hillenbrand, Peña, et al. (2018). The 2018 epoch lacks a contemporaneous visible range spectrum, so I apply a similar color correction to the 2019 DBSP spectrum using the ZTF photometry for the dates of the TSPEC observation. I then perform a 2 epoch fit similar to that for the objects in previous sections. Since the spectroscopic evolution of Gaia 17bpi appears especially colorless (see Figure 9.10), I allow both $R_{\rm inner}$ and A_V to vary between epochs, in addition to $\dot{M}$.

The posterior distributions for the fit are shown in Figures 9.11 and 9.12. The best-fit models for each epoch are shown in Figure 9.13. The mass of the source is well-constrained at $M_* = 0.2 \pm 0.03\ M_\odot$. The best-fit $R_{\rm inner}$ for both epochs are essentially equal: $R_{\rm inner,1} = 0.82 \pm 0.03\ R_\odot$ and $R_{\rm inner,2} = 0.80 \pm 0.01\ R_\odot$. Although these radii are still a bit small, they are reasonable for a 0.2 M_* protostar at an age of 4 Myr. The best-fit $\dot{M}_1 = 10^{-5.84\pm0.03}\ M_\odot\ {\rm yr}^{-1}$ and $\dot{M}_2 = 10^{-5.65\pm0.06}\ M_\odot\ {\rm yr}^{-1}$. Although the accretion rate increases as the outburst peaks, this is slightly offset by a 0.3 mag increase in A_V, as $A_{V,1} = 2.12 \pm 0.1$ mag and $A_{V,2} = 2.45 \pm 0.06$ mag. This may explain why the brightening and fading of the source near the peak of the outburst appear relatively colorless.

The best-fit $\cos i = 0.19$ is equivalent to $i = 80°$, as discussed above. Although this is only a 5° and $0.2 - 0.3$ mag difference from the i and A_V values used in the bolometric corrections to the lightcurve presented in Chapter 2, the $L_{\rm acc}$ values increase to $6 - 9\ L_\odot$, compared to the $3 - 7\ L_\odot$ estimated previously. Gaia 17bpi remains one of the lowest-luminosity FUOrs yet discovered, but this example demonstrates the importance of precise constraints on the inclination to the source, especially when the source is nearly edge-on.

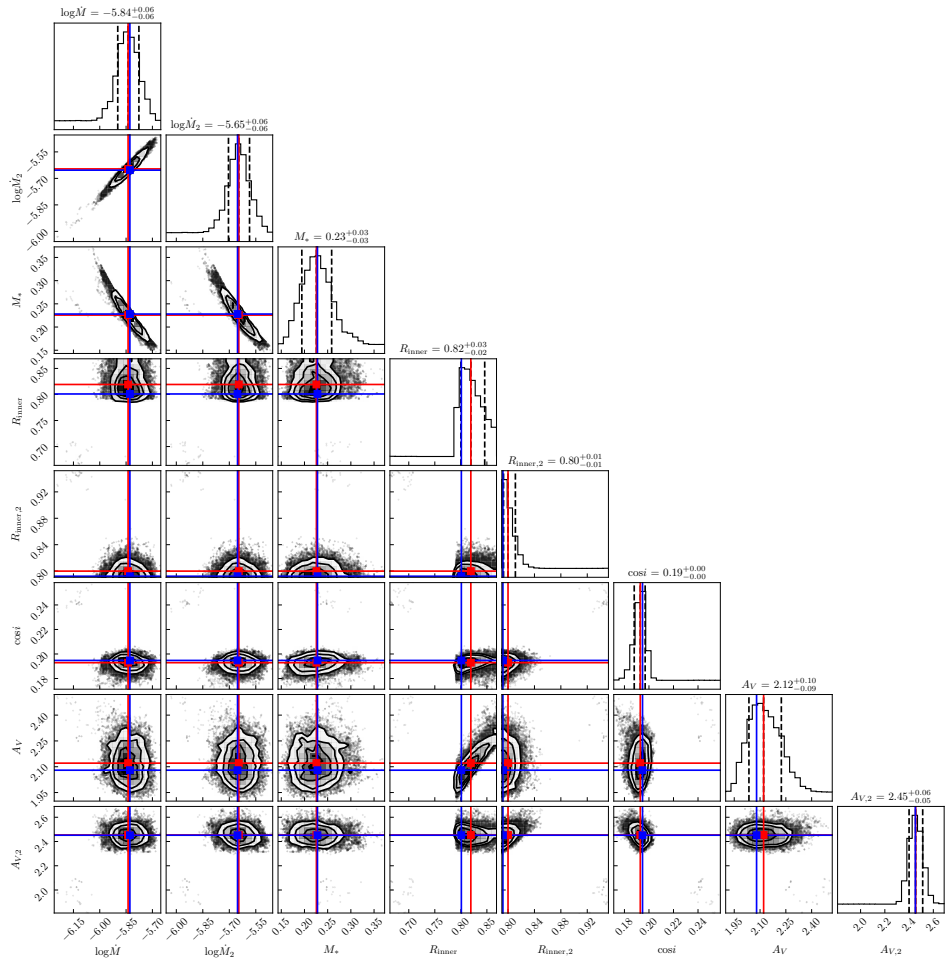

Figure 9.11: The posterior distributions for the 7 parameter 2 epoch SED fit for Gaia 17bpi.

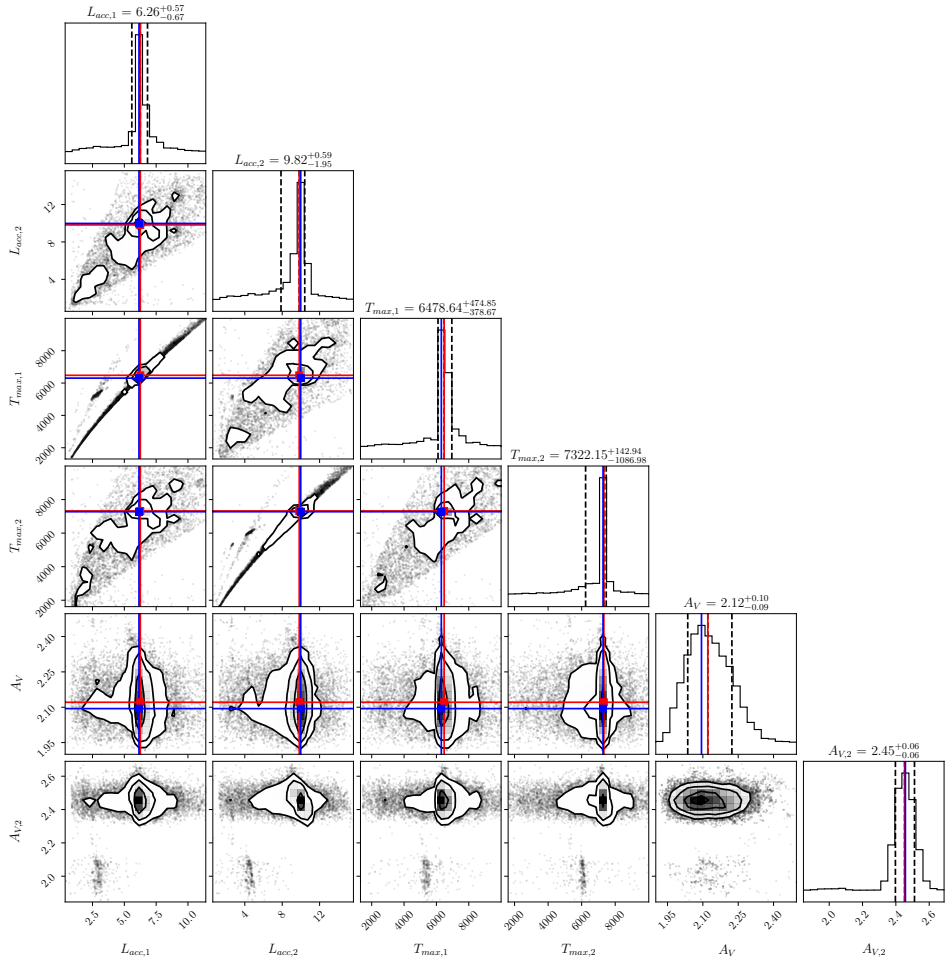

Figure 9.12: The $L_{\rm acc}$, $T_{\rm max}$, and A_V distributions for each epoch in the Gaia 17bpi SED fit.

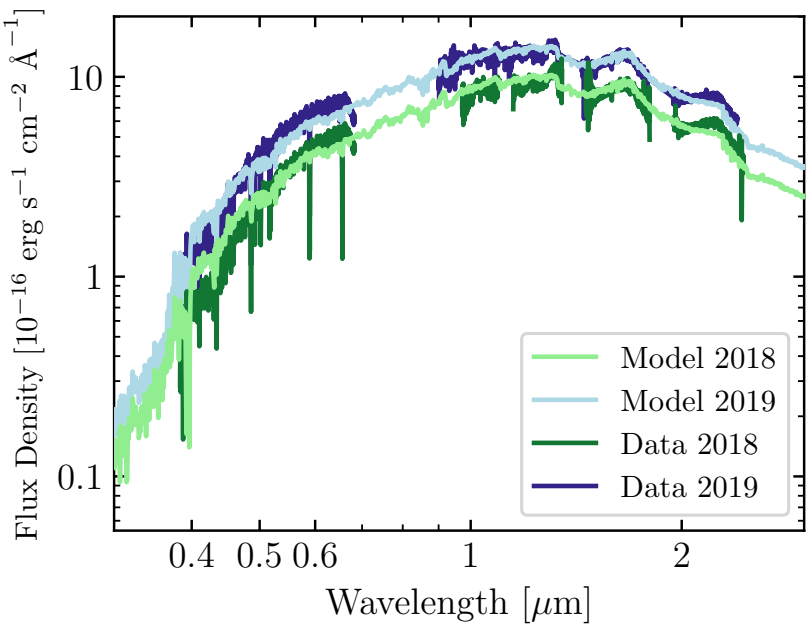

Figure 9.13: The two-epoch best-fit models for Gaia 17bpi.

Chapter 10

AN FUV-DETECTED ACCRETION SHOCK AT THE STAR-DISK BOUNDARY OF FU ORI

Carvalho, Adolfo S., Lynne A. Hillenbrand, Kevin France, and Gregory J. Herczeg (Oct. 2024). "A Far-ultraviolet-detected Accretion Shock at the Star–Disk Boundary of FU Ori." In: *ApJL* 973.2, L40, p. L40. DOI: 10.3847/2041-8213/ad74eb. arXiv: 2408.11033 [astro-ph.SR].

Abstract: FU Ori objects are the most extreme eruptive young stars known. Their 4 to 5 magnitude photometric outbursts last for decades and are attributed to a factor of up to 10,000 increase in the stellar accretion rate. The nature of the accretion disk-to-star interface in FU Ori objects has remained a mystery for decades. To date, attempts to directly observe a shock or boundary layer have been thwarted by the apparent lack of emission in excess of the accretion disk photosphere down to $\lambda = 2300$ Å. We present a new NUV and the first high-sensitivity FUV spectrum of FU Ori. The FUV continuum is detected for the first time and, at $\lambda = 1400$ Å, is more than 10^4 times brighter than predicted by a viscous accretion disk. We interpret the excess as arising from a shock at the boundary between the disk and the stellar surface. We model the shock emission as a blackbody and find that the temperature of the shocked material is $T_{\rm FUV} \approx 16,000 \pm 2000$ K. The shock temperature corresponds to an accretion flow along the surface of the disk that reaches a velocity of 40 km s^{-1} at the boundary, consistent with predictions from simulations.

10.1 Introduction

FU Ori is a young stellar object (YSO) that underwent an enormous photometric outburst in 1937 (Wachmann, 1954; Herbig, 1966). As other outbursting YSOs were discovered in the following decades (Herbig, 1977), the nature of the outbursts was eventually understood as a sudden increase in stellar mass accretion rate (Hartmann and Kenyon, 1996). FU Ori became the prototype for these outbursting YSOs, and FU Ori objects came to represent the most rapidly accreting YSOs known.

In this interpretation, FU Ori objects are classical T Tauri stars (CTTSs) that have undergone a disk instability and, as a result, their accretion rates increased from

the typical CTTS rate of 10^{-8} $M_\odot$ yr^{-1} to 10^{-4} $M_\odot$ yr^{-1}. Kenyon, Hartmann, and Hewett (1988) demonstrated that the absorption line profiles and spectral energy distributions from FU Ori objects were consistent with those predicted by a modified version of the Shakura and Sunyaev (1973) viscous accretion disk model. However, unlike the situation for the Shakura and Sunyaev (1973) theory that had been developed for black hole disk accretion, CTTS have finite radius. This necessitates both a different form for the temperature profile at small radii in the disk, and revised expectations regarding a “boundary layer" between the disk and the star (Lynden-Bell and Pringle, 1974a; Pringle, 1981).

For CTTS, it is generally accepted that accreting material is transported along stellar magnetic field lines and deposited near the poles of the star. Observed blue optical and ultraviolet excess emission, relative to non-accreting young stars of the same spectral type, is then understood as matter shocking onto the stellar photosphere at free-fall velocities (Uchida and Shibata, 1984; Koenigl, 1991; Valenti, Basri, et al., 1993; Calvet and Gullbring, 1998). For FU Ori objects the detailed structure of the accretion boundary layer, which is expected to be equatorial, remains largely unconstrained.

Popham, Narayan, et al. (1993) developed a boundary layer model in which the angular momentum transport efficiency onto the star governed the excess heating at the disk-star interface and led to different temperature profiles parameterized by that efficiency. They then used their model to predict the resulting temperature profiles and observed SEDs and line profiles of FU Ori objects (Popham, Kenyon, et al., 1996). A comparison with visible range observations favored temperature profiles resembling that constructed by Kenyon, Hartmann, and Hewett (1988), which had $T_{\rm max}$ = 6800 K.

Between 1979 and 1987, near- and far-ultraviolet (NUV/FUV) spectra of FU Ori were taken by the International Ultraviolet Explorer (IUE). The FUV spectrum[1] revealed line emission from the Si IV, C IV, and He II features, which are typically interpreted as emission from the accretion shock in CTTSs (Johns-Krull et al., 2000; Ardila et al., 2013), although the observations of FU Ori were not sensitive enough to analyze the line profiles or to detect the continuum. The NUV spectrum (Kenyon, Hartmann, Imhoff, et al., 1989) indicated a relatively high maximum disk temperature (9,000 K).

[1]We visually inspected the FUV spectrum in the IUE Newly Extracted Spectra (INES) archive at `http://ines.oat.ts.astro.it/` without further processing. The published spectrum can be seen in Valenti, Johns-Krull, et al. (2000)

This high temperature complemented theories of a boundary layer region where the heating is dominated by the enormous shear between the disk material, which is orbiting at near-Keplerian speeds, $v_{\rm kep} \sim 200$ km s^{-1}, and the slower-rotating central star, $v_{\rm rot} < 50$ km s^{-1} (Nofi et al., 2021). However, the temperature profiles of Popham, Kenyon, et al. (1996) that give $T_{\rm max} \sim 9000$ K predict absorption line profiles that are inconsistent with both the optical and ultraviolet observations.

Subsequently, the IUE NUV-derived $T_{\rm max} \sim 9000$ K was re-affirmed with a 2001 NUV spectrum of FU Ori taken with HST/STIS. This spectrum is almost identical to the IUE spectrum and Kravtsova, Lamzin, et al. (2007) found that a $T_{\rm max} = 9000$ K model is required to match the absorption in the 2300 – 3200 Å range. Yet, using the radiative transfer model from Zhu, Hartmann, et al. (2007) and a lower $A_V = 1.5$ mag (rather than 2.2 mag), Hartmann, Zhu, et al. (2011) demonstrate that the NUV continuum can be produced with a much lower $T_{\rm max} = 5840$ K.

We present in this Letter the first high-sensitivity FUV spectrum of FU Ori, with a clear continuum detection down to $\lambda \approx 1150$ Å. The FUV continuum flux is in excess of that predicted by a viscous disk model by a factor of $> 10^4$. We treat the FUV excess as a blackbody and find a $T_{\rm FUV} \sim 16,000$ K and a filling factor of 0.02% on the surface of the 3.52 $R_\odot$ star. The small emission region and relatively high temperature indicate that the FUV flux arises from shock-heated material where the surface accretion in the disk meets the stellar photosphere.

In Section 10.2, we describe our HST observations and how we discriminate between continuum and line emission. We show our FUV spectrum for both COS and STIS in Section 10.3. We then introduce our disk model and describe how we fit the observed FUV excess relative to the disk model in Section 10.4. In Section 10.5 we discuss our interpretation of the continuum spectrum in the context of previous boundary layer models.

10.2 Data and Calibration

We obtained spectra of FU Ori using the HST Space Telescope Imaging Spectrograph (STIS) and Cosmic Origins Spectrograph (COS) as part of the Guest Observer (GO) program 17176[2].

The STIS observations were taken using the $52'' \times 2''$ arcsec slit in the grating settings: G140L (FUV-MAMA), G230L (NUV-MAMA), and G430L. The three

[2]The data can be accessed at the Mikulski Archive for Space Telescopes (MAST) via https://doi.org/10.17909/3p42-jw31.

settings cover 1150-5500 Å with a typical $R \equiv \lambda/\Delta\lambda = 600$.

The COS spectra were obtained using the G130M and G160M gratings and 4 central wavelength ($\lambda_{\rm cen}$) settings: 1222, 1309, 1589, and 1623 Å to ensure maximal coverage of the FUV at high resolution. The exposure times were 2350, 2348, 2118, and 1666 s, respectively. We used the Primary Science Aperture, which is a spherical aperture with a 2.5″ diameter. We combined the four exposures into a single FUV spectrum spanning 1065-1800 Å with a typical $R \sim 15,000$. To increase the signal-to-noise of the COS spectrum, we bin by a factor of 5 using the flux-conserving rebinning code `spectres` (Carnall, 2017).

The COS spectrum is shown in Figure 10.1. For the purposes of our FUV excess fit, we carefully identified regions of continuum emission, free of emission line contamination, following the method outlined in France, Schindhelm, et al. (2014). In order to minimize contamination from line emission, we masked any points within ±500 km s^{-1} of atomic lines and ±100 km s^{-1} of H_2 lines. The line list we used includes both features we clearly detect in the spectrum of FU Ori and, to be thorough, known bright features in CTTS spectra (regardless of their strength in FU Ori). There are several features with uncertain identification that we masked, and we leave identifying these features to a future paper. The selected continuum regions are shown in light blue in Figure 10.1.

We then bin those regions further down to 12 points spanning 1150 Å to 1780 Å to represent the FUV continuum flux (as indicated in Figure 10.1). We assume the uncertainties are normally distributed and propagate them accordingly, including the 5% COS absolute flux uncertainty[3]. The effective wavelength of each bin is the flux-weighted mean wavelength. As a result, some bins are assigned effective wavelengths that coincide with bright emission lines (e.g., the bin at 1336 Å), although the bin does not contain flux from that line. We also bin down the 1800 Å to 2400 Å region of the STIS G230L spectrum to the same wavelength spacing to construct a full spectrum of the FUV continuum. This 1150 – 2400 Å continuum spectrum is what we use for the model fit described in Section 10.4.

The different apertures between the STIS (52″ × 2″) and COS (2.5″) do not seem to produce any significant differences between the spectra. Both apertures capture the major features at < 1″ scale in the FU Ori system (see Weber, Pérez, Guidi, et al., 2023, for a scattered light image as a reference). The companion, FU Ori S, is

[3] `https://hst-docs.stsci.edu/cosihb/chapter-5-spectroscopy-with-cos/5-1-the-capabilities-of-cos`

detected in line emission in the STIS G140L spectrum. We report this in Carvalho et al. (2024, in prep). The binary is clearly resolved in the spatial direction such that extraction of the spectrum of FU Ori N does not include emission from FU Ori S.

10.3 The FUV Spectrum of FU Ori

The COS spectrum of FU Ori is the first FUV spectrum sensitive enough to detect continuum emission from the source. The continuum is detected from 1170 Å $< \lambda <$ 1780 Å at a signal-to-noise ratio (SNR) greater than 5. The emission blueward of 1170 Å is extremely low SNR and therefore undetected, and redward of 1800 Å is near the detector edges where the spectrum data quality drops rapidly.

As can be seen in Figure 10.1 the spectrum is line rich, though there are several emission lines that are often seen in CTTS systems but are very weak or only marginally detected here (e.g., C III 1175 Å multiplet and the N V 1238.8/1242.8 Å doublet). The detected emission lines typically targeted in FUV studies of CTTSs are marked, as are bright H_2 features.

A more detailed discussion of the line profiles and plots of the individual lines in velocity space are given in Appendix 10.8. As this Letter is focused on the properties of the FUV continuum, we reserve an analysis of the emission line profiles for a future paper.

The full STIS UV spectrum of FU Ori is shown in Figure 10.2. We include the binned continuum points derived from the COS spectrum, which are in good agreement with the continuum level of the STIS G140L spectrum. The continuum points from the 1800 Å to 2400 Å region of the STIS G230L spectrum used for our fit to the FUV excess are also marked.

The three bright lines in the G230L spectrum are the C II] 2335 Å, Fe II 2507/2509 Å, and Mg II 2795/2802 Å features, respectively. We further discuss their appearance in Appendix 10.9.

10.4 Fitting the FUV Excess Emission

We identify the NUV/FUV excess emission by comparing the observed spectrum to a viscous gas accretion disk model spectrum. Our model is described in detail in Carvalho, Hillenbrand, Hambsch, et al. (2023) but we summarize it here.

We assume that for $r < 150\ R_\odot$ (43 R_*), the FU Ori accretion disk is thin ($H/R <$ 0.01, Zhu, Jiang, et al., 2020) and viscously heated. We then adopt a modified

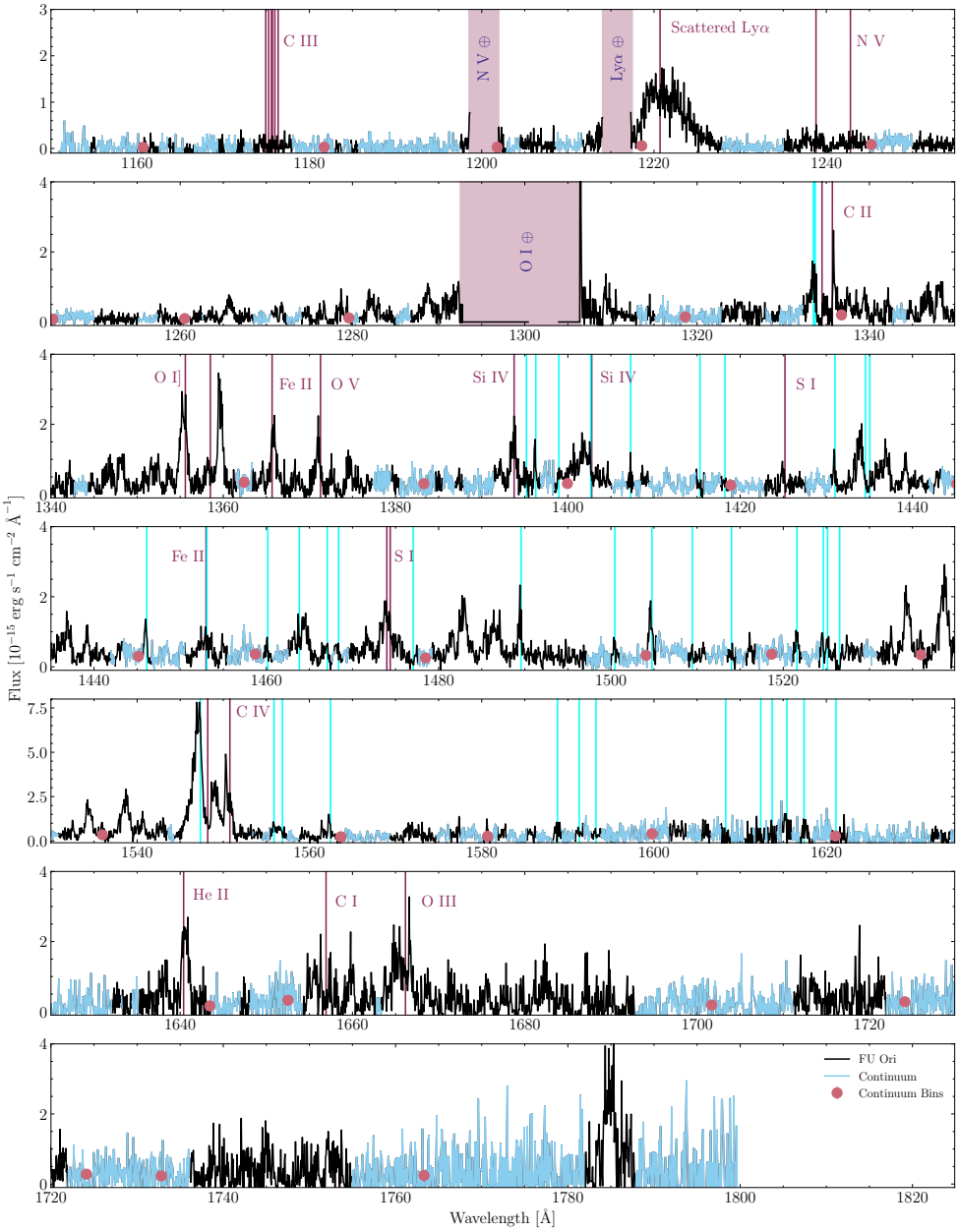

Figure 10.1: The COS spectrum of FU Ori with the regions selected to represent continuum highlighted in light blue. Regions in black represent those masked out due to observed or potential line emission. The pink points with error bars mark the binned down continuum points we fit in Section 10.4. The vertical cyan lines mark locations of prominent H_2 features in typical CTTS spectra France, Arulanantham, et al. (2023), while identified bright or well-known (but marginally detected) atomic emission lines are marked and labeled in maroon. The vertical shaded regions denote masked geocoronal emission.

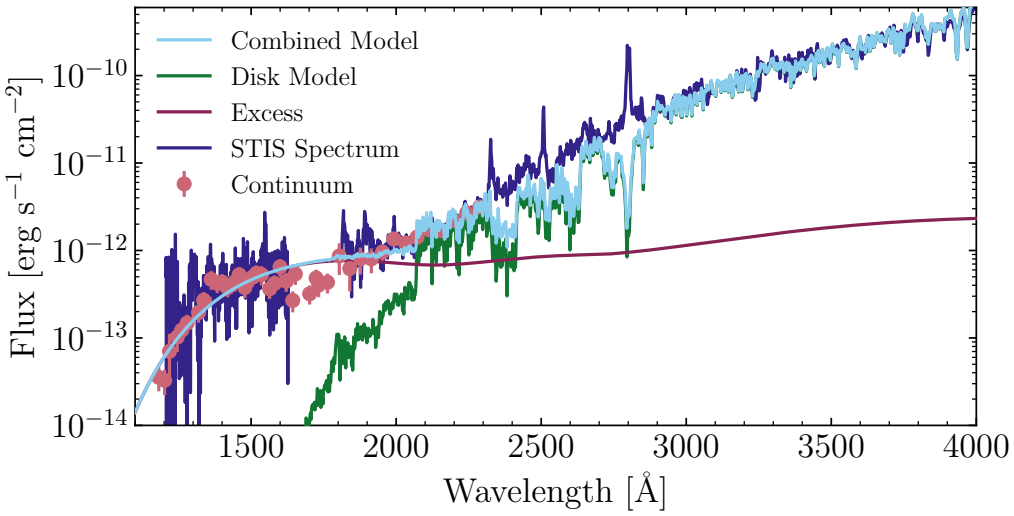

Figure 10.2: The FUV and NUV STIS spectra (dark blue) and the continuum points we derived from the COS spectrum (pink circles with error bars). Our combined disk + shock model fit is shown (light blue) along with the individual model components, with the disk model in green and the 16,275 K blackbody component in maroon. Notice the sharp transition from the disk-dominated spectrum to the excess emission dominated spectrum at the 2060 Å continuum break. The model components have all been reddened to our adopted A_V = 1.5 mag and using the Whittet et al. (2004) extinction curve, which has a weaker 2200 Å bump than the commonly used Cardelli et al. (1989) curve. The effect of the bump can be seen as an undulation from 2000 Å to 2800 Å in the otherwise featureless reddened excess component blackbody spectrum.

version of the Shakura and Sunyaev (1973) α-disk temperature profile,

$$T_{\rm eff}^4(r) = \frac{3GM_*\dot{M}}{8\pi\sigma r^3}\left(1-\sqrt{\frac{R_{\rm inner}}{r}}\right), \tag{10.1}$$

where $R_{\rm inner}$ is the inner radius of the accretion disk, M_* is the mass of the central star, $\dot{M}$ is the stellar accretion rate, G is the gravitational constant, and σ is the Stefan-Boltzmann constant. We assume that for $r < \frac{49}{36}R_{\rm inner}$, $T_{\rm eff}(\frac{49}{36}R_{\rm inner}) = T_{\rm max}$ (Kenyon, Hartmann, and Hewett, 1988).

We populate the annuli of the disk using PHOENIX model stellar spectra (Husser et al., 2013) with log$g$ = 1.5 and the appropriate $T_{\rm eff}(r)$. For the FU Ori system parameters, we adopt most of those reported in Zhu, Jiang, et al. (2020): M_* = 0.6 $M_\odot$, $R_{\rm inner}$ = 3.52 $R_\odot$, $R_{\rm outer}$ = 0.7 AU. For the distance to the system, we use the Gaia-derived distance of 404 pc to the λ Ori cluster, of which FU Ori is a member (Kounkel et al., 2018; Roychowdhury and Hillenbrand, 2024a). We assume

an inclination of 35° (Pérez et al., 2020). We initially explored models across a range of $\dot{M}$ and A_V (described in Appendix 10.10) and found that $\dot{M} = 10^{-4.49}\ M_\odot$ yr $^{-1}$ is a better fit to the NUV spectrum than the $\dot{M} = 10^{-4.42}\ M_\odot\ \mathrm{yr}^{-1}$ used by Zhu, Jiang, et al. (2020). This analysis also showed that the A_V is weakly constrained but agrees with the Zhu, Jiang, et al. (2020) value of $A_V = 1.5$ mag. Therefore, in our fiducial disk model we use $\dot{M} = 10^{-4.49}\ M_\odot$ yr $^{-1}$ and $A_V = 1.5$ mag.

For our extinction correction, we adopt the Whittet et al. (2004) extinction curve, which was based on stars located behind the Taurus Molecular Cloud. This curve has a much weaker 2175 Å "bump" than the typically-used Cardelli et al. (1989) and has been found to be a better fit to the ISM conditions in star forming regions. In our STIS spectrum, the Cardelli et al. (1989) curve over-predicts the 2175 Å extinction. For simplicity, we fix $R_V = 3.1$.

The STIS spectrum is well matched by the viscous disk component of our model until the sharp continuum break at $\sim$ 2060 Å. The break is due to the Al I continuum opacity, which has a jump in that region that grows stronger with temperature for $T_{\mathrm{eff}} > 5000$ K (Travis and Matsushima, 1968). The Al I continuum opacity may be overestimated in the model atmospheres, or it is possible that in this innermost region of the disk our assumption of an LTE plane-parallel atmosphere no longer holds. Regardless, the agreement between the continuum level of the disk model and the continuum in the 2100 – 3100 Å range covered by the E230M spectrum confirms that the disk model does not require $T_{\mathrm{max}} \sim 9000$ K to match the observed flux (Hartmann, Zhu, et al., 2011).

Blueward of 2100 Å, the observed FUV continuum exceeds the disk model spectrum by several orders of magnitude, requiring the an additional component in the model to match the data. We model the component as a simple Planck function of a single temperature, T_{FUV} having an effective radius R_{eff}. The additional flux is $F_{\mathrm{BL}} = \pi B_\lambda(T_{\mathrm{FUV}}) \left(\frac{R_{\mathrm{eff}}}{d}\right)^2$, where $d = 404$ pc. To determine the best-fit R_{eff} and T_{FUV} of the emitting region, we use Markov-Chain Monte-Carlo ensemble sampling from the `emcee` package (Foreman-Mackey et al., 2013). We summarize the posterior distributions for the T_{FUV} and R_{eff} of the emission region in Figure 10.3, constructed using the `corner` (Foreman-Mackey, 2016) package.

Although we considered multi-temperature models, we ultimately find that a single-temperature component provides the best fit to the spectrum. Introducing even one additional emission component with a different temperature results in a bimodal posterior distribution with one peak at $T_1 \sim 6000$ K, essentially the T_{max} in our

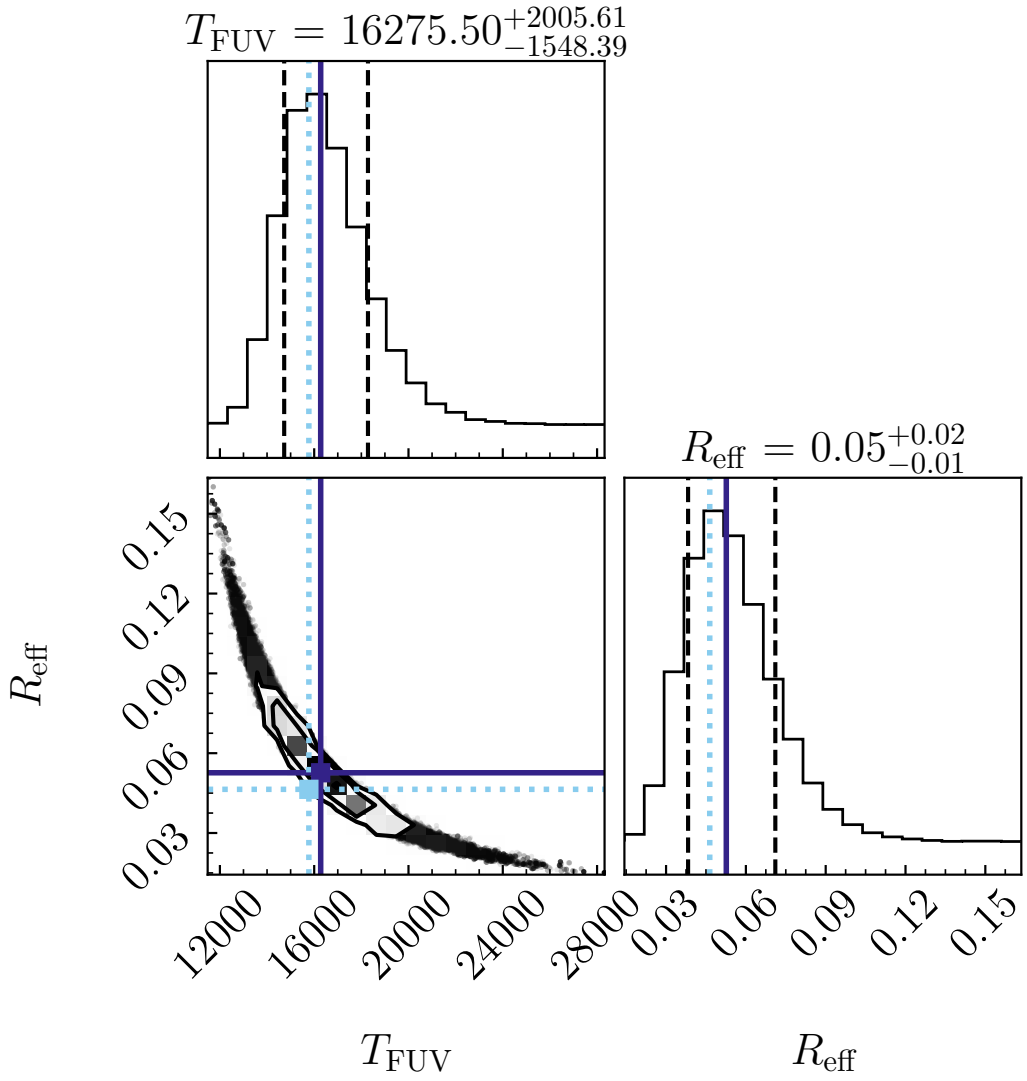

Figure 10.3: The `corner` plot for our MCMC fit for the FU Ori FUV excess. Our adopted best-fit values are marked by the navy vertical lines, showing the medians of the histograms. The modal values, marked by light blue dotted lines, are identical to the median values. The contours in the 2-d histogram mark the 0.5, 1.0, 1.5, and 2.0 σ levels, while the vertical dashed lines mark the 16th and 84th percentiles in the 1-d histograms.

disk model, and another at $T_2 \sim 14000 - 16000$ K, the same as the $T_{\rm FUV}$ of the one-temperature solution.

We also considered the commonly-used hydrogen slab model (Valenti, Basri, et al., 1993). However, as mentioned above, $T > 12,000$ K is necessary to explain the shape of the FUV continuum we detect. At these temperatures, hydrogen is almost entirely ionized, and the continuous opacity is dominated by emission from metals, particularly C, Si, Mg, and Al (Travis and Matsushima, 1968). Since we do not see the distinct jumps at the wavelengths where each particular species opacity should dominate (e.g., 2070 Å for Al), we can assume that the emission is largely blackbody.

The best-fit parameters for our single temperature model are $T_{\rm FUV} = 16275^{+2005}_{-1548}$ K and $R_{\rm eff} = 0.05^{+0.02}_{-0.01}\ R_\odot$. These values are robust to allowing A_V and $\dot{M}$ to vary in the model, as we demonstrate in Appendix 10.10. Our best fit model[4] is shown along with the spectra in Figure 10.2.

If we assume that the geometry of the emission region is a disk or torus at the equator the $R_{\rm eff}$ corresponds to an annulus with $R_{\rm outer} = 3.52\ R_\odot$ and a $\Delta r = 4 \times 10^{-4}\ R_\odot$. We interpret this extremely narrow width as evidence of an accretion shock at the disk-star boundary due to the disk surface accretion flow impacting the stellar surface.

Continuing to assume a disk-like geometry for the emission region, the FUV excess luminosity, $L_{\rm FUV}$, is given by $L_{\rm FUV} = \frac{2\pi}{\cos i} R_{\rm eff}^2 \sigma T_{\rm FUV}^4 = 0.11\ L_\odot$. Considering only the projected area we observe, instead of a disk-like geometry, $L_{\rm FUV} = \pi R_{\rm eff}^2 \sigma T_{\rm FUV}^4 = 0.04\ L_\odot$. We compare those values with the CTTS population in Section 10.5.

The fiducial model that we adopt is distinct from previously proposed boundary layer models that modify the temperature profile of the disk assuming sheer between the disk and star contributes to excess heating (e.g., Regev, 1983; Popham, Narayan, et al., 1993; Kley and Lin, 1996). We explored such modified temperature profiles and found that they were insufficient to reproduce the full UV spectrum. Our results of these tests are presented in Section 10.5.

[4]In the 1700-1800 Å region, the model appears to over-estimate the continuum. However, this is near the detector cut-off at the reddest points of the COS spectrum and it is likely that the uncertainties on those photometric points are underestimated. The detected continuum in that wavelength range should thus be considered a lower bound.

10.5 Discussion

The observed FUV emission for FU Ori exceeds the viscous disk model by a factor of $> 10^4$ (see Figure 10.2), indicating the presence of a bright emission source at the disk-star interface. In this Section, we compare our results with previous theoretical predictions of a boundary layer in the FU Ori system. We then compare our measured $T_{\rm FUV}$ with estimates of boundary layer properties based on analyses of the 2001 STIS E230M spectrum. We also discuss other potential mechanisms for the FUV emission and why we disfavor them in our interpretation.

A shock at the star-disk interface

Our best-fit model for the FUV continuum excess is of an emission source with a single temperature of 16,000 K and a filling factor of 0.02% on the surface of the star. We also constrain the α-disk component of the system to have a $T_{\rm max}$ = 5,800 K, a bit cooler than, but consistent with, the $T_{\rm max}$ =6,050 K reported by Zhu, Jiang, et al. (2020). Notably, we do not find evidence in the spectrum from components with temperatures in between 5,800 K and 16,000 K as would be expected from shear-heated boundary layer models.

Given the small filling factor of the 16,000 K component relative to the $r \sim R_{\rm inner}$ region of the disk or the stellar surface, which is presumably also at $R_* \sim R_{\rm inner}$, and the sudden jump in temperature, we conclude that the emission arises from a shock at the star-disk interface.

In previous magneto-hydro-dynamical simulations of accretion disks vertically threaded by magnetic fields (like we expect to be the case in FU Ori, Donati et al., 2005), the accretion flow does not occur along the midplane but the radially inward mass flux is concentrated in a vertically thin region above the disk photosphere (Gammie, 1996; Zhu and Stone, 2018). This accretion geometry is termed “surface accretion" (Zhu, Jiang, et al., 2020) and the shock we observe is at the boundary where the supersonic surface accretion flow, with velocity $v_{\rm inflow}$, collides with the stellar photosphere.

Assuming the temperature of the material is near the $T_{\rm max}$ of the system implies a Mach number of $v_{\rm inflow}/c_s \sim 4$. Therefore, when the supersonic flow reaches the stellar surface, it should produce a strong shock. The temperature of the shocked material can be then computed using the typical Hugoniot strong shock conditions,

$$T_{\rm shock} = \frac{3}{16}\frac{\mu m_H}{k_B} v_{\rm inflow}^2, \tag{10.2}$$

where $\mu = 0.5$ is the mean molecular weight assuming the gas is dominated by ionized hydrogen, and m_H is the proton mass. If we use an inflow velocity of 38 km s^{-1}, then $T_{\rm shock} \approx 16,000$ K. This is consistent with the $v_{\rm inflow} = 20 - 40$ km s^{-1} of the surface accretion layer seen in simulations of the FU Ori accretion disk (Zhu, Jiang, et al., 2020).

Is this emission consistent with the presence of a boundary layer?

While we interpret the FUV emission as arising from a shock, here we consider the necessary properties of a boundary layer that might produce the FUV emission. We will first discuss the nature of boundary layers in the context of YSO accretion disks and compare predictions of such boundary layers with our observed spectra. In the following sections, we turn toward specific boundary layer models and directly contrast those with the data.

In the work by Lynden-Bell and Pringle (1974a), Pringle (1981), and Popham, Narayan, et al. (1993), the boundary layer is a region where material that is moving at Keplerian orbit velocities of 200 – 300 km s^{-1} at $r \approx R_{\rm inner}$ slows to the stellar rotational velocity of 10 – 30 km s^{-1} (Nofi et al., 2021). The energy released by the shear is expected to heat the gas nearest the star sufficiently that $L_{\rm BL} \sim L_{\rm acc}$. The region is also predicted to have a width comparable to the scale height of the disk at $R_{\rm inner}$, or $dR_{\rm BL} = 0.1\ R_{\rm inner}$.

Compared with the observed FUV emission, which has a luminosity of 0.1 $L_\odot$, the continuum is more than 700 times underluminous for a shear-heated boundary layer. The expected total area of a boundary layer of thickness 0.1 $R_{\rm inner}$ is 880 times greater than that which we find for our best-fit model. Matching both the size and luminosity of the boundary layer predicted for an FU Ori system would require that the FUV emission source be obscured by an $A_V > 6$ mag. This may be the case if a majority of the boundary layer is buried by cooler upper layers of the disk atmosphere that trap the hot photons in the innermost region of the disk.

It is possible to match only the size of a boundary layer by treating the source of the FUV continuum as optically thin, rather than the optically thick model which we estimate to have $dR = 4 \times 10^{-4}\ R_\odot$. Then, the expected $dR_{\rm BL}$ of would imply an optical depth of $\tau = -\ln(1 - 0.0004/0.352) < 0.001$. Given the high density expected in this region ($n > 10^{15}$ cm^{-3}, Zhu, Jiang, et al., 2020), the emission is unlikely to be optically thin.

Another prediction in the boundary layer model is that there should be a continuous

temperature increase as $r \rightarrow R_{\rm inner}$, rather than the sharp jump we find with our single temperature model. To investigate the potential for a continuous temperature model to fit the FUV excess, we tested using a temperature profile with a power law dependence on the area of the emission region. Then the flux of such a boundary layer would be given by $F_{\rm FUV} = \pi \sum_i^{N_T} B_\lambda(T_i)(A_i/d^2)$, where $N_T = 10$ is the total number of temperature components we used and A_i is the area of each component of temperature T_i. The power law is given by $A_i = A_0(T_0/T_i)^\gamma$, where A_0 is the reference area for the lowest temperature component, T_0.

We again performed an MCMC fit and found that $T_0 = 6400 \pm 1000$ K, $A_0 = 0.04 \pm 0.03$, and $\gamma = 5.03 \pm 0.8$. The total area of the boundary layer integrated over the 10 temperature components is 0.4 $R_\odot^2$, which would correspond to an annulus of $dR_{\rm BL} = 0.017\ R_\odot = 0.005\ R_{\rm inner}$. Even allowing a continuous temperature increase, the preferred model yields a thin boundary layer (or one that requires $\tau << 1$) and a steep dependence on the size of each emitting region. The boundary layer here is not much thicker than is expected for our single-temperature model, implying it is either much thinner than expected for FU Ori systems or that the FUV continuum is not produced by such a boundary layer.

Comparison of the shock model with previous boundary layer models

We find good agreement between the thin viscous accretion disk + blackbody shock model and the observed FUV spectrum. Moving towards the NUV, the component of the spectrum that remains relatively dominated by the viscous accretion disk continuum is consistent with the modified Shakura and Sunyaev (1973) model we adopt, including the isothermal $T(r < \frac{49}{36} R_{\rm inner}) = T_{\rm max}$ assumption.

With our FUV spectrum, we can also test boundary layer models wherein the sheer between the star and disk produce a boundary layer with a temperature dependent on the efficiency of angular momentum accretion, j, of the star (Popham, Narayan, et al., 1993; Popham, Kenyon, et al., 1996). As a result of the increased heating from less efficient angular momentum transport, the Shakura and Sunyaev (1973) temperature profile in the thin disk case becomes,

$$T_{\rm eff}^4(r) = \frac{3GM_*\dot{M}}{8\pi\sigma r^3}\left(1 - j\sqrt{\frac{R_{\rm inner}}{r}}\right), \tag{10.3}$$

where $j \equiv \dot{J}/\dot{M}\Omega(R_*)R_*^2$, $\dot{J}$ is the angular momentum transfer rate onto the star, $\Omega(R_*)$ is the Keplerian frequency at the stellar surface and the new location of $T_{\rm max}$ in the disk is at $r = \frac{49}{36} j^2 R_{\rm inner}$.

We tested varying the j parameter in our model and found that it was inadequate to simultaneously reproduce the visible, NUV, and FUV spectra. If we allow j to vary and include a shock component with a variable $T_{\rm FUV}$ and $R_{\rm eff}$, the fit converges to $j \sim 0.95$ and $T_{\rm eff}$ and $R_{\rm eff}$ values close to those in our fiducial model. The $j \sim 0.95$ temperature profile is almost isothermal for $r < \frac{49}{36} j^2 R_{\rm inner}$ and produces an SED that is indistinguishable from our fiducial model temperature profile.

We note that our model relies on the thin disk approximation, which may break down in the shear-heated region closest to the central star. The models in Popham, Narayan, et al. (1993) account for changes to the disk scale height due to the excess heating, which can produce different temperature profiles at $r \sim R_{\rm inner}$ than the thin disk approximation. For instance, in all of their temperature profiles, the $T(r < 1.2\, R_{\rm inner}) < T_{\rm max}$, regardless of choice of j. In the thin disk case, this is only true for $j > 0.9$. Furthermore, the line profiles predicted for $j < 0.6$ reproduce the flat-bottomed square line profiles observed in the visible and NIR spectra of FU Ori (Kenyon, Hartmann, and Hewett, 1988; Petrov and Herbig, 2008; Zhu, Espaillat, et al., 2009b) best, though the thin disk models with j values in this range are inconsistent with the SED from the NUV to the NIR.

Another potential boundary layer model for FU Ori objects may be found in the accreting compact object literature. Existing white dwarf accretion disk boundary layer models could be good analogs for the very narrow, hot boundary layer that we attribute to a shock (Hertfelder and Kley, 2017). In these models, in the final $r < 1.01\ R_{\rm inner}$ of the disk, the temperature of the boundary layer increases rapidly to $5 - 10\times$ the temperature at $r \sim 1.1\ R_{\rm inner}$. The boundary layer typically has a thickness of $\Delta r < 0.006\ R_{\rm inner}$ and spread upward along the surface of the compact object, reaching latitudes of 35°. This is a factor of 10 greater than our limit on the thickness of a toroidal boundary layer region around FU Ori, but if such a boundary layer were present in this system, we can compare the measured T_{BL} with a prediction based on the white dwarf case.

As a crude estimate of how the boundary layer temperature from Hertfelder and Kley (2017) might scale going from a white dwarf system to an FU Ori system, we can use the fact that $T_{\rm max} \propto (M_* \dot{M} / R_{\rm inner}^3)^{1/4}$. Scaling then from the white dwarf

parameters adopted by Hertfelder and Kley (2017), we get

$$T_{\rm BL,FU} = 350 \times 10^3 \text{ K} \left(\frac{0.6\ M_\odot}{1.0\ M_\odot}\right)^{0.25} \times \left(\frac{10^{-4.49}\ M_\odot \text{yr}^{-1}}{10^{-8}\ M_\odot \text{yr}^{-1}}\right)^{0.25} \left(\frac{3.52\ R_\odot}{5.6 \times 10^8 \text{cm}}\right)^{-0.75} = 24,000 \text{ K},$$

which is 50% larger than the $T_{\rm FUV} \approx 16,000$ K we find. This is a simple scaling exercise, but demonstrates that boundary layer models based on compact object accretion disks may be applicable to the FU Ori disk and should be explored further.

If we consider a geometry similar to that of the white dwarf boundary layer described above, where the emission region is a rectangular band on the surface of the star with a latitudinal size of h and wraps around the equator of the star, then its area projected along our line of sight is given by $2\pi R_* h \sin i$. Requiring that the observed area be equal to $\pi R_{\rm eff}^2$ and solving for h in this case yields a similar value to the annular emission geometry: $h = 6 \times 10^{-4}\ R_\odot$. In this geometry, it is likely that we are only seeing a very small part of the total emission surface, and that the rest is obscured by the dense disk midplane.

Ultimately, we believe our proposed accretion shock interpretation to be the most reasonable explanation for our observations. The interpretation is complementary to what may be expected from the flows predicted by the radiation MHD models in Zhu, Jiang, et al. (2020).

Excluding magnetic activity as a source of FUV continuum emission

A potential source of FUV continuum emission is magnetic activity, particularly in events like stellar flares. In FU Ori objects, the X-ray emission has been established as likely arising from heightened magnetic activity due to the extreme temperatures of the X-rays (Kuhn and Hillenbrand, 2019). Here, we consider whether the FUV emission might arise from a transition region between the star and the X-ray emitting corona or from serendipitous flare-like activity during our observation.

Studies of superflares in magnetically active M dwarfs, known to have ~ kG field strengths like YSOs, describe the FUV continuum during flares as 15,000 - 30,000 K blackbodies, with significant enhancement in several high temperature emission lines (Kowalski, 2024). While we find a continuum temperature at the lower end of this range, and detect common features like the C IV and Si IV doublets and He II 1640 Å, there are other bright emission lines seen in flare spectra that we at best marginally

detect (e.g., C III 1175, Si III 1206.51, the N V doublet, and the C I multiplet, Loyd et al., 2018; MacGregor et al., 2021).

Although the continuum may be similar to that observed in flares, the brightness and persistence of the emission would imply extraordinary flare activity. Integrating the FUV luminosity of 0.1 $L_\odot$ over the 8482 s of exposure time gives a total emitted energy of 3.5×10^{36} erg. This is comparable to the *bolometric* energy of the most powerful superflares observed in flare stars (Simões et al., 2024). The FUV flux level is also constant during the four COS exposures. For flares to have produced the emission would require 4 almost identical, extremely powerful flares to have occurred consecutively during the time of observation, each lasting no longer than the time of an individual exposure.

It may be that the high temperature lines like the C IV and Si IV doublets and He II 1640 Å feature are emitted from a transition region between the star-disk interface and the corona from which the X-rays are emitted. However, it is unlikely that the FUV continuum is produced by magnetic activity. This is supported by the stability of the FUV continuum emission and the fact that while coronal line emission is observed in magnetically active stars, bright continuum emission is only seen during flares.

Excluding 2-photon emission as the source of FUV emission

In addition to multi-component models and variations on the viscous disk temperature profile, we considered the hydrogen two-photon process as a source of the FUV emission. We expect that the number densities associated with the process ($n_e < 10^3$ cm^{-3}) are much lower than those predicted for the region near the star in the FU Ori system (Zhu, Jiang, et al., 2020). Therefore, if the FUV emission were indeed two-photon, it would instead suggest a nebular origin, rather than a boundary layer or shock.

To test the possibility that we are seeing two-photon emission, we substitute the Planck function in the model with the two-photon model given in France, McCray, et al. (2011). Following the procedure in Section 10.4, the best-fit $R_{\rm eff} = 0.2\ R_\odot$ and the hydrogen column density is 3×10^{21} cm^{-2}.

Although the model fits the FUV continuum well for 1220 Å $< \lambda <$ 1600 Å, the flux at 1800 Å $< \lambda <$ 2200 Å is insufficient to match the observed spectrum. Analyzing the count rate in the COS spectrum, we also detect the continuum blueward of λ = 1200 Å at a 10σ level (see Appendix 10.11). The spectrum of the two-photon process has a sharp cutoff at $\lambda <$ 1215 Å and would therefore not be detected. This

rules out the two-photon process as the source of the FUV continuum.

The UV luminosity of FU Ori in context

With our two assumptions about the geometry of the FUV emission source (isotropic versus disk-like), we estimate the FUV luminosity of FU Ori to be $L_{\rm FUV} = 0.04 - 0.11\ L_\odot$. The ratio of FUV luminosity to accretion luminosity is $L_{\rm FUV}/L_{\rm disk} = 0.5 - 1.2 \times 10^{-3}$. Considering the $L_{\rm X} = 1.6 \times 10^{-3}\ L_\odot$, the $L_{\rm X}/L_{\rm disk} = 2.5 \times 10^{-5}$ (Kuhn and Hillenbrand, 2019).

To better contextualize these values relative to magnetospherically accreting young stars, we compare the continuum (i.e., excluding Lyα) $L_{\rm FUV}$ and $L_{\rm X}$ for FU Ori with CTTSs in Taurus using data from (Yang et al., 2012). For the median CTTS in the sample, $L_{\rm FUV} = 10^{-2.7}\ L_\odot$. FU Ori is more FUV-luminous than the median object in the CTTS sample by almost a factor of 100. FU Ori is also much more X-ray luminous than typical members of the CTTS sample. The objects in this parameter space that have comparable FUV and X-ray luminosities to FU Ori are K0 or G type stars and up to 2× more massive than FU Ori.

The increased disk luminosity during an FU Ori outburst is predicted to drive disk chemistry by sublimating volatiles on icy dust grains, leading to enrichment of complex organic molecules (Molyarova et al., 2018). The increased hard radiation from FU Ori in outburst may also have significant implications for disk chemistry during outbursts. If we calculate the FUV energy density, $u_{FUV}(10\,{\rm au}) = \frac{1}{4\pi c}\sigma_{SB}T_{\rm eff}^4\left(\frac{0.05\ R_\odot}{10\ {\rm AU}}\right)^2 = 1.15{\times}10^{-8}\,{\rm erg\,cm^{-3}}$, or $10^{5.3}\ G_0$. Closer-in, $u_{\rm FUV}(1\ {\rm AU}) \sim 10^7\ G_0$. As expected from the larger $L_{\rm FUV}$, this is a factor of 10-100 greater than the typical continuum $u_{\rm FUV}$ near the central star in a CTTS system (France, Schindhelm, et al., 2014). It is also greater than the FUV energy density from the Orion Trapezium Cluster found to drive a photoevaporative disk outflow in nearby YSO (Berné et al., 2024). The total $u_{\rm FUV}$ can be even greater if Lyα is accounted for in the system, which in CTTSs can contribute 10× the continuum FUV flux (France, Schindhelm, et al., 2014). Studies considering the effects of FU Ori outbursts on the chemical environment in protoplanetary disks should take into account both the increased $L_{\rm bol}$ and $L_{\rm FUV}$.

10.6 Conclusions

The HST COS/STIS spectra of FU Ori contain FUV emission exceeding by a factor of $> 10^4$ at 1400 Åthe flux predicted by the viscous disk accretion model that

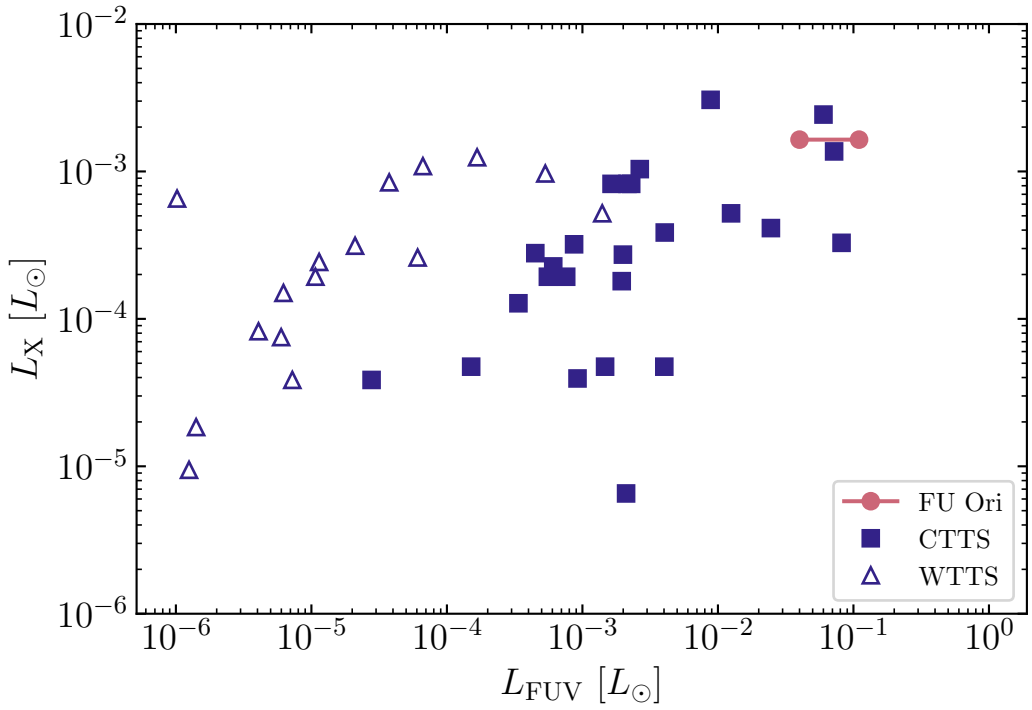

Figure 10.4: The $L_{\rm FUV}$ (this work) and L_X (Kuhn and Hillenbrand, 2019) for FU Ori, compared with YSOs in Taurus (Yang et al., 2012). FU Ori has among the highest L_X and has the highest $L_{\rm FUV}$ of the sample. The range of $L_{\rm FUV}$ for FU Ori reflects the two values we calculate depending on the assumed geometry of the emission region. The sources that have $L_{\rm FUV} > 0.05\ L_\odot$ are T Tau, HD 143006, and RY Tau, which are much earlier spectral types than the FU Ori central object would be (K1, G3, and G0, respectively, Herczeg and Hillenbrand, 2014).

explains in full the 4000 – 22,000 Å wavelength range. To understand the nature of the excess, we isolated the continuum emission in the COS spectrum. We carefully masked out several regions that either showed clear line emission or are known to show line emission in accreting YSOs. We then fit the FUV spectrum with a viscous disk model combined with a blackbody spectrum, varying the $T_{\rm FUV}$ of the spectrum and the $R_{\rm eff}$ of the emitting region. Our combined model shows that the temperature and effective radius of the emitting region are $T_{\rm FUV} = 16,000 \pm 2,000$ K and $R_{\rm eff} = 0.05 \pm 0.02\ R_\odot$.

The measured temperature and the size of the FUV emission region are consistent with expectations for a shock at the disk-star boundary. The shock arises from the collision of the highly supersonic disk surface accretion flow with the stellar photosphere. The FUV continuum luminosity is $L_{\rm FUV} = 0.04 - 0.11\ L_\odot$, which is $\sim 100\times$ greater than typical values for CTTSs. The resulting FUV energy density

is 10^7 G_0 at 1 AU and $10^{5.3}$ G_0 at 10 AU, comparable with the most extreme FUV interstellar radiation fields. The large increase in FUV flux from the inner disk could drive photochemistry in a larger portion of the outer disk relative to quiescent systems.

We encourage detailed theoretical modeling of the innermost $r < 0.1$ AU of the FU Ori system at outburst, incorporating a disk-star boundary layer in order to better understand the gas dynamics in the region. In future work, we will present an analysis of the many emission lines in the COS spectrum to understand their origin and the properties of the massive, high velocity outflows near the star.

10.7 Acknowledgements

This research was supported, in part, by grant HST-GO-17176.001-A from STScI. The authors thank Lee Hartmann for his insightful comments on the analysis and interpretation of the data. The authors acknowledge Will Fischer, for many things over the years, but most relevant here is the volunteering of valuable, unsolicited advice regarding our *cenwave* choice.

10.8 Appendix: Line Profiles of Common CTTS FUV Emission Features

The COS spectrum shown in Section 10.2 has several bright emission lines, many of which have profiles similar to those seen in CTTS systems with accretion and strong outflows, wherein the lines are highly self-absorbed. The brightest features in the COS spectrum are Lyα, the C II 1334.5/1335.7 doublet, the C IV 1548.2/1550.77 doublet, the Si IV 1393/1402 doublet, and He II 1640.4 (Figure 10.5, 10.6). In this Appendix, we discuss the lines shown in Figures 10.5 and 10.6 and compare them with their counterparts in quiescent young stars. A detailed analysis of the lines will be presented in a future paper.

There is almost no C I detected in the spectrum. We marginally detect the features at 1656/1657, which at $T \sim 16,000$ K (according to the CHIANTI atomic line database, assuming Local Thermodynamic Equilibrium; LTE) are predicted to be the brightest C I features (Dere et al., 1997; Del Zanna et al., 2021a). It is possible that the *SNR* in this spectrum is not high enough to clearly establish the presence or absence of C I.

In the case of the Lyα feature, we do not see the core due to the strong geocoronal emission and significant resonant scattering in the circumstellar and interstellar media. Emission from $-800 < v < 800$ km s^{-1} is entirely absorbed by the wind,

but the emission from 800 – 2000 km s^{-1} is strong. Emission at these velocities indicates large amounts of scattering by the dense material ($n \sim 10^{15}$ cm^{-3} Zhu, Jiang, et al., 2020) surrounding the accretion shock.

The C II doublet is highly wind-absorbed and only the red wings of the line profiles are visible. The same wind absorption is seen in GM Aur or DE Tau (Xu et al., 2021a). The absorption in the lines extends to > -200 km s^{-1}, like the $i = 35°$ systems observed by Xu et al. (2021a).

The C IV doublet line profiles are less analogous to their CTTS counterparts (Ardila et al., 2013). The C IV profiles in GM Aur and DE Tau are relatively symmetric, whereas in FU Ori the blue component of the doublet cannot be clearly identified. It is possible that there is some wind absorption of C IV, which would point to the wind in FU Ori being hotter than in quiescent YSOs. This has been proposed to be the case for FU Ori objects by Carvalho, Hillenbrand, Seebeck, and Covey (2024) in their analysis of the visible range wind emission lines of HBC 722. Ardila et al. (2013) also note that the only object in their sample for which the C IV lines have P Cygni profile is DX Cha, a Herbig Ae star that may have a wind temperature greater than 10^5 K.

The He II 1640.4 Å line is narrow and appears redshifted to 50 km s^{-1} with a FWHM of ~ 150 km s^{-1}. The line may be wind-absorbed so that we are only seeing red-shifted emission. Since the C IV lines tend to form at higher temperatures than the He II line, this is expected if there is indeed wind absorption is seen in C IV.

The H_2 emission in FU Ori is very weak. There are a few features that are almost as bright as the C II and C IV emission, but many of the H_2 emission lines seen in CTTSs are not detected in the COS or STIS FUV spectra (see the line locations marked in Figure 10.1). The lines are almost all blue-shifted to -30 km s^{-1}. The features are narrow, with typical FWHM values of 10 km s^{-1}, although their profiles vary from feature to feature. This variation may point to multiple origins for the H_2 emission in the system. It is possible that the emission is weaker than might be expected for such a rapidly accreting system due to strong absorption of Lyα in the wind, preventing photons from reaching the H_2 to excite emission. Furthermore, the wind temperature estimated for FU Ori objects by Carvalho, Hillenbrand, Seebeck, and Covey (2024) is sufficiently high that combined with the fact that many of the features are blue-shifted, a significant fraction of the H_2 we observe may be from the wind.

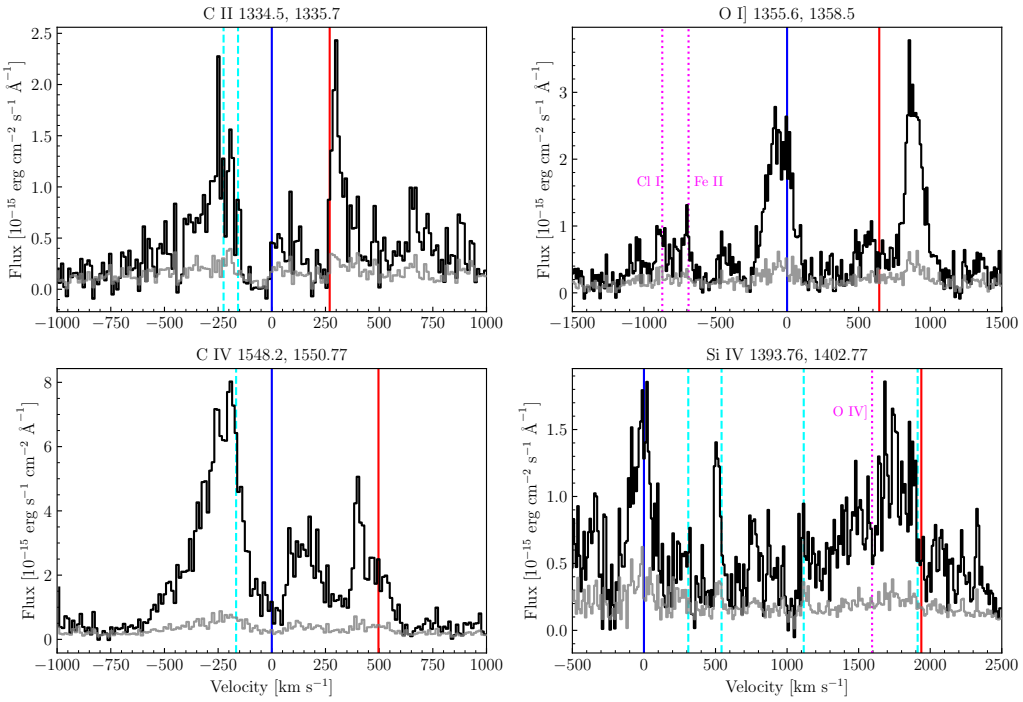

Figure 10.5: Selected bright emission line doublets commonly studied in the FUV spectra of YSOs. The data are plotted in black and the uncertainty on each point is shown in light grey. The blue and red lines mark the blue and red components of the doublets. The vertical cyan dashed lines mark the rest-wavelengths of H_2 lines and the vertical magenta dotted lines mark the rest frequencies of known features that may be contaminating the doublet line profiles (Cl I 1351.657, Fe II 1352.487, and O IV] 1401.17).

One feature that is present in many CTTSs and clearly absent in the FU Ori spectrum is the "bump" at 1600 Å (France, Roueff, et al., 2017). It is suggested by France, Roueff, et al. (2017) that the bump is due to H_2O dissociation by Lyα in the inner 2 AU of the disk. If so, the lack of a bump here indicates that either the Lyα flux does not reach the disk surface due to strong self-absorption in the outflow, as discussed above, or that the bump emission is not bright enough to compare with the shock continuum emission.

10.9 Appendix: Previous Analysis of the FU Ori NUV Spectrum

While we present the first detection of the FUV continuum in FU Ori, previous studies have used the 2001 STIS/E230M spectrum to estimate the potential for boundary layer emission in the system (Kravtsova, Lamzin, et al., 2007). Here, we compare our findings with these results.

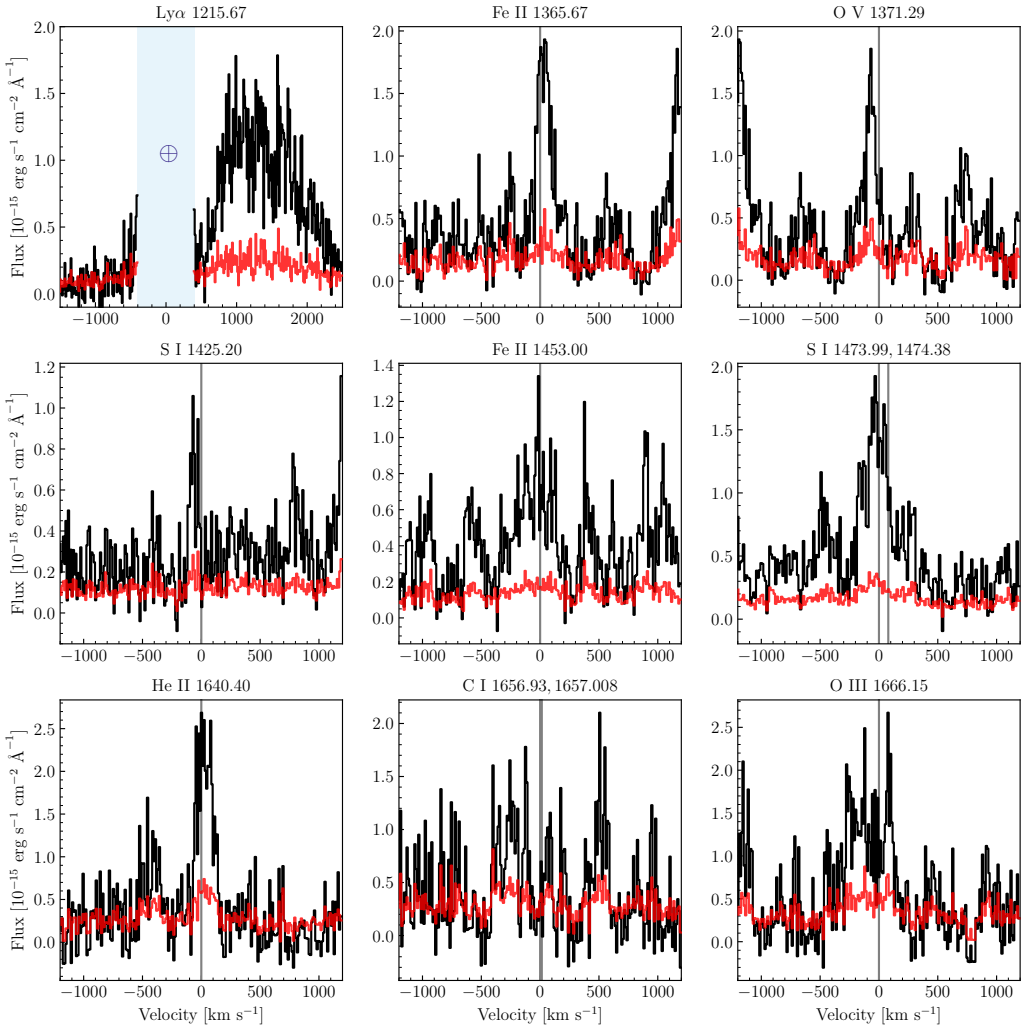

Figure 10.6: Detected bright emission lines commonly seen in the FUV spectra of YSOs. The data are plotted in black and the uncertainty on each point is shown in red. The rest-frequency of each line marked by the vertical grey line. Notice that, if present, the C I 1656 feature is only marginally detected.

Our 16,000 K best-fit shock temperature is close to that reported in López-Martínez and Gómez de Castro (2014) based on modeling of the C II] 2325 Å emission line and nearby Fe II] and Si II] emission line ratios. Their analysis finds that the lines arise from a region with $T_e = 15,135$ K and $n_e = 1.78 \times 10^{10}$ cm^{-3}, assuming the emission is optically thin. Such a low n_e is typical of the densities expected in the funnel flow of a CTTS with magnetospheric accretion (Calvet and Gullbring, 1998).

However, López-Martínez and Gómez de Castro (2014) also report that the lines they analyzed in FU Ori are all blue-shifted to $v = -45$ km s^{-1} and have full-width at half-maximum (FWHM) values of 221 km s^{-1}. The velocity offset matches the blue-shifted wind absorption found in the Mg II 2796/2803 Å doublet (Kravtsova, Lamzin, et al., 2007), while the FWHM is comparable with the broadening seen in the red-shifted emission of the NUV Mg II doublet and the Hα line in the visible (Herbig et al., 2003).

These facts together indicate that both sets of emission lines may be formed in a strong outflow near the star. The absorption in Mg II and emission in C II] may trace the launch points of the outflow, whereas the broader (and red-shifted in Mg II) emission traces scattering and turbulence in the wind at larger distances. The outflow may include material heated by the shock, which would explain the similar temperatures of the two components.

In the low resolution G230L spectrum we detect the C II] 2325 Å, Si II] 2350 Å, and Mg II 2795/2802 Å lines, previously identified by Kravtsova, Lamzin, et al. (2007) at high resolution. The doublet reported at 2506 Å is the second-brightest feature in the G230L spectrum. We identify the feature as likely being the 2507/2509 Fe II doublet, which has been previously studied in the Weigelt blobs of η Carinae (Johansson and Hamann, 1993a; Johansson and Letokhov, 2004). The doublet is blue-shifted at the same velocity as the Si II] and C II] features, so it likely traces the same material. The appearance of this doublet in FU Ori is mysterious because it is not seen in the spectra of any other YSOs. Nevertheless the temperature of the outflowing material near the shock may be close to that of the Weigelt blobs (Mehner et al., 2010) and we expect the density is higher here than in the blobs.

10.10 Appendix: Revisiting the $\dot{M}$ and A_V of FU Ori

In addition to modeling the excess FUV emission, we sought to also revisit the literature $\dot{M}$ and A_V estimates for FU Ori. Using a recent SED model produced from a radiation-magneto-hydro-dynamical simulation of the system and an updated

system inclination (Pérez et al., 2020), Zhu, Jiang, et al. (2020) reported that the system has a $\dot{M} = 10^{-4.42}\ M_\odot\ \mathrm{yr}^{-1}$ and an $A_V = 1.5$ mag. Using $\dot{M} = 10^{-4.42}\ M_\odot\ \mathrm{yr}^{-1}$ in the disk + shock model causes it to greatly overestimate the continuum redward of 2100 Å, even in the visible range, due to the Rayleigh-Jeans tail of the shock emission.

Using the same SED fitting procedure we describe in Section 10.4, we allowed the $\dot{M}$ and A_V to vary along with the T_{FUV} and R_{eff}. We require that $T_{\mathrm{FUV}} < 20,000$ K in this fit due to the slight degeneracy between T_{FUV}, $\dot{M}$, and A_V. When higher temperatures are allowed, the peak of the shock emission shifts blueward, requiring a higher A_V to match the shape of the FUV continuum and a higher corresponding $\dot{M}$ to match the NUV. This produces a poorer overall fit to the UV and visible spectrum, especially in the 2100 to 2400 Å and 3000 to 3800 Å regions. The posterior distributions of the $\dot{M}$, T_{FUV}, and R_{eff}, are well-constrained, as shown in Figure 10.7. The A_V posterior distribution is poorly constrained, although the fit clearly favors $A_V < 2$ mag. The $A_V = 1.5$ from previous literature, derived from fits to the visible range data (Zhu, Hartmann, et al., 2007), is well within the 1σ uncertainty of the best-fit A_V here. Given the good agreement between our best-fit $\dot{M}$ and the existing literature value, we adopt $\dot{M} = 10^{-4.49}\ M_\odot\ \mathrm{yr}^{-1}$ for our fiducial model. Due to the poor constraint on A_V, we simply adopt the historical value of $A_V = 1.5$.

10.11 Appendix: Detecting the Continuum Blueward of 1200 Å

In Section 10.5, we stated that we observe emission blueward of Lyα, which rules out the two photon process as the dominant source of FUV emission. In order to confirm the significance of the continuum detection in this range, we examined the background-subtracted count rate of the two G130M spectra ($\lambda_{\mathrm{cen}} = 1222$ Å and $\lambda_{\mathrm{cen}} = 1309$ Å).

We compute the total net counts during the integration by multiplying the count rate by the 2348 s and 2350 s exposure times. We then mask the wavelengths that are known to have emission lines, following the procedure given in Section 10.2. We then resample the data onto a grid with bin widths of 100 pixels each. We assume that the count rates are Poisson-distributed to estimate the uncertainties. We show the resulting spectrum in Figure 10.8.

The continuum emission at $\lambda < 1216$ Å is detected in most of the bins with several exceeding 9 counts, or 3σ assuming Poisson-distributed noise. If we bin all counts

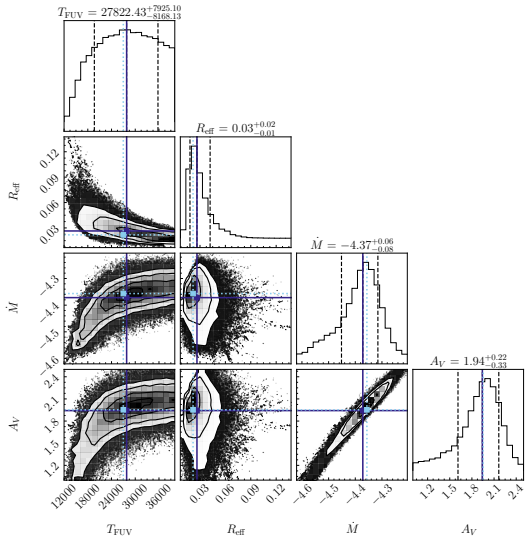

Figure 10.7: The `corner` plot for the fit with a variable $T_{\rm FUV}$, $R_{\rm eff}$, $\dot{M}$ and A_V. The dark blue vertical and horizontal solid lines mark the median values of the histograms, while the light blue dotted lines mark the modal values. The agreement between the two in all but the $T_{\rm FUV}$ parameter show that the posterior distributions are well-behaved. The contours in the 2-d histogram mark the 0.5, 1.0, 1.5, and 2.0 σ levels, while the vertical dashed lines mark the 16th and 84th percentiles in the 1-d histograms.

blueward of 1200 Å into a one, the detection significance rises to 10σ. The two photon process has a sharp emission cut-off at $\sim$ 1215 Å, so if it cannot be the source of the continuum we see in this wavelength range. Therefore, we rule-out the possibility that the two photon process produces the observed FUV excess in FU Ori.

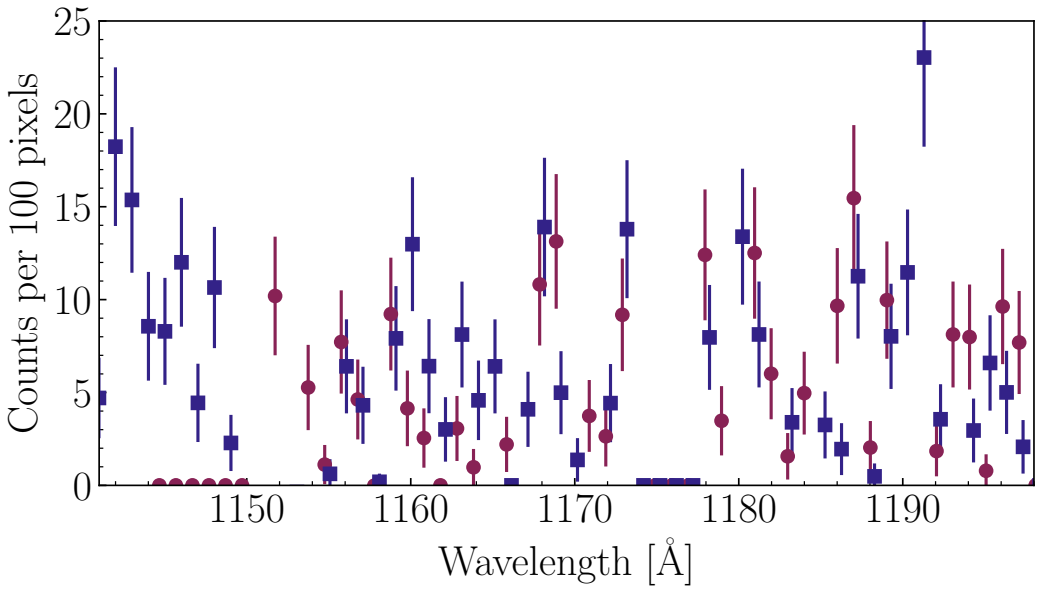

Figure 10.8: The net counts in the COS G130M spectra from 1150 Å to 1200 Å. The $\lambda_{\rm cen}$ = 1309 Å points are shown in maroon and the $\lambda_{\rm cen}$ = 1222 Å points are shown as dark blue squares. The counts have been resampled to a grid with 100-pixel-wide bins. Prior to binning, we masked the spectrum following the procedure described in Section 10.2. We assume the uncertainties on each bin are Poisson-distributed. Notice that there are several bins with $\sim$ 10 counts, indicating a $> 3\ \sigma$ continuum emission detection.

Chapter 11

THE NEAR-ULTRAVIOLET SPECTRA OF FU ORIONIS ACCRETION DISKS

Abstract: We present the results of the first high-sensitivity NUV (1800 to 3200 Å) survey of FU Ori objects, using the *Hubble Space Telescope* (HST) STIS spectrograph. We compare new low resolution spectra for 6 sources with predictions from accretion disk models and find that all show emission in excess of the disk model spectrum. The physical properties of the NUV emission excess are very consistent among the sample, with a mean luminosity of $0.04 \pm 0.02\ L_\odot$ and temperature of 16200 ± 2400 K – despite spanning 0.9 dex in M_*, 1.3 dex in $\dot{M}$, and 0.7 dex in $L_{\rm acc}$. We use the spectra to conclusively rule out the existence of a hot boundary layer in FU Ori accretion disks. We then discuss the source of the excess emission in the context of recent simulations of FU Ori outbursts and boundary layer accretion. The UV spectra also show the often-seen C II] 2326 Å multiplet and Mg II 2796/2803 Å doublet, as well as the unusual Fe II] 2507/2509 Å doublet, a feature that is not seen in the existing UV spectra of other young stellar objects. We measure and compare the luminosities of these lines in outbursting with those in non-outbursting objects.

11.1 Introduction

There is class of young stellar objects (YSOs) called FU Ori objects, or FUOrs (Herbig, 1977), which are observed to undergo eruptive episodes during which they accrete mass at rates up to 10,000 times greater than typical YSOs (Hartmann and Kenyon, 1996). These accretion-driven outbursts can last for several decades, with some appearing to have been in outburst for well over 100 years (e.g., V883 Ori and RNO 54, Strom and Strom, 1993; Hillenbrand, Carvalho, van Roestel, et al., 2023). The class is named for FU Ori, which underwent a $\Delta V = 4$ magnitudes outburst in 1937 (Wachmann, 1954) and has remained at nearly its peak brightness for the past 87 years. Since the start of the FU Ori outburst, approximately 40 FUOrs have been found (Connelley and Reipurth, 2018, Contreras-Pena et al. 2025, in prep). The enormous mass accretion rates of FUOrs ($10^{-5} - 10^{-4}\ M_\odot\ {\rm yr}^{-1}$) radically alter the geometry of the accretion of material from the disk onto the star.

In non-outbursting YSOs, the classical T Tauri stars (CTTSs), the accretion geometry is that of magnetospheric accretion (Uchida and Shibata, 1984). As material flows

toward the star in the inner disk, it eventually meets an opposing pressure from the strong stellar magnetic field, which is stronger nearer the star. There the magnetic field energy density becomes comparable with the ram pressure of the inflowing material and the charged matter is lifted along the stellar magnetic field lines and deposited on the surface of the star (e.g., Zhu, Stone, and Calvet, 2024). The mass flow reaches the star at freefall velocities ($300 - 400$ km s^{-1}) and creates a shock buried in the stellar photosphere. The shock-heated photospheric material at the location of the accretion column emits brightly at ultraviolet (UV) and blue visible wavelengths (Calvet and Gullbring, 1998; Hartmann, Herczeg, et al., 2016; Pittman, Espaillat, Robinson, Thanathibodee, Calvet, et al., 2022). The UV spectra of CTTSs are thus typically dominated by accretion emission, rather than emission from the photosphere of the star.

In FUOrs, by contrast, when the disk undergoes an instability that dramatically increases the accretion rate, $\dot{M}$, the pressure balance is disrupted. For sufficiently high $\dot{M}$, the magnetosphere is overwhelmed by the accretion flow and the disk engulfs the star. The disk material accretes directly onto the stellar surface modulated by a boundary layer. The boundary layer itself has been theorized to be a region dominated by shear heating as the disk material in Keplerian rotation slows to the rotation rate of the central star (Popham, Narayan, et al., 1993). Models of the shear heated boundary layer predict a high maximum temperature, $T_{\rm max}$, of the disk at radii approaching the stellar radius, R_* (Popham, Kenyon, et al., 1996). This high temperature shear-heated component should produce as a bright UV spectrum.

The accretion disk itself can reach temperatures of $7,000 - 8,500$ K (Welty, Strom, Edwards, et al., 1992; Kenyon, Hartmann, Imhoff, et al., 1989; Hartmann and Kenyon, 1996; Carvalho, Hillenbrand, Hambsch, et al., 2023) and is thus intrinsically UV-bright. The extreme luminosity of the accretion disk and its high maximum temperature have thus far made detection of any UV excess relative to the disk challenging. Identifying a UV excess requires going bluer than 3500-4500 Å, which is where the hottest components of the disk are brightest. Unfortunately, FUOrs are typically highly extincted (Connelley and Reipurth, 2018) and appear quite faint in the UV. Altogether, detecting the predicted boundary layer excess would require high sensitivity FUV and NUV spectra.

We recently completed a Hubble Space Telescope (HST) survey aimed at detecting this predicted UV excess. We targeted 6 FUOrs that had previous U or B band measurements bright enough to ensure they would be detected in the NUV, and

obtained low resolution spectra spanning 1800 – 5500 Å. We also sought a high resolution, deep spectrum of FU Ori in the FUV, in order to fully characterize the disk spectrum and any potential boundary layer excess emission at the disk-star interface.

In Carvalho, Hillenbrand, France, et al. (2024, hereafter C24), we published the finding that the FUV spectrum of FU Ori shows clear excess UV emission but its continuum shape and effective temperature are inconsistent with previous shear-heating models. We found that the continuum was instead more consistent with a magnetic heating or surface accretion shock origin.

In this article we present the UV spectra of the six FUOrs in our survey, including a re-discussion of FU Ori. All six objects have UV emission in excess of the viscous accretion disk. The luminosity of the excess component is correlated with the system luminosity, indicating the UV excess emission mechanism is related to accretion outburst itself. We also discuss the emission lines in the NUV spectra.

11.2 Data

We obtained visible and NUV spectra of 6 FUOrs: FU Ori, V1057 Cyg, V1515 Cyg, V960 Mon, HBC 722, and BBW 76 as part of the Guest Observer (GO) program 17176[1]. The sample was selected as the most blue/UV bright FU Ori objects known in 2022 ($B < 16$ mag). The spectra were taken with the Hubble Space Telescope (HST) Space Telescope Imaging Spectrograph (STIS) using the $52'' \times 2''$ arcsec slit in 2 grating settings: G230L (NUV-MAMA) and G430L. An observation log is provided in Table 11.1.

The spectra cover the wavelength range 1800 Å to 5500 Å at a spectral resolution of $R \equiv \lambda/\Delta\lambda \sim 600$. The signal-to-noise (SNR) ratio per pixel varies depending on the brightness of the source. In order to improve the SNR of the spectra at the bluest wavelengths, we bin the G230L spectra in 30 Å increments, masking out the bright emission features at 2326 Å, 2505 Å, and 2800 Å. The three faintest objects in the sample, V1057 Cyg, BBW 76, and HBC 722, have very little flux to the blue of 2300 Å, as can be seen in the 2D spectra presented in Appendix 11.7.

For our fainter objects, we consider the source detected if the peak of the spectral trace is 3× the noise value in a given wavelength bin (see Appendix 11.7 for details). V1057 Cyg, BBW 76, and HBC 722 are not detected blueward of 2300 Å, 2000 Å,

[1]The data can be accessed at the Mikulski Archive for Space Telescopes (MAST) via `https://doi.org/10.17909/tpk0-8h65`.

Table 11.1: HST/STIS Observations Log

Target	Date	Obs Time (s)	Grating	Wavelengths (Å)
FU Ori	2023-10-08	1381	G230L	1580 – 3160
	2023-10-08	45	G430L	2900 – 5700
V1057 Cyg	2023-04-05	1886	G230L	1580 – 3160
	2023-04-05	2818	G230L	1580 – 3160
	2023-04-05	150	G430L	2900 – 5700
V1515 Cyg	2025-01-01	1812	G230L	1580 – 3160
	2025-01-01	2796	G230L	1580 – 3160
	2025-01-01	150	G430L	2900 – 5700
HBC 722	2023-08-27	1856	G230L	1580 – 3160
	2023-08-27	180	G430L	2900 – 5700
BBW 76	2024-02-15	1848	G230L	1580 – 3160
	2024-02-15	2760	G230L	1580 – 3160
	2024-02-15	130	G430L	2900 – 5700
V960 Mon	2024-09-26	130	G230L	1580 – 3160
	2024-09-26	1810	G230L	1580 – 3160
	2024-09-26	2722	G430L	2900 – 5700

and 2300 Å, respectively, so for those objects we also computed 3σ upper limits on the flux in those wavelength bins. The upper limits are derived from the dark count level, cts_d, in each observation[2]. We assume that the uncertainty is Poisson-distributed and thus $\sigma_d = \sqrt{cts_d}$. We then converted σ_d to an effective flux level using the response function of the detector. The spectra and upper limits are all shown in Figure 11.1.

11.3 Modeling the Spectra

We model the NUV spectra with a two component model comprising a thin, viscously heated accretion disk and a single blackbody. We fit the two components generally following the same procedure described in C24, which we will summarize below.

The choice of extinction curve cannot be neglected in the analysis of UV data. The assumed shape of the 2175 Å feature can significantly impact continuum shape of dereddened spectra. As in C24, we adopt the extinction curve from Whittet et al. (2004), which has been demonstrated to be more appropriate for the interstellar

[2]The average dark counts subtracted per pixel from the image during processing is given in the `x1d` file header under the header key `MEANDARK`. We multiply this by the extraction region size, which is saved under the header key `EXTRSIZE`. This yields the total dark counts contributing to the uncertainty along the extraced object trace.

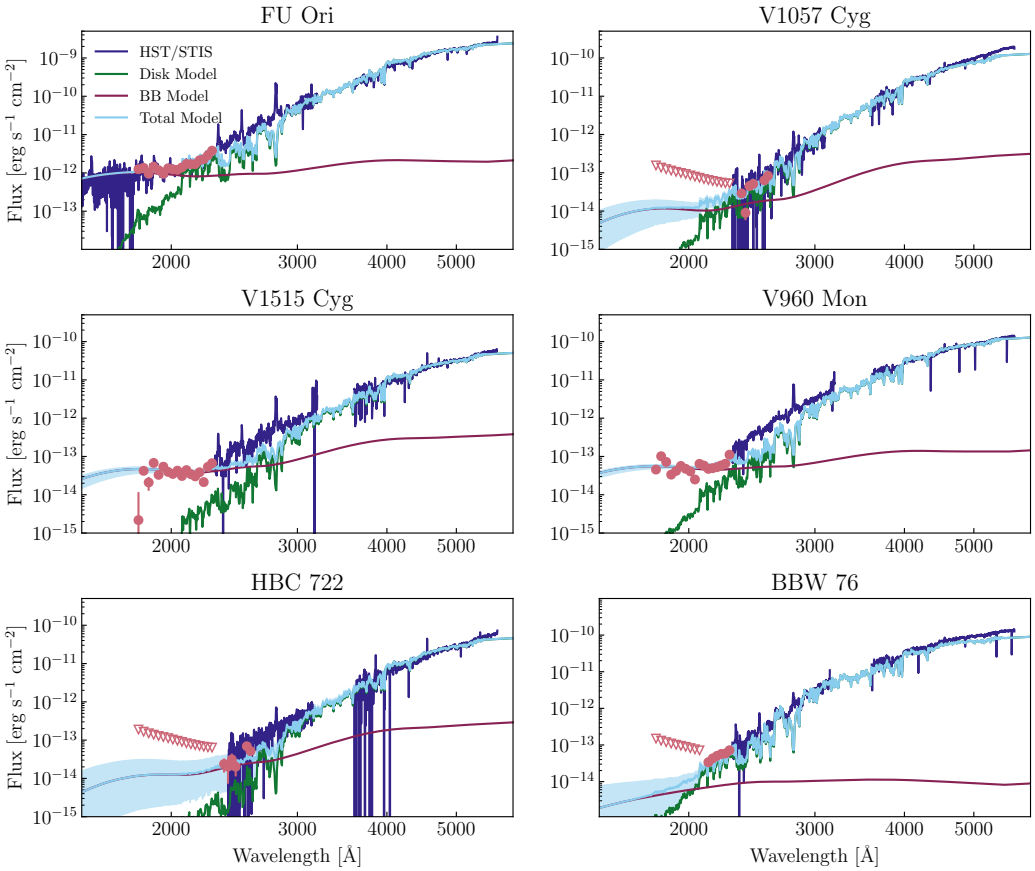

Figure 11.1: The G230L and G430L spectra for each of our objects (dark blue), along with the disk (green) and disk + UV excess (light blue) models for each of the FUOrs in the survey. The shaded regions show the range of the 16th and 84th percentile models from the MCMC samples. The UV excess in each panel (maroon) matches the flux level of the binned continuum points (salmon) blueward of 2300 Å. The flux upper limits for V1057 Cyg, HBC 722, and BBW 76 are shown as empty triangles.

environment surrounding YSOs. The extinction curve contains two important features: a weak 2175 Å "bump" and a total-to-selective reddening factor, or R_V, of 3.63 (greater than the typically adopted galactic average from Cardelli et al., 1989). Recent extensive work aimed at measuring R_V along several Milky Way sightlines indicates that R_V values that are greater than the galactic average are found in dense environments near star-forming regions, and that R_V can reach 3.5 – 3.7 in the densest regions probed by the study (Zhang and Green, 2025). For sources with sufficient SNR at 2100 Å (FU Ori, V1515 Cyg, and V960 Mon, see Figure 11.1), the spectrum does not show the strong 2170 Å absorption feature predicted by the often-used Cardelli et al. (1989) or Fitzpatrick (1999) extinction laws.

The Accretion Disk Component

The accretion disk model is the same that we successfully applied to model the spectra of FUOrs and is described in detail in Carvalho, Hillenbrand, and Seebeck (2023) and Carvalho, Hillenbrand, Seebeck, and Covey (2024). The primary assumption of the model is that the radial temperature profile of inner disk, $T_{\rm eff}(r)$, near the star can be described using the Shakura and Sunyaev (1973) α disk prescription,

$$T_{\rm eff}^4(r) = \frac{3GM_*\dot{M}}{8\pi\sigma_{\rm SB}r^3}\left(1-\sqrt{\frac{R_{\rm inner}}{r}}\right), \tag{11.1}$$

where M_* is the stellar mass, $\dot{M}$ is the disk-to-star mass accretion rate, $R_{\rm inner}$ is the innermost boundary of the disk, G is the universal gravitational constant, and $\sigma_{\rm SB}$ is the Stefan-Boltzmann constant. We modify the temperature profile so that $T_{\rm eff}(r < \frac{49}{36}R_{\rm inner}) = T_{\rm eff}(\frac{49}{36}R_{\rm inner}) \equiv T_{\rm max}$, following (Kenyon, Hartmann, and Hewett, 1988). This modification has been rigorously tested and upheld as an accurate description of the observed spectrum in both simulations (Zhu, Jiang, et al., 2020) and observations in the visible range (Rodriguez and Hillenbrand, 2022; Liu et al., 2022) and the UV (C24).

Table 11.2: The adopted disk model parameters for each object in the sample. Note that parameters like $\dot{M}$, $R_{\rm inner}$ and the emergent $T_{\rm max}$ and $L_{\rm acc}$ all vary over the course of an outburst. The parameters reported in this Table reflect the state of each system at the time of observation. The distance references are as follows: FU Ori (Kounkel et al., 2018; Roychowdhury and Hillenbrand, 2024a); V1057 Cyg (Szabó, Kóspál, Ábrahám, Park, Siwak, Green, Moór, et al., 2021); V1515 Cyg (Szabó, Kóspál, Ábrahám, Park, Siwak, Green, Pál, et al., 2022a); V960 Mon (Kuhn and Hillenbrand, 2019); HBC 722 (Kuhn and Hillenbrand, 2019); BBW 76 (Gaia Collaboration, Vallenari, et al., 2023).

Object	M ($M_\odot$)	$\log\dot{M}$ ($M_\odot$ yr^{-1})	$R_{\rm inner}$ ($R_\odot$)	inc (deg)	A_V (mag)	d (pc)	$T_{\rm max}$ (K)	$L_{\rm acc}$ ($L_\odot$)
FU Ori	0.60	−4.49	3.52	35	1.50	404	5970	86
V1057 Cyg	1.61	−5.32	2.67	8	2.72	795	5858	46
V1515 Cyg	1.0	−5.68	1.82	2	2.23	960	5609	89
V960 Mon	0.59	−4.96	2.69	15	1.60	1120.0	5550	38
HBC 722	0.20	−4.18	3.65	79	2.30	745.0	5840	85
BBW 76	0.20	−5.38	1.41	21	0.43	1040.0	5398	9

For each of the objects in the sample, the disk model parameters we use are presented in Table 11.2. The disk model component for each object is shown in light blue in Figure 11.1. In the case of FU Ori, we adopted the best-fit parameters we found

in C24. For HBC 722, we adopted the M_* and $R_{\rm inner}$ from Carvalho, Hillenbrand, Seebeck, and Covey (2024) and scaled the $\dot{M}$ downward to account for slightly fainter source brightness when the STIS spectrum was taken. For V960 Mon, we followed the prescription from Carvalho, Hillenbrand, Hambsch, et al. (2023) in order to scale the $\dot{M}$ and $R_{\rm inner}$ in the model spectrum from the 2017 epoch to the 2023 epoch of the STIS observation.

The remaining three objects, BBW 76, V1515 Cyg, and V1057 Cyg required new model fits. The details of the fits are given in Chapter 9. We follow the general disk fitting procedure we have applied successfully to the other FUOrs. The SEDs we fit are combinations of the near-infrared (NIR) spectra from Connelley and Reipurth (2018) and the STIS G430L spectra, scaled to the flux of each target in 2015, when the NIR spectra were taken. We also use rotational broadening of lines in high resolution spectra to constrain the maximum Keplerian velocity in the disk (see Chapter 8.1).

The Excess Blackbody Component

As can be seen in Figure 11.1, the disk model alone is insufficient to match the NUV continuum emission in all of the sources. The upper panel of Figure 11.2 shows the excess is stronger toward bluer wavelengths, with the observed flux diverging rapidly from the disk model flux for $\lambda < 2200$ Å.

In order to model the excess UV emission, we use a single-temperature blackbody, which we showed in C24 accurately matches the FUV and NUV excess emission in FU Ori. The blackbody component model has only two variable parameters: the effective radius of the emission region, $R_{\rm BB}$, and the effective temperature of the blackbody, $T_{\rm BB}$. We treat the emission as isotropic, since we do not know what the geometry of the emission is.

In order to model the excess UV emission, we use a single-temperature blackbody, which we showed in C24 accurately matches the FUV and NUV excess emission in FU Ori. The blackbody component model is given by

$$F_\lambda = \pi B_\lambda(T_{\rm BB}) \left(\frac{R_{\rm BB}}{d}\right)^2, \tag{11.2}$$

where d is the distance to the source, $R_{\rm BB}$ is the effective radius of the emission region, and $T_{\rm BB}$ is the effective temperature of the blackbody, B_λ. We treat the emission as a disk projected in the plane of the sky, since we do not know its true geometry and to maintain consistency with the assumption in C24.

For the sources with the highest signal-to-noise spectra (FU Ori, V1515 Cyg, and V960 Mon), we apply the model to the binned continuum points with $\lambda < 2300$ Å, as this is where the excess relative to the disk model is strongest and where there are few bright emission lines contributing to the continuum bins. For the fainter sources (V1057 Cyg, BBW 76, and HBC 722), we use the bluest wavelength bins in which they are detected, according to the detection criteria in Section 11.2. The wavelength ranges used for the fits are reported in Table 11.3. We then fit the two-parameter model using the log-likelihood based Markov-Chain Monte Carlo nested sampling code `dynesty` (Speagle, 2020). The median values from the posterior distributions, which we adopt as our best-fits, are reported in Table 11.3. The posterior distributions themselves are shown in Appendix 11.8.

Due to the lack of signal for $\lambda < 1800$ Å in our spectra, we are unable to adequately constrain the maximum possible temperature of the blackbody. However, we confidently rule out temperatures below 7,000 K for all of our objects. For FU Ori, V960 Mon, and V1515 Cyg, $T_{\rm BB} > 12000$ K is strongly preferred. The posterior distributions follow the expected $R_{\rm BB}^2 \propto T_{\rm eff}^4$ for a fixed luminosity, enabling us to compute the luminosity of the UV excess as $L_{\rm excess} = 4\pi R_{\rm BB}^2 \sigma_{\rm SB} T_{\rm BB}^4$. We report the luminosities in Table 11.3 and discuss them in Section 11.3.

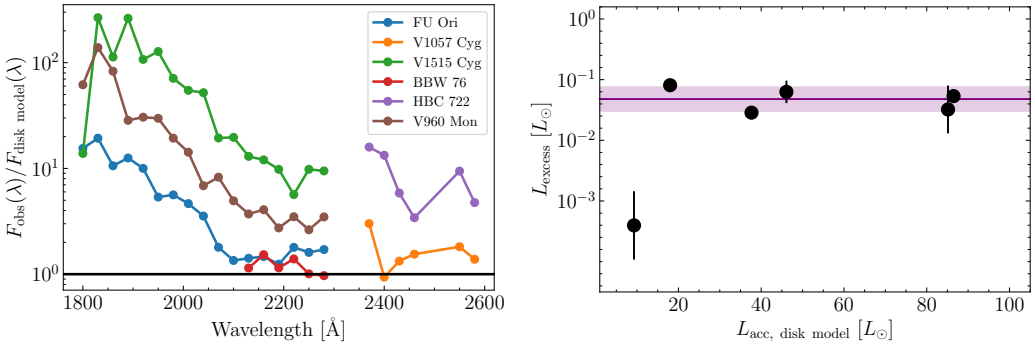

Figure 11.2: The excess emission observed in the STIS spectra and its luminosity for each FUOr in the survey. **Upper Panel:** The ratio of the observed binned STIS spectra used to fit the blackbody excess model and the disk models binned to the same wavelength sampling. Notice that for all the FUOrs in the sample, the NUV flux is at least 2× as bright as the disk model predicts at 2200 Å and for many the flux ratio is > 10 (for HBC 722 and V1057 Cyg, this is true at 2400 Å, despite the lack of data at 2200 Å). **Lower Panel:** The $L_{\rm excess}$ measurements for each of the FUOrs compared with their disk-model-derived $L_{\rm acc}$. The mean and standard deviation on the UV excess luminosities (excluding BBW 76) are marked by the purple line and shading, respectively.

Results of the Blackbody Fits and UV Excess Component Properties

Our spectra of five additional FUOrs confirm the observed properties of the UV excess in FU Ori itself. In particular, the excess components all have temperatures in excess of 12,000 K and filling factors of $< 10^{-3}$ of the stellar surface (Table 11.3).

In our sample of 6 objects, the mean $L_{\rm excess} = 0.04 \pm 0.02\ L_{\odot}$, excluding BBW 76, which shows almost no excess. The mean temperature $T_{\rm BB} = 16,200 \pm 2,400$ K and size $R_{\rm BB} = 0.05 \pm 0.01\ R_{\odot}$ are consistent with what we found for the UV excess of FU Ori using continuum regions of a COS FUV spectrum (C24).

As can be seen in the lower panel of Figure 11.2, the $L_{\rm excess}$ values show little dependence on the $L_{\rm acc}$ of the system. There is also no correlation between $L_{\rm excess}$ and $\dot{M}$, M_{*}, $R_{\rm inner}$, or i. The uniformity of the UV excess across the sample may have provide hints as to its origin and its relation to boundary layer accretion in general. We discuss this in detail in Section 11.5.

11.4 NUV Emission Lines

The NUV spectra of the FUOrs show 3 prominent emission features: the often-seen C II] 2326 Å multiplet and Mg II 2796/2803 Å doublet, as well as the unusual Fe II] 2507/2509 Å doublet. We discuss each of these features in detail below.

In order to understand the differences between these emission lines in FUOrs and their counterparts in CTTSs, we compute the line luminosities for each feature and discuss the measurements in the following Section. The CTTS we select for comparison is BP Tau. We justify the choice of BP Tau as a representative CTTS in Appendix 11.9. We measure its line luminosities in the STIS G230L spectrum obtained in 2002 in the HST GO program 9081 (PI: N. Calvet; Kravtsova and Lamzin, 2003), which was accessed through MAST. We adopt a distance of 131 pc (Gaia Collaboration, Vallenari, et al., 2023) and an $A_V = 0.41$ mag to the source (Herczeg and Hillenbrand, 2014).

The line fluxes were measured from the dereddened spectra, which were extinction-corrected using the A_V values reported in Table 11.2 and the Whittet et al. (2004) extinction law. We then fit a pseudocontinuum near the line using the `specutils` function `fit_continuum` and compute the line flux via direct integration. The integration limits for each lines are: 2310 – 2340 Å (C II]), 2503 – 2515 Å (Fe II]), and 2780 – 2820 Å (Mg II). The flux is then converted to a luminosity using the source distances in Table 11.3. The luminosity measurements are shown in Figure 11.4.

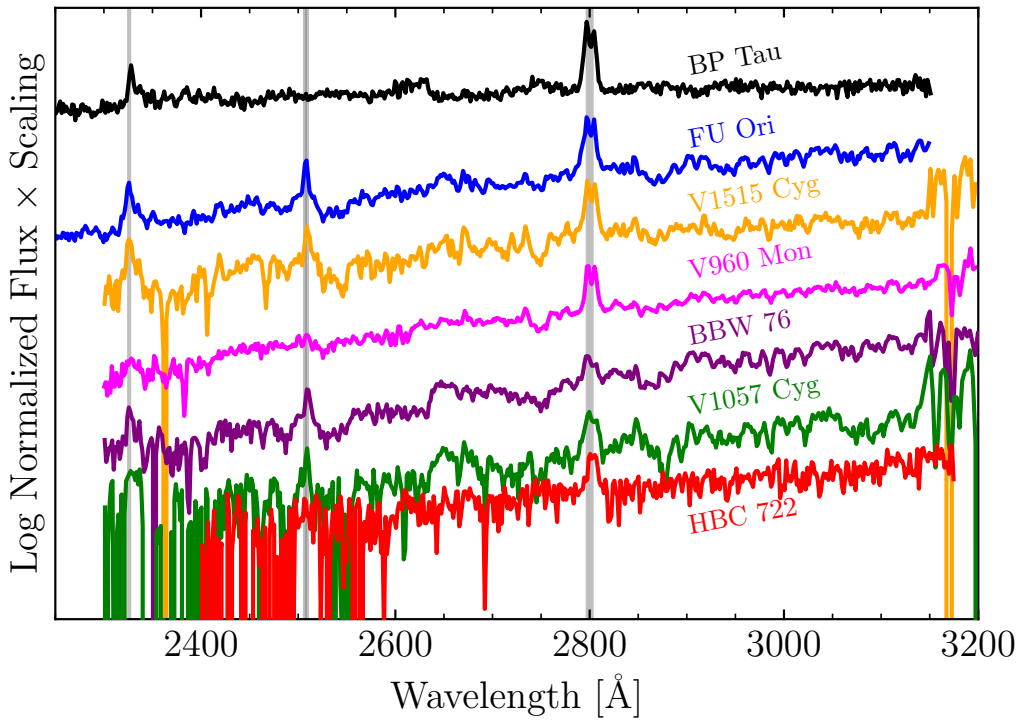

Figure 11.3: The STIS G230L spectra of the 6 FUOrs and the CTTS BP Tau for reference. The spectra are sorted top-to-bottom in order of decreasing signal-to-noise. The grey vertical lines mark the locations of the emission features discussed in Section 11.4.

The Mg II Doublet

The brightest feature in the NUV spectra of all 6 objects is the Mg II 2796/2803 Å doublet. Although doublet luminosity has been shown to correlate with the accretion luminosity of CTTSs, it can display P Cygni profiles typical of lines that trace outflows and has been seen in non-accreting, but magnetically active, YSO spectra (Ingleby et al., 2013; Xu et al., 2021b). The high resolution 2001 HST/STIS E230M spectrum of FU Ori also reveals strong outflow absorption in the Mg II doublet, as both features are in clear P Cygni profiles (Kravtsova, Lamzin, et al., 2007).

Despite the unknown degree of outflow absorption in the profiles, we measure and report the doublet luminosity for each object. The high resolution E230M spectrum of the FU Ori (Kravtsova, Lamzin, et al., 2007) shows that the deep blue-shifted absorption removes approximately half of the flux from the total line emission. Therefore, our reported luminosities should be considered lower limits on the intrinsic Mg II doublet luminosity of FUOrs.

Visually, the Mg II line strengths look similar across the sample, with the exception of BBW 76 and V1057 Cyg. In these two objects, the Mg II emission is much weaker relative to the other two emission features, an effect that is quantified in the ratios plotted in Figure 11.4. We discuss the potential implications of this in Section 11.5.

The C II] Complex at 2326 Å

The C II] emission feature at 2326 Å is in fact a blend of multiplets from three species: C II], Si II], and Fe II]. The features in the wavelength range over which we measure line flux that contribute most strongly to the line are: C II] 2324.21, 2325.4, 2326.11, 2327.64, and 2328.83, Si II] 2329.23, and 2335.12/2335.32, and Fe II] 2328.11. In the STIS E230M spectrum of FU Ori, the Si II] 2335.12/2335.32 doublet has a blue-shifted absorption/red-shifted emission P Cygni profile. The emission from the Fe II] features in the region is also mildly red-shifted, suggesting they may be in P Cygni profiles as well. This indicates that at least the Fe II] and Si II] features trace an outflow in the system.

Looking closely at the C II] multiplet in the STIS E230M spectrum of FU Ori reveals that the lines are unlikely to arise from an optically thin plasma in collisional equilibrium. In CTTSs, this assumption has enabled the estimation of temperature and number density of the line-emitting material based on flux ratios of lines in this complex (López-Martínez and Gómez de Castro, 2014). We test this assumption in FU Ori using line emissivities from the CHIANTI database. Over a broad range of electron densities ($n_e = 10^2 - 10^{15}$ cm^{-3}) and temperatures ($T_e = 10^4 - 10^6$ cm^{-3}), the ratio of C II] 2325.4/2326.11 intensities is at most 0.2 – 0.3. In the FU Ori E230M spectrum, the ratio is 0.74, indicating the level population of the multiplet is in disequilibrium.

Although in CTTSs the C II] 2326 Å luminosity is a reliable tracer and diagnostic of accretion, its luminosity in FUOrs does not follow the same scaling. If we apply the Ingleby et al. (2013) relation found for CTTSs, $\log L_{\rm acc} = 1.1 \log(L_{\rm CII]}) + 2.7$, the $L_{\rm acc}$ values for the FUOrs are underpredicted by factors of 40 – 160. There is some mild correlation between the $L_{\rm CII]}$ and $L_{\rm acc}$ values, however, which can be fit by $\log(L_{\rm acc}) = 1.3 \log(L_{\rm CII]}) - 4.75$ (omitting the HBC 722 upper bound in the fit). The best fit is shown in Figure 11.4.

The Fe II Doublet and Its Origin

There is a strong feature at 2508 that we identified as the Fe II] 2507/2509 doublet in the spectrum of FU Ori (C24). The luminosity of the line closely matches the

luminosity of the C II] feature in all of the sources, even matching the $L_{\rm CII]}$ upper limit in HBC 722. This indicates that the feature may also correlate with the $L_{\rm acc}$ of FUOrs (except HBC 722). However, as we discuss below, the origin of the feature is not well-understood.

The presence of the Fe II] 2507/2509 doublet in the spectra of FUOrs is surprising. It is not seen at all in the spectra of other accreting YSOs, but has been observed in spectra of evolved systems like symbiotic binaries, η Carinae, and chromospherically-active giants (Johansson and Hamann, 1993b; de la Reza, 2025), indicating it may be diagnostic of boundary layer accretion. The feature is not expected to appear as brightly as we see it in the FUOr spectra in isolation. For an optically thin plasma in local thermodynamic equilibrium, there are several Fe II emission lines around 2495 – 2520 Å that should be as bright as or brighter than the 2507/2509 doublet (Dere et al., 1997; Del Zanna et al., 2021b). However, the high resolution STIS E230M spectrum of FU Ori confirms that the doublet is much brighter than any nearby Fe II features (Kravtsova, Lamzin, et al., 2007).

The strength of the doublet relative to other Fe II features in the same wavelength range is attributed to fluorescence via one of two proposed mechanisms: photoexcitation by accidental resonance or photoexcitation by continuum resonance (termed PAR or PCR, respectively, Johansson and Hamann, 1993b). Both mechanisms rely on photons in the 1000-1300 Å wavelength range to pump Fe II transitions that populate energy levels around 11-12 eV, which eventually cascade downward and through the 2507/2509 lines (Johansson and Hamann, 1993b)[3]. While it is beyond the scope of this paper to model the emission of this doublet in detail, we did investigate the PAR/PCR mechanisms discussed in Johansson and Hamann (1993b) and their plausibility in FUOrs.

The PAR mechanism relies on the coincidence between the wavelength of an existing emission line and that of a transition in another species. In the case of the 2507/2509 doublet, Johansson and Hamann (1993b) propose that very red-shifted Lyα might excite electrons via transitions at 1217.85 Å and 1218.21 Å, which would require Lyα emission reaching 500 – 600 km s^{-1}. Alternatively, −70 km s^{-1} emission by the O V 1218.5 Å line could also excite the same transition. In C24, we found high velocity red-shifted Lyα in the high resolution FUV spectrum of FU Ori, as well as blue-shifted emission from O V at 1371 Å with a velocity of −80 km s^{-1}. Though this

[3]The specific transitions are identified by Johansson and Hamann (1993b) as $5p^6F^\circ_{9/2} \rightarrow 4s\ c^4F_{7/2}$ and $4p^4G^\circ_{9/2} \rightarrow 4s\ c^4F_{7/2}$ for 2507 Å and 2509 Å, respectively.

suggests Lyα emission as a promising PAR source, CTTSs have extremely bright Lyα at velocities of 500 – 600 km s^{-1} (Arulanantham et al., 2023) but do not show the Fe II doublet.

In the case of PCR, all that is necessary is bright continuum emission in the correct wavelength range to excite the desired transition. Johansson and Hamann (1993b) propose that Fe II ground transitions around 1100-1115 Å can be excited by continuum emission. A clear signature of this excitation mechanism would be a series of absorption features in 1100-1115 Å wavelength range, though that may depend on the geometry of the absorbing material. There is also the case of the 1785 Å Fe II feature, which can result from PCR of ground transitions around 1270 Å (Hempe and Reimers, 1982). While the signal-to-noise ratio of the FUV spectrum of FU Ori is insufficient to detect the predicted line absorption, PCR would explain the strength of the bright feature at 1785 Å seen in the FUV spectrum of FU Ori C24. Given the bright FUV continuum of FU Ori, which we showed extends beyond 1150 Å (C24), it is possible that PCR in the 1100 Å range could pump the upper transitions of the 2507/2509 doublet.

Both PAR and PCR can also produce fluorescent line emission at wavelengths around 9000 Å, but the lines would be significantly fainter than the accretion disk and therefore not observable in the spectra of FUOrs. Clearly identifying or ruling out PAR/PCR as the source of the transition pumping photons would require both careful modeling of this mechanism in FUOrs and a much more sensitive FUV spectrum of FU Ori.

11.5 Discussion

In Section 11.3, we demonstrated that all six FUOrs in the sample possess excess UV continuum emission that reaches more than 10× the disk model flux, as shown in Figure 11.2. We also found that the excess emission spans a narrow range of luminosities ($L_{\rm excess} \sim 0.04\ L_{\odot}$), temperatures ($T_{\rm BB} \sim 12000 - 18000$ K), and physical size ($R_{\rm BB} \sim 0.02 - 0.06\ R_{\odot}$). Despite the 0.9 dex range in stellar mass and 1.2 dex range in mass accretion rate, the $L_{\rm excess}$ excess varies little across the sample. Here, we discuss the potential source of the emission in the context of the classical boundary layer accretion model for FUOrs and the exceptional case of the source BBW 76.

The UV Excess Emission in FUOrs compared with CTTSs

To contextualize the luminosity of the UV excess in FU Ori objects relative to other YSOs, we compare our measurements with the UV survey of CTTSs compiled by Yang et al. (2012). We restrict our comparison to the lower mass and lower luminosity subset of CTTSs ($L_{\rm acc} < 1\ L_{\odot}$), since they better reflect the pre-outburst FUOrs in our survey.

Directly comparing the UV emission from both sets of objects is challenging due to the different accretion geometries in each. In CTTSs, for instance, a large fraction ($10 - 50\%$) of the accretion luminosity is emitted at $2000 < \lambda < 3100$ Å (termed $L_{\rm space}$ in Pittman, Espaillat, Robinson, Thanathibodee, Lopez, et al., 2025). Integrating our disk + blackbody models in the range $2000 < \lambda < 3100$ Å, we find a median $L_{\rm space} = 10^{-1.7\pm0.4}\ L_{\odot}$, which is only a bit smaller than $L_{\rm UV}$. Dividing by the $L_{\rm acc}$ values in Table 11.2, we obtain $L_{\rm space}/L_{\rm acc} = 10^{-3.4\pm0.2}$. In other words, only a very small fraction of the total $L_{\rm acc}$ in FUOrs is emitted in the NUV, though the actual NUV luminosities themselves are high.

Comparing the luminosities of the CTTSs and FUOrs in the FUV is further complicated by the lack of FUV spectra in our survey (with the exception of FU Ori). Although we do not have FUV spectra for the other 5 objects in the sample, we can extrapolate the blackbodies into the FUV. The blackbodies have similar best-fit $T_{\rm BB}$ and $R_{\rm BB}$ to the FUV-derived best-fit values for FU Ori, indicating the FUV continuum emission in our sample is likely well-represented by these blackbody fits.

We then integrate the blackbodies in the range $1250 - 1700$ Å, as was done to measure the $L_{\rm FUV}$ of CTTSs reported in Yang et al. (2012). The mean $L_{\rm FUV,FUOr} = 0.012 \pm 0.007\ L_{\odot}$ following this process. This is 7.5× greater than the mean $L_{\rm FUV,CTTS} = 0.0016 \pm 0.002 L_{\odot}$ for the CTTSs in the Yang et al. (2012) with $L_{\rm acc} < 1\ L_{\odot}$. The true difference between the FUV continuum luminosities of the two samples is likely greater, since the FUV spectra of CTTSs are emission-line-dominated, with continuum emission matching the typical accretion shock models for $T_{\rm eff} = 10^4$ K (France, Yang, et al., 2011).

The Missing Boundary Layer in FUOrs

In the viscous accretion disk model applied to FUOrs (Lynden-Bell and Pringle, 1974b; Kenyon, Hartmann, and Hewett, 1988), only half of the viscous dissipation of gravitational energy ($GM_*\dot{M}/R_{\rm inner}$) is expected to be radiated by the disk itself.

A key assumption is that as material approaches the star, it must decelerate from its large Keplerian rotation rate to the much slower stellar rotation rate. This requires dissipating the remaining half of the initial gravitational energy over a region known as the dynamical boundary layer.

If the energy dissipation mechanism in the dynamical boundary layer is viscosity, then the energy should be efficiently radiated away as the material is heated. The dynamical boundary layer would then have a luminosity as great as the accretion disk due to this extreme shear ($L_{\rm BL} = L_{\rm acc}$). In our survey, the median value of $L_{\rm excess}/L_{\rm acc}$ measured for the 6 FUOrs is 0.002 ± 0.001, which is several orders of magnitude below what would be expected of a shear-heated boundary layer.

A potential solution is to assume that the boundary layer may be confined to latitudes near disk midplane and obscured from our view due to the surface accretion layer. Could the UV spectrum be reproduced by adopting a higher temperature ($T_{\rm BL} \sim 30,000$ K, Hartmann and Kenyon, 1985b) and luminosity ($L_{\rm BL} = 85\ L_\odot$) for the boundary layer but obscuring it under some larger A_V? We explored this using the FUV spectrum of FU Ori and found that even for large $T_{\rm BL}$, adopting $A_V > 2$ mag results in model spectra that underpredict the flux for $\lambda < 1600$ Å.

We note that the obscuring material is probably not dust, and thus A_V may not be an appropriate proxy for its absorption. However, if we were to instead model the gas absorption against the 30,000 K continuum, the absorption would be dominated by the bound-free transitions in metallic species like C and Si, which have even greater continuous opacities than dust at FUV wavelengths (Travis and Matsushima, 1968). We do not see these features in the FUV spectrum of FU Ori, but it is possible that the continuum sensitivity is insufficient to detect them. Perhaps future large UV/optical telescopes with greater senstivity will reveal these continuum features in the FUV spectra of FUOrs. In either case, for the large column densities necessary to diminish the observed $L_{\rm BL}/L_{\rm acc}$ by several orders of magnitude, the FUV continuum at $\lambda < 1600$ Å is severely underestimated.

The upper limit on extinction also places an upper limit of $0.6\ L_\odot$ on the luminosity of an obscured boundary layer. It is therefore unlikely that the FUV continuum in FU Ori is due to a classical boundary layer obscured by disk material along the line of sight. Furthermore, (Popham, Narayan, et al., 1993) found that for the high accretion rates in FUOrs, the boundary layer should extend over as much as $0.2\ R_*$, which is incompatible with the median $R_{\rm BB} = 0.04\ R_\odot$.

The uniformly low luminosity and small spatial scale of the UV excess in FUOrs is inconsistent with the classical models for a hot boundary layer. In C24, we also provide a more extensive discussion of other models for shear-heated boundary layers, both in the literature of YSOs and compact objects, and why the UV excess in FU Ori is inconsistent with those.

In short, the remaining gravitational energy of the gas near the stellar surface is not dissipated by heating the boundary layer. It is instead likely that the pressure support from the strong magnetic fields near the surface of the star slows the material as it approaches. The interacting disk and stellar fields in the boundary layer are capable of efficiently removing large amounts of angular momentum via Maxwell stresses (Takasao et al., 2025). The magnetic field is thus capable of slowing material down to the stellar rotation rate without strongly heating the gas.

The Source of the UV Continuum Excess in FUOrs

As we established in Section 11.5, the UV excess emission in FUOrs does not arise from a classical hot boundary layer. What could the source of the excess be, then?

In CTTSs, the UV excess emission arises from the heated pre-shock and post-shock material in the photosphere (Calvet and Gullbring, 1998; Hartmann, Herczeg, et al., 2016). This material is expected to be $8,000 - 10,000$ K, while the shock temperature is expected to be $\sim 9 \times 10^5$ K due to the high free-fall velocities of matter flowing along the accretion funnel.

The picture we presented in C24 was that the FUV continuum in FU Ori is from a directly-observed accretion shock that is much cooler than that of CTTS systems. The velocity of material producing this shock is the surface accretion flow velocity at the disk-star interface, which is found to be $\sim 40\%$ of the Keplerian velocity near the star (Zhu, Jiang, et al., 2020). For most of our sources, the Keplerian velocity at $r = R_*$ is 160 ± 20 km s^{-1}, indicating a surface flow velocity of $v_{\rm surf} = 64 \pm 8$ km s^{-1}. If we assume that the resulting shock is a strong shock, we estimate the shock temperature: $T_s = \frac{3}{16}\frac{\mu m_H}{k} v_{\rm surf}^2 = 45,500$ K, where k is the Boltzmann constant, m_H the mass of the hydrogen atom, and μ the mean atomic weight, set to 0.5 here since the material is likely fully ionized. $T_s = 45,500$ is much greater than the maximum $T_{\rm BB}$ in the sample.

If we assume that the the magnetic pressure support from the star/disk field at the boundary further slows the material (Takasao et al., 2025), we can adopt 40 km s^{-1} as the inflow shock velocity and compute $T_s = 17,300$ K, which is in better agreement

with the $T_{\rm BB}$ values. The range of temperatures observed in the sample can then be reproduced by increasing or decreasing $v_{\rm surf}$ by just 5 km s^{-1}, while the range of $v_{\rm Kep}(R_*)$ in our sample is more than 100 km s^{-1}. We observe a weak correlation between $T_{\rm BB}$ and $v_{\rm Kep}(R_*)$, supporting the idea that $v_s \propto v_{\rm Kep}(R_*)$ subject to some braking effect.

It is also conceivable that the magnetic deceleration of the surface flow may be more efficient in systems with greater $v_{\rm Kep}(R_*)$. The magnetic deceleration depends in part on the strength of the bundled fields near the stellar surface, which depend on the shear between the star and disk (Takasao et al., 2025). Systems with larger $v_{\rm Kep}(R_*)$ may thus have stronger fields at R_* and more effectively brake the more rapid flow. In this way the deceleration may regulate the accretion flow velocity to produce the narrow range of observed temperatures.

An alternative hypothesis is that the UV emission arises from material above the star that is heated by rapidly recurring magnetic reconnection events at the star-disk interface. These events are seen in simulations of boundary layer accretion and are proposed to be the energy source heating the material emitting soft X-rays in FUOrs (Takasao et al., 2025). This would also explain the high temperatures of the X-rays in FUOrs (Kuhn and Hillenbrand, 2019), as well as the hour-to-hour variability of X-ray luminosity in FU Ori (Skinner et al., 2010).The UV emission may then be from material between the stellar surface and the hot corona above.

The Strange Case of BBW 76

A potential hint to the UV excess emission source lies in the outlier of our sample: BBW 76. We do detect the UV excess in the source, but it has an $L_{\rm excess}$ that 13× smaller than the median in the sample. Our upper limits on the flux blueward of 2000 Å also rule out the potential of a hotter or brighter component with $L_{\rm excess} > 0.02\ L_\odot$ (5× fainter than the rest of the sample), despite an accretion luminosity of $L_{\rm acc} = 13\ L_\odot$. Furthermore, BBW 76 has an NUV line emission spectrum that is distinct from the other FUOrs. The Mg II 2800 Å doublet is much less luminous than in the other objects, even the CTTS BP Tau, and there is a strong continuum break or emission feature at 2650 Å, which appears only weakly in the other objects.

While its large (relative to CTTSs) accretion luminosity confirms it is still in outburst, recent photometry from ASAS-SN and NEOWISE (Shappee et al., 2014a; Mainzer et al., 2011; Hart et al., 2023) shows that BBW 76 has faded monotonically by more than $\Delta V = 0.3$ mag and $\Delta W1 = 0.8$ mag in 10 years, while a recent near-infrared

spectrum of the source shows significant spectroscopic evolution in the past 5 years (Carvalho 2025, in prep). It is possible that the source has entered an intermediate stage between boundary layer accretion and magnetospheric accretion, wherein the proximity of the inner disk to the central star still produces a bright disk-dominated visible range continuum.

A transition between boundary layer accretion and magnetospheric accretion could result in a rapid decline in the UV excess luminosity. In the shock case, once the magnetospheric funnel flows re-establish themselves, the disk and stellar fields will separate spatially, lowering the magnetic flux (and therefore magnetic pressure) near the location of the former boundary layer. The pressure support will no longer slow the surface accretion flow, enabling it to impact the photosphere at velocities more similar to the CTTS case, embedding the shock in the photosphere. The lower $T_{\rm BB}$ in BBW 76 implies we may be seeing the heated photosphere re-processing this buried shock, rather than the shock itself.

The magnetic reconnection events that may produce the excess rely on the interaction of the stellar and disk fields at the boundary layer (Takasao et al., 2025). Once again, as the magnetospheric accretion funnels re-establish themselves, the disk and stellar surface will be separated, lessening the frequency of reconnection events. The heating would diminish and the temperature and luminosity of the emission would decrease as the system evolves away from boundary layer accretion.

11.6 Conclusions

Our recent HST/STIS survey of FUOrs reveals that FUV continuum emission in excess of the viscous accretion disk is common. The typical properties of the FUV continuum in the sample are: $L_{\rm excess} = 0.04 \pm 0.02\ L_{\odot}$, $T_{\rm BB} = 16,200 \pm 2,400$ K, and $R_{\rm BB} = 0.04 \pm 0.01\ R_{\odot}$. The consistent luminosities, temperatures, and physical sizes of the emitting material indicate a common source for the emission in all FUOrs.

The NUV line emission from the sample is also bright, though not as bright as predicted by correlations between line and accretion luminosity in CTTSs. The presence of strong Fe II] 2507/2509 doublet emission relative to other Fe II features also imply that the physical conditions of the plasma emitting the NUV lines differ significantly from those in the NUV emitting accretion flows of CTTSs.

Recent magnetohydrodynamical simulations of both the FU Ori system and boundary layer accretion in protostars support two potential origins for the UV continuum

emission: a shock where the surface accretion flow impacts the stellar surface or material above the star heated by magnetic reconnection events at the star/disk interface. The comparison of the properties of the UV emission and physical properties (M_*, $\dot{M}$, $R_{\rm inner}$) of the sample do not highlight a preference for one mechanism over another.

More detailed study and modeling of the emission lines in the NUV spectra will help to establish whether they share a common origin with the UV continuum emission. A UV-sensitive spectrograph on a future large space telescope will be critical for expanding the number of FUOrs with NUV and FUV spectroscopy beyond the 6 covered in this study.

11.7 Appendix: STIS 2D Spectra and Detection Criteria For Fainter Sources

The 2 dimensional recitified `x2d` G230L spectra of each object in the sample. For sources with 2 G230L exposures (see Table 11.1), the images have been coadded via an uncertainty-weighted mean. The traces can clearly be identified, as well as the 3 bright emission lines discussed in Section 11.4. In FU Ori, the diffuse emission from the bright scattered light nebula (Zurlo et al., 2024b) can be seen, as well as the trace of FU Ori S (Carvalho, Herczeg, et al., 2024).

In order to check the wavelengths where the faintest 3 sources (V1057 Cyg, HBC 722, and BBW 76) were detected, we cut spatial profiles of the 2d spectra in ~ 78 Å bins. The spectrally-binned mean spatial profiles are shown in Figure 11.6. We then computed the maximum surface brightness (within $0.2''$ of the slit center) and standard deviation (within $0.2''$ of the slit center) for each spatial profile. The source was considered “detected" in a given spectral bin if the maximum surface density was greater than $3\times$ the standard deviation.

11.8 Appendix: Posterior Distributions for the UV Excess Blackbody Fits

The posterior distributions for the blackbody fits to the UV excess are shown in Figure 11.7 as `corner` plots (Foreman-Mackey, 2016). Notice that for the sources with the strongest detected excess, the maximum temperature is poorly constrained by the NUV-only data. This is confirmed by the case of FU Ori, which has a well-constrained $T_{\rm BB}$ and $R_{\rm BB}$ in C24 when the fit included the FUV continuum but not in this paper when the fit is restricted to only the NUV. The luminosity of the emission, however, is clearly well-constrained. This can be seen from the fact that the posteriors of the two parameters lie along a locus well-described by $R_{\rm BB} \propto T_{\rm BB}^{-2}$.

11.9 Appendix: BP Tau as a Representative CTTS

We select BP Tau as our reference CTTS for the comparison between the NUV spectra of FUOrs and those of non-outbursting YSOs. The $M_* \sim 0.5\ M_\odot$ of BP Tau is comparable to those of the central objects in our sample, while its accretion rate ($\dot{M} = 10^{-7.29}\ M_\odot\ \mathrm{yr}^{-1}$) is typical for a CTTS (Manara et al., 2023).

To determine how well the NUV spectrum of BP Tau represents typical NUV spectra of CTTSs, we query all 87 of the STIS/G230L for sources classified as T Tauri Stars in the ULLYSES archive on MAST (Roman-Duval et al., 2025). The stellar properties of the sample span spectral types of M6 to A2 (though most are M2-K1) and a broad range of accretion rates.

We then perform a signal-to-noise selection, keeping only the 50 spectra that have a median signal-to-noise ratio of 5 for $\lambda > 2100$ Å. We divide each spectrum by an approximate continuum, estimated using the asymmetric least-squares fitting code described in (Carvalho, Hillenbrand, and Seebeck, 2023). We use an extremely inflexible regularization parameter of 10^12 and fit only the 10th percentile of flux, to avoid emission features and divide out only the general slope of each spectrum. We then interpolate each spectrum to a common wavelength grid and compute the 16th, 50th, and 84th percentile normalized flux over all spectra in each wavelength bin. This enables us to estimate the median spectrum in the sample as well as the typical object-to-object variation in features like strong emission lines.

Figure 11.8 shows the G230L spectrum of BP Tau compared with the median ULLYSES spectrum. The upper and lower ranges of spectra are shown in the shaded region. Notice that BP Tau almost perfectly matches the median spectrum.

Table 11.3: The best-fit blackbody component parameters and NUV emission line luminosities for each object in the sample. The best-fit blackbody component parameters for FU Ori are adopted from C24, since that analysis includes FUV data that can better constrain $T_{\rm BB}$.

Object	Fit Range (Å)	$\log R_{\rm BB}$ ($R_\odot$)	$T_{\rm BB}$ (K)	$\log(L_{\rm excess})$ ($L_\odot$)	$L_{\rm MgII}$ (10^{-3} $L_\odot$)	$L_{\rm CII]}$ (10^{-3} $L_\odot$)	$L_{\rm FeII]}$ (10^{-3} $L_\odot$)
FU Ori	1800 – 2300	-1.3 ± 0.2	$16,000 \pm 1,000$	-0.68 ± 0.01	78.9 ± 0.3	7.0 ± 0.1	7.0 ± 0.1
V1057 Cyg	2350 – 2500	-1.2 ± 0.3	$14,200 \pm 4,000$	-1.20 ± 0.19	26.1 ± 2.5	9.9 ± 0.6	3.8 ± 0.2
V1515 Cyg	1800 – 2300	-1.2 ± 0.2	$16,600 \pm 2,500$	-1.09 ± 0.04	31.4 ± 4.7	5.3 ± 0.2	4.5 ± 0.7
V960 Mon	1800 – 2300	-1.5 ± 0.1	$18,500 \pm 1,500$	-1.54 ± 0.03	23.4 ± 3.5	1.1 ± 0.3	0.9 ± 0.5
HBC 722	2350 – 2500	-1.2 ± 0.5	$12,750 \pm 5,000$	-1.49 ± 0.34	5.2 ± 0.4	< 9.0	0.34 ± 0.01
BBW 76	2100 – 2300	-2.2 ± 0.5	$11,600 \pm 5,000$	-3.4 ± 0.56	0.38 ± 0.17	0.01 ± 0.01	0.1 ± 0.01
Average	···	-1.27 ± 0.13	$16,200 \pm 2,400$	-1.34 ± 0.18	···	···	···

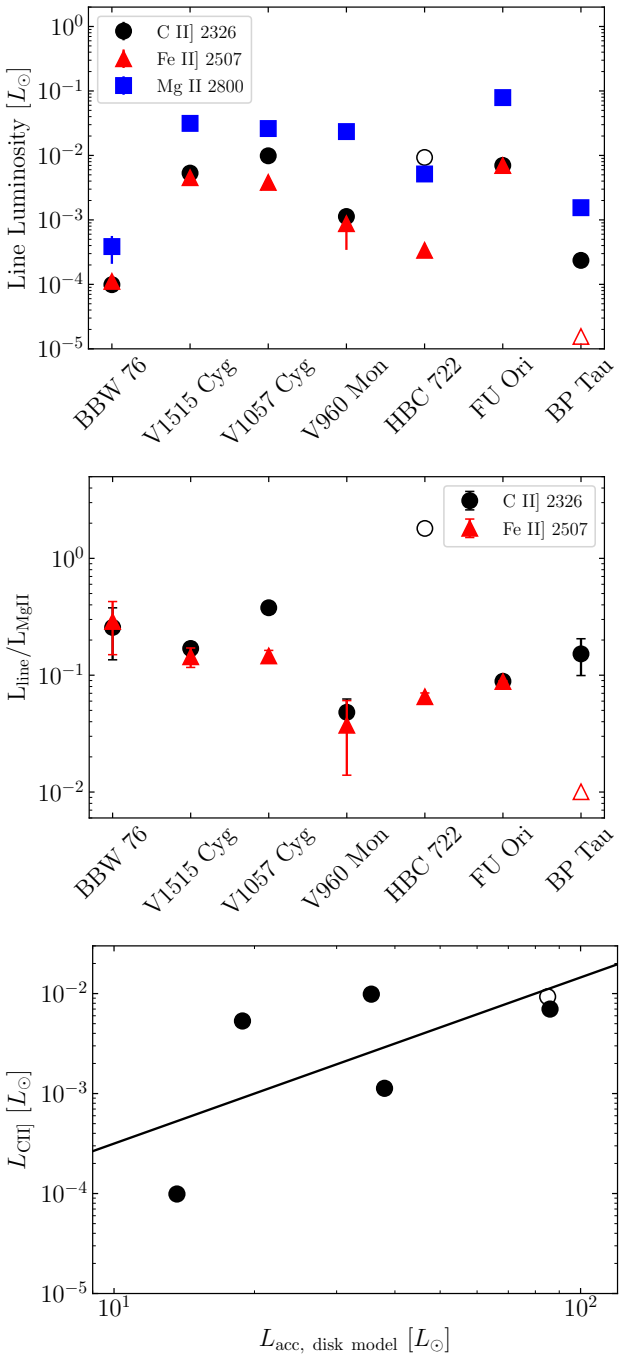

Figure 11.4: Comparisons of the line luminosities in the FUOr sample and a representative CTTS (BP Tau). **Top:** The C II] (black circles), Fe II] (red triangles), and Mg II (blue squares) line luminosities for the FUOr sample and the CTTS BP Tau. Error bars are drawn but are smaller than the symbols for most measurements. The empty circle (triangle) for HBC 722 (BP Tau) represents the 3σ upper limit on the C II] (Fe II]) luminosity. The FUOrs are sorted left-to-right in order of increasing $L_{\rm acc}$. **Middle:** The same line C II] and Fe II] luminosities divided by the Mg II luminosities. **Bottom:** The $L_{\rm CII]}$ measurements plotted against the $L_{\rm acc}$ for the FUOrs. The black line shows the best-fit relation described in Section 11.4.

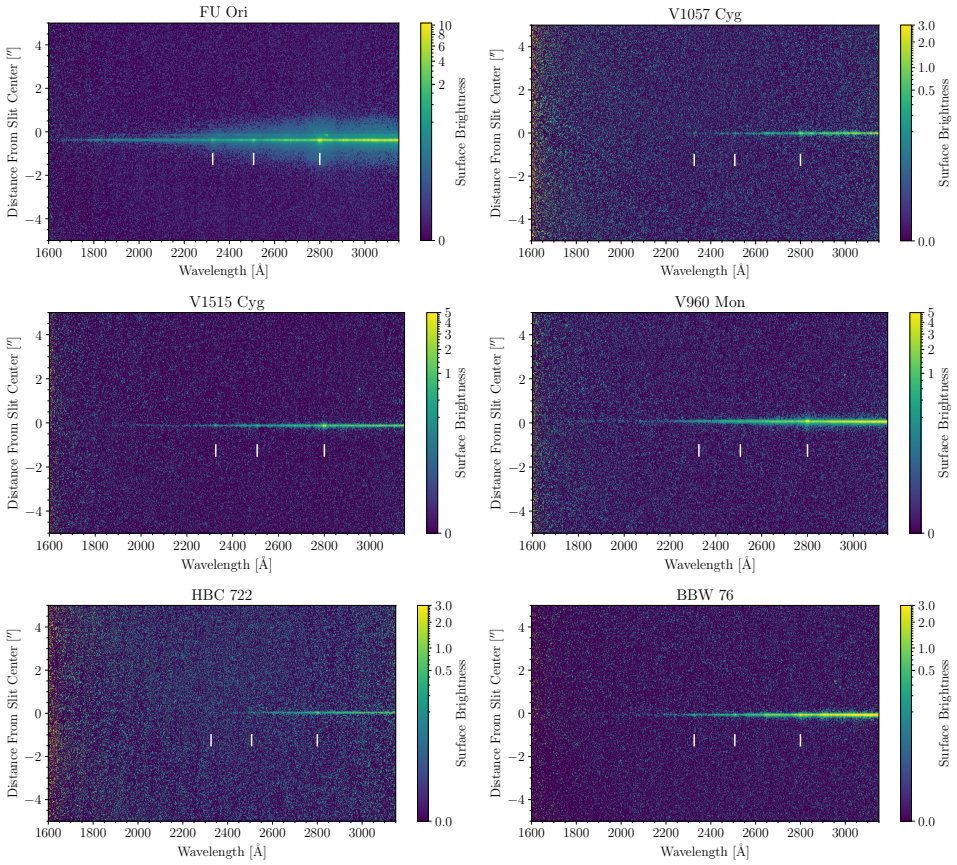

Figure 11.5: The two-dimensional rectified `x2d` HST/STIS images for each of our sources. The white hashes mark the locations of the C II] 2326, Fe II] 2500, and Mg II 2800 features and the surface brightness units are 10^{-14} erg s^{-1} cm^{-2} Å^{-1} arcsec^{-2}. Notice that the traces of FU Ori, V1515 Cyg, and V960 Mon are all detected down to at 1800 Å. BBW 76 is only marginally detected at 2100 Å. V1057 Cyg is only detected redward of the C II feature, with barely any continuum until 2400 Å, and HBC 722 is only detected redward of 2450 Å.

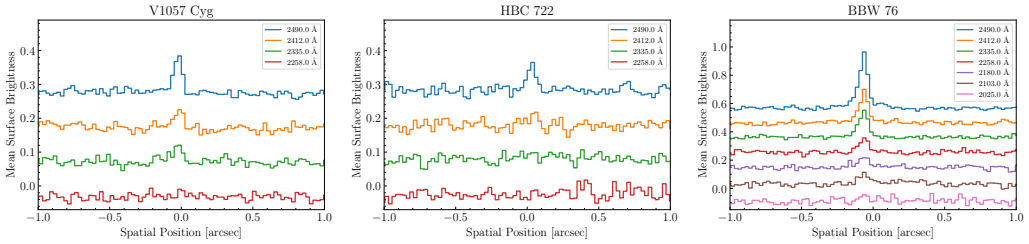

Figure 11.6: Spectrally averaged spatial cuts in the 2d spectra of V1057 Cyg (left), HBC 722 (middle) and BBW 76 (right). The spectral averaging was over ∼ 75 Å and the legend shows the mean wavelength of each bin.

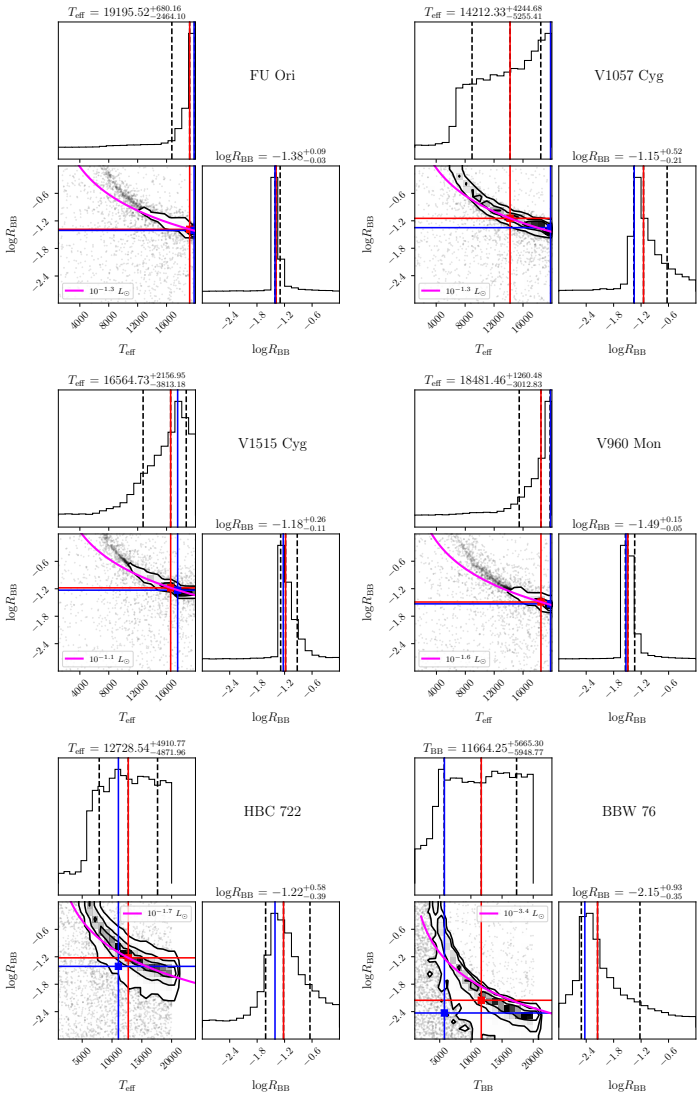

Figure 11.7: **The posterior distributions for the blackbody fit described in Section 11.3. The red vertical and horizontal lines mark the median values for histogram, while the blue lines mark the modal values. The magenta line marks the $R_{\rm BB} \propto T_{\rm BB}^{-2}$ relation, anchored at the median $L_{\rm excess}$ value for each source.**

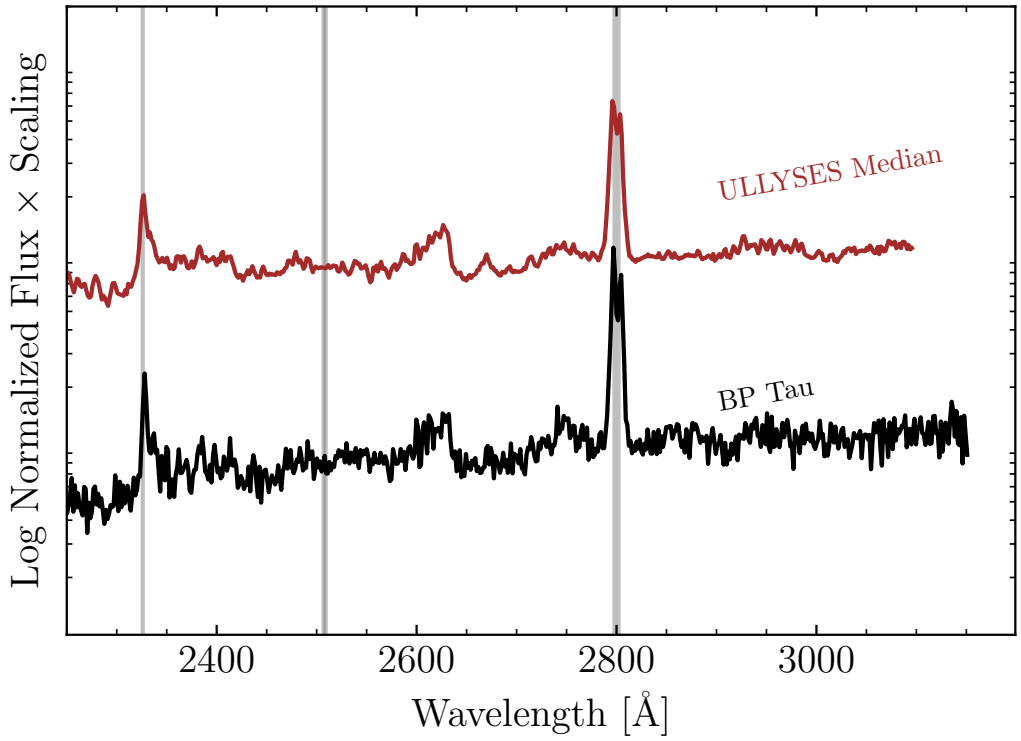

Figure 11.8: The G230L spectrum of BP Tau (black) compared with the median (brown line) and range (brown filled region) of G230L spectra of 50 CTTSs in the ULLYSES sample. The grey lines mark the locations of the NUV emission lines discussed in Section 11.4. Notice that there is no sign of the Fe II] emission feature at 2505 in either BP Tau or the ULLYSES sample.

Chapter 12

A KECK/HIRES SPECTRAL ATLAS OF FU ORI OBJECTS

The high resolution spectra of FU Ori objects are extremely information-rich. While obtaining sensitive spectra of these often faint objects can be expensive, requiring large apertures and long exposure times, the data provide an unparalleled ability to study the dynamics of their inner disk regions.

I present here a compilation of visible range high signal-to-noise (SNR), high resolution Keck/HIRES spectra for 14 FUOrs. The spectra span approximately 4800 – 9200 Å, though I omit the low signal-to-noise orders of the reddest objects like V900 Mon, V733 Cep, and RNO 1b.

I also include the object PTF 15afq. It is not formally a FUOr, but it is one of two objects known to undergo a short-lived EX Lup-type outburst while showing a FUOr-like disk spectrum (Park, Kóspál, et al., 2022; Siwak, Hillenbrand, et al., 2023). It is possible that objects undergoing outbursts of sufficiently high amplitudes will produce disk-absorption-dominated spectra regardless of the longevity of the outburst.

Several objects have multiple epochs of Keck/HIRES data available, but for the illustrative plots shown in this Chapter I have selected the highest SNR data to plot. For the objects V960 Mon and HBC 722, I show all of the spectra analyzed in Carvalho, Hillenbrand, and Seebeck (2023) and Carvalho, Hillenbrand, Seebeck, and Covey (2024), respectively. The spectra were taken during the first 5-10 years following the peak of each object's outburst and show significant evolution in lines known to trace outflows and the disk. More details about these objects can be found in Chapters 3, 4, and 5.

12.1 Outflow-tracing features

The lines that commonly trace outflows in YSOs, like Hα, Hβ, the Na I D 5889/5895 Å doublet, and the Ca II Infrared Triplet (IRT), all have strong, high velocity blue-shifted absorption in the spectra of FUOrs. The profiles of Hα and the Ca II IRT are also frequently accompanied by red-shifted emission, producing the classic P Cygni profiles associated with stellar winds. These lines are highlighted in Figures 12.1, 12.2, 12.3, and 12.4.

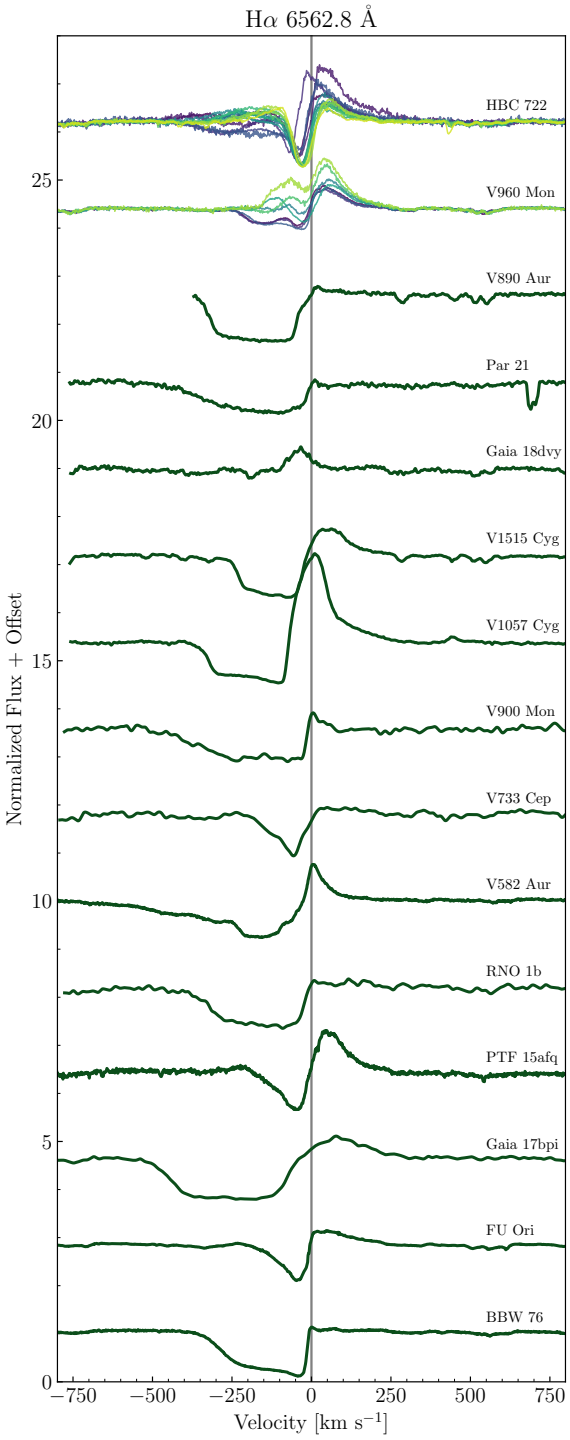

Figure 12.1: The Hα line profiles of FUOrs captured with Keck/HIRES. As can be seen in the spectra of V960 Mon and HBC 722, the profiles can be highly variable. The lines all show a wide range of absorption velocities, sometimes reaching -500 km s^{-1}. The vertical grey line indicates the rest velocity of each line.

The fact that the Hα, Hβ, and Na I D line profiles are all highly saturated indicates that the outflowing material obscures a large fraction of the continuum-emitting region from 4800 – 6600 Å. Furthermore, the line profiles of Gaia 17bpi, BBW 76, V1057 Cyg, and V1515 Cyg are saturated at blue-shifted velocities > 200 km s^{-1}, indicating a large column of material even at high velocities. Furthermore, the multi-component structure of the Na I D line profiles, called the "shell" features by Herbig et al. (2003), reveal a complex vertical and kinematic structure in the outflow near its launch point.

In simulations, an MRI-driven outburst has been shown to produce powerful outflows (Zhu, Jiang, et al., 2020), with mass loss rates comparable to 0.1 $\dot{M}_{\rm acc} \sim 10^{-6}$ $M_\odot$ yr^{-1}. There are also observations of large scale outflows seen with millimeter CO emission that may be the result of past outburst activity (Ruíz-Rodríguez et al., 2017; Cruz-Sáenz de Miera et al., 2023; Hales et al., 2024). Comparison with models of Hα line profiles produced by stellar and disk winds also indicate high mass outflow rates. The models of Muzerolle et al. (2001) and Lima et al. (2010) in particular highlight the Stark broadening in the red-shifted emission component of Hα, as is seen in FUOrs, is diagnostic of wind emission. When compared with models computed for different wind temperatures, the line profiles of FUOrs seem generally consistent with wind temperatures > 4000 K (Lima et al., 2010; Carvalho, Hillenbrand, Seebeck, and Covey, 2024). This is discussed more specifically in the context of HBC 722 in Chapter 5 but the discussion can be broadened to include all FUOrs, given the similarity of their Hα profiles.

One enduring mystery in the high resolution spectra of FUOrs is the surprisingly dynamic Li I 6707 Å doublet. Among FGKM spectral types, the strength of the doublet can be diagnostic of stellar age (Herbig, 1965; Xiong and Deng, 2009) and its presence was one of the first indicators used to identify FUOrs as YSOs (Herbig, 1977). As a weak feature of a sparse species, the doublet is should only trace the Keplerian motion of the disk atmosphere (Calvet, Hartmann, et al., 1993). However, as can be seen in Figure 12.5, the absorption profiles do not, in fact, only show disk broadening.

Many of the Li I profiles are asymmetric, often with blue-shifted absorption. This is also seen in the profiles of HBC 722, where the blue-shifted absorption strength increases in the years following its outburst peak (see Chapter 5). The bizarre profile of the Li I feature in V1057 Cyg also highlights the fact that this line must trace non-disk components in addition to the disk atmosphere in FUOrs.

12.2 The HIRES Spectral Atlas

In the remaining Figures in this Chapter, I present all 34 spectral orders from the Keck/HIRES spectra I have discussed so far. As was discussed in Chapter 2, the spectra in this wavelength range are affected by both rotational broadening and the maximum temperature of the disk. There are also several features like Fe II 5018 Å and Fe II 5316 Å that trace low velocity winds, likely near their launch points (Calvet, Hartmann, et al., 1993; Hartmann and Calvet, 1995a).

The absorption profiles in visible range spectra have also been shown to be sensitive to the oscillator strengths and excitation potentials of the lines (Welty, Strom, Edwards, et al., 1992; Calvet, Hartmann, et al., 1993; Carvalho, Hillenbrand, and Seebeck, 2023). Features at higher excitation potential trace warmer regions of the disk, which are closer to the star. These features are thus expected to show broader wings, as the absorbing material is in more rapid Keplerian rotation. However, these features can also at times exhibit deeper cores than predicted by the disk model, potentially indicating that they are tracing highly sub-Keplerian material near the boundary layer (Popham, Kenyon, et al., 1996; Carvalho, Hillenbrand, and Seebeck, 2023).

Lines with high oscillator strengths, or generally high opacities, tend to trace outflows. Since the lines are sufficiently sensitive to probe low density material, they absorb the disk continuum well above the disk surface, either in the wind launching region or well into the jet/wind itself. A surprising discovery in the shortly post-peak spectra of V960 Mon and HBC 722 has been the emergence of narrow, blue-shifted absorption features in weak absorption lines (Carvalho, Hillenbrand, and Seebeck, 2023; Carvalho, Hillenbrand, Seebeck, and Covey, 2024). The features have deepened over time, indicating that they are tracing an increasingly large column of outflowing material. They also persist into the NIR, a sign that the material covers a large fraction of the projected disk area. The properties of the lines and their origin are discussed in Chapters 4 and 5.

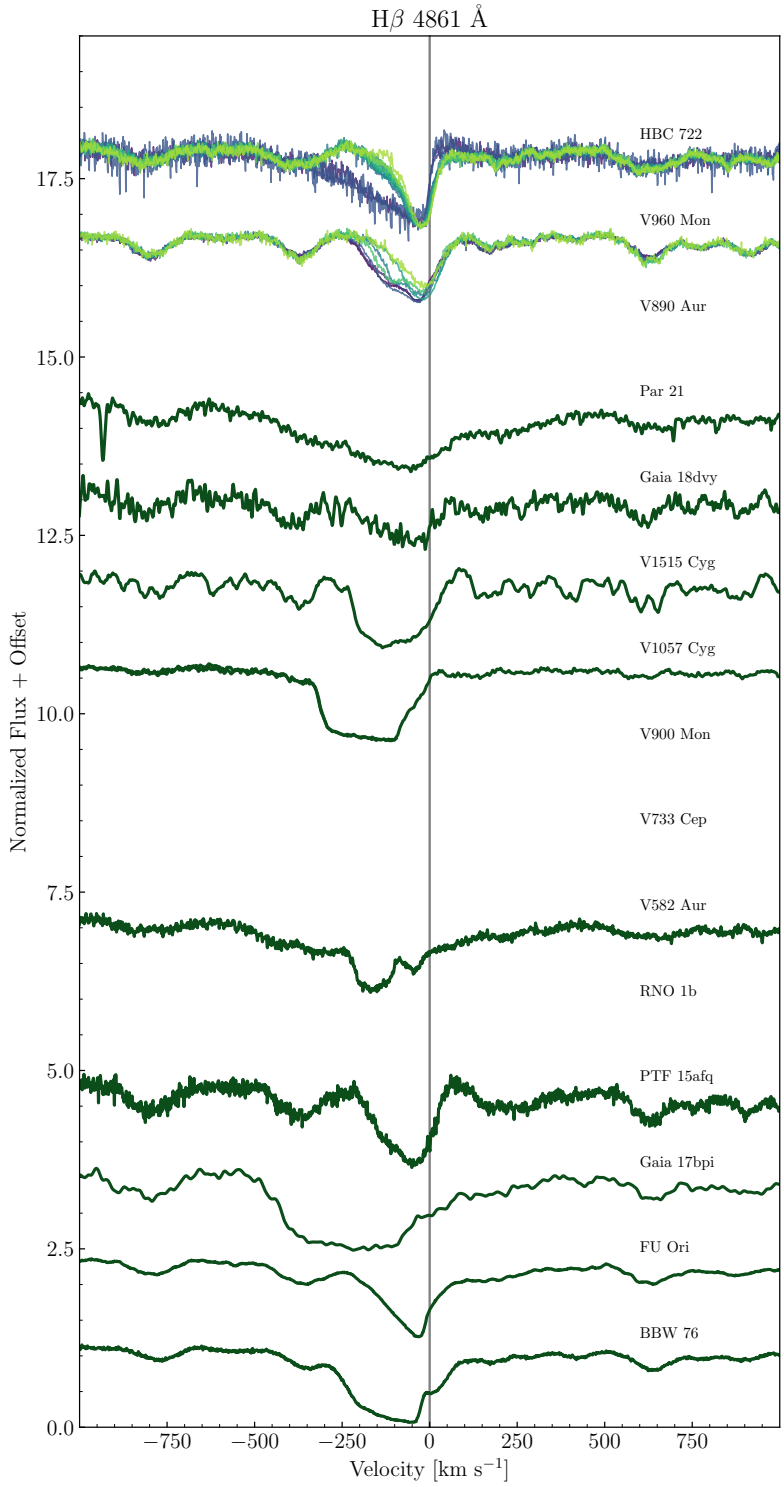

Figure 12.2: The Hβ line profiles of FUOrs captured with Keck/HIRES. As can be seen in the spectra of V960 Mon and HBC 722, the profiles can be highly variable. The lines all show a wide range of absorption velocities, sometimes reaching -500 km s^{-1}. The vertical grey line indicates the rest velocity of each line.

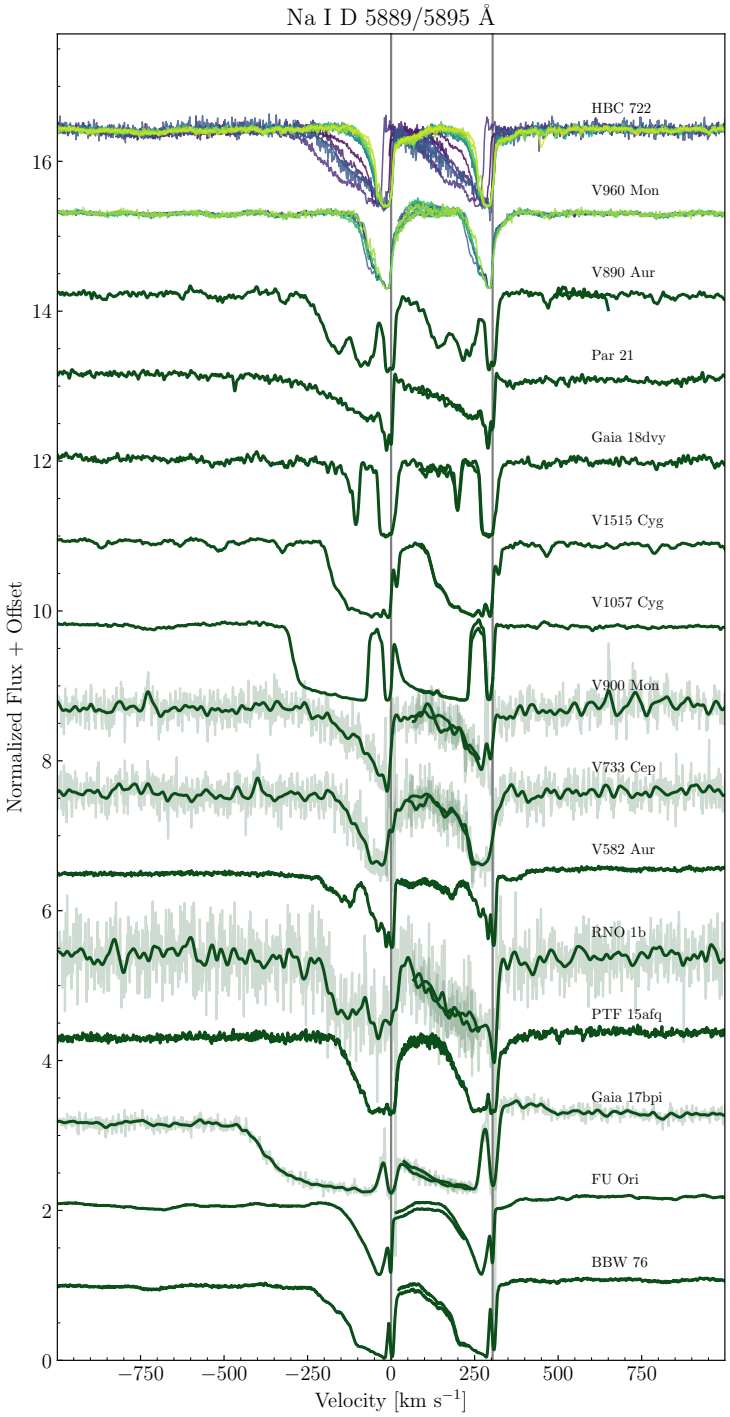

Figure 12.3: Na I D line profiles of FUOrs captured with Keck/HIRES. As can be seen in the spectra of V960 Mon and HBC 722, the profiles can be highly variable. The lines all have several absorption components, indicating a multi-layered structure to the outflow. The vertical grey line indicates the rest velocity of each line.

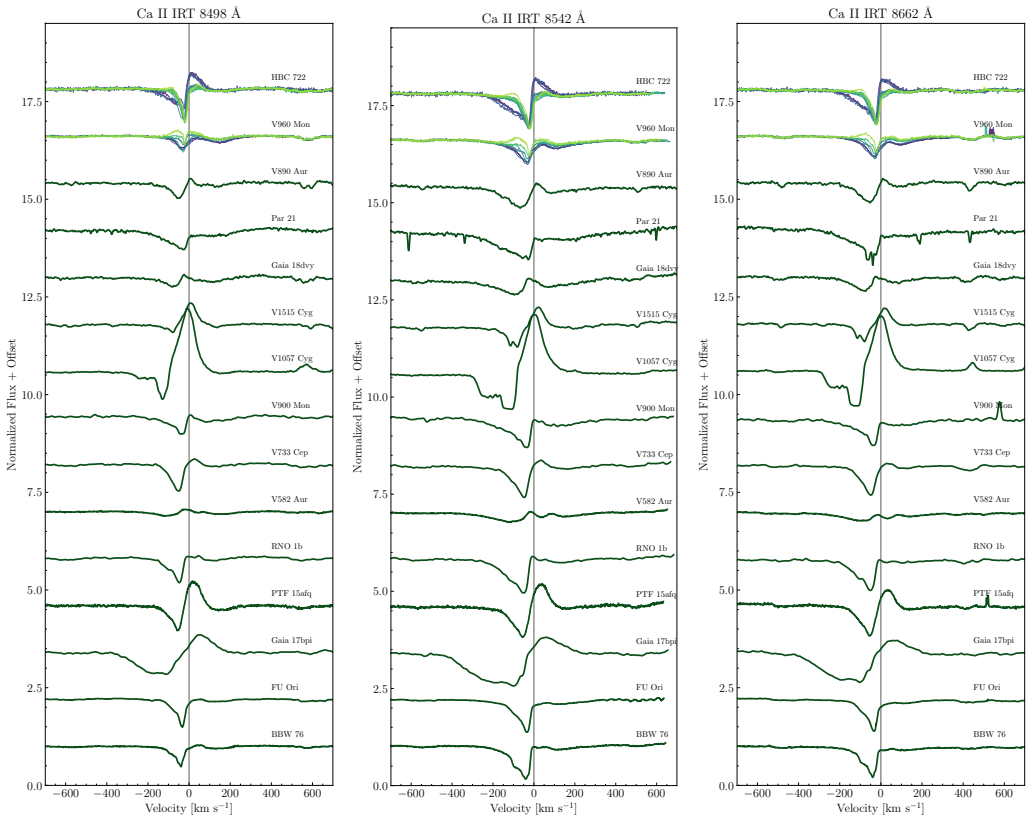

Figure 12.4: The Ca II IRT line profiles for each component of the triplet. Each of the three components is impacted on the red-shifted side by increasingly severe HP absorption from the 8502 Å, 8545 Å, and 8665 Å lines. The blue-shifted absorption profiles vary between the components due to the relative line strengths of the three. The vertical grey line indicates the rest velocity of each line.

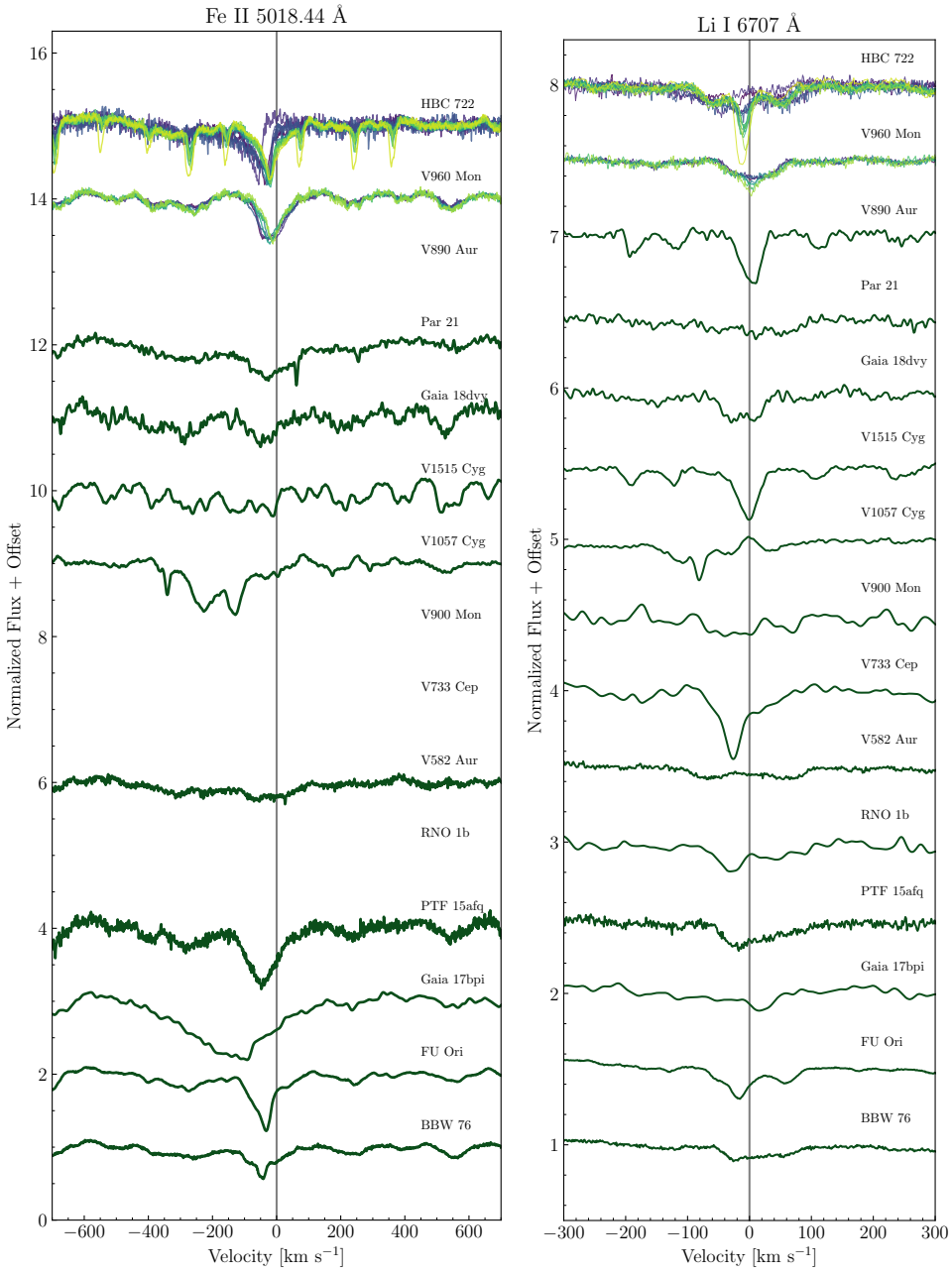

Figure 12.5: The line profiles for the Fe II 5018 Å and Li I 6707 Å features. In most FUOrs, the Fe II 5018 line shows both disk-broadened absorption in the wings and a blue-shifted core indicative of low-velocity wind absorption. The Li I 6707 line, despite expectations that it should trace the disk atmosphere closely, shows surprising diversity in its profiles.

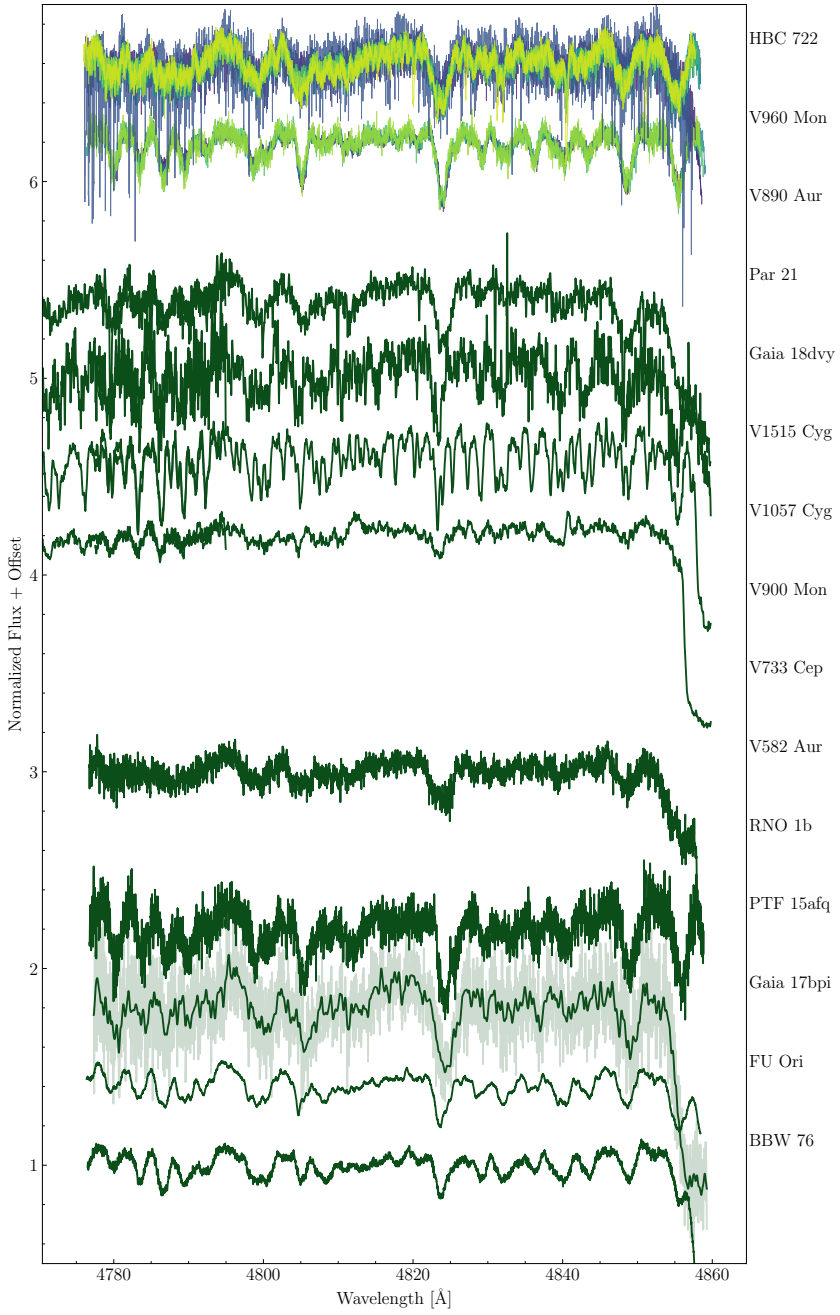

Figure 12.6: The Keck/HIRES spectra of 15 FUOrs, continuum normalized and offset for ease of comparison. The colors of the spectra of HBC 722 and V960 Mon mark different epochs spanning the first few years after the peaks of each the outbursts in each object. The spectra of Gaia 17bpi, V900 Mon, V733 Cep, and RNO 1b are all low signal-to-noise and have been smoothed by a Gaussian kernel with $\sigma = 5$ pixels. The non-smoothed spectra for the sources are also shown in light green.

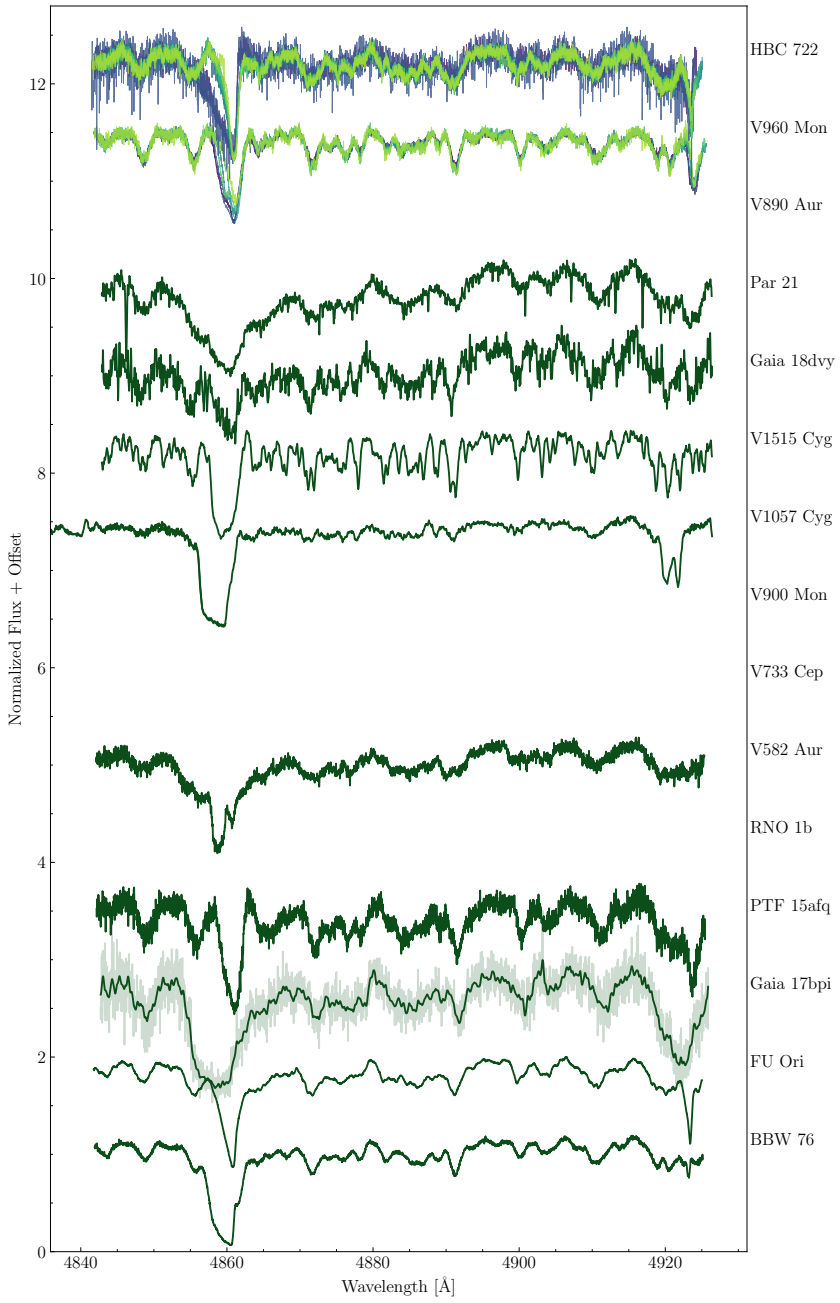

Figure 12.7: Figure 12.6 continued.

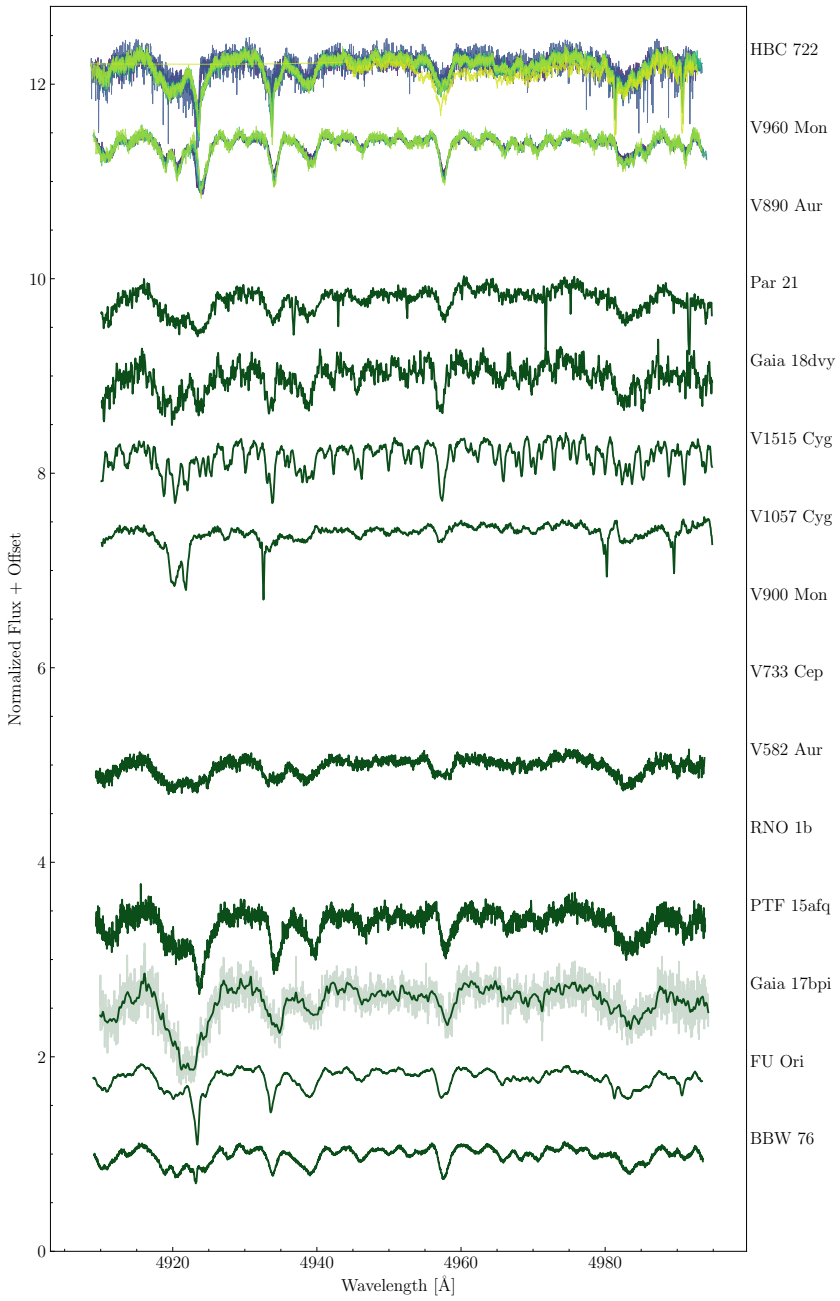

Figure 12.8: Figure 12.6 continued.

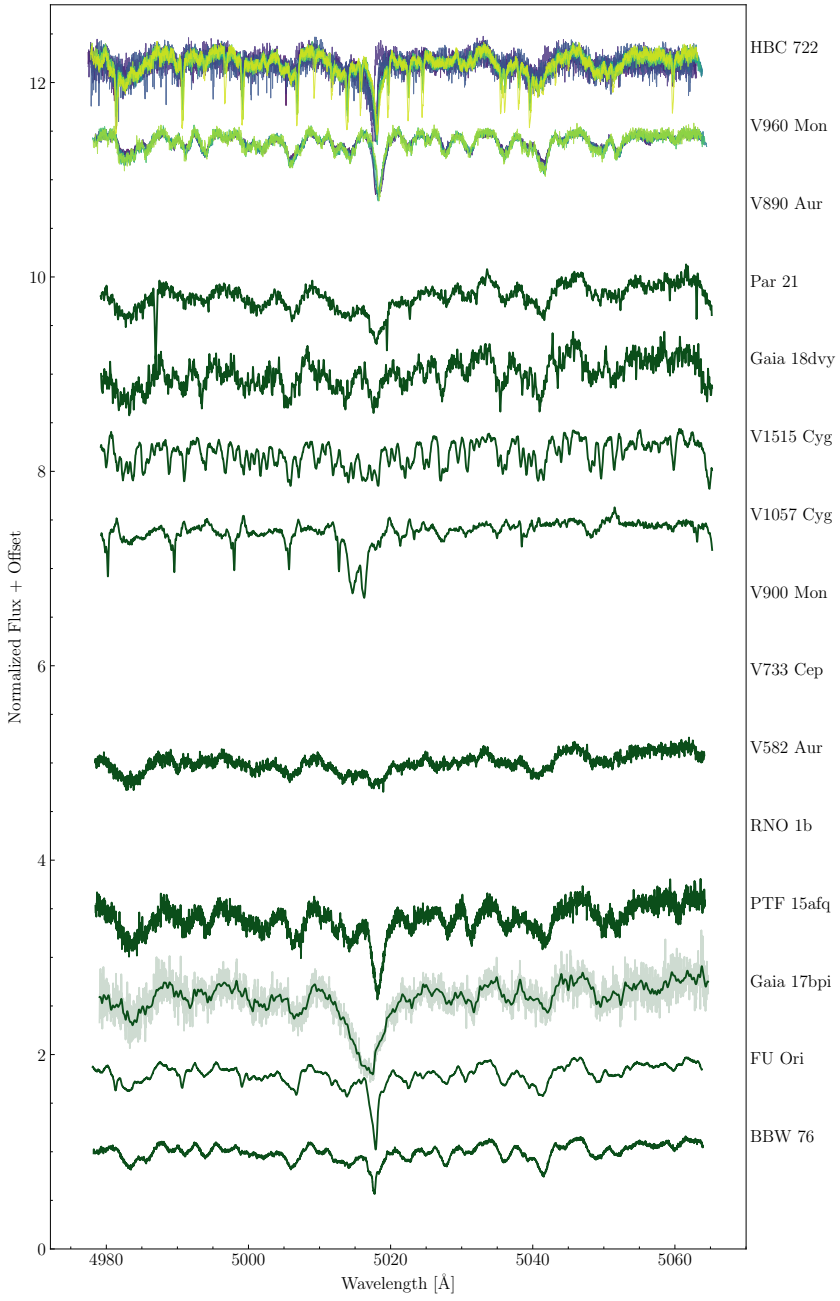

Figure 12.9: Figure 12.6 continued.

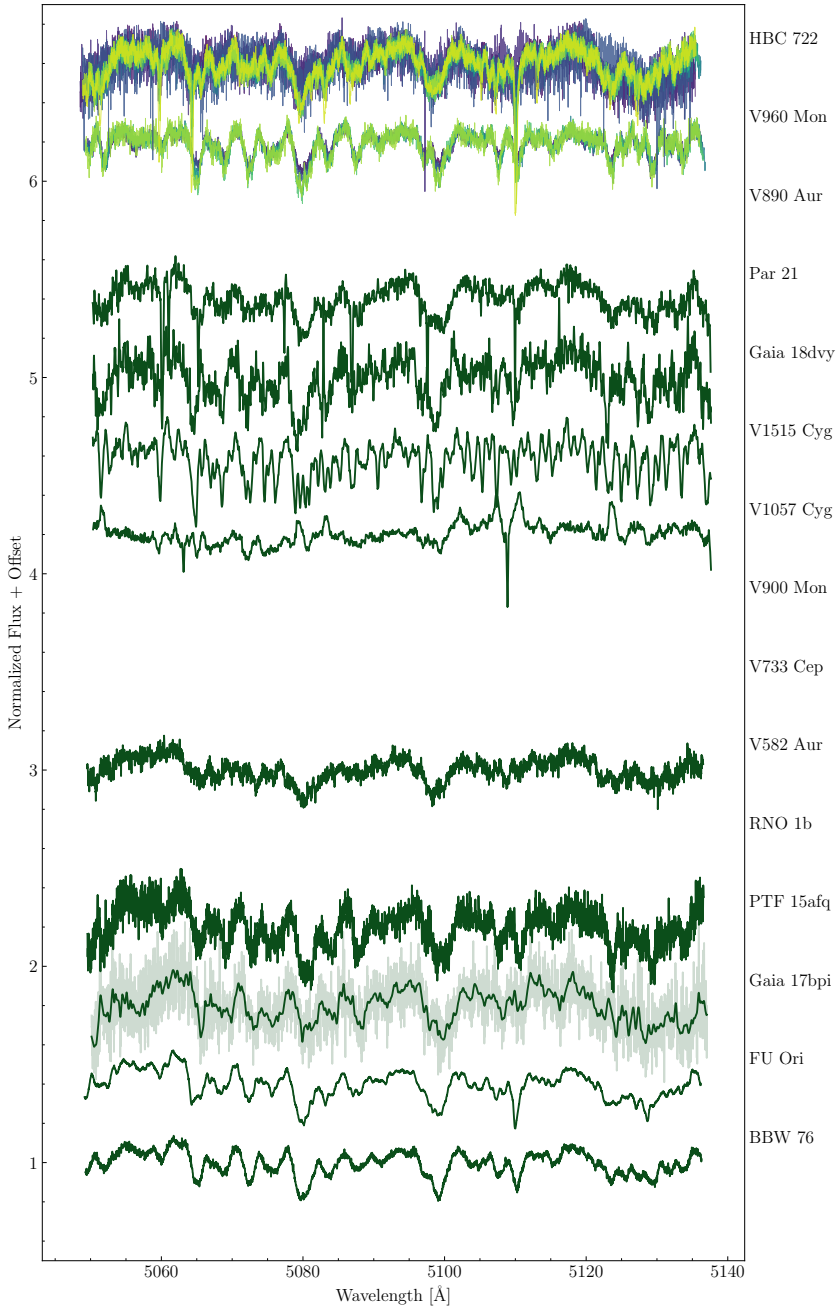

Figure 12.10: Figure 12.6 continued.

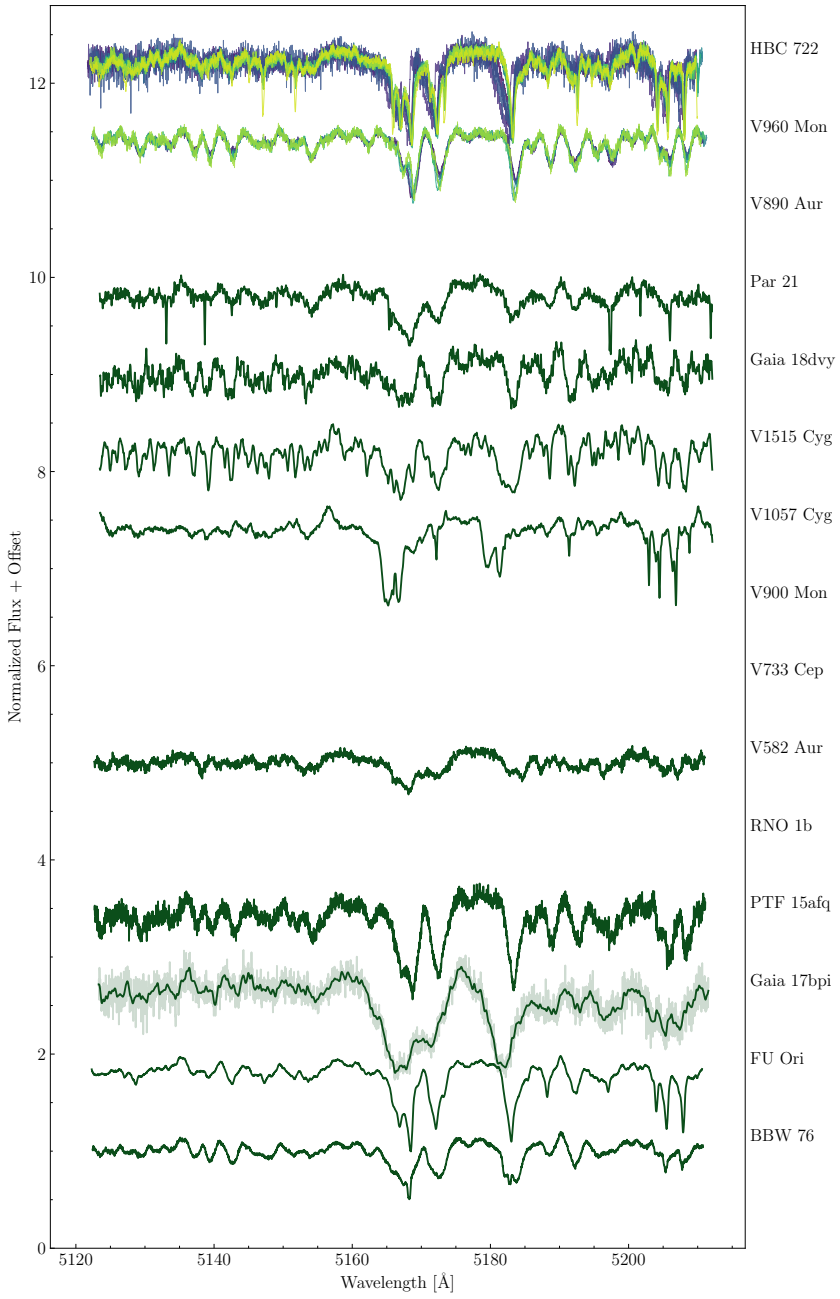

Figure 12.11: Figure 12.6 continued.

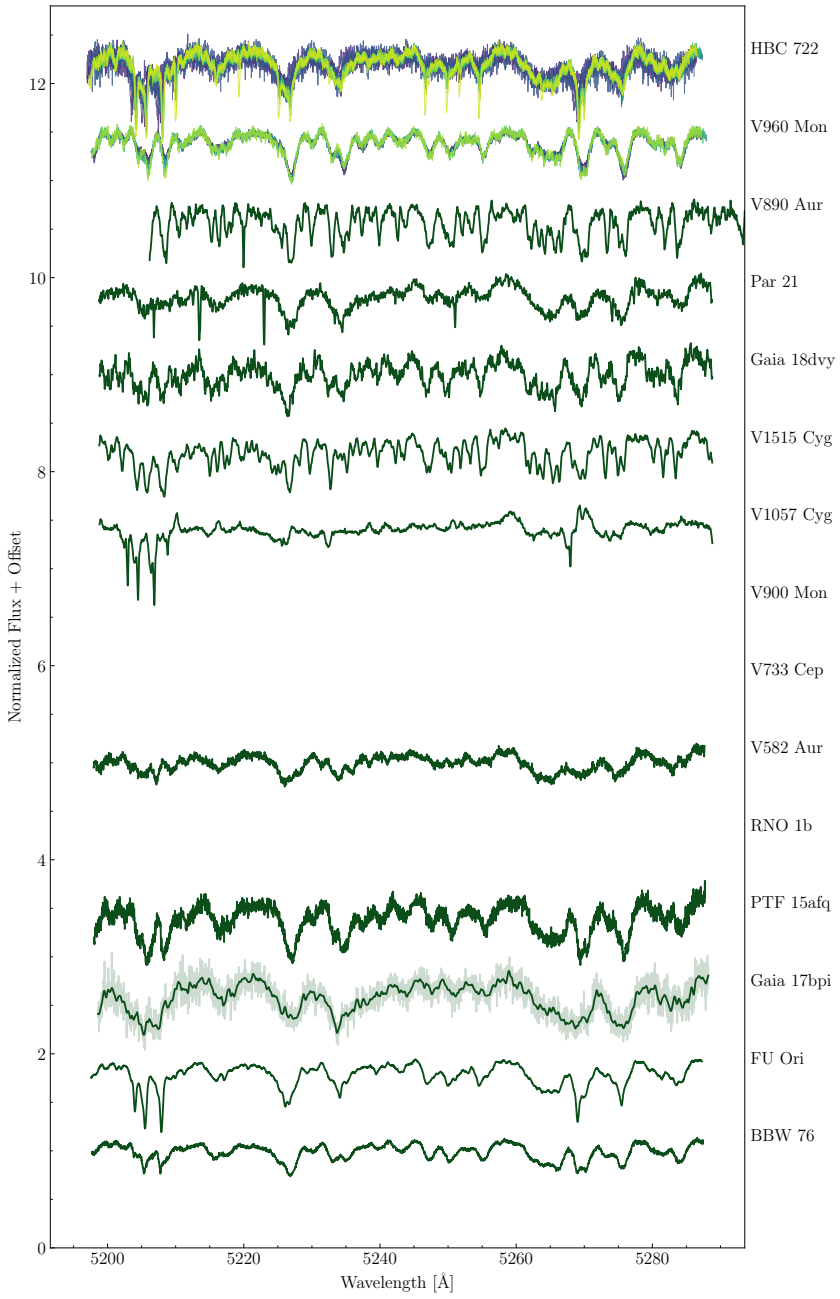

Figure 12.12: Figure 12.6 continued.

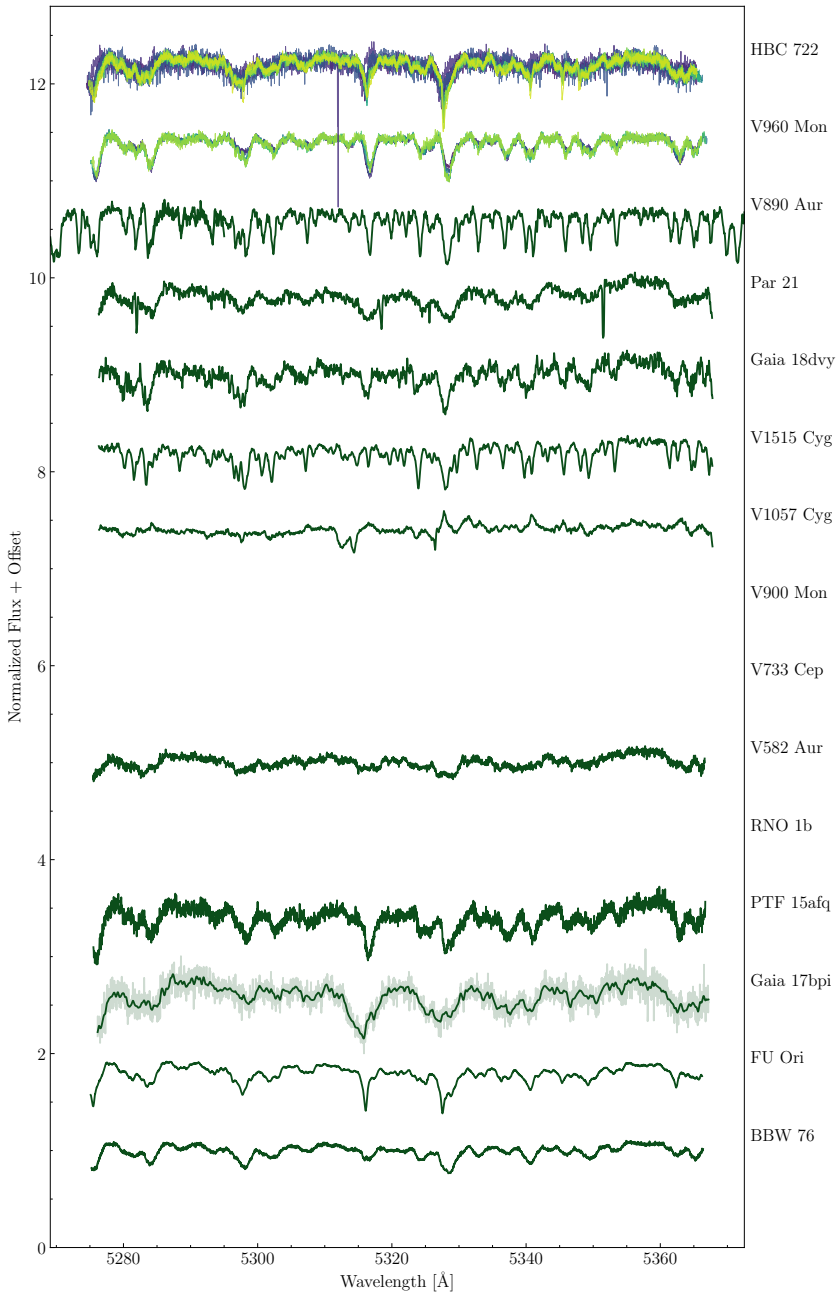

Figure 12.13: Figure 12.6 continued.

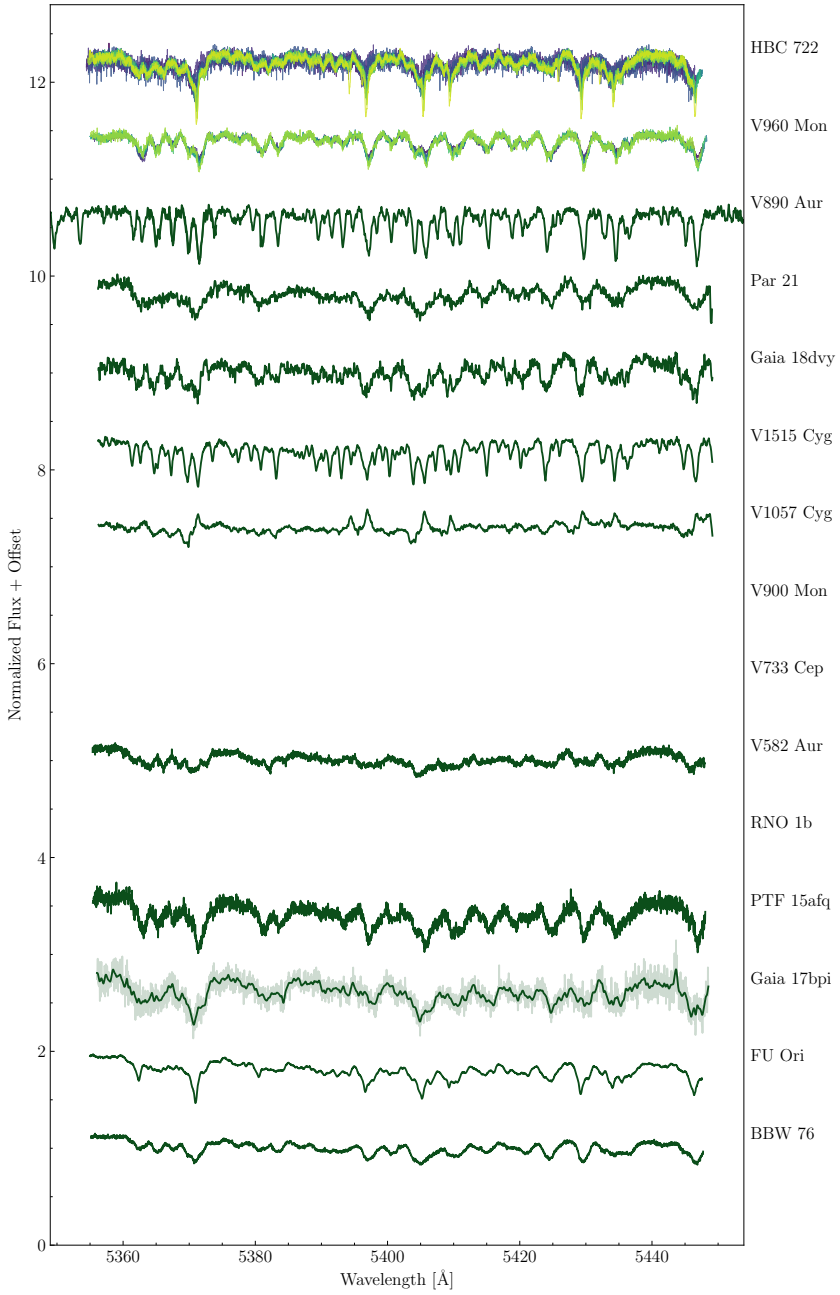

Figure 12.14: Figure 12.6 continued.

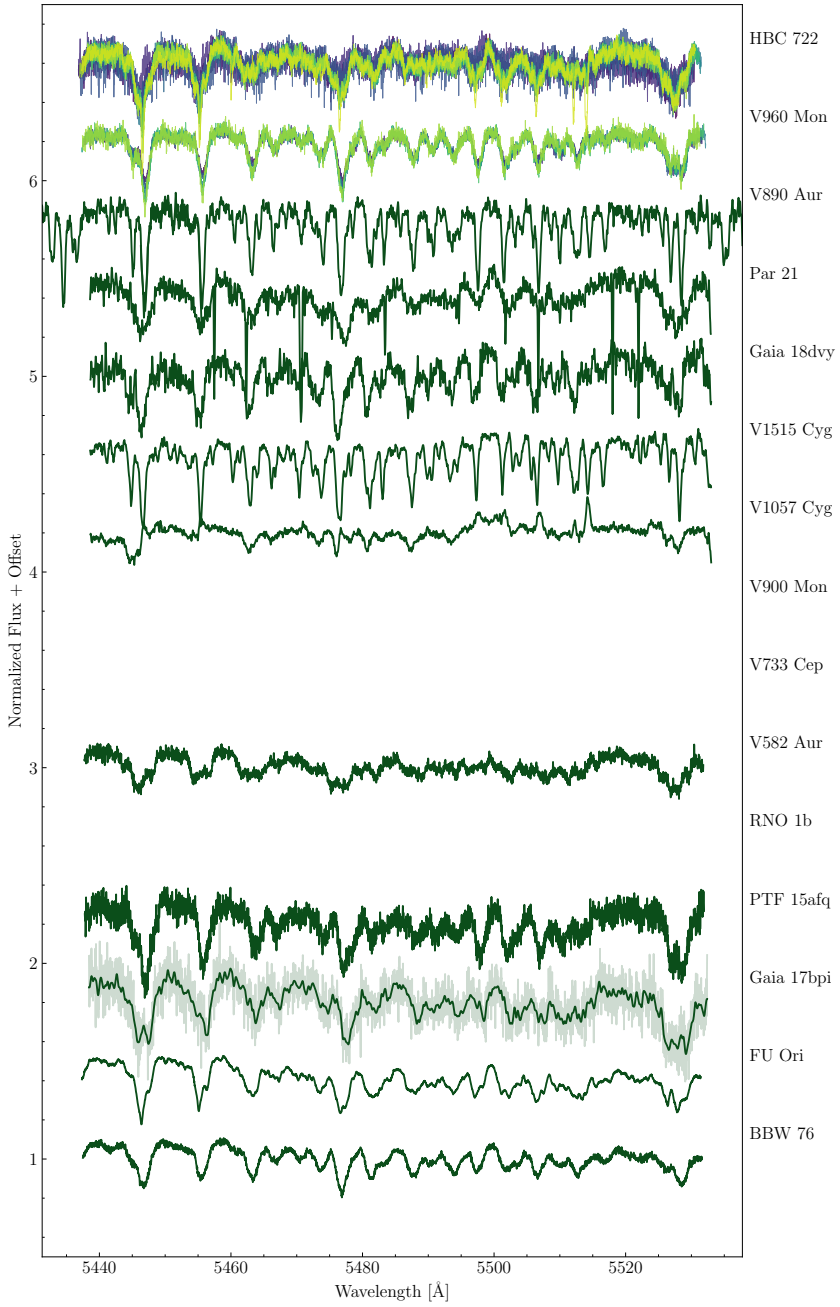

Figure 12.15: Figure 12.6 continued.

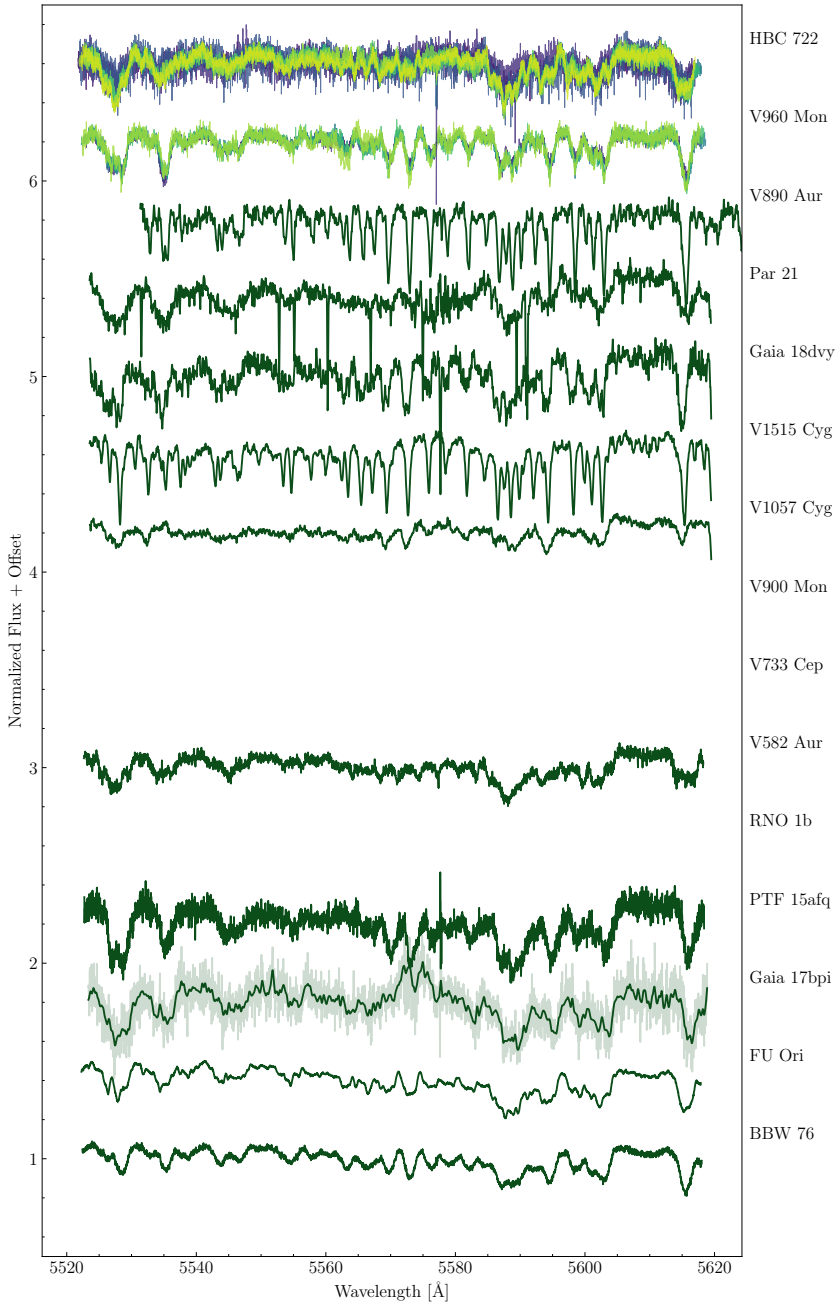

Figure 12.16: Figure 12.6 continued.

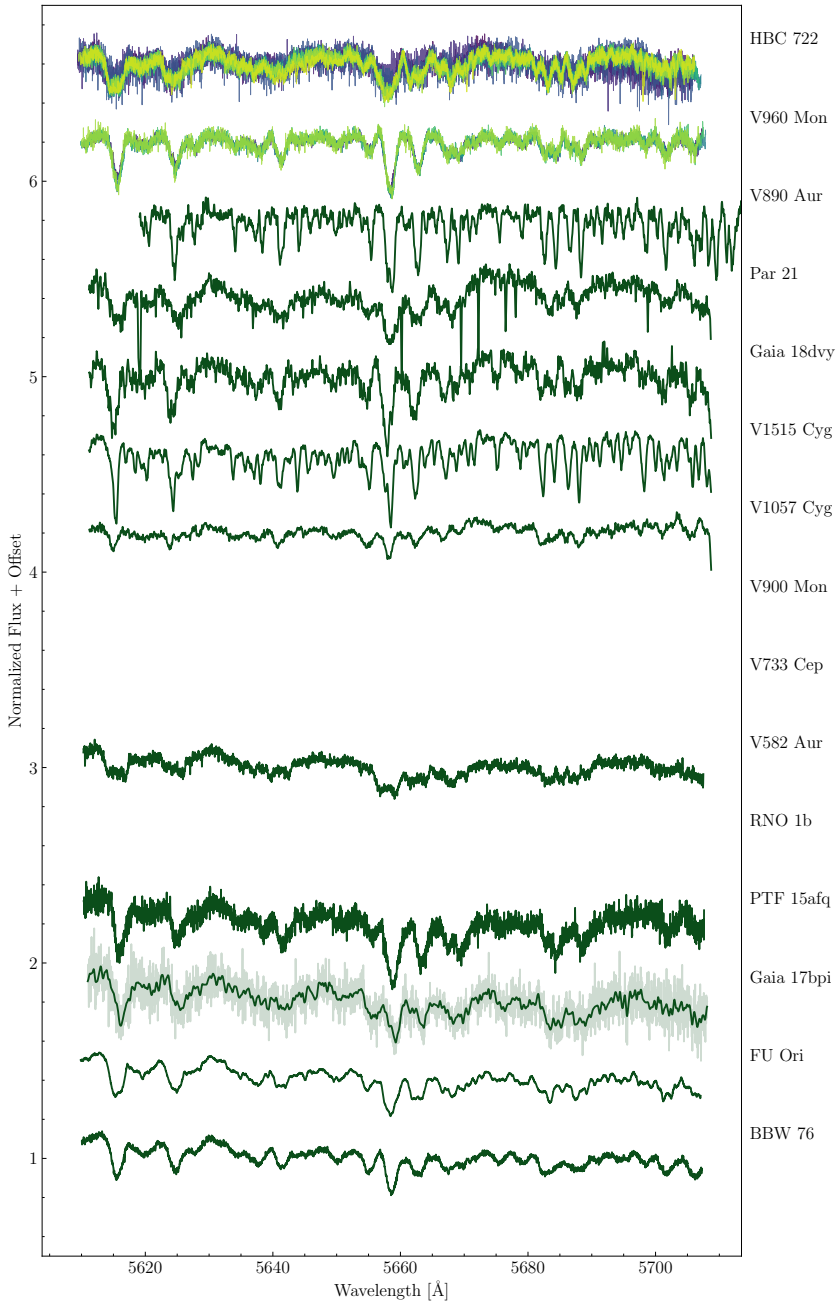

Figure 12.17: Figure 12.6 continued.

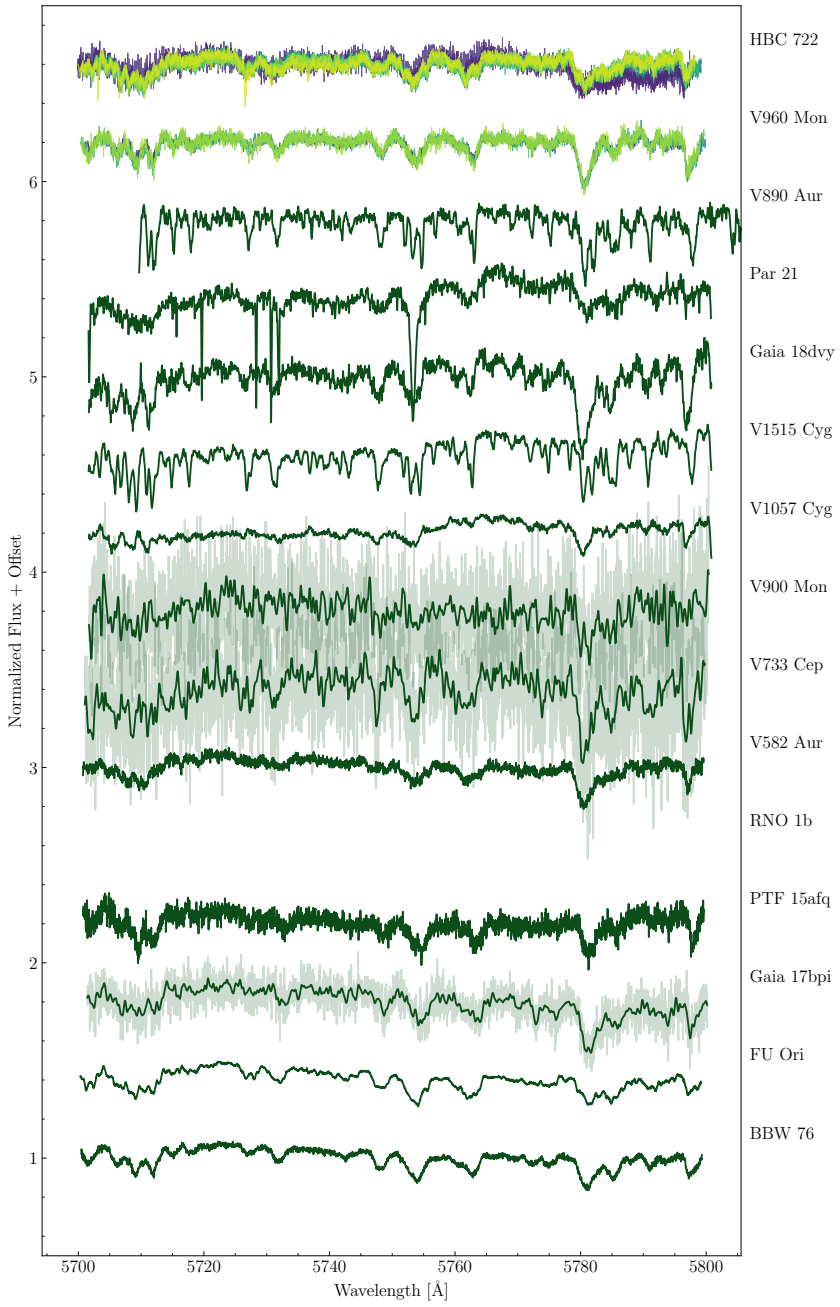

Figure 12.18: Figure 12.6 continued.

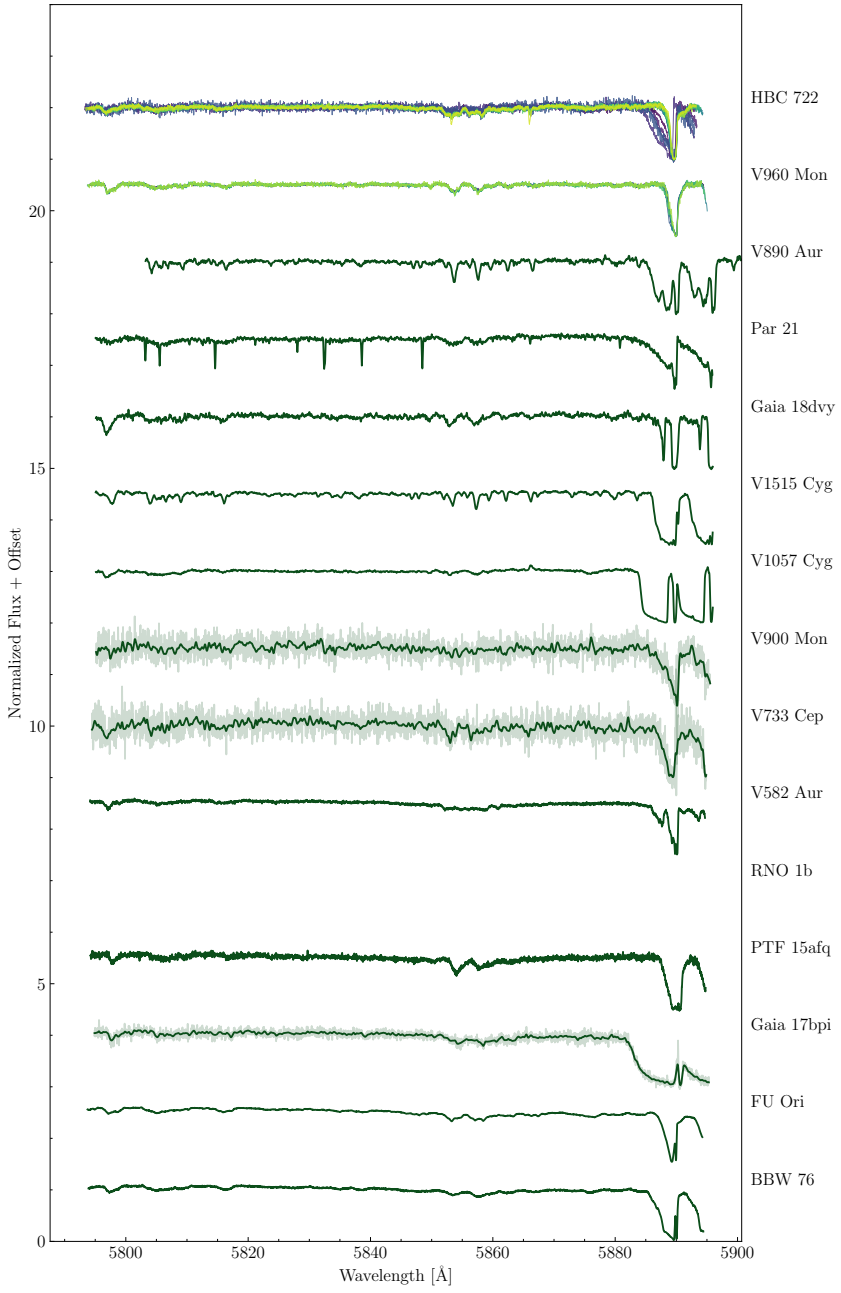

Figure 12.19: Figure 12.6 continued.

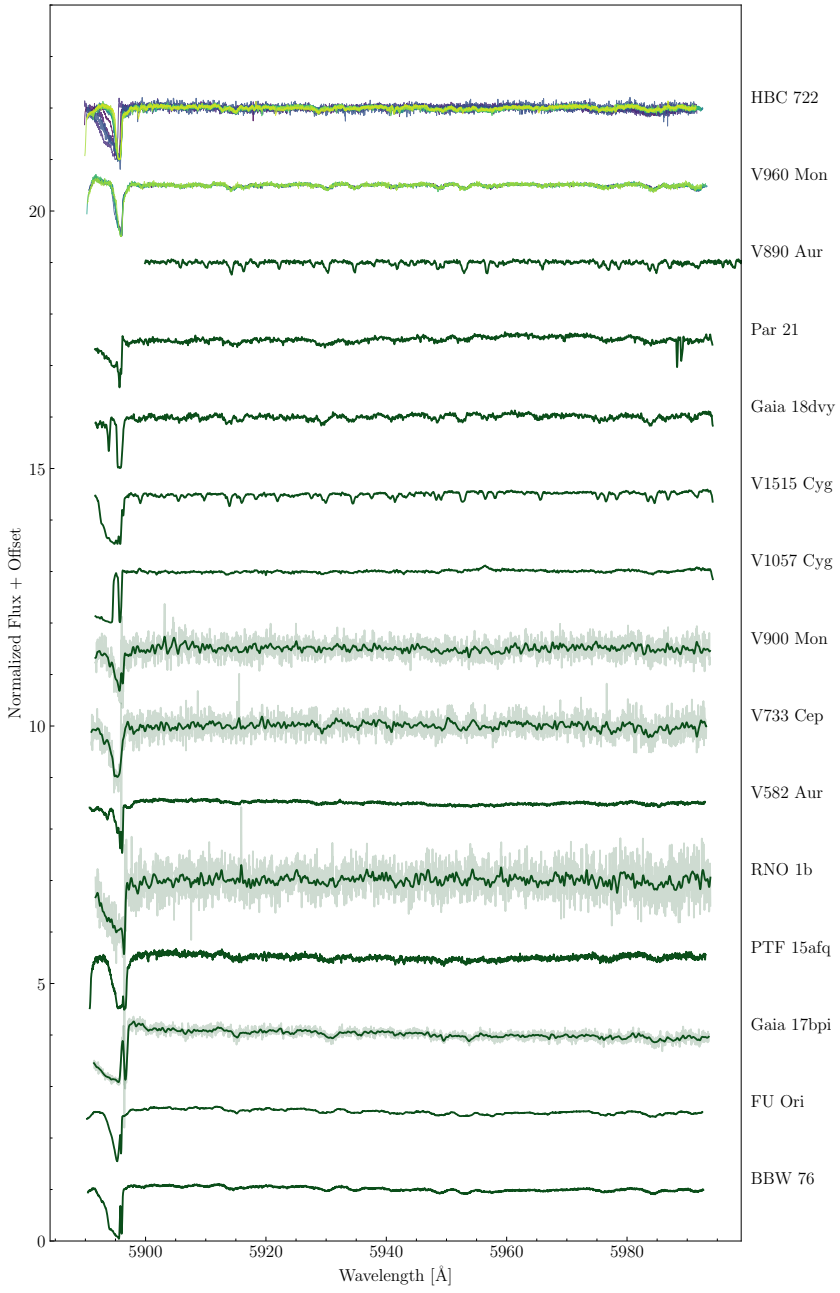

Figure 12.20: Figure 12.6 continued.

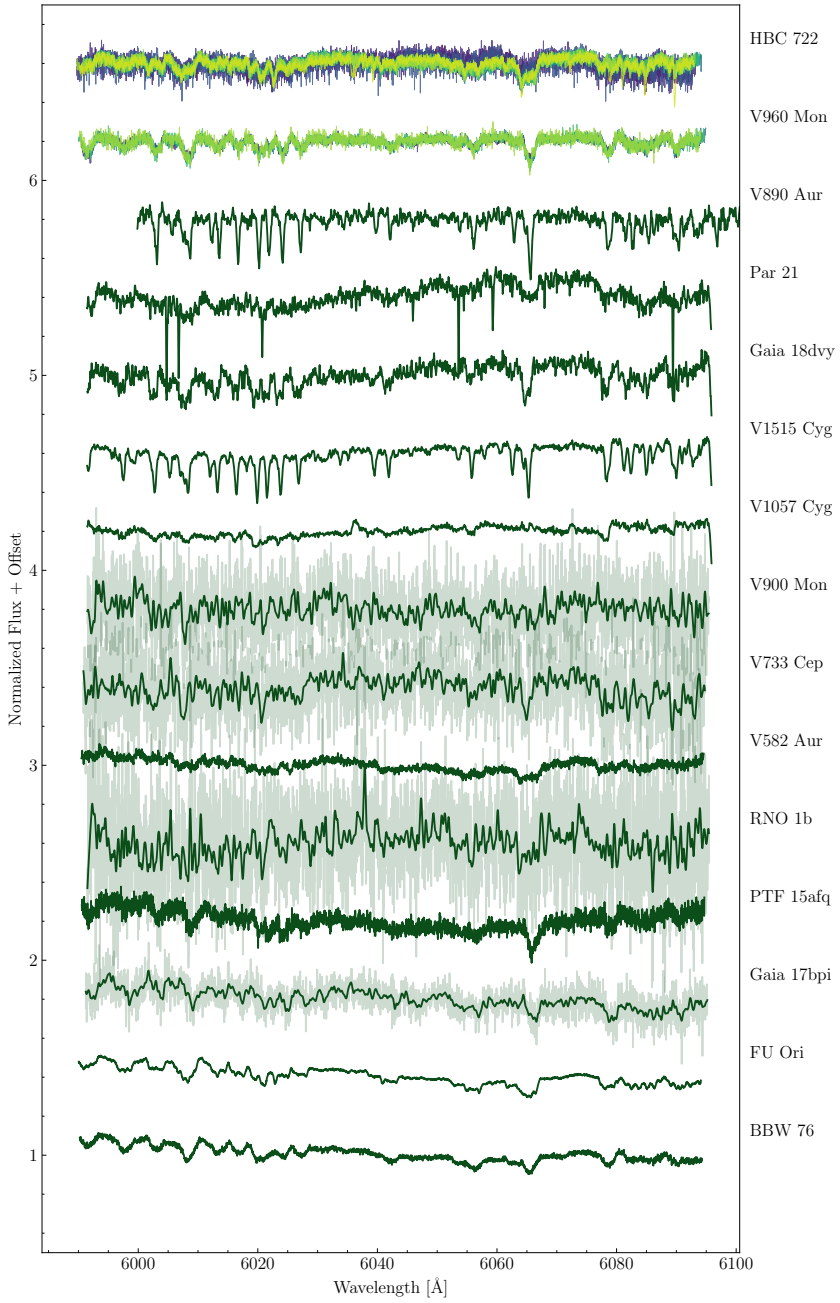

Figure 12.21: Figure 12.6 continued.

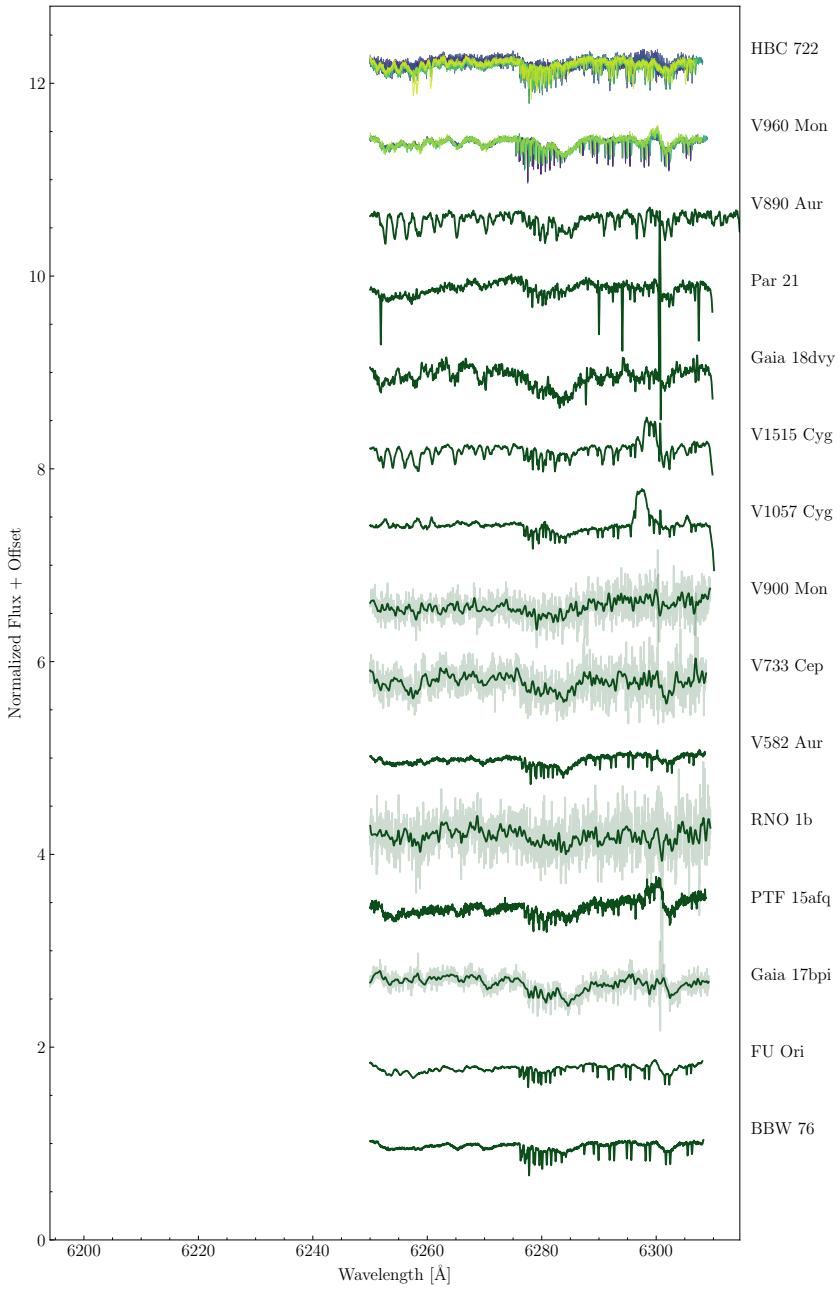

Figure 12.22: Figure 12.6 continued.

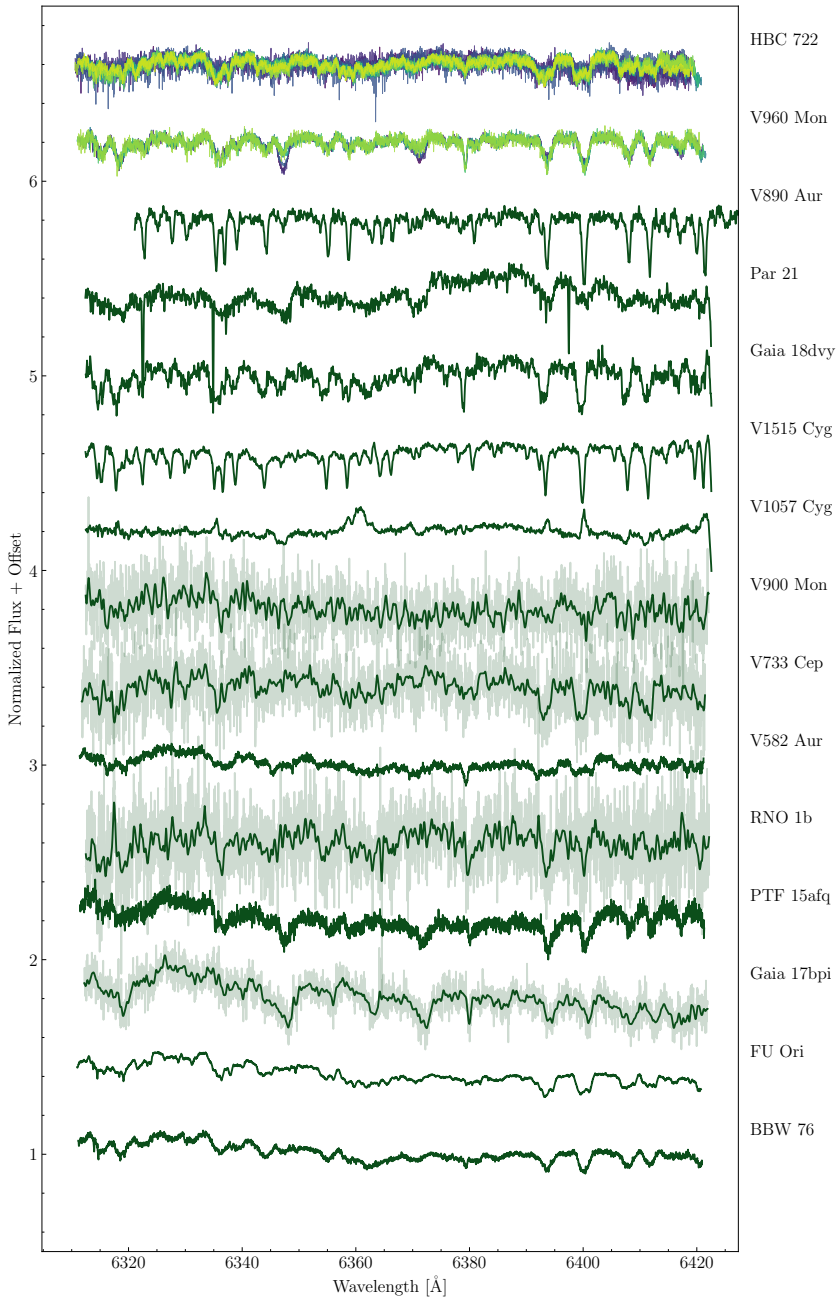

Figure 12.23: Figure 12.6 continued.

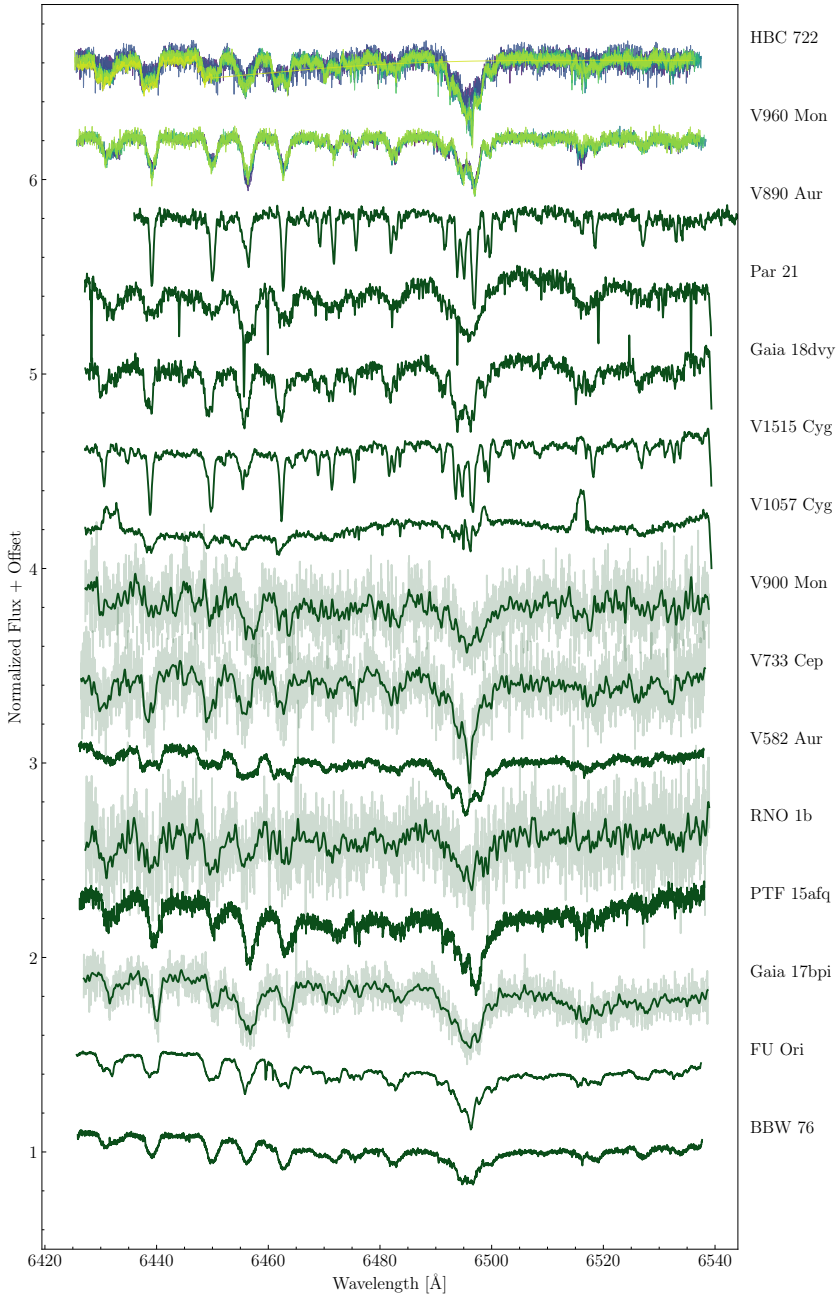

Figure 12.24: Figure 12.6 continued.

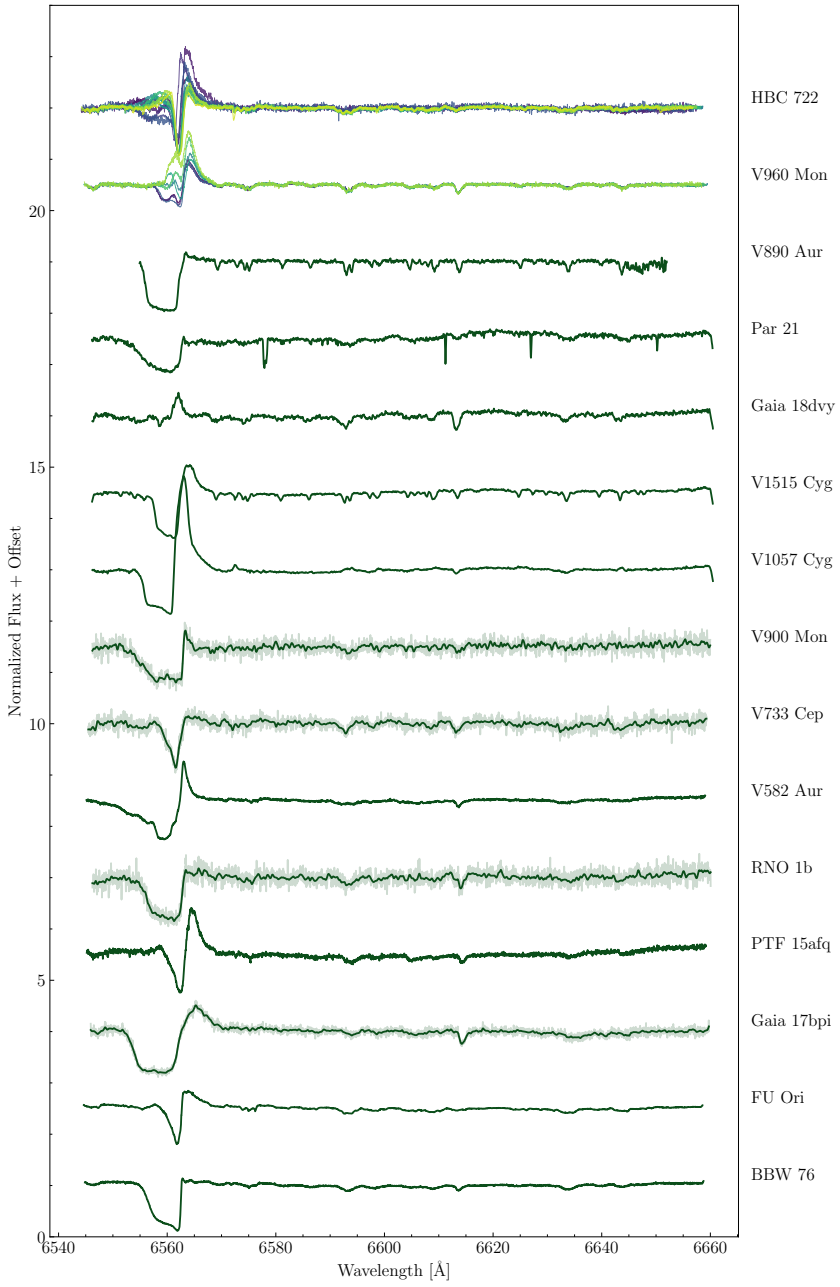

Figure 12.25: Figure 12.6 continued.

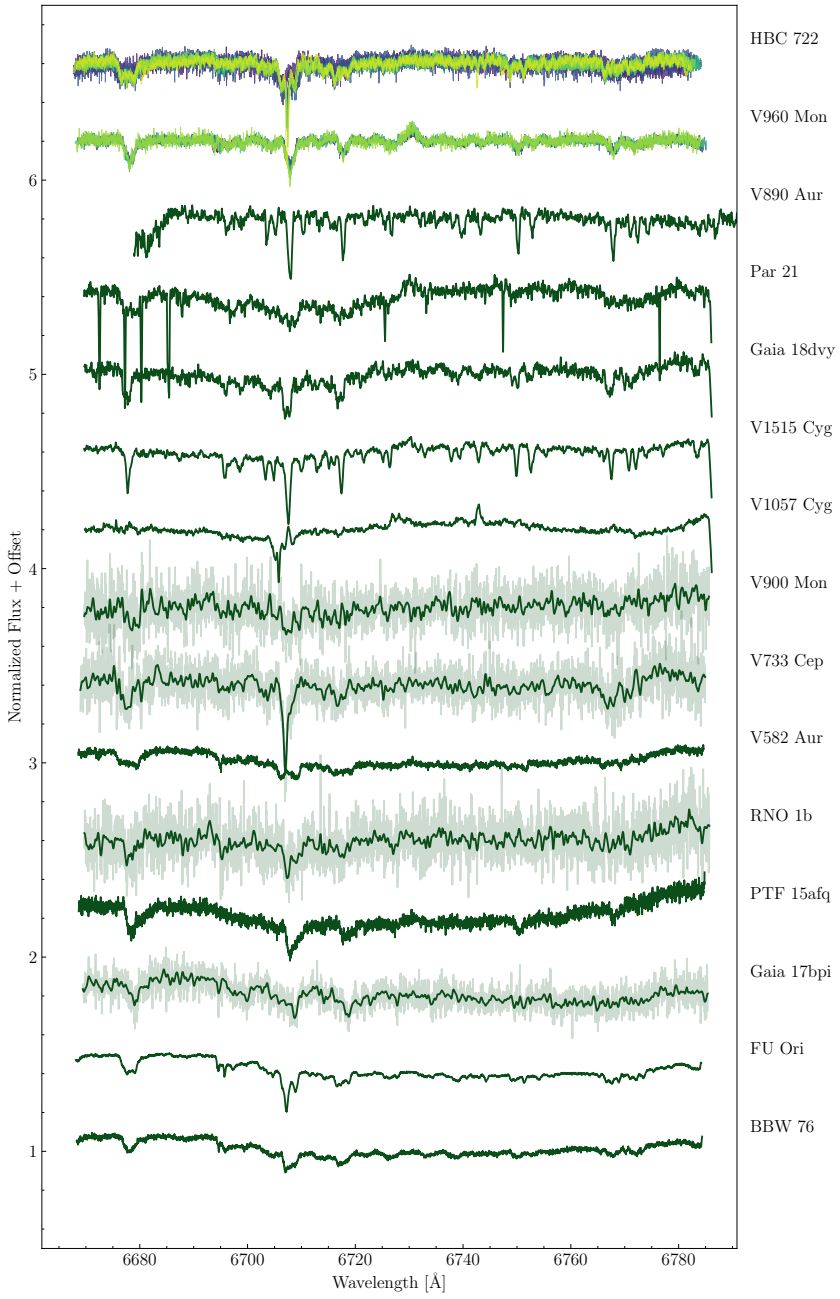

Figure 12.26: Figure 12.6 continued.

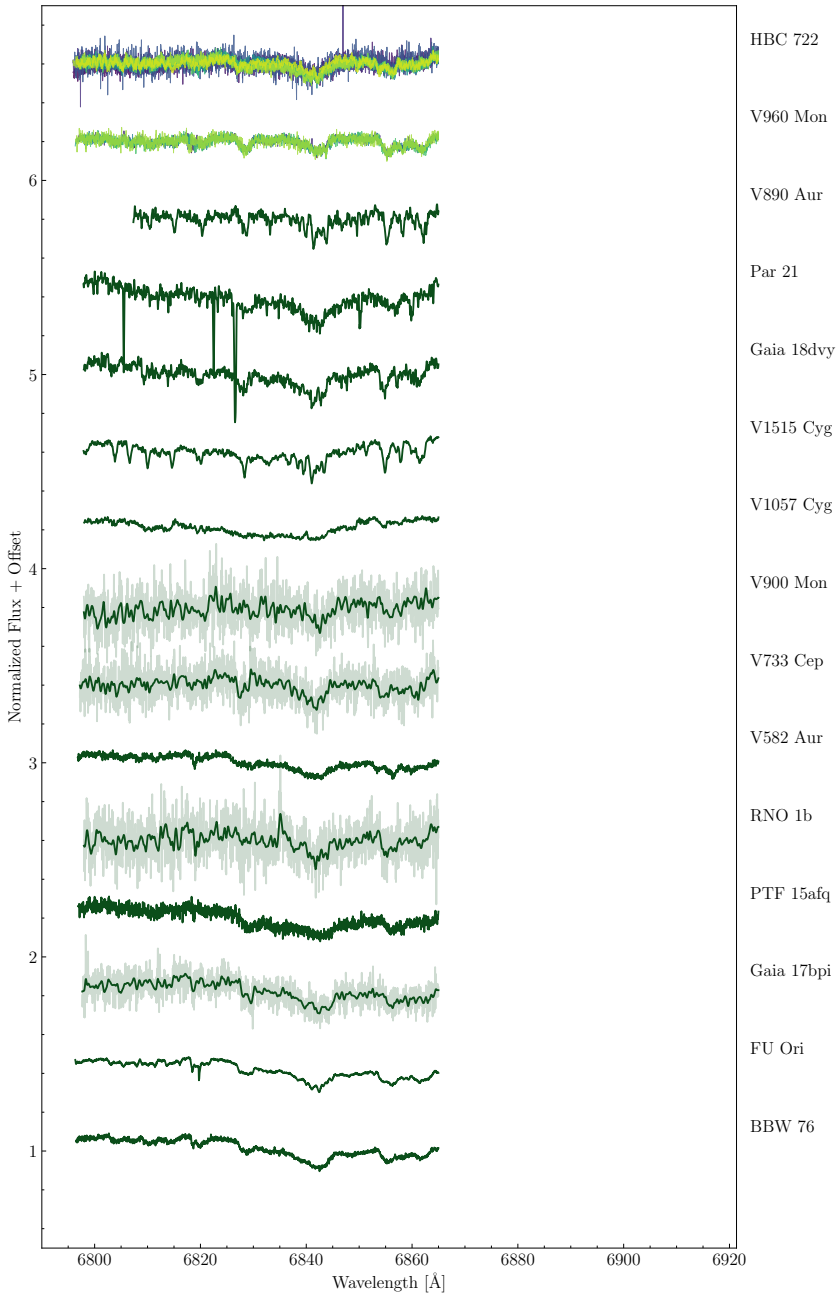

Figure 12.27: Figure 12.6 continued.

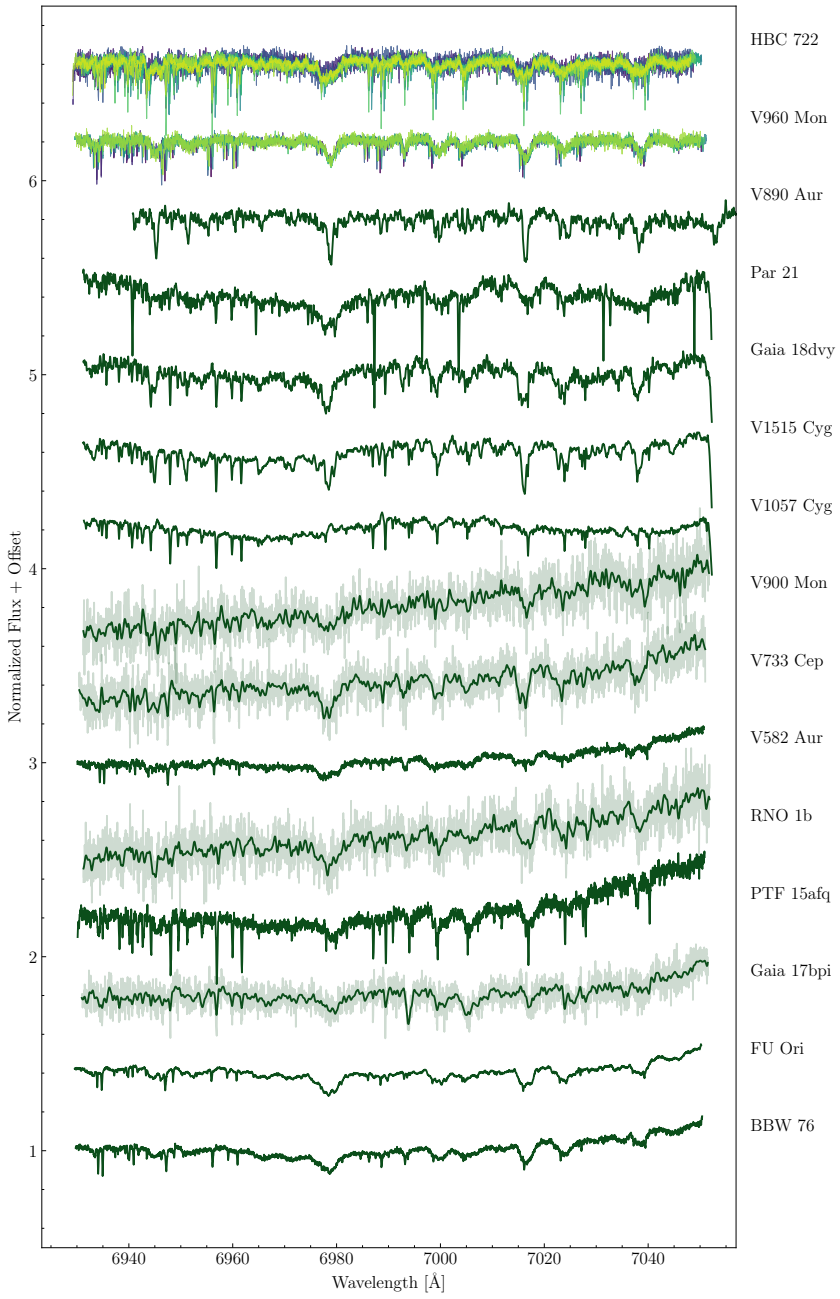

Figure 12.28: Figure 12.6 continued.

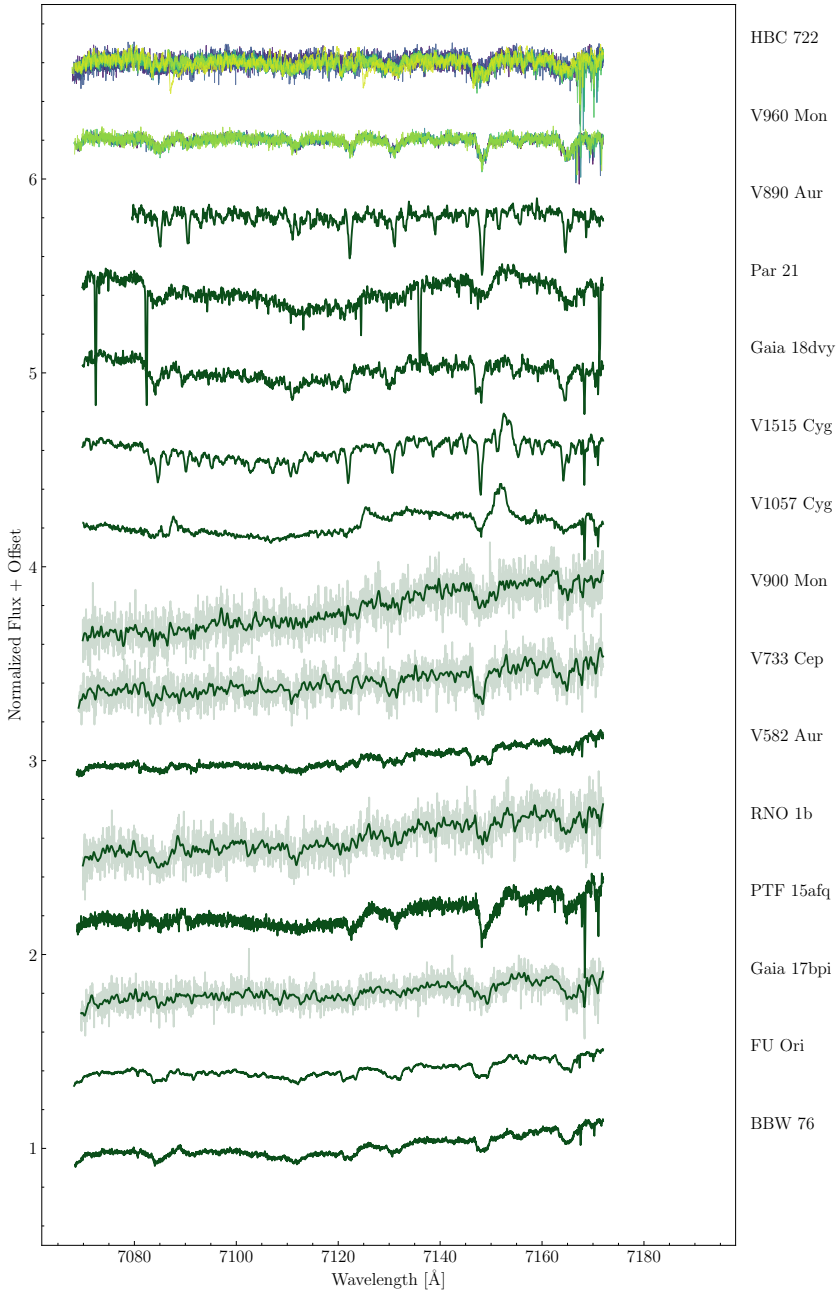

Figure 12.29: Figure 12.6 continued.

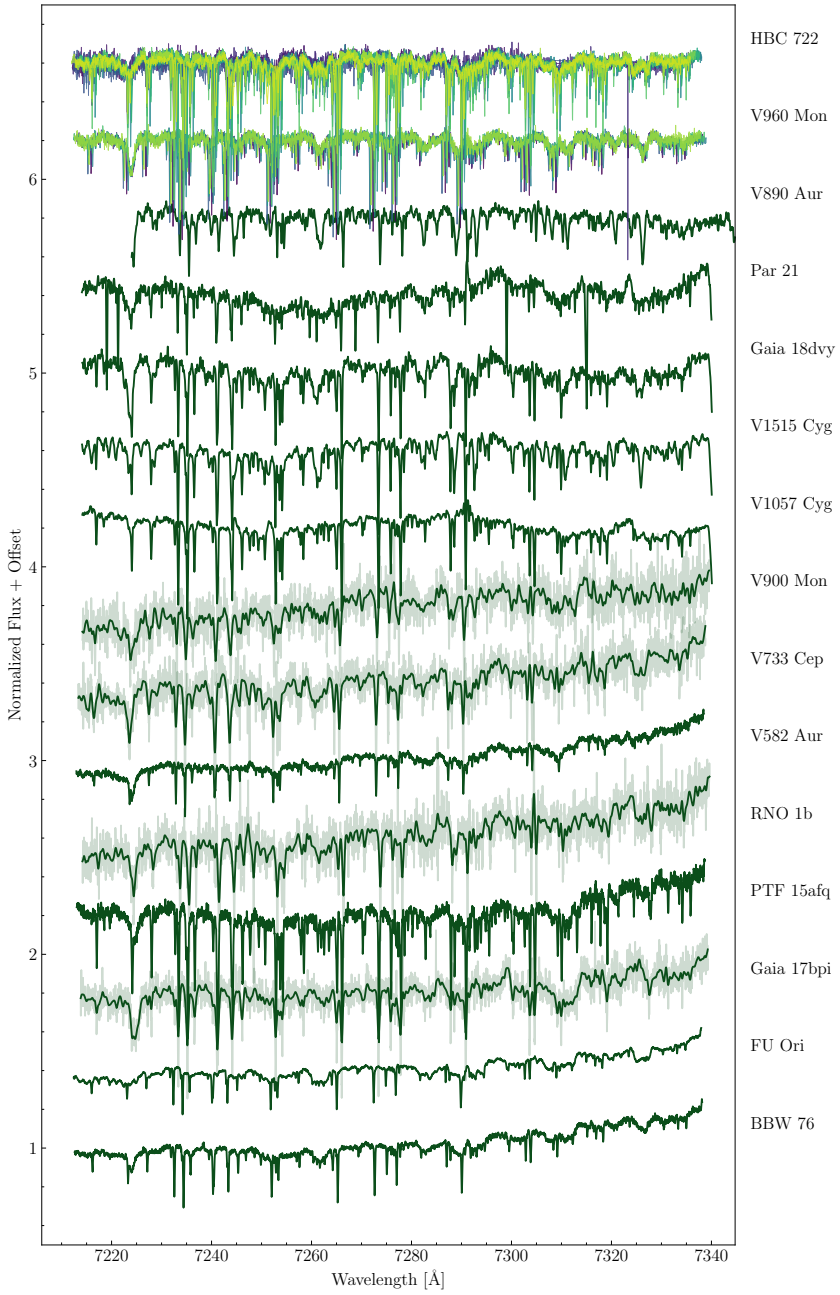

Figure 12.30: Figure 12.6 continued.

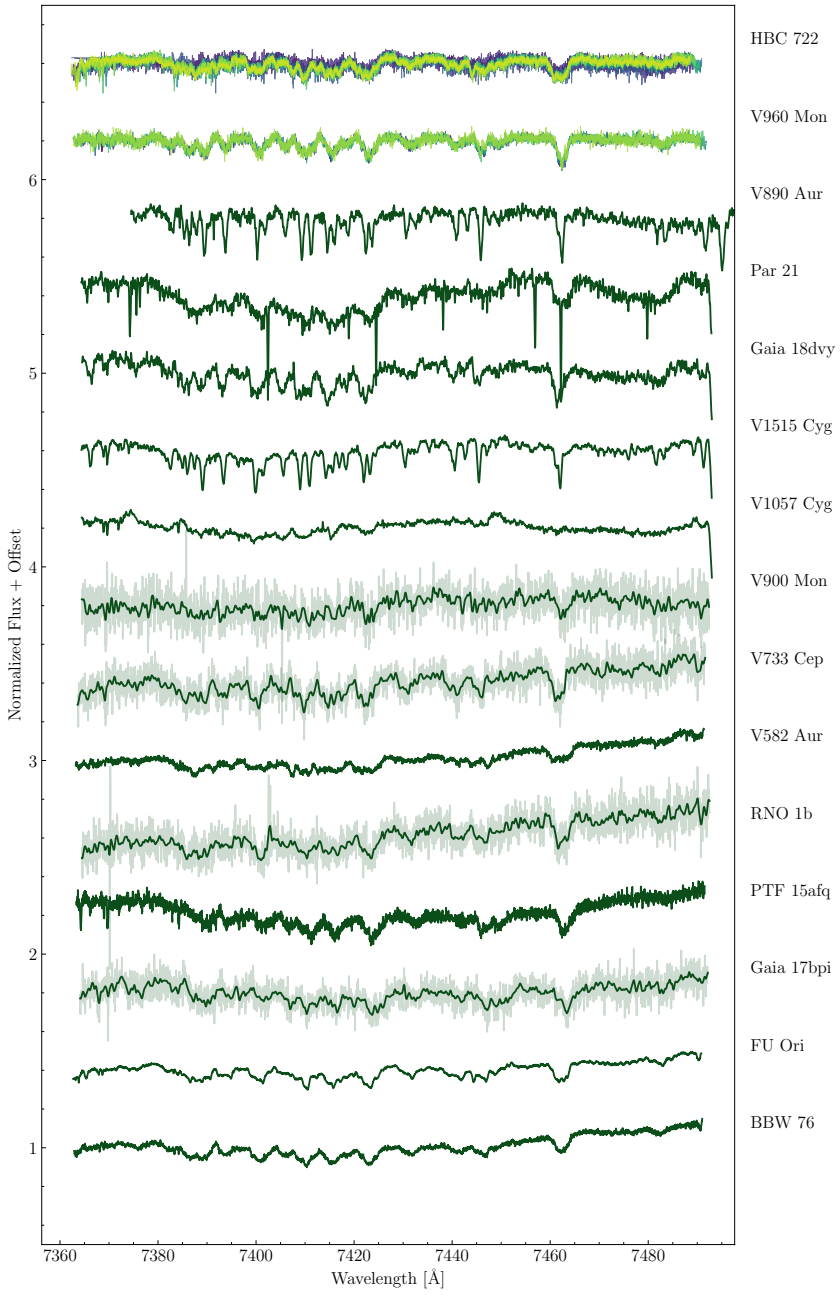

Figure 12.31: Figure 12.6 continued.

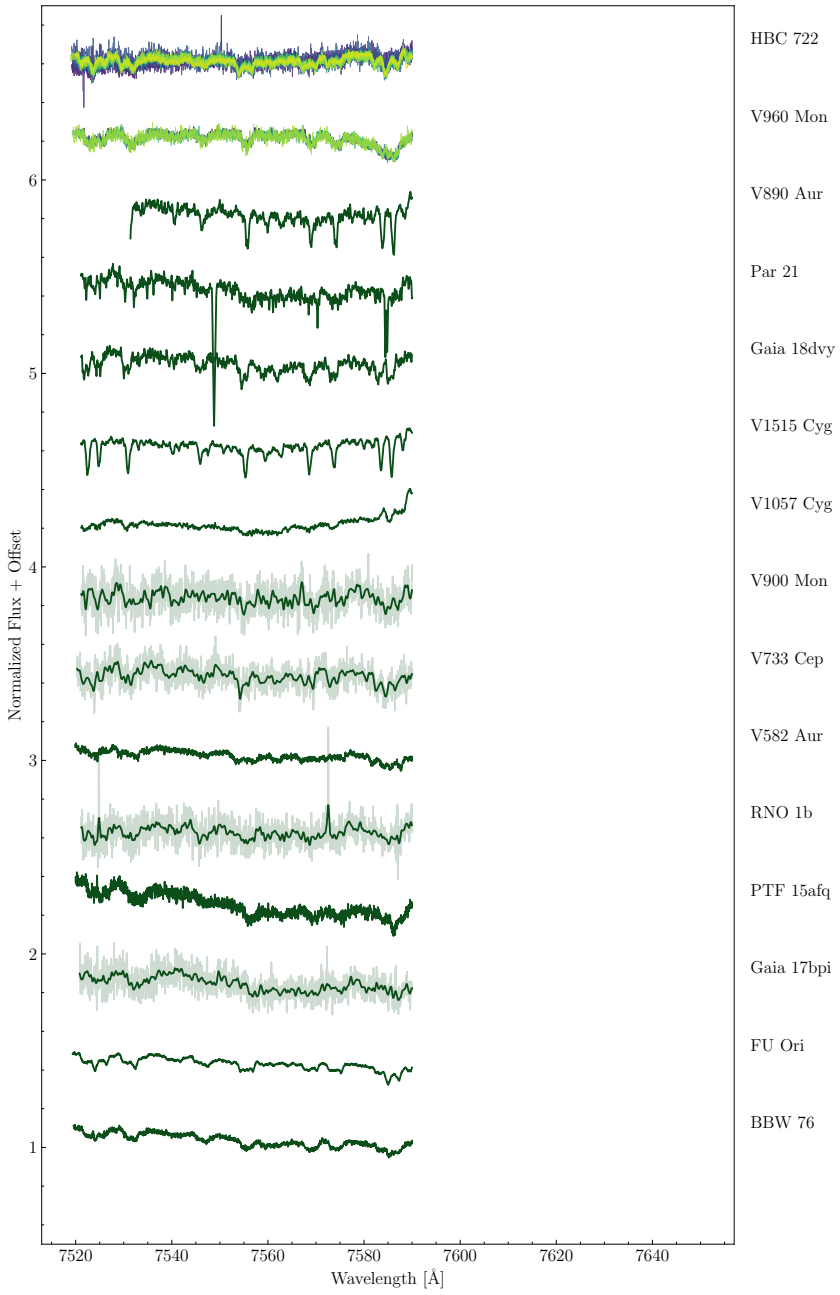

Figure 12.32: Figure 12.6 continued.

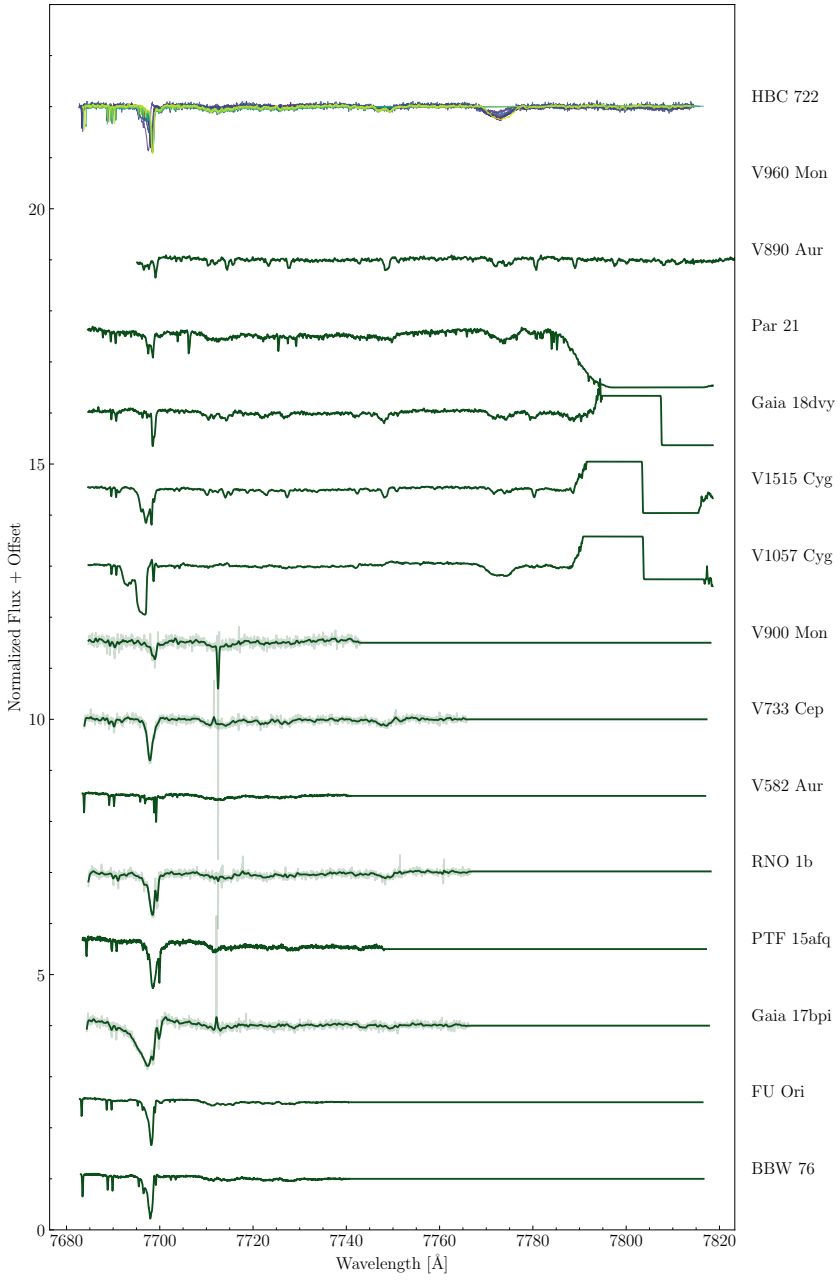

Figure 12.33: Figure 12.6 continued.

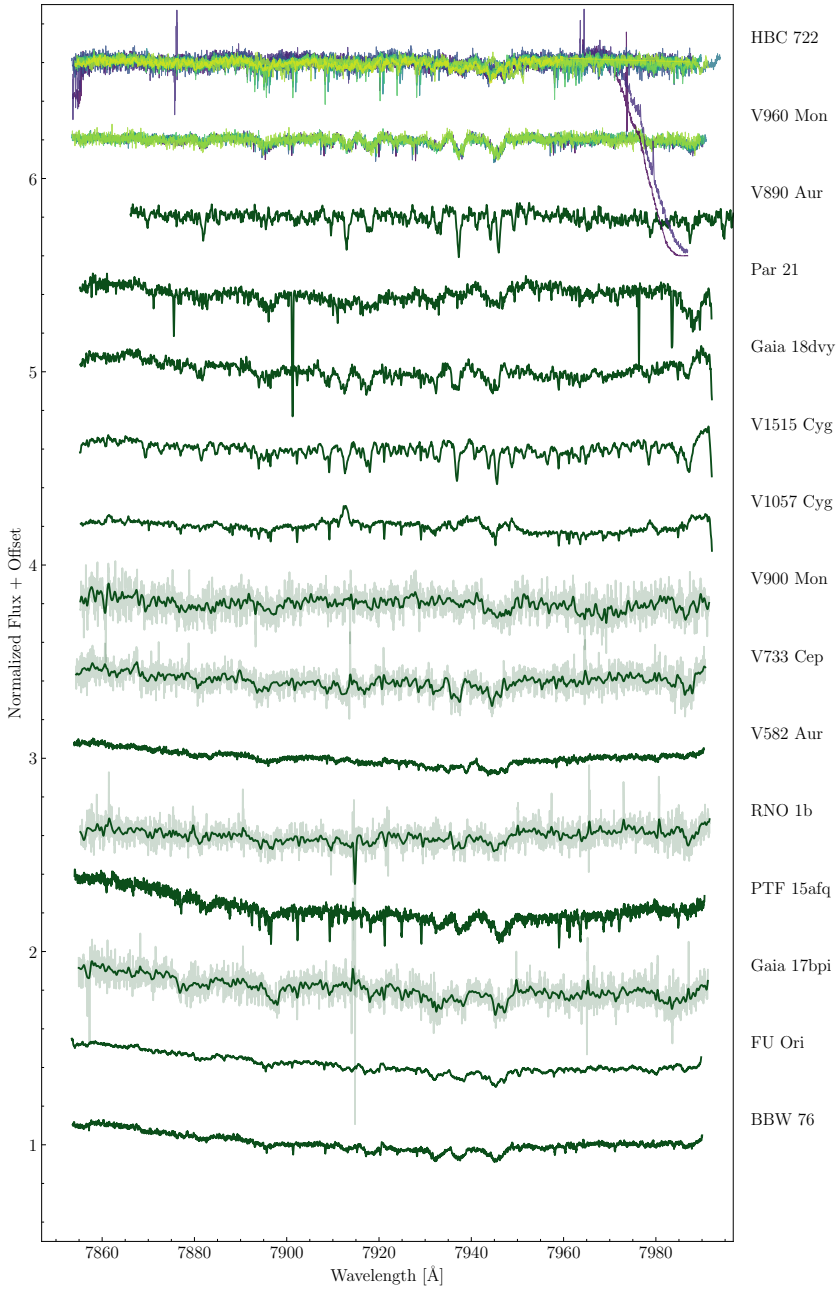

Figure 12.34: Figure 12.6 continued.

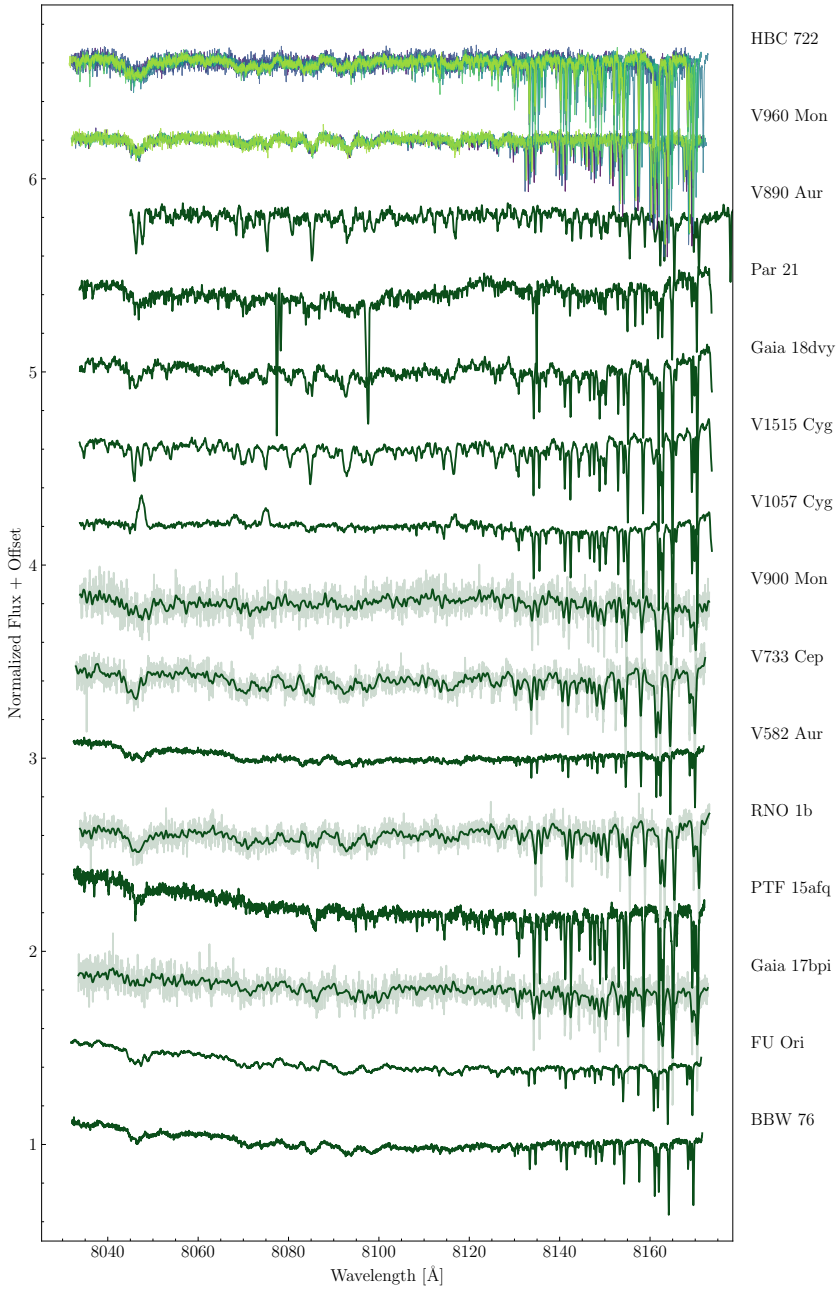

Figure 12.35: Figure 12.6 continued.

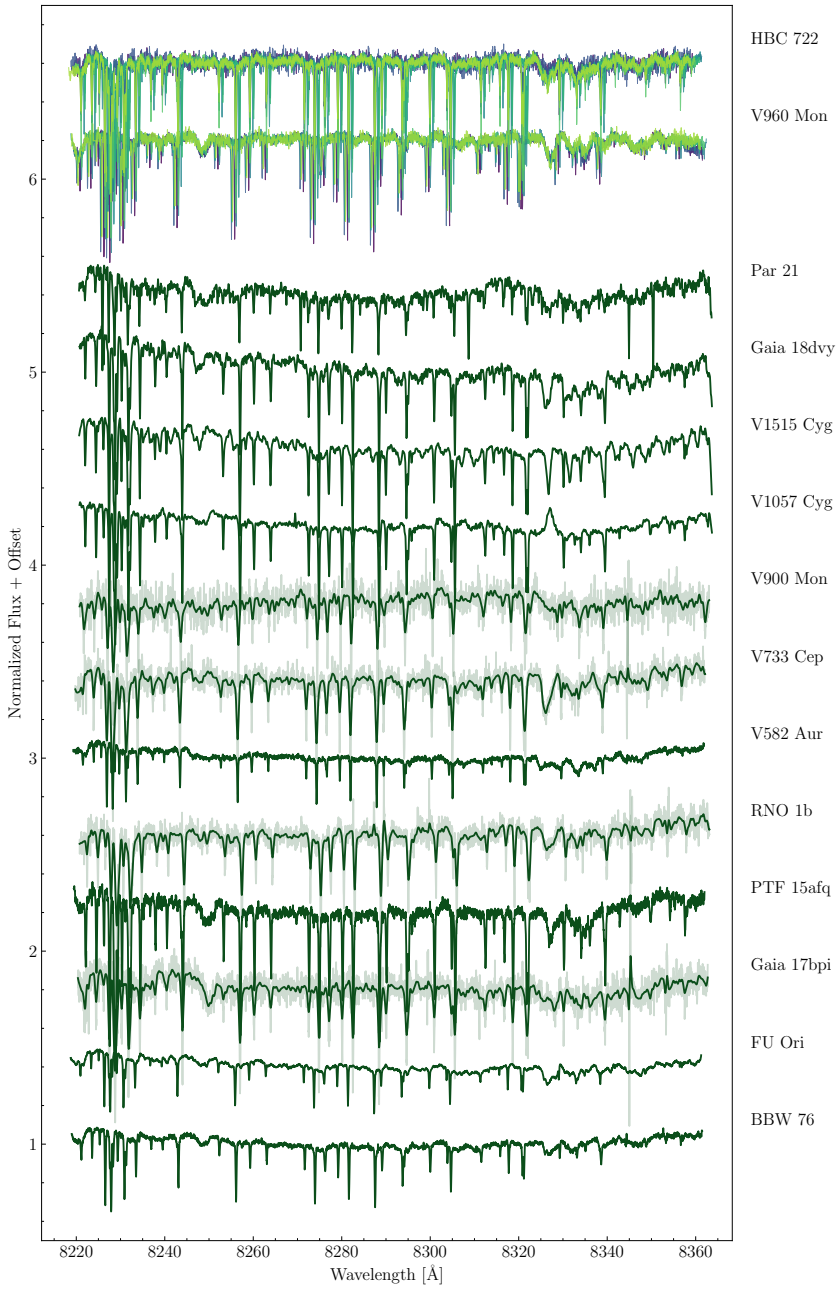

Figure 12.36: Figure 12.6 continued.

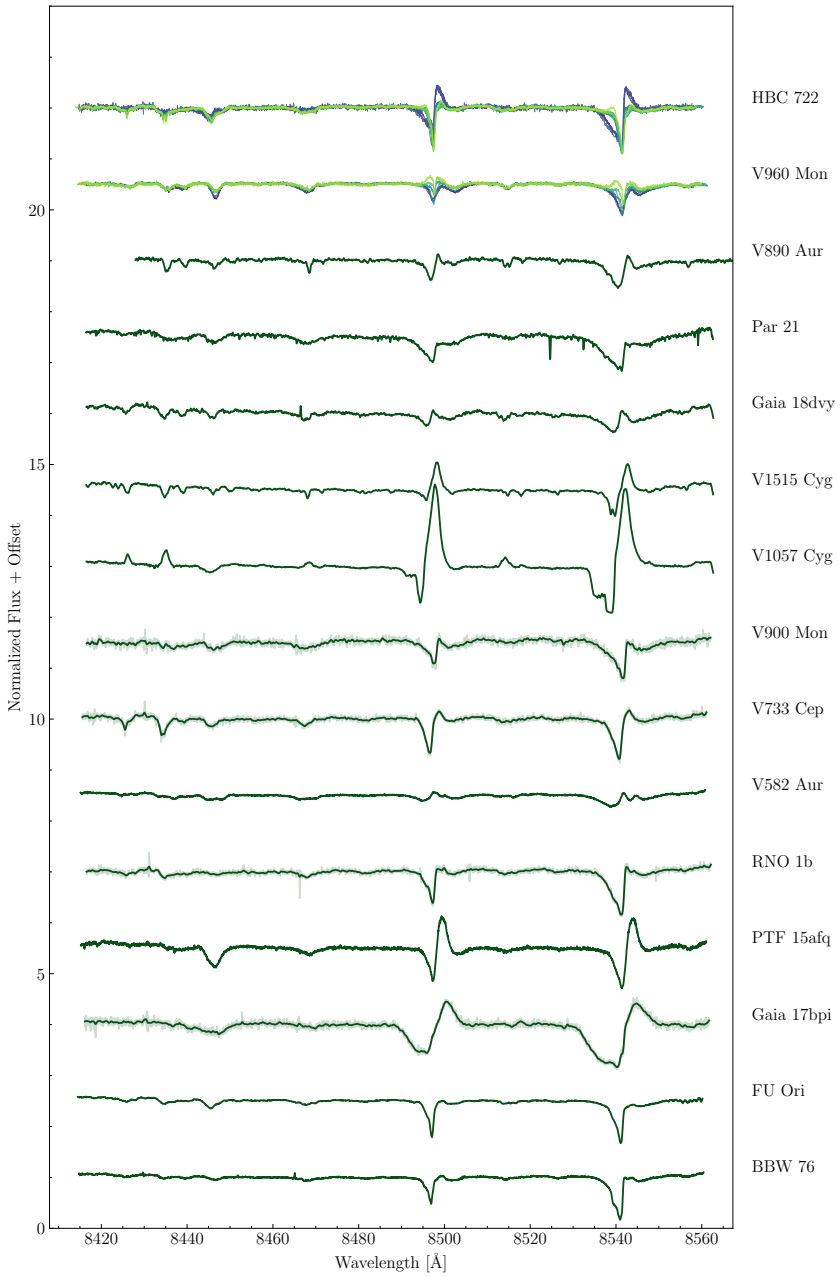

Figure 12.37: Figure 12.6 continued.

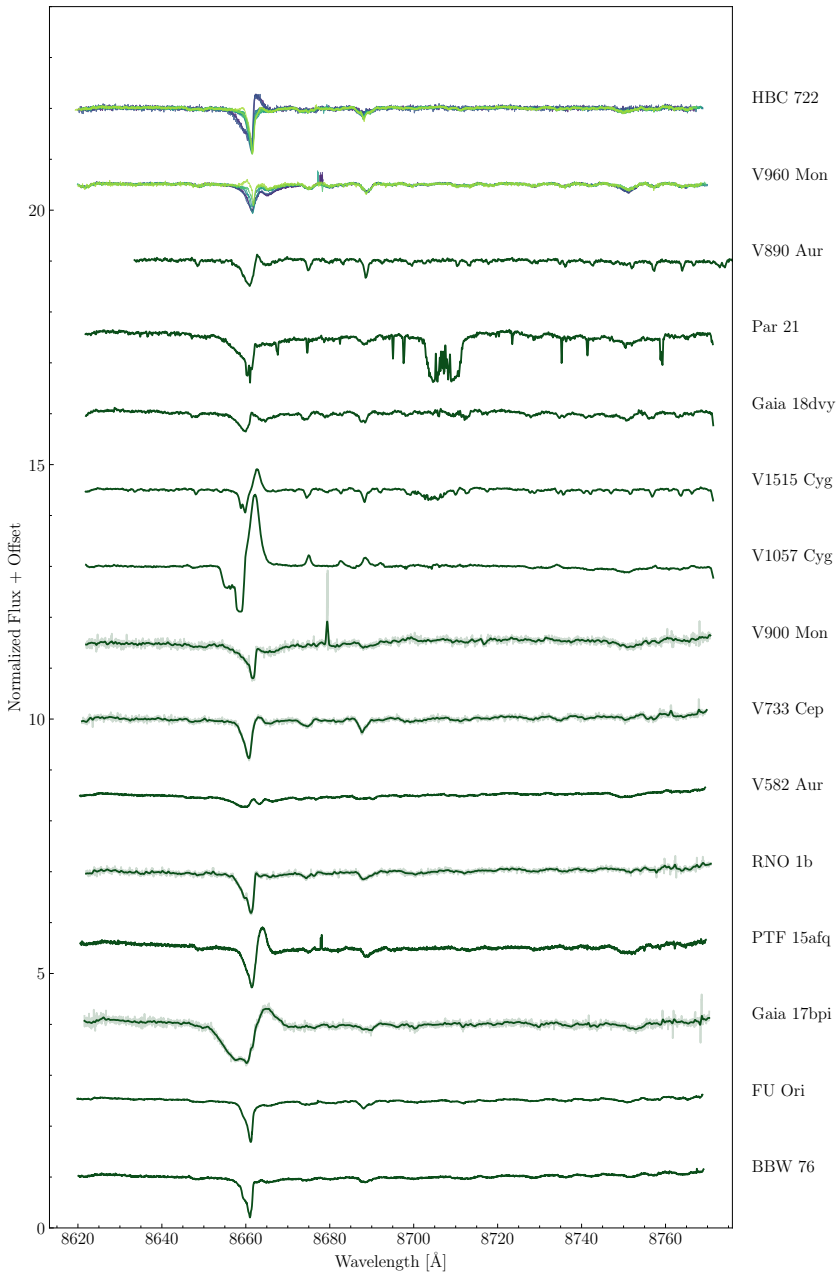

Figure 12.38: Figure 12.6 continued.

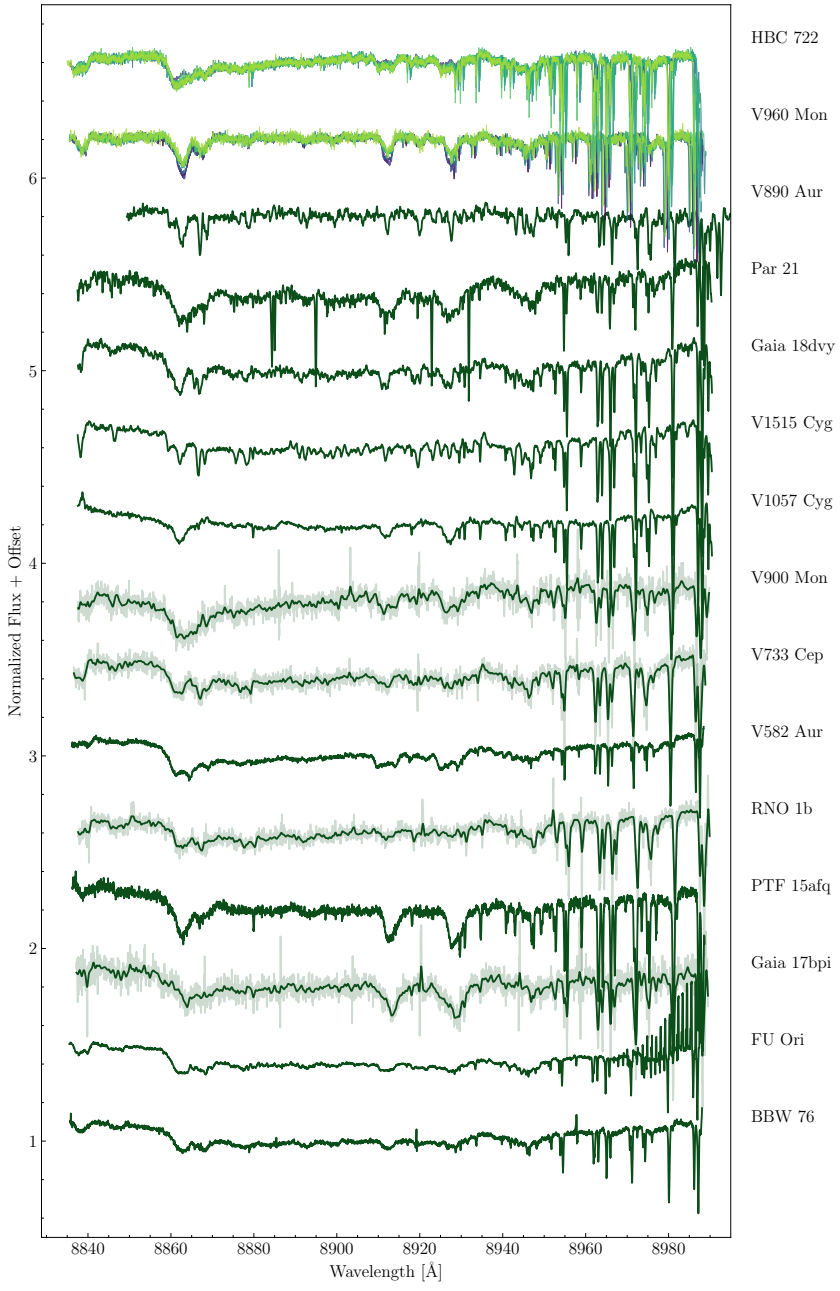

Figure 12.39: Figure 12.6 continued.

Chapter 13

A KECK/NIRSPEC ATLAS OF FUORS

Complementing the Keck/HIRES atlas of FUOrs is a Keck/NIRSPEC atlas, spanning Y to K band, though Y band is not available for the most embedded ($A_V > 40$ mag) objects. An observation log for each band is provided in Tables 13.1, 13.2, and 13.3. The spectra were all taken via standard ABBA nod sequences in generally good weather[1]. The spectra were extracted, deblazed, coadded, and telluric corrected using the `PypeIt` (Prochaska et al., 2020) module written for Keck/NIRSPEC and the telluric correction procedure described in Carvalho, Doppmann, et al. (2024). The telluric standards used were A0V stars that were easily accessible throughout the nights of the observing run.

This survey was conducted in part to provide a maximally complete set of high resolution spectra for known FUOrs. Since the survey began in 2022, 3 – 4 new FUOrs have been discovered that are bright enough for NIRSPEC spectra. Follow-up observations of these objects will be conducted to maintain an up-to-date data set. The need for high resolution spectra of FUOrs is discussed in detail in Section 4.3 and all of the spectra shown below are used somewhere in this Thesis.

13.1 Plots of the Keck/NIRSPEC Spectra

Figure 13.1 shows the He I 10830 Å and Paschen β features in all of the Y band spectra collected as a part of this survey. There are additional Y band spectra in the Keck Observatory Archive, though at lower SNR. In Class I/II YSOs, Paβ is typically an emission line and serves as an accretion tracer, as its luminosity can be used to estimate the accretion luminosity of a source. In FUOrs, the feature is only ever seen in absorption or in a P Cygni profile, indicating it instead traces the strong outflows near the star.

The He 10830 Å triplet frequently traces outflows in FUOr spectra, as can be seen by the very high blue-shifted velocities in Figure 13.1. The diversity of line profiles

[1] A fun bit of trivia: the spectra taken in Dec 2022 were taken during the peak of the eruption of Mauna Loa during that year. Lynne Hillenbrand and I were baffled by the highly variable sky background to the South until we realized we were seeing lava glow reflecting off the clouds. The temperature of the lava was exactly right to increase K band sky backgrounds so much that even the reddest objects were difficult to see in K using the slit camera and we had to resort to finding the objects in J band, first.

from object to object is comparable to that of Hα, shown in Chapter 12. Identifying the true highest velocities in the He I 10830 triplet is confounded by contamination from Mg I and Si I features blueward of the triplet. The feature is also known to the variable on month-to-year timescales, as Connelley and Reipurth (2018) show for V1735 Cyg. This further supports the idea that it traces outflowing material relatively close to the star.

Following the outflow lines, the atlas spans Figures 13.2 to 13.32. There are some objects which have multiple epochs of spectra, enabling comparison between visits to search for variability. With the exception of features that have been shown to trace outflows (see Chapters 5 and 6), the line profiles in the NIR spectra show little variability. This is consistent with the disk model demonstration in Chapter 2 that showed the NIR is relatively insensitive to $T_{\rm max}$ in the disk, which is the parameter most likely to vary on short timescales.

13.2 Recommendations for Future Keck/NIRSPEC Observers

Any future Keck/NIRSPEC observers, particularly those seeking to maximize the wavelength coverage of single-observations in K band, should heed the final set of plots in this Chapter as a warning about the predictive power of the Echelle Format Simulator (EFS). While the location of the echellogram on the detector is reasonably well-represented in the simulator, the detector cutoff location can be uncertain by as many as 100 pixels. If there are important spectral features that are predicted to appear near the edge of the detector in the EFS, observers should confirm the desired wavelengths are covered when performing calibrations. It is sufficient to select one or two bright arc lamp lines to estimate a linear wavelength solution and ensure the attained wavelength coverage is as expected.

The location of the echellogram on detector can drift over the course of a night if alternating between different filter settings or grating/cross-disperser angles. When conducting this survey, the observations usually were taken in cycles of Y, J, H, K, K, H, J, Y to minimize the number of motor steps in any single filter change operation. Despite this, the echellogram drifts by several pixels so that the absolute wavelength solution for any given spectrum may be offset from the start of night solution by $10 - 20$ km s^{-1}. If the absolute wavelength calibration is critical to the science and this shift cannot be corrected for by, e.g., using photospheric lines as references, it is best to remain in one filter/setting throughout the night. Alternatively, OH emission lines can provide contemporaneous wavelength solutions for exposures exceeding

$\sim$ 300s.

Finally, it is important to take good telluric standards throughout the night. If possible, mapping the airmass throughout the night is the minimal requirement to ensure reliable telluric correction. For high airmass targets, it is best to take a standard close in time to the observation as well, in the event that weather conditions change during the night. The larger atmospheric column for these targets rapidly compounds the otherwise small time dependence of telluric features. At high resolution, this can make correction especially challenging due to the increased sensitivity to the precise line shape in addition to its depth.

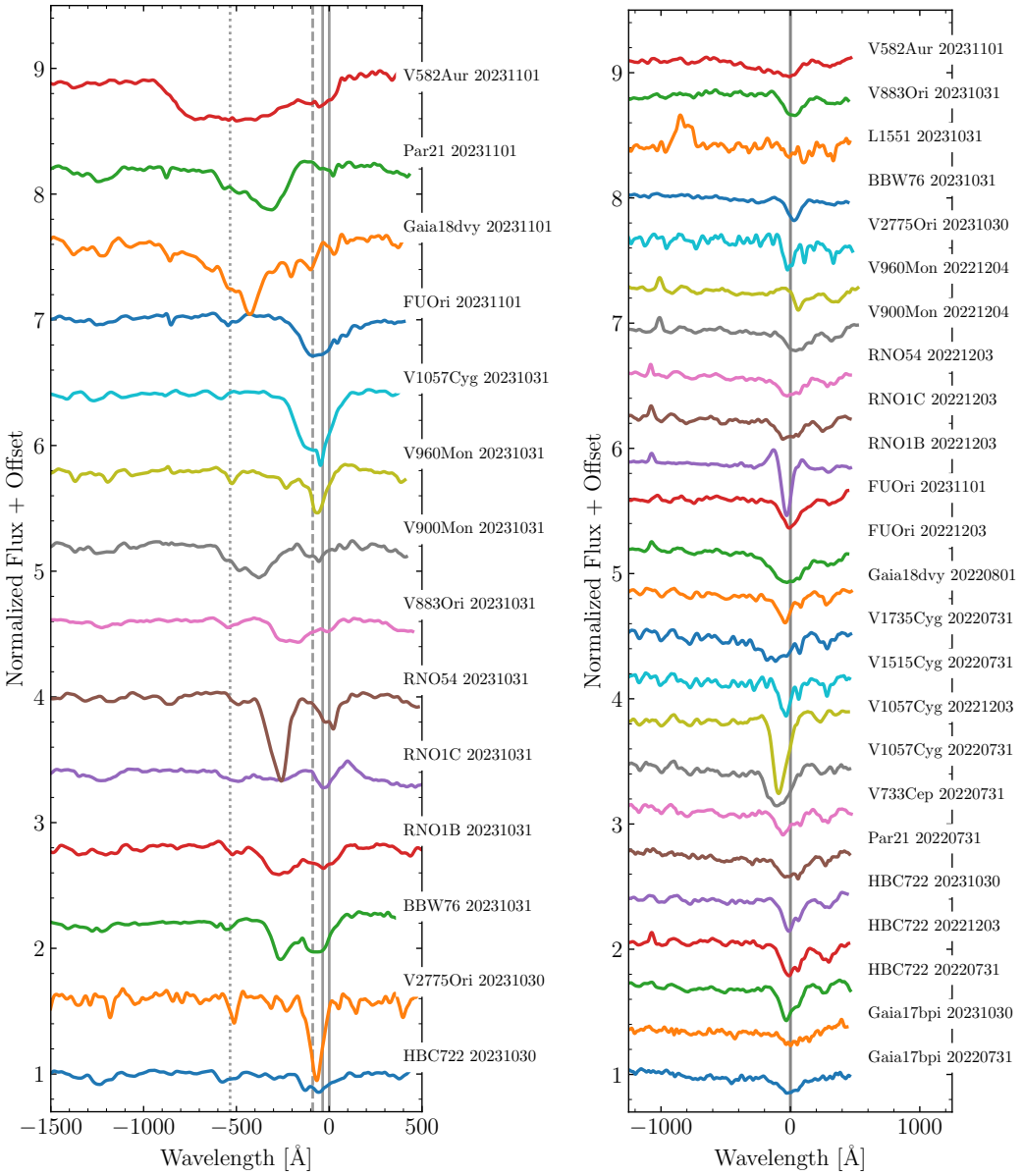

Figure 13.1: The line profiles of He I 10830 and Paβ in FUOrs. **Left:** The He I 10830 Å triplet for the FUOrs in our NIRSPEC survey. Notice the diversity of line profiles and maximum outflow absorption velocities. The vertical solid grey lines mark the components of the triplet, while the dashed line marks the nearby Si I 10827 Å line and the dotted line marks an Mg I 10811 Å line. **Right:** The Paβ line for the FUOrs in the survey. It is much weaker than the visible range Hα or Hβ (see Chapter 12), but does show variability between epochs. The spectra of FU Ori and V1057 Cyg show this most dramatically, but it can also be seen in HBC 722.

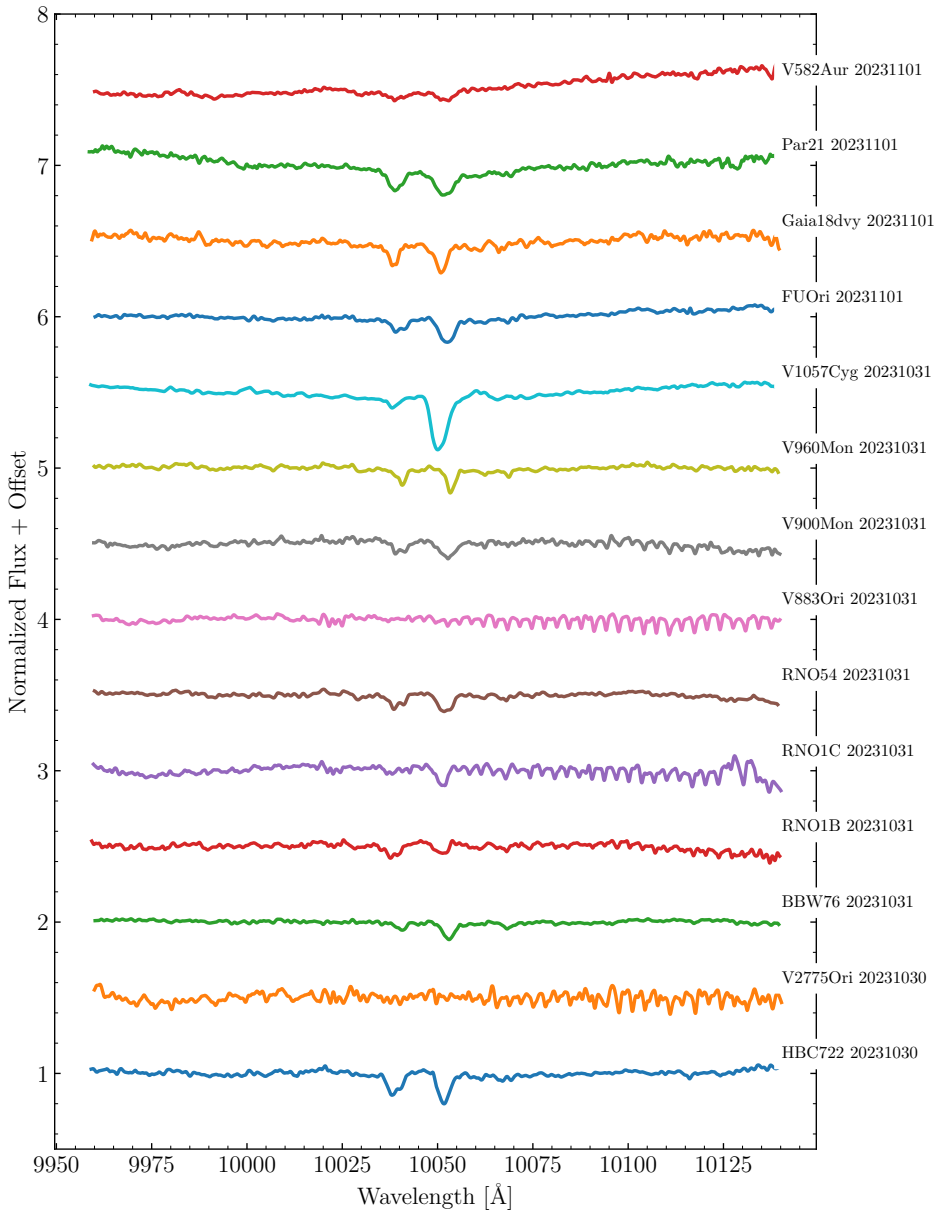

Figure 13.2: All of the FUOr spectra taken for the Keck/NIRSPEC survey with sufficient signal at 1 μm for high resolution spectroscopy. Shown here is Y Band order 76.

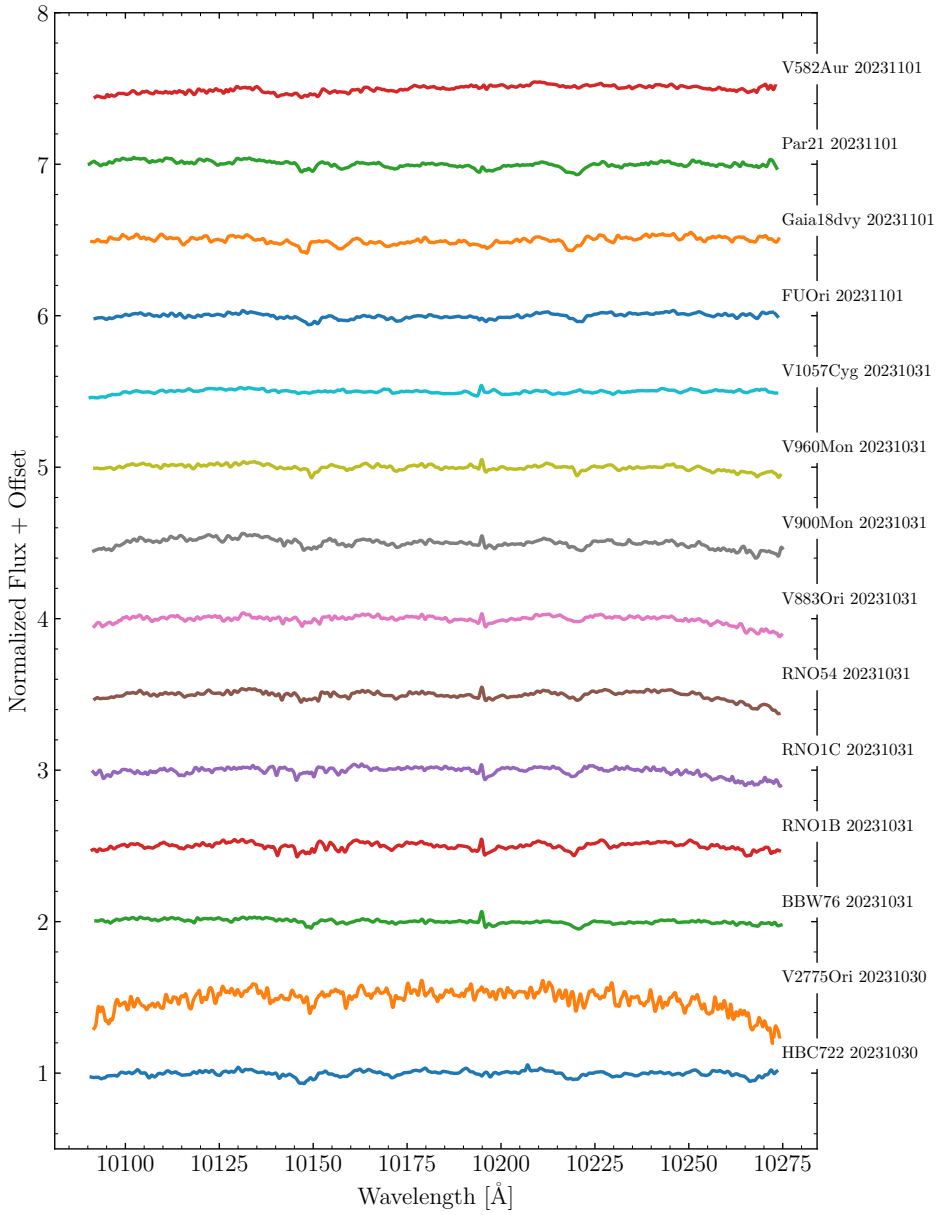

Figure 13.3: Same as Figure 13.2 for Y Band order 75.

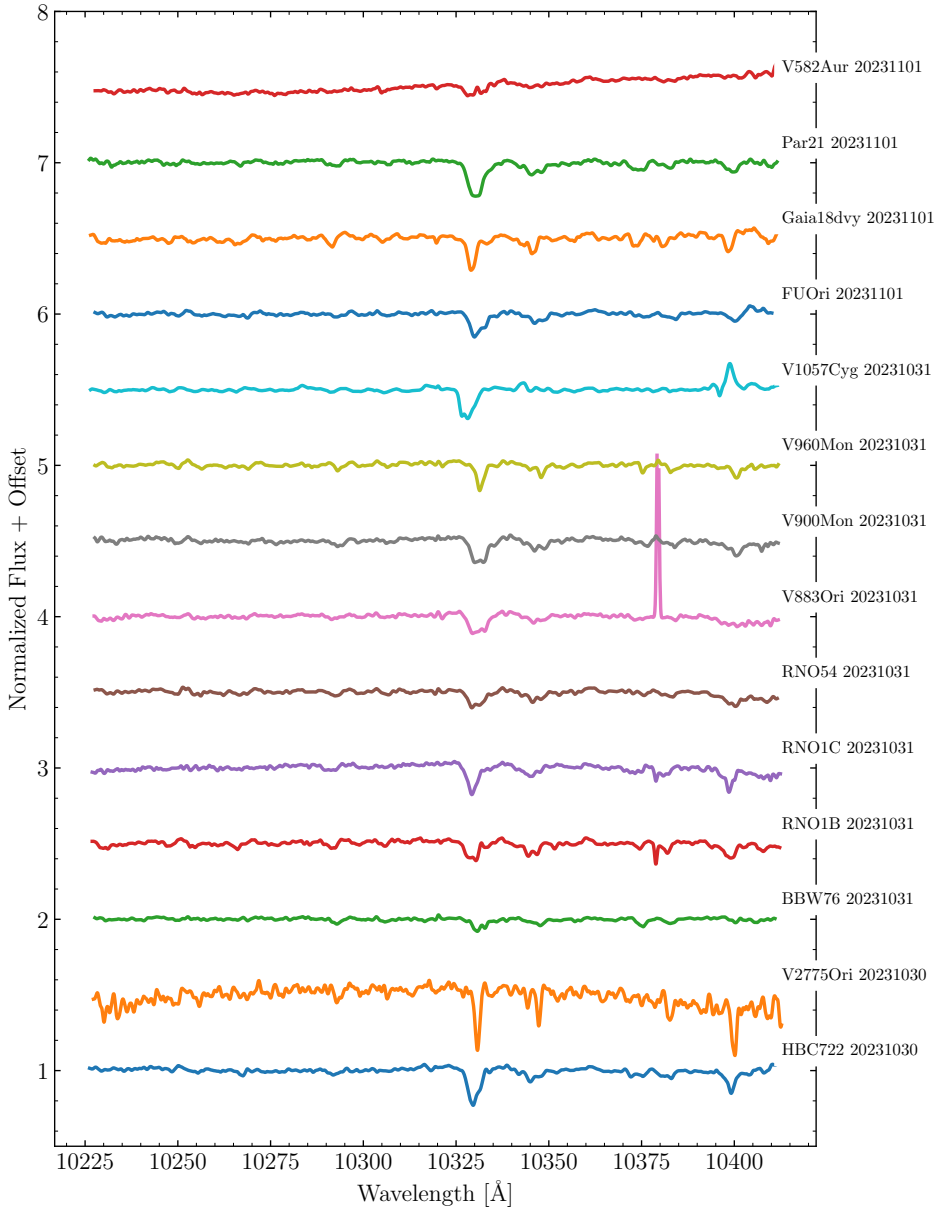

Figure 13.4: Same as Figure 13.2 for Y Band order 74.

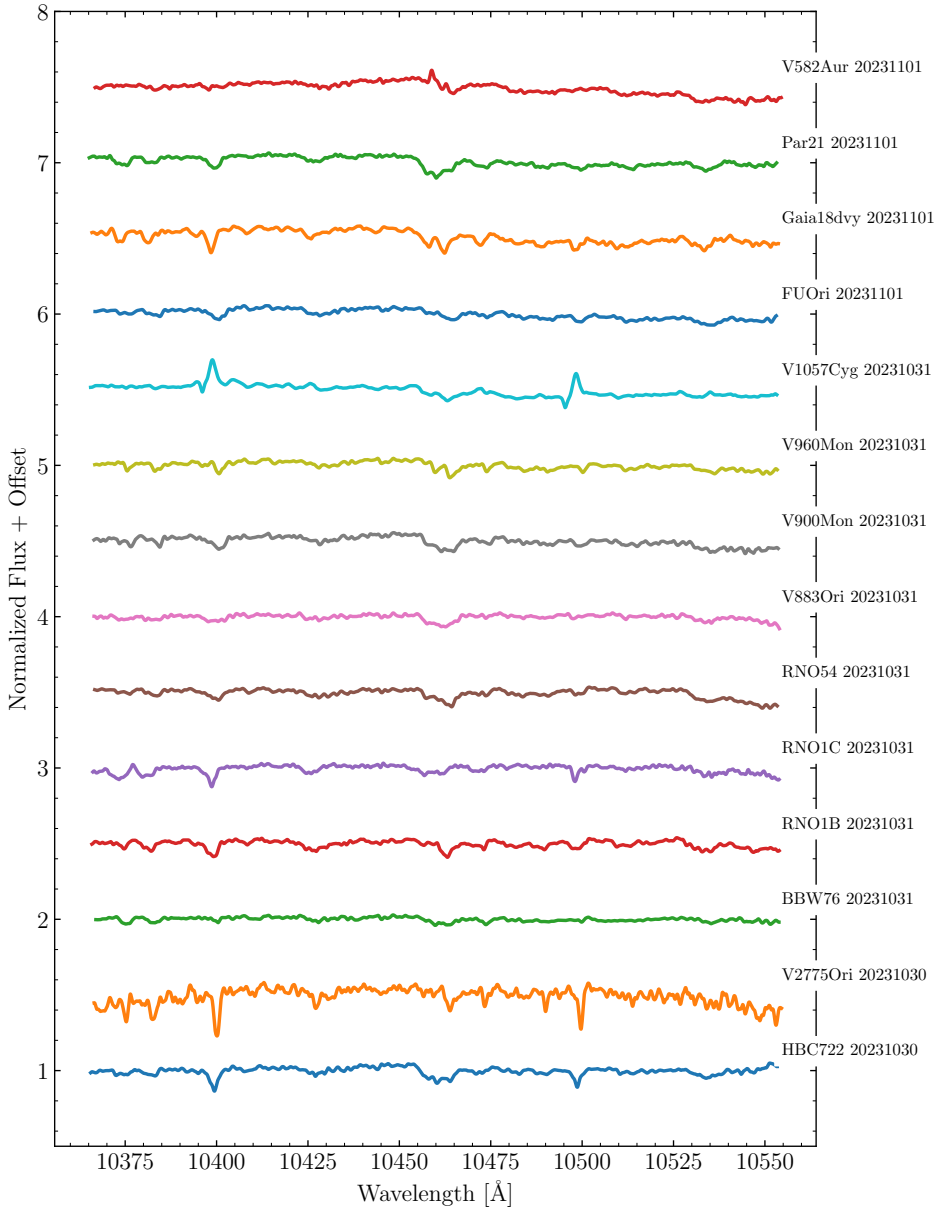

Figure 13.5: Same as Figure 13.2 for Y Band order 73.

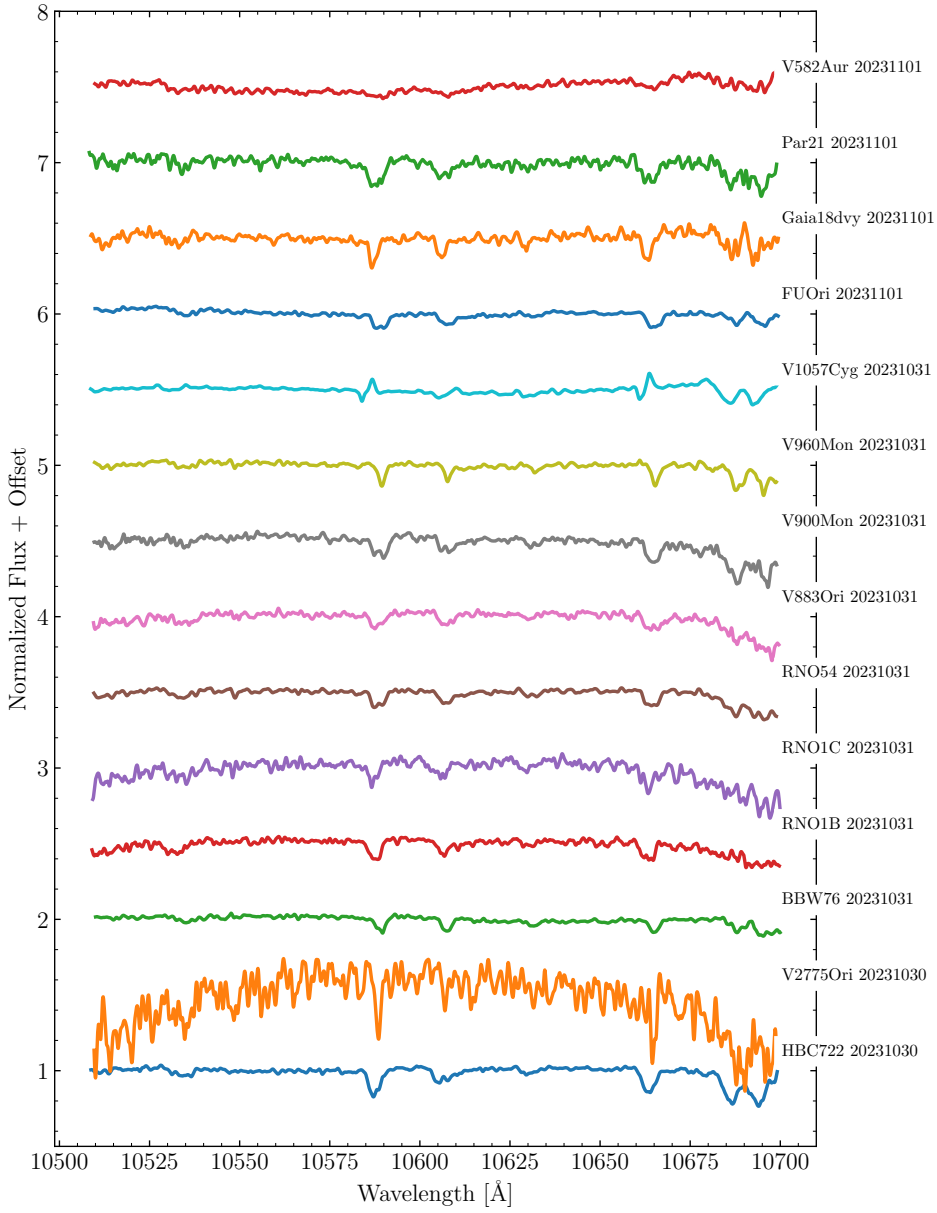

Figure 13.6: Same as Figure 13.2 for Y Band order 72.

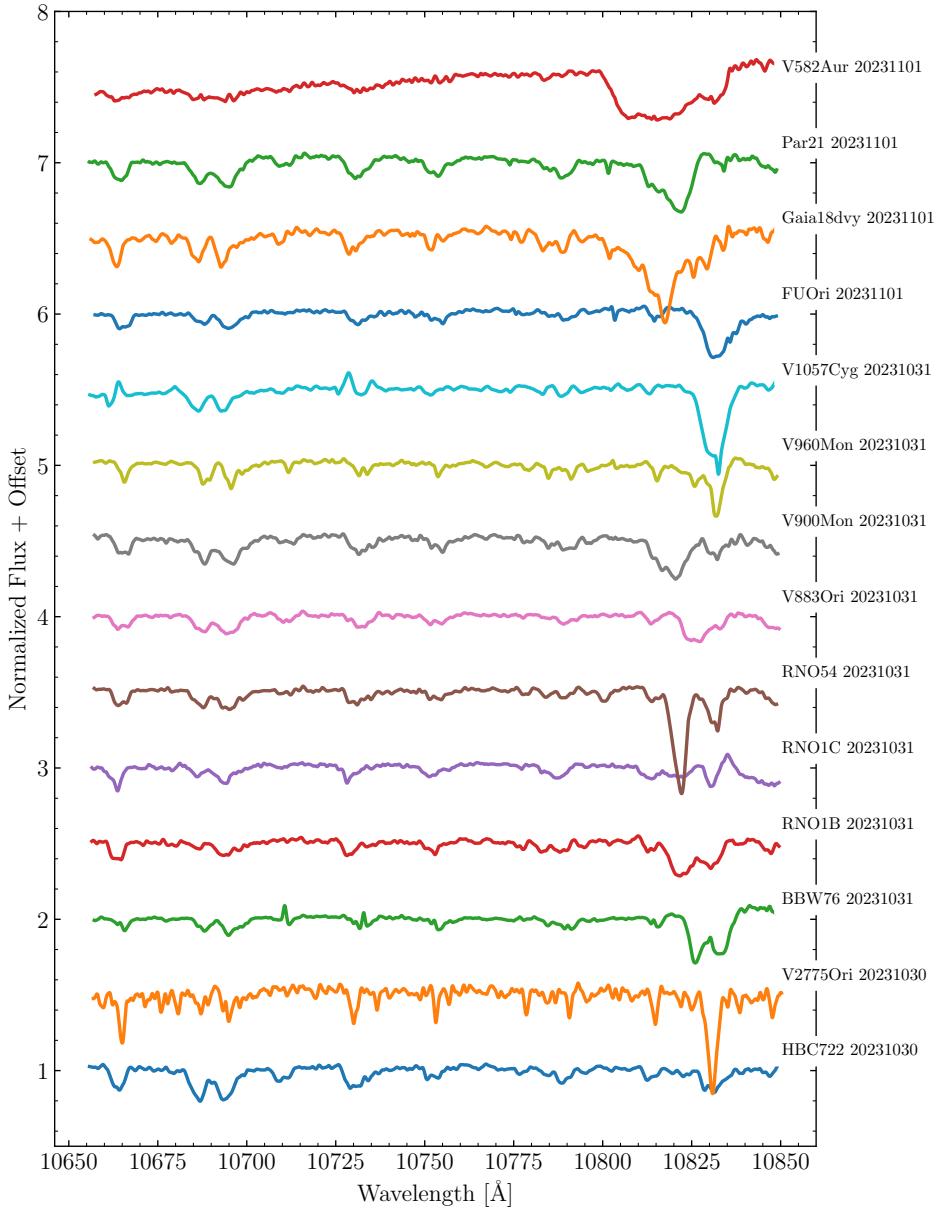

Figure 13.7: Same as Figure 13.2 for Y Band order 71.

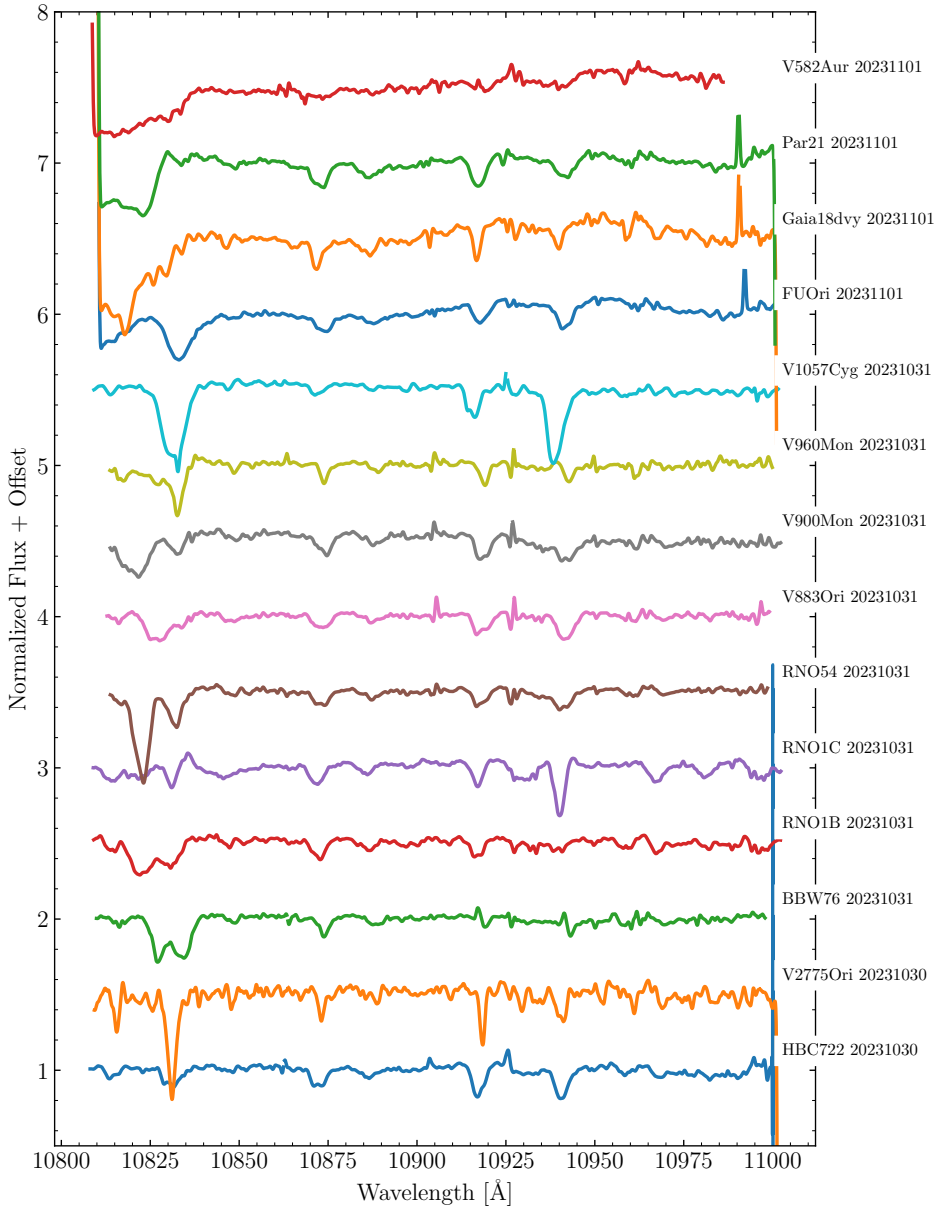

Figure 13.8: Same as Figure 13.2 for Y Band order 70.

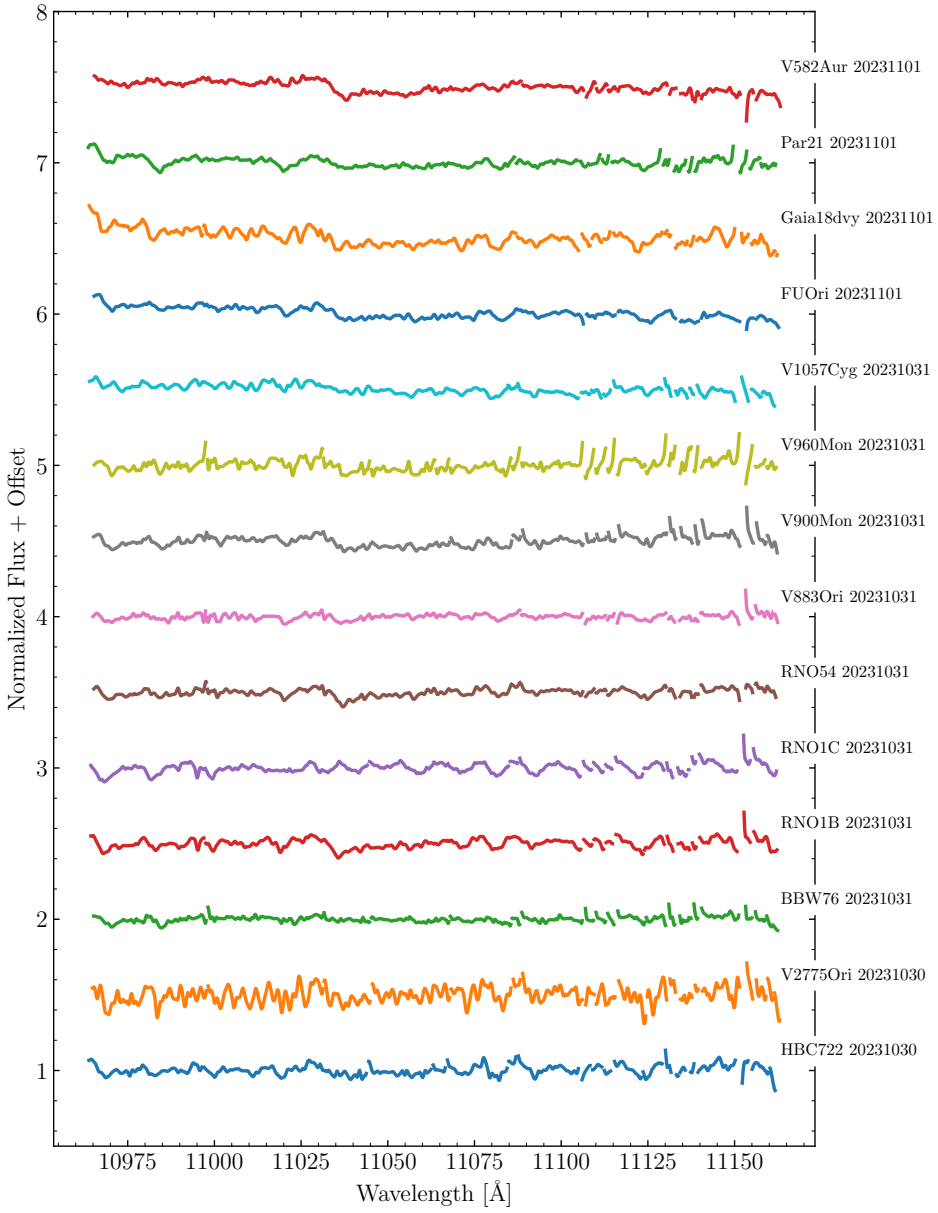

Figure 13.9: Same as Figure 13.2 for Y Band order 69.

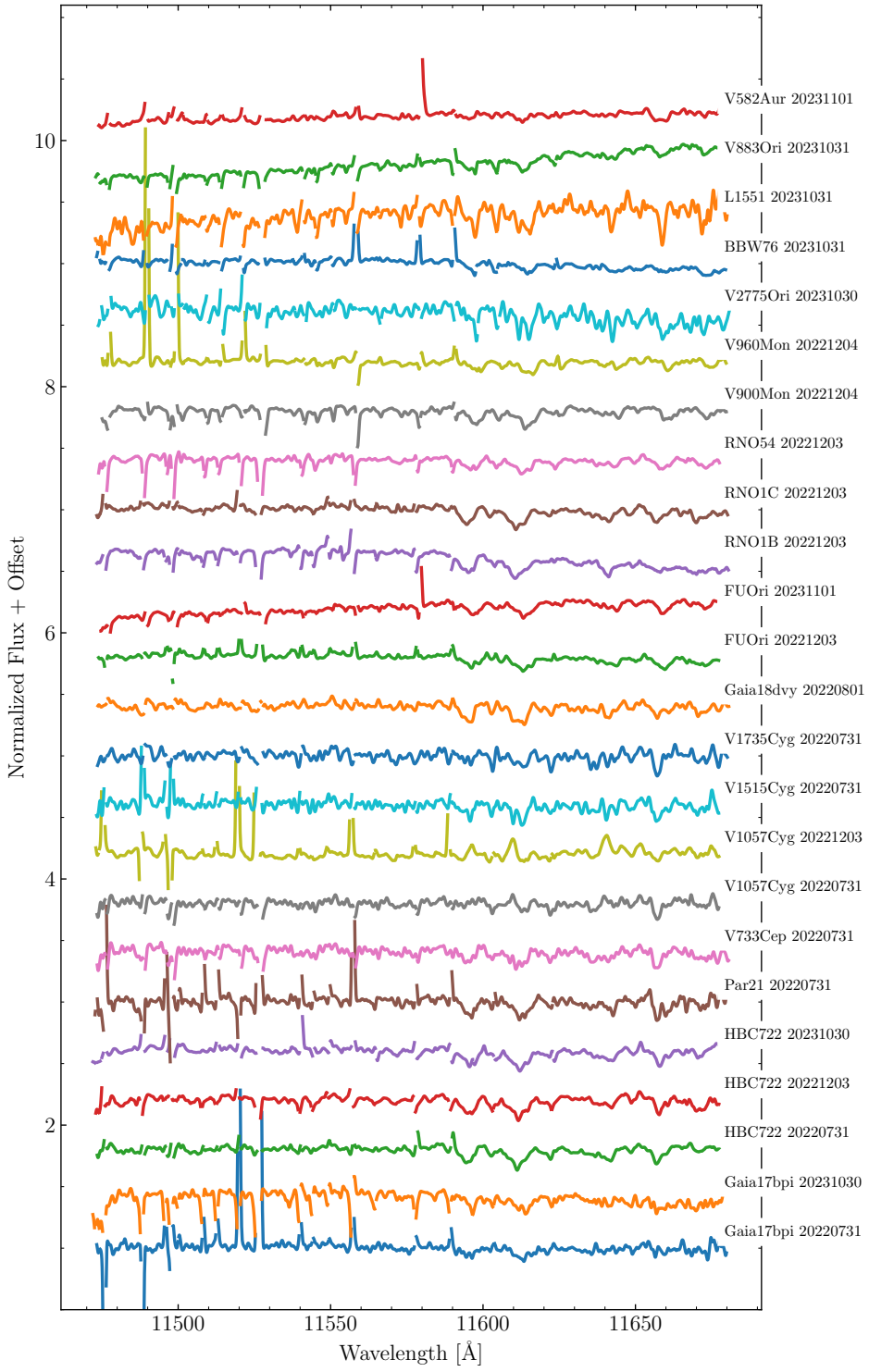

Figure 13.10: All of the FUOr spectra taken for the Keck/NIRSPEC survey with sufficient signal at 1.2 μm for high resolution spectroscopy. Shown here is J Band order 66.

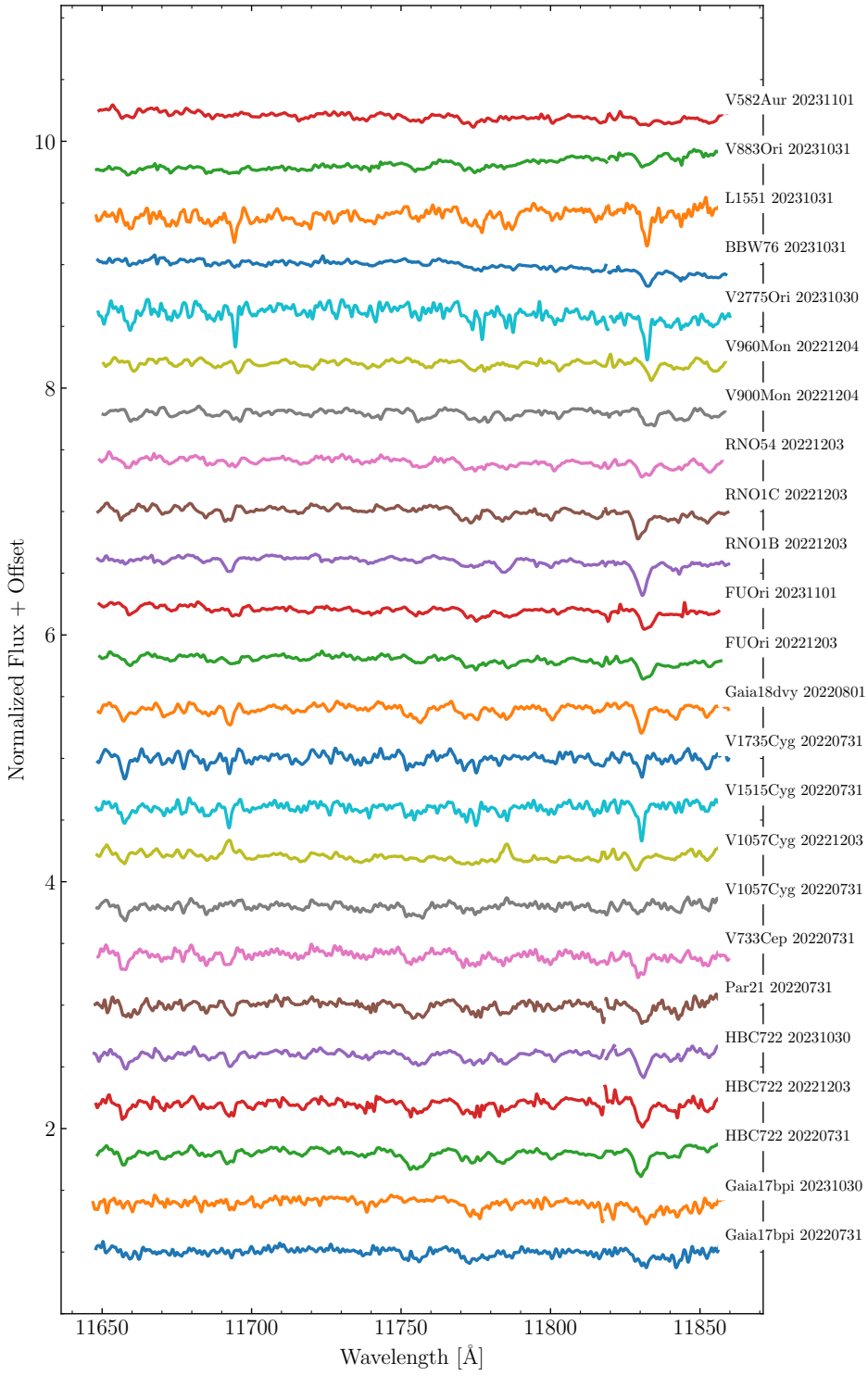

Figure 13.11: Same as Figure 13.10 for *J* Band order 65.

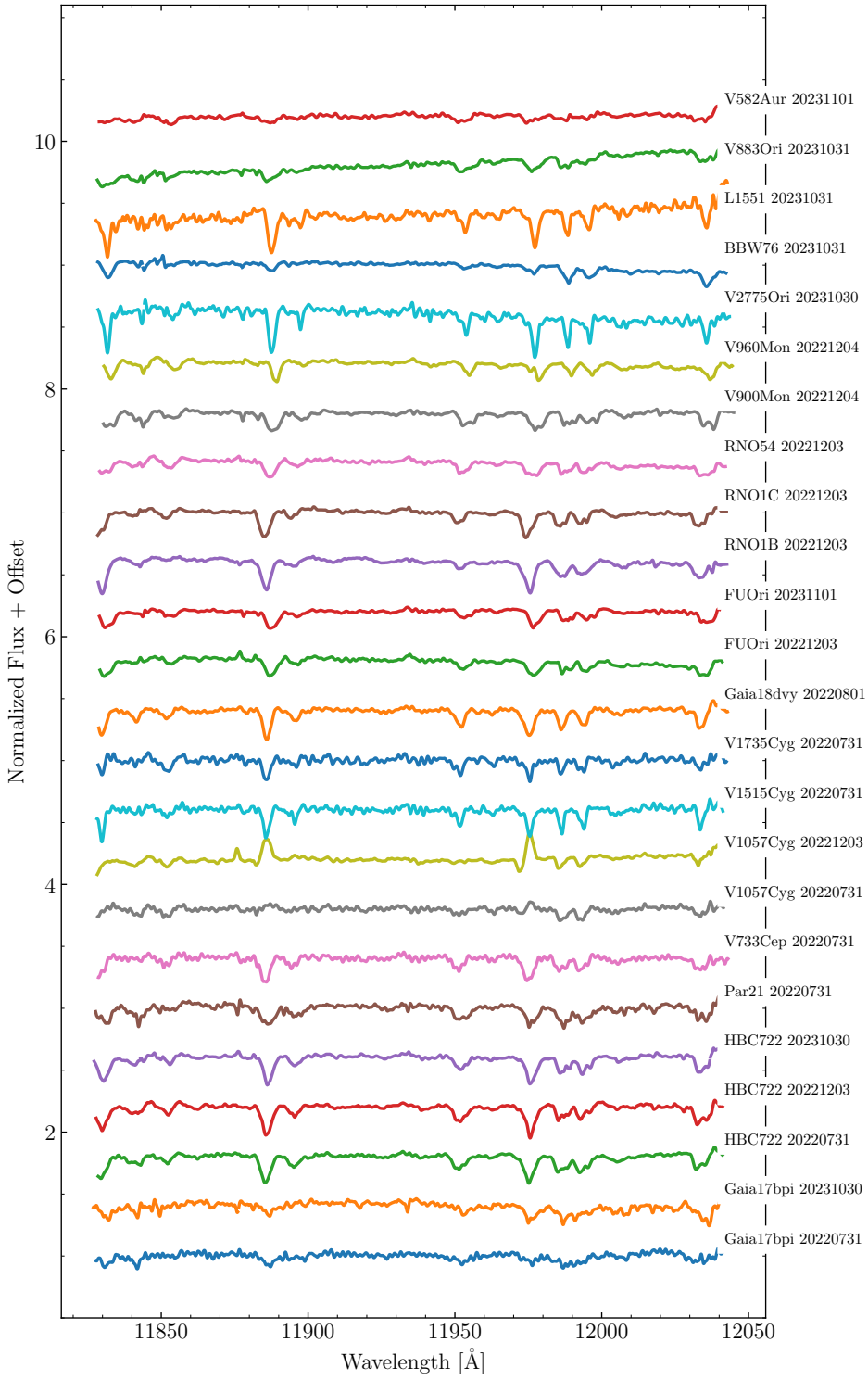

Figure 13.12: Same as Figure 13.10 for *J* Band order 64.

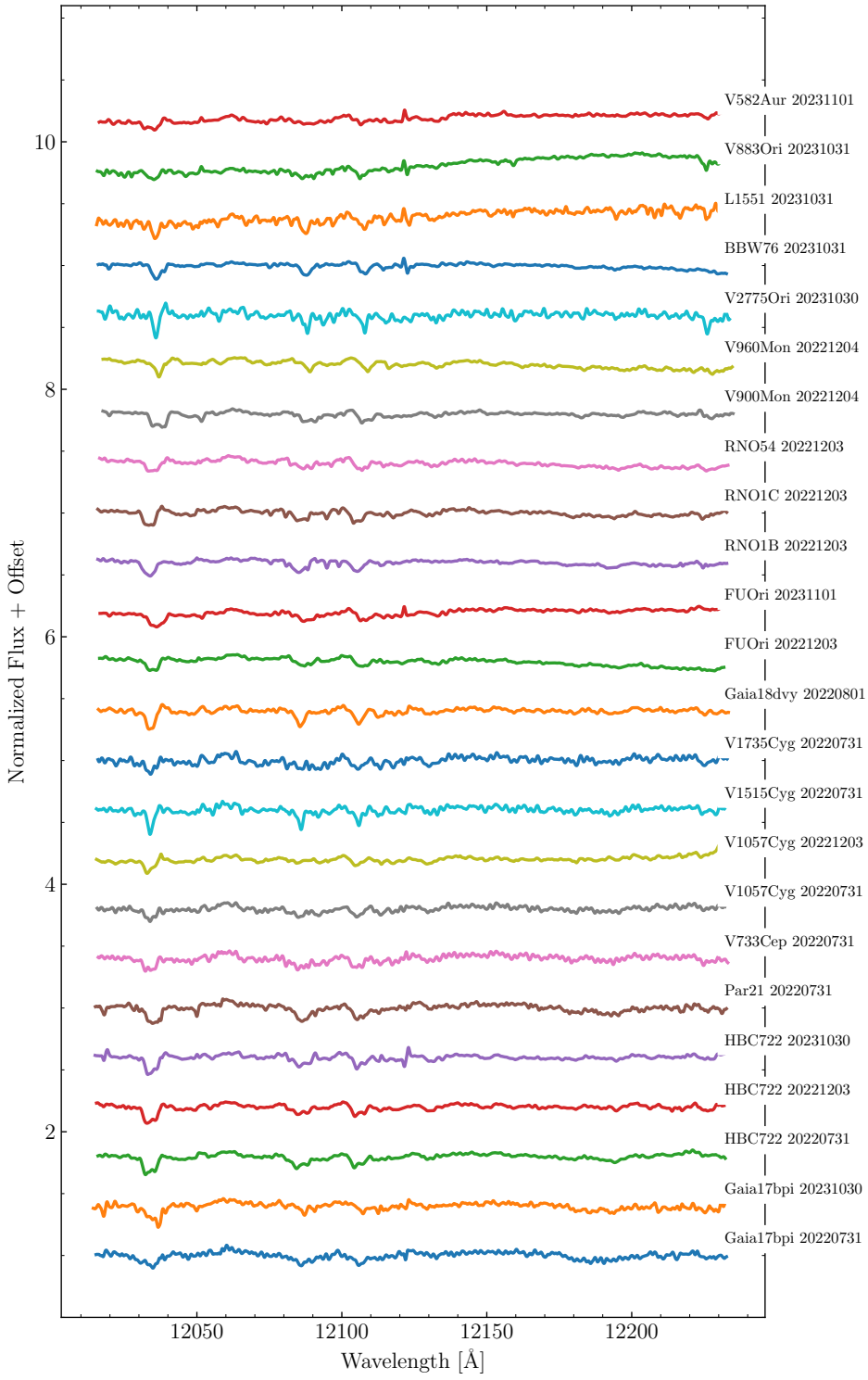

Figure 13.13: Same as Figure 13.10 for *J* Band order 63.

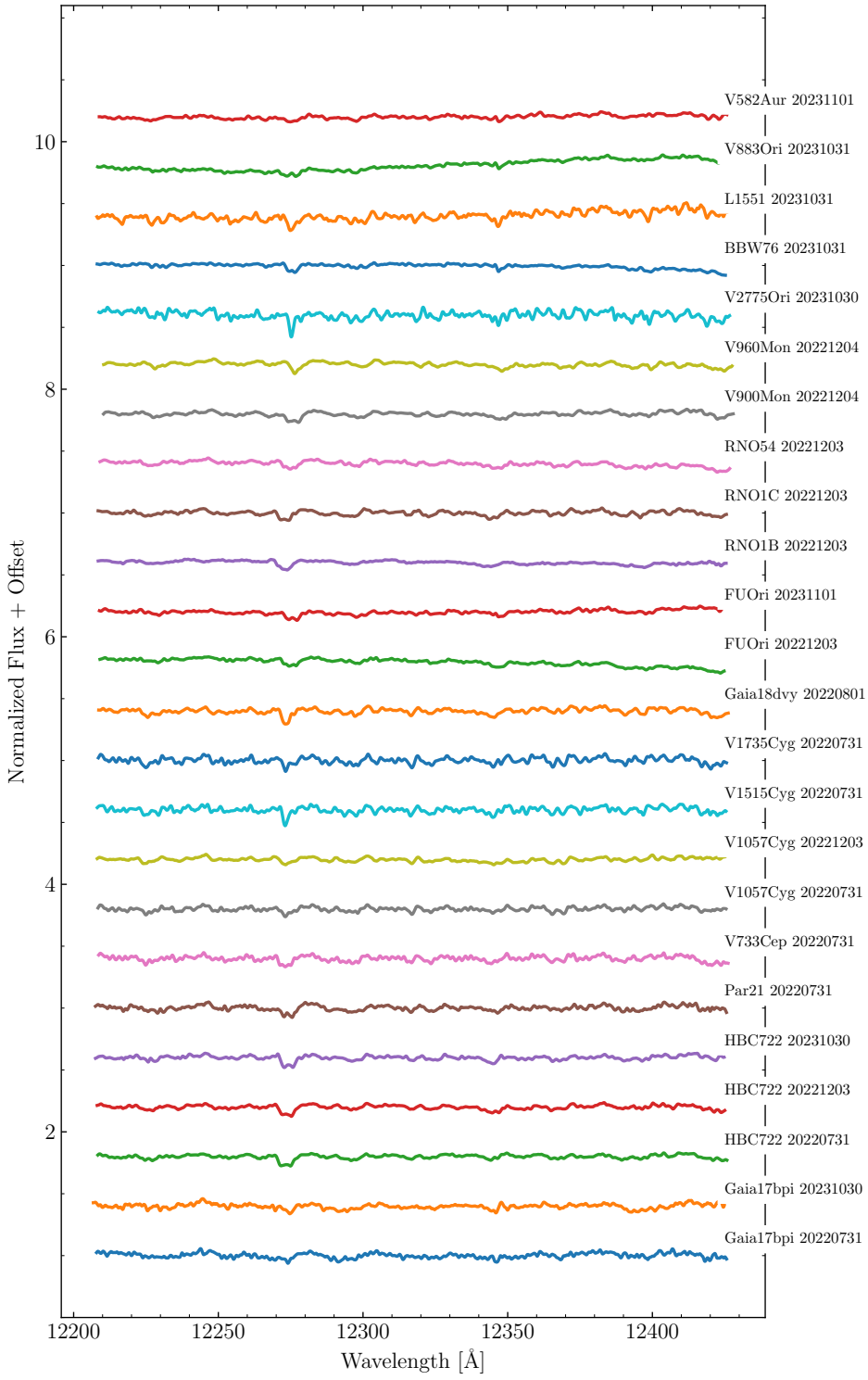

Figure 13.14: Same as Figure 13.10 for *J* Band order 62.

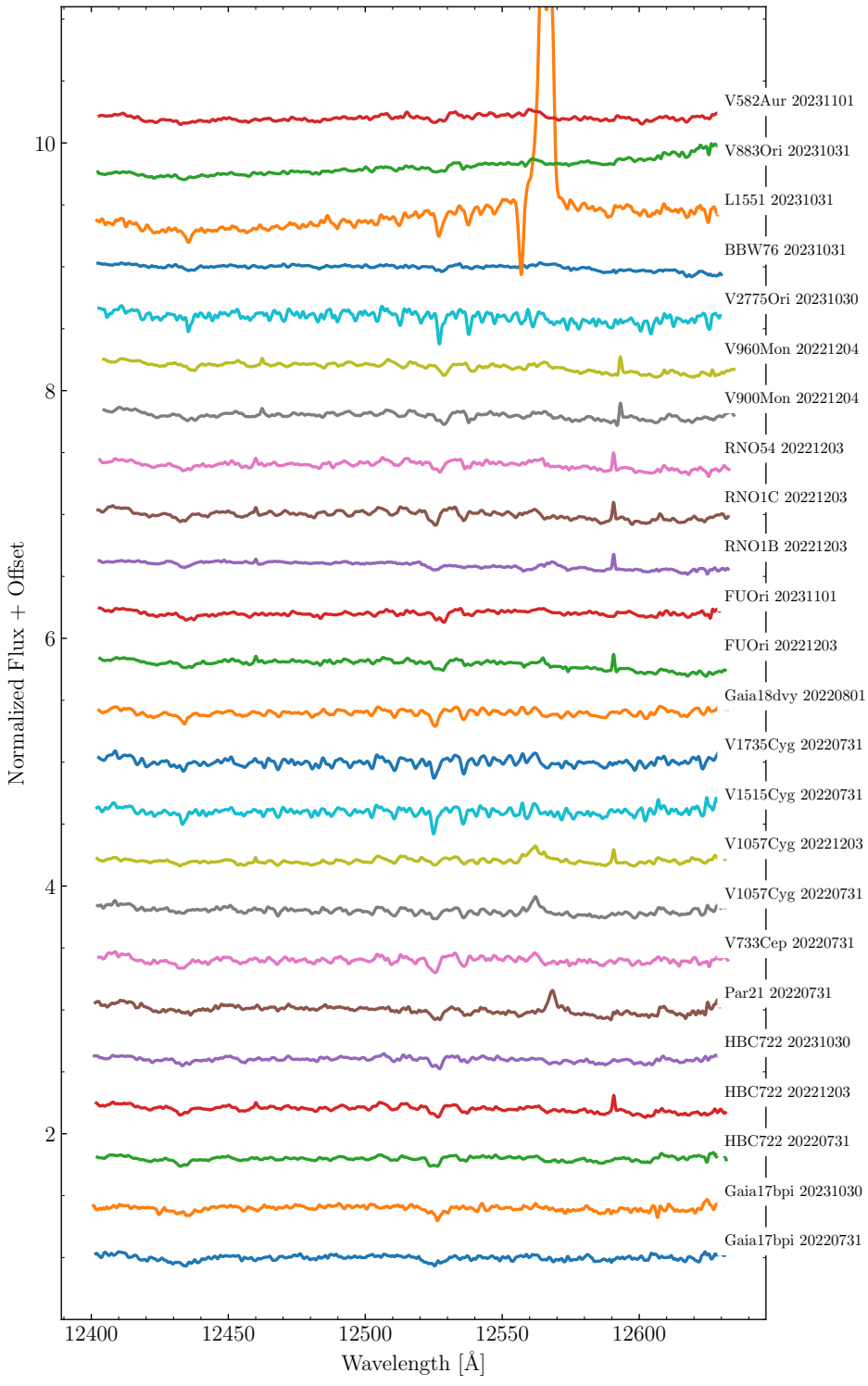

Figure 13.15: Same as Figure 13.10 for *J* Band order 61.

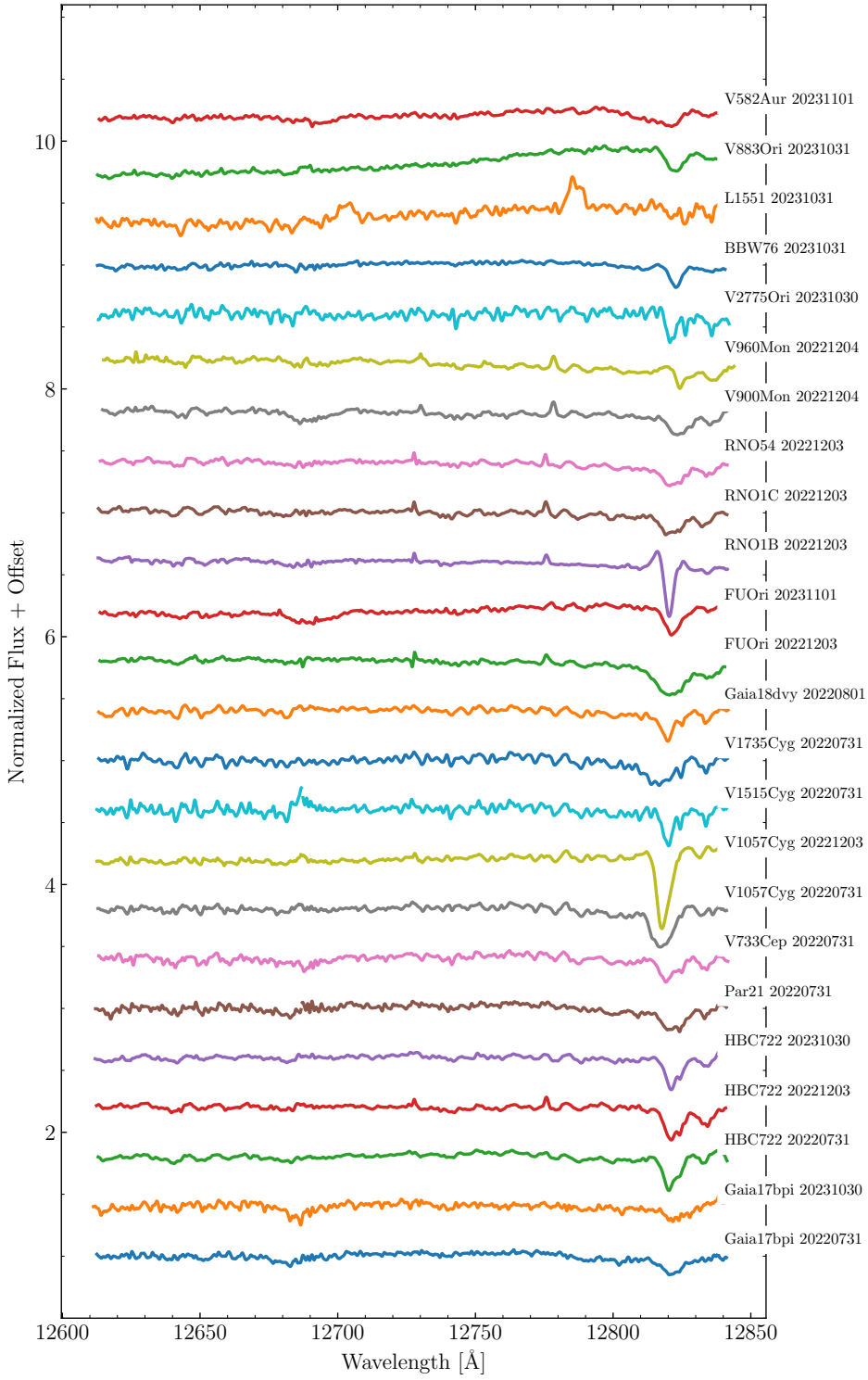

Figure 13.16: Same as Figure 13.10 for *J* Band order 60.

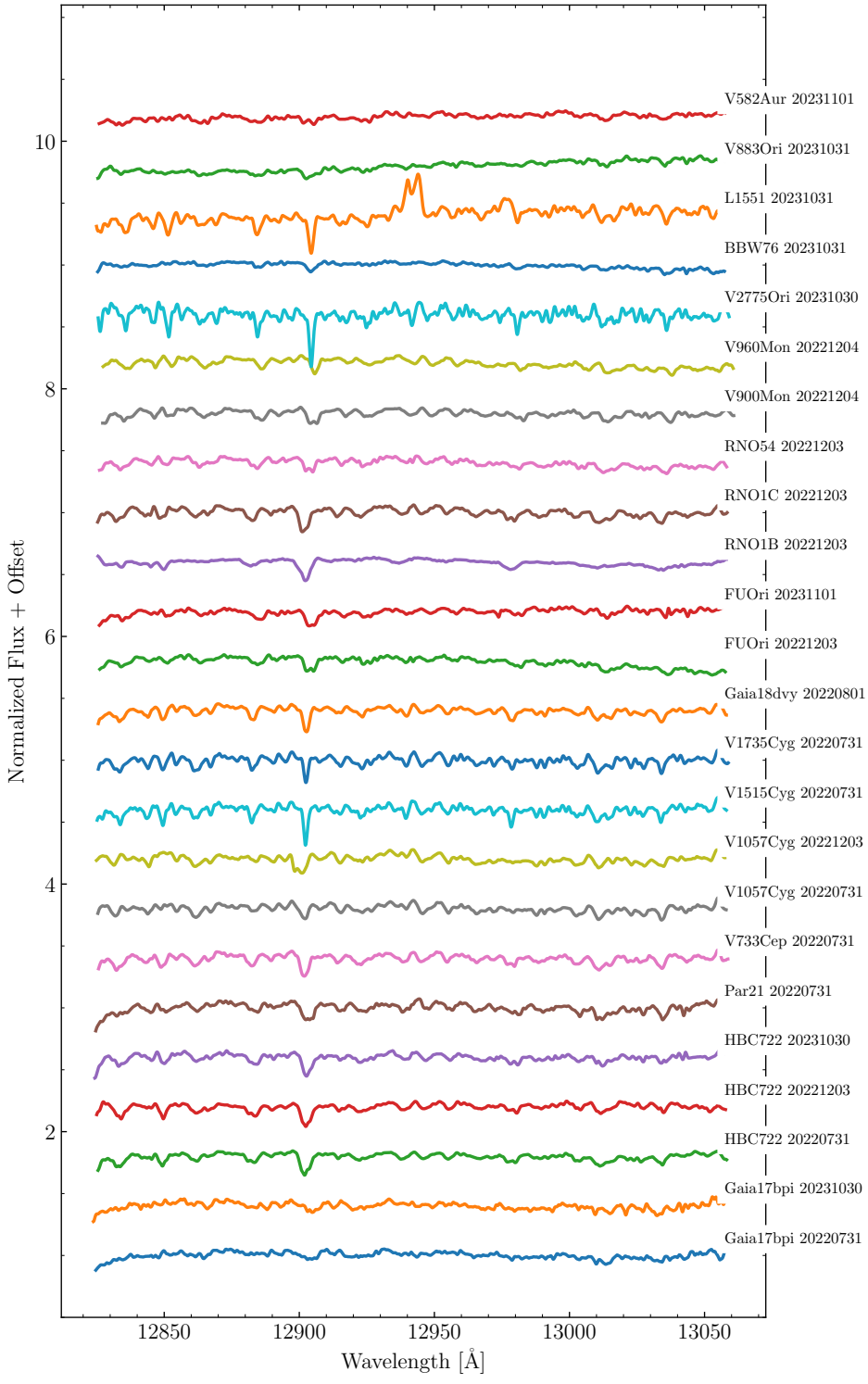

Figure 13.17: Same as Figure 13.10 for *J* Band order 59.

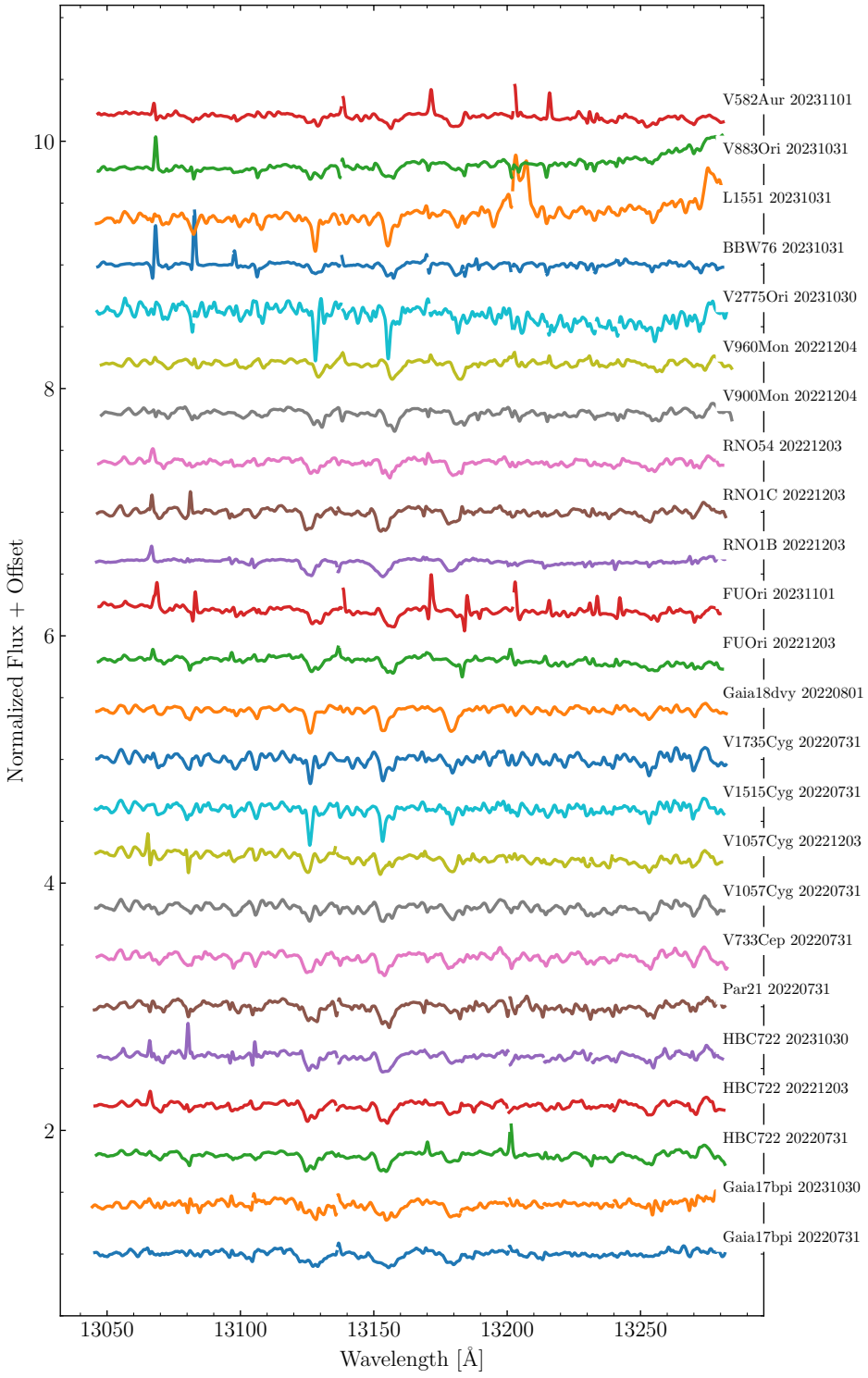

Figure 13.18: Same as Figure 13.10 for *J* Band order 58.

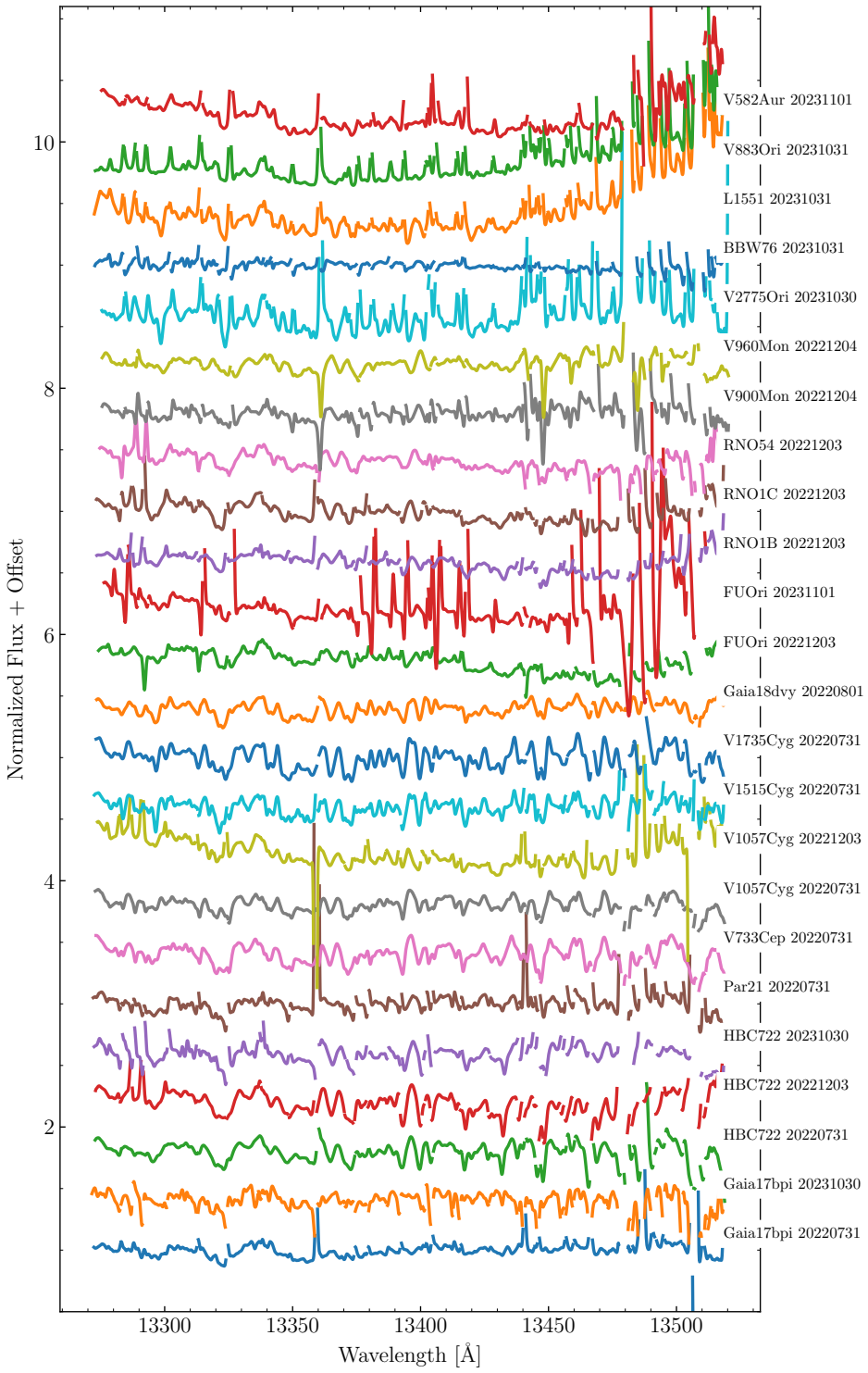

Figure 13.19: Same as Figure 13.10 for *J* Band order 57.

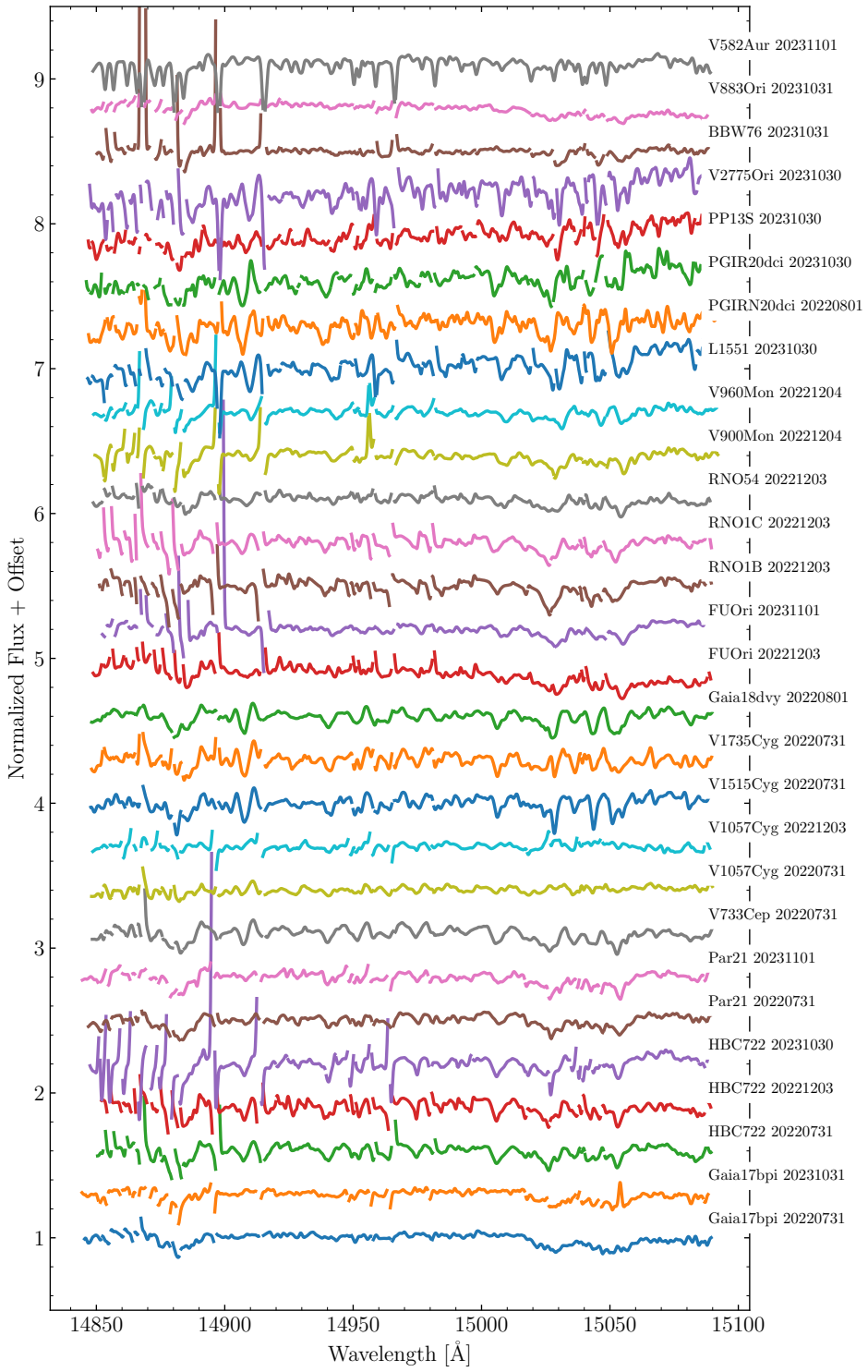

Figure 13.20: All of the FUOr spectra taken for the Keck/NIRSPEC survey with sufficient signal at 1.6 μm for high resolution spectroscopy. Shown here is *H* Band order 51.

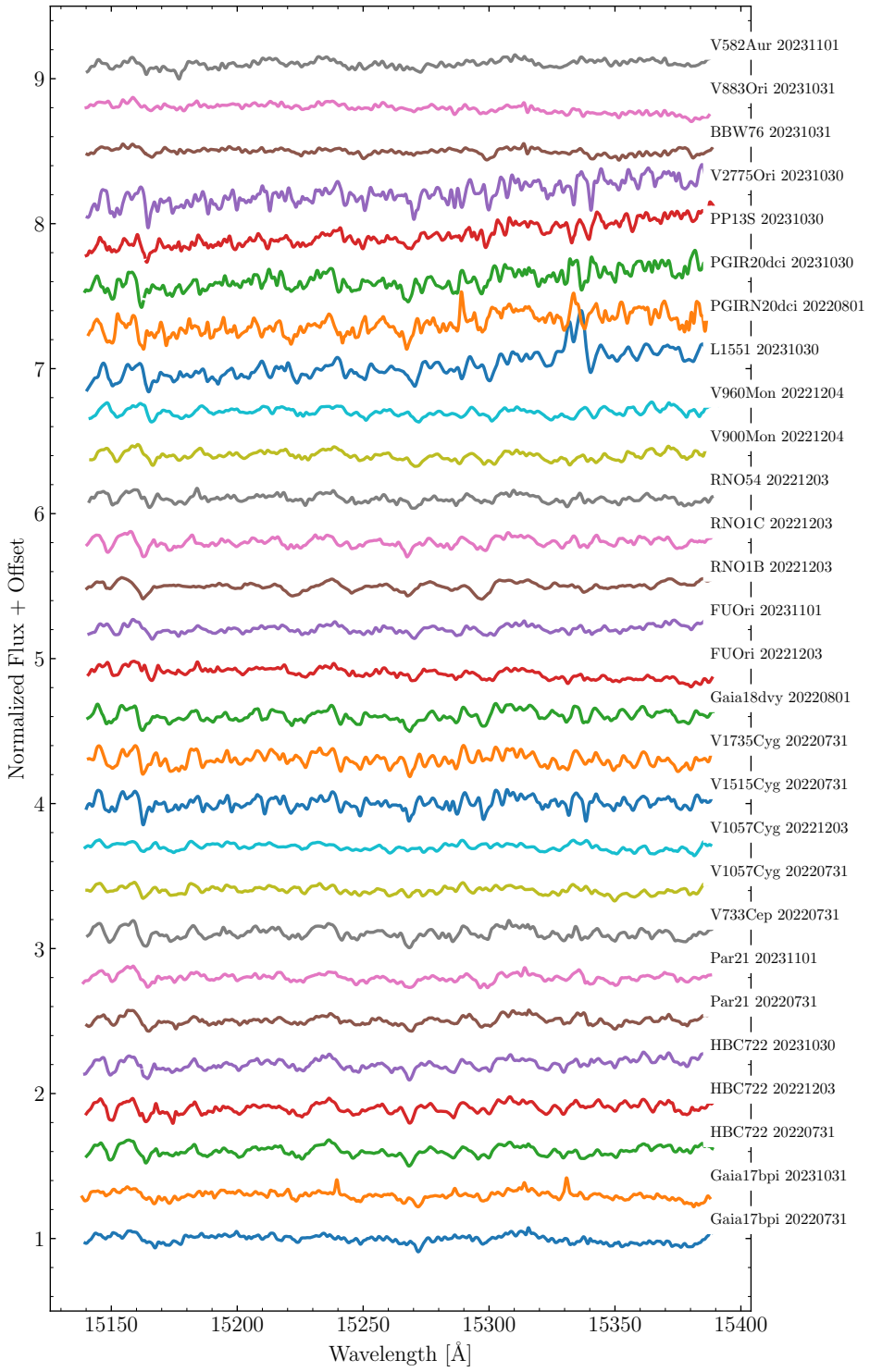

Figure 13.21: Same as Figure 13.20 for *H* Band order 50.

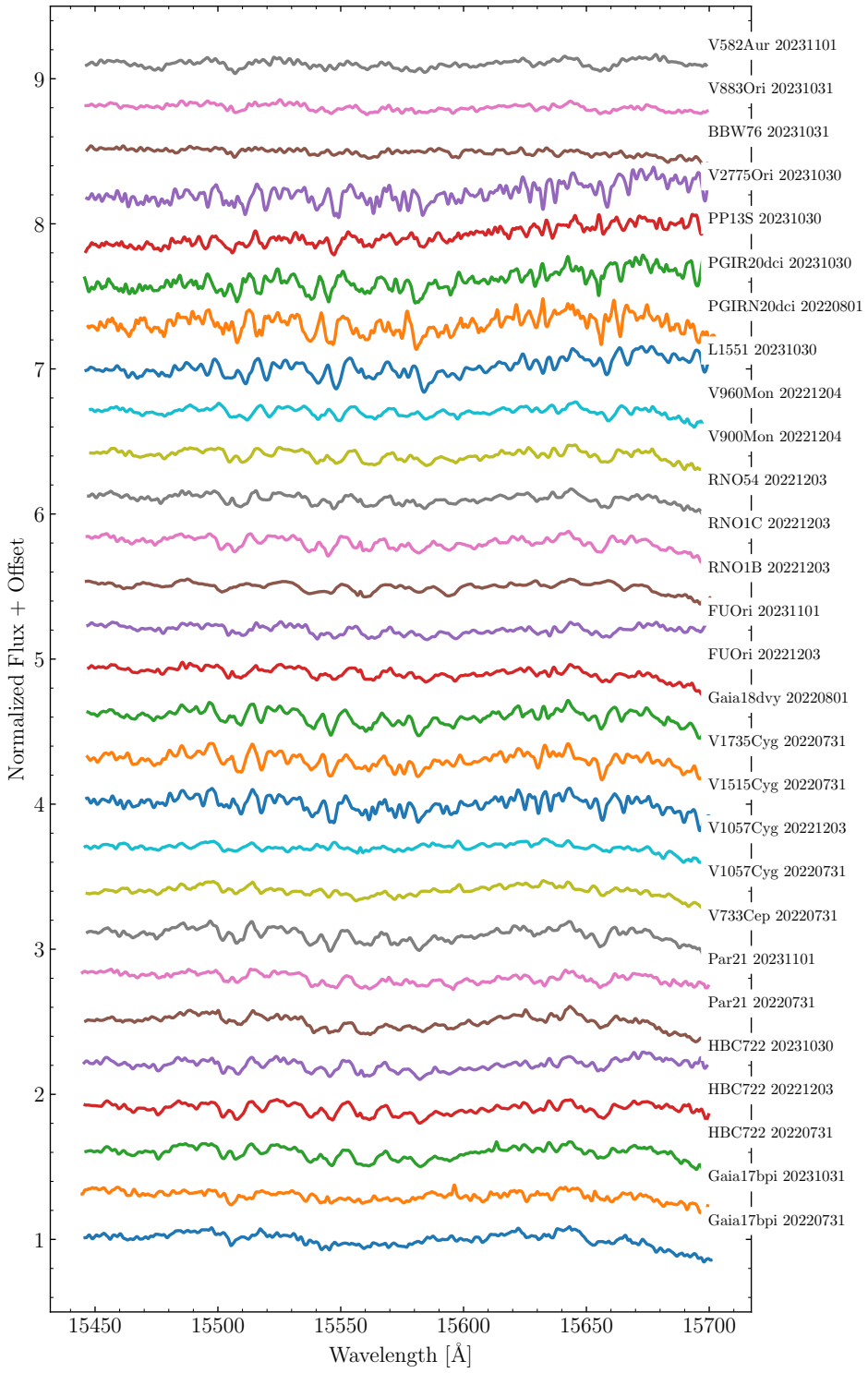

Figure 13.22: Same as Figure 13.20 for *H* Band order 49.

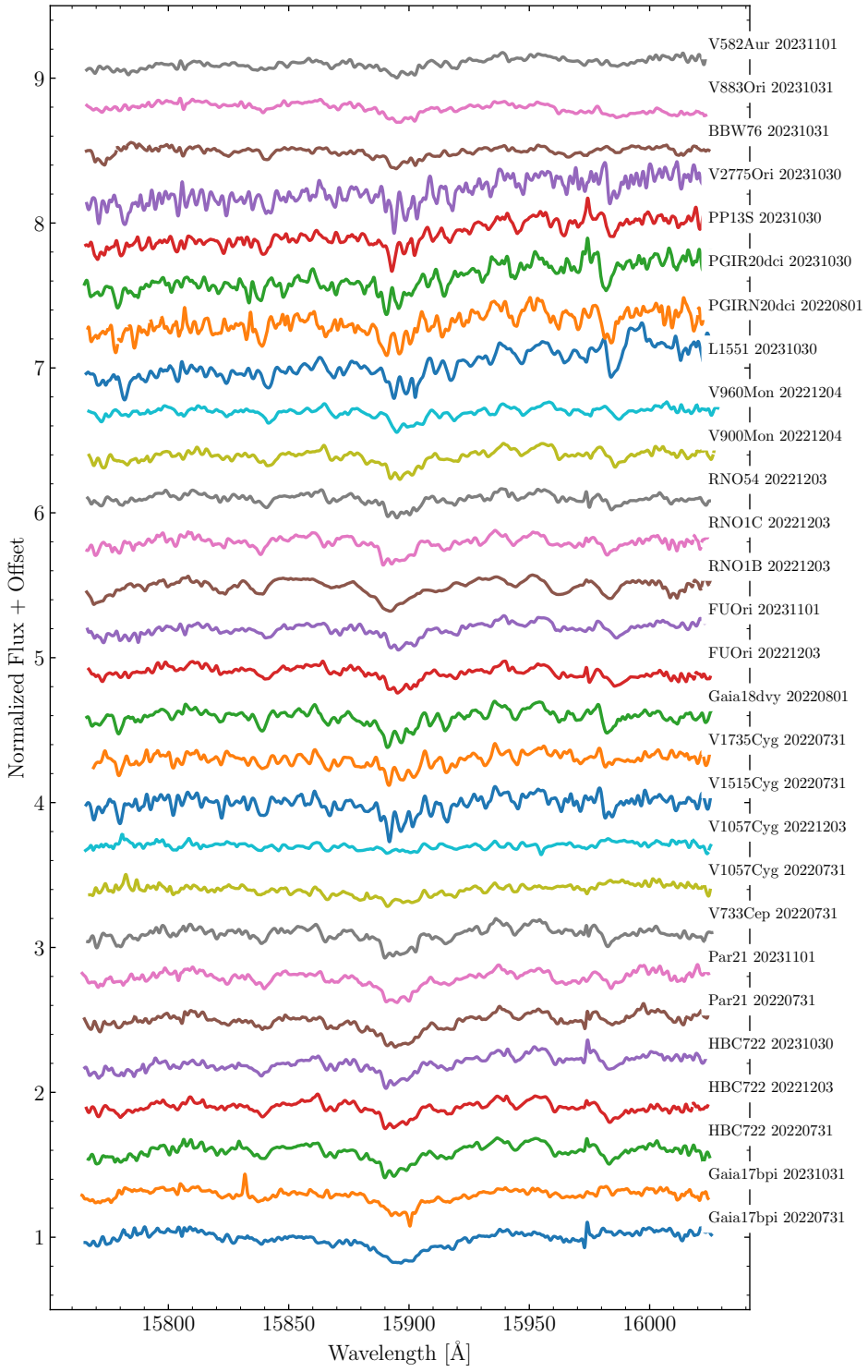

Figure 13.23: Same as Figure 13.20 for *H* Band order 48.

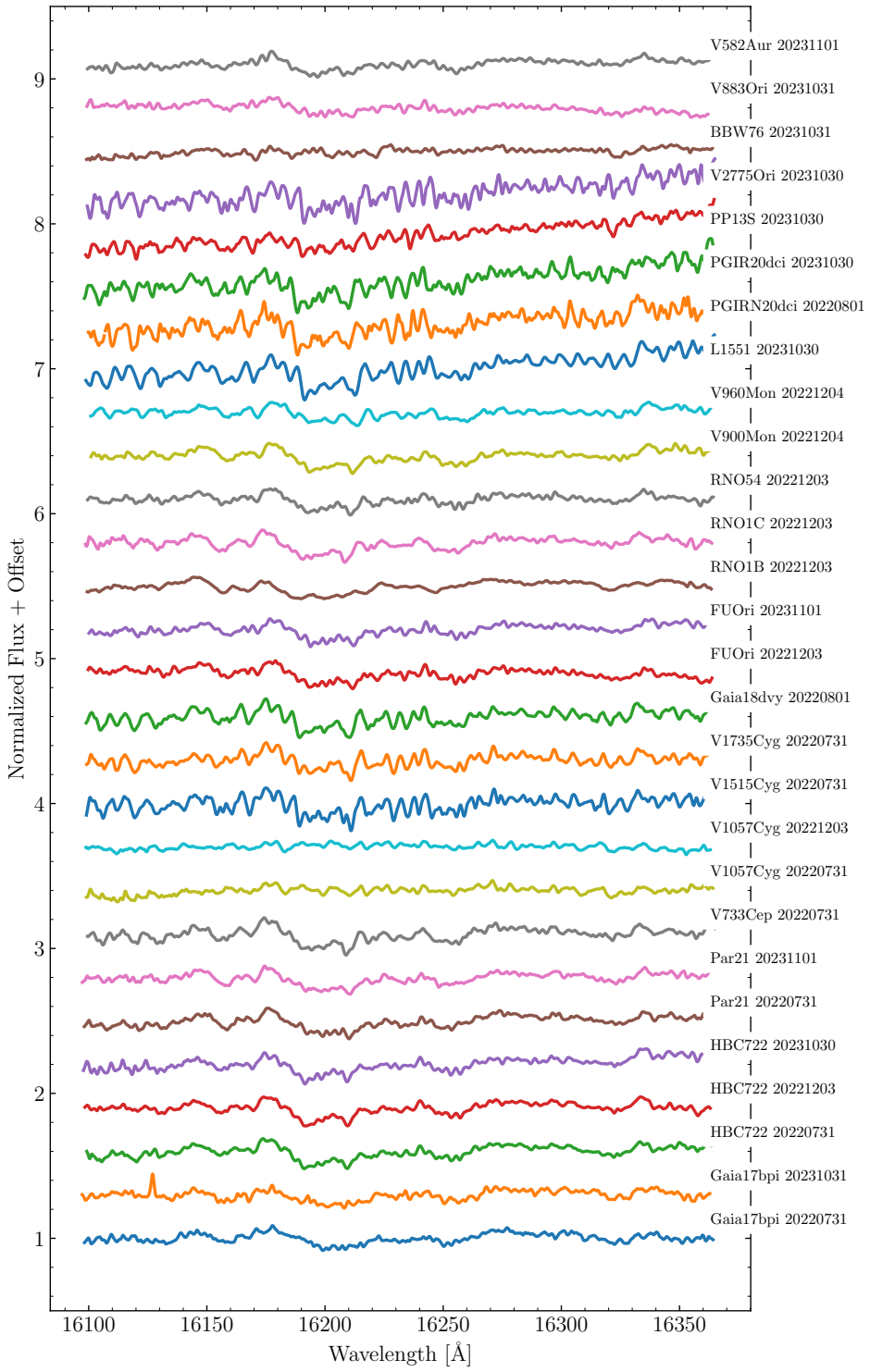

Figure 13.24: Same as Figure 13.20 for *H* Band order 47.

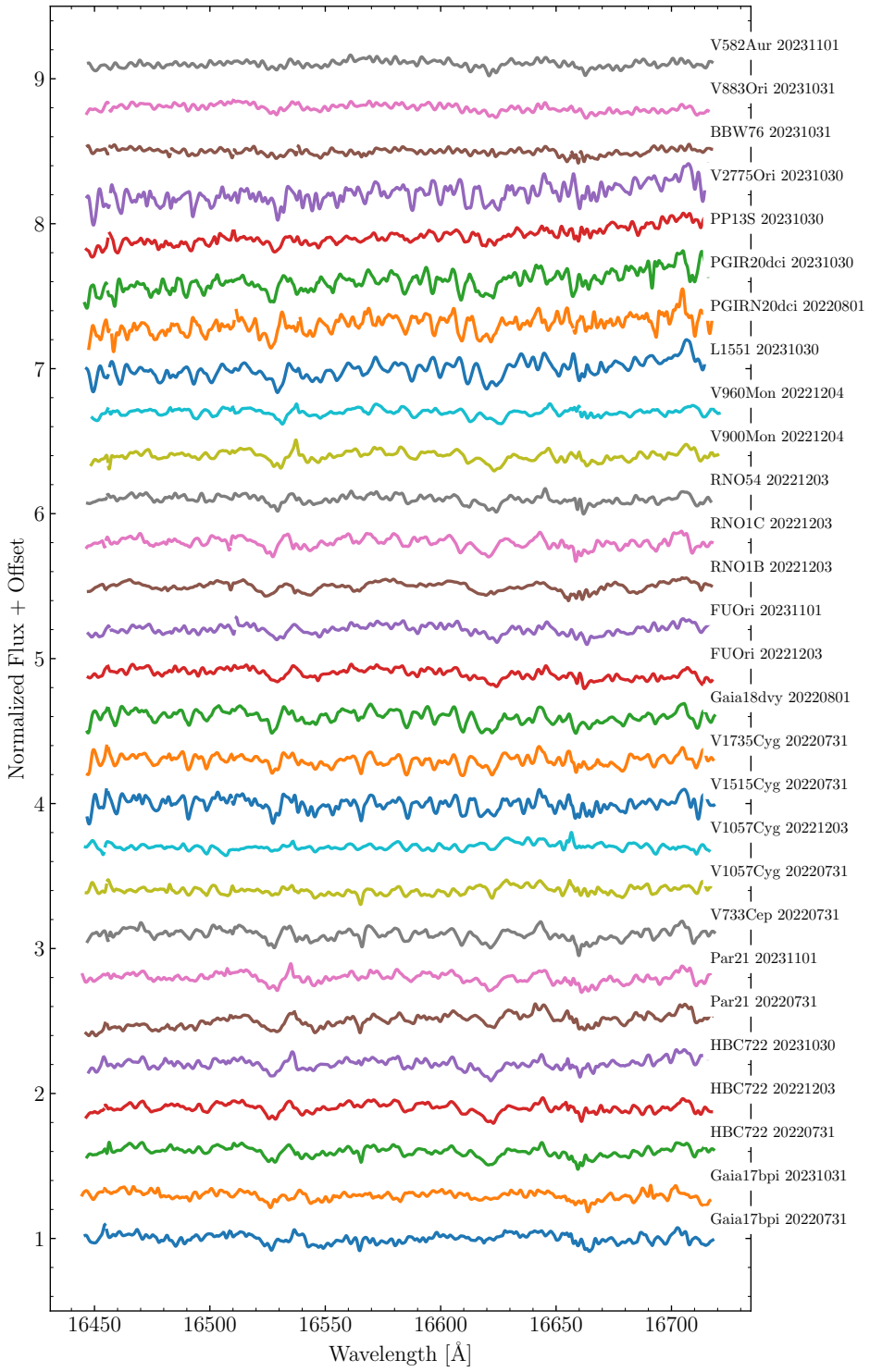

Figure 13.25: Same as Figure 13.20 for *H* Band order 46.

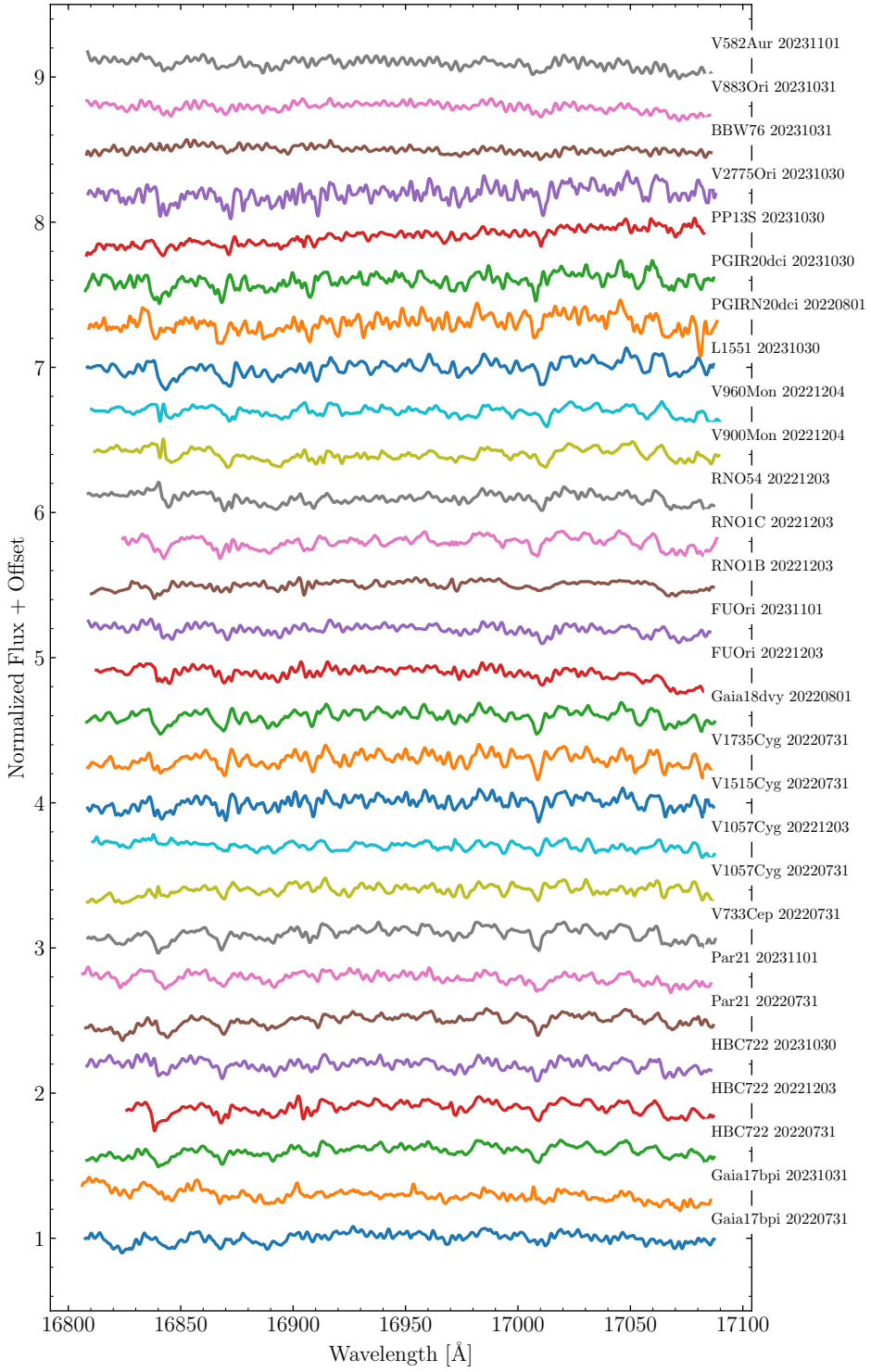

Figure 13.26: Same as Figure 13.20 for *H* Band order 45.

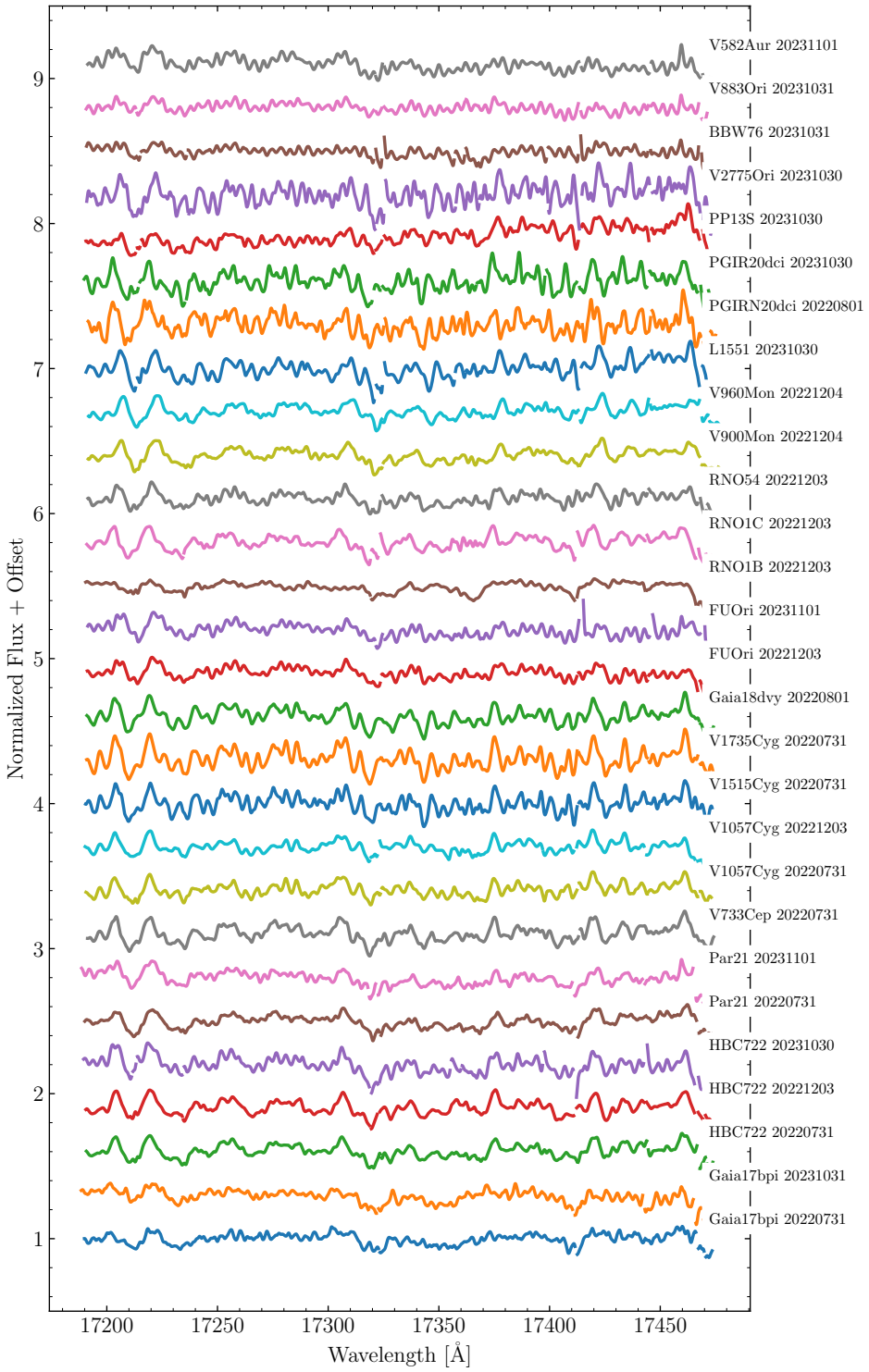

Figure 13.27: Same as Figure 13.20 for *H* Band order 44.

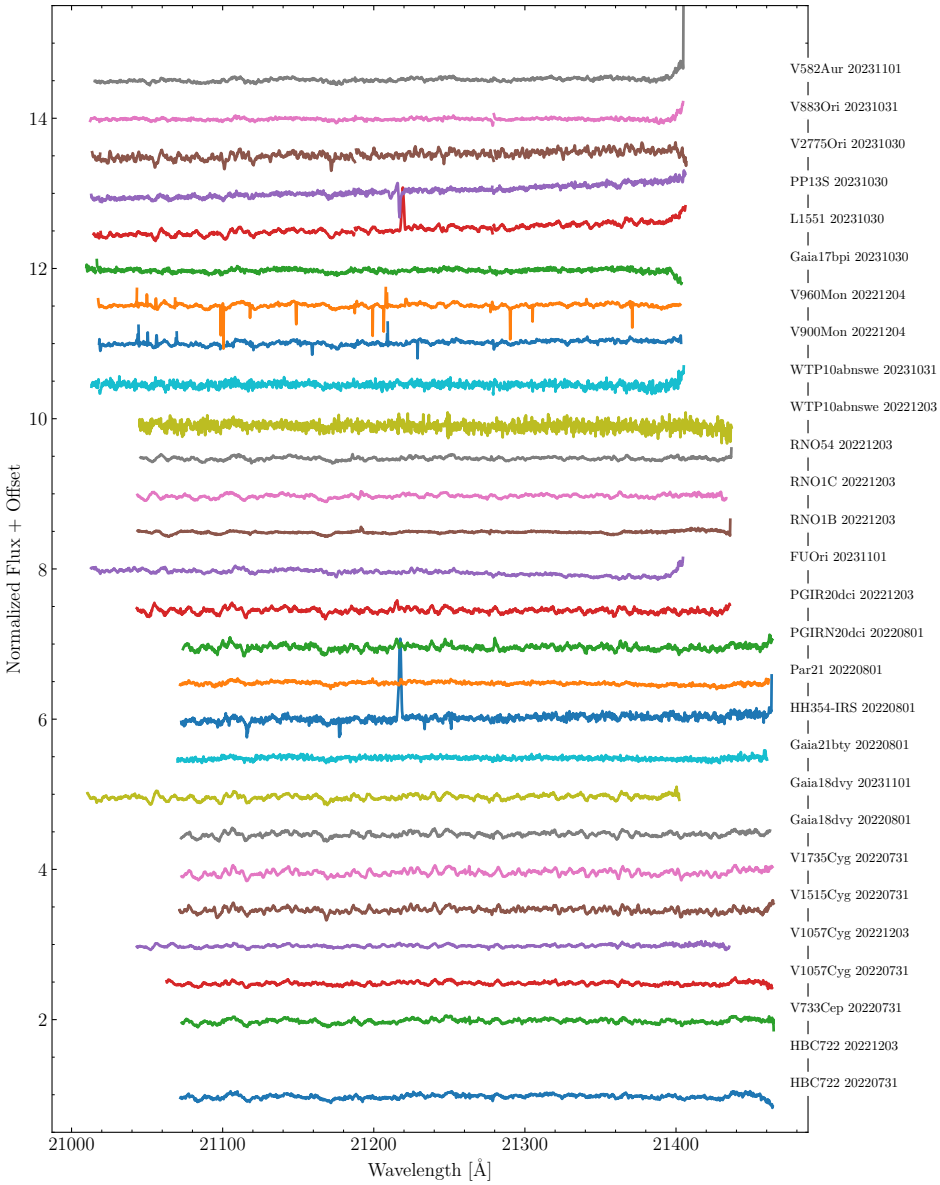

Figure 13.28: All of the FUOr spectra taken for the Keck/NIRSPEC survey. Shown here is *K* Band order 36.

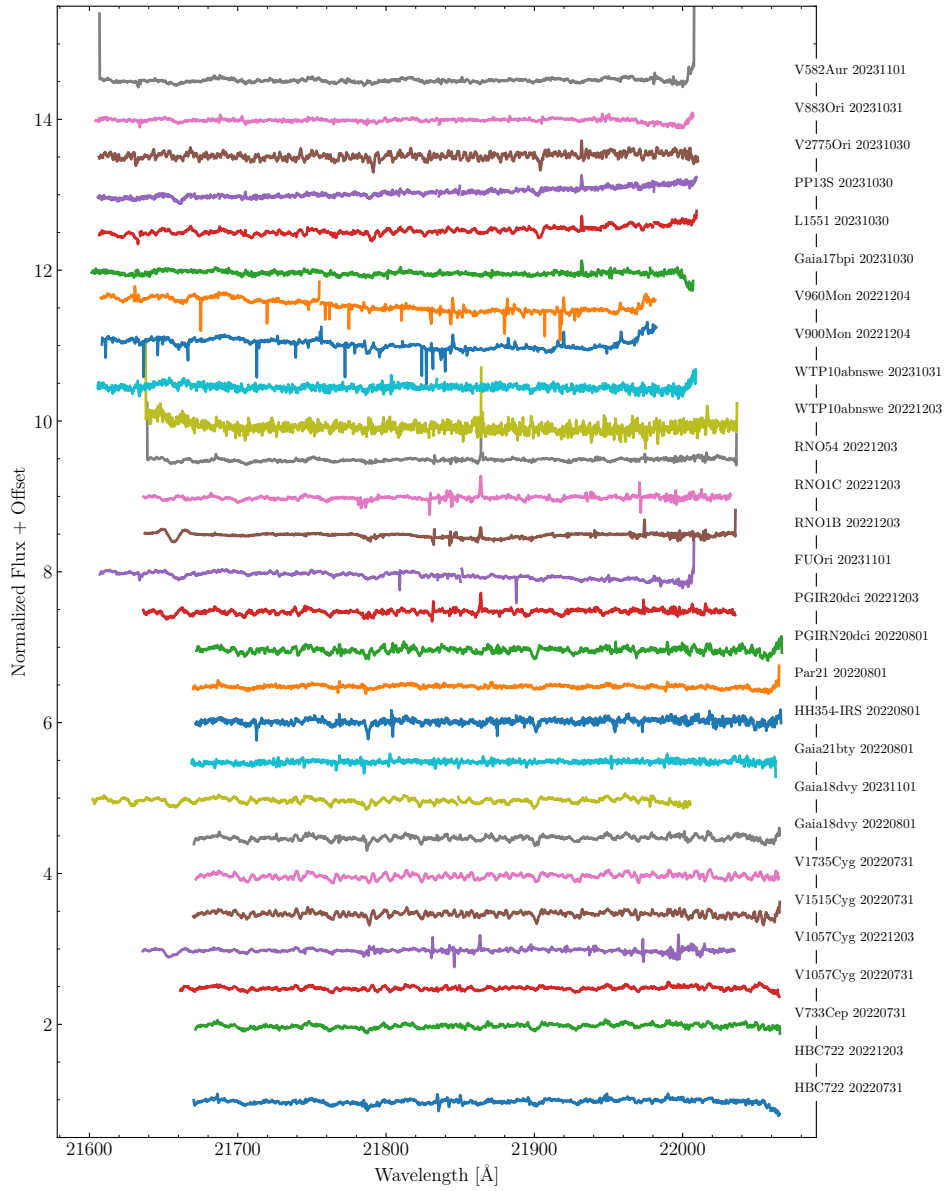

Figure 13.29: Same as Figure 13.28 for *K* Band order 35.

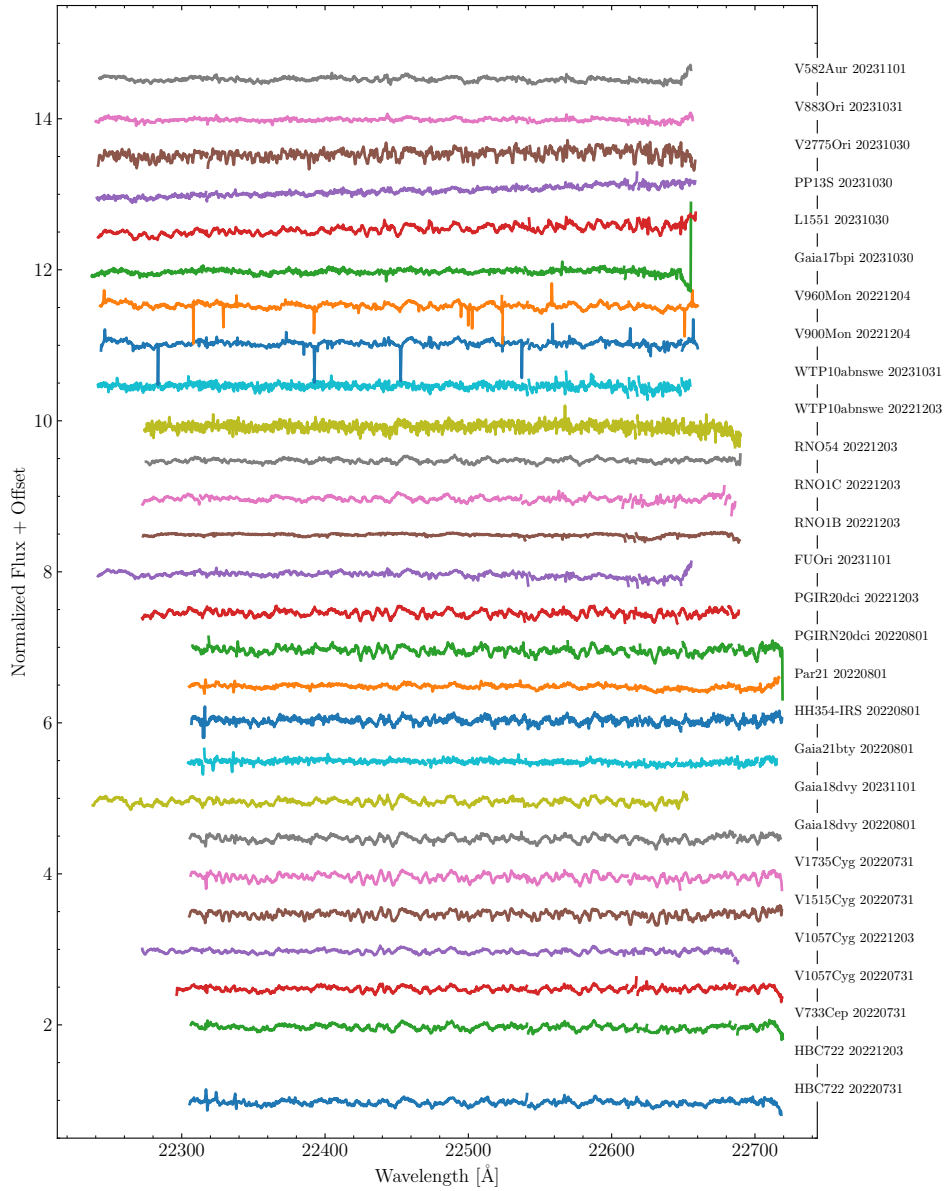

Figure 13.30: Same as Figure 13.28 for *K* Band order 34.

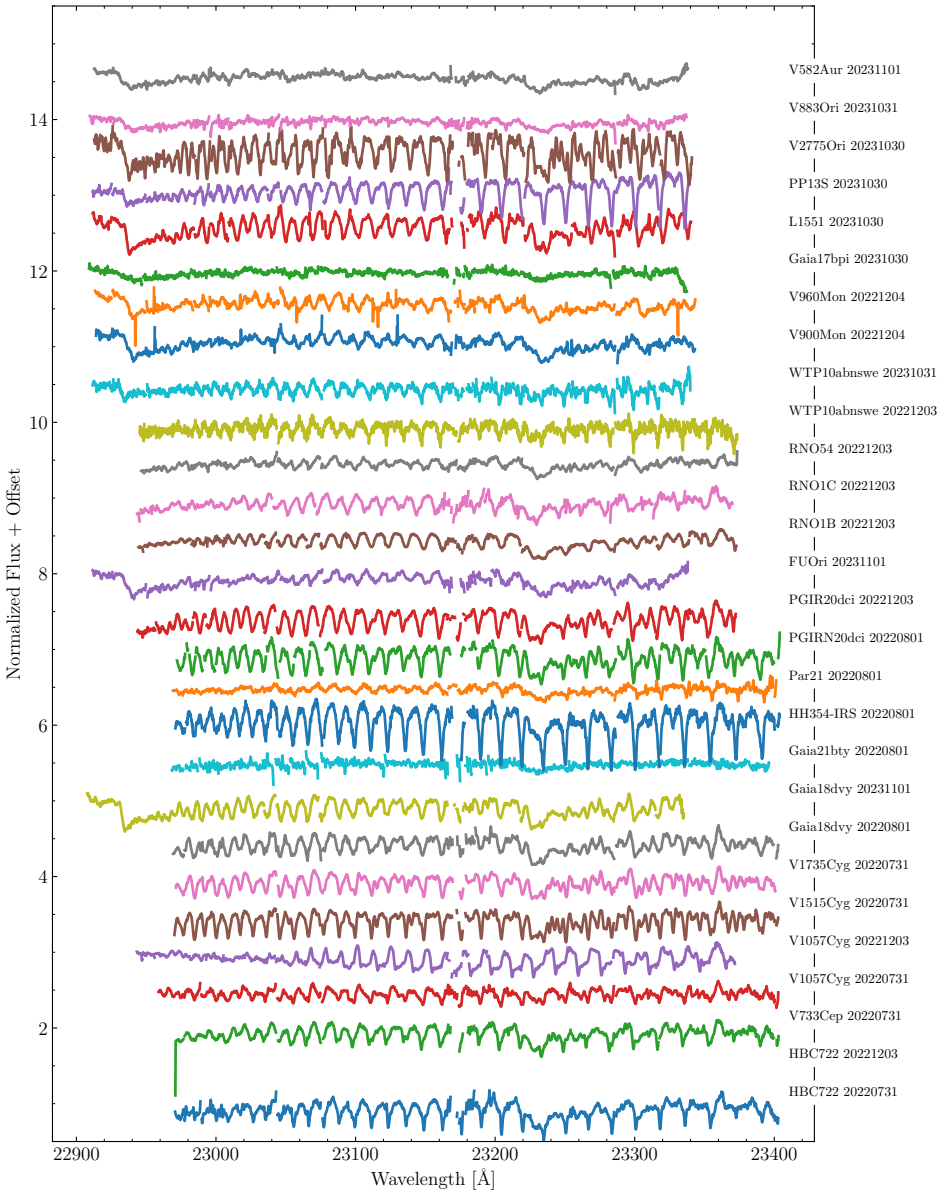

Figure 13.31: Same as Figure 13.28 for *K* Band order 33.

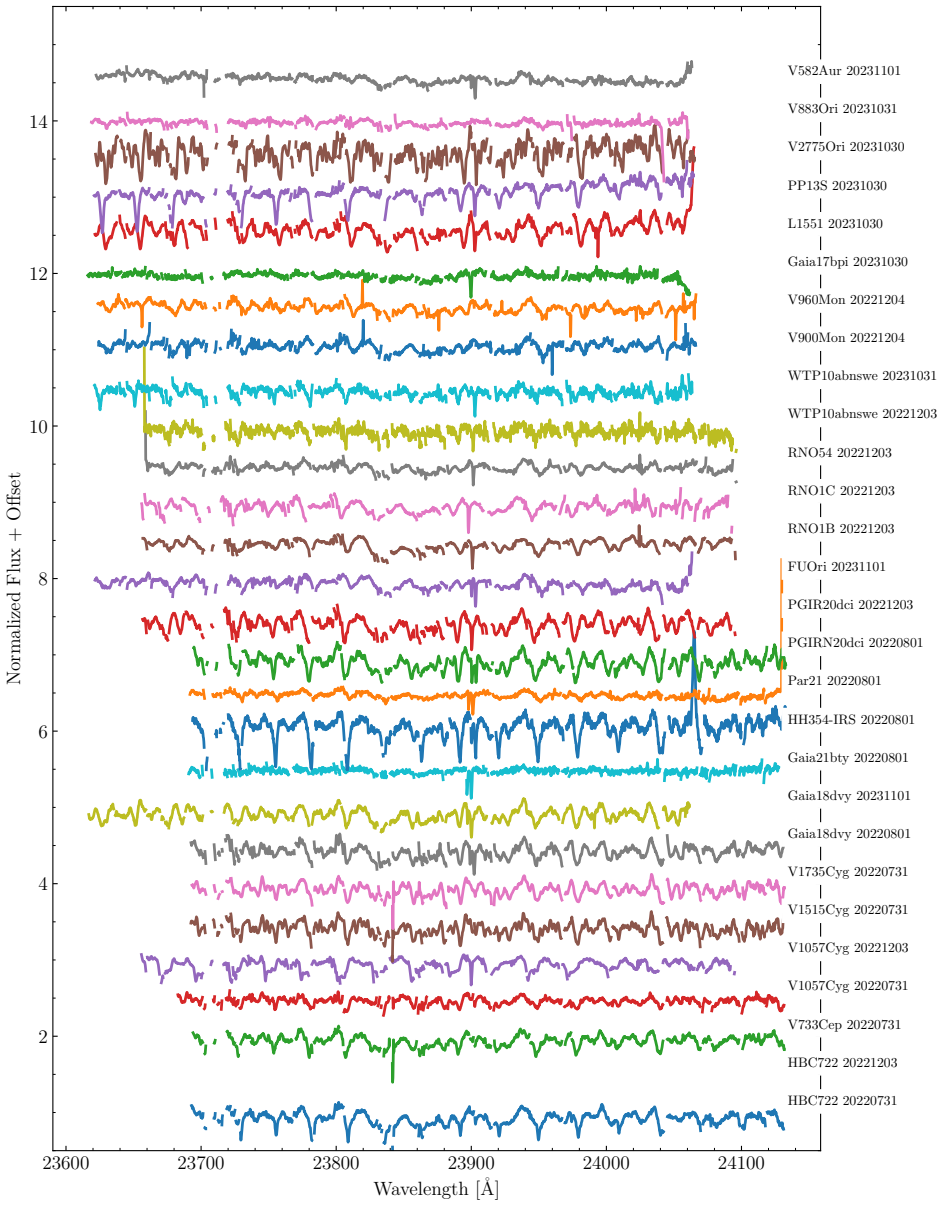

Figure 13.32: Same as Figure 13.28 for *K* Band order 32.

Table 13.1: The observing log for the Keck/NIRSPEC Survey we conducted from 2022-2023. The exposure times are the total on-source integration time and are reported in seconds.

Target	Date	Band	Exposure Time
FU Ori	2023-11-01	*K*	120
	2023-11-01	*H*	240
	2022-12-03		80
	2023-11-01	*J*	240
	2022-12-03		80
	2023-11-01	*Y*	240
V1057 Cyg	2022-12-03	*K*	120
	2022-07-31		80
	2022-12-03	*H*	160
	2022-07-31		160
	2022-12-03	*J*	120
	2022-07-31		120
	2023-10-31	*Y*	480
V1515 Cyg	2022-07-31	*K*	112
	2022-07-31	*H*	240
	2022-07-31	*J*	160
HBC 722	2022-12-03	*K*	80
	2022-07-31		40
	2022-10-30	*H*	240
	2022-12-03		400
	2022-07-31		400
	2022-10-30	*J*	240
	2022-12-03		80
	2022-07-31		200
	2022-10-30	*Y*	240
V733 Cep	2022-07-31	*K*	480
	2022-07-31	*H*	1200
	2022-07-31	*J*	1200
V1735 Cyg	2022-07-31	*K*	240
	2022-07-31	*H*	720
	2022-07-31	*J*	720
Gaia 18dvy	2023-11-01	*K*	600
	2022-08-01		1200
	2022-08-01	*H*	1800
	2022-08-01	*J*	1800
	2023-11-01	*Y*	1200
HH 354 IRS	2022-08-01	*K*	1200

Table 13.2: Table 13.1 continued.

Target	Date	Band	Exposure Time
Parsamian 21	2022-08-01	*K*	720
	2023-11-01	*H*	
	2022-07-31		1000
	2022-07-31	*J*	960
	2023-11-01	*Y*	2400
PGIR 20dci	2022-12-03	*K*	2400
	2022-08-01		1200
	2023-10-30	*H*	4800
	2022-08-01		1200
RNO 1B	2022-12-03	*K*	120
	2022-12-03	*H*	400
	2022-12-03	*J*	960
	2023-10-31	*Y*	2400
RNO 1C	2022-12-03	*K*	240
	2022-12-03	*H*	480
	2022-12-03	*J*	960
	2023-10-31	*Y*	3600
RNO 54	2022-12-03	*K*	240
	2022-12-03	*H*	480
	2022-12-03	*J*	480
	2023-10-31	*Y*	480
WTP10abnswe	2023-10-31	*K*	1200
	2022-12-03		960
V900 Mon	2022-12-04	*K*	240
	2022-12-04	*H*	800
	2022-12-04	*J*	800
	2023-10-31	*Y*	720
V960 Mon	2022-12-04	*K*	720
	2022-12-04	*H*	960
	2022-12-04	*J*	480
	2023-10-31	*Y*	480
Gaia 17bpi	2023-10-30	*K*	2400
	2023-10-31	*H*	4320
	2022-07-31		2400
	2023-10-30	*J*	2880
	2022-07-31		2400
L1551 IRS 5	2023-10-30	*K*	480
	2023-10-30	*H*	1800
	2023-10-30	*J*	2400

Table 13.3: Table 13.1 continued.

Target	Date	Band	Exposure Time
V2775 Ori	2023-10-30	*K*	240
	2023-10-30	*H*	1200
	2023-10-30	*J*	1200
	2023-10-30	*Y*	2400
V883 Ori	2023-10-31	*K*	80
	2023-10-31	*H*	360
	2023-10-31	*J*	720
	2023-10-31	*Y*	1200
V582 Aur	2023-11-01	*K*	960
	2023-11-01	*H*	1200
	2023-11-01	*J*	1200
	2023-11-01	*Y*	1200
PP 13S	2023-10-30	*H*	1800
BBW 76	2023-10-31	*H*	720
	2023-10-31	*J*	1200
	2023-10-31	*Y*	1200

Chapter 14

SUMMARY AND FUTURE DIRECTIONS

The goal of this thesis has been to establish a framework for constraining the physical parameters of FUOrs to enable comparative analysis of the objects across the class. Given the relatively small number of objects available for study, and their highly variable natures, comparing FUOrs across the class requires accurate measurements of their physical parameters. In the final 2 years of my thesis, I have used this framework to constrain the M_*, $\dot{M}$, and $R_{\rm inner}$ of 9 FUOrs. Using the high resolution spectra presented in this thesis, it is possible to expand that number to between 15 and 21 total objects over the next 1-2 years. This will be crucial to answering some of the questions raised in the Introduction, in particular concerning the mass distribution and mass accretion rate distributions of FUOrs.

I would like to conclude this thesis by discussing how this framework will be used in the near future in conjunction with new and exciting observing capabilities to expand our understanding of FUOrs and what triggers their outbursts. I will also explore how recent developments in interferometry at both millimeter and visible and NIR wavelengths establish a course for better understanding FUOrs relative to other YSOs, both eruptive and non.

14.1 New Visible and NIR Surveying Capabilities

The many all-sky time-domain survey experiments that have operated in the past 15 years have almost doubled the number of FUOrs discovered (Contreras-Pena et al. 2025, submitted). Many of the space-based surveys, like Gaia and WISE/NEOWISE, have concluded in the past year. Ground-based surveys like VVV/VVVX (Southern Hemisphere, Minniti et al., 2010; Saito et al., 2024), ZTF (Bellm et al., 2019, Northern Hemisphere,), and ASAS-SN (all sky, Shappee et al., 2014b; Kochanek et al., 2017) continue to be renewed and are still operational today, although their coverage of the sky is limited by time of day, seasons, and weather[1].

Just this year, the first images and data products have been released by three exciting

[1]Other impactful time-domain experiments that have contributed to the known population of FUOrs are the Palomar Transient Factory (PTF, Law et al., 2009; Rau et al., 2009), which contributed to the early detection of HBC 722 (Miller, Hillenbrand, et al., 2011) and the Catalina Real-Time Transient Survey (CRTS), which detected the outburst of V899 Mon (Wils et al., 2009).

new missions/surveys: the Rubin Observatory's Legacy Survey of Space and Time (LSST, Ivezić et al., 2019), the Roman Space Telescope's Core Community Surveys (Akeson et al., 2019), and the SPHEREx Mission's all sky survey (Doré et al., 2014). Over the next 5-10 years, each of these surveys will provide different means of searching for new outbursting YSOs in the Galaxy.

A Broadband Spectroscopic Survey in SPHEREx

The WISE/NEOWISE and VVV/VVVX surveys showed that there are several eruptive YSOs that show high amplitude NIR outbursts that were overlooked in, or altogether undetected by, optical surveys (e.g., Tran et al., 2024; Guo et al., 2024). This is in part due to the limited coverage of ground-based surveys, but also it is a consequence of the fact that many of these youngest YSOs are deeply embedded and thus faint in the optical. Many of the known FUOrs surveyed in Connelley and Reipurth (2018) are not detected in ZTF even in their outbursting states.

Another unexpected revelation in the NEOWISE survey was that the 6-month cadence was sufficient to resolve the outbursts of many FUOrs (see the lightcurves in Contreras-Pena et al. 2025, submitted) and that some objects, like Gaia 17bpi, have a NIR precursor to the visible range eruption (Hillenbrand, Peña, et al., 2018). However, assembling SEDs for objects during the rising part of the outburst as proven challenging, as it requires coincident observation by multiple (mostly ground-based) photometric surveys. Furthermore, prior to the Palomar/Gattini experiment (in J band, Moore, Kasliwal, et al., 2016), there was no dedicated Northern Hemisphere NIR time-domain survey.

With the SPHEREx mission, there will now be an unprecedented $0.7-5\,\mu$m spectrum of objects as faint as $\sim$ 19 mag every 6 months. This will enable monitoring of existing FUOrs and reveal the broadband evolution of newly outbursting FUOrs as they transition from magnetospheric accretion to boundary layer accretion. The sensitivity to hot dust emission (which for FUOrs becomes relevant at around 3 μm, Carvalho, Hillenbrand, Hambsch, et al., 2023; Carvalho, Hillenbrand, Seebeck, and Covey, 2024) from the inner disk will also reveal how the passive component of the disk responds to the changing heating source, from primarily stellar-dominated to primarily active accretion-dominated. There is also the potential to observe how ices in the circumstellar envelope respond to the excess heat from the outburst by studying the evolution of the 3μm H_2O ice feature.

The broadband high-sensitivity monitoring will also help to constrain how common

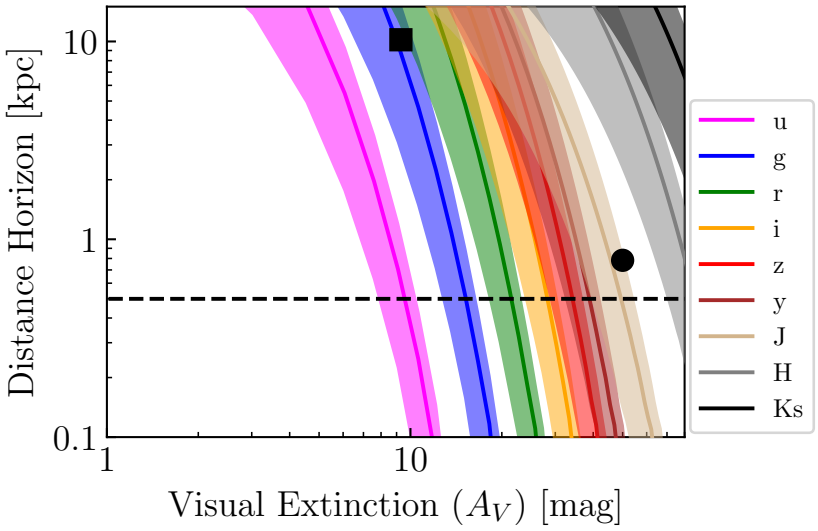

Figure 14.1: The distance horizon to FUOrs for LSST and SPHEREx, calculated from the bolometric corrections for a range of A_V to the source. The shaded regions represent a range of assumed FUOr luminosities from 10 $L_\odot$ to 300 $L_\odot$. The square marks the furthest known FUOr, L222_1 and the circle marks the most embedded known FUOr. The dashed line marks the horizon for VLT/GRAVITY to resolve the < 2 AU inner region FUOrs to measure the disk inclination.

NIR precursors to FUOr outbursts are with precise contemporaneous NIR and visible-range data. Trigger mechanisms that rely on instabilities occurring around 1-10 au in the disk (see the Introduction) often predict a NIR precursor to the outburst, but the precise NIR to optical colors are difficult to constrain without contemporaneous reliable visible range photometry to compare with the NEOWISE lightcurves.

Deeper Visible Range Surveying

The LSST being conducted by the Rubin Observatory will greatly extend the horizon of detectability of FUOrs to 10s of kpc, depending on the band and A_V. The distance horizons to LSST and SPHEREx, calculated using bolometric corrections and assuming a FUOr luminosity range of $10 - 300$ $L_\odot$, are shown in Figure 14.1. The assumed sensitivities for each observatory are based on the single-epoch 5σ detection thresholds for LSST (Bianco et al., 2022) and the Maximum Expected Value 5σ detection thresholds for SPHEREx [2].

Compared with ZTF, LSST will have a distance horizon that is 10× further for

[2] https://spherex.caltech.edu/page/survey

$4 < A_V < 20$. For detecting FUOrs in the Southern Hemisphere, LSST will be a formidable complement to SPHEREx. The main challenge for future detailed study of FUOrs detected with the high sensitivity surveys is follow-up. For objects near the distance horizons of these surveys (i.e., $K \sim 19$), there are few spectrographs sensitive enough to perform even low resolution follow-up. Obtaining a spectrum of a source capable of constraining the rotational broadening in the disk requires a resolution of $R > 10,000$ and $SNR > 20$. The only spectrograph with the current combination of sensitivity and resolution to attain this, VLT/X-shooter, would still require almost 4 hours on source[3].

However, with the deeper coverage of both LSST and SPHEREx, many of the detected FUOrs will be accessible to X-shooter and some to Keck/NIRSPEC. Rapid confirmation of these outbursts as bonafide FUOrs can be achieved by JWST/NIRSPEC, Keck/NIRES, Keck/MOSFIRE, and lower resolution modes of VLT/X-shooter. Coordinating study of the FUOrs in the early days of their outbursts will enrich our understanding of the outburst onset and how it propagates through the disk. It will be crucial to understanding if the outwardly expanding instability seen in HBC 722 (see Chapter 5) or the widening $R_{\rm inner}$ in V960 Mon (see Chapter 3) are unique to those sources or characteristic of objects with their lightcurves.

14.2 Millimeter Observations of FUOrs Can Probe Disk Chemistry

There is a growing sample of FUOrs with high sensitivity millimeter wavelength spectra showing bright molecular emission from FUOrs (e.g., Lee, Lee, et al., 2019; Szabó, Gong, et al., 2023; Calahan et al., 2024; Szabó, Belloche, et al., 2025). The bright emission is suggested to be due to the rapid sublimation of ices, in the disk midplane due to the intense heat of the outburst. The newly sublimated molecules are free to mix into the disk atmosphere and can thus be detected.

Connecting the emission of particular molecules to the outburst has proven challenging. The molecular inventory reported so far for FUOrs varies greatly across the sample. The source V1057 Cyg, which has been noted as an exception among FUOrs in previous Chapters (see Chapters 11 and 12), has the brightest and most molecule-rich millimeter spectrum of the class (Calahan et al., 2024; Szabó, Belloche, et al., 2025). Meanwhile, sources that are much brighter, like V883 Ori, have much fainter molecular emission.

[3]see the ESO P116 X-shooter user manual at `https://www.eso.org/sci/facilities/paranal/instruments/xshooter/doc.html`

To clarify the connection between the properties of a FUOr and the observed molecular line emission requires detailed chemical network modeling of the response of a disk to an outburst. In principle, when the outburst heats the disk and liberates molecules from ices to interact in the atmosphere, thermochemical processing may alter abundance ratios between species or between isotopologues of those species. Recent modeling of outbursts in disks shows that the ratios of $C^{18}O$ and ^{13}CO to ^{12}CO can be diagnostic of past outburst activity (Zwicky et al., 2024). However, the existing models do not incorporate the effect of both the intense viscous heating from the midplane in addition to a fully detailed prescription for the spectrum of the inner disk.

As is demonstrated in Chapter 6, the irradiation heating from the inner disk dominates the heating budget exterior to $\sim$ 5 AU, while heating in the inner disk is dominated by accretion in the midplane. At the same time, the work presented in Chapters 10 and 11 shows that during outbursts, the NUV and FUV irradiation of the disk are greatly elevated. This, along with the increased X-ray luminosity of FUOrs relative to quiescent YSOs (Kuhn and Hillenbrand, 2019), may ionize large molecules liberated from ices and drive new photochemistry in the disk atmosphere.

New modeling efforts that incorporate the full high energy spectrum of a FUOr in outburst, as well as the multiple enhanced sources of heating in the disk, can be combined with the detailed modeling in this thesis to predict the molecular emission line spectra of FUOrs. This modeling can expand upon the efforts of Zwicky et al. (2024) to predict other molecular tracers of outbursts. Existing observations of FUOrs can begin testing the predictions of such a chemical network model.

Unfortunately, many of the objects in this thesis, for which we best know the M_*, $L_{\rm acc}$, $T_{\rm max}$, $L_{\rm UV}$, and the evolution of $L_{\rm acc}$, lack deep millimeter observations like those performed by Calahan et al. (2024). The relatively large distances ($>$ 400 pc) to these FUOrs requires both high sensitivity and high angular resolution observations to detect the molecular emission (or tightly constrain it, if absent) and disentangle disk from envelope emission. In the case of V1057 Cyg, the emission cannot be uniquely attributed to the disk, since the $> 2''$ angular resolution of the observations in Calahan et al. (2024) and Szabó, Belloche, et al. (2025) span almost 1000 AU.

Today, only ALMA is capable of providing the combined angular resolution and sensitivity to perform the survey for molecular emission from FUOrs. The data in this thesis are both necessary and sufficient to contextualize the irradiation from the inner disk and source properties for several FUOrs accessible to ALMA. The necessary

exposure times to ensure tight constraints on the gaseous molecular inventory of these objects will require an ambitious Large Program. Nevertheless, the endeavor is worthwhile to illuminate the ways in which outbursts may alter or reset the chemical inventories of disks. The process of cloud to disk to planet chemical inheritance cannot be understood without this.

14.3 JWST as a Rapid Follow-Up Instrument of Newly Discovered Outbursts

The wideband, high sensitivity of JWST, as well as its ability to probe ice emission/absorption in YSOs may prove crucial to illuminating the ability of FUOr outbursts to sublimate ices rapidly. The cases of V960 Mon and HBC 722 both show that FUOrs undergo significant spectroscopic evolution in the years immediately following their outbursts. There is also evidence, as summarized in (Herbig, 1977), that V1057 Cyg similarly underwent dramatic evolution in the first 10 years after the peak of its outburst.

As is discussed above, there is the expectation that in the early stages of the outburst, the intense heating of the disk drives sublimation lines in the disk significantly outward. There is some evidence of this in the millimeter HDO emission from V883 Ori, as well (Tobin et al., 2023), that the water sublimation line in that source is at $\sim 40 - 80$ AU.

JWST is uniquely capable of identifying, immediately following the onset of an outburst, the sublimation of ices. The results of the JDISCS survey (Pontoppidan et al., 2024) show that spectra from the MIRI instrument can reveal both cold, warm, and hot molecular emission from H_2O and several hydrocarbon species. With the sensitivity of its instruments, medium resolution spectroscopy from $0.7 - 28$ μm can be easily obtained for any FUOr detected by SPHEREx or LSST.

14.4 Upgraded Interferometry for FUOr Multiplicity and Disk Inclinations

Over the coming decade, two major interferometric capabilities will expand our ability to search for multiplicity in FUOrs and to better constrain the disk inclinations. The first is interferometry in the near-infrared with VLT. The second is the Next Generation VLA (ngVLA, Carilli et al., 2015). I discuss the exciting opportunities for studying FUOrs with these capabilities below.

VLTI and GRAVITY+

In the next year, the GRAVITY+ upgrade to the GRAVITY instrument on the VLT will enable infrared interferometric observations of sources as faint as $K \sim 19$.

This will make almost any FUOr detected with SPHEREx or LSST accessible to the instrument, potentially enabling direct radial temperature profile and inclination measurements of the inner disks of these sources.

The primary limitation to studying FUOrs with GRAVITY+ is the small size of the K band continuum emitting region of the sources. The largest $R_{\rm outer}$ values we find in our spectroscopic fits to FUOrs have been typically < 1 au. A similar size for the region is reported in existing infrared interferometry of FUOrs (Lykou, Ábrahám, Chen, et al., 2022; Lykou, Ábrahám, Cruz-Sáenz de Miera, et al., 2024).

In the search for close-in binary companions to FUOrs, the distance horizon for GRAVITY+ can be much greater. As is discussed in the Introduction, an interaction with a companion that could trigger a recently discovered outburst would require a binary separation < 50 AU. This is easily resolvable for GRAVITY+ out to 20 kpc. As long as the companion was of comparable brightness to the primary pre-outburst ($L_{\rm companion} \sim L_{\rm preouburst}$), and assuming $L_{\rm acc} \sim 100\ L_{\rm preoutburst}$, the contrast between companion and FUOr is $\Delta K < 5$. This contrast level is easily attainable even by GRAVITY (Pourré et al., 2024).

ngVLA

The current performance estimates for the ngVLA[4] indicates that the post-upgrade array will attain an angular resolution at its maximum baseline of 0.08 mas at 93 GHz frequencies, while reaching a continuum sensitivity of 0.4 μJy in 1 hour. At the same frequency, and in the same on-source time, ALMA attains a sensitivity of 10 μJy and an angular resolution of 40 mas.

This enormous improvement in angular resolution will enable us to resolve the outer disks of all known FUOrs with Declination $> -40°$. The improvement in sensitivity will make disks with dust masses of $M_d = 20\ M_\oplus$[5] detectable at a 3σ level out to 10 kpc. This expands several avenues of investigation that have been difficult for FUOrs even with ALMA.

The ability to resolve the outer disks of FUOrs with sufficient sensitivity to search for substructure will place strong constraints on the plausibility of certain outburst trigger mechanisms in a given source. There is existing theoretical guidance on what substructure is to be expected from different triggers (Vorobyov et al., 2021).

[4] `https://ngvla.nrao.edu/page/performance`

[5] The mass of the FU Ori disk, which is less massive than typical FUOr disks (Pérez et al., 2020; Kóspál, Cruz-Sáenz de Miera, et al., 2021)

To date, we lack the sensitivity to detect most of those that have been predicted. Even in the case of gravitational instability, the relevant spiral substructures should be within radii of 10s of AU, not, e.g., the 1000 AU spirals detected in V960 Mon (Weber, Pérez, Zurlo, et al., 2023a).

The sharper angular resolution will enable improved measurements of outer disk inclinations, which often prove necessary or extremely helpful to modeling the SEDs and high resolution spectra of the disks (see Chapter 3). For nearby FUOrs, GRAVITY+ inner disk inclination measurements can be compared with outer disk inclination measurements from ngVLA to calibrate the likelihood of inner disk misalignment relative to the outer disk. In FU Ori, there is a persistent discrepancy between the VLTI-based inner disk inclination measurements of $i \sim 50°$ and the ALMA-based outer disk inclination measurements of $i \sim 35°$ (Lykou, Ábrahám, Chen, et al., 2022). However, the optical interferometric data are not sufficiently sensitive to rule out an inner disk aligned with the 35° value. If alignment between inner and outer disks in outbursting sources can be expected, then the ngVLA will prove a powerful instrument for constraining visible/NIR SED models.

BIBLIOGRAPHY

Adams, Fred C., Charles J. Lada, and Frank H. Shu (Jan. 1987). "Spectral Evolution of Young Stellar Objects." In: *ApJ* 312, p. 788. DOI: 10.1086/164924.

Akeson, Rachel et al. (Feb. 2019). "The Wide Field Infrared Survey Telescope: 100 Hubbles for the 2020s." In: *arXiv e-prints*, arXiv:1902.05569, arXiv:1902.05569. DOI: 10.48550/arXiv.1902.05569. arXiv: 1902.05569 [astro-ph.IM].

Alencar, S. H. P., G. Basri, L. Hartmann, and N. Calvet (Sept. 2005). "The extreme T Tauri star RW Aur: accretion and outflow variability." In: *A&A* 440.2, pp. 595–608. DOI: 10.1051/0004-6361:20053315.

Allen, D. A., K. M. Strom, G. L. Grasdalen, S. E. Strom, and K. M. Merrill (Oct. 1975). "Haro 13a: a luminous, heavily obscured star in Orion?" In: *MNRAS* 173, 47P–50. DOI: 10.1093/mnras/173.1.47P.

Ardila, David R., Gregory J. Herczeg, Scott G. Gregory, Laura Ingleby, Kevin France, Alexander Brown, Suzan Edwards, Christopher Johns-Krull, Jeffrey L. Linsky, Hao Yang, Jeff A. Valenti, Hervé Abgrall, Richard D. Alexander, Edwin Bergin, Thomas Bethell, Joanna M. Brown, Nuria Calvet, Catherine Espaillat, Lynne A. Hillenbrand, Gaitee Hussain, Evelyne Roueff, Rebecca N. Schindhelm, and Frederick M. Walter (July 2013). "Hot Gas Lines in T Tauri Stars." In: *ApJs* 207.1, 1, p. 1. DOI: 10.1088/0067-0049/207/1/1. arXiv: 1304.3746 [astro-ph.SR].

Armitage, Philip J., Cathie J. Clarke, and Francesco Palla (July 2003). "Dispersion in the lifetime and accretion rate of T Tauri discs." In: *MNRAS* 342.4, pp. 1139–1146. DOI: 10.1046/j.1365-8711.2003.06604.x. arXiv: astro-ph/0303343 [astro-ph].

Arulanantham, Nicole, Max Gronke, Eleonora Fiorellino, Jorge Filipe Gameiro, Antonio Frasca, Joel Green, Seok-Jun Chang, Rik A. B. Claes, Catherine C. Espaillat, Kevin France, Gregory J. Herczeg, Carlo F. Manara, Laura Venuti, Péter Ábrahám, Richard Alexander, Jerome Bouvier, Justyn Campbell-White, Jochen Eislöffel, William J. Fischer, Ágnes Kóspál, and Miguel Vioque (Feb. 2023). "Lyα Scattering Models Trace Accretion and Outflow Kinematics in T Tauri Systems." In: *ApJ* 944.2, 185, p. 185. DOI: 10.3847/1538-4357/acaf70. arXiv: 2301.01761 [astro-ph.SR].

Audard, M., P. Ábrahám, M. M. Dunham, J. D. Green, N. Grosso, K. Hamaguchi, J. H. Kastner, Á. Kóspál, G. Lodato, M. M. Romanova, S. L. Skinner, E. I. Vorobyov, and Z. Zhu (Jan. 2014). "Episodic Accretion in Young Stars." In: *Protostars and Planets VI*. Ed. by Henrik Beuther, Ralf S. Klessen, Cornelis P. Dullemond, and Thomas Henning, pp. 387–410. DOI: 10.2458/azu_uapress_9780816531240-ch017. arXiv: 1401.3368 [astro-ph.SR].

Ballesteros, F. J. (Feb. 2012). "New insights into black bodies." In: *EPL (Europhysics Letters)* 97.3, p. 34008. DOI: 10.1209/0295-5075/97/34008. arXiv: 1201.1809 [astro-ph.IM].

Baraffe, Isabelle, Derek Homeier, France Allard, and Gilles Chabrier (May 2015). "New evolutionary models for pre-main sequence and main sequence low-mass stars down to the hydrogen-burning limit." In: *A&A* 577, A42, A42. DOI: 10.1051/0004-6361/201425481. arXiv: 1503.04107 [astro-ph.SR].

Barsony, M. (Jan. 1994). "Class 0 Protostars." In: *Clouds, Cores, and Low Mass Stars*. Ed. by Dan P. Clemens and Richard Barvainis. Vol. 65. Astronomical Society of the Pacific Conference Series, p. 197.

Beck, Tracy L. and C. Aspin (Mar. 2012). "The Nature and Evolutionary State of the FU Orionis Binary System." In: *The Astronomical Journal* 143.3, 55, p. 55. DOI: 10.1088/0004-6256/143/3/55.

Bell, K. R. and D. N. C. Lin (June 1994). "Using FU Orionis Outbursts to Constrain Self-regulated Protostellar Disk Models." In: *ApJ* 427, p. 987. DOI: 10.1086/174206. arXiv: astro-ph/9312015 [astro-ph].

Bellm, Eric C. et al. (Jan. 2019). "The Zwicky Transient Facility: System Overview, Performance, and First Results." In: *PASP* 131.995, p. 018002. DOI: 10.1088/1538-3873/aaecbe. arXiv: 1902.01932 [astro-ph.IM].

Berné, Olivier et al. (Mar. 2024). "A far-ultraviolet–driven photoevaporation flow observed in a protoplanetary disk." In: *Science* 383.6686, pp. 988–992. DOI: 10.1126/science.adh2861. arXiv: 2403.00160 [astro-ph.GA].

Bianco, Federica B., Željko Ivezić, R. Lynne Jones, Melissa L. Graham, Phil Marshall, Abhijit Saha, Michael A. Strauss, Peter Yoachim, Tiago Ribeiro, Timo Anguita, A. E. Bauer, Franz E. Bauer, Eric C. Bellm, Robert D. Blum, William N. Brandt, Sarah Brough, Márcio Catelan, William I. Clarkson, Andrew J. Connolly, Eric Gawiser, John E. Gizis, Renée Hložek, Sugata Kaviraj, Charles T. Liu, Michelle Lochner, Ashish A. Mahabal, Rachel Mandelbaum, Peregrine McGehee, Eric H. Neilsen Jr., Knut A. G. Olsen, Hiranya V. Peiris, Jason Rhodes, Gordon T. Richards, Stephen Ridgway, Megan E. Schwamb, Dan Scolnic, Ohad Shemmer, Colin T. Slater, Anže Slosar, Stephen J. Smartt, Jay Strader, Rachel Street, David E. Trilling, Aprajita Verma, A. K. Vivas, Risa H. Wechsler, and Beth Willman (Jan. 2022). "Optimization of the Observing Cadence for the Rubin Observatory Legacy Survey of Space and Time: A Pioneering Process of Community-focused Experimental Design." In: *ApJ Supplement Series* 258.1, 1, p. 1. DOI: 10.3847/1538-4365/ac3e72. arXiv: 2108.01683 [astro-ph.IM].

Blandford, R. D. and D. G. Payne (June 1982). "Hydromagnetic flows from accretion disks and the production of radio jets." In: *MNRAS* 199, pp. 883–903. DOI: 10.1093/mnras/199.4.883.

Bonnell, Ian and Pierre Bastien (Dec. 1992). "A Binary Origin for FU Orionis Stars." In: *ApJL* 401, p. L31. DOI: 10.1086/186663.

Bradley, Larry, Brigitta Sipőcz, Thomas Robitaille, Erik Tollerud, Zè Vinícius, Christoph Deil, Kyle Barbary, Tom J Wilson, Ivo Busko, Axel Donath, Hans Moritz Günther, Mihai Cara, P. L. Lim, Sebastian Meßlinger, Simon Conseil, Zach Burnett, Azalee Bostroem, Michael Droettboom, E. M. Bray, Lars Andersen Bratholm, Adam Ginsburg, William Jamieson, Geert Barentsen, Matt Craig, Brett M. Morris, Marshall Perrin, Shivangee Rathi, Sergio Pascual, and Iskren Y. Georgiev (Oct. 2024). *astropy/photutils: 2.0.2*. Version 2.0.2. DOI: 10.5281/zenodo.13989456. URL: https://doi.org/10.5281/zenodo.13989456.

Burrows, Christopher J., Karl R. Stapelfeldt, Alan M. Watson, John E. Krist, Gilda E. Ballester, John T. Clarke, David Crisp, John S. Gallagher III, Richard E. Griffiths, J. Jeff Hester, John G. Hoessel, Jon A. Holtzman, Jeremy R. Mould, Paul A. Scowen, John T. Trauger, and James A. Westphal (Dec. 1996). "Hubble Space Telescope Observations of the Disk and Jet of HH 30." In: *ApJ* 473, p. 437. DOI: 10.1086/178156.

Calahan, Jenny K., Edwin A. Bergin, Merel van't Hoff, Alice S. Booth, Karin Öberg, Ke Zhang, Nuria Calvet, and Lee Hartmann (Nov. 2024). "Complex Organics Surrounding the FU Ori–type Object V1057 Cyg Indicative of Sublimated Ices." In: *ApJ* 975.2, 170, p. 170. DOI: 10.3847/1538-4357/ad78d1. arXiv: 2409.04530 [astro-ph.SR].

Calvet, Nuria and Erik Gullbring (Dec. 1998). "The Structure and Emission of the Accretion Shock in T Tauri Stars." In: *ApJ* 509.2, pp. 802–818. DOI: 10.1086/306527.

Calvet, Nuria, Lee Hartmann, and Scott J. Kenyon (Jan. 1993). "Mass Loss from Pre–Main-Sequence Accretion Disks. I. The Accelerating Wind of FU Orionis." In: *ApJ* 402, p. 623. DOI: 10.1086/172164.

Caratti o Garatti, A., R. Garcia Lopez, T. P. Ray, J. Eislöffel, B. Stecklum, A. Scholz, S. Kraus, G. Weigelt, A. Kreplin, and V. Shenavrin (June 2015). "Investigating 2MASS J06593158-0405277: AN FUor Burst in a Triple System?" In: *ApJL* 806.1, L4, p. L4. DOI: 10.1088/2041-8205/806/1/L4. arXiv: 1505.03691 [astro-ph.SR].

Cardelli, Jason A., Geoffrey C. Clayton, and John S. Mathis (Oct. 1989). "The relationship between infrared, optical, and ultraviolet extinction." In: *ApJ* 345, pp. 245–256. ISSN: 0004-637X. DOI: 10.1086/167900. URL: http://adsabs.harvard.edu/abs/1989ApJ...345..245C (visited on 03/10/2021).

Carilli, C. L., M. McKinnon, J. Ott, A. Beasley, A. Isella, E. Murphy, A. Leroy, C. Casey, A. Moullet, M. Lacy, J. Hodge, G. Bower, P. Demorest, C. Hull, M. Hughes, J. di Francesco, D. Narayanan, B. Kent, B. Clark, and B. Butler (Oct. 2015). "Next Generation Very Large Array Memo No. 5: Science Working Groups – Project Overview." In: *arXiv e-prints*, arXiv:1510.06438, arXiv:1510.06438. DOI: 10.48550/arXiv.1510.06438. arXiv: 1510.06438 [astro-ph.IM].

Carnall, A. C. (May 2017). "SpectRes: A Fast Spectral Resampling Tool in Python." In: *arXiv e-prints*, arXiv:1705.05165, arXiv:1705.05165. DOI: 10.48550/arXiv.1705.05165. arXiv: 1705.05165 [astro-ph.IM].

Carvalho, Adolfo S., Greg Doppmann, Kyle B. Westfall, Debora Pelliccia, J. Xavier Prochaska, Joseph Hennawi, Frederick B. Davies, Max Brodheim, Feige Wang, and Ryan Cooke (Oct. 2024). "Robust Support for Semi-automated Reductions of Keck/NIRSPEC Data Using PypeIt." In: *RNAAS* 8.10, 271, p. 271. DOI: 10.3847/2515-5172/ad8bb5. arXiv: 2410.19991 [astro-ph.IM].

Carvalho, Adolfo S., Gregory J. Herczeg, Kevin France, and Lynne A. Hillenbrand (Sept. 2024). "The Far-ultraviolet Spectrum of FU Ori South." In: *RNAAS* 8.9, 232, p. 232. DOI: 10.3847/2515-5172/ad7ba3. arXiv: 2409.10796 [astro-ph.SR].

Carvalho, Adolfo S., Lynne Hillenbrand, and Jerome Seebeck (Dec. 2023). "Disk Cooling and Wind Lines as Seen in the Spectral Line Evolution of V960 Mon." In: *ApJ* 958.2, 140, p. 140. DOI: 10.3847/1538-4357/acff59. arXiv: 2310.02465 [astro-ph.SR].

Carvalho, Adolfo S., Lynne Hillenbrand, Jerome Seebeck, and Kevin Covey (Aug. 2024). "An Expanding Accretion Disk and a Warm Disk Wind as Seen in the Spectral Evolution of HBC 722." In: *ApJ* 971.1, 44, p. 44. DOI: 10.3847/1538-4357/ad5286. arXiv: 2405.20251 [astro-ph.SR].

Carvalho, Adolfo S. and Lynne A. Hillenbrand (Dec. 2022). "Measuring Optical Extinction toward Young Stellar Objects Using Diffuse Interstellar Bands." In: *ApJ* 940.2, 156, p. 156. DOI: 10.3847/1538-4357/ac9d8e. arXiv: 2204.06061 [astro-ph.SR].

– (Nov. 2024). "Bolometric Corrections for FU Ori Object Accretion Disk Luminosities." In: *ApJL* 976.1, L5, p. L5. DOI: 10.3847/2041-8213/ad8cdf. arXiv: 2410.22270 [astro-ph.SR].

Carvalho, Adolfo S., Lynne A. Hillenbrand, Kevin France, and Gregory J. Herczeg (Oct. 2024). "A Far-ultraviolet-detected Accretion Shock at the Star–Disk Boundary of FU Ori." In: *ApJL* 973.2, L40, p. L40. DOI: 10.3847/2041-8213/ad74eb. arXiv: 2408.11033 [astro-ph.SR].

Carvalho, Adolfo S., Lynne A. Hillenbrand, Franz-Josef Hambsch, Shawn Dvorak, Michael Sitko, Ray W. Russell, Victoria Hammond, Michael Connelley, Michael C. B. Ashley, and Matthew J. Hankins (Aug. 2023). "Modeling the Multiwavelength Evolution of the V960 Mon System." In: *ApJ* 953.1, 86, p. 86. DOI: 10.3847/1538-4357/ace2cb. arXiv: 2306.15107 [astro-ph.SR].

Carvalho, Adolfo S. and Christopher M. Johns-Krull (May 2023a). "A Simple Code for Rotational Broadening of Broad Wavelength Range High-Dispersion Spectra." In: *RNAAS* 7.5, 91, p. 91. DOI: 10.3847/2515-5172/acd37e. arXiv: 2305.09693 [astro-ph.IM].

Carvalho, Adolfo S. and Christopher M. Johns-Krull (May 2023b). *RotBroadInt*. DOI: 10.5281/zenodo.7905357. URL: https://doi.org/10.5281/zenodo.7905357.

Cecil, Michael and Mario Flock (Dec. 2024). "Variability of the inner dead zone edge in 2D radiation hydrodynamic simulations." In: *A & A* 692, A171, A171. DOI: 10.1051/0004-6361/202451175. arXiv: 2411.05444 [astro-ph.EP].

Chambers, K. C. et al. (2019). *The Pan-STARRS1 Surveys*. arXiv: 1612.05560 [astro-ph.IM]. URL: https://arxiv.org/abs/1612.05560.

Chiang, E. I. and P. Goldreich (Nov. 1997). "Spectral Energy Distributions of T Tauri Stars with Passive Circumstellar Disks." In: *ApJ* 490.1, pp. 368–376. DOI: 10.1086/304869. arXiv: astro-ph/9706042 [astro-ph].

Cieza, Lucas A., Simon Casassus, John Tobin, Steven P. Bos, Jonathan P. Williams, Sebastian Perez, Zhaohuan Zhu, Claudio Caceres, Hector Canovas, Michael M. Dunham, Antonio Hales, Jose L. Prieto, David A. Principe, Matthias R. Schreiber, Dary Ruiz-Rodriguez, and Alice Zurlo (July 2016). "Imaging the water snow-line during a protostellar outburst." In: *Nature* 535.7611, pp. 258–261. DOI: 10.1038/nature18612. arXiv: 1607.03757 [astro-ph.SR].

Cieza, Lucas A., Dary Ruíz-Rodríguez, Sebastian Perez, Simon Casassus, Jonathan P. Williams, Alice Zurlo, David A. Principe, Antonio Hales, Jose L. Prieto, John J. Tobin, Zhaohuan Zhu, and Sebastian Marino (Mar. 2018). "The ALMA early science view of FUor/EXor objects - V. Continuum disc masses and sizes." In: *MNRAS* 474.4, pp. 4347–4357. DOI: 10.1093/mnras/stx3059. arXiv: 1711.08693 [astro-ph.SR].

Clarke, C., G. Lodato, S. Y. Melnikov, and M. A. Ibrahimov (Aug. 2005). "The photometric evolution of FU Orionis objects: disc instability and wind-envelope interaction." In: *MNRAS* 361.3, pp. 942–954. DOI: 10.1111/j.1365-2966.2005.09231.x. arXiv: astro-ph/0505515 [astro-ph].

Cleaver, Jacob, Lee Hartmann, and Jaehan Bae (Aug. 2023). "Magnetically activated accretion outbursts of pre-main-sequence discs." In: *MNRAS* 523.4, pp. 5522–5534. DOI: 10.1093/mnras/stad1784. arXiv: 2306.11098 [astro-ph.SR].

Connelley, Michael S. and Bo Reipurth (July 2018). "A Near-infrared Spectroscopic Survey of FU Orionis Objects." In: *ApJ* 861, p. 145. ISSN: 0004-637X. DOI: 10.3847/1538-4357/aaba7b. URL: http://adsabs.harvard.edu/abs/2018ApJ...861..145C (visited on 02/25/2021).

Croswell, Ken, L. Hartmann, and E. H. Avrett (Jan. 1987). "Mass Loss from FU Orionis Objects." In: *ApJ* 312, p. 227. DOI: 10.1086/164865.

Cruz-Sáenz de Miera, Fernando, Ágnes Kóspál, Péter Ábrahám, Timea Csengeri, Orsolya Fehér, Rolf Güsten, and Thomas Henning (Mar. 2023). "An APEX Study of Molecular Outflows in FUor-type Stars." In: *ApJ* 945.1, 80, p. 80. DOI: 10.3847/1538-4357/acb332. arXiv: 2301.03387 [astro-ph.SR].

Cuello, Nicolás, Giovanni Dipierro, Daniel Mentiplay, Daniel J. Price, Christophe Pinte, Jorge Cuadra, Guillaume Laibe, François Ménard, Pedro P. Poblete, and Matías Montesinos (Mar. 2019). "Flybys in protoplanetary discs: I. Gas and dust dynamics." In: *MNRAS* 483.3, pp. 4114–4139. DOI: 10.1093/mnras/sty3325. arXiv: 1812.00961 [astro-ph.EP].

Cuello, Nicolás, Fabien Louvet, Daniel Mentiplay, Christophe Pinte, Daniel J. Price, Andrew J. Winter, Rebecca Nealon, François Ménard, Giuseppe Lodato, Giovanni Dipierro, Valentin Christiaens, Matías Montesinos, Jorge Cuadra, Guillaume Laibe, Lucas Cieza, Ruobing Dong, and Richard Alexander (Jan. 2020). "Flybys in protoplanetary discs - II. Observational signatures." In: *MNRAS* 491.1, pp. 504–514. DOI: 10.1093/mnras/stz2938. arXiv: 1910.06822 [astro-ph.EP].

Cushing, Michael C., William D. Vacca, and John T. Rayner (Apr. 2004). "Spextool: A Spectral Extraction Package for SpeX, a 0.8-5.5 Micron Cross-Dispersed Spectrograph." In: *PASP* 116.818, pp. 362–376. DOI: 10.1086/382907.

Cutri, R. M., A. Mainzer, T. Conrow, F. Masci, J. Bauer, J. Dailey, J. D. Kirkpatrick, S. Fajardo-Acosta, C. Gelino, C. Grillmair, S. L. Wheelock, L. Yan, M. Harbut, R. Beck, M. Wittman, E. L. Wright, J. Masiero, T. Grav, S. Sonnett, C. Nugent, E. Kramer, R. Stevenson, P. R. M. Eisenhardt, B. Fabinsky, D. Tholen, M. Papin, J. Fowler, and H. McCallon (Mar. 2015). *Explanatory Supplement to the NEOWISE Data Release Products*.

Cutri, R. M., M. F. Skrutskie, S. van Dyk, C. A. Beichman, J. M. Carpenter, T. Chester, L. Cambresy, T. Evans, J. Fowler, J. Gizis, E. Howard, J. Huchra, T. Jarrett, E. L. Kopan, J. D. Kirkpatrick, R. M. Light, K. A. Marsh, H. McCallon, S. Schneider, R. Stiening, M. Sykes, M. Weinberg, W. A. Wheaton, S. Wheelock, and N. Zacarias (June 2003). "VizieR Online Data Catalog: 2MASS All-Sky Catalog of Point Sources (Cutri+ 2003)." In: *VizieR Online Data Catalog*, II/246, pp. II/246.

Czesla, Stefan, Sebastian Schröter, Christian P. Schneider, Klaus F. Huber, Fabian Pfeifer, Daniel T. Andreasen, and Mathias Zechmeister (June 2019). *PyA: Python astronomy-related packages*. ascl: 1906.010.

Dawson, Rebekah I. and John Asher Johnson (Sept. 2018). "Origins of Hot Jupiters." In: *ARA&A* 56, pp. 175–221. DOI: 10.1146/annurev-astro-081817-051853. arXiv: 1801.06117 [astro-ph.EP].

De, Kishalay, Matthew J. Hankins, Mansi M. Kasliwal, Anna M. Moore, Eran O. Ofek, Scott M. Adams, Michael C. B. Ashley, Aliya-Nur Babul, Ashot Bagdasaryan, Kevin B. Burdge, Jill Burnham, Richard G. Dekany, Alexander Declacroix, Antony Galla, Tim Greffe, David Hale, Jacob E. Jencson, Ryan M. Lau, Ashish Mahabal, Daniel McKenna, Manasi Sharma, Patrick L. Shopbell, Roger M. Smith, Jamie Soon, Jennifer Sokoloski, Roberto Soria, and Tony Travouillon (Feb. 2020). "Palomar Gattini-IR: Survey Overview, Data Processing System, On-sky Performance and First Results." In: *PASP* 132.1008, 025001, p. 025001. DOI: 10.1088/1538-3873/ab6069. arXiv: 1910.13319 [astro-ph.IM].

de la Reza, R. (Jan. 2025). "The lithium-rich giant stars puzzle: New observational trends for a general-mass-loss scenario." In: *A&A* 693, A98, A98. DOI: 10.1051/0004-6361/202451727. arXiv: 2412.04624 [astro-ph.SR].

Del Zanna, G., K. P. Dere, P. R. Young, and E. Landi (Mar. 2021a). "CHIANTI—An Atomic Database for Emission Lines. XVI. Version 10, Further Extensions." In: *ApJ* 909.1, 38, p. 38. DOI: 10.3847/1538-4357/abd8ce. arXiv: 2011.05211 [physics.atom-ph].

– (Mar. 2021b). "CHIANTI—An Atomic Database for Emission Lines. XVI. Version 10, Further Extensions." In: *ApJ* 909.1, 38, p. 38. DOI: 10.3847/1538-4357/abd8ce. arXiv: 2011.05211 [physics.atom-ph].

Dere, K. P., E. Landi, H. E. Mason, B. C. Monsignori Fossi, and P. R. Young (Oct. 1997). "CHIANTI - an atomic database for emission lines." In: *A&A Supplements* 125, pp. 149–173. DOI: 10.1051/aas:1997368.

Donati, Jean-François, Fréderic Paletou, Jérome Bouvier, and Jonathan Ferreira (Nov. 2005). "Direct detection of a magnetic field in the innermost regions of an accretion disk." In: *Nature* 438.7067, pp. 466–469. DOI: 10.1038/nature04253. arXiv: astro-ph/0511695 [astro-ph].

Dong, Ruobing, Hauyu Baobab Liu, Nicolás Cuello, Christophe Pinte, Péter Ábrahám, Eduard Vorobyov, Jun Hashimoto, Ágnes Kóspál, Eugene Chiang, Michihiro Takami, Lei Chen, Michael Dunham, Misato Fukagawa, Joel Green, Yasuhiro Hasegawa, Thomas Henning, Yaroslav Pavlyuchenkov, Tae-Soo Pyo, and Motohide Tamura (Jan. 2022). "A likely flyby of binary protostar Z CMa caught in action." In: *Nature Astronomy* 6, pp. 331–338. DOI: 10.1038/s41550-021-01558-y. arXiv: 2201.05617 [astro-ph.SR].

Doré, Olivier, Jamie Bock, Matthew Ashby, Peter Capak, Asantha Cooray, Roland de Putter, Tim Eifler, Nicolas Flagey, Yan Gong, Salman Habib, Katrin Heitmann, Chris Hirata, Woong-Seob Jeong, Raj Katti, Phil Korngut, Elisabeth Krause, Dae-Hee Lee, Daniel Masters, Phil Mauskopf, Gary Melnick, Bertrand Mennesson, Hien Nguyen, Karin Öberg, Anthony Pullen, Alvise Raccanelli, Roger Smith, Yong-Seon Song, Volker Tolls, Steve Unwin, Tejaswi Venumadhav, Marco Viero, Mike Werner, and Mike Zemcov (Dec. 2014). "Cosmology with the SPHEREX All-Sky Spectral Survey." In: *arXiv e-prints*, arXiv:1412.4872, arXiv:1412.4872. DOI: 10.48550/arXiv.1412.4872. arXiv: 1412.4872 [astro-ph.CO].

Draine, Bruce T. (2011). *Physics of the Interstellar and Intergalactic Medium*.

Dupree, A. K., N. S. Brickhouse, Graeme H. Smith, and Jay Strader (June 2005). "A Hot Wind from the Classical T Tauri Stars: TW Hydrae and T Tauri." In: *ApJL* 625.2, pp. L131–L134. DOI: 10.1086/431323. arXiv: astro-ph/0505037 [astro-ph].

Eilers, Paul HC and Hans FM Boelens (2005). "Baseline correction with asymmetric least squares smoothing." In: *Leiden University Medical Centre Report* 1.1, p. 5.

Eisner, J. A. and L. A. Hillenbrand (Sept. 2011). "Resolving the Sub-AU-scale Gas and Dust Distribution in FU Orionis Sources." In: *ApJ* 738.1, 9, p. 9. DOI: 10.1088/0004-637X/738/1/9. arXiv: 1106.1440 [astro-ph.GA].

Evans, Neal J. (Apr. 2011). "Low-mass Star Formation: Observations." In: *Computational Star Formation*. Ed. by João. Alves, Bruce G. Elmegreen, Josep M. Girart, and Virginia Trimble. Vol. 270, pp. 25–32. DOI: 10.1017/S1743921311000123. arXiv: 1007.5214 [astro-ph.GA].

Fang, Min, Lynne A. Hillenbrand, Jinyoung Serena Kim, Krzysztof Findeisen, Gregory J. Herczeg, John M. Carpenter, Luisa M. Rebull, and Hongchi Wang (Dec. 2020). "The First Extensive Spectroscopic Study of Young Stars in the North America and Pelican Nebulae." In: *ApJ* 904.2, 146, p. 146. DOI: 10.3847/1538-4357/abba84. arXiv: 2009.11995 [astro-ph.SR].

Fang, Min, Ilaria Pascucci, Suzan Edwards, Uma Gorti, Andrea Banzatti, Mario Flock, Patrick Hartigan, Gregory J. Herczeg, and Andrea K. Dupree (Nov. 2018). "A New Look at T Tauri Star Forbidden Lines: MHD-driven Winds from the Inner Disk." In: *ApJ* 868.1, 28, p. 28. DOI: 10.3847/1538-4357/aae780. arXiv: 1810.03366 [astro-ph.SR].

Fang, Min, Lile Wang, Gregory J. Herczeg, Jun Hashimoto, Ziyan Xu, Ahmad Nemer, Ilaria Pascucci, Sebastiaan Y. Haffert, and Yuhiko Aoyama (June 2023). "High-resolution [O I] line spectral mapping of TW Hya supportive of a magnetothermal wind." In: *Nature Astronomy*. DOI: 10.1038/s41550-023-02004-x. arXiv: 2305.07929 [astro-ph.SR].

Fiorellino, Eleonora, Łukasz Tychoniec, Fernando Cruz-Sáenz de Miera, Simone Antoniucci, Ágnes Kóspál, Carlo F. Manara, Brunella Nisini, and Giovanni Rosotti (Feb. 2023). "The Mass Accretion Rate and Stellar Properties in Class I Protostars." In: *ApJ* 944.2, 135, p. 135. DOI: 10.3847/1538-4357/aca320. arXiv: 2211.07653 [astro-ph.SR].

Fischer, W. J., L. A. Hillenbrand, G. J. Herczeg, D. Johnstone, A. Kospal, and M. M. Dunham (July 2023a). "Accretion Variability as a Guide to Stellar Mass Assembly." In: *Protostars and Planets VII*. Ed. by S. Inutsuka, Y. Aikawa, T. Muto, K. Tomida, and M. Tamura. Vol. 534. Astronomical Society of the Pacific Conference Series, p. 355. DOI: 10.48550/arXiv.2203.11257. arXiv: 2203.11257 [astro-ph.SR].

– (July 2023b). "Accretion Variability as a Guide to Stellar Mass Assembly." In: *Astronomical Society of the Pacific Conference Series*. Ed. by S. Inutsuka, Y. Aikawa, T. Muto, K. Tomida, and M. Tamura. Vol. 534. Astronomical Society of the Pacific Conference Series, p. 355.

Fitzpatrick, Edward L. (Jan. 1999). "Correcting for the Effects of Interstellar Extinction." In: *PASP* 111.755, pp. 63–75. DOI: 10.1086/316293. arXiv: astro-ph/9809387 [astro-ph].

Flewelling, H. A., E. A. Magnier, K. C. Chambers, J. N. Heasley, C. Holmberg, M. E. Huber, W. Sweeney, C. Z. Waters, A. Calamida, S. Casertano, X. Chen, D. Farrow, G. Hasinger, R. Henderson, K. S. Long, N. Metcalfe, G. Narayan, M. A. Nieto-Santisteban, P. Norberg, A. Rest, R. P. Saglia, A. Szalay, A. R. Thakar, J. L. Tonry, J. Valenti, S. Werner, R. White, L. Denneau, P. W. Draper, K. W. Hodapp, R. Jedicke, N. Kaiser, R. P. Kudritzki, P. A. Price, R. J. Wainscoat, S. Chastel, B. McLean, M. Postman, and B. Shiao (Nov. 2020). "The Pan-STARRS1 Database and Data Products." In: *ApJS* 251.1, 7, p. 7. DOI: 10.3847/1538-4365/abb82d. arXiv: 1612.05243 [astro-ph.IM].

Foreman-Mackey, Daniel (June 2016). "corner.py: Scatterplot matrices in Python." In: *The Journal of Open Source Software* 1.2, p. 24. DOI: 10.21105/joss.00024. URL: https://doi.org/10.21105/joss.00024.

Foreman-Mackey, Daniel, David W. Hogg, Dustin Lang, and Jonathan Goodman (Mar. 2013). "emcee: The MCMC Hammer." In: *PASP* 125.925, p. 306. DOI: 10.1086/670067. arXiv: 1202.3665 [astro-ph.IM].

France, Kevin, Nicole Arulanantham, Erin Maloney, P. Wilson Cauley, P. Ábrahám, Juan M. Alcalá, Justyn Campbell-White, Eleonora Fiorellino, Gregory J. Herczeg, Brunella Nisini, and Miguel Vioque (Aug. 2023). "The Radial Distribution and Excitation of H_2 around Young Stars in the HST-ULLYSES Survey." In: *AJ* 166.2, 67, p. 67. DOI: 10.3847/1538-3881/ace34c. arXiv: 2307.03780 [astro-ph.SR].

France, Kevin, Richard McCray, Steven V. Penton, Robert P. Kirshner, Peter Challis, J. Martin Laming, Patrice Bouchet, Roger Chevalier, Peter M. Garnavich, Claes Fransson, Kevin Heng, Josefin Larsson, Stephen Lawrence, Peter Lundqvist, Nino Panagia, Chun S. J. Pun, Nathan Smith, Jesper Sollerman, George Sonneborn, Ben Sugerman, and J. Craig Wheeler (Dec. 2011). "HST-COS Observations of Hydrogen, Helium, Carbon, and Nitrogen Emission from the SN 1987A Reverse Shock." In: *ApJ* 743.2, 186, p. 186. DOI: 10.1088/0004-637X/743/2/186. arXiv: 1111.1735 [astro-ph.SR].

France, Kevin, Evelyne Roueff, and Hervé Abgrall (Aug. 2017). "The 1600 Å Emission Bump in Protoplanetary Disks: A Spectral Signature of H_2O Dissociation." In: *ApJ* 844.2, 169, p. 169. DOI: 10.3847/1538-4357/aa7cee. arXiv: 1706.09940 [astro-ph.SR].

France, Kevin, Rebecca Schindhelm, Edwin A. Bergin, Evelyne Roueff, and Hervé Abgrall (Apr. 2014). "High-resolution Ultraviolet Radiation Fields of Classical T Tauri Stars." In: *ApJ* 784.2, 127, p. 127. DOI: 10.1088/0004-637X/784/2/127. arXiv: 1402.6341 [astro-ph.SR].

France, Kevin, Hao Yang, and Jeffrey L. Linsky (Mar. 2011). "The Far-ultraviolet "Continuum" in Protoplanetary Disk Systems. I. Electron-impact H_2 and Accretion Shocks." In: *ApJ* 729.1, 7, p. 7. DOI: 10.1088/0004-637X/729/1/7. arXiv: 1101.0165 [astro-ph.EP].

Fukue, Jun (May 2013). "Radiative transfer in protoplanetary disks under irradiation by the protostar." In: *Progress of Theoretical and Experimental Physics* 2013.5, 053E02, 053E02. DOI: 10.1093/ptep/ptt028.

Gaia Collaboration, A. G. A. Brown, et al. (May 2021). "Gaia Early Data Release 3. Summary of the contents and survey properties." In: *A&A* 649, A1, A1. DOI: 10.1051/0004-6361/202039657. arXiv: 2012.01533 [astro-ph.GA].

Gaia Collaboration, T. Prusti, et al. (Nov. 2016). "The Gaia mission." In: *A&A* 595, A1, A1. DOI: 10.1051/0004-6361/201629272. arXiv: 1609.04153 [astro-ph.IM].

Gaia Collaboration, A. Vallenari, et al. (June 2023). "Gaia Data Release 3. Summary of the content and survey properties." In: *A&A* 674, A1, A1. DOI: 10.1051/0004-6361/202243940. arXiv: 2208.00211 [astro-ph.GA].

Gammie, Charles F. (Jan. 1996). "Layered Accretion in T Tauri Disks." In: *ApJ* 457, p. 355. DOI: 10.1086/176735.

Gramajo, Luciana V., Javier A. Rodón, and Mercedes Gómez (June 2014). "Spectral Energy Distribution Analysis of Class I and Class II FU Orionis Stars." In: *The Astronomical Journal* 147, p. 140. ISSN: 0004-6256. DOI: 10.1088/0004-6256/147/6/140. URL: http://adsabs.harvard.edu/abs/2014AJ...147..140G (visited on 02/25/2021).

GRAVITY Collaboration, K. Perraut, L. Labadie, J. Bouvier, F. Ménard, L. Klarmann, C. Dougados, M. Benisty, J. -P. Berger, Y. -I. Bouarour, W. Brandner, A. Caratti O Garatti, P. Caselli, P. T. de Zeeuw, R. Garcia-Lopez, T. Henning, J. Sanchez-Bermudez, A. Sousa, E. van Dishoeck, E. Alécian, A. Amorim, Y. Clénet, R. Davies, A. Drescher, G. Duvert, A. Eckart, F. Eisenhauer, N. M. Förster-Schreiber, P. Garcia, E. Gendron, R. Genzel, S. Gillessen, R. Grellmann, G. Heißel, S. Hippler, M. Horrobin, Z. Hubert, L. Jocou, P. Kervella, S. Lacour, V. Lapeyrère, J. -B. Le Bouquin, P. Léna, D. Lutz, T. Ott, T. Paumard, G. Perrin, S. Scheithauer, J. Shangguan, T. Shimizu, J. Stadler, O. Straub, C. Straubmeier, E. Sturm, L. Tacconi, F. Vincent, S. von Fellenberg, and F. Widmann (Nov. 2021). "The GRAVITY young stellar object survey. VII. The inner dusty disks of T Tauri stars." In: *A & A* 655, A73, A73. DOI: 10.1051/0004-6361/202141624. arXiv: 2109.11826 [astro-ph.SR].

Gray, David F. (2005). *The Observation and Analysis of Stellar Photospheres*. 3rd ed. Cambridge University Press. DOI: 10.1017/CBO9781316036570.

– (2008). *The Observation and Analysis of Stellar Photospheres*.

Green, Joel D., Adam L. Kraus, Aaron C. Rizzuto, Michael J. Ireland, Trent J. Dupuy, Andrew W. Mann, and Rajika Kuruwita (Oct. 2016). "Testing the Binary Trigger Hypothesis in FUors." In: *ApJ* 830.1, 29, p. 29. DOI: 10.3847/0004-637X/830/1/29. arXiv: 1605.03270 [astro-ph.SR].

Greene, Thomas P., Bruce A. Wilking, Philippe Andre, Erick T. Young, and Charles J. Lada (Oct. 1994). "Further Mid-Infrared Study of the rho Ophiuchi Cloud Young Stellar Population: Luminosities and Masses of Pre–Main-Sequence Stars." In: *ApJ* 434, p. 614. DOI: 10.1086/174763.

Guo, Zhen, P. W. Lucas, R. Kurtev, J. Borissova, C. Contreras Peña, S. N. Yurchenko, L. C. Smith, D. Minniti, R. K. Saito, A. Bayo, M. Catelan, J. Alonso-García, A. Caratti o Garatti, C. Morris, D. Froebrich, J. Tennyson, K. Maucó, A. Aguayo, N. Miller, and H. D. S. Muthu (Feb. 2024). "Spectroscopic confirmation of high-amplitude eruptive YSOs and dipping giants from the VVV survey." In: *MNRAS* 528.2, pp. 1769–1788. DOI: 10.1093/mnras/stad3700. arXiv: 2401.14464 [astro-ph.SR].

Hackstein, M., M. Haas, Á. Kóspál, F. -J. Hambsch, R. Chini, P. Ábrahám, A. Moór, F. Pozo Nuñez, M. Ramolla, Ch. Westhues, L. Kaderhandt, Ch. Fein, A. Barr Domínguez, and K. -W. Hodapp (Oct. 2015). "Light curves of the latest FUor: Indication of a close binary." In: *A&A* 582, L12, p. L12. DOI: 10.1051/0004-6361/201527127. arXiv: 1510.06612 [astro-ph.SR].

Hackstein, Moritz, Rolf Chini, Martin Haas, Peter Abraham, and Agnes Kospal (Dec. 2014). "The light curve of the FU Ori type object 2MASS J06593158-0405277." In: *The Astronomer's Telegram* 6838, p. 1.

Hales, A. S., A. Gupta, D. Ruíz-Rodríguez, J. P. Williams, S. Pérez, L. Cieza, C. González-Ruilova, J. E. Pineda, A. Santamaría-Miranda, J. Tobin, P. Weber, Z. Zhu, and A. Zurlo (May 2024). "Discovery of an Accretion Streamer and a Slow Wide-angle Outflow around FU Orionis." In: *ApJ* 966.1, 96, p. 96. DOI: 10.3847/1538-4357/ad31a1. arXiv: 2405.03033 [astro-ph.SR].

Hamann, Fred and S. E. Persson (Sept. 1992a). "Emission-Line Studies of Young Stars. I. The T Tauri Stars." In: *ApJS* 82, p. 247. DOI: 10.1086/191715.

– (Sept. 1992b). "Emission-Line Studies of Young Stars. II. The Herbig Ae/Be Stars." In: *ApJS* 82, p. 285. DOI: 10.1086/191716.

Haro, Guillermo (Jan. 1953). "Hα Emission Stars and Peculiar Objects in the Orion Nebula." In: *ApJ* 117, p. 73. DOI: 10.1086/145669.

Hart, K., B. J. Shappee, D. Hey, C. S. Kochanek, K. Z. Stanek, L. Lim, S. Dobbs, M. Tucker, T. Jayasinghe, J. F. Beacom, T. Boright, T. Holoien, J. M. Joel Ong, J. L. Prieto, T. A. Thompson, and D. Will (Apr. 2023). "ASAS-SN Sky Patrol V2.0." In: *arXiv e-prints*, arXiv:2304.03791, arXiv:2304.03791. DOI: 10.48550/arXiv.2304.03791. arXiv: 2304.03791 [astro-ph.IM].

Hartmann, L. and S. J. Kenyon (Dec. 1985a). "On the nature of FU Orionis objects." In: *ApJ* 299, pp. 462–478. DOI: 10.1086/163713.

– (Dec. 1985b). "On the nature of FU Orionis objects." In: *ApJ* 299, pp. 462–478. DOI: 10.1086/163713.

Hartmann, Lee and Nuria Calvet (Apr. 1995a). "Observational Constraints on FU ORI Winds." In: *AJ* 109, p. 1846. DOI: 10.1086/117411.

– (Apr. 1995b). "Observational Constraints on FU ORI Winds." In: *AJ* 109, p. 1846. DOI: 10.1086/117411.

Hartmann, Lee, Gregory Herczeg, and Nuria Calvet (Sept. 2016). "Accretion onto Pre-Main-Sequence Stars." In: *ARA&A* 54, pp. 135–180. DOI: 10.1146/annurev-astro-081915-023347.

Hartmann, Lee and Scott J. Kenyon (1996). "The FU Orionis Phenomenon." In: *ARA&A* 34, pp. 207–240. ISSN: 0066-4146. DOI: 10.1146/annurev.astro.34.1.207. URL: http://adsabs.harvard.edu/abs/1996ARA%26A..34..207H (visited on 01/19/2021).

Hartmann, Lee, Zhaohuan Zhu, and Nuria Calvet (June 2011). "On Rapid Disk Accretion and Initial Conditions in Protostellar Evolution." In: *arXiv e-prints*, arXiv:1106.3343, arXiv:1106.3343. DOI: 10.48550/arXiv.1106.3343. arXiv: 1106.3343 [astro-ph.SR].

Hempe, K. and D. Reimers (Mar. 1982). "On excitation through radiative pumping of the Fe II UV-mult. 191 lambda lambda 1785-88 angstrom observed with the IUE during the eclipse of 32 Cyg." In: *A&A* 107, pp. 36–38.

Herbig, G. H. (Feb. 1965). "Lithium Abundances in F5-G8 Dwarfs." In: *ApJ* 141, p. 588. DOI: 10.1086/148147.

– (Jan. 1966). "On the interpretation of FU orionis." In: *Vistas in Astronomy* 8.1, pp. 109–125. DOI: 10.1016/0083-6656(66)90025-0.

– (Nov. 1977). "Eruptive phenomena in early stellar evolution." In: *ApJ* 217, pp. 693–715. ISSN: 0004-637X. DOI: 10.1086/155615. URL: http://adsabs.harvard.edu/abs/1977ApJ...217..693H (visited on 02/25/2021).

Herbig, G. H., P. P. Petrov, and R. Duemmler (Sept. 2003). "High-Resolution Spectroscopy of FU Orionis Stars." In: *ApJ* 595, pp. 384–411. ISSN: 0004-637X. DOI: 10.1086/377194. URL: http://adsabs.harvard.edu/abs/2003ApJ...595..384H (visited on 02/25/2021).

Herczeg, Gregory J. and Lynne A. Hillenbrand (July 2008). "UV Excess Measures of Accretion onto Young Very Low Mass Stars and Brown Dwarfs." In: *ApJ* 681.1, pp. 594–625. DOI: 10.1086/586728. arXiv: 0801.3525 [astro-ph].

– (May 2014). "An Optical Spectroscopic Study of T Tauri Stars. I. Photospheric Properties." In: *ApJ* 786.2, 97, p. 97. DOI: 10.1088/0004-637X/786/2/97. arXiv: 1403.1675 [astro-ph.SR].

Herter, Terry L., Charles P. Henderson, John C. Wilson, Keith Y. Matthews, Gustavo Rahmer, Marco Bonati, Philip S. Muirhead, Joseph D. Adams, James P. Lloyd, Michael F. Skrutskie, Dae-Sik Moon, Stephen C. Parshley, Matthew J. Nelson, Frantz Martinache, and George E. Gull (July 2008). "The performance of TripleSpec at Palomar." In: *Ground-based and Airborne Instrumentation for Astronomy*

II. Ed. by Ian S. McLean and Mark M. Casali. Vol. 7014. Society of Photo-Optical Instrumentation Engineers (SPIE) Conference Series, 70140X, p. 70140X. DOI: 10.1117/12.789660.

Hertfelder, Marius and Wilhelm Kley (Sept. 2017). "The vertical structure of the boundary layer around compact objects." In: *A&A* 605, A24, A24. DOI: 10.1051/0004-6361/201730847. arXiv: 1705.07658 [astro-ph.SR].

Hillenbrand, Lynne (Dec. 2014). "Confirmation of the FU Orionis Type Outburst of 2MASS J06593158-0405277." In: *The Astronomer's Telegram* 6797, p. 1.

Hillenbrand, Lynne A., Adolfo S. Carvalho, Dan Stern, Michael Connelley, Facundo Pérez Paolino, Ahaan Shetty, Zachariah Milby, and Howard Isaacson (July 2025a). "FUOr-Aur 0544+3330: A New Young Stellar Object Outburst in the Outskirts of Auriga OB1, Viewed Face-on." In: *ApJ* 988.1, 77, p. 77. DOI: 10.3847/1538-4357/ade14d. arXiv: 2505.11440 [astro-ph.SR].

– (May 2025b). "FUOr-Aur 0544+3330: A New YSO Outburst in the Outskirts of Auriga OB1, Viewed Face-On." In: *arXiv e-prints*, arXiv:2505.11440, arXiv:2505.11440. DOI: 10.48550/arXiv.2505.11440. arXiv: 2505.11440 [astro-ph.SR].

Hillenbrand, Lynne A., Adolfo S. Carvalho, Jan van Roestel, and Kishalay De (Dec. 2023). "RNO 54: A Previously Unappreciated FU Ori Star." In: *ApJL* 958.2, L27, p. L27. DOI: 10.3847/2041-8213/ad0be0. arXiv: 2310.17227 [astro-ph.SR].

Hillenbrand, Lynne A., Carlos Contreras Peña, Sam Morrell, Tim Naylor, Michael A. Kuhn, Roc M. Cutri, Luisa M. Rebull, Simon Hodgkin, Dirk Froebrich, and Amy K. Mainzer (Dec. 2018). "Gaia 17bpi: An FU Ori–type Outburst." en. In: *ApJ* 869.2. Publisher: American Astronomical Society, p. 146. ISSN: 0004-637X. DOI: 10.3847/1538-4357/aaf414. URL: https://doi.org/10.3847/1538-4357/aaf414 (visited on 02/18/2021).

Hillenbrand, Lynne A., Bo Reipurth, and M. S. Connelley (Nov. 2015). "Optical Spectroscopy of the Eruptive Variable ASASSN-15qi." In: *The Astronomer's Telegram* 8331. URL: http://adsabs.harvard.edu/abs/2015ATel.8331...1H (visited on 02/25/2021).

Hillenbrand, Lynne A. and Antonio C. Rodriguez (Jan. 2022). "Expected FU Ori Outburst Amplitudes from the Optical to the Mid-infrared." In: *RNAAS* 6.1, 6, p. 6. DOI: 10.3847/2515-5172/ac4807. arXiv: 2201.01012 [astro-ph.SR].

Hinkley, Sasha, Lynne Hillenbrand, Ben R. Oppenheimer, Emily L. Rice, Laurent Pueyo, Gautam Vasisht, Neil Zimmerman, Adam L. Kraus, Michael J. Ireland, Douglas Brenner, Charles Beichman, Richard Dekany, Jennifer E. Roberts, Ian R. Parry, Lewis C. Roberts Jr., Justin R. Crepp, Rick Burruss, J. Kent Wallace, Eric Cady, Chengxing Zhai, Michael Shao, Thomas Lockhart, Rémi Soummer, and Anand Sivaramakrishnan (Jan. 2013). "High-resolution Infrared Imaging and Spectroscopy of the Z Canis Majoris System during Quiescence and Outburst."

In: *ApJL* 763.1, L9, p. L9. DOI: 10.1088/2041-8205/763/1/L9. arXiv: 1212.2637 [astro-ph.SR].

Hodapp, Klaus W., Rolf Chini, Bo Reipurth, Miguel Murphy, Roland Lemke, Ramon Watermann, Shane Jacobson, Karsten Bischoff, Taylor Chonis, Denny Dement, Ryan Terrien, Kimberley Bott, and Sydney Provence (July 2010). "Commissioning of the infrared imaging survey (IRIS) system." In: *Ground-based and Airborne Instrumentation for Astronomy III*. Ed. by Ian S. McLean, Suzanne K. Ramsay, and Hideki Takami. Vol. 7735. Society of Photo-Optical Instrumentation Engineers (SPIE) Conference Series, 77351A, 77351A. DOI: 10.1117/12.856288.

Hodgkin, S. T. et al. (Aug. 2021). "Gaia Early Data Release 3. Gaia photometric science alerts." In: *A&A* 652, A76, A76. DOI: 10.1051/0004-6361/202140735. arXiv: 2106.01394 [astro-ph.IM].

Howard, Andrew W., John Asher Johnson, Geoffrey W. Marcy, Debra A. Fischer, Jason T. Wright, David Bernat, Gregory W. Henry, Kathryn M. G. Peek, Howard Isaacson, Kevin Apps, Michael Endl, William D. Cochran, Jeff A. Valenti, Jay Anderson, and Nikolai E. Piskunov (Oct. 2010). "The California Planet Survey. I. Four New Giant Exoplanets." In: *ApJ* 721.2, pp. 1467–1481. DOI: 10.1088/0004-637X/721/2/1467. arXiv: 1003.3488 [astro-ph.EP].

Husser, T. -O., S. Wende-von Berg, S. Dreizler, D. Homeier, A. Reiners, T. Barman, and P. H. Hauschildt (May 2013). "A new extensive library of PHOENIX stellar atmospheres and synthetic spectra." In: *A&A* 553, A6, A6. DOI: 10.1051/0004-6361/201219058. arXiv: 1303.5632 [astro-ph.SR].

Ingleby, Laura, Nuria Calvet, Gregory Herczeg, Alex Blaty, Frederick Walter, David Ardila, Richard Alexander, Suzan Edwards, Catherine Espaillat, Scott G. Gregory, Lynne Hillenbrand, and Alexander Brown (Apr. 2013). "Accretion Rates for T Tauri Stars Using Nearly Simultaneous Ultraviolet and Optical Spectra." In: *ApJ* 767.2, 112, p. 112. DOI: 10.1088/0004-637X/767/2/112. arXiv: 1303.0769 [astro-ph.SR].

Ivezić, Željko et al. (Mar. 2019). "LSST: From Science Drivers to Reference Design and Anticipated Data Products." In: *ApJ* 873.2, 111, p. 111. DOI: 10.3847/1538-4357/ab042c. arXiv: 0805.2366 [astro-ph].

Jeans, J. H. (Jan. 1902). "The Stability of a Spherical Nebula." In: *Philosophical Transactions of the Royal Society of London Series A* 199, pp. 1–53. DOI: 10.1098/rsta.1902.0012.

Johansson, S. and F. W. Hamann (Jan. 1993a). "Fluorescence lines in ultraviolet spectra of stars." In: *Physica Scripta Volume T* 47, p. 157. DOI: 10.1088/0031-8949/1993/T47/025.

– (Jan. 1993b). "Fluorescence lines in ultraviolet spectra of stars." In: *Physica Scripta Volume T* 47, p. 157. DOI: 10.1088/0031-8949/1993/T47/025.

Johansson, S. and V. S. Letokhov (Dec. 2004). "Astrophysical lasers operating in optical Fe II lines in stellar ejecta of η Carinae." In: *A&A* 428, pp. 497–509. DOI: 10.1051/0004-6361:20040379. arXiv: astro-ph/0409069 [astro-ph].

Johns-Krull, Christopher M. (Aug. 2007). "The Magnetic Fields of Classical T Tauri Stars." In: *ApJ* 664.2, pp. 975–985. DOI: 10.1086/519017. arXiv: 0704.2923 [astro-ph].

Johns-Krull, Christopher M., Jeff A. Valenti, and Jeffrey L. Linsky (Aug. 2000). "An IUE Atlas of Pre-Main-Sequence Stars. II. Far-Ultraviolet Accretion Diagnostics in T Tauri Stars." In: *ApJ* 539.2, pp. 815–833. DOI: 10.1086/309259.

Jurdana-Šepić, Rajka and Ulisse Munari (Feb. 2016). "The past photometric history of the FU Ori-type young eruptive star 2MASS J06593158-0405277 = V960 Mon." In: *Nature Astronomy* 43, pp. 87–90. DOI: 10.1016/j.newast.2015.08.001. arXiv: 1509.04642 [astro-ph.SR].

Kenyon, S. J., L. Hartmann, and R. Hewett (Feb. 1988). "Accretion Disk Models for FU Orionis and V1057 Cygni: Detailed Comparisons between Observations and Theory." In: *ApJ* 325, p. 231. DOI: 10.1086/165999.

Kenyon, S. J., L. Hartmann, C. L. Imhoff, and A. Cassatella (Sept. 1989). "Ultraviolet Spectroscopy of Pre–Main-Sequence Accretion Disks." In: *ApJ* 344, p. 925. DOI: 10.1086/167860.

Kenyon, Scott J. and Lee Hartmann (Nov. 1995). "Pre-Main-Sequence Evolution in the Taurus-Auriga Molecular Cloud." In: *ApJS* 101, p. 117. DOI: 10.1086/192235.

Kenyon, Scott J., Lee W. Hartmann, Karen M. Strom, and Stephen E. Strom (Mar. 1990). "An IRAS Survey of the Taurus-Auriga Molecular Cloud." In: *AJ* 99, p. 869. DOI: 10.1086/115380.

Kley, W. and D. N. C. Lin (Apr. 1996). "The Structure of the Boundary Layer in Protostellar Disks." In: *ApJ* 461, p. 933. DOI: 10.1086/177115.

Kochanek, C. S., B. J. Shappee, K. Z. Stanek, T. W. -S. Holoien, Todd A. Thompson, J. L. Prieto, Subo Dong, J. V. Shields, D. Will, C. Britt, D. Perzanowski, and G. Pojmański (Oct. 2017). "The All-Sky Automated Survey for Supernovae (ASAS-SN) Light Curve Server v1.0." In: *PASP* 129.980, p. 104502. DOI: 10.1088/1538-3873/aa80d9. arXiv: 1706.07060 [astro-ph.SR].

Koenigl, Arieh (Mar. 1991). "Disk Accretion onto Magnetic T Tauri Stars." In: *ApJL* 370, p. L39. DOI: 10.1086/185972.

Koresko, Chris D., Steven V. W. Beckwith, Andrea M. Ghez, Keith Matthews, and Gerry Neugebauer (Dec. 1991). "An Infrared Companion to Z Canis Majoris." In: *AJ* 102, p. 2073. DOI: 10.1086/116031.

Korotin, S. A., S. M. Andrievsky, E. Caffau, P. Bonifacio, and E. Oliva (Aug. 2020). "Study of the departures from LTE in the unevolved stars infrared spectra." In: *MNRAS* 496.2, pp. 2462–2473. DOI: 10.1093/mnras/staa1707. arXiv: 2006.10998 [astro-ph.SR].

Kóspál, Á., P. Ábrahám, J. A. Acosta-Pulido, M. M. Dunham, D. García-Álvarez, M. R. Hogerheijde, M. Kun, A. Moór, A. Farkas, G. Hajdu, G. Hodosán, T. Kovács, L. Kriskovics, G. Marton, L. Molnár, A. Pál, K. Sárneczky, Á. Sódor, R. Szakáts, T. Szalai, E. Szegedi-Elek, A. Szing, I. Tóth, K. Vida, and J. Vinkó (Nov. 2016). "Multiwavelength study of the low-luminosity outbursting young star HBC 722." In: *A&A* 596, A52, A52. DOI: 10.1051/0004-6361/201528061. arXiv: 1607.05925 [astro-ph.SR].

Kóspál, Á., P. Ábrahám, T. Csengeri, O. Fehér, M. R. Hogerheijde, Ch. Brinch, M. M. Dunham, E. I. Vorobyov, D. M. Salter, and Th. Henning (July 2017). "Mass Transport from the Envelope to the Disk of V346 Nor: A Case Study for the Luminosity Problem in an FUor-type Young Eruptive Star." In: *ApJ* 843.1, 45, p. 45. DOI: 10.3847/1538-4357/aa7683. arXiv: 1707.09883 [astro-ph.SR].

Kóspál, Á., P. Ábrahám, A. Moór, M. Haas, R. Chini, and M. Hackstein (Mar. 2015). "The Progenitor of the FUor-Type Young Eruptive Star 2MASS J06593158-0405277." In: *ApJL* 801.1, L5, p. L5. DOI: 10.1088/2041-8205/801/1/L5. arXiv: 1501.07735 [astro-ph.SR].

Kóspál, Á., F. Cruz-Sáenz de Miera, J. A. White, P. Ábrahám, L. Chen, T. Csengeri, R. Dong, M. M. Dunham, O. Fehér, J. D. Green, J. Hashimoto, Th. Henning, M. Hogerheijde, T. Kudo, H. B. Liu, M. Takami, and E. I. Vorobyov (Oct. 2021). "Massive Compact Disks around FU Orionis-type Young Eruptive Stars Revealed by ALMA." In: *ApJS* 256.2, 30, p. 30. DOI: 10.3847/1538-4365/ac0f09. arXiv: 2106.14409 [astro-ph.SR].

Kounkel, Marina, Kevin Covey, Genaro Suárez, Carlos Román-Zúñiga, Jesus Hernandez, Keivan Stassun, Karl O. Jaehnig, Eric D. Feigelson, Karla Peña Ramírez, Alexandre Roman-Lopes, Nicola Da Rio, Guy S. Stringfellow, J. Serena Kim, Jura Borissova, José G. Fernández-Trincado, Adam Burgasser, D. A. García-Hernández, Olga Zamora, Kaike Pan, and Christian Nitschelm (Sept. 2018). "The APOGEE-2 Survey of the Orion Star-forming Complex. II. Six-dimensional Structure." In: *AJ* 156.3, 84, p. 84. DOI: 10.3847/1538-3881/aad1f1. arXiv: 1805.04649 [astro-ph.SR].

Kowalski, Adam F. (Apr. 2024). "Stellar flares." In: *Living Reviews in Solar Physics* 21.1, 1, p. 1. DOI: 10.1007/s41116-024-00039-4. arXiv: 2402.07885 [astro-ph.SR].

Kravtsova, A. S. and S. A. Lamzin (Sept. 2003). "Peculiarities of the UV Continuum Energy Distribution for T Tauri Stars." In: *Astronomy Letters* 29, pp. 612–620. DOI: 10.1134/1.1607499.

Kravtsova, A. S., S. A. Lamzin, L. Errico, and A. Vittone (Nov. 2007). "Ultraviolet spectrum of FU Ori and a "Compromise" model of the FUor." In: *Astronomy Letters* 33.11, pp. 755–765. DOI: 10.1134/S1063773707110060.

Kroupa, Pavel (Apr. 2001). "On the variation of the initial mass function." In: *MNRAS* 322.2, pp. 231–246. DOI: 10.1046/j.1365-8711.2001.04022.x. arXiv: astro-ph/0009005 [astro-ph].

Kuhn, Michael A. and Lynne A. Hillenbrand (Oct. 2019). "A Comparison of the X-Ray Properties of FU Ori-type Stars to Generic Young Stellar Objects." In: *ApJ* 883, p. 117. ISSN: 0004-637X. DOI: 10.3847/1538-4357/ab3a3f. URL: http://adsabs.harvard.edu/abs/2019ApJ...883..117K (visited on 02/25/2021).

– (Dec. 2020). "Distance and Tangential Velocity of the Main Ionizing Star in the North America/Pelican Nebulae with Gaia EDR3." In: *RNAAS* 4.12, 224, p. 224. DOI: 10.3847/2515-5172/abd18a. arXiv: 2012.05074 [astro-ph.GA].

Kurosawa, Ryuichi, M. M. Romanova, and T. J. Harries (Oct. 2011). "Multidimensional models of hydrogen and helium emission line profiles for classical T Tauri stars: method, tests and examples." In: *MNRAS* 416.4, pp. 2623–2639. DOI: 10.1111/j.1365-2966.2011.19216.x. arXiv: 1102.0828 [astro-ph.SR].

Labdon, Aaron, Stefan Kraus, Claire L. Davies, Alexander Kreplin, John D. Monnier, Jean-Baptiste Le Bouquin, Narsireddy Anugu, Theo ten Brummelaar, Benjamin Setterholm, Tyler Gardner, Jacob Ennis, Cyprien Lanthermann, Gail Schaefer, and Anna Laws (Feb. 2021). "Viscous heating in the disk of the outbursting star FU Orionis." In: *A&A* 646, A102, A102. DOI: 10.1051/0004-6361/202039370. arXiv: 2011.07865 [astro-ph.SR].

Lada, Charles J. (Jan. 1987). "Star formation: from OB associations to protostars." In: *Star Forming Regions*. Ed. by Manuel Peimbert and Jun Jugaku. Vol. 115. IAU Symposium, p. 1.

Lada, Charles J. and Burkhard A. Wilking (Dec. 1984). "The nature of the embedded population in the rho Ophiuchi dark cloud : mid-infrared observations." In: *ApJ* 287, pp. 610–621. DOI: 10.1086/162719.

Lau, Mike Y. M., Ryosuke Hirai, Ilya Mandel, and Christopher A. Tout (May 2024). "Expansion of Accreting Main-sequence Stars during Rapid Mass Transfer." In: *ApJL* 966.1, L7, p. L7. DOI: 10.3847/2041-8213/ad3d50. arXiv: 2401.09570 [astro-ph.SR].

Law, Nicholas M., Shrinivas R. Kulkarni, Richard G. Dekany, Eran O. Ofek, Robert M. Quimby, Peter E. Nugent, Jason Surace, Carl C. Grillmair, Joshua S. Bloom, Mansi M. Kasliwal, Lars Bildsten, Tim Brown, S. Bradley Cenko, David Ciardi, Ernest Croner, S. George Djorgovski, Julian van Eyken, Alexei V. Filippenko, Derek B. Fox, Avishay Gal-Yam, David Hale, Nouhad Hamam, George Helou, John Henning, D. Andrew Howell, Janet Jacobsen, Russ Laher, Sean Mattingly, Dan McKenna, Andrew Pickles, Dovi Poznanski, Gustavo Rahmer, Arne Rau,

Wayne Rosing, Michael Shara, Roger Smith, Dan Starr, Mark Sullivan, Viswa Velur, Richard Walters, and Jeff Zolkower (Dec. 2009). "The Palomar Transient Factory: System Overview, Performance, and First Results." In: *PASP* 121.886, p. 1395. DOI: 10.1086/648598. arXiv: 0906.5350 [astro-ph.IM].

Lee, Jae-Joon, Kevin Gullikson, and Kyle Kaplan (Aug. 2017). *igrins/plp 2.2.0*. DOI: 10.5281/zenodo.845059.

Lee, Jeong-Eun, Seokho Lee, Giseon Baek, Yuri Aikawa, Lucas Cieza, Sung-Yong Yoon, Gregory Herczeg, Doug Johnstone, and Simon Casassus (Feb. 2019). "The ice composition in the disk around V883 Ori revealed by its stellar outburst." In: *Nature Astronomy* 3, pp. 314–319. DOI: 10.1038/s41550-018-0680-0. arXiv: 1809.00353 [astro-ph.SR].

Lee, Jeong-Eun, Sunkyung Park, Joel D. Green, William D. Cochran, Wonseok Kang, Sang-Gak Lee, and Hyun-Il Sung (July 2015). "High Resolution Optical and NIR Spectra of HBC 722." In: *ApJ* 807.1, 84, p. 84. DOI: 10.1088/0004-637X/807/1/84. arXiv: 1505.03206 [astro-ph.SR].

Lima, G. H. R. A., S. H. P. Alencar, N. Calvet, L. Hartmann, and J. Muzerolle (Nov. 2010). "Modeling the Hα line emission around classical T Tauri stars using magnetospheric accretion and disk wind models." In: *A&A* 522, A104, A104. DOI: 10.1051/0004-6361/201014490. arXiv: 1007.3976 [astro-ph.SR].

Liu, Hanpu, Gregory J. Herczeg, Doug Johnstone, Carlos Contreras-Peña, Jeong-Eun Lee, Haifeng Yang, Xingyu Zhou, Sung-Yong Yoon, Ho-Gyu Lee, Masanobu Kunitomo, and Jessy Jose (Sept. 2022). "Diagnosing FU Ori-like Sources: The Parameter Space of Viscously Heated Disks in the Optical and Near-infrared." In: *ApJ* 936.2, 152, p. 152. DOI: 10.3847/1538-4357/ac84d2. arXiv: 2207.13324 [astro-ph.SR].

López, Ronald A., Erika B. Hoffman, Greg Doppmann, Michael P. Fitzgerald, Chris Johnson, Marc Kassis, Kyle Lanclos, Jim Lyke, Emily C. Martin, Ian McLean, Ji Man Sohn, and Jason Weiss (Dec. 2020). "Characterization and performance of the upgraded NIRSPEC on the W. M. Keck Telescope." In: *Ground-based and Airborne Instrumentation for Astronomy VIII*. Ed. by Christopher J. Evans, Julia J. Bryant, and Kentaro Motohara. Vol. 11447. Society of Photo-Optical Instrumentation Engineers (SPIE) Conference Series, 114476B, 114476B. DOI: 10.1117/12.2563075.

López-Martínez, Fatima and Ana Inés Gómez de Castro (Aug. 2014). "Constraints to the magnetospheric properties of T Tauri stars - I. The C II], Fe II] and Si II] ultraviolet features." In: *MNRAS* 442.4, pp. 2951–2962. DOI: 10.1093/mnras/stu1045. arXiv: 1405.7180 [astro-ph.SR].

Lourie, Nathan P., John W. Baker, Richard S. Burruss, Mark Egan, Gábor Fżrész, Danielle Frostig, Allan A. Garcia-Zych, Nicolae Ganciu, Kari Haworth, Erik Hinrichsen, Mansi M. Kasliwal, Viraj R. Karambelkar, Andrew Malonis, Robert A. Simcoe, and Jeffrey Zolkower (Dec. 2020). "The wide-field infrared tran-

sient explorer (WINTER).” In: *Ground-based and Airborne Instrumentation for Astronomy VIII*. Ed. by Christopher J. Evans, Julia J. Bryant, and Kentaro Motohara. Vol. 11447. Society of Photo-Optical Instrumentation Engineers (SPIE) Conference Series, 114479K, 114479K. DOI: 10.1117/12.2561210. arXiv: 2102.01109 [astro-ph.IM].

Loyd, R. O. Parke, Kevin France, Allison Youngblood, Christian Schneider, Alexander Brown, Renyu Hu, Antígona Segura, Jeffrey Linsky, Seth Redfield, Feng Tian, Sarah Rugheimer, Yamila Miguel, and Cynthia S. Froning (Nov. 2018). “The MUSCLES Treasury Survey. V. FUV Flares on Active and Inactive M Dwarfs.” In: *ApJ* 867.1, 71, p. 71. DOI: 10.3847/1538-4357/aae2bd. arXiv: 1809.07322 [astro-ph.SR].

Lykou, F., P. Ábrahám, L. Chen, J. Varga, Á. Kóspál, A. Matter, M. Siwak, Zs. M. Szabó, Z. Zhu, H. B. Liu, B. Lopez, F. Allouche, J. -C. Augereau, P. Berio, P. Cruzalèbes, C. Dominik, Th. Henning, K. -H. Hofmann, M. Hogerheijde, W. J. Jaffe, E. Kokoulina, S. Lagarde, A. Meilland, F. Millour, E. Pantin, R. Petrov, S. Robbe-Dubois, D. Schertl, M. Scheuck, R. van Boekel, L. B. F. M. Waters, G. Weigelt, and S. Wolf (July 2022). “The disk of FU Orionis viewed with MATISSE/VLTI. First interferometric observations in L and M bands.” In: *A&A* 663, A86, A86. DOI: 10.1051/0004-6361/202142788. arXiv: 2205.10173 [astro-ph.SR].

Lykou, F., P. Ábrahám, F. Cruz-Sáenz de Miera, J. Varga, Á. Kóspál, J. Bouwman, L. Chen, S. Kraus, M. L. Sitko, R. W. Russell, and M. Pikhartova (Feb. 2024). “The disk of the eruptive protostar V900 Mon. A MATISSE/VLTI and MUSE/VLT perspective.” In: *A&A* 682, A75, A75. DOI: 10.1051/0004-6361/202245740. arXiv: 2311.07250 [astro-ph.SR].

Lynden-Bell, D. and J. E. Pringle (Sept. 1974a). “The evolution of viscous discs and the origin of the nebular variables.” In: *MNRAS* 168, pp. 603–637. DOI: 10.1093/mnras/168.3.603.

– (Sept. 1974b). “The evolution of viscous discs and the origin of the nebular variables.” In: *MNRAS* 168, pp. 603–637. DOI: 10.1093/mnras/168.3.603.

MacGregor, Meredith A., Alycia J. Weinberger, R. O. Parke Loyd, Evgenya Shkolnik, Thomas Barclay, Ward S. Howard, Andrew Zic, Rachel A. Osten, Steven R. Cranmer, Adam F. Kowalski, Emil Lenc, Allison Youngblood, Anna Estes, David J. Wilner, Jan Forbrich, Anna Hughes, Nicholas M. Law, Tara Murphy, Aaron Boley, and Jaymie Matthews (Apr. 2021). “Discovery of an Extremely Short Duration Flare from Proxima Centauri Using Millimeter through Far-ultraviolet Observations.” In: *ApJL* 911.2, L25, p. L25. DOI: 10.3847/2041-8213/abf14c. arXiv: 2104.09519 [astro-ph.SR].

Maehara, Hiroyuki, Tadashi Kojima, and Mitsugu Fujii (Nov. 2014). “FU Ori-type outburst of 2MASS J06593158-0405277.” In: *The Astronomer’s Telegram* 6770, p. 1.

Magnier, Eugene A., K. C. Chambers, H. A. Flewelling, J. C. Hoblitt, M. E. Huber, P. A. Price, W. E. Sweeney, C. Z. Waters, L. Denneau, P. W. Draper, K. W. Hodapp, R. Jedicke, N. Kaiser, R. -P. Kudritzki, N. Metcalfe, C. W. Stubbs, and R. J. Wainscoat (Nov. 2020). "The Pan-STARRS Data-processing System." In: *ApJS* 251.1, 3, p. 3. DOI: 10.3847/1538-4365/abb829. arXiv: 1612.05240 [astro-ph.IM].

Mainzer, A., J. Bauer, T. Grav, J. Masiero, R. M. Cutri, J. Dailey, P. Eisenhardt, R. S. McMillan, E. Wright, R. Walker, R. Jedicke, T. Spahr, D. Tholen, R. Alles, R. Beck, H. Brandenburg, T. Conrow, T. Evans, J. Fowler, T. Jarrett, K. Marsh, F. Masci, H. McCallon, S. Wheelock, M. Wittman, P. Wyatt, E. DeBaun, G. Elliott, D. Elsbury, IV Gautier T., S. Gomillion, D. Leisawitz, C. Maleszewski, M. Micheli, and A. Wilkins (Apr. 2011). "Preliminary Results from NEOWISE: An Enhancement to the Wide-field Infrared Survey Explorer for Solar System Science." In: *ApJ* 731.1, 53, p. 53. DOI: 10.1088/0004-637X/731/1/53. arXiv: 1102.1996 [astro-ph.EP].

Maksimova, L. A., Ya. N. Pavlyuchenkov, and A. V. Tutukov (Oct. 2020). "Evolution of a Viscous Protoplanetary Disk with Convectively Unstable Regions. II. Accretion Regimes and Long-Term Dynamics." In: *Astronomy Reports* 64.10, pp. 815–826. DOI: 10.1134/S1063772920110050. arXiv: 2009.07750 [astro-ph.SR].

Manara, C. F., M. Ansdell, G. P. Rosotti, A. M. Hughes, P. J. Armitage, G. Lodato, and J. P. Williams (July 2023). "Demographics of Young Stars and their Protoplanetary Disks: Lessons Learned on Disk Evolution and its Connection to Planet Formation." In: *Protostars and Planets VII*. Ed. by S. Inutsuka, Y. Aikawa, T. Muto, K. Tomida, and M. Tamura. Vol. 534. Astronomical Society of the Pacific Conference Series, p. 539. DOI: 10.48550/arXiv.2203.09930. arXiv: 2203.09930 [astro-ph.SR].

Martin, Emily C., Michael P. Fitzgerald, Ian S. McLean, Gregory Doppmann, Marc Kassis, Ted Aliado, John Canfield, Chris Johnson, Evan Kress, Kyle Lanclos, Kenneth Magnone, Ji Man Sohn, Eric Wang, and Jason Weiss (Aug. 2018). "An overview of the NIRSPEC upgrade for the Keck II telescope." In: *Ground-based and Airborne Instrumentation for Astronomy VII*. Ed. by Christopher J. Evans, Luc Simard, and Hideki Takami. Vol. 10702. Society of Photo-Optical Instrumentation Engineers (SPIE) Conference Series, 107020A, 107020A. DOI: 10.1117/12.2312266. arXiv: 1808.06024 [astro-ph.IM].

Mathis, John S. (Jan. 1990). "Interstellar dust and extinction." In: *ARA&A* 28, pp. 37–70. DOI: 10.1146/annurev.aa.28.090190.000345.

Mayor, Michel and Didier Queloz (Nov. 1995). "A Jupiter-mass companion to a solar-type star." In: *Nature* 378.6555, pp. 355–359. DOI: 10.1038/378355a0.

McCarthy, James K., Judith G. Cohen, Brad Butcher, John Cromer, Ernest Croner, William R. Douglas, Richard M. Goeden, Tony Grewal, Barry Lu, Harold L. Petrie, Tianxiang Weng, Bob Weber, Donald G. Koch, and John M. Rodgers (July 1998). "Blue channel of the Keck low-resolution imaging spectrometer."

In: *Optical Astronomical Instrumentation*. Ed. by Sandro D'Odorico. Vol. 3355. Society of Photo-Optical Instrumentation Engineers (SPIE) Conference Series, pp. 81–92. DOI: 10.1117/12.316831.

McLean, Ian S., Eric E. Becklin, Oddvar Bendiksen, George Brims, John Canfield, Donald F. Figer, James R. Graham, Jonah Hare, Fred Lacayanga, James E. Larkin, Samuel B. Larson, Nancy Levenson, Nick Magnone, Harry Teplitz, and Woon Wong (Aug. 1998). "Design and development of NIRSPEC: a near-infrared echelle spectrograph for the Keck II telescope." In: *Infrared Astronomical Instrumentation*. Ed. by Albert M. Fowler. Vol. 3354. Society of Photo-Optical Instrumentation Engineers (SPIE) Conference Series, pp. 566–578. DOI: 10.1117/12.317283.

Mehner, Andrea, Kris Davidson, Gary J. Ferland, and Roberta M. Humphreys (Feb. 2010). "High-excitation Emission Lines near Eta Carinae, and Its Likely Companion Star." In: *ApJ* 710.1, pp. 729–742. DOI: 10.1088/0004-637X/710/1/729. arXiv: 0912.1067 [astro-ph.SR].

Miller, Adam A., Lynne A. Hillenbrand, Kevin R. Covey, Dovi Poznanski, Jeffrey M. Silverman, Io K. W. Kleiser, Bárbara Rojas-Ayala, Philip S. Muirhead, S. Bradley Cenko, Joshua S. Bloom, Mansi M. Kasliwal, Alexei V. Filippenko, Nicholas M. Law, Eran O. Ofek, Richard G. Dekany, Gustavo Rahmer, David Hale, Roger Smith, Robert M. Quimby, Peter Nugent, Janet Jacobsen, Jeff Zolkower, Viswa Velur, Richard Walters, John Henning, Khanh Bui, Dan McKenna, Shrinivas R. Kulkarni, Christopher R. Klein, Michael Kandrashoff, and Alekzandir Morton (Apr. 2011). "Evidence for an FU Orionis-like Outburst from a Classical T Tauri Star." In: *ApJ* 730, p. 80. ISSN: 0004-637X. DOI: 10.1088/0004-637X/730/2/80. URL: http://adsabs.harvard.edu/abs/2011ApJ...730...80M (visited on 02/25/2021).

Miller, J.S. and R.P.S. Stone (1993). "The Kast Double Spectrograph." In: *Lick Observatory Technical Report* 66.

Milliner, Kelly, James H. Matthews, Knox S. Long, and Lee Hartmann (Feb. 2019a). "Disc wind models for FU Ori objects." In: *MNRAS* 483.2, pp. 1663–1673. DOI: 10.1093/mnras/sty3197. arXiv: 1811.12453 [astro-ph.SR].

– (Feb. 2019b). "Disc wind models for FU Ori objects." In: *MNRAS* 483.2, pp. 1663–1673. DOI: 10.1093/mnras/sty3197. arXiv: 1811.12453 [astro-ph.SR].

Minniti, D., P. W. Lucas, J. P. Emerson, R. K. Saito, M. Hempel, P. Pietrukowicz, A. V. Ahumada, M. V. Alonso, J. Alonso-Garcia, J. I. Arias, R. M. Bandyopadhyay, R. H. Barbá, B. Barbuy, L. R. Bedin, E. Bica, J. Borissova, L. Bronfman, G. Carraro, M. Catelan, J. J. Clariá, N. Cross, R. de Grijs, I. Dékány, J. E. Drew, C. Fariña, C. Feinstein, E. Fernández Lajús, R. C. Gamen, D. Geisler, W. Gieren, B. Goldman, O. A. Gonzalez, G. Gunthardt, S. Gurovich, N. C. Hambly, M. J. Irwin, V. D. Ivanov, A. Jordán, E. Kerins, K. Kinemuchi, R. Kurtev, M. López-Corredoira, T. Maccarone, N. Masetti, D. Merlo, M. Messineo, I. F. Mirabel, L. Monaco, L. Morelli, N. Padilla, T. Palma, M. C. Parisi, G. Pignata, M. Rejkuba,

A. Roman-Lopes, S. E. Sale, M. R. Schreiber, A. C. Schröder, M. Smith, Jr. L. Sodré, M. Soto, M. Tamura, C. Tappert, M. A. Thompson, I. Toledo, M. Zoccali, and G. Pietrzynski (July 2010). "VISTA Variables in the Via Lactea (VVV): The public ESO near-IR variability survey of the Milky Way." In: *Nature Astronomy* 15.5, pp. 433–443. DOI: 10.1016/j.newast.2009.12.002. arXiv: 0912.1056 [astro-ph.GA].

Molyarova, Tamara, Vitaly Akimkin, Dmitry Semenov, Péter Ábrahám, Thomas Henning, Ágnes Kóspál, Eduard Vorobyov, and Dmitri Wiebe (Oct. 2018). "Chemical Signatures of the FU Ori Outbursts." In: *ApJ* 866.1, 46, p. 46. DOI: 10.3847/1538-4357/aadfd9. arXiv: 1809.01925 [astro-ph.EP].

Momose, Munetake, Nagayoshi Ohashi, Ryohei Kawabe, Takenori Nakano, and Masahiko Hayashi (Sept. 1998). "Aperture Synthesis $C^{18}O$ J = 1-0 Observations of L1551 IRS 5: Detailed Structure of the Infalling Envelope." In: *ApJ* 504.1, pp. 314–333. DOI: 10.1086/306061.

Moore, Anna M., Mansi M. Kasliwal, Christopher R. Gelino, Jacob E. Jencson, Mike I. Jones, J. Davy Kirkpatrick, Ryan M. Lau, Eran Ofek, Yuri Petrunin, Roger Smith, Valery Terebizh, Eric Steinbring, and Lin Yan (Aug. 2016). "Unveiling the dynamic infrared sky with Gattini-IR." In: *Ground-based and Airborne Telescopes VI*. Ed. by Helen J. Hall, Roberto Gilmozzi, and Heather K. Marshall. Vol. 9906. Society of Photo-Optical Instrumentation Engineers (SPIE) Conference Series, 99062C, p. 99062C. DOI: 10.1117/12.2233694. arXiv: 1608.04510 [astro-ph.IM].

Moore, Charlotte E. and Paul W. Merrill (1968). *Partial Grotrian Diagrams of Astrophysical Interest*.

Muzerolle, James, Nuria Calvet, and Lee Hartmann (Apr. 2001). "Emission-Line Diagnostics of T Tauri Magnetospheric Accretion. II. Improved Model Tests and Insights into Accretion Physics." In: *ApJ* 550.2, pp. 944–961. DOI: 10.1086/319779.

Myers, Philip C. (May 2010). "Star-forming Gas in Young Clusters." In: *ApJ* 714.2, pp. 1280–1289. DOI: 10.1088/0004-637X/714/2/1280. arXiv: 1003.4900 [astro-ph.GA].

Nayakshin, Sergei, Fernando Cruz Sáenz de Miera, Ágnes Kóspál, Aleksandra Ćalović, Jochen Eislöffel, and Douglas N. C. Lin (May 2024). "Episodic eruptions of young accreting stars: the key role of disc thermal instability due to Hydrogen ionization." In: *MNRAS* 530.2, pp. 1749–1765. DOI: 10.1093/mnras/stae877. arXiv: 2403.04439 [astro-ph.SR].

Nayakshin, Sergei and Vardan Elbakyan (Feb. 2024). "On the origin of accretion bursts in FU Ori." In: *MNRAS* 528.2, pp. 2182–2198. DOI: 10.1093/mnras/stae049. arXiv: 2309.12072 [astro-ph.EP].

Nayakshin, Sergei, James E. Owen, and Vardan Elbakyan (July 2023). "Extreme evaporation of planets in hot thermally unstable protoplanetary discs: the case of FU Ori." In: *MNRAS* 523.1, pp. 385–403. DOI: 10.1093/mnras/stad1392. arXiv: 2305.03392 [astro-ph.EP].

Nguyen, C. T., G. Costa, L. Girardi, G. Volpato, A. Bressan, Y. Chen, P. Marigo, X. Fu, and P. Goudfrooij (Sept. 2022). "PARSEC V2.0: Stellar tracks and isochrones of low- and intermediate-mass stars with rotation." In: *A&A* 665, A126, A126. DOI: 10.1051/0004-6361/202244166. arXiv: 2207.08642 [astro-ph.SR].

Nofi, Larissa A., Christopher M. Johns-Krull, Ricardo López-Valdivia, Lauren Biddle, Adolfo S. Carvalho, Daniel Huber, Daniel Jaffe, Joe Llama, Gregory Mace, Lisa Prato, Brian Skiff, Kimberly R. Sokal, Kendall Sullivan, and Jamie Tayar (Apr. 2021). "Projected Rotational Velocities and Fundamental Properties of Low-mass Pre-main-sequence Stars in the Taurus-Auriga Star-forming Region." In: *ApJ* 911.2, 138, p. 138. DOI: 10.3847/1538-4357/abeab3. arXiv: 2103.01246 [astro-ph.SR].

Öberg, Karin I., Stefano Facchini, and Dana E. Anderson (Aug. 2023). "Protoplanetary Disk Chemistry." In: *ARA&A* 61, pp. 287–328. DOI: 10.1146/annurev-astro-022823-040820. arXiv: 2309.05685 [astro-ph.EP].

Oke, J. B., J. G. Cohen, M. Carr, J. Cromer, A. Dingizian, F. H. Harris, S. Labrecque, R. Lucinio, W. Schaal, H. Epps, and J. Miller (Apr. 1995). "The Keck Low-Resolution Imaging Spectrometer." In: *PASP* 107, p. 375. DOI: 10.1086/133562.

Oller-Moreno, Sergio, Antonio Pardo, Juan Manuel Jiménez-Soto, Josep Samitier, and Santiago Marco (2014). "Adaptive Asymmetric Least Squares baseline estimation for analytical instruments." In: *2014 IEEE 11th International Multi-Conference on Systems, Signals & Devices (SSD14)*. IEEE, pp. 1–5.

Padgett, Deborah L., Wolfgang Brandner, Karl R. Stapelfeldt, Stephen E. Strom, Susan Terebey, and David Koerner (Mar. 1999). "HUBBLE SPACE TELESCOPE/NICMOS Imaging of Disks and Envelopes around Very Young Stars." In: *AJ* 117.3, pp. 1490–1504. DOI: 10.1086/300781. arXiv: astro-ph/9902101 [astro-ph].

Park, Chan, Daniel T. Jaffe, In-Soo Yuk, Moo-Young Chun, Soojong Pak, Kang-Min Kim, Michael Pavel, Hanshin Lee, Heeyoung Oh, Ueejeong Jeong, Chae Kyung Sim, Hye-In Lee, Huynh Anh Nguyen Le, Joseph Strubhar, Michael Gully-Santiago, Jae Sok Oh, Sang-Mok Cha, Bongkon Moon, Kwijong Park, Cynthia Brooks, Kyeongyeon Ko, Jeong-Yeol Han, Jakyoung Nah, Peter C. Hill, Sungho Lee, Stuart Barnes, Young Sam Yu, Kyle Kaplan, Gregory Mace, Hwihyun Kim, Jae-Joon Lee, Narae Hwang, and Byeong-Gon Park (July 2014). "Design and early performance of IGRINS (Immersion Grating Infrared Spectrometer)." In: *Ground-based and Airborne Instrumentation for Astronomy V*. Ed. by Suzanne K. Ramsay, Ian S. McLean, and Hideki Takami. Vol. 9147. Society of Photo-Optical Instrumentation Engineers (SPIE) Conference Series, 91471D, p. 91471D. DOI: 10.1117/12.2056431.

Park, Sunkyung, Ágnes Kóspál, Péter Ábrahám, Fernando Cruz-Sáenz de Miera, Eleonora Fiorellino, Michał Siwak, Zsófia Nagy, Teresa Giannini, Roberta Carini, Zsófia Marianna Szabó, Jeong-Eun Lee, Jae-Joon Lee, Fabrizio Vitali, Mária Kun, Borbála Cseh, Máté Krezinger, Levente Kriskovics, András Ordasi, András Pál, Róbert Szakáts, Krisztián Vida, and József Vinkó (Dec. 2022). "Photometric and Spectroscopic Study of the EXor-like Eruptive Young Star Gaia19fct." In: *ApJ* 941.2, 165, p. 165. DOI: 10.3847/1538-4357/aca01e. arXiv: 2211.02137 [astro-ph.SR].

Park, Sunkyung, Jeong-Eun Lee, Tae-Soo Pyo, Daniel T. Jaffe, Gregory N. Mace, Hyun-Il Sung, Sang-Gak Lee, Wonseok Kang, Hyung-Il Oh, Tae Seog Yoon, Sung-Yong Yoon, and Joel D. Green (Aug. 2020). "High-resolution Spectroscopic Monitoring Observations of FU Orionis–type Object, V960 Mon." en. In: *ApJ* 900.1. Publisher: American Astronomical Society, p. 36. ISSN: 0004-637X. DOI: 10.3847/1538-4357/aba532. URL: https://doi.org/10.3847/1538-4357/aba532 (visited on 02/18/2021).

Pascucci, I., S. Cabrit, S. Edwards, U. Gorti, O. Gressel, and T. K. Suzuki (July 2023). "The Role of Disk Winds in the Evolution and Dispersal of Protoplanetary Disks." In: *Astronomical Society of the Pacific Conference Series*. Ed. by S. Inutsuka, Y. Aikawa, T. Muto, K. Tomida, and M. Tamura. Vol. 534. Astronomical Society of the Pacific Conference Series, p. 567.

Pavlyuchenkov, Ya. N., A. V. Tutukov, L. A. Maksimova, and E. I. Vorobyov (Mar. 2020). "Evolution of a Viscous Protoplanetary Disk with Convectively Unstable Regions." In: *Astronomy Reports* 64.1, pp. 1–14. DOI: 10.1134/S1063772920010060. arXiv: 1912.08572 [astro-ph.SR].

Pérez, Sebastián, Antonio Hales, Hauyu Baobab Liu, Zhaohuan Zhu, Simon Casassus, Jonathan Williams, Alice Zurlo, Nicolás Cuello, Lucas Cieza, and David Principe (Jan. 2020). "Resolving the FU Orionis System with ALMA: Interacting Twin Disks?" In: *ApJ* 889.1, 59, p. 59. DOI: 10.3847/1538-4357/ab5c1b. arXiv: 1911.11282 [astro-ph.EP].

Petrov, P. P. and G. H. Herbig (Aug. 2008). "Line Structure in the Spectrum of FU Orionis." In: *AJ* 136.2, pp. 676–683. DOI: 10.1088/0004-6256/136/2/676. arXiv: 0806.4053 [astro-ph].

Petrov, P. P., R. Kurosawa, M. M. Romanova, J. F. Gameiro, M. Fernandez, E. V. Babina, and S. A. Artemenko (Aug. 2014). "Facing the wind of the pre-FUor V1331 Cyg." In: *MNRAS* 442.4, pp. 3643–3652. DOI: 10.1093/mnras/stu1131. arXiv: 1406.1660 [astro-ph.SR].

Pickering, Edward Charles (Jan. 1890). "Detection of new nebulae by photography." In: *Annals of Harvard College Observatory* 18.6, pp. 113–117.

Pittman, Caeley V., C. C. Espaillat, Connor E. Robinson, Thanawuth Thanathibodee, Sophia Lopez, Nuria Calvet, Zhaohuan Zhu, Frederick M. Walter, John Wendeborn, Carlo Felice Manara, Justyn Campbell-White, Rik A. Claes, Min

Fang, Antonio Frasca, J. F. Gameiro, Manuele Gangi, Jesus Hernández, Ágnes Kóspál, Karina Maucó, James Muzerolle, Michał Siwak, Łukasz Tychoniec, and Laura Venuti (July 2025). "The ODYSSEUS Survey. Characterizing magnetospheric geometries and hotspot structures in T Tauri stars." In: *arXiv e-prints*, arXiv:2507.01162, arXiv:2507.01162. DOI: 10.48550/arXiv.2507.01162. arXiv: 2507.01162 [astro-ph.SR].

Pittman, Caeley V., Catherine C. Espaillat, Connor E. Robinson, Thanawuth Thanathibodee, Nuria Calvet, John Wendeborn, Jesus Hernández, Carlo F. Manara, Fred Walter, Péter Ábrahám, Juan M. Alcalá, Sílvia H. P. Alencar, Nicole Arulanantham, Sylvie Cabrit, Jochen Eislöffel, Eleonora Fiorellino, Kevin France, Manuele Gangi, Konstantin Grankin, Gregory J. Herczeg, Ágnes Kóspál, Ignacio Mendigutía, Javier Serna, and Laura Venuti (Nov. 2022). "Towards a Comprehensive View of Accretion, Inner Disks, and Extinction in Classical T Tauri Stars: An ODYSSEUS Study of the Orion OB1b Association." In: *AJ* 164.5, 201, p. 201. DOI: 10.3847/1538-3881/ac898d. arXiv: 2208.04986 [astro-ph.SR].

Pontoppidan, Klaus M., Colette Salyk, Andrea Banzatti, Ke Zhang, Ilaria Pascucci, Karin I. Öberg, Feng Long, Carlos E. Romero-Mirza, John Carr, Joan Najita, Geoffrey A. Blake, Nicole Arulanantham, Sean Andrews, Nicholas P. Ballering, Edwin Bergin, Jenny Calahan, Douglas Cobb, Maria Jose Colmenares, Annie Dickson-Vandervelde, Anna Dignan, Joel Green, Phoebe Heretz, Gregory Herczeg, Anusha Kalyaan, Sebastiaan Krijt, Tyler Pauly, Paola Pinilla, Leon Trapman, and Chengyan Xie (Mar. 2024). "High-contrast JWST-MIRI Spectroscopy of Planet-forming Disks for the JDISC Survey." In: *ApJ* 963.2, 158, p. 158. DOI: 10.3847/1538-4357/ad20f0. arXiv: 2311.17020 [astro-ph.EP].

Popham, Robert, Scott Kenyon, Lee Hartmann, and Ramesh Narayan (Dec. 1996). "Spectra and Line Profiles of FU Orionis Objects: Comparisons between Boundary Layer Models and Observations." In: *ApJ* 473, p. 422. DOI: 10.1086/178155. arXiv: astro-ph/9606111 [astro-ph].

Popham, Robert, Ramesh Narayan, Lee Hartmann, and Scott Kenyon (Oct. 1993). "Boundary Layers in Pre-Main-Sequence Accretion Disks." In: *ApJL* 415, p. L127. DOI: 10.1086/187049.

Pourré, N. et al. (June 2024). "High contrast at short separation with VLTI/GRAVITY: Bringing Gaia companions to light." In: *A&A* 686, A258, A258. DOI: 10.1051/0004-6361/202449507. arXiv: 2406.04003 [astro-ph.IM].

Pringle, J. E. (Jan. 1981). "Accretion discs in astrophysics." In: *ARA&A* 19, pp. 137–162. DOI: 10.1146/annurev.aa.19.090181.001033.

Prochaska, J., Joseph Hennawi, Kyle Westfall, Ryan Cooke, Feige Wang, Tiffany Hsyu, Frederick Davies, Emanuele Farina, and Debora Pelliccia (Dec. 2020). "PypeIt: The Python Spectroscopic Data Reduction Pipeline." In: *The Journal of Open Source Software* 5.56, 2308, p. 2308. DOI: 10.21105/joss.02308. arXiv: 2005.06505 [astro-ph.IM].

Pueyo, Laurent, Lynne Hillenbrand, Gautam Vasisht, Ben R. Oppenheimer, John D. Monnier, Sasha Hinkley, Justin Crepp, Jr. Roberts Lewis C., Douglas Brenner, Neil Zimmerman, Ian Parry, Charles Beichman, Richard Dekany, Mike Shao, Rick Burruss, Eric Cady, Jenny Roberts, and Rémi Soummer (Sept. 2012). "Constraining Mass Ratio and Extinction in the FU Orionis Binary System with Infrared Integral Field Spectroscopy." In: *ApJ* 757.1, 57, p. 57. DOI: 10.1088/0004-637X/757/1/57. arXiv: 1211.6741 [astro-ph.SR].

Rau, Arne, Shrinivas R. Kulkarni, Nicholas M. Law, Joshua S. Bloom, David Ciardi, George S. Djorgovski, Derek B. Fox, Avishay Gal-Yam, Carl C. Grillmair, Mansi M. Kasliwal, Peter E. Nugent, Eran O. Ofek, Robert M. Quimby, William T. Reach, Michael Shara, Lars Bildsten, S. Bradley Cenko, Andrew J. Drake, Alexei V. Filippenko, David J. Helfand, George Helou, D. Andrew Howell, Dovi Poznanski, and Mark Sullivan (Dec. 2009). "Exploring the Optical Transient Sky with the Palomar Transient Factory." In: *PASP* 121.886, p. 1334. DOI: 10.1086/605911. arXiv: 0906.5355 [astro-ph.CO].

Rayner, J. T., D. W. Toomey, P. M. Onaka, A. J. Denault, W. E. Stahlberger, W. D. Vacca, M. C. Cushing, and S. Wang (Mar. 2003). "SpeX: A Medium-Resolution 0.8-5.5 Micron Spectrograph and Imager for the NASA Infrared Telescope Facility." In: *PASP* 115.805, pp. 362–382. DOI: 10.1086/367745.

Rayner, John T., Michael C. Cushing, and William D. Vacca (Dec. 2009). "The Infrared Telescope Facility (IRTF) Spectral Library: Cool Stars." In: *ApJS* 185.2, pp. 289–432. DOI: 10.1088/0067-0049/185/2/289. arXiv: 0909.0818 [astro-ph.SR].

Regev, O. (Sept. 1983). "The disk-star boundary layer and its effect on the accretion disk structure." In: *A&A* 126.1, pp. 146–151.

Reipurth, Bo and Colin Aspin (June 2004). "The FU Orionis Binary System and the Formation of Close Binaries." In: *ApJL* 608.1, pp. L65–L68. DOI: 10.1086/422250.

Reipurth, Bo and M. S. Connelley (Jan. 2015). "Infrared Spectroscopy of the FU Orionis Type Object 2MASS J06593158-0405277." In: *The Astronomer's Telegram* 6862, p. 1.

Reipurth, Bo, Lee Hartmann, Scott J. Kenyon, Alain Smette, and Patrice Bouchet (Oct. 2002). "Evolution of the FU Orionis Object BBW 76." In: *The Astronomical Journal* 124, pp. 2194–2206. ISSN: 0004-6256. DOI: 10.1086/342740. URL: http://adsabs.harvard.edu/abs/2002AJ....124.2194R (visited on 02/25/2021).

Riello, M., F. De Angeli, D. W. Evans, P. Montegriffo, J. M. Carrasco, G. Busso, L. Palaversa, P. W. Burgess, C. Diener, M. Davidson, N. Rowell, C. Fabricius, C. Jordi, M. Bellazzini, E. Pancino, D. L. Harrison, C. Cacciari, F. van Leeuwen, N. C. Hambly, S. T. Hodgkin, P. J. Osborne, G. Altavilla, M. A. Barstow, A. G. A. Brown, M. Castellani, S. Cowell, F. De Luise, G. Gilmore, G. Giuffrida, S.

Hidalgo, G. Holland, S. Marinoni, C. Pagani, A. M. Piersimoni, L. Pulone, S. Ragaini, M. Rainer, P. J. Richards, N. Sanna, N. A. Walton, M. Weiler, and A. Yoldas (May 2021). "Gaia Early Data Release 3. Photometric content and validation." In: *A&A* 649, A3, A3. DOI: 10.1051/0004-6361/202039587. arXiv: 2012.01916 [astro-ph.IM].

Rockosi, C., R. Stover, R. Kibrick, C. Lockwood, M. Peck, D. Cowley, M. Bolte, S. Adkins, B. Alcott, S. L. Allen, B. Brown, G. Cabak, W. Deich, D. Hilyard, M. Kassis, K. Lanclos, J. Lewis, T. Pfister, A. Phillips, L. Robinson, M. Saylor, M. Thompson, J. Ward, M. Wei, and C. Wright (July 2010). "The low-resolution imaging spectrograph red channel CCD upgrade: fully depleted, high-resistivity CCDs for Keck." In: *Ground-based and Airborne Instrumentation for Astronomy III*. Ed. by Ian S. McLean, Suzanne K. Ramsay, and Hideki Takami. Vol. 7735. Society of Photo-Optical Instrumentation Engineers (SPIE) Conference Series, 77350R, 77350R. DOI: 10.1117/12.856818.

Rodriguez, Antonio C. and Lynne A. Hillenbrand (Mar. 2022). "Application of a Steady-state Accretion Disk Model to Spectrophotometry and High-resolution Spectra of Two Recent FU Ori Outbursts." In: *ApJ* 927.2, 144, p. 144. DOI: 10.3847/1538-4357/ac496b. arXiv: 2112.01549 [astro-ph.SR].

Roman-Duval, Julia, William J. Fischer, Alexander W. Fullerton, Jo Taylor, Rachel Plesha, Charles Proffitt, TalaWanda Monroe, Travis C. Fischer, Alessandra Aloisi, Jean-Claude Bouret, Christopher Britt, Nuria Calvet, Joleen K. Carlberg, Paul A. Crowther, Gisella De Rosa, William V. Dixon, Catherine C. Espaillat, Christopher J. Evans, Andrew J. Fox, Kevin France, Miriam Garcia, Scott W. Fleming, Elaine M. Frazer, Ana I. Gómez de Castro, Gregory J. Herczeg, Svea Hernandez, Alec S. Hirschauer, Bethan L. James, Christopher M. Johns-Krull, Claus Leitherer, Sean Lockwood, Joan Najita, M. S. Oey, Cristina Oliveira, Tyler Pauly, I. Neill Reid, Adric Riedel, David R. Rodriguez, David Sahnow, Ravi Sankrit, Kenneth R. Sembach, Richard Shaw, Linda J. Smith, S. Tony Sohn, Debopam Som, Leonardo Úbeda, and Daniel E. Welty (May 2025). "The UV Legacy Library of Young Stars as Essential Standards (ULLYSES) Large Director's Discretionary Program with Hubble. I. Goals, Design, and Initial Results." In: *ApJ* 985.1, 109, p. 109. DOI: 10.3847/1538-4357/adc45b. arXiv: 2504.05446 [astro-ph.SR].

Roychowdhury, Tamojeet and Lynne A. Hillenbrand (June 2024a). "Kinematic Association of Two FU Orionis Stars with Young Clusters in Orion." In: *RNAAS* 8.6, 171, p. 171. DOI: 10.3847/2515-5172/ad5a9c.

– (June 2024b). "Kinematic Association of Two FU Orionis Stars with Young Clusters in Orion." In: *RNAAS* 8.6, 171, p. 171. DOI: 10.3847/2515-5172/ad5a9c.

Ruíz-Rodríguez, D., L. A. Cieza, J. P. Williams, D. Principe, J. J. Tobin, Z. Zhu, and A. Zurlo (July 2017). "The ALMA early science view of FUor/EXor objects - III. The slow and wide outflow of V883 Ori." In: *MNRAS* 468.3, pp. 3266–3276. DOI: 10.1093/mnras/stx703. arXiv: 1703.07006 [astro-ph.SR].

Ryabchikova, T., N. Piskunov, R. L. Kurucz, H. C. Stempels, U. Heiter, Yu Pakhomov, and P. S. Barklem (May 2015). "A major upgrade of the VALD database." In: *Physica Scripta* 90.5, 054005, p. 054005. DOI: 10.1088/0031-8949/90/5/054005.

Saito, R. K. et al. (Sept. 2024). "The VISTA Variables in the Vía Láctea extended (VVVX) ESO public survey: Completion of the observations and legacy." In: *A&A* 689, A148, A148. DOI: 10.1051/0004-6361/202450584. arXiv: 2406.16646 [astro-ph.GA].

Schoonenberg, Djoeke, Satoshi Okuzumi, and Chris W. Ormel (Sept. 2017). "What pebbles are made of: Interpretation of the V883 Ori disk." In: *A&A* 605, L2, p. L2. DOI: 10.1051/0004-6361/201731202. arXiv: 1708.03328 [astro-ph.EP].

Semkov, E. and S. Peneva (Aug. 2010). "A possible new FUor star in NGC 7000." In: *The Astronomer's Telegram* 2801, p. 1.

Semkov, E. H., S. P. Peneva, U. Munari, M. Dennefeld, H. Mito, D. P. Dimitrov, S. Ibryamov, and K. A. Stoyanov (Aug. 2013). "Photometric and spectroscopic variability of the FUor star V582 Aurigae." en. In: *Astronomy & Astrophysics* 556. Publisher: EDP Sciences, A60. ISSN: 0004-6361, 1432-0746. DOI: 10.1051/0004-6361/201321732. URL: https://www.aanda.org/articles/aa/abs/2013/08/aa21732-13/aa21732-13.html (visited on 02/19/2021).

Semkov, Evgeni, Sunay Ibryamov, and Stoyanka Peneva (Dec. 2021). "The FUor Star V2493 Cyg (HBC 722)—Eleven Years at Maximum Brightness." In: *Symmetry* 13.12, p. 2433. DOI: 10.3390/sym13122433. arXiv: 2112.09406 [astro-ph.SR].

Shakura, N. I. and R. A. Sunyaev (Jan. 1973). "Black holes in binary systems. Observational appearance." In: *A&A* 24, pp. 337–355.

Shappee, B. J., J. L. Prieto, D. Grupe, C. S. Kochanek, K. Z. Stanek, G. De Rosa, S. Mathur, Y. Zu, B. M. Peterson, R. W. Pogge, S. Komossa, M. Im, J. Jencson, T. W.-S. Holoien, U. Basu, J. F. Beacom, D. M. Szczygieł, J. Brimacombe, S. Adams, A. Campillay, C. Choi, C. Contreras, M. Dietrich, M. Dubberley, M. Elphick, S. Foale, M. Giustini, C. Gonzalez, E. Hawkins, D. A. Howell, E. Y. Hsiao, M. Koss, K. M. Leighly, N. Morrell, D. Mudd, D. Mullins, J. M. Nugent, J. Parrent, M. M. Phillips, G. Pojmanski, W. Rosing, R. Ross, D. Sand, D. M. Terndrup, S. Valenti, Z. Walker, and Y. Yoon (June 2014a). "The Man behind the Curtain: X-Rays Drive the UV through NIR Variability in the 2013 Active Galactic Nucleus Outburst in NGC 2617." In: *ApJ* 788.1, 48, p. 48. DOI: 10.1088/0004-637X/788/1/48. arXiv: 1310.2241 [astro-ph.HE].

– (June 2014b). "The Man behind the Curtain: X-Rays Drive the UV through NIR Variability in the 2013 Active Galactic Nucleus Outburst in NGC 2617." In: *ApJ* 788.1, 48, p. 48. DOI: 10.1088/0004-637X/788/1/48. arXiv: 1310.2241 [astro-ph.HE].

Sheehan, Patrick D., John J. Tobin, Leslie W. Looney, and S. Thomas Megeath (Apr. 2022). "The VLA/ALMA Nascent Disk and Multiplicity (VANDAM) Survey of Orion Protostars. VI. Insights from Radiative Transfer Modeling." In: *ApJ* 929.1, 76, p. 76. DOI: 10.3847/1538-4357/ac574d. arXiv: 2203.00029 [astro-ph.SR].

Sicilia-Aguilar, A., Á. Kóspál, J. Setiawan, P. Ábrahám, C. Dullemond, C. Eiroa, M. Goto, Th. Henning, and A. Juhász (Aug. 2012). "Optical spectroscopy of EX Lupi during quiescence and outburst. Infall, wind, and dynamics in the accretion flow." In: *A&A* 544, A93, A93. DOI: 10.1051/0004-6361/201118555. arXiv: 1206.3081 [astro-ph.SR].

Sicilia-Aguilar, Aurora, Min Fang, Veronica Roccatagliata, Andrew Collier Cameron, Ágnes Kóspál, Thomas Henning, Peter Ábrahám, and Nikoletta Sipos (Aug. 2015). "Accretion dynamics of EX Lupi in quiescence. The star, the spot, and the accretion column." In: *A&A* 580, A82, A82. DOI: 10.1051/0004-6361/201525970. arXiv: 1505.08011 [astro-ph.SR].

Simões, Paulo J. A., Alexandre Araújo, Adriana Válio, and Lyndsay Fletcher (Feb. 2024). "Hydrogen recombination continuum as the radiative model for stellar optical flares." In: *MNRAS* 528.2, pp. 2562–2567. DOI: 10.1093/mnras/stae186. arXiv: 2401.07824 [astro-ph.SR].

Siwak, Michał, Lynne A. Hillenbrand, Ágnes Kóspál, Péter Ábrahám, Teresa Giannini, Kishalay De, Attila Moór, Máté Szilágyi, Jan Janík, Chris Koen, Sunkyung Park, Zsófia Nagy, Fernando Cruz-Sáenz de Miera, Eleonora Fiorellino, Gábor Marton, Mária Kun, Philip W. Lucas, Andrzej Udalski, and Zsófia Marianna Szabó (Oct. 2023). "Gaia21bty: An EXor light curve exhibiting a FUor spectrum." In: *MNRAS* 524.4, pp. 5548–5565. DOI: 10.1093/mnras/stad2135. arXiv: 2307.08802 [astro-ph.SR].

Siwak, Michał, Waldemar Ogłoza, and Jerzy Krzesiński (Dec. 2020). "Disc light variability in the FUor star V646 Puppis as observed by TESS and from the ground." In: *A&A* 644, A135, A135. DOI: 10.1051/0004-6361/202037607. arXiv: 2011.00254 [astro-ph.SR].

Skinner, Stephen L., Manuel Güdel, Kevin R. Briggs, and Sergei A. Lamzin (Oct. 2010). "Chandra Reveals Variable Multi-component X-ray Emission From FU Orionis." In: *ApJ* 722.2, pp. 1654–1665. DOI: 10.1088/0004-637X/722/2/1654. arXiv: 1008.4090 [astro-ph.SR].

Speagle, Joshua S. (Apr. 2020). "DYNESTY: a dynamic nested sampling package for estimating Bayesian posteriors and evidences." In: *MNRAS* 493.3, pp. 3132–3158. DOI: 10.1093/mnras/staa278. arXiv: 1904.02180 [astro-ph.IM].

Strom, Karen M. and Stephen E. Strom (Aug. 1993). "The Discovery of Two FU Orionis Objects in L1641." In: *ApJL* 412, p. L63. DOI: 10.1086/186941. arXiv: astro-ph/9305012 [astro-ph].

Szabó, Zs. M., A. Belloche, K. M. Menten, Y. Gong, Á. Kóspál, P. Ábrahám, W. Yang, C. J. Cyganowski, and F. Wyrowski (Feb. 2025). "Molecular inventory of the environment of a young eruptive star: Case study of the classical FU Orionis star V1057 Cyg." In: *A&A* 694, A329, A329. DOI: 10.1051/0004-6361/202451851. arXiv: 2501.14553 [astro-ph.SR].

Szabó, Zs. M., Y. Gong, K. M. Menten, W. Yang, C. J. Cyganowski, Á. Kóspál, P. Ábrahám, A. Belloche, and F. Wyrowski (Apr. 2023). "The Effelsberg survey of FU Orionis and EX Lupi objects. I. Host environments of FUors and EXors traced by NH_3." In: *A&A* 672, A158, A158. DOI: 10.1051/0004-6361/202244911. arXiv: 2302.03371 [astro-ph.SR].

Szabó, Zs. M., Á. Kóspál, P. Ábrahám, S. Park, M. Siwak, J. D. Green, A. Moór, A. Pál, J. A. Acosta-Pulido, J. -E. Lee, B. Cseh, G. Csörnyei, O. Hanyecz, R. Könyves-Tóth, M. Krezinger, L. Kriskovics, A. Ordasi, K. Sárneczky, B. Seli, R. Szakáts, A. Szing, and K. Vida (Aug. 2021). "A Study of the Photometric and Spectroscopic Variations of the Prototypical FU Orionis-type Star V1057 Cyg." In: *ApJ* 917.2, 80, p. 80. DOI: 10.3847/1538-4357/ac04b3. arXiv: 2105.10405 [astro-ph.SR].

Szabó, Zs. M., Á. Kóspál, P. Ábrahám, S. Park, M. Siwak, J. D. Green, A. Pál, J. A. Acosta-Pulido, J. -E. Lee, M. Ibrahimov, K. Grankin, B. Kovács, Zs. Bora, A. Bódi, B. Cseh, G. Csörnyei, Marek Dróżdż, O. Hanyecz, B. Ignácz, Cs. Kalup, R. Könyves-Tóth, M. Krezinger, L. Kriskovics, Waldemar Ogłoza, A. Ordasi, K. Sárneczky, B. Seli, R. Szakáts, Á. Sódor, A. Szing, K. Vida, and J. Vinkó (Sept. 2022a). "A Multi-epoch, Multiwavelength Study of the Classical FUor V1515 Cyg Approaching Quiescence." In: *ApJ* 936.1, 64, p. 64. DOI: 10.3847/1538-4357/ac82f5. arXiv: 2206.12446 [astro-ph.SR].

– (Sept. 2022b). "A Multi-epoch, Multiwavelength Study of the Classical FUor V1515 Cyg Approaching Quiescence." In: *ApJ* 936.1, 64, p. 64. DOI: 10.3847/1538-4357/ac82f5. arXiv: 2206.12446 [astro-ph.SR].

Takasao, Shinsuke, Takashi Hosokawa, Kengo Tomida, and Kazunari Iwasaki (May 2025). "Connecting a Magnetized Disk to a Convective Low-mass Protostar: A Global 3D Model of Boundary Layer Accretion." In: *ApJ* 985.1, 16, p. 16. DOI: 10.3847/1538-4357/adc37b. arXiv: 2503.15350 [astro-ph.SR].

Tobin, John J., Merel L. R. van't Hoff, Margot Leemker, Ewine F. van Dishoeck, Teresa Paneque-Carreño, Kenji Furuya, Daniel Harsono, Magnus V. Persson, L. Ilsedore Cleeves, Patrick D. Sheehan, and Lucas Cieza (Mar. 2023). "Deuterium-enriched water ties planet-forming disks to comets and protostars." In: *Nature* 615.7951, pp. 227–230. DOI: 10.1038/s41586-022-05676-z.

Tran, Vinh, Kishalay De, and Lynne Hillenbrand (May 2024). "WTP 10aaauow: discovery of a new FU Ori outburst towards the RCW 49 star-forming region in NEOWISE data." In: *MNRAS* 530.2, pp. 2076–2086. DOI: 10.1093/mnras/stae953. arXiv: 2310.10832 [astro-ph.SR].

Travis, Larry D. and Satoshi Matsushima (Nov. 1968). "Radiative Opacity in Stellar Atmospheres. I. Metal Absorption Coefficients." In: *ApJ* 154, p. 689. DOI: 10.1086/149790.

Uchida, Y. and K. Shibata (Jan. 1984). "Magnetically buffered accretion to a young star and the formation of bipolar flows." In: *PASJ* 36, pp. 105–118.

Vacca, William D., Michael C. Cushing, and John T. Rayner (Mar. 2003). "A Method of Correcting Near-Infrared Spectra for Telluric Absorption." In: *PASP* 115.805, pp. 389–409. DOI: 10.1086/346193. arXiv: astro-ph/0211255 [astro-ph].

Valenti, Jeff A., Gibor Basri, and Christopher M. Johns (Nov. 1993). "T Tauri Stars in Blue." In: *AJ* 106, p. 2024. DOI: 10.1086/116783.

Valenti, Jeff A., Christopher M. Johns-Krull, and Jeffrey L. Linsky (July 2000). "An IUE Atlas of Pre-Main-Sequence Stars. I. Co-added Final Archive Spectra from the SWP Camera." In: *ApJ Supplement Series* 129.1, pp. 399–420. DOI: 10.1086/313408.

van 't Hoff, Merel L. R., John J. Tobin, Leon Trapman, Daniel Harsono, Patrick D. Sheehan, William J. Fischer, S. Thomas Megeath, and Ewine F. van Dishoeck (Sept. 2018). "Methanol and its Relation to the Water Snowline in the Disk around the Young Outbursting Star V883 Ori." In: *ApJL* 864.1, L23, p. L23. DOI: 10.3847/2041-8213/aadb8a. arXiv: 1808.08258 [astro-ph.SR].

Vogt, S. S., S. L. Allen, B. C. Bigelow, L. Bresee, B. Brown, T. Cantrall, A. Conrad, M. Couture, C. Delaney, H. W. Epps, D. Hilyard, D. F. Hilyard, E. Horn, N. Jern, D. Kanto, M. J. Keane, R. I. Kibrick, J. W. Lewis, J. Osborne, G. H. Pardeilhan, T. Pfister, T. Ricketts, L. B. Robinson, R. J. Stover, D. Tucker, J. Ward, and M. Z. Wei (June 1994). "HIRES: the high-resolution echelle spectrometer on the Keck 10-m Telescope." In: *Instrumentation in Astronomy VIII*. Ed. by David L. Crawford and Eric R. Craine. Vol. 2198. Society of Photo-Optical Instrumentation Engineers (SPIE) Conference Series, p. 362. DOI: 10.1117/12.176725.

Vorobyov, Eduard I., Vardan G. Elbakyan, Hauyu Baobab Liu, and Michihiro Takami (Mar. 2021). "Distinguishing between different mechanisms of FU-Orionis-type luminosity outbursts." In: *A&A* 647, A44, A44. DOI: 10.1051/0004-6361/202039391. arXiv: 2101.01596 [astro-ph.SR].

Wachmann, A. (Jan. 1954). "Das bisherige Verhalten von FU Orionis. Mit 7 Textabbildungen." In: *Zeitschrift fur Astrophysik* 35, p. 74.

Wang, Hongchi, Dániel Apai, Thomas Henning, and Ilaria Pascucci (Jan. 2004). "FU Orionis: A Binary Star?" In: *ApJL* 601.1, pp. L83–L86. DOI: 10.1086/381705. arXiv: astro-ph/0311606 [astro-ph].

Wang, Mu-Tian, Gregory J. Herczeg, Hui-Gen Liu, Min Fang, Doug Johnstone, Ho-Gyu Lee, Frederick M. Walter, Franz-Josef Hambsch, Carlos Contreras Peña, Jeong-Eun Lee, Mervyn Millward, Andrew Pearce, Berto Monard, and Lihang Zhou (Nov. 2023). "The Accretion History of EX Lup: A Century of Bursts,

Outbursts, and Quiescence." In: *ApJ* 957.2, 113, p. 113. DOI: 10.3847/1538-4357/acf2f4. arXiv: 2308.11895 [astro-ph.SR].

Waters, C. Z., E. A. Magnier, P. A. Price, K. C. Chambers, W. S. Burgett, P. W. Draper, H. A. Flewelling, K. W. Hodapp, M. E. Huber, R. Jedicke, N. Kaiser, R. -P. Kudritzki, R. H. Lupton, N. Metcalfe, A. Rest, W. E. Sweeney, J. L. Tonry, R. J. Wainscoat, and W. M. Wood-Vasey (Nov. 2020). "Pan-STARRS Pixel Processing: Detrending, Warping, Stacking." In: *ApJS* 251.1, 4, p. 4. DOI: 10.3847/1538-4365/abb82b. arXiv: 1612.05245 [astro-ph.IM].

Weber, Philipp, Sebastián Pérez, Greta Guidi, Nicolás T. Kurtovic, Alice Zurlo, Antonio Garufi, Paola Pinilla, Satoshi Mayama, Rob G. van Holstein, Cornelis P. Dullemond, Nicolás Cuello, David Principe, Lucas Cieza, Camilo González-Ruilova, and Julien Girard (Feb. 2023). "The SPHERE view of three interacting twin disc systems in polarized light." In: *MNRAS* 518.4, pp. 5620–5642. DOI: 10.1093/mnras/stac3478. arXiv: 2211.14322 [astro-ph.SR].

Weber, Philipp, Sebastián Pérez, Alice Zurlo, James Miley, Antonio Hales, Lucas Cieza, David Principe, Miguel Cárcamo, Antonio Garufi, Ágnes Kóspál, Michihiro Takami, Joel Kastner, Zhaohuan Zhu, and Jonathan Williams (July 2023a). "Spirals and Clumps in V960 Mon: Signs of Planet Formation via Gravitational Instability around an FU Ori Star?" In: *ApJL* 952.1, L17, p. L17. DOI: 10.3847/2041-8213/ace186. arXiv: 2307.13433 [astro-ph.EP].

– (July 2023b). "Spirals and Clumps in V960 Mon: Signs of Planet Formation via Gravitational Instability around an FU Ori Star?" In: *ApJL* 952.1, L17, p. L17. DOI: 10.3847/2041-8213/ace186. arXiv: 2307.13433 [astro-ph.EP].

Welty, Alan D., Stephen E. Strom, Suzan Edwards, Scott J. Kenyon, and Lee W. Hartmann (Sept. 1992). "Optical Spectroscopy of Z Canis Majoris, V1057 Cygni, and FU Orionis: Accretion Disks and Signatures of Disk Winds." In: *ApJ* 397, p. 260. DOI: 10.1086/171785.

Welty, Alan D., Stephen E. Strom, Karen M. Strom, Lee W. Hartmann, Scott J. Kenyon, Gary L. Grasdalen, and John R. Stauffer (Jan. 1990). "Further Evidence for Differential Rotation in V1057 Cygni." In: *ApJ* 349, p. 328. DOI: 10.1086/168316.

Whelan, E. T., I. Pascucci, U. Gorti, S. Edwards, R. D. Alexander, M. F. Sterzik, and C. Melo (May 2021). "Evidence for an MHD Disk Wind via Optical Forbidden Line Spectroastrometry." In: *ApJ* 913.1, 43, p. 43. DOI: 10.3847/1538-4357/abf55e. arXiv: 2104.05561 [astro-ph.SR].

Whittet, D. C. B., S. S. Shenoy, Geoffrey C. Clayton, and Karl D. Gordon (Feb. 2004). "The Ultraviolet Extinction Curve of Intraclump Dust in Taurus (TMC-1): Constraints on the 2175 Å Bump Absorber." In: *ApJ* 602.1, pp. 291–297. DOI: 10.1086/380837.

Williams, Jonathan P. and Conor McPartland (Oct. 2016). "Measuring Protoplanetary Disk Gas Surface Density Profiles with ALMA." In: *ApJ* 830.1, 32, p. 32. DOI: 10.3847/0004-637X/830/1/32. arXiv: 1606.05646 [astro-ph.GA].

Willmer, Christopher N. A. (June 2018). "The Absolute Magnitude of the Sun in Several Filters." In: *ApJS* 236.2, 47, p. 47. DOI: 10.3847/1538-4365/aabfdf. arXiv: 1804.07788 [astro-ph.SR].

Wils, P., J. Greaves, M. Catelan, S. G. Djorgovski, A. J. Drake, M. J. Graham, A. A. Mahabal, R. Williams, E. C. Beshore, S. M. Larson, and E. Christensen (Nov. 2009). "Discovery of a likely FU-Ori-type system." In: *The Astronomer's Telegram* 2307, p. 1.

Wolff, Schuyler G., Marshall D. Perrin, Karl Stapelfeldt, Gaspard Duchêne, Francois Ménard, Deborah Padgett, Christophe Pinte, Laurent Pueyo, and William J. Fischer (Dec. 2017). "Hubble Space Telescope Scattered-light Imaging and Modeling of the Edge-on Protoplanetary Disk ESO-Hα 569." In: *ApJ* 851.1, 56, p. 56. DOI: 10.3847/1538-4357/aa9981. arXiv: 1711.03322 [astro-ph.SR].

Wright, Edward L., Peter R. M. Eisenhardt, Amy K. Mainzer, Michael E. Ressler, Roc M. Cutri, Thomas Jarrett, J. Davy Kirkpatrick, Deborah Padgett, Robert S. McMillan, Michael Skrutskie, S. A. Stanford, Martin Cohen, Russell G. Walker, John C. Mather, David Leisawitz, Thomas N. Gautier III, Ian McLean, Dominic Benford, Carol J. Lonsdale, Andrew Blain, Bryan Mendez, William R. Irace, Valerie Duval, Fengchuan Liu, Don Royer, Ingolf Heinrichsen, Joan Howard, Mark Shannon, Martha Kendall, Amy L. Walsh, Mark Larsen, Joel G. Cardon, Scott Schick, Mark Schwalm, Mohamed Abid, Beth Fabinsky, Larry Naes, and Chao-Wei Tsai (Dec. 2010). "The Wide-field Infrared Survey Explorer (WISE): Mission Description and Initial On-orbit Performance." In: *AJ* 140.6, pp. 1868–1881. DOI: 10.1088/0004-6256/140/6/1868. arXiv: 1008.0031 [astro-ph.IM].

Xiong, D. R. and L. Deng (June 2009). "Lithium depletion in late-type dwarfs." In: *MNRAS* 395.4, pp. 2013–2028. DOI: 10.1111/j.1365-2966.2009.14581.x.

Xu, Ziyan, Gregory J. Herczeg, Christopher M. Johns-Krull, and Kevin France (Nov. 2021a). "Probing Protoplanetary Disk Winds with C II Absorption." In: *ApJ* 921.2, 181, p. 181. DOI: 10.3847/1538-4357/ac1739. arXiv: 2107.11188 [astro-ph.SR].

– (Nov. 2021b). "Probing Protoplanetary Disk Winds with C II Absorption." In: *ApJ* 921.2, 181, p. 181. DOI: 10.3847/1538-4357/ac1739. arXiv: 2107.11188 [astro-ph.SR].

Yang, Hao, Gregory J. Herczeg, Jeffrey L. Linsky, Alexander Brown, Christopher M. Johns-Krull, Laura Ingleby, Nuria Calvet, Edwin Bergin, and Jeff A. Valenti (Jan. 2012). "A Far-ultraviolet Atlas of Low-resolution Hubble Space Telescope Spectra of T Tauri Stars." In: *ApJ* 744.2, 121, p. 121. DOI: 10.1088/0004-637X/744/2/121. arXiv: 1205.4789 [astro-ph.SR].

Ysard, N., A. P. Jones, K. Demyk, T. Boutéraon, and M. Koehler (Sept. 2018). "The optical properties of dust: the effects of composition, size, and structure." In: *A&A* 617, A124, A124. DOI: 10.1051/0004-6361/201833386. arXiv: 1806.05420 [astro-ph.GA].

Zhang, Ruoyi and Haibo Yuan (Jan. 2023). "Empirical Temperature- and Extinction-dependent Extinction Coefficients for the GALEX, Pan-STARRS 1, Gaia, SDSS, 2MASS, and WISE Passbands." In: *ApJS* 264.1, 14, p. 14. DOI: 10.3847/1538-4365/ac9dfa. arXiv: 2210.15918 [astro-ph.GA].

Zhang, Xiangyu and Gregory M. Green (Mar. 2025). "Three-dimensional maps of the interstellar dust extinction curve within the Milky Way galaxy." In: *Science* 387.6739, pp. 1209–1214. DOI: 10.1126/science.ado9787. arXiv: 2407.14594 [astro-ph.GA].

Zhu, Zhaohuan, Catherine Espaillat, Kenneth Hinkle, Jesus Hernandez, Lee Hartmann, and Nuria Calvet (Mar. 2009a). "The Differential Rotation of FU Ori." In: *ApJL* 694.1, pp. L64–L68. DOI: 10.1088/0004-637X/694/1/L64. arXiv: 0902.4469 [astro-ph.SR].

– (Mar. 2009b). "The Differential Rotation of FU Ori." In: *ApJL* 694.1, pp. L64–L68. DOI: 10.1088/0004-637X/694/1/L64. arXiv: 0902.4469 [astro-ph.SR].

Zhu, Zhaohuan, Lee Hartmann, Nuria Calvet, Jesus Hernandez, James Muzerolle, and Ajay-Kumar Tannirkulam (Nov. 2007). "The Hot Inner Disk of FU Orionis." In: *ApJ* 669.1, pp. 483–492. DOI: 10.1086/521345. arXiv: 0707.3429 [astro-ph].

Zhu, Zhaohuan, Yan-Fei Jiang, and James M. Stone (Jan. 2020). "Global 3D radiation magnetohydrodynamic simulations for FU Ori's accretion disc and observational signatures of magnetic fields." In: *MNRAS* 495.3, pp. 3494–3514. DOI: 10.1093/mnras/staa952. arXiv: 1912.01632 [astro-ph.EP].

Zhu, Zhaohuan and James M. Stone (Apr. 2018). "Global Evolution of an Accretion Disk with a Net Vertical Field: Coronal Accretion, Flux Transport, and Disk Winds." In: *ApJ* 857.1, 34, p. 34. DOI: 10.3847/1538-4357/aaafc9. arXiv: 1701.04627 [astro-ph.EP].

Zhu, Zhaohuan, James M. Stone, and Nuria Calvet (Feb. 2024). "A global 3D simulation of magnetospheric accretion - I. Magnetically disrupted discs and surface accretion." In: *MNRAS* 528.2, pp. 2883–2911. DOI: 10.1093/mnras/stad3712. arXiv: 2309.15318 [astro-ph.SR].

Zucker, S. (July 2003). "Cross-correlation and maximum-likelihood analysis: a new approach to combining cross-correlation functions." In: *MNRAS* 342.4, pp. 1291–1298. DOI: 10.1046/j.1365-8711.2003.06633.x. arXiv: astro-ph/0303426 [astro-ph].

Zurlo, A., P. Weber, S. Pérez, L. Cieza, C. Ginski, R. G. van Holstein, D. Principe, A. Garufi, A. Hales, J. Kastner, E. Rigliaco, G. Ruane, M. Benisty, and C. Manara (June 2024a). "The environment around young eruptive stars. SPHERE/IRDIS polarimetric imaging of seven protostars." In: *A&A* 686, A309, A309. DOI: 10.1051/0004-6361/202348526. arXiv: 2403.12124 [astro-ph.SR].

– (June 2024b). "The environment around young eruptive stars. SPHERE/IRDIS polarimetric imaging of seven protostars." In: *A&A* 686, A309, A309. DOI: 10.1051/0004-6361/202348526. arXiv: 2403.12124 [astro-ph.SR].

Zwicky, Lis, Tamara Molyarova, Vitaly Akimkin, Grigorii V. Smirnov-Pinchukov, Dmitry Semenov, Ágnes Kóspál, and Péter Ábrahám (Jan. 2024). "Observational chemical signatures of the past FU Ori outbursts." In: *MNRAS* 527.3, pp. 7652–7671. DOI: 10.1093/mnras/stad3713. arXiv: 2311.17499 [astro-ph.SR].

Appendix A

ROBUST SUPPORT FOR SEMI-AUTOMATED REDUCTIONS OF KECK/NIRSPEC DATA USING PYPEIT

Carvalho, Adolfo S., Greg Doppmann, Kyle B. Westfall, Debora Pelliccia, J. Xavier Prochaska, Joseph Hennawi, Frederick B. Davies, Max Brodheim, Feige Wang, and Ryan Cooke (Oct. 2024). "Robust Support for Semi-automated Reductions of Keck/NIRSPEC Data Using PypeIt." In: *RNAAS* 8.10, 271, p. 271. DOI: 10.3847/2515-5172/ad8bb5. arXiv: 2410.19991 [astro-ph.IM].

Abstract: We present a data reduction pipeline (DRP) for Keck/NIRSPEC built as an addition to the PypeIt Python package. The DRP is capable of reducing multi-order echelle data taken both before and after the detector upgrade in 2018. As part of developing the pipeline, we implemented major improvements to the capabilities of the PypeIt package, including manual wavelength calibration for multi-order data and new output product that returns a coadded spectrum order-by-order. We also provide a procedure for correcting telluric absorption in NIRSPEC data by using the spectra of telluric standard stars taken near the time of the science spectra. At high resolutions, this is often more accurate than modeling-based approaches.

A.1 Introduction

The high resolution Near InfraRed SPECtrograph (NIRSPEC, McLean et al., 1998) on the W. M. Keck Observatory delivers a resolving power $R \equiv \lambda/\Delta\lambda = 15,000 - 35,000$ from 0.95 to 5.5 μm. Prior to 2018, there were three recommended software options for reducing NIRSPEC data: the IDL package REDSPEC[1], the IRAF package WMKONSPEC[2], and the semi-automated Python pipeline NSDRP[3]. In 2018, the instrument underwent a major detector upgrade, in which the 1024x1024 detector was replaced by a 2048x2048 detector. Post-upgrade, only REDSPEC was updated to reduce the data from the new detector, rendering NSDRP and WMKONSPEC usable only for pre-upgrade data.

In order to enable NIRSPEC users to rapidly reduce new and archival data, we used the existing data reduction pipeline package PypeIt (Prochaska et al., 2020). PypeIt

[1] https://www2.keck.hawaii.edu/inst/nirspec/redspec.html
[2] https://www2.keck.hawaii.edu/inst/nirspec/wmkonspec.html
[3] https://www2.keck.hawaii.edu/koa/nsdrp/nsdrp.html

is a python-based data-reduction package that enables automated processing of raw on-sky observations and calibration data from slit-based spectrographs. Separate workflows are implemented for long-slit, multi-slit, slicer-based integral-field units, and cross-dispersed echelle observations; however, all workflows leverage the same core code to perform common tasks. Instrument-specific code is isolated from the core code in a way that limits the development needed to introduce new spectrographs into the PypeIt architecture. Although *enabling* PypeIt to read and apply its routines to data from additional spectrographs is streamlined, ensuring that the PypeIt reductions are *reliable and robust* requires dedicated development effort.

In this Note, we detail this effort for PypeIt reductions of Keck/NIRSPEC data, applicable to data obtained both before and after the detector upgrade in 2018. The pipeline includes improvements to the main PypeIt code and a procedure for the removal of telluric absorption in NIRSPEC spectra using telluric standard star spectra. The pipeline is available at the PypeIt Github page (`https://github.com/pypeit/PypeIt`) and an example script outlining the telluric removal procedure is provided in the Keck/NIRSPEC instrument webpage and linked in Section A.3.

A.2 Updates to PypeIt

Developing the PypeIt-NIRSPEC module required two major upgrades to the PypeIt main data reduction code. The first, and most impactful, was the expansion of the PypeIt manual wavelength calibration program to operate on echelle data. The second was the construction of a new data structure as a default output for PypeIt reductions of echelle data. Here, we will briefly describe the two upgrades.

The original user-interface-based manual wavelength calibration in PypeIt was written for calibrating only a single trace, which is appropriate in the case of long-slit spectroscopy or for multi-object spectroscopy where each trace is expected to have approximately the same wavelength solution. To wavelength calibrate the multi-trace echelle spectra, the script now iterates through each extracted order, prompts the user to compute a solution for the order through a user-interface, then saves the solution and proceeds to the next order. Upon completing all of the orders, the multi-trace solution is saved so that it may be used for any data set taken with the same grating settings. The script was tested with data and calibrations taken at different times with independent instrument configurations. It can handle spectral shifts and spatial shifts (8 and 25 pix, respectively) typical of the variation in the

positioning accuracy of NIRSPEC's gratings.

The second major update to PypeIt was in the output products. Previously, the final co-added output spectrum, even for high resolution echelle spectrographs, was presented in a single masked vector spanning the entire wavelength range of the spectrum. While this is ideal for low and medium resolution spectroscopy, particularly when the spectra are properly flux-calibrated, this can make working with high resolution spectra challenging. Now, for high resolution echelle spectra, a second output product is offered: the co-added spectrum given as an $N \times M$ array for the N orders of the spectrum and M columns on the detector. This is an output format that is standard in other data reduction pipelines for high resolution spectra, including NSDRP.

A.3 Telluric Contamination Correction

The recommended telluric correction technique for NIRSPEC data is to use standard A0V star spectra taken throughout the night at varying airmasses to ensure accurate removal of atmospheric absorption features. To then remove the telluric features from the observed spectrum requires the following steps:

1. Continuum normalizing the standard star and science target spectra.
2. Fitting and dividing out the stellar photospheric features of the (ideally A0V) standard.
3. Shifting the newly-obtained telluric absorption spectrum to match the science target in case of instrumental wavelength shifts between observations.
4. Uniform scaling the line depths of the telluric absorption spectrum to account for differences in airmass between observations.
5. Dividing the shifted and scaled telluric absorption spectrum from the science target spectrum.

We make use of several tools in the PypeIt package for this procedure, particularly the cross-correlation-based approach used to compute the relative shifts between spectra. A well-documented notebook showing how to extract the output PypeIt data and implement the steps above is provided at `https://www2.keck.hawaii.edu/inst/nirspec/pypeit_nirspec.html` to guide the user. We recommend this as a means of telluric correction, which is based on the popularly-used telluric

correction program in IRAF. An example showcasing the efficacy of our telluric correction is shown in Figure A.1.

In the Y and J bands, observations taken using the thin blocker filter are also subject to severe fringing that is worse in bluer orders. The fringing is stable as a function of wavelength over the course of the night and appears in both the standard and science spectra at the same amplitude relative to continuum. As such, using a standard star for telluric correction in the same night as the observed science target enables easy removal of the fringing as well. This is demonstrated in the case of the J band spectrum presented in Figure A.1.

If standard star observations are not available for a particular night or a desired spectrograph setup, PypeIt offers a modeling-based means of telluric line removal. However, the model-based removal is less reliable at the highest resolutions and performs poorly in Y and J band spectra that have significant fringing.

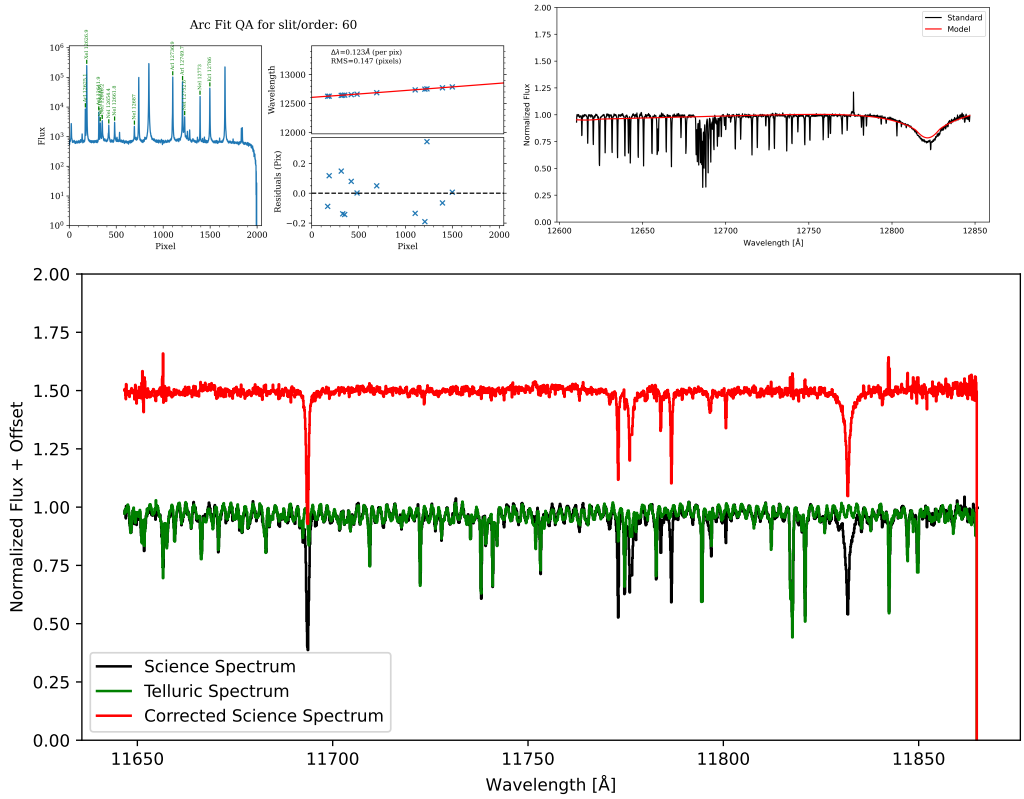

Figure A.1: An example of plots from PypeIt showing major steps in the data reduction process. **Upper Left:** A sample quality assurance plot from the wavelength calibration of Order 60 in the J band. **Upper Right:** Order 60 of the A0V telluric standard spectrum (black) and the PHOENIX model (red) used to remove the Paβ line to produce a telluric absorption spectrum. **Bottom Panel:** A plot of Order 65 of the science spectrum (black), the telluric spectrum (green) and the telluric-corrected spectrum (red). Notice that the fringing is also removed by the division by the telluric absorption spectrum.

Appendix B

A SIMPLE CODE FOR ROTATIONAL BROADENING OF BROAD WAVELENGTH RANGE HIGH-DISPERSION SPECTRA

Carvalho, Adolfo S. and Christopher M. Johns-Krull (May 2023). "A Simple Code for Rotational Broadening of Broad Wavelength Range High-Dispersion Spectra." In: *RNAAS* 7.5, 91, p. 91. DOI: 10.3847/2515-5172/acd37e. arXiv: 2305.09693 [astro-ph.IM].

Abstract: In high dispersion spectra of rotating bodies such as stars and planets, the rotation contributes significantly to, and sometimes dominates, the line broadening. We present a simple method for rotationally broadening large wavelength ranges of high-dispersion spectra. The broadening is rapid and scales linearly with the length of the spectrum array. For large wavelength ranges, the method is much faster than the popular convolution-based broadening. We provide the code implementation of this method in a publicly accessible repository.

B.1 Introduction

As faster and more intricate techniques for fitting and modeling high-dispersion spectra of stars and planets develop, one step in the calculation that is often overlooked is the rotational broadening of templates or models. The rotation of these bodies contributes significantly to the overall line broadening, sometimes dominating over all other broadening mechanisms, so accurately implementing this is crucial to properly modeling spectra. A popular technique to rapidly broaden a small region of a spectrum is to convolve the spectrum by the kernel prescribed in Gray (2005).

Unfortunately this method typically relies on a wavelength grid that is sampled at constant $d\lambda$ and computes the Doppler shifts in wavelength space. This is only valid for a small region of the spectrum, $\Delta v \sim 3000$ km s^{-1}, where the wavelength dependence of the Doppler shift is small and can be ignored.

In order to apply the method to larger wavelength ranges accurately, the spectrum must be separated into many smaller $\Delta v \sim 3000$ km s^{-1} arrays which are each broadened then reassembled into a single broadened spectrum. Even a single echelle order on Keck/HIRES or other similar high-dispersion spectrographs must be separated into at least two segments for accurate convolutional broadening.

In this note we present a simple code which directly integrates the stellar (or planetary) disk, allowing for accurate rotational broadening across a broad wavelength range.

B.2 Broadening by Direct Integration

Rotational broadening by direct integration is relatively simple and the time taken for the broadening depends mainly linearly on the length of the vector being broadened.

We compute the broadening by projecting the spherical stellar surface onto the two-dimensional sky. We first segment the disk into polar coordinates, r and θ, with $r \in [0, 1]$. The radial grid size is given by N_r, with the corresponding spacing $dr = 1/N_r$, and the maximum number of θ steps in the outermost ring is given by N_θ. At each radial point, the number of θ steps $n_\theta(r) = rN_\theta$, rounded to the nearest integer, and $d\theta = (2\pi)/n_\theta$. At each $r,\ \theta$ point, we then define the projected area by

$$dA(r, \theta) = \frac{\pi(r + dr/2)^2 - \pi(r - dr/2)^2}{n_\theta}. \tag{B.1}$$

We also incorporate the a linear limb-darkening law, defined by the parameter ϵ, which ranges from 0 to 1, by rescaling the areas such that

$$\hat{dA} = dA(r, \theta) \times (1 - \epsilon + \epsilon \cos(\arcsin(r))). \tag{B.2}$$

We then compute the projected velocity by $v(r, \theta) = v\ r\ sin(\theta)$. To incorporate differential rotation, we adopt a solar-like differential rotation law by scaling the projected velocity according to:

$$\hat{v} = v(r, \theta) \times \left[1 - \frac{\delta}{2} - \frac{\delta}{2} \cos(2 \arccos(r \cos(\theta)))\right] \tag{B.3}$$

We can then integrate the disk by:

$$\hat{s}(\lambda) = \int_0^1 \int_0^{2\pi} s(\lambda(\hat{v}(r, \theta))) \hat{dA}(r, \theta), \tag{B.4}$$

where $s(\lambda(\hat{v}(r, \theta)))$ is the spectrum interpolated onto the wavelength scale that has been Doppler shifted to the new velocity $\hat{v}$. We then normalize by

$$\hat{A} = \int_0^1 \int_0^{2\pi} \hat{dA}(r, \theta), \tag{B.5}$$

to account for any under or over estimation of the disk area. We provide the code implementation of this method in a static Zenodo repository (Carvalho and Johns-Krull, 2023b). A live version of the code can be found on Github[1].

[1] `https://github.com/Adolfo1519/RotBroadInt`

The accuracy of the method is a function of the resolution used in the disk integration (N_r and N_θ) and the length of the spectrum being broadened. We provide in the code the default N_r, N_θ values for which the broadening is computed accurately but still rapidly in most cases.

We show the result of broadening a $T_{\rm eff}$ = 5500 K PHOENIX (Husser et al., 2013) atmosphere model spectrum using direct integration versus convolution in Figure B.1. We use the convolutional broadening code in the package `PyAstronomy` (Czesla et al., 2019) for this example. For the sake of comparing the accuracy of the methods across broad wavelength ranges, we use the "fast" version of convolution, wherein the spectrum is not subdivided. We do this to demonstrate the inaccurate results it produces for regions of the spectrum far from the central wavelength adopted in the convolution.

For the smaller $\Delta\lambda$ shown in Figure B.1, the convolutional broadening produces an identical result to direct integration. In this case, the $\Delta\lambda$ is small enough to be valid for the kernel approximation and the "fast" convolution is essentially the same as the "slow" convolution. For the larger $\Delta\lambda$, the "fast" convolution is insufficient to accurately reproduce the rotational broadening.

We also compare the computation times for direct integration compared with the more properly done "slow" convolution (subdividing the spectrum into smaller wavelength bins). For a fixed resolution, the computation time of integration scales approximately linearly with the length of the spectrum. This compares quite favorably with the exponential increase in computation time for convolution.

For a high-dispersion spectrum sampled at $d\lambda < 0.1$, a wavelength range of $\Delta\lambda \sim$ 2000 Å has $\sim$ 20000 points. The computation time of the convolutional broadening for an input this long is several minutes. While this may be acceptable for a single demonstration, it makes broadband fitting impossible.

An additional benefit of our implementation of the direct integration is that it does not reply on having an evenly sampled wavelength grid. The convolution method requires that the spectrum being convolved has a constant $\Delta\lambda$ throughout. However, this is not possible if the spectra are sampled at constant Δv. If representing the data at a consistent resolution ($R = \lambda/\Delta\lambda$) across a broadband spectrum is important, the convolution method should not be used.

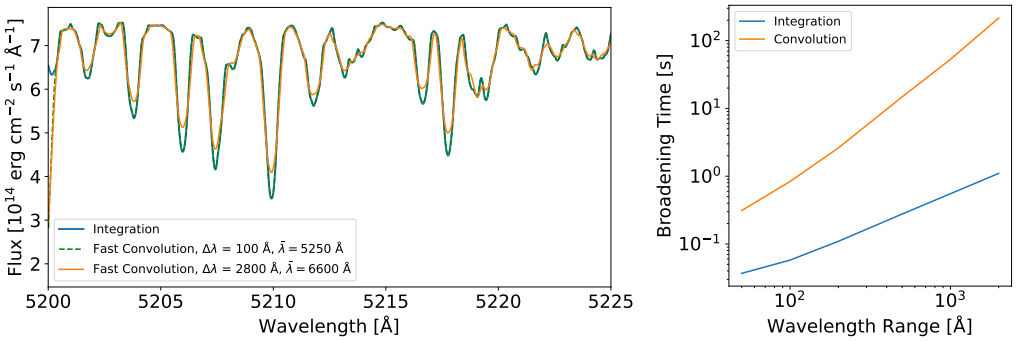

Figure B.1: Results from rotationally broadening spectra using the two methods, direct integration and convolution. **Left:** A 5500 K PHOENIX (Husser et al., 2013) atmosphere model, broadened to 30 km s^{-1} using the two methods and assuming a limb darkening coefficient of 0.6. We show a small piece of spectrum to better distinguish the individual line profiles. The wavelength ranges ($\Delta\lambda$) and mean wavelengths ($\bar{\lambda}$) of each spectrum are given in the legend. Notice the "fast" convolution matches the direct integration almost perfectly when the wavelength range is small and the region of interest is near the center of that range. In that case, the result is the same as using the "slow" method. However, for the larger wavelength range, where we are now far from the mean central wavelength, the broadening accuracy is much worse. The direct integration case is computed on the $\Delta\lambda = 2800$ Å case. **Right:** The times for the two broadening method as a function of the length of the array being broadened. Notice the rapid increase in time for the convolution method compared to integration. The spectra shown are sampled at $d\lambda \sim 0.01$, so $\Delta\lambda = 1000$ is a 10^5 element array. The grid used for the integration has $N_r = 10$ and $N_\theta = 100$, the default values for our function.

B.3 Conclusion

We encourage the use of our public, open-source rotational broadening code for anyone doing broadband high-dispersion spectroscopy. The method is simple but powerful and effective.